Editors:
M. RAHMAN, C.A. BREBBIA

Advances in Fluid Mechanics VII

WIT PRESS

Advances in Fluid Mechanics VII

WIT PRESS

WIT Press publishes leading books in Science and Technology.
Visit our website for the current list of titles.
www.witpress.com

WIT eLibrary

Home of the Transactions of the Wessex Institute.
Papers presented at Advances in Fluid Mechanics VII are archived
in the WIT eLibrary in volume 59 of WIT Transactions on
Engineering Sciences (ISSN 1743-3533). The WIT eLibrary provides the international
scientific community with immediate and permanent access to individual papers presented
at WIT conferences.
http://library.witpress.com.

SEVENTH INTERNATIONAL CONFERENCE ON
ADVANCES IN FLUID MECHANICS

Advances in Fluid Mechanics VII

CONFERENCE CHAIRMEN

M. Rahman
Dalhousie University, Canada

C.A. Brebbia
Wessex Institute of Technology, UK

INTERNATIONAL SCIENTIFIC ADVISORY COMMITTEE

R. Bourisli
A. Chakrabarti
G. Comini
M. Davidson
L. Debnath
J.P. Du Plessis
R.H.J. Grimshaw
W. Harris
T.B. Moodie
V. Popov
M. Rahman
L. Skerget
G. Swaters
R. Verhoeven

ORGANISED BY
The Wessex Institute of Technology, UK
Dalhousie University, Canada

SPONSORED BY
WIT Transactions on Engineering Sciences

WIT Transactions

Transactions Editor

Carlos Brebbia
Wessex Institute of Technology
Ashurst Lodge, Ashurst
Southampton SO40 7AA, UK
Email: carlos@wessex.ac.uk

Editorial Board

Advances in Fluid Mechanics VII

Editors

M. Rahman
Dalhousie University, Canada

C.A. Brebbia
Wessex Institute of Technology, UK

WIT*PRESS* **Southampton, Boston**

Editors:

M. Rahman
Dalhousie University, Canada

C.A. Brebbia
Wessex Institute of Technology, UK

Published by

WIT Press
Ashurst Lodge, Ashurst, Southampton, SO40 7AA, UK
Tel: 44 (0) 238 029 3223; Fax: 44 (0) 238 029 2853
E-Mail: witpress@witpress.com
http://www.witpress.com

For USA, Canada and Mexico

WIT Press
25 Bridge Street, Billerica, MA 01821, USA
Tel: 978 667 5841; Fax: 978 667 7582
E-Mail: infousa@witpress.com
http://www.witpress.com

British Library Cataloguing-in-Publication Data

A Catalogue record for this book is available
from the British Library.

ISBN: 978-1-84564-109-2
ISSN: (print) 1746-4471
ISSN: (on-line) 1743-3533

The texts of the papers in this volume were set individually by the authors or under their supervision. Only minor corrections to the text may have been carried out by the publisher.

Printed in Great Britain by Cambridge Printing

Preface

This book covers a wide range of papers in the areas of fluid mechanics presented at the Seventh International Conference on Advances in Fluid Mechanics held at The New Forest, UK on 21-23 May 2008. The conference was organised by the Wessex Institute of Technology, UK and Dalhousie University, Canada, and was sponsored by the WIT Transactions on Engineering Sciences.

The conference emphasizes the advancement of knowledge in fluid mechanics problems and new applications. The basic mathematical formulations and their solutions by analytical and numerical methods are discussed together with the experimental work.

The conference has been reconvened every two years since 1996 and was motivated by previous Meetings and well-established book series, *Advances in Fluid Mechanics,* also published by WIT Press. The series has so far produced over 55 volumes. The Scientific Advisory Committee of the conference comprises the experienced scientists who are members of the Editorial Board of the book series.

The conference was first held in New Orleans, USA(1996), followed by Udine, Italy(1998), Montreal, Canada (2000), Ghent, Belgium (2002), Lisbon, Portugal (2004), and Skiathos, Greece (2006). Many world renowned scientists, engineers, applied mathematicians and professionals presented their research findings in those conferences.

This book comprises the following sections: Computational Methods in Fluid Mechanics; Environmental Fluid Mechanics; Experimental versus Simulation Methods; Multiphase Flow; Hydraulics and Hydrodynamics; Heat and Mass Transfer; Industrial Applications; Wave Studies.

The editors are very grateful to the contributors as well as the Board Members for their enthusiastic support and participation in the Meeting. We are also thankful to the staff of the WIT Press for their excellent job in producing this beautiful book.

The Editors
The New Forest, 2008

This page intentionally left blank

Contents

Section 1: Computational methods in fluid mechanics

Section 2: Environmental fluid mechanics

Section 3: Experimental versus simulation methods

Section 4: Multiphase flow

Section 5: Hydraulics and hydrodynamics

Section 6: Heat and mass transfer

Section 7: Industrial applications

Section 8: Wave studies

This page intentionally left blank

Section 1
Computational methods in fluid mechanics

This page intentionally left blank

Ice accretion simulation on finite wings with extended Messinger Method

S. Özgen[1] & M. Canibek[2]
[1]*Department of Aerospace Engineering,*
Middle East Technical University, 06531, Ankara, Turkey
[2]*Flight Sciences Department, Turkish Aerospace Industries,*
Middle East Technical University Technopolis, 06531, Ankara, Turkey

Abstract

Numerical icing simulations on finite wings are performed using a quasi-3D approach. The solution method consists of computations of the flowfield using the Hess-Smith panel method, droplet trajectories, droplet collection efficiencies, convective heat transfer coefficients and finally ice accretion rates and ice shapes. Inputs to the problem are the ambient temperature T_a, freestream velocity V_∞, liquid water content of air ρ_a, droplet diameter d_p, total icing time t_{exp}, angle of attack α and the wing geometry. Droplet trajectories are calculated by integrating the differential equations of motion for the droplets over time. Droplet impact locations and collection efficiencies are thus determined. Convective heat transfer coefficients are calculated using empirical relations and the solutions of the 2-D integral boundary layer equations. Extended Messinger Method is employed for the prediction of the ice accretion rates. At low temperatures and liquid water contents rime ice occurs and the ice thickness is obtained using an algebraic equation. At higher temperatures and liquid water contents, glaze ice forms for which the energy and mass conservation equations are combined to yield a first order ordinary differential equation, solved numerically. In this case, a thin layer of water is present over a layer of ice and effects of runback water are accounted for. A computer code is developed using the outlined theory, which is validated with experimental ice shapes reported in the literature. Ice shapes are obtained for a wing having taper, twist, dihedral and sweep.
Keywords: ice accretion simulation, Messinger Method, droplet collection efficiency, rime ice, glaze ice.

WIT Transactions on Engineering Sciences, Vol 59, © 2008 WIT Press
www.witpress.com, ISSN 1743-3533 (on-line)
doi:10.2495/AFM080011

1 Introduction

Ice accumulation on parts of the airframe during flight is one of the fundamental problems of aviation. Ice growth on wings, tail surfaces, fuselage, etc. result in severe performance degradation. For example, modification of the wing shape due to ice accumulation results in lift reduction together with increases in drag and weight. Ice formation on control surfaces and stabilizers results in serious and unpredictable degradations in the control characteristics of airplanes. Therefore, it is important to be able to simulate the effects of icing on performance and flight characteristics.

Messinger's study [1] is an important milestone in numerical ice accretion simulation. Increases in capacities and speeds of digital computers in the 1970s allowed theoretical and numerical researchers to analyze realistic geometries such as airfoils, wings and helicopter rotor blades.

In a review paper, Gent *et al*. [2] present the background and the status of analysis developed to address the problem of icing on aircraft. Methods for water droplet trajectory calculation, ice accretion prediction and aerodynamic performance degradation are discussed.

Myers [3] presents a one-dimensional mathematical model describing ice growth, which is an extension of the original Messinger model. It is shown that the model can also be extended to two and three-dimensions and it is the two-dimensional extension that is employed in the current study.

Potapczuk and Bidwell [4] report an effort to develop a three-dimensional ice accretion modeling. Three-dimensional flowfield methods and particle trajectories are combined with two-dimensional ice accretion calculations.

Mingione *et al*. [5] discuss a three-dimensional ice accretion code. Ice accretion on the NASA MS-317 30° swept wing and on the Agusta A109 air intake protection grid are evaluated.

In this article, Section 2 summarizes the approaches used for problem formulation and the solution method. Methods used for computing the flowfield, droplet trajectories, collection efficiencies and convective heat transfer coefficients are explained. Extended Messinger Method is outlined in the same Section. Section 3 is devoted to code validation and presentation of the results. Finally, Section 4 summarizes the study and makes recommendations for future work.

2 Problem formulation and solution method

2.1 Flowfield solution

In order to determine the pressure distribution around the wing and provide the air velocities required for droplet trajectory calculations, 3-D Hess-Smith panel method is employed [6]. The pressure distribution around the wing is also used for boundary-layer calculations in order to determine the convective heat transfer coefficients.

2.2 Droplet trajectories and collection efficiencies

The following assumptions are made for the formulation of the 3-D equations of motion for the water droplets:

- Droplet sizes are small, hence remain spherical,
- The flowfield is not affected by the presence of the droplets,
- Gravity and aerodynamic drag are the only forces involved.

These assumptions are valid for $d_p \leq 500\ \mu m$. The governing equations are:

$$m\ddot{x}_p = -Dcos\gamma_1, \tag{1}$$

$$m\ddot{y}_p = -Dcos\gamma_2, \tag{2}$$

$$m\ddot{z}_p = -(Dcos\gamma_3 + mg), \tag{3}$$

where

$$\gamma_1 = \tan^{-1}\frac{\dot{x_p} - V_x}{V_{rel}}, \quad \gamma_2 = \tan^{-1}\frac{\dot{y_p} - V_y}{V_{rel}}, \quad \gamma_3 = \tan^{-1}\frac{\dot{z_p} - V_z}{V_{rel}}, \tag{4}$$

$$V_{rel} = \sqrt{(\dot{x_p} - V_x)^2 + (\dot{y_p} - V_y)^2 + (\dot{z_p} - V_z)^2}, \tag{5}$$

$$D = 1/2\rho V_{rel}^2 C_D A_p. \tag{6}$$

V_x, V_y and V_z are the flowfield velocity components at the droplet location obtained from the flowfield solution, while $\dot{x_p}$, $\dot{y_p}$, $\dot{z_p}$, $\ddot{x_p}$, $\ddot{y_p}$ and $\ddot{z_p}$ are the components of the droplet velocity and acceleration. A_p is the droplet cross-sectional area. The drag coefficients of the droplets are calculated using the following drag law [2]:

$$\begin{aligned} C_D &= 1 + 0.197Re^{0.63} + 2.6 \times 10^{-4}Re^{-1.34}, \quad Re \leq 3500, \\ C_D &= (1.699 \times 10^{-5})Re^{1.92}, \qquad\qquad\qquad\quad Re > 3500, \end{aligned} \tag{7}$$

where $Re = \rho V_{rel} d_p/\mu$ is the Reynolds number based on droplet diameter d_p and relative velocity V_{rel}. The droplet impact pattern on the wing determines the amount of water that impinges on the surface and the region subject to icing. The local collection efficiency is defined as the ratio, of the area of impingement to the area through which water passes at some distance upstream of the wing. The three-dimensional collection efficiency can be defined as $\beta = A_o/A$, where A_o is the area constituted by four droplets in the release plane, while A is the area of impingement constituted by the same four droplets neighboring a control point. Figure 1 shows the computed particle trajectories and how the collection efficiency is calculated.

2.3 Convective heat transfer coefficients

After flowfield and droplet trajectory calculations, the wing is divided into spanwise strips. Boundary-layer and icing calculations are performed for each of these

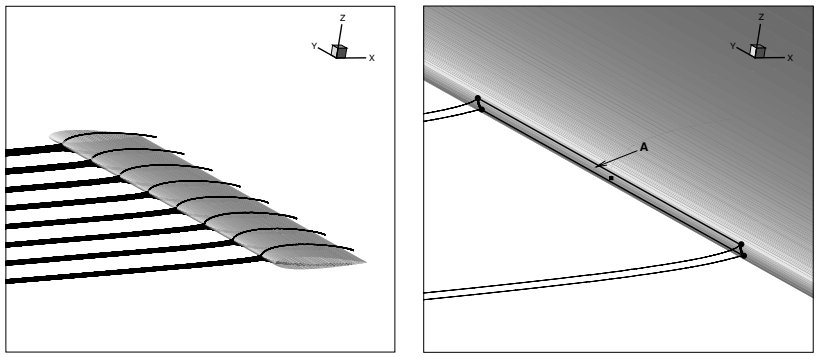

(a) (b)

Figure 1: Particle trajectories and collection efficiency calculation.

strips using 2-D approaches. The current study employs a 2-D Integral Boundary Layer Method for the calculation of the convective heat transfer coefficients. With this method, the laminar and turbulent boundary layer properties are calculated fairly accurately provided that the crossflow velocity component due to 3-D effects is not too high compared to the streamwise component. Transition prediction is based on the roughness Reynolds number, $Re_k = \rho U_e k_s/\mu$, where k_s is the roughness height and U_e is the velocity of the external flow at the roughness location. For laminar flow ($Re_k < 600$), formulation of Smith and Spalding is used to calculate the convective heat transfer coefficient [2]:

$$h_c = \frac{0.296 k U_e^{1.435}}{\sqrt{\nu \int_0^s U_e^{1.87} ds}}, \tag{8}$$

where, k is the thermal conductivity of air obtained by assuming constant Prandtl number and viscosity obtained from Sutherland's law as a function of ambient temperature. Streamwise distance along the wing strip starting at the stagnation point is denoted by$s$. For turbulent flow ($Re_k \geq 600$), the method of Kays and Crawford is employed [2]. Accordingly, the turbulent momentum thickness is given by:

$$\theta = \frac{0.036 \nu^{0.2}}{U_e^{3.29}} \left(\int_{s_{tr}}^{s} U_e^{3.86} ds \right)^{0.8} + \theta_{tr}, \tag{9}$$

where θ_{tr} is the laminar momentum thickness at transition location. Skin friction coefficient is found from the Makkonen relation [2]:

$$\frac{C_f}{2} = \frac{0.1681}{[\ln(864\theta/k_s + 2.568)]^2}. \tag{10}$$

The Stanton number can be calculated from [2]:

$$St = \frac{C_f/2}{Pr_t + \sqrt{(C_f/2)/St_k}}. \tag{11}$$

The roughness Stanton number is calculated from [2]:

$$St_k = 1.92 Re_k^{-0.45} Pr^{-0.8}. \tag{12}$$

Finally, turbulent convective heat transfer coefficient is found from [2]:

$$h_c = St \rho U_e C_{pa}. \tag{13}$$

The roughness height is calculated from $k_s = 0.00117 K_{V_\infty} K_{LWC} K_{T_a} K_{d_p} \bar{c}$, where K_{V_∞}, K_{LWC}, K_{T_a} and K_{d_p} are empirical factors accounting for freestream velocity, liquid water content, ambient temperature and droplet size effects [7]. The mean aerodynamic chord of the wing is denoted by $\bar{c}$.

2.4 Extended Messinger method

Icing prediction is based on phase change or the Stefan problem. The Stefan problem is governed by four equations: heat equations in the ice and water, a mass balance and a phase change condition at the ice/water interface [3]:

$$\frac{\partial T}{\partial t} = \frac{k_i}{\rho_i C_{pi}} \frac{\partial^2 T}{\partial y^2}, \tag{14}$$

$$\frac{\partial \theta}{\partial t} = \frac{k_w}{\rho_w C_{pw}} \frac{\partial^2 \theta}{\partial y^2}, \tag{15}$$

$$\rho_i \frac{\partial B}{\partial t} + \rho_w \frac{\partial h}{\partial t} = \rho_a \beta V_\infty + \dot{m}_{in} - \dot{m}_{e,s}, \tag{16}$$

$$\rho_i L_F \frac{\partial B}{\partial t} = k_i \frac{\partial T}{\partial y} - k_w \frac{\partial \theta}{\partial y}, \tag{17}$$

where θ and T are the temperatures, k_w and k_i are the thermal conductivities, C_{pw} and C_{pi} are the specific heats and h and B are the thicknesses of water and ice layers, respectively. In equation (16), $\dot{m}_{in}$ and $\dot{m}_{e,s}$ are runback and evaporating (or sublimating) water mass flow rates, respectively. On the other hand, ρ_i and L_F denote the density of ice and the latent heat of solidification of water, respectively. Ice density is assumed to have different values for rime ice, ρ_r and glaze ice, ρ_g. The coordinate y is normal to the surface. In order to determine the ice and water thicknesses together with the temperature distribution at each layer, boundary and initial conditions must be specified. These are based on the following assumptions:

- Ice is in perfect contact with the wing surface (surface temperature is assumed to be equal to the ambient temperature, $T_s = T_a$):

$$T(0, t) = T_s. \tag{18}$$

- The temperature is continuous at the ice/water boundary and is equal to the freezing temperature, T_f:

$$T(B,t) = \theta(B,t) = T_f. \tag{19}$$

- At the air/water (glaze ice, $y = B+h$) or air/ice (rime ice, $y = B$) interface, heat flux is determined by convection $Q_c = h_c(T_s - T_a)$, heat from incoming droplets $Q_d = \rho_a \beta V_\infty C_{pw}(T_s - T_a)$, heat brought in by runback water $Q_{in} = \dot{m}_{in} C_{pw}(T_f - T_s)$, evaporation $Q_e = \chi_e e_o (T_s - T_a)$ or sublimation $Q_s = \chi_s e_o (T_s - T_a)$, aerodynamic heating $Q_a = r h_c {V_\infty}^2/2C_{pa}$, kinetic energy of incoming droplets $Q_k = \rho_a \beta {V_\infty}^3/2$, and latent heat release $Q_l = \rho_r L_F \partial B/\partial t$:

$$\begin{aligned} \text{Glaze ice} &: -k_w \frac{\partial \theta}{\partial y} = (Q_c + Q_e + Q_d) - (Q_a + Q_k + Q_{in}), \\ \text{Rime ice} &: -k_i \frac{\partial T}{\partial y} = (Q_c + Q_s + Q_d) - (Q_a + Q_k + Q_{in} + Q_l). \end{aligned} \tag{20}$$

  Evaporation and sublimation coefficients are expressed as:

$$\chi_e = \frac{0.622 h_c L_E}{C_{pa} P_t Le^{2/3}}, \quad \chi_s = \frac{0.622 h_c L_S}{C_{pa} P_t Le^{2/3}}, \tag{21}$$

  and P_t is the total pressure of the freestream flow.
- The wing surface is initially clean:

$$B = h = 0, \quad t = 0. \tag{22}$$

2.4.1 Rime ice growth and temperature profile

Rime ice thickness follows from the mass balance in equation (16), since water droplets freeze entirely on impact:

$$B(t) = \frac{\rho_a \beta V_\infty + \dot{m}_{in} - \dot{m}_s}{\rho_r} t. \tag{23}$$

2.4.2 Glaze ice growth

Glaze ice thickness is obtained by time-integration of the ordinary differential equation obtained by combining mass and energy equations:

$$\rho_g L_f \frac{\partial B}{\partial t} = \frac{k_i (T_f - T_s)}{B} + k_w \frac{(Q_c + Q_e + Q_d) - (Q_a + Q_k)}{k_w + h(Q_c + Q_e + Q_d)/(T_s - T_a)} - Q_{in}. \tag{24}$$

It is assumed that, all unfrozen water runs back to the neighboring downstream cell for the upper surface, while all water sheds for the lower surface [8]. To calculate the glaze ice thickness, equation (24) is integrated numerically, using a Runge–Kutta–Fehlberg method. Water layer thickness for glaze ice conditions is found

Table 1: Parameter values used in the calculations.

Symbol	Definition	Value
C_{pa}	Specific heat of air	1006 J/kg.K
C_{pi}	Specific heat of ice	2050 J/kg.K
C_{pw}	Specific heat of water	4218 J/kg.K
e_o	Saturation vapor pressure constant	27.03
g	Gravitational acceleration	9.81 m/s^2
k_i	Thermal conductivity of ice	2.18 W/m.K
k_w	Thermal conductivity of water	0.571 W/m.K
Le	Lewis number	$1/Pr$
L_F	Latent heat of solidification	3.344×10^5 J/kg
L_E	Latent heat of evaporation	2.5×10^6 J/kg
L_S	Latent heat of sublimation	2.8344×10^6 J/kg
Pr	Laminar Prandtl number of air	0.72
Pr_t	Turbulent number of air	0.9
r	Adiabatic recovery factor	1/2: laminar flow 1/3: turbulent flow
μ_w	Viscosity of water	1.795×10^{-3} Pa.s
ρ_r	Density of rime ice	880 kg/m^3
ρ_g	Density of glaze ice	917 kg/m^3
ρ_w	Density of water	999 kg/m^3

from the following expression:

$$h = \frac{(\rho_a \beta V_\infty + \dot{m}_{in} - \dot{m}_e)}{\rho_w}(t - t_g) - \frac{\rho_g}{\rho_w}(B - B_g). \tag{25}$$

where B_g is the rime ice thickness at which glaze ice first forms, and t_g is the corresponding time given as:

$$B_g = \frac{k_i(T_f - T_s)}{(\rho_a \beta V_\infty + \dot{m}_{in} - \dot{m}_s)L_F + (Q_a + Q_k + Q_{in}) - (Q_c + Q_e + Q_d)}, \tag{26}$$

$$t_g = \frac{\rho_r}{(\rho_a \beta V_\infty + \dot{m}_{in} - \dot{m}_s)} B_g. \tag{27}$$

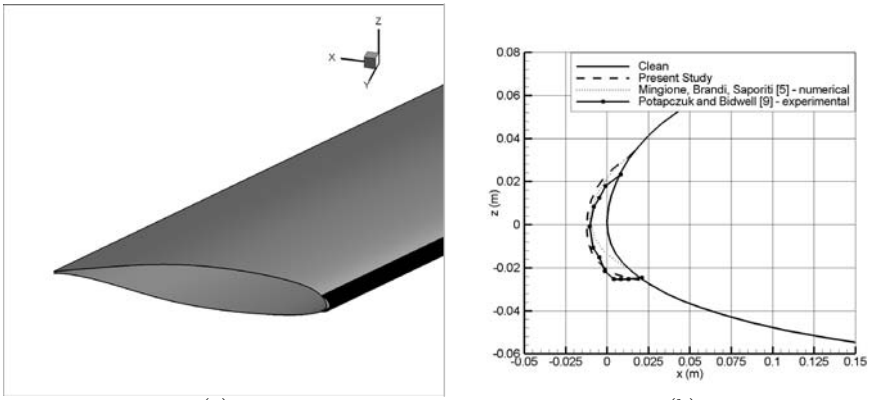

(a) (b)

Figure 2: Ice shapes on a 30° swept wing having NASA MS-317 section.

Table 2: Icing conditions for the cases presented in Figures 2 and 3.

Variable	**Value (Figure 2)**	**Value (Figure 3)**
Angle of attack, α	0°	4°
Freestream velocity, V_∞	74 m/s	129 m/s
Wingroot chord length, c_r	0.9 m	1 m
Wing span, b	7.3 m	8 m
Taper ratio, λ	1	0.5
Leading edge sweep, Λ_{le}	30°	10°
Dihedral angle, Γ	0°	4°
Geometric twist, θ	0°	4°
Ambient temperature, T_a	$-18.1°C$	$-12.6°C$
Exposure time, t_{exp}	390 s	120 s
Droplet size, d_p	20 μm	20 μm
Liquid water content, ρ_a	1 g/m^3	1 g/m^3

3 Validation of the method, results and discussion

Figure 2 shows the ice shapes and comparisons with numerical and experimental data in the literature for a 30° swept NASA MS-317 wing. Icing and geometrical conditions for this case are given in the second column of Table 2. As can be seen, a typical rime ice shape is obtained and it is in very good agreement with the experimental and the numerical ice shapes reported in the literature. Also, the extent of the iced region is well predicted.

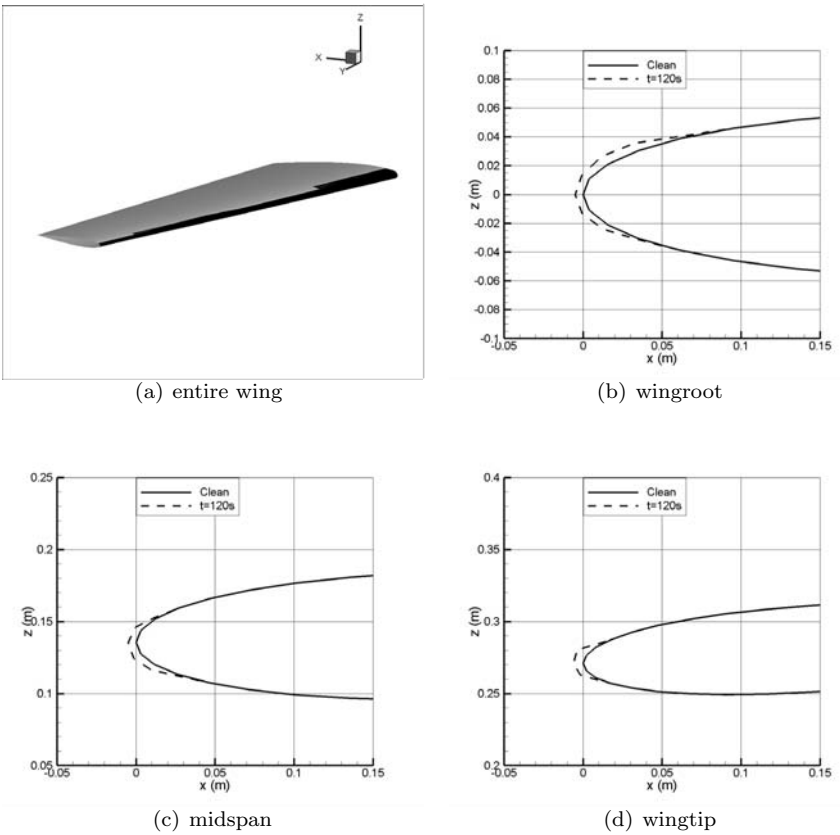

(a) entire wing (b) wingroot

(c) midspan (d) wingtip

Figure 3: Ice shapes on a 10° swept wing having NACA 0012 section.

Figure 3 shows the results for a wing with taper, twist, dihedral and sweep having NACA 0012 section. This wing is representative of wings that one would see on real airplanes. Icing and geometrical conditions for this case are given in the third column of Table 2. As expected, there is a spanwise variation of both the ice thickness and the iced region. At the wingroot, the ice is thin but extends through a wide portion of the leading edge. On the other hand, at the wingtip, the ice is thicker but is confined to a narrower region of the leading edge. These inferences are in qualitative agreement with the results reported by Özgen *et al*. [9]. As reported in [9] smaller wing sections yield higher collection efficiencies, hence leading to thicker and more severe icing. The ice shape in Figure 3b suggests that there is glaze ice formation, at least on some parts of the wing.

4 Conclusions and recommendations for future work

Ice accretion predictions on finite wings have been performed using a quasi-3D approach. Results indicate that the strip approach is capable of predicting ice

shapes with success, although the boundary-layer and thermodynamical models used are 2-D. The tool can be used for preliminary design purposes for the selection of a de/anti-icing system or for certification.

The current tool can be developed to a full 3-D code by implementing a 3-D boundary-layer solver and a thermodynamical model. This will be at the expense of computational complexity and increased run time. Then, the user has to decide what to use such a tool for and trades between simplicity, good accuracy versus complexity, improved accuracy need to be considered. However, if more complex geometries like intakes or highly swept wings are to be studied, then these improvements are almost imperative. As a further improvement, a more sophisticated liquid water model can be introduced, like those described by Fortin *et al*. [8] and Myers *et al*. [10].

References

[1] Messinger, B., Equilibrium temperature of an unheated icing surface as a function of airspeed. *Journal of Aeronautical Sciences*, **January 1953**, pp. 29–42, 1953.
[2] Gent, R., Dart, N. & Cansdale, J., Aircraft icing. *Phil Trans R Soc Lond A*, **358**, pp. 2873–2911, 2000.
[3] Myers, T., Extension to the Messinger model for aircraft icing. *AIAA J*, **39**, pp. 211–218, 2001.
[4] Potapczuk, M. & Bidwell, C., Swept wing ice accretion modeling. Technical report, NASA TM–103114, 1990.
[5] Mingione, G., Brandi, V. & Saporiti, A., A 3d ice accretion simulation code. AIAA Paper 99-0247, 1999.
[6] Katz, J. & Plotkin, *Low-Speed Aerodynamics*. Springer-Verlag: Berlin and New York, pp. 11–13, 1984.
[7] Wright, W., Genat, R. & Guffond, D., Dra/nasa/onera collaboration on icing research part ii, prediction of airfoil ice accretion. Technical report, NASA CR–202349, 1997.
[8] G. Fortin, J.L.L. & Ilinca, A., Heat and mass transfer during ice accretion on aircraft wings with an improved roughness model. *Int J Thermal Sciences*, **45**, pp. 595–606, 2006.
[9] Özgen, S., Ortakaya, Y. & Korkem, B., Ice accretion simulation on multi-element airfoils. *Proc. of the 2nd European Conf. for Aerospace Sciences*, Brussels, 2007.
[10] Myers, T., Charpin, J. & Thompson, C., Slowly accreting ice due to supercooled water impacting on a cold surface. *Physics of Fluids*, **14**, pp. 240–256, 2002.

Influence of linear and non-linear constitutive models on thermoacoustic waves in an enclosure

L. Škerget & J. Ravnik
University of Maribor, Faculty of Mechanical Engineering, Smetanova ulica 17, SI-2000 Maribor, Slovenia

Abstract

The problem of unsteady compressible fluid flow in an enclosure induced by thermoacoustic waves is studied numerically. Full compressible set of Navier-Stokes equations are considered and numerically solved by boundary-domain integral equations approach, coupled with wavelet compression and domain decomposition to achieve numerical efficiency. The thermal energy equation is written in its most general form including the Rayleigh and reversible expansion rate terms. Both the classical Fourier heat flux model and wave heat conduction model are investigated. The momentum flux is modelled using standard Newtonian viscous model and linear viscoelastic Maxwell model.

The velocity-vorticity formulation of the governing Navier-Stokes equations is employed, while the pressure field is evaluated from the corresponding pressure Poisson equation. Material properties are taken to be for the perfect gas and assumed to be pressure and temperature dependent.
Keywords: compressible fluid flow, velocity-vorticity formulation, Navier-Stokes equations, thermoacoustic waves.

1 Introduction

In the paper the generation and transmission of thermoacoustic waves in an perfect gas filled closed cavity is studied numerically. When a compressible fluid is subjected to a rapid increase in temperature at a solid wall, a sudden expansion of the adjacent gas occurs. This phenomenon generates a fast increase in the local pressure and leads to the production of pressure waves. These thermally generated waves are referred to as thermoacoustic waves.

Thermoacoustic transport phenomena may be very interesting, when the fluid is close to thermodynamic critical point or when other modes of transport mechanism

WIT Transactions on Engineering Sciences, Vol 59, © 2008 WIT Press
www.witpress.com, ISSN 1743-3533 (on-line)
doi:10.2495/AFM080021

are weak or absent. Thermoacoustic waves enhance heat transport by converting the thermal energy into compression work and by inducing convection motion away from the heated wall. This mode of heat transfer is dominant in the space environment under zero- or reduced-gravity conditions, where natural convection of heat transport may be absent or low, and when heat conduction is the only mode of heat transport mechanism.

The problem of thermoacoustic transport phenomena in a perfect gas confined in an enclosure subjected to a sudden increase in temperature at a solid wall, have been considered experimentally and numerically by Huang and Bau [1] as well as by Brown and Churchill [2]. In the literature one can find analytical attempts to study the phenomenon limited mainly to simplified models, while the solutions to general cases have been performed by numerical approximative methods. In the present paper the boundary element method (BEM) is used. Previous studies of Lin and Farouk [3], Aktas and Farouk [4], Škerget and Ravnik [5], observed strong thermoacoustic waves as a consequence of impulsive heating. Horizontal velocity component reverses sign after reflection from the side walls. The flow field is essentially one-dimensional.

2 Governing equations for the primitive variables formulation

The field functions of interest are velocity vector field v_i, scalar pressure field p, temperature field T and the field of mass density ρ, so that the mass, momentum and energy equations are given by the following set of nonlinear equations:

$$\frac{\partial v_j}{\partial x_j} = \mathcal{D} = -\frac{1}{\rho}\frac{D\rho}{Dt}, \tag{1}$$

$$\rho\frac{Dv_i}{Dt} = -e_{ijk}\frac{\partial \eta\omega_k}{\partial x_j} + 2e_{ijk}\frac{\partial \eta}{\partial x_j}\omega_k + 2\frac{\partial \eta}{\partial x_j}\frac{\partial v_i}{\partial x_j} + \frac{4}{3}\frac{\partial \eta\mathcal{D}}{\partial x_i} - 2\mathcal{D}\frac{\partial \eta}{\partial x_i} - \frac{\partial p}{\partial x_i} + \rho g_i, \tag{2}$$

$$c\frac{DT}{Dt} = \frac{\partial}{\partial x_j}\left(k\frac{\partial T}{\partial x_j} + \lambda\frac{\partial q_j}{\partial t}\right) + \beta T\frac{Dp}{Dt} + \Phi, \tag{3}$$

in the Cartesian frame x_i, where c denotes changeable isobaric specific heat capacity per unit volume, $c = c_p\rho$, t is time, g_i is gravitational acceleration vector, while β is a volume coefficient of thermal expansion, λ is a heat relaxation time and Φ is the Rayleigh viscous dissipation function. Because of the analytical reasons required by the derivation of the velocity-vorticity formulation of the governing equations, the momentum equation is given in the second extended form.

The Newton momentum viscous and Maxwell viscoelastic constitutive models are considered, such as

$$\tau_{ij} = \tau_{ij}^{v} + \tau_{ij}^{e} = 2\eta\dot{\varepsilon}_{ij} - \frac{2}{3}\eta\mathcal{D}\delta_{ij} - \lambda_1\frac{\partial \tau_{ij}}{\partial t}, \tag{4}$$

where the extra stress tenzor or the momentum flux tenzor is given as a sum of viscous τ_{ij}^{v} and elastic τ_{ij}^{e} effects. $\mathcal{D} = div\vec{v} = \dot{\varepsilon}_{ii}$ represents the divergence of the velocity field or local expansion field. The parameter λ_1 is the stress relaxation time. The Rayleigh dissipation function may be stated as

$$\Phi = \tau_{ij}\frac{\partial v_i}{\partial x_j} = \eta\left(\frac{\partial v_i}{\partial x_j}\frac{\partial v_i}{\partial x_j} + \frac{\partial v_j}{\partial x_i}\frac{\partial v_j}{\partial x_i}\right) - \frac{2}{3}\eta\mathcal{D}^2. \tag{5}$$

In the case of intensive unsteady heat transfer, it is important to take into account a terminal velocity of a moving temperature frontier, namely the following form of heat flux constitutive model

$$q_i = -k\frac{\partial T}{\partial x_i} - \lambda\frac{\partial q_i}{\partial t}, \tag{6}$$

where material constants k and λ are the heat conductivity and the heat relaxation time. For most heat transfer problems of practical importance, the simplification known as the Fourier law of heat diffusion is accurate enough, namely $q_i = -k\frac{\partial T}{\partial x_i}$.

Representing the material properties of the fluid the dynamic viscosity η, heat conductivity k, the specific heat per unit volume c, and the mass density ρ, are written as sums of a constant and variable part, e.g. $\eta = \eta_o + \widetilde{\eta}$, $k = k_o + \widetilde{k}$, $c = c_o + \widetilde{c}$, and $\rho = \rho_o + \widetilde{\rho}$, so the momentum and energy eqs. (2) and (3) may be written in analogy to the basic conservation equations formulated for the constant material properties

$$\frac{D\vec{v}}{Dt} = -\nu_o\vec{\nabla}\times\vec{\omega} - \frac{1}{\rho_o}\vec{\nabla}p + \frac{\rho}{\rho_o}\vec{g} + \frac{1}{\rho_o}\vec{f}^{m} + \frac{1}{\rho_o}\vec{\nabla}\cdot\underline{\tau}^{e}, \tag{7}$$

$$\frac{DT}{Dt} = a_o\triangle T + \frac{S^m}{c_o}, \tag{8}$$

where the pseudo body force term $\vec{f}^{m}$ and pseudo heat source term S^m are introduced into the momentum eq. (7) and into energy eq. (8) respectively, capturing the variable material property effects, and the nonlinear effects due to rate of reversible and irreversible work, and given by expressions, e.g. for plane flow problems

$$f_i^m = -e_{ij}\frac{\partial\widetilde{\eta}\omega}{\partial x_j} + 2e_{ij}\frac{\partial\widetilde{\eta}}{\partial x_j}\omega + 2\frac{\partial\eta}{\partial x_j}\frac{\partial v_i}{\partial x_j} + \frac{4}{3}\frac{\partial\eta\mathcal{D}}{\partial x_i} - 2\mathcal{D}\frac{\partial\eta}{\partial x_i} - \widetilde{\rho}a_i, \tag{9}$$

while the pseudo heat source term is given by an expression

$$S^m = \vec{\nabla}\left(\widetilde{k}\vec{\nabla}T + \lambda\frac{\partial\vec{q}}{\partial t}\right) - \widetilde{c}\frac{DT}{Dt} + \beta T\frac{Dp}{Dt} + \Phi, \tag{10}$$

in which the kinematic viscosity is $\nu_o = \eta_o/\rho_o$, the heat diffusivity $a_o = k_o/c_o$ and the inertia acceleration vector is $\vec{a} = D\vec{v}/Dt$.

3 Governing equations for the velocity-vorticity formulation

The kinematics of the flow motion is governed by the following vector elliptic Poisson equation for the velocity vector

$$\nabla^2 \vec{v} + \vec{\nabla} \times \vec{\omega} - \vec{\nabla}\mathcal{D} = 0. \tag{11}$$

The kinetics of the flow representing the vorticity transport equation is obtained by applying the curl differential operator to the both sides of eq. (7), rendering the following statement for the two-dimensional plane flow written in Cartesian tensor notation form as

$$\frac{\partial \omega}{\partial t} + \frac{\partial v_j \omega}{\partial x_j} = \nu_o \frac{\partial^2 \omega}{\partial x_j \partial x_j} - \frac{1}{\rho_o} e_{ij} \frac{\partial \rho g_i}{\partial x_j} - \frac{1}{\rho_o} e_{ij} \frac{\partial f_i^m}{\partial x_j} - \frac{1}{\rho_o} e_{ij} \frac{\partial}{\partial x_j} \left(\frac{\partial \tau_{ik}^e}{\partial x_k} \right). \tag{12}$$

To derive the pressure equation, depending on known velocity field, vorticity field and material functions, the divergence of momentum equation should be calculated, resulting in the elliptic Poisson pressure equation

$$\triangle p - \vec{\nabla} \cdot \vec{f}_p = 0, \tag{13}$$

where the pressure force term $\vec{f}_p$ is for the planar flow cases

$$\frac{\partial p}{\partial x_i} = f_{pi} = -\eta_o e_{ij} \frac{\partial \omega}{\partial x_j} - \rho_o a_i + \rho g_i + f_i^m + \vec{\nabla} \cdot \underline{\tau}^e. \tag{14}$$

The Neumann boundary conditions for pressure equation may be determined for the whole solution domain and the following relation is valid

$$\frac{\partial p}{\partial n} = \vec{f}_p \cdot \vec{n} \quad on \quad \Gamma. \tag{15}$$

Due to the variable material property terms, and rate of reversible and irreversible work acting as additional temperature, pressure and velocity field dependent source terms, the vorticity, thermal energy, and pressure equations are coupled, making the numerical solution procedure of this highly nonlinear coupled set of equations very severe. Already, the vorticity transport equation as itself is highly nonlinear partial differential equation due to the inherent nonlinearity caused by the compatibility and restriction conditions among velocity, vorticity and dilatation fields. The dilatation and the vortical part of the flow, $\mathcal{D}$ and $\vec{\omega}$ field functions respectively, and all other nonlinear terms have to be under-relaxed to achieve the convergence of the numerical solution procedure.

4 Numerical algorithm

The nonlinear system of partial differential equation described in the previous section is solved by a combination of two BEM techniques. The wavelet compressed BEM (Ravnik et al. [6]) is used to calculated boundary values of vorticity and

pressure, while a macro element BEM governed by a square system matrix is used to solve other equations. The algorithm is presented in detail below:

- calculate integrals, that depend solely on the mesh geometry
- use wavelet compression on matrices of integrals
- begin time step loop
  - begin global nonlinear loop
    - begin local kinematic-vorticity loop
      - *KINEMATICS*
      * calculate boundary values by solving the kinematics equation by wavelet compressed single domain BEM
      * calculate domain velocity values by solving the kinematics equation by subdomain BEM
      - *VORTICITY KINETICS*
      * solve vorticity transport equation by subdomain BEM using the boundary values from single domain BEM calculation
      * check convergence - repeat steps in the local loop until convergence is achieved
    - end local kinematic-vorticity loop
    - *ENERGY KINETICS*
    * temperature
    - *PRESSURE COMPUTATION*
    * calculate boundary values by solving the pressure equation by wavelet compressed single domain BEM
    * calculate domain pressure values by solving the pressure equation by subdomain BEM
    - *NON-LINEAR EFFECTS*
    * calculate all nonlinear terms (dilatation, reversible and irreversible rate of work, nonlinear material properties)
    - *CONSTITUTIVE FLUX MODELS*
    * Fourier and non-Fourier heat flux model
    * Newton viscous and Maxwell viscoelastic models
    * check convergence - repeat steps in the nonlinear loop until convergence is achieved
  - end global nonlinear loop
- end time step
- output results

With the aim of decreasing storage and CPU time requirements of the single domain BEM we employ the macro element approach. The idea is to use a collocation scheme for equation for each domain cell separately and require that the functions must be continuous over the domain cell boundaries. Since every domain cell neighbours only to a few cells, we end up with a sparse system of equations. In a nutshell we are using single domain BEM on every domain cell separately and connect them via compatibility and equilibrium conditions (Škerget et al. [7], Ravnik et al. [8]).

In order to be able to perform simulations on dense grids, we used a wavelet compression algorithm on fully populated matrices, resulting from the BEM calculation of boundary vorticity. A discrete wavelet transform for vectors of arbitrary length, developed by Ravnik et al. [6, 9], was used.

5 Numerical example

Using the developed numerical scheme we analysed the onset of thermoacoustic waves in an enclosure. The enclosure is 13 mm wide and 13 mm high. It is filled with nitrogen gas at $p = 101325$ Pa and $T_0 = 300$ K. In the beginning the fluid is at rest. At $t = 0$ the left wall is impulsively heated to $T_L = 400$ K. During the simulation ($t > 0$) a constant temperature of $T_R = 300$ K is kept on the right wall and $T_L = 400$ K on the left. The top and bottom walls of the enclosure are considered adiabatic, i.e. there is no heat flux through them. Gravity is neglected. The enclosure is closed by walls, which have a no-slip velocity boundary condition.

The ideal gas is chosen as a working fluid, thus the equation of state for the perfect gas is applied

$$p = \rho RT, \tag{16}$$

to relate the temperature to the other thermodynamic quantities. In the present research the Prandtl (Pr) number is assumed to remain constant, e.g. the following constant physical values are selected for the nitrogen (N_2): $\kappa = 1.4$, $R = 296.7$ and $Pr = 0.713$. The temperature dependence of the material properties are taken into account using the following polynomial expressions, e.g. for the dynamic viscosity η

$$\eta(T) = -1.253 \cdot 10^{-6} + 8.983 \cdot 10^{-8} T - 1.139 \cdot 10^{-10} T^2 + 9.101 \cdot 10^{-14} T^3, \tag{17}$$

the heat conductivity

$$k(T) = 1.494 \cdot 10^{-4} + 1.108 \cdot 10^{-4} T - 1.045 \cdot 10^{-7} T^2 + 6.958 \cdot 10^{-11} T^3, \tag{18}$$

while the heat relaxation time value $\lambda = 0.1$ was selected. The influence of temperature on c_p is neglected.

For the impulsive heating, the temperature of the left wall is given as

$$T_L(t) = T_0(1 + A), \tag{19}$$

where the over heat ratio A is given by an expression

$$A = \frac{T_L - T_0}{T_0}, \tag{20}$$

and $A = 1/3$ for all cases presented for spatially uniform wall heating, thus the left wall temperature is equated to $T_L = 400$ K.

Three meshes were used in simulations. The coarse mesh with 20×20 elements (1681 nodes), the middle mesh with 30×30 elements (3721 nodes) and the fine

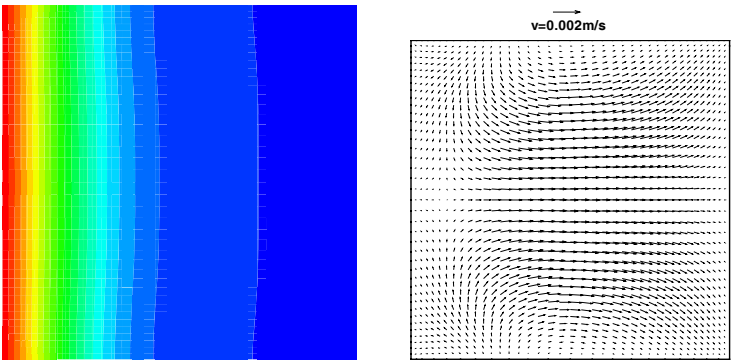

Figure 1: Temperature contours (left) and velocity vectors (right) at $t = 0.15$ s, zero gravity condition, 20×20 element mesh, $\Delta t = 10^{-4}$ s.

mesh with 40×40 elements (6561 nodes). Two time steps were used for simulation. The long time step of $\Delta t = 10^{-4}$ s, which enabled a long-term simulation reaching steady state. The short time step of $\Delta t = 10^{-6}$ s enabled an insight into the physics of the phenomenon. The short time step was used on the coarse and middle meshes, while the long time step was employed on the fine mesh.

The short time step simulation lasted for 0.8 s. On Figure 1 we are showing the temperature field and the velocity fields at $t = 0.15$ s. Since there is no gravity and hence no buoyancy the flow field appears to be one-dimensional.

A point in the middle of the enclosure ($x = 0.065$ m, $y = 0.065$ m) was chosen for demonstration of the time development of the flow. On Figure 2 (left) a pressure and temperature evolution with time is shown. We observe a gradual increase of pressure, faster in the first tenth of a second and slower after that. No pressure waves are observed, which was expected since the time step is too long to capture phenomena which occur with the speed of sound. The pressure distribution in the

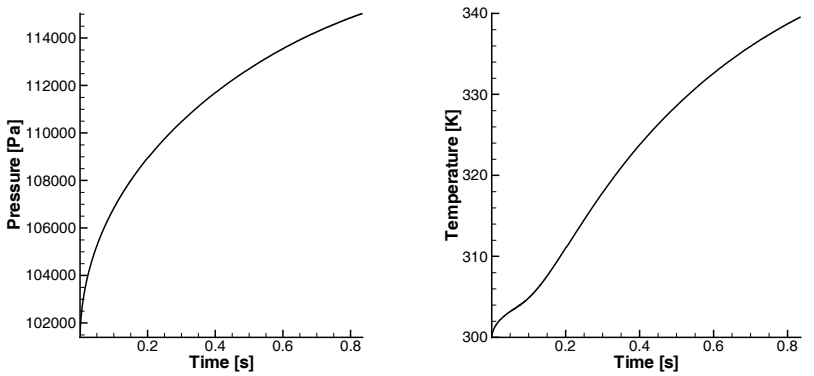

Figure 2: Pressure (left) and temperature (right) in the centre of the enclosure ($x = 0.065$ m, $y = 0.065$ m) versus time; $\Delta t = 10^{-4}$ s.

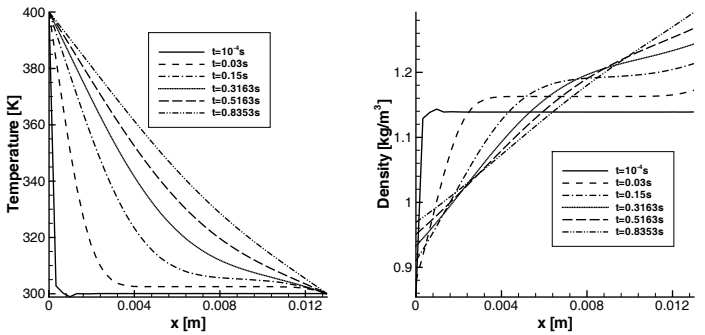

Figure 3: Temperature (left) and density (right) profiles through the centreline of the cavity. Development of the profile with time can be seen; $\Delta t = 10^{-4}$ s.

enclosure is uniform. At $t = 0.8$ s the pressure reaches about $p = 114000$ Pa. Looking at the evolution of the temperature of nitrogen in the middle of the enclosure on Figure 2 (right) we observe that the temperature increase is more or less linear. The nitrogen in the centre of the enclosure reaches $T = 340$ K.

To show the variation of flow fields across the enclosure we examined profiles along the horizontal centreline (x, 0.065 m). Figure 3 shows temperature and density profiles for six time instants. The very sharp temperature profile in the beginning of the simulation is caused by the application of boundary conditions. At long times, a steady state diffusive temperature profile is observed. Since the ideal gas approximation of nitrogen is assumed and since the pressure distribution in the cavity is uniform the density profiles are reciprocal to those of temperature.

The simulation on the fine mesh was preformed using a time step of 10^{-6} s. Figure 4 shows the time evolution of pressure and horizontal velocity component

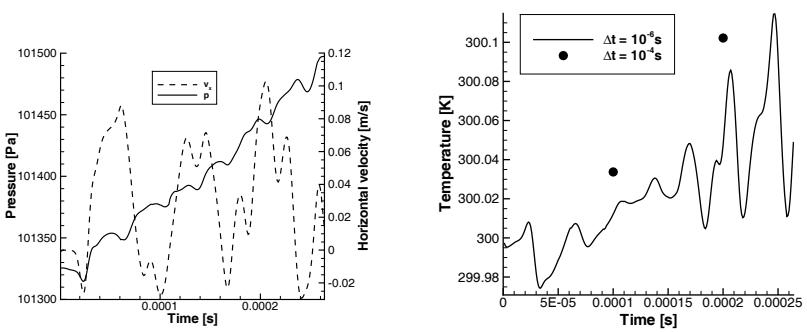

Figure 4: Pressure and horizontal velocity in the centre of the enclosure with time (left); Temperature in the centre of the enclosure with time (right); 40 × 40 element mesh, $\Delta t = 10^{-6}$ s.

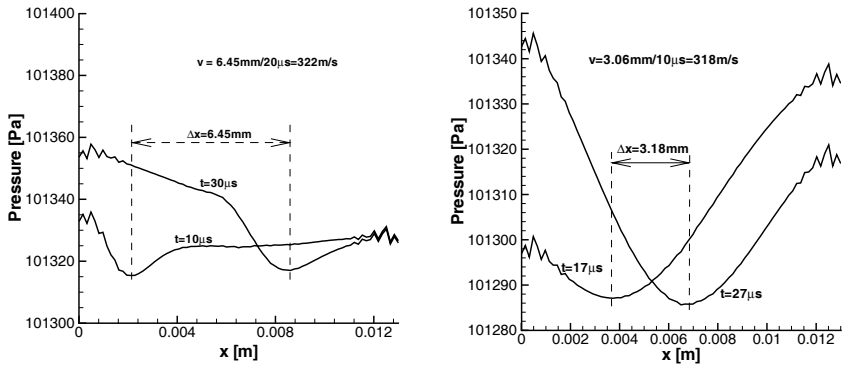

Figure 5: Pressure profiles through the centre of the enclosure; 40×40 element mesh, $\Delta t = 10^{-6}$ s. Left Fourier heat diffusion rheological model, right non-Fourier heat diffusion rheological model.

in the centre of the enclosure. Due to the presence of thermoacoustic waves a fluctuating increase of pressure and changing sign of horizontal velocity is observed. At the same time a fluctuating increase of temperature is also observed.

Figure 5, left, shows pressure profiles across the centreline of the enclosure at $t = 10$ μs and $t = 30$ μs. By measuring the distance travelled by the thermoacoustic wave between these time instants we were able to estimate the speed of sound to about 322m/s, which is within 10% of the correct value for nitrogen.

The non-Fourier heat transfer model was also simulated on the fine mesh with a time step of $\Delta t = 10^{-6}s$. Using subsequent pressure profiles we were able to estimate the distance travelled by the pressure wave in a specified time interval. This enabled the estimation of the speed of sound, which amounted to about 318 m/s. The two profiles were selected to be 10 μs apart and are displayed on Figure 5, right.

6 Conclusions

In this work a numerical algorithm for solving laminar compressible viscous flow and heat transfer is presented. The method is used to simulate the onset of thermoacoustic waves in a nitrogen filled enclosure subjected to a high temperature gradient. The results show the occurrence of thermoacoustic waves travelling across the enclosure at the speed of sound. During the expansion phase, the wave temperature dips bellow the average medium temperature. The thermoacoustic waves propagate at approximately the speed of sound within the fluid and gradually damp out due to heat and momentum diffusion. Extremely high gradients are present in the flow field, which generate the pressure waves and are difficult to model numerically. Our findings are consistent with numerical and experimental results of other authors, confirming the applicability of BEM for such flows.

Detailed investigation of the influence of different constitutive models on the flow phenomenon will be presented at the conference.

References

[1] Huang, Y. & Bau, H., Thermoacoustic waves in a confined medium. *Int J Heat Mass Transfer*, **40**, pp. 407–419, 1997.
[2] Brown, M. & Churchill, S., Experimental measurements of pressure waves generated by impulsive heating of a surface. *AIChE Journal*, **41**, pp. 205–213, 1995.
[3] Lin, Y. & Farouk, B., Flows induced by thermoacoustic waves in an enclosure: efffect of gravity. *J Thermophys Heat Transfer*, **20**, pp. 376–383, 2006.
[4] Aktas, M. & Farouk, B., Numerical simulation of developing natural convection in an enclosure due to rapid heating. *Int J Heat Mass Transfer*, **46**, pp. 2253–2261, 2003.
[5] Škerget, L. & Ravnik, J., Numerical simulation of compressible fluid flow in an enclosure induced by thermoacoustic waves. *Numerical analysis and applied mathematics, (AIP Conference Proceedings, 936)*, ed. T. Simos, American Institute of Physics, pp. 523–526, 2007.
[6] Ravnik, J., Škerget, L. & Hriberšek, M., The wavelet transform for BEM computational fluid dynamics. *Eng Anal Bound Elem*, **28**, pp. 1303–1314, 2004.
[7] Škerget, L., Hriberšek, M. & Žunič, Z., Natural convection flows in complex cavities by BEM. *Int J Num Meth Heat & Fluid Fl*, **13**, pp. 720–735, 2003.
[8] Ravnik, J., Škerget, L. & Žunič, Z., Combined single domain and subdomain BEM for 3D laminar viscous flow. *Eng Anal Bound Elem*, **submitted**, 2008.
[9] Ravnik, J., Škerget, L. & Hriberšek, M., 2D velocity vorticity based LES for the solution of natural convection in a differentially heated enclosure by wavelet transform based BEM and FEM. *Eng Anal Bound Elem*, **30**, pp. 671–686, 2006.

Prediction of laminar flow over a back facing step using new formula of penalty parameter

Mahmud A. Mehemed Abughalia
Department of Mechanical Engineering, Al-Fateh University, Libya

Dedication: To the soul of my Fiancée, the architecture engineer Rima

Abstract

This paper introduces a numerical solution for flow over a back facing step. In this study, the continuity equation is replaced by a penalty function and a new formula of penalty parameter is derived and implemented. The new formula of penalty parameter is restricted only to the finite element method and the formula requires the existence of the second derivative of the trial function so that a rectangular element with exponential trial function is proposed and used.

A laminar flow over a back facing step is chosen as a test model to examine the numerical solution. The location of the reattachment point is captured accurately only if the penalty parameter is multiplied by a suitable factor and this factor depends on the Jacobian.

The current numerical results are validated through a comparison to available numerical and experimental results for the case of flow over a back facing step. The tested range of Reynolds number was 200, 400 and 1000 and the ratio between the step height to the duct height was 0.5. The reattachment point is tabulated against Reynolds number. The comparison shows that the finite element solution using the new penalty parameter is closer to the experimental results than the available numerical results.

Keywords: penalty method, back facing step, finite element, laminar flow, Navier Stokes equations, numerical solution.

1 Introduction

The Navier Stokes equations govern the physical behavior of most of the fluid flow applications. Thus they have attracted a great deal of attention by most engineering fields, chemical, civil, aeronautical, oil and mechanical engineering. These equations usually are solved numerically and the challenge of the

WIT Transactions on Engineering Sciences, Vol 59, © 2008 WIT Press
www.witpress.com, ISSN 1743-3533 (on-line)
doi:10.2495/AFM080031

numerical studies usually focuses on predicting more precise results for the case study.

The well known methods for solving the Navier Stokes equations are finite difference, finite volume and finite element method. The numerical solution by these methods faces three aspects of instability sources.

- *The direct solution of continuity equation.*

The direct solution of continuity equation is unstable and this equation is used to be replaced by pressure Poisson equation, pressure or velocity correction methods, artificial compressibility or penalty methods.

- *Advection dominant.*

At Reynolds number greater than 2, the advection term dominants the solution and observed that the solution is unstable where the variable oscillating from node to node. This problem studied early and many techniques are developed to handle the problem as Pertov Galerkin or upwinding streamline techniques.

- *Using equal order element.*

For Navier Stokes equations, the using of the same element order to the velocity and pressure leads to non physical oscillation in the pressure and in the velocity. The pressure field usually interpolated at lower order than the velocity field but equal order elements for the pressure and velocity can be used and that requires a stabilization technique.

The current work considers a numerical solution to laminar flow over a back facing step. The numerical solution adopts the penalty method instead of the continuity equation in order to reduce the computation time. The validation of the results is achieved by a comparison to numerical and experimental results.

2 Previous studies

There are a vast number of publications devoted to employ the finite element method to solve Navier Stokes equations. The applications go back to 1950's. The numerical studies usually consider the effect of the element type, the numerical scheme and the stabilization techniques. Among the early studies using finite element method, the study of Taylor and Frances 1981 in which they employed finite element method to very low Reynolds number flow over a back facing step using second order element for velocity field and less order for pressure field.

Back facing step model is preferred as test study and usually the developing of the numerical schemes is validated over this model due to the well experimental investigations.

Numerical and experimental results to flow over a back facing step is available from the work of Mateescu [3], and Barber and Fonty [2].

Mateescu presented efficient solutions of the steady and unsteady Navier-Stokes equations based on a finite difference formulation and using artificial compressibility. His numerical method is validated for steady incompressible flows past a downstream-facing step. The method is used to obtain efficient solutions for several 2D and 3D unsteady flow problems with oscillating walls.

The comparison with experimental results of Armaly and by Lee presented in [2] indicated a good agreement for Reynolds numbers between 400 and 700, with a deteriorating agreement between Re=800 and 1200; this agreement deterioration was attributed by Gartling [26], Kim and Moin presented in [2] and Armaly to the three-dimensional effects occurring in the experimental flows due to the side walls, as opposed to the rigorous two-dimensional numerical analysis.

Barber and Fonty [2] introduced a novel vortex element method for simulating incompressible laminar flow over a two-dimensional backward-facing step. Their model employs an operator-splitting technique to compute the evolution of the vorticity field downstream of abrupt changes in flow geometry. They validate the model by comparing the length of the recirculating eddy behind a confined backward-facing step against data from experimental and numerical investigations and commercial finite-volume computational fluid dynamics code, CFD-ACE+. The results show that the vortex element scheme over-predicts the length of the downstream re-circulating eddy.

The current work is devoted to employ the penalty method. This method is widely implemented to solve the Navier Stokes equations. The basic of the penalty method is relating the pressure explicitly to the velocity gradients as;

$$P = -\lambda\left(\frac{\partial u}{\partial x} + \frac{\partial v}{\partial y}\right) \tag{1}$$

where λ is the penalty parameter. The magnitude of the penalty parameter can not determined easily and must be assigned a large value in order to approximate the incompressibility. Small value of penalty parameter increases the error and large value may lead to ill condition system of equations.

Recent works that conducted to the penalty method that have used different penalty parameter are surveyed next. Most of the penalty parameter are determined by numerical experiments. There are two trends in handling the penalty parameter. In the first one, penalty parameter is set as constant may depend on the fluid properties.

In the study of Vellando et al [20], they employed penalty function to study laminar flow over a back facing step, flow in square cavity and the flow past a cylinder. Numerically they used a SUPG type algorithm as a stabilization procedure, in order to eliminate the numerical oscillations. The results for the penalty algorithm for Reynolds numbers of 100, 1000, 5000 and 10000 considered, the penalty parameter as 10^4.

Another study presented in [21] employed penalty method to study the laminar flow over a back facing step at Re = 900. The penalty parameter was suggested to be in the range between 10^7 and 10^9. The study showed oscillating pressure field from one element to the next because of the discretization of the pressure.

Among the studies employed constant penalty parameter that related to the fluid density, Roylance [24], where he set the penalty parameter as,

$$\lambda = 10^7 \times \mu \tag{2}$$

The other trend in the expressing the penalty parameter is setting the parameter as function of Reynolds number as that presented by Baker [10] who suggested to use penalty parameter as;

$$\lambda = \max(v\,\mathrm{Re}, \mathrm{Re}) \tag{3}$$

and John et al [28], relates the penalty parameter to Reynolds number as follows;

$$\lambda = \frac{h.\mathrm{Re}}{\sqrt{\pi\delta}} \tag{4}$$

where h is the element width. Hozman [25] also employed the penalty method to compressible flow using penalty parameter as;

$$\lambda = \mathrm{Re} \tag{5}$$

In the manual of FIDAP, the penalty parameter is picked according to the relation,

$$\lambda = c \times D \tag{6}$$

where *c* depends on the machine accuracy and D is a measure of the dominant contribution in stiffness matrix. All versions of FIDAP use floating point word lengths of 64 bits and numerical studies reveal that for this range of lengths, an appropriate choice of c is 10^6 and D can be chosen as,

$$D = \max(\mu\,\mathrm{Re}, \mu) \tag{7}$$

when μ is the viscosity, Re is the Reynolds number, lie within a range of 10^{-3} to 10^3 it is not necessary to be very particular about the selection of λ as it may vary over several orders of magnitude with essentially insignificant effect on results; however, outside this range the penalty parameter should be decreased accordingly from its default value of 10^6.

Chan et al [23] employed a finite element and penalty method to single-phase viscous incompressible fluid, or single-phase elastic solid, as limiting cases of a biphasic material. Interface boundary conditions allow the solution of problems involving combinations of biphasic, fluid and solid regions. The results are compared to independent, analytic solution for the problem of Couette flow over rigid and deformable porous biphasic layers and show that the finite element code accurately predicts the viscous fluid flows and deformation in the porous biphasic region. The study use penalty parameter as function of fluid properties as

$$\lambda = Ct_O \frac{\beta + 2\mu^s}{N_i} + C\frac{\mu^f}{N_i} \tag{8}$$

where t_o is a reference time, C is a computer-dependent parameter related to the accuracy of the numerical calculations C is usually chosen in the range 10^7 to 10^9, β and μ^s are the solid phase Lamé parameters and μ^f mf is the viscosity of the fluid.

Generally, in practical computations, the selection of the value of the penalty parameter is of crucial importance. The following section considers a derivation of penalty parameter formula.

3 The determination of the penalty parameter

In the present paper, we assume a generalized formula to the penalty parameter based on mathematical ground where such a formula does not exist in the extensive survey. The penalty parameter is intended to be derived based on the momentum equations.

If the momentum equations are differentiated with respect to their corresponding velocity component, we obtain

$$\rho(u^* \frac{\partial N_J}{\partial x} + v^* \frac{\partial N_J}{\partial y}) - \lambda(\frac{\partial^2 N_J}{\partial x^2}) = \mu(\frac{\partial^2 N_J}{\partial x^2} + \frac{\partial^2 N_J}{\partial y^2}) \tag{9}$$

and

$$\rho(u^* \frac{\partial N_J}{\partial x} + v^* \frac{\partial N_J}{\partial y}) - \lambda(\frac{\partial^2 N_J}{\partial y^2}) = \mu(\frac{\partial^2 N_J}{\partial x^2} + \frac{\partial^2 N_J}{\partial y^2}) \tag{10}$$

Adding the two equations and obtain penalty parameter;

$$\lambda = \left| 2\frac{\rho(u^* \frac{\partial N_J}{\partial x} + v^* \frac{\partial N_J}{\partial y})}{(\frac{\partial^2 N_J}{\partial x^2} + \frac{\partial^2 N_J}{\partial y^2})} - 2\mu \right| \tag{11}$$

The above formula gives a continuous distribution of penalty parameter over the element.

4 The element type

The usual strategy in the applications of the finite element method is using a polynomial trial functions. The pressure field is recommended to be of lower order than that used for the velocity field and should satisfy the inf-sub condition. The *usage* of such elements is summarized by Gresho et al [17]. They tabulated the advantages and disadvantages of the most known 2D-3D polynomial elements. Table 1, shows some elements that can be used when penalty method employed.

Patankar [27] used exponential trial function for triangle element as

$$N_i = A + B\exp(\frac{\rho U x}{\Gamma}) + Cy$$

where $A, B\,and\,C$ are evaluated as in the traditional way.

The approach in this paper is to use an element that simulates the mathematical solution of the governing equations. The penalty parameter in Eqn (11) requires an existence of the second derivative of the trial function, so polynomial elements are excluded from the study where higher order elements do not recommended in the Navier Stokes equations. According to the solution nature, an element with exponential distribution is suggested and used. The using of exponential distribution over triangular or rectangular elements works well

with the penalty method. The pressure and velocity elements are of equal order and the trial functions of the element are,

Table 1: Working elements with penalty method [17].

Q_2P_{-1}	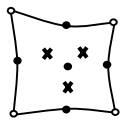	Q_2Q_0	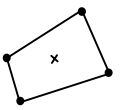
Q_2Q_{-1}	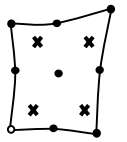	P_1P_0	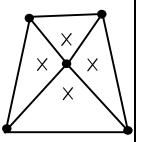

Table 2: The trial functions of exponential elements using parent coordinates.

$N_1 = 1 - \frac{e^{\zeta} - e^{-1}}{e^{1} - e^{-1}} - \frac{e^{\eta} - e^{-1}}{e^{1} - e^{-1}} + \frac{e^{\zeta} - e^{-1}}{e^{1} - e^{-1}} \times \frac{e^{\eta} - e^{-1}}{e^{1} - e^{-1}}$ $N_2 = \frac{e^{\zeta} - e^{-1}}{e^{1} - e^{-1}} - \frac{e^{\zeta} - e^{-1}}{e^{1} - e^{-1}} \times \frac{e^{\eta} - e^{-1}}{e^{1} - e^{-1}}$ $N_3 = \frac{e^{\zeta} - e^{-1}}{e^{1} - e^{-1}} \times \frac{e^{\eta} - e^{-1}}{e^{1} - e^{-1}}$ $N_4 = \frac{e^{\eta} - e^{-1}}{e^{1} - e^{-1}} - \frac{e^{\zeta} - e^{-1}}{e^{1} - e^{-1}} \times \frac{e^{\eta} - e^{-1}}{e^{1} - e^{-1}}$	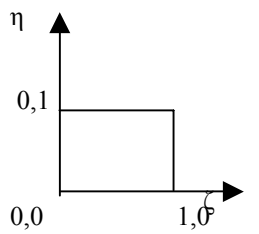
$N_1 = 1 - \frac{e^{\zeta} - 1}{e^{1} - 1} - \frac{e^{\eta} - 1}{e^{1} - 1}$ $N_2 = \frac{e^{\zeta} - 1}{e^{1} - 1}$ $N_3 = \frac{e^{\eta} - 1}{e^{1} - 1}$	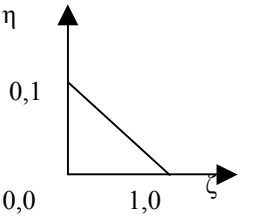

5 Numerical scheme

It is observed from the current numerical experiments that the direct implementation and linear iterative solvers are inefficient to get precise results. In order to get a convergent solution, the following discretization is stabilized through the Pertove Galerkin method and the residual of the previous iterations is added to current iteration.

The current technique is based on varying inlet boundary condition from zero. For very small inlet boundary condition, the advection term can be neglected and the system looks like the diffusion problem. This solution can be considered as exact for the next iteration in which the inlet boundary condition is increased linearly.

$$\tau_{ps}^{n}\begin{bmatrix}\Theta_{ad}\dfrac{\rho u^{*}}{2}\int(N_i+\dfrac{\beta}{\|u\|}(u^{*}\dfrac{\partial N_i}{\partial x}+v^{*}\dfrac{\partial N_i}{\partial y}))\dfrac{\partial u}{\partial x}dA\\ -\Theta_{ad}\dfrac{\rho u^{*}}{2}\int(N_i+\dfrac{\beta}{\|u\|}(u^{*}\dfrac{\partial N_i}{\partial x}+v^{*}\dfrac{\partial N_i}{\partial y}))\dfrac{\partial v}{\partial y}dA+\\ \Theta_{ad}\rho v^{*}\int(N_i+\dfrac{\beta}{\|u\|}(u^{*}\dfrac{\partial N_i}{\partial x}+v^{*}\dfrac{\partial N_i}{\partial y}))\dfrac{\partial u}{\partial y}dA+\\ \Theta_{p}\lambda\int\dfrac{\partial N_i}{\partial x}(\dfrac{\partial u}{\partial x}+\dfrac{\partial v}{\partial y})dA+\mu\int(\dfrac{\partial N_i}{\partial x}\dfrac{\partial u}{\partial x}+\dfrac{\partial N_i}{\partial y}\dfrac{\partial u}{\partial y})dA\end{bmatrix}^{n}+$$

$$\sum_{jk=0}^{jk=n-1}\tau_{ps}^{jk}\begin{bmatrix}\Theta_{ad}\dfrac{\rho u^{*}}{2}\int(N_i+\dfrac{\beta}{\|u\|}(u^{*}\dfrac{\partial N_i}{\partial x}+v^{*}\dfrac{\partial N_i}{\partial y}))\dfrac{\partial u}{\partial x}dA\\ -\Theta_{ad}\dfrac{\rho u^{*}}{2}\int(N_i+\dfrac{\beta}{\|u\|}(u^{*}\dfrac{\partial N_i}{\partial x}+v^{*}\dfrac{\partial N_i}{\partial y}))\dfrac{\partial v}{\partial y}dA+\\ \Theta_{ad}\rho v^{*}\int(N_i+\dfrac{\beta}{\|u\|}(u^{*}\dfrac{\partial N_i}{\partial x}+v^{*}\dfrac{\partial N_i}{\partial y}))\dfrac{\partial u}{\partial y}dA+\\ \Theta_{p}\lambda\int\dfrac{\partial N_i}{\partial x}(\dfrac{\partial u}{\partial x}+\dfrac{\partial v}{\partial y})dA+\mu\int(\dfrac{\partial N_i}{\partial x}\dfrac{\partial u}{\partial x}+\dfrac{\partial N_i}{\partial y}\dfrac{\partial u}{\partial y})dA\end{bmatrix}^{jk}=0 \tag{12}$$

$$\tau_{ps}^{n}\begin{bmatrix}\Theta_{ad}\rho u^{*}\int(N_i+\dfrac{\beta}{\|u\|}(u^{*}\dfrac{\partial N_i}{\partial x}+v^{*}\dfrac{\partial N_i}{\partial y}))\dfrac{\partial v}{\partial x}dA+\\ -\Theta_{ad}\dfrac{\rho v^{*}}{2}\int(N_i+\dfrac{\beta}{\|u\|}(u^{*}\dfrac{\partial N_i}{\partial x}+v^{*}\dfrac{\partial N_i}{\partial y}))\dfrac{\partial u}{\partial x}dA\\ \Theta_{ad}\dfrac{\rho v^{*}}{2}\int(N_i+\dfrac{\beta}{\|u\|}(u^{*}\dfrac{\partial N_i}{\partial x}+v^{*}\dfrac{\partial N_i}{\partial y}))\dfrac{\partial v}{\partial y}dA+\\ \Theta_{p}\lambda\int\dfrac{\partial N_i}{\partial y}(\dfrac{\partial u}{\partial x}+\dfrac{\partial v}{\partial y})dA+\mu\int(\dfrac{\partial N_i}{\partial x}\dfrac{\partial v}{\partial x}+\dfrac{\partial N_i}{\partial y}\dfrac{\partial v}{\partial y})dA\end{bmatrix}^{n}+$$

$$\sum_{jk=0}^{jk=n-1}\tau_{ps}^{jk}\begin{bmatrix}\Theta_{ad}\rho u^{*}\int(N_i+\dfrac{\beta}{\|u\|}(u^{*}\dfrac{\partial N_i}{\partial x}+v^{*}\dfrac{\partial N_i}{\partial y}))\dfrac{\partial v}{\partial x}dA+\\ -\Theta_{ad}\dfrac{\rho v^{*}}{2}\int(N_i+\dfrac{\beta}{\|u\|}(u^{*}\dfrac{\partial N_i}{\partial x}+v^{*}\dfrac{\partial N_i}{\partial y}))\dfrac{\partial u}{\partial x}dA\\ \Theta_{ad}\dfrac{\rho v^{*}}{2}\int(N_i+\dfrac{\beta}{\|u\|}(u^{*}\dfrac{\partial N_i}{\partial x}+v^{*}\dfrac{\partial N_i}{\partial y}))\dfrac{\partial v}{\partial y}dA+\\ \Theta_{p}\lambda\int\dfrac{\partial N_i}{\partial y}(\dfrac{\partial u}{\partial x}+\dfrac{\partial v}{\partial y})dA+\mu\int(\dfrac{\partial N_i}{\partial x}\dfrac{\partial v}{\partial x}+\dfrac{\partial N_i}{\partial y}\dfrac{\partial v}{\partial y})dA\end{bmatrix}^{jk}=0 \tag{13}$$

where n is the current iteration number and β is defined

$$\beta = \frac{\bar{\xi}.u.\Delta x + \bar{\eta}.v.\Delta y}{2},\ \bar{\xi} = \coth(\alpha_\xi) - \frac{1}{\alpha_\xi},$$

$$\bar{\eta} = \coth(\alpha_\eta) - \frac{1}{\alpha_\eta},\ \alpha_\xi = \frac{\rho.u.\Delta x}{2\mu},\ \alpha_\eta = \frac{\rho.v.\Delta y}{2\mu}$$

and τ_{PS} is defined

$$\tau_{PS} = 1$$

where $\Theta_{\text{ad}} = 2$ and this value also multiplied to the term includes fluid density in equation 11. . The factor Θ_{ad} depends on related parameters.

$$\Theta_P = \max(|J_{11}|, |J_{12}|, |J_{21}|, |J_{22}|)$$

Where J_{ij} is the element of Jacobian matrix and the relaxation factor is taken as 0.75 and the number of iterations is 4000. Another workable scheme is increasing the Θ_P linearly with the iterations.

6 Laminar flow over a back facing step

The behavior of the flow over a back facing step in laminar mode is sensitive to the Reynolds number and also sensitive to the ratio between the step height to the duct height. The main feature of such flow is the circulation that formed behind the step as a result of the abrupt change in geometry.

In flows at $ST = 0.33$ only one circulation behind the step observed while at $ST = 0.5$ another circulation occurs at the upper wall. For ST greater than 0.33, the upper circulation occurs as a result of the vacuum induced by the lower circulation and it occurs before the reattachment point of the lower circulation and extends afterwards.

Irrespective to dependency of the numerical solution on grid concentration and size, the current study is intended to be performed on uniform equal size rectangular elements to exhibit the efficiency of the developed numerical model.

The study is performed over a wide range of laminar flow and the Reynolds number ranged from 400 to 1200. The Reynolds number is based on the mean velocity and duct height as a characteristic length as in the study of Mateescu [3] but Barber and Fonty [2], calculated the Reynolds number based on the step height.

The locations of the separation and reattachment points are commonly used as a validation criteria for the computational and experimental results. Thus, the separation and the reattachment points for laminar flow is tabulated versus Reynolds number in table 1 and the table also shows a comparison to the data given in [2] and in [3].

Table 3 shows a change of lower reattachment point with change of Reynolds number that presented in [2] and [3].

Kim and Moin's study that presented in [2] used a computational domain that does not include an inlet region and they directly impose the inflow boundary condition at the step edge itself. In this study and the study of Mateescu [3], the domain contains an inlet region which has made the problem more physically realistic.

The linear iterative solvers are inefficient to solve the system of equations so that gauss elimination method is applied to compressed matrices in each iteration.

The numerical solution is very sensitive to Θ_P and relaxation factor. Their changes have great effect on the numerical prediction of the reattachment point. Although of that, the comparison of the current results shows the efficiency of the current numerical solution. The current results are more accurate than the numerical results presented in both [2] and [3]. The consistency of accuracy is hold over all tested range of Reynolds number. But for the study of [2] and [3] the accuracy is lost for Reynolds number greater than 400.

For real flow, a secondary bubble circulation is observed experimentally behind and closer to the step and the current numerical technique is capable to predict this bubble circulation.

7 Conclusions

In this study, a new formula of penalty method is derived from momentum equations and used with an element of exponential trial function to study a laminar flow over a back facing step. A special technique to handle the problem is employed hence linear iterative solvers are found inefficient. Validation of the code is achieved through a comparison over a wide range of Reynolds number of flow over a back facing step in laminar mode. The comparison shows that a precise results are obtainable if the multipliers to the advection and penalty parameter are well employed. The coefficients, θ_{ad} , θ_p needs a mathematical optimization and generally the present numerical technique shows efficiency over the numerical results presented in the references.

Table 3: The effect of Reynolds number and step height at ST =0.5.

Re_D	Lower Reattachment point: R1			upper separation point: R2			upper Reattachment point: R3		
	Curr	**Ref [2]**	**EXP [3]**	**Curr**	**Ref [2]**	**EXP [3]**	**Curr**	**Ref [2]**	**EXP [3]**
400	4.6	5.5	4.1-4.3	-	-	-	-	-	-
600	5.6	7	5.21-5.8	4.3	-	4	7	-	8
800	7	8.5	6.45-7.1	5.2	-	5-5.25	10	-	9.8-10
1200	9.1	11	8.4-8.9	4.7	-	7.8	9.8	-	11-11.5

Curr: Current results, **Exp [3]**: Experimental results presented in [3].
Re_D : Reynolds number based on the hydraulic diameter.

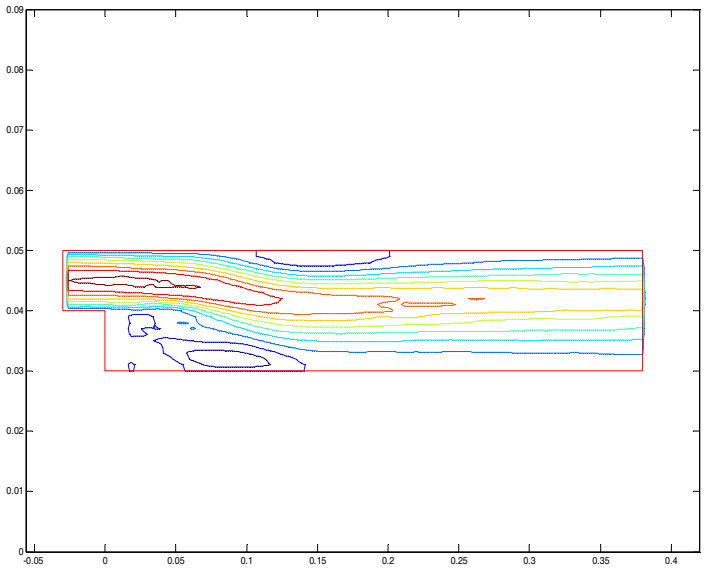

Figure 1: Backward facing step problem for Re_D =800.

Nomenclature

ρ: Fluid density.
μ: Fluid dynamic viscosity.
ν: Fluid kinematics viscosity.
λ: Penalty parameter.
Re: Reynolds number.
δ: Boundary layer thickness.
h: Element size.
N_I: Weighting function.
N_J: Trial function at node J.
ST: The ratio between the step height to the duct height.

References

[1] Mahmud A. Mehemed Abughalia, *Numerical study of reattachment point to flow over Back Facing Step*, M. Sc. Thesis, AL-Fateh University, Libya,2007.
[2] Robert W. Barber and Anne Fonty, *Comparison of vortex-element and finite-volume simulations of low reynolds umber flow over a confined backward-facing step*, 4th GRACM Congress on Computational Mechanics, GRACM 2002,Patra, 27-29 June, 2002.

[3] Dan Mateescu, *Efficient methods for 2D and 3D steady and unsteady confined flows based on the solution of the Navier-Stokes equations*, aerospace program director, Department Of Mechanical Engineering, Mcgill University, Montreal, Canada, email: Dan.Mateescu@mcgill.ca, 2004.

[4] J.G. Barbosa Saldana and N. K. Anand, *Forced convection over a three-dimensional horizontal backward facing step*, Department Of Mechanical Engineering, Department Of Computer Science, Texas University.

[5] H. M. Blackburn, D. Barkley and S. J. Sherwin, *Convective instability and transient growth in flow over a backward-facing step*, Department Of Mechanical Engineering, Monash University, australia, mathematics institute, University of warwick, UK and Department Of Aeronautics, Imperial College London, UK.

[6] E. Creus´e, a. Giovannini, and I. Mortazavi, *Active control strategies for transitional backward-facing step flows*, lamav, universit´e de valenciennes, france equipe simpaf, inria futurs, site de lille ecreuse@univ-valenciennes.fr 2 imft, 118, route de narbonne, 31062 toulouse, france giova@cict.fr 3 universit´e de bordeaux, 33405 talence cedex, france projet mc2, inria futurs, site de bordeaux mortaz@math.u-bordeaux1.fr.

[7] T. M. Shih, numerical heat transfer, hemisphere, 1984.

[8] Gianni Comini, Stefano Del Giudice, Carlo Nonino, *finite element analysis heat transfe*r, Taylor & Francis, 1994.

[9] Suhas V. Patanker, *Numerical heat transfer and fluid flow*, Taylor & Francis, 1980.

[10] A. J. Baker, *Finite element computational fluid mechanics*, Hemisphere, 1983.

[11] Klaus Jurgen Bathe, F*inite element procedure*, Prentice Hall, 1996.

[12] Roald Akberov, Darrell W. Pepper, Yitung Chen, *Turbulent flow over a backward facing step using penalty and equal order methods*, Nevada Center For Advanced Computational Methods.

[13] A. Kolesnikov and A. J. Baker, *Efficient implementation of high order methods for advection diffusion equation*, PROC of the third ASME-JSME Joint Fluids Engineering Conference, July 18-23 1999, San Francisco, California.

[14] T. Chen and L. S. Raju, *Coupling finite element and meshless local petrov- galerkin methods for two dimensional problems*, AIAA-2002 - 1659,2002.

[15] Jahrul Alam and Md. Ashaque Meah*, Finite element simulation of two dimensional fluid flow*.

[16] S. A. Mohsen Karimian, Anthony G. Straaman, *An improved scheme for pressure velocity coupling in control volume based finite element discretization*, the University of Western Ontario, London, Ontario, Canada n6a 5b9.

[17] P. M. Gresho, R. L. Sani and M. S. Engelman, *incompressible flow and the finite element method*, John Wiley & Sons, 1998.

[18] Rajiv Sampath and Nicholas Zabaras, D*esign and object-oriented implementation of a preconditioned-stabilized incompressible Navier Stokes solver using equal-order-interpolation velocity pressure elements*, Cornell University.

[19] B. S. Varaprasad Patnaik et al, *simulation of internal flows with heat transfer using velocity correction*.

[20] P. Vellando, J. Puertas, j. Bonillo, J. Fe. *On the resolution of the viscous incompressible flow for various supg finite element formulations*, European Congress on Computational Methods in applied sciences and engineering. Eccomas 2000 Barcelona, 11-14 September 2000. Ó ECCOMAS.

[21] Numerical Methods, *Finite element for modeling fluid flow*, section 410.4,fluid flow division, march 1999. Genium Publishing.

[22] R.D. Lazarov, J.E. Pasciak, J. Sch¨oberl, and P.S. Vassilevski, *Almost optimal interior penalty discontinuous approximations of symmetric elliptic problems on non-matching grids*, 1991 Mathematics Subject classification. 65f10, 65n20, 65n30. Science foundation under grant dms-9973328. 2000- 2001.

[23] B. Chan, P. S. Donzelli and R. L. Spilker, *A mixed-penalty biphasic finite element formulation incorporating viscous fluids and material interfaces*, Department Of Mechanical Engineering, Aeronautical Engineering, and Mechanics Department of biomedical engineering, Scientific computation Research center 9 Rensselaer Polytechnic Institute 10 Troy, New York 12180.

[24] David Roylance, *Finite element analysis of non-isothermal reactive flows*, Department Of Materials Science and Engineering, Massachusetts Institute of Technology, Cambridge, 2003.

[25] J. Hozman, *Numerical solution of the Navier–Stokes equations by semi–implicit schemes*, Charles University, Faculty of Mathematics and Physics, Prague, Czech Republic. Wds'06 PROC of contributed papers, part i, pp 59–64, 2006.

[26] Gartling D.K. *A test problem for outflow boundary conditions – Flow over a backward-facing step*. International Journal for Numerical Methods in Fluids 11: 953-967, 1990.

[27] Suhas V. Patanker, *Numerical heat transfer and fluid flow*, Hemisphere Publishing corporation, 1980.

[28] V. John, W. Layton and N. Sahin, *Derivation and analysis of near wall models for channel and re-circulating flows*, Faculty of Mathematics Ottovon-Guericke- University Magdeburg, Germany, 0898-1221/04/ - 2004 Elsevier ltd.

An inverse approach for airfoil design

M. T. Rahmati[1], G. A. Aggidis[1] & M. Zangeneh[2]
[1]*Lancaster University, Engineering Department, UK*
[2]*University College London, Mechanical Engineering Department, UK*

Abstract

Inverse design methods directly compute geometry for specified design parameters such as surface pressure or velocity, which is related to the performance of an airfoil (or a blade) geometry. These methods replace the time consuming iterative procedure of direct methods in which a large number of different blade shapes are designed and analysed to find the one which creates the surface velocity or pressure distribution closest to the desired one. In this paper a viscous inverse method for airfoil design is described. The inverse design approach computes an airfoil shape based on the target surface pressure distribution. The re-design of an airfoil, starting from an initial arbitrary profile in subsonic flow regimes, demonstrates the merits and robustness of this approach.

Keywords: inverse method, CFD, airfoil design, RANS equations.

1 Introduction

The Computational Fluid Dynamics (CFD) codes can be directly used for airfoil shape design based on 'trial and error' approaches. By guessing an airfoil shape, the flow solution can be obtained using the CFD codes. The flow solution is then compared with the desired flow conditions. If these are not met then the airfoil geometry is altered. The whole process is repeated again, until the required flow conditions are achieved. In fact, these direct design procedures are very inefficient and time consuming. In order to reduce the development and design time and their associated costs, a more systematic method is required. The inverse method is an alternative approach that replaces the time consuming iterative procedure of direct methods. A pioneering airfoil inverse method based on conformal mapping was developed by Lighthill [1] in 1945. Since then many inverse methods for airfoil (or blade) design have been developed. These

WIT Transactions on Engineering Sciences, Vol 59, © 2008 WIT Press
www.witpress.com, ISSN 1743-3533 (on-line)
doi:10.2495/AFM080041

methods are mainly based on potential flow equations [2, 3] or Euler flow equations [4, 5]. These methods provide inviscid geometries so many characteristics of real flow fields are ignored. Unfortunately the inverse design based on inviscid flow calculations cannot directly be extended to methods based on Navier-Stokes equations. This is because the blade modification algorithm of these inverse design methods requires a non-zero relative velocity on the surface whereas the relative wall velocity is zero in viscous flow calculations due to the non-slip condition. However, in certain flow fields accurate modelling of viscous flow by utilizing Navier-Stokes equations is essential in order to design the blade or airfoil shape more precisely [6].

The current viscous inverse design approach computes an airfoil shape based on the target surface pressure distribution. In order to determine the required geometrical modification to accomplish the target design specification the following steps are carried out. First, the surface pressure coefficients distribution of an initial blade is calculated using the viscous flow analysis algorithm. Then, the difference between the target and the initial surface pressure coefficient distribution is used for blade modification. Subsequently, the mesh of the domain is adapted to the modified blade. The modified airfoil is then considered as an initial airfoil and this procedure is carried out iteratively until the differences between the target and initial surface pressure coefficients are negligible. These steps and the application of the method for the design of an airfoil are described hereafter. It is then followed by the application of the method for airfoil shape design.

2 Flow analysis algorithm

Taking the time average of the steady incompressible Navier-Stokes equations in a Cartesian coordinate system and applying the Boussinesq hypothesis for closure of the equations yields the following RANS equations:

$$\frac{\partial}{\partial x_i}\left(\rho U_i\right) = 0 \tag{1}$$

$$\frac{\partial}{\partial x_j}\left[\rho U_i U_j - \left(\mu + \mu_t\right)\left(\frac{\partial U_i}{\partial x_j} + \frac{\partial U_j}{\partial x_i}\right)\right] = -\frac{\partial P}{\partial x_i} \tag{2}$$

U and P are the time averaged components of velocity and pressure vectors respectively, μ is viscosity, μ_t is turbulent viscosity and ρ is density. The standard k-ε model is implemented for turbulence modelling as it has a good compromise in terms of accuracy and robustness [6]. In this model μ_t is given by:

$$\mu_t = \rho C_\mu \frac{k^2}{\varepsilon} \tag{3}$$

An approximate transport equation for k and ε can be written in the following form:

$$\frac{\partial \rho U_i k}{\partial x_i} = \frac{\partial}{\partial x_i}\left(\frac{\mu_t}{\sigma_k}\frac{\partial k}{\partial x_i}\right) + G_k - \rho\varepsilon \tag{4}$$

$$\frac{\partial \rho U_i \varepsilon}{\partial x_i} = \frac{\partial}{\partial x_i}\left(\frac{\mu_t}{\sigma_\varepsilon}\frac{\partial \varepsilon}{\partial x_i}\right) + C_1 \frac{\varepsilon}{k} G_k - C_2 \rho \frac{\varepsilon^2}{k} \tag{5}$$

Here G_k represents the generation of k and is defined as

$$G_k = \mu_t \left(\frac{\partial U_i}{\partial x_j} + \frac{\partial U_j}{\partial x_i}\right)\frac{\partial U_i}{\partial x_j} \tag{6}$$

Based on experimental data from a variety of turbulent flows Launder and Spalding [7] recommended the following values for the empirical constants which appear in equation (3) to equation (5):

C_1=1.44, C_2=1.92, C_μ=.09, σ_k =1 and σ_ε =1.3.

The pressure correction method developed by Patankar [8] has been used to solve the incompressible Navier-Stokes equations on unstructured meshes. A cell centred finite volume discretisation of the governing equation based on the work of Mathur and Murthy [9] was developed. The flow analysis algorithm and discretisation method is explained in details in Rahmati et al. [10].

3 Airfoil modifying algorithm

The blade surface pressure coefficient instead of surface velocity is used to modify the blade. This is because the velocity on the surface is considered zero to satisfy the non-slip conditions. The airfoil surface is treated as elastic membrane, which is modified based on the differences between target and calculated pressure coefficient. The airfoil modifying algorithm is based on the method of Dulikravich and Baker [11] who suggested the following linear partial differential equations can be used as a residual corrector to modify the top and bottom contour of the blade respectively:

$$-\beta_1 \partial(\Delta y_{top}) + \beta_2 \partial\ (\Delta y_{top})/\partial s + \beta_3 \partial^2 (\Delta y_{top})/\partial s^2 = \Delta Cp \tag{7}$$

$$\beta_1 \partial(\Delta y_{bottom}) + \beta_2 \partial\ (\Delta y_{bottom})/\partial s - \beta_3 \partial^2 (\Delta y_{bottom})/\partial s^2 = \Delta Cp \tag{8}$$

In equation (7) and equation (8), s is the airfoil contour following coordinate, L_E is the lower airfoil contour length, L is the total airfoil counter length and Δy_{top} and Δy_{bottom} are the blade normal displacement at the top and bottom counter of the airfoil respectively. β_1, β_2, β_3 in equation (7) and equation (8) are user specified coefficients while ΔCp is the local differences between the target and computed surface pressure coefficient i.e.

$$\Delta Cp = Cp^{Target} - Cp^{Calculated} \tag{9}$$

By using two different equations, appropriate boundary conditions for the airfoil shape design such as leading edge closure and stacking conditions can be implemented. The solution of this equation provides the geometry correction, which is used to modify the initial geometry to form a new geometry. If, after having checked the convergence, the design requirements are not satisfied, the design cycle is repeated with the new geometry. The process is repeated until the pressure coefficient differences are negligible.

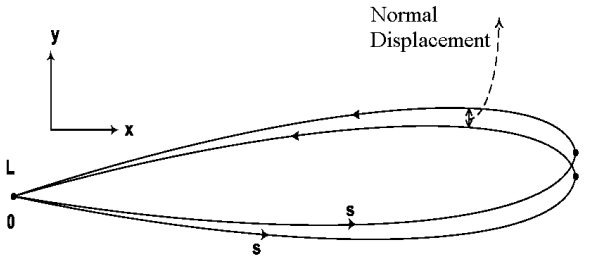

Figure 1: Blade modification method using elastic membrane concept.

Equation (7) and equation (8) are non-homogeneous second order equations with constant coefficients. The complementary functions of these equations for the upper and lower contours are:

$$\Delta y^{top} = C_1 e^{\lambda_1 s} + C_2 e^{\lambda_2 s} \tag{10}$$

$$\Delta y^{Bottom} = C_3 e^{-\lambda_1 s} + C_4 e^{-\lambda_2 s} \tag{11}$$

where

$$\lambda_{1,2} = \frac{-\beta_2 \pm \sqrt{\beta_2^2 + 4\beta_1 . \beta_2}}{2\beta_3} \tag{12}$$

C_1, C_2, C_3 and C_4 are constants that will be computed from the boundary conditions at the leading and trailing edges. To find out the particular integral of equation (7) and equation (8) the surface distribution of ΔCp is represented by utilising the Fourier series expansion as follow:

$$\Delta C_P(s) = a_0 + \sum_{n=1}^{n_{\max}} \left[a_n \cos(N_n s) + b_n \sin(N_n s) \right] \tag{13}$$

where $N_n = 2n\pi/L$ and a_0, a_n and b_n are the Fourier series coefficients. The particular integral of equation (7) and equation (8) are represented in the form of Fourier series as:

$$\Delta y^{top} = A_0^{top} + \sum_{n=1}^{n_{\max}} \left[A_n^{top} \cos(N_n s) + B_0^{top} \sin(N_n s) \right] \tag{14}$$

$$\Delta y^{bottom} = A_0^{bottom} + \sum_{n=1}^{n_{\max}} \left[A_0^{bottom} \cos(N_n s) + B_0^{bottom} \sin(N_n s) \right] \tag{15}$$

The values of A_0, A_n and B_n are found by substitution of equation (14) and equation (15) into equation (7) and equation (8) respectively: These values are as follow:

$$A^{top}_{\ n} = \frac{a_n(\beta_1 + N^2{}_n\beta_3) - b_n(\beta_2 N_n)}{(\beta_1 + N^2{}_n\beta_3) + (\beta_2 N_n)^2} \qquad 0 \le n \le n_{\max} \tag{16}$$

$$B^{top}{}_n = \frac{b_n(\beta_1 + N^2{}_n\beta_3) + a_n(\beta_2 N_n)}{(\beta_1 + N^2{}_n\beta_3) + (\beta_2 N_n)^2} \qquad 1 \le n \le n_{\max} \tag{17}$$

$$A^{bottom}{}_n = -\frac{a_n(\beta_1 + N^2{}_n\beta_3) + b_n(\beta_2 N_n)}{(\beta_1 + N^2{}_n\beta_3) + (\beta_2 N_n)^2} \qquad 0 \le n \le n_{\max} \tag{18}$$

$$B^{bottom}{}_n = -\frac{b_n(\beta_1 + N^2{}_n\beta_3) - a_n(\beta_2 N_n)}{(\beta_1 + N^2{}_n\beta_3) + (\beta_2 N_n)^2} \qquad 1 \le n \le n_{\max} \tag{19}$$

Having found the particular integral and complementary functions of equations (7) and equation (8), the complete solution of these equations are given by the following equations:

$$\Delta y^{top} = C_1 e^{\lambda_1 s} + C_2 e^{\lambda_2 s} + \sum_{n=0}^{n_{\max}} \left[\; A_n^{top} \cos(N_n s) + B_n^{top} \sin(N_n s) \; \right] \tag{20}$$

$$\Delta y^{bottom} = C_3 e^{-\lambda_1 s} + C_4 e^{-\lambda_2 s} + \sum_{n=0}^{n_{\max}} \left[\; A_n^{bottom} \cos(N_n s) + B_n^{bottom} \sin(N_n s) \; \right] \tag{21}$$

Equation (20) and equation (21) contain four unknown constants C_1, C_2, C_3 and C_4. To compute these constants, the following boundary conditions are applied: zero trailing edge displacement, trailing edge closure, leading edge closure, and smooth leading edge. Consequently, these boundary conditions, for the airfoil shown in figure 1, yield four equations with four unknown: C_1, C_2, C_3 and C_4. These constants are found by the following matrix:

$$\begin{bmatrix} C_1 \\ C_2 \\ C_3 \\ C_4 \end{bmatrix} = \begin{bmatrix} 1 & 1 & 0 & 0 \\ 0 & 0 & e^{L\lambda_1} & e^{L\lambda_2} \\ e^{-\lambda_1 L_E} & e^{-\lambda_2 L_E} & -e^{\lambda_1 L_E} & -e^{\lambda_2 L_E} \\ -\lambda_1 e^{-\lambda_1 L_E} & -\lambda_2 e^{-\lambda_2 L_E} & -\lambda_1 e^{\lambda_1 L_E} & -\lambda_2 e^{\lambda_2 L_E} \end{bmatrix}^{-1} \times$$

$$\begin{bmatrix} -\sum_{n=1}^{n_{\max}} A^{bottom}{}_n \\ -\sum_{n=1}^{n_{\max}} A^{top}{}_n \\ \sum_{n=1}^{n_{\max}} \left[\Delta A_{\;n} \cos(N_n L_E) + \Delta B_n \sin(N_n L_E) \; \right] \\ \sum_{n=1}^{n_{\max}} \left[-\Delta A_{\;n} N_n \sin(N_n L_E) + \Delta B_n N_n \cos(N_n L_E) \; \right] \end{bmatrix} \tag{22}$$

where

$$\Delta A_n = A_n^{top} - A_n^{bottom} \tag{23}$$

$$\Delta B_n = B_n^{top} - B_n^{bottom} \tag{24}$$

In the formulation of this method three arbitrary contents; β_1, β_2, β_3 are used. Ideally the design method for different applications should be independent of these user-specified constants. However, the choice of these arbitrary constants controls the convergence and stability of the inverse design. So optimising these values for successful convergence of iterative design procedure in reasonable time is essential. Though, the only method to specify these user-specified values for different applications is based on trail and error. This is the major disadvantage of the method as the success of inverse design depends on the specification of these arbitrary constants. For airfoil design the amount of β_1 =1.2, β_2 =0, β_3=0.4 was considered which are the same values which was proposed by Dulikravich and Baker [11].

4 Mesh movement algorithm

Mesh movement algorithm is an integral part of the current inverse design method as once the blade surface is modified by inverse algorithm the corresponding triangular mesh has to be adapted too. The mesh movement algorithm is based on the linear tension spring analogy concept of Batina [12]. In this method each unstructured meshes edges are modeled as springs with the stiffness inversely proportional to the length of the edges. By displacement of the boundaries of the domain, the spring forces are calculated. Then the displacement of every interior vertex is solved iteratively until all forces are in equilibrium. A linear tension spring analogy is applied here because only the nodal displacements are important and no purely elasticity variables such as local stress or strains. Also this method is a robust method with a low computational cost, see Rahmati [6].

5 Inverse design application

The task of inverse design is usually to improve the performance of a known blade or create a new design based on earlier design that operates under the same conditions. Thus, the initial blade is usually known prior to the design. In the case of inverse design of airfoil, a known airfoil, NACA0012 with zero angle of incidence, is used as an initial blade. The blade modification algorithms of the inverse design method require an initial condition, which is given by a stacking point that remains fixed throughout the iterative design procedure. In this case the stacking point is a point at the trailing edge of the airfoil. This initial condition is required to satisfy the boundary conditions of equation (20) and equation (21).

The NACA0012 airfoil with zero angle of incidence is utilised as an initial blade to re-design of NACA0012 with 6 degree angle of incidence by imposing the target surface pressure coefficient distribution. The air flow velocity is 55 m/s. Figure 2 and figure 3 show the initial airfoil, the airfoil shape after five and ten iterations, the designed airfoil and their corresponding surface pressure coefficients. The meshes of these airfoils, which contain 10216 triangular cells, are shown in figure 4 to figure 7. Twenty five calls to the analysis code are

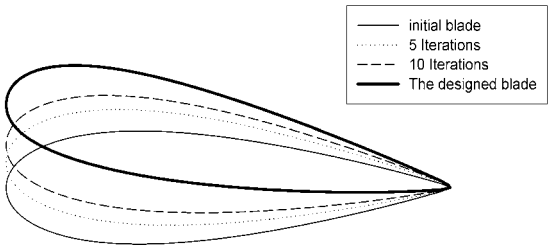

Figure 2: Reproducing NACA0012 airfoil with 6 degree angle of incidence.

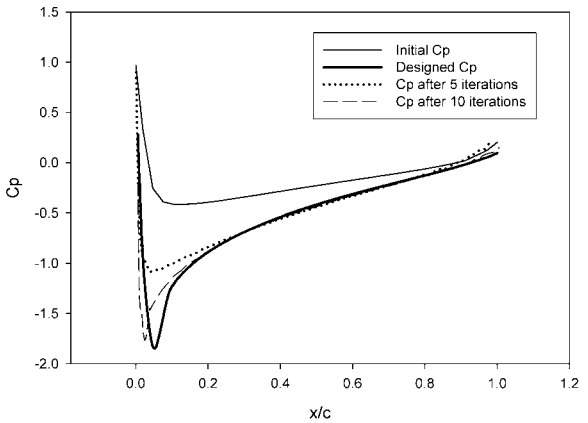

Figure 3: Initial, intermediates and target surface pressure coefficient.

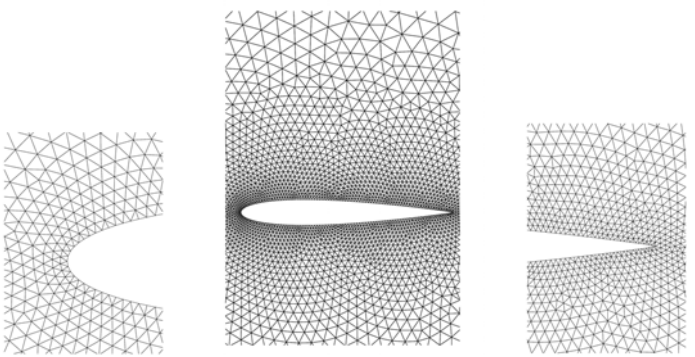

Figure 4: The initial mesh around the blade.

required for the convergence of the geometry. The flow analysis algorithm is considered to be converged when the normalised residuals of the governing equations had reduced to 10^{-4}. The design process for the computation of blade geometry is considered to have converged when the calculated design parameters

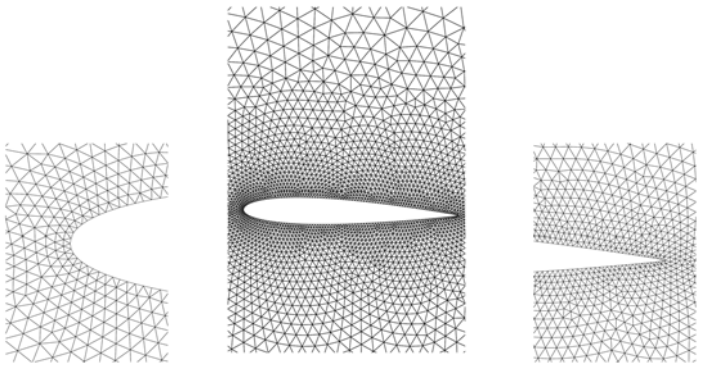

Figure 5: The mesh around the blade after 5 iterations.

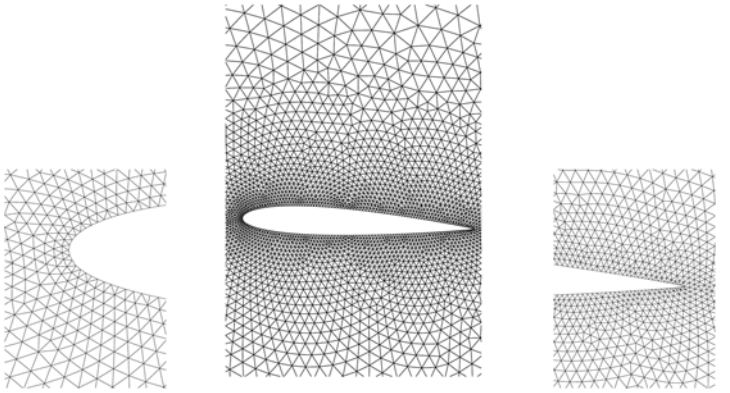

Figure 6: The mesh around the blade after 10 iterations.

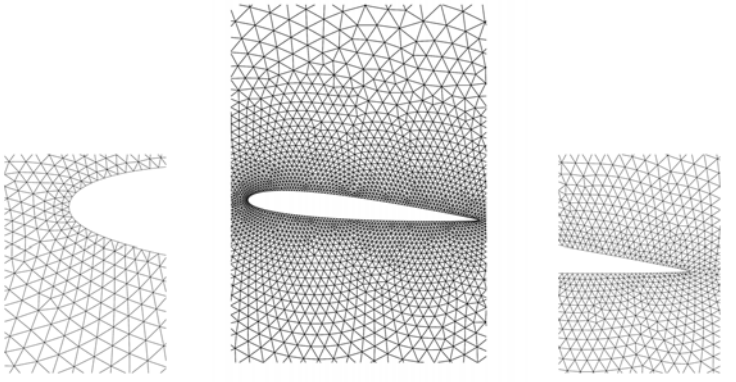

Figure 7: The mesh around the designed blade.

match the target design parameter within the specific tolerance of 1%. This tolerance is defined as the percentage of the discrepancy between the target and calculated design specification.

6 Conclusion

A Navier-Stokes inverse design method based on the specification of surface pressure coefficient distribution on the blade is developed. One of the improvements of the present methods over previous methods is that the flow field is treated as viscous turbulent flow. Also one of the advantages of the current design method and flow analysis algorithm is that they are based on the unstructured meshes. So most complex fluid regions can be meshed automatically which yields to significant reduction in the time and effort required to generate meshes. The capabilities of this design methodology have been verified by reproducing an airfoil based on a target surface pressure coefficient distribution. The numerical results show the efficiency of the method for airfoil inverse design. However the convergence rate of the shape design process relies on the specifications of three arbitrary constants. These arbitrary constants are required in the formulation of the blade modifying algorithm. The method can be extended for three-dimensional inverse design of wings by rewriting equation (7) and equation (8) for three-dimensional surfaces using more arbitrary constants. So, the convergence rate of the shape design process for three-dimensional applications will depend on the specifications of more than three arbitrary constants.

References

[1] Lighthill, M.J., A New Method of Two Dimensional Aerodynamics Design, *Aeronautical Research Council,* London R& M*,* 2112, 1945.

[2] Sobieczky, H., Fung, N.J., & Seebass, R.S., New Method for Designing Shock-Free Transonic Configuration, *AIAA Journal*, (17): pp. 722–729, 1978.

[3] Zangeneh, M., A Compressible Three-Dimensional Design Method for Radial and Mixed Flow Turbomachinery Blades, *International Journal of Numerical Methods in Fluids,* pp. 599–624, 1991.

[4] Demeulenaere, A.R., & Braembussche, V.D, Three-Dimensional Inverse Method for Turbomachinery Blading Design, *Trans. ASME, Journal of Turbomachinery,* (120), pp. 247–255,1998.

[5] Dang, T., & Jiang, J., Design Method for Turbomachine Blades With Finite Thickness By The Circulation Method, *Journal of Turbomachinery,* (119), 1997.

[6] Rahmati, M.T., Incompressible Navier-Stokes Inverse Design Method Based on Unstructured Meshes, PhD *thesis*, University College London, 2006.

[7] Launder, B.E., & Spalding, D.B., Lectures in Mathematical Models of Turbulence, *Academic Press*, London, 1972.

[8] Patankar, S.V., Numerical Heat Transfer and Fluid Flow, *Taylor and Francis*, U.S.A, 1980.
[9] Mathur, S.R., & Murthy, Y.T., A Pressure-Based Method for Unstructured Meshes, *Numerical Heat Transfer,* Part B. 31, pp. 195–215, 1997.
[10] Rahmati, M.T., Charlesworth, D., & Zangeneh, M., Incompressible Navier-Stokes Inverse Design Method Based On Adaptive Unstructured Mesh, *The 13th Annual Conference on Computational Fluid Dynamics*, St. John's, Canada, 2005.
[11] Dulikravich, G. S., & Baker, D.P., Fourier Series Solution for Inverse Design of Aerodynamic Shape, *Inverse Problems in Engineering*, pp. 427–436, 1998.
[12] Batina, J.T., Unsteady Euler Airfoil Solutions Using Unstructured Dynamic Meshes, *AIAA Journal,* 28(8), pp. 1381–1388, 1990.

Simulation of flow in two-sided lid-driven square cavities by the lattice Boltzmann method

D. Arumuga Perumal & A. K. Dass
Department of Mechanical Engineering,
Indian Institute of Technology Guwahati, Guwahati 781039, India

Abstract

Due to the presence of corner eddies that change in number and pattern, the classical one-sided lid-driven cavity problem has been found to be particularly suitable to study various aspects of the performance of solution algorithms for incompressible viscous flows. More recently, the flow induced by the motion of two facing walls (two-sided lid-driven cavity) has also been investigated by Kuhlmann et al. For some aspect ratios this study demonstrates the existence of a multiplicity of solutions. However, for the aspect ratio of unity no multiplicity of solutions has been observed. Also it is found that for parallel motion of the walls, there appears a pair of counter-rotating secondary vortices of equal size near the centre of a wall. Because of symmetry, this pair of counter-rotating vortices has similar shapes and their detailed study as to how they grow with increasing Reynolds number has not yet been made. Such a study is attempted in this paper through the lattice Boltzmann method (LBM), as the problem has the potential of being used for testing various solution methods for incompressible viscous flows. The results for the antiparallel motion of the walls are also presented in detail. As the problem has not been investigated before, to lend credibility to the results they are further compared with those obtained from a finite difference method (FDM) code developed for this purpose.

Keywords: two-sided lid-driven cavity, lattice Boltzmann method, finite difference method, D2Q9 model, bounce-back boundary condition.

1 Introduction

A number of experimental and numerical studies have been conducted to investigate the flow field of a lid-driven cavity flow in recent decades. Ghia et al.

WIT Transactions on Engineering Sciences, Vol 59, © 2008 WIT Press
www.witpress.com, ISSN 1743-3533 (on-line)
doi:10.2495/AFM080051

[1] have applied a multi-grid strategy and presented solutions for Reynolds numbers starting from Re = 100 to as high as Re = 10000. A review on computational and also experimental studies on lid-driven cavity flow can be found in Shankar and Deshpande [2]. They have studied and analyzed corner eddies, nonuniqueness, transition and turbulence in the lid-driven cavity. Kuhlmann et al. [3] have done several experiments on a two-sided lid-driven cavity with various spanwise aspect ratios. Blohm and Kuhlmann [4] experimentally investigated the incompressible fluid flow in a rectangular container driven by two facing sidewalls that move steadily in an anti-parallel direction up to Reynolds number 1200.

Albensoeder et al. [5] were the first to investigate the nonlinear regime and found multiple two-dimensional states. They have found seven and five flow states in antiparallel and parallel motion respectively. Kalita et al. [6] developed an HOC algorithm for Stream-function vorticity formulation of the 2D N-S equations on graded Cartesian meshes. They used the algorithm to compute the flow in a two-sided 2D lid-driven cavity [7] where, besides wall shear, free shear flow is also encountered.

Many researchers [9] carried out simulations of one-sided lid-driven cavity flow by lattice Boltzmann method. Yong G Lai et al. [10] compared the lattice Boltzmann method and the finite volume Navier-Stokes solver and concluded that bounce-back boundary condition has better than first order accuracy. The present work uses lattice Boltzmann BGK model (LBGK) with single time relaxation and bounce-back boundary condition to investigate the flow driven by parallel and antiparallel motion of two facing walls in a square cavity for Reynolds number up to 2000. A nine-bit square lattice incompressible LB model in 2D space has been used in the present work since it is known to give more accurate results compared to seven-bit incompressible LB model.

The rest of the paper is organized as follows. In Section 2, LBGK with single time relaxation and 2D nine-velocity lattice model is defined. The numerical procedures for LBM and stream function-vorticity based FDM is also described in this section. In Section 3, the two-sided lid-driven cavity problem is described and the results from LBM simulation with parallel and antiparallel motion of the walls are presented. The results are discussed in Section 4. Based on the results obtained concluding remarks are made in Section 5.

2 Numerical methods

2.1 Lattice Boltzmann method

The lattice Boltzmann method represents an alternative possibility for the direct simulation of the incompressible flow. It has been shown that the accuracy of the lattice Boltzmann method is of second order both in space and time [9]. The lattice Boltzmann equation, which can be linked to the Boltzmann equation in kinetic theory, is formulated as [8]

$$f_i(\mathbf{x} + c_i\Delta t, t + \Delta t) - f_i(\mathbf{x}, t) = \Omega_i \tag{1}$$

where f_i is the particle distribution function, c_i is the particle velocity along the ith direction and Ω_i is the collision operator. The so-called lattice BGK model

with single time relaxation, which is a commonly used lattice Boltzmann method, is given by

$$f_i(\mathbf{x} + c_i\Delta t, t + \Delta t) - f_i(\mathbf{x}, t) = -\frac{1}{\tau}\left(f_i(\mathbf{x},t) - f_i^{(0)}(\mathbf{x},t)\right) \tag{2}$$

Here $f_i^{(0)}(\mathbf{x},t)$ is the equilibrium distribution function at **x**,t and τ is the time relaxation parameter.

The D2Q9 square lattice used here has nine discrete velocities. A square lattice with unit spacing is used on each node with eight neighbours connected by eight links. Particles residing on a node move to their nearest neighbours along these links in unit time step. The occupation of the rest particle is defined as f_0. The occupation of the particles moving along the axes are defined as f_1, f_2, f_3, f_4, while the occupation of diagonally moving particles are defined as f_5, f_6, f_7, f_8. The particle velocities are defined as

$$\begin{aligned} \mathrm{c}_i &= 0, \quad i = 0 \\ \mathrm{c}_i &= (\cos(\pi/4(i-1)), \sin(\pi/4(i-1))), \quad i = 1, 2, 3, 4 \\ \mathrm{c}_i &= \sqrt{2}(\cos(\pi/4(i-1)), \sin(\pi/4(i-1))), \quad i = 5, 6, 7, 8. \end{aligned} \tag{3}$$

The macroscopic quantities such as density ρ and momentum density ρu are defined as velocity moments of the distribution function f_i as follows:

$$\rho = \sum_{i=0}^{N} f_i, \tag{4}$$

$$\rho u = \sum_{i=0}^{N} f_i c_i. \tag{5}$$

The density is determined from the particle distribution function. The density and the velocities satisfy the Navier-Stokes equations in the low-Mach number limit by using the Chapman-Enskog expansion [8]. In the nine-velocity square lattice, a suitable equilibrium distribution function has been proposed [9] with,

$$\begin{aligned} f_i^{(0)} &= \frac{4}{9}\rho\left[1 - \frac{3}{2}u^2\right], \quad i = 0 \\ f_i^{(0)} &= \frac{1}{9}\rho\left[1 + 3(c_i.u) + 4.5\,(c_i.u)^2 - 1.5\,u^2\right], \quad i = 1, 2, 3, 4 \\ f_i^{(0)} &= \frac{1}{36}\rho\left[1 + 3(c_i.u) + 4.5\,(c_i.u)^2 - 1.5\,u^2\right], \quad i = 5, 6, 7, 8 \end{aligned} \tag{6}$$

where the lattice weights are $w_0 = 4/9$, $w_1 = w_2 = w_3 = w_4 = 1/9$ and $w_5 = w_6 = w_7 = w_8 = 1/36$. The relaxation time τ is related to the viscosity by

$$\tau = \frac{6\upsilon - 1}{2} \tag{7}$$

where υ is the kinematic viscosity. It was seen that $\tau = 0.5$ is the critical value for ensuring a non-negative kinematic viscosity. Numerical instability can be expected for τ close to this critical value. This situation takes place at high Reynolds numbers. In this work Reynolds numbers up to 2000 in a lattice size of 257^2 have been investigated.

In LBM several boundary conditions have been proposed [10]. The bounce-back scheme was used in these simulations to copy the velocity no-slip condition

on walls. In this scheme, the particle distribution function at the wall lattice node is assigned to be the particle distribution function of its opposite direction. The basic argument for the use of 'on-grid bounce-back model' is that it is both mathematically applicable and quite relevant for LBE simulations of fluid flows in simple bounded domains. For this reason, this boundary condition has been employed here on the two stationary walls. However for the moving walls, the equilibrium boundary condition is applied [9]. At the lattice nodes on the moving walls, flow-variables are re-set to their pre-assumed values at the end of every streaming-step. A lid-velocity of U = 0.1 has been considered in this work.

2.1.1 Numerical algorithm

The velocities at all nodes except those on the moving walls are assumed to be zero at the time of starting the simulation. Initially, the equilibrium distribution function that corresponds to the flow-variables is assumed as the unknown particle distribution function for all nodes at t = 0. Uniform density ρ = 1.0 is imposed initially.

The solution procedure of the LBM at each time step comprise streaming and collision step, application of boundary conditions, calculation of particle distribution function followed by calculation of macroscopic variables.

The lattice Boltzmann Equation (LBE) is solved in the solution domain subjected to the above initial and boundary conditions on a uniform 2D mesh. It is seen that the numerical algorithm of the LBM is relatively simpler compared with conventional Navier-Stokes methods. Another benefit of the present approach is the easiness of programming.

2.2 Finite difference (FD) stream function-vorticity based solver

As the LBM method is intended to be used to compute an unexplored problem, need was felt to develop a finite difference code to attack the same problem thus providing a basis for comparison. The FD code numerically solves the 2D Navier-Stokes equation in stream function-vorticity formulation given by

$$\frac{\partial^2 \psi}{\partial x^2} + \frac{\partial^2 \psi}{\partial y^2} = -\omega \tag{8}$$

$$\frac{\partial \omega}{\partial \mathrm{t}} + u\frac{\partial \omega}{\partial x} + v\frac{\partial \omega}{\partial y} = \frac{1}{Re}\left(\frac{\partial^2 \omega}{\partial x^2} + \frac{\partial^2 \omega}{\partial y^2}\right). \tag{9}$$

In the code all space derivatives are centrally differenced and ADI method is used for time integration to the steady state. This code will provide a legitimate basis for comparison only after it has been validated and this exercise is presented in the next sub-section.

2.3 Code validation

The developed FD code is used to compute the single lid-driven flow in a square cavity on a 129^2 grid. Well established results computed by Ghia et al. [1] exist for the same problem on a similar grid and this work is used for validating the present FD code. Figure 1 shows the steady-state u-velocity profile along a

vertical line passing through the geometric centre of the cavity at Re = 1000. Here the top lid moves from left to right and it is observed that the agreement between our FD results and those of Ghia et al. [1] is excellent. The same figure also displays our LBM results, which again are in excellent agreement with the two results described earlier. In the next section the LBM results for the unexplored two-sided lid-driven cavity flow will be presented and the credibility of these results will be established through comparison with the results of the FD code.

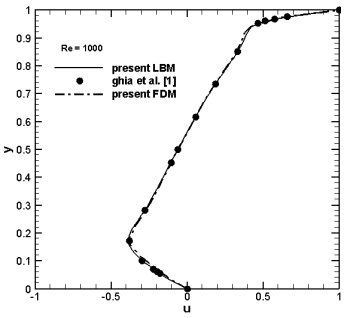

Figure 1: u-velocity profile at the vertical centreline for single lid-driven square cavity flow (Re = 1000).

3 Two-sided lid-driven cavity flow

An incompressible viscous flow in a square cavity whose top and bottom walls move in the same (parallel motion) or opposite (antiparallel motion) direction with a uniform velocity is the problem investigated in the present paper. In the case of parallel wall motion, a free shear layer exists midway between the top and bottom walls apart from the wall bounded shear layers whereas in the case of antiparallel wall motion, only wall bounded shear layers exist.

3.1 Parallel wall motion

LBM results on a lattice size of 257× 257 for the parallel wall motion are shown in Figure 2. When both the walls, say, the top and the bottom move in the same direction with the same velocity, the streamlines are found to be symmetric with respect to a line parallel to these walls and passing through the cavity centre. Figure 2(a) shows the streamline pattern for the parallel wall motion at Re = 100 with the top and bottom walls moving from left to right. Two counter-rotating primary vortices symmetric to each other are seen to form with a free shear layer in between. At this Reynolds number the primary vortex cores are seen to be somewhat away from the centres of the top and bottom halves of the lid-driven cavity towards the right-hand top and right-hand bottom corners respectively. At Re = 400 (Figure 2(b)), apart from the primary vortices two counter-rotating secondary vortices symmetrically placed about the horizontal centreline are seen to appear near the centre of the right wall. Figures 2(c) and 2(d) show the

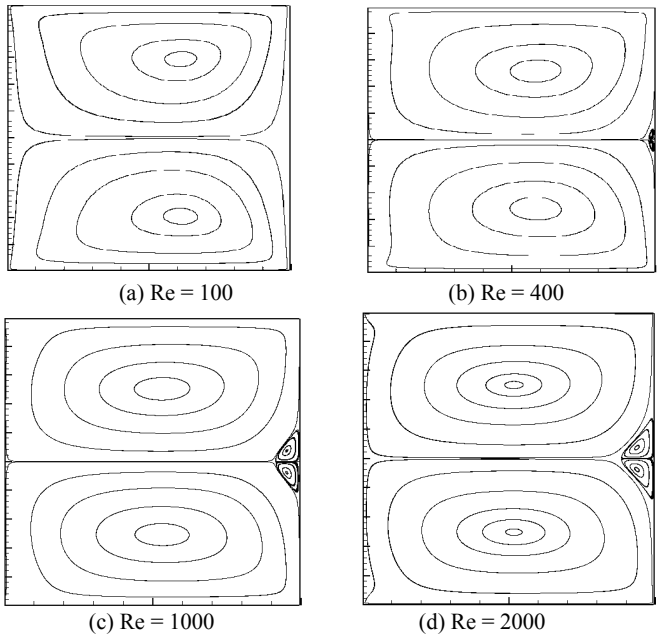

Figure 2: Streamline pattern for parallel wall motion at (a) Re = 100 (b) Re = 400 (c) Re = 1000 and (d) Re = 2000 by LBM on a 257^2 lattice.

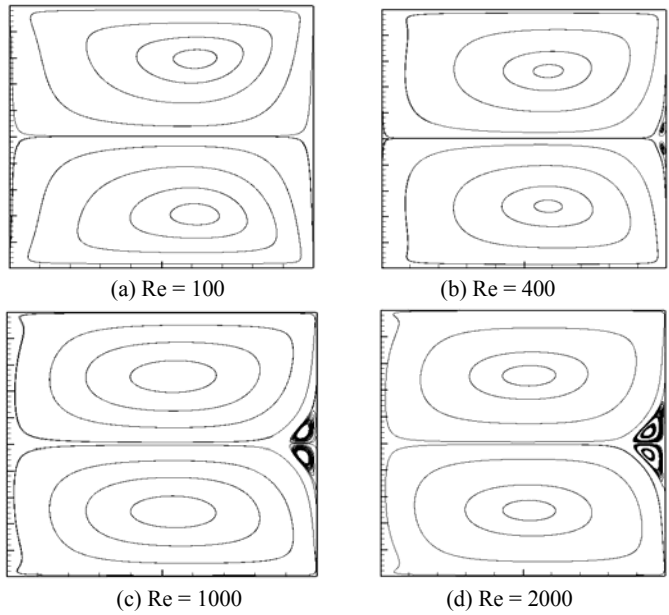

Figure 3: Streamline pattern for parallel wall motion at (a) Re = 100 (b) Re = 400 (c) Re = 1000 and (d) Re = 2000 by FDM on a 129^2 grid.

streamline patterns at Re = 1000 and Re = 2000 respectively. From Figure 2 it is observed that as the Reynolds number increases the cores of the primary vortices move from near the top right and bottom right corners to the centres of the top and bottom halves of the cavity respectively. Also as the Reynolds number increases the secondary vortices near the centre of the right wall grow in size. The counter-rotating pairs of primary and secondary vortices maintain their centro-symmetry for all the Reynolds number investigated in this work. As mentioned earlier these results are now substantiated by comparison with the results given by the validated FDM code. Figure 3 shows the FDM streamline patterns on a 129^2 grid for Re = 100, 400, 1000 and 2000 as before. Comparison with Figure 2 shows that LBM streamline patterns compare very well with those for the FDM. Figure 4(a) shows the comparison for horizontal velocity along the vertical centreline of the cavity and Figure 4(b) shows the comparison of vertical velocity on a horizontal line at a height of three quarters from the bottom wall. Agreement of the velocity profiles given by both methods is again excellent. Table 1 gives the locations of the vortices given by LBM and FDM for Re = 100, 400, 1000, 1500 and 2000. All these results show that the agreement is very good thus lending credibility to the results for these unexplored problems.

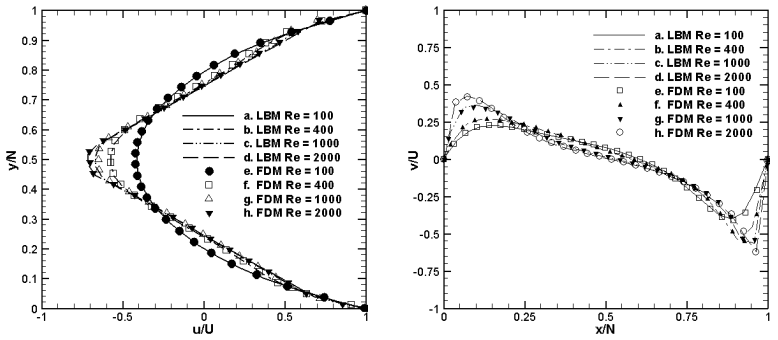

(a) (b)

Figure 4: For parallel wall motion (a) u-velocity along vertical line passing through x = 0.50 (b) v-velocity along horizontal line passing through y = 0.75.

3.2 Antiparallel wall motion

LBM results on a lattice size of 257^2 for the antiparallel wall motion are shown in Figure 5. When both the walls move in opposite direction with the same velocity, top to the right and bottom to the left in this paper, a single primary vortex centred at the geometric centre of the cavity is formed (Figures 5(a) and 5(b)). These two figures show the streamline patterns for Re = 100 and 400 respectively. Figures 5(c) and 5(d) show the streamline patterns for Re = 1000 and 2000, which show the appearance of also two secondary vortices near the top left and the bottom right corners of the cavity. It may be noted that the corresponding vortex for a single lid-driven cavity flow does not appear at a Reynolds number as low as 1000 but much later (i.e. at a higher value beyond

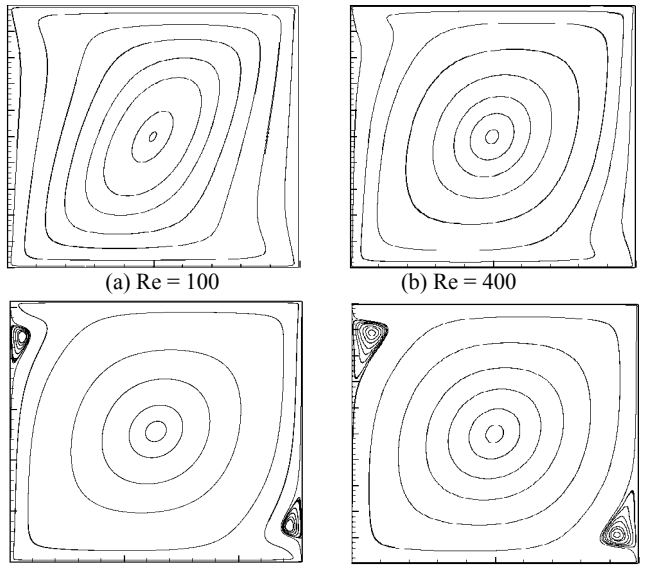

Figure 5: Streamline pattern for antiparallel wall motion at (a) Re = 100 (b) Re = 400 (c) Re = 1000 and (d) Re = 2000 by LBM on a 257^2 lattice.

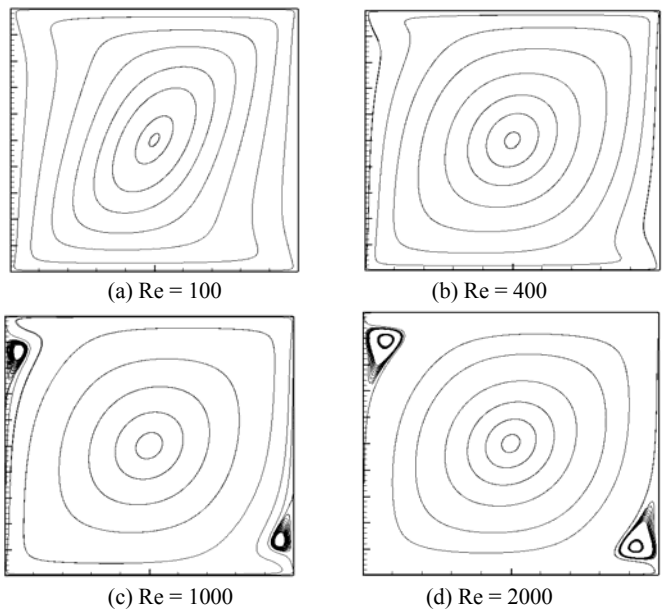

Figure 6: Streamline pattern for antiparallel wall motion at (a) Re = 100 (b) Re = 400 (c) Re = 1000 and (d) Re = 2000 by FDM on a 129^2 lattice.

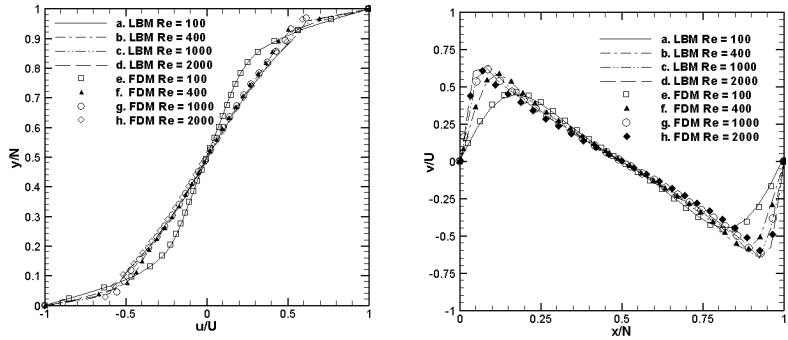

(a) (b)

Figure 7: For antiparallel wall motion (a) u-velocity along vertical line passing through x = 0.50 (b) v-velocity along horizontal line passing through y = 0.50.

Table 1: Locations of the vortices for parallel wall motion: a. FDM, b. LBM.

Re	Primary vortex centres				Secondary vortex centres			
	Bottom		Top		Bottom		Top	
	x	y	x	y	x	y	x	y
100	a. 0.6146	0.2025	0.6146	0.7956	…	…	…	…
	b. 0.6145	0.2024	0.6145	0.7949	…	…	…	…
400	a. 0.5844	0.2387	0.5844	0.7552	0.9872	0.4636	0.9872	0.5262
	b. 0.5845	0.2388	0.5845	0.7549	0.9875	0.4713	0.9874	0.5283
1000	a. 0.5352	0.2453	0.5352	0.755	0.9550	0.4572	0.9550	0.5408
	b. 0.5314	0.2431	0.5314	0.7556	0.9528	0.4619	0.9528	0.5365
1500	a. 0.5245	0.2453	0.5267	0.7528	0.9444	0.4572	0.9443	0.5429
	b. 0.5234	0.2434	0.5234	0.7518	0.9434	0.4569	0.9433	0.5385
2000	a. 0.5132	0.2474	0.5132	0.7528	0.9400	0.4573	0.9400	0.5478
	b. 0.5108	0.2489	0.5108	0.7497	0.9378	0.4598	0.9377	0.5389

2000). It has also been observed that primary vortex centre remains at the geometric centre of the cavity even for these higher values of Re = 1000 and 2000. However the size of the secondary vortices are seen to increase between Re = 1000 and 2000. Similar increase in size of the secondary vortices with Reynolds numbers was also observed for the parallel wall motion. These results are now substantiated by comparison with the results of the validated FDM code. Figure 6 gives for the same configuration the FDM streamline patterns on a 129^2 grid for Re = 100, 400, 1000 and 2000. Comparisons with Figure 5 shows that LBM streamline patterns compare very well with those for the FDM. Figures 7(a) and 7(b) show the comparison between LBM and FDM for the horizontal velocity along the vertical centreline and the vertical velocity along the horizontal centreline and the agreement is excellent once again.

Table 2: Locations of the vortices for antiparallel motion: a. FDM, b. LBM.

Re	Primary Vortex (PV)		Secondary Vortices (SV)			
	x	y	Bottom Right		Top Left	
			x	y	x	y
100	a. 0.4999 b. 0.5002	0.5001 0.5001	… …	… …	… …	… …
400	a. 0.5002 b. 0.5001	0.4980 0.4982	… …	… …	… …	… …
1000	a. 0.5007 b. 0.5012	0.4981 0.4982	0.9507 0.9512	0.1319 0.1326	0.0492 0.0449	0.8663 0.8609
1500	a. 0.5005 b. 0.5010	0.4982 0.4979	0.9214 0.9336	0.1146 0.1175	0.0727 0.0642	0.8856 0.8829
2000	a. 0.5003 b. 0.5002	0.5001 0.4991	0.9229 0.9250	0.1082 0.1082	0.0791 0.0727	0.8920 0.8855

Table 2 gives the locations of the vortices given by LBM and FDM for Re = 100, 400, 1000, 1500 and 2000. It is seen that LBM results given by the figures and the table are in excellent agreement with the FDM results produced through the validated code. This lends credibility to the current LBM results for this unexplored problem.

References

[1] Ghia, U. Ghia, N. & Shin, T., High-Re solutions for incompressible flow using N-S eqns and a multigrid method. J. Comp. Phys, 43, pp. 387–441, 1982.

[2] Shankar, P.N. & Deshpande, M.D., Fluid Mechanics in the Driven Cavity. Ann. Rev. of Fluid Mech, 32, pp. 93–136, 2000.

[3] Kuhlmann, Wanschura, & Rath, J., Flow in 2-sided lid-driven cavities: non-uniqueness, instability, cellular structures. J. F. Mech, 336 pp 267–299, 2001.

[4] Blohm, H. & Kuhlmann, C., The two-sided lid-driven cavity: experiment on stationary and time-dependent flows. J. Fluid Mech, 450, pp. 67–95, 2002.

[5] Albensoeder, S. Kuhlmann, C. & Rath J., Multiplicity of steady 2-D flow in two-sided lid-driven cavities. The Com. fluid Dym, 14, pp. 223–241, 2001.

[6] Kalita, J.C. Dass, A.K. & Dalal, D., A trans.-free HOC scheme for steady conv-diff. on nonuniform grid. I. J. N. Me in Engg, 38, pp. 3497–3521, 2004.

[7] Kumar, N, Kalita, C, & Dass, A.K., HOC computation of 2-Sided lid-driven cavity flow. Int Con on Com. Mech & Sim, Vol 2 B073, 1695–1701, 2006.

[8] He, X. & Luo, L.S., Theory of the LBM: From the Boltzmann eqn to the lattice Boltzmann eqn. Phys. Rev. E, 56, pp. 6811–6817, 1997.

[9] Hou, S. Zou, Q. Chen, S. Doolen, G. & Cogley, A.C., Simulation of Cavity Flow by the LBM. J. of Comput. Phys, 118, pp. 329–347, 1995.

[10] Lai, G. Lin, L. & Huang, J., Accuracy and Efficiency study of a LBM for steady-state flow simulation. Num. Heat Transfer-B, 39, pp. 21–43, 2001.

Validation of a CFD model for flow in meandering rivers using an experimental test-setup: first results

K. Delecluyse[1], W. Brantegem[1], P. Troch[1], R. Verhoeven[1] & J. Vierendeels[2]
[1]*Laboratory of Hydraulics, Department of Civil Engineering, Ghent University, Ghent, Belgium*
[2]*Department of Flow, Heat and Combustion Mechanics, Ghent University, Ghent, Belgium*

Abstract

A 3D Reynolds Averaged Navier Stokes (RANS) model of a meandering channel with rectangular cross-section has been developed using the commercial software package FLUENT 6.2. This model solves the 3D Navier-Stokes equations using the PISO scheme for the pressure-velocity coupling and the realizable k-ε model for turbulence closure. Output of the numerical model is compared to validation experiments conducted in a physical model, which represents two wavelengths of a regime channel and allows for the measurement of flow patterns at several discharges and variable bed forms. The computed water depths and velocity profiles of the CFD model output are in good agreement with the physical model results. The simulations slightly underpredict the streamwise velocities, which reach a maximum just before the apex of the meander bend, at the inner bank in the lower part of the flow depth. The CFD model also captures the motion of the secondary current or transverse flow well, showing the same direction of current along the entire second wavelength.

Keywords: CFD, numerical model, meandering rivers, open channel flow, experimental results.

WIT Transactions on Engineering Sciences, Vol 59, © 2008 WIT Press
www.witpress.com, ISSN 1743-3533 (on-line)
doi:10.2495/AFM080061

1 Introduction

During the last century, a large number of rivers have been artificially straightened in order to improve the manoeuvrability of ships, ease the drainage of rain water and make more space for expanding urban areas. These measures however brought along a number of drawbacks. Nowadays, the trend in river management is to give the river back its former space and to restore its natural flow and meandering pattern.

In order to accurately predict this remeandering process of artificially straightened rivers, a detailed knowledge of the flow characteristics and sediment transport processes in meandering river bends is required. The study of two- and three-dimensional flow in open channels has recently experienced a surge of interest in the application of computational fluid dynamics (CFD) to hydrological and geomorphological problems, showing great potential in those problems where the spatio-temporal boundary conditions may vary over a wide range, thus often making field study either impracticable or impossible.

In this paper a 3D CFD model is presented to investigate and predict the flow in a meandering river. To validate the numerical model, an experimental model was built which represents two wavelengths of a regime channel. Previous studies have shown that combining the numerical models with a physical model is a useful method to validate the numerical output, although it can be difficult to trace whether any differences between the two are caused by numerical simplifications or experimental errors (e.g. Olsen and Kjellesvig [1]; Rajendran et al [2]). A first set of experiments with rectangular, fixed cross-section and steady discharge rate was performed, and the results are presented in this paper. Both the experimental and numerical results are compared to the theory of flow in a meandering river, and discussed in detail.

2 Experimental model

The experimental model shown in Figure 1 represents two wavelengths of a regime channel, the dimensions of which were determined according to Williams [3]. At the inlet, the discharge is determined by means of a calibrated triangular weir. Before entering the channel geometry, the water flows through a series of parallel tubes, to ensure a uniform velocity profile. At the outlet, the water flows over a rectangular weir with adjustable height, and is collected in a container after which the water gets pumped into the inlet construction again, thus forming a closed circuit. The sides and bottom of the entire second wavelength are made out of a transparent material to allow for the future use of Particle Image Velocimetry (PIV) measurement techniques. In the early stages of the research, this model is solely used to measure velocity profiles in a meander bend, without incorporating sediment transport processes. For this reason, the rectangular cross section and the discharge remain constant during the experiment. Later on, when the sediment transport module will be introduced into the numerical model, the experimental model will be adjusted to enable variable cross-sections and discharges.

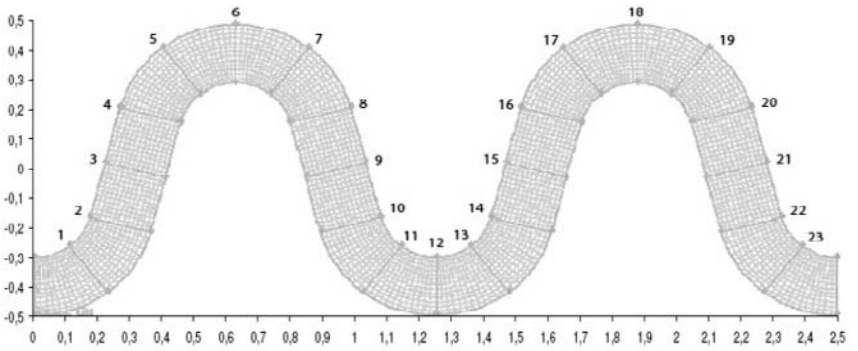

Figure 1: Geometry and computational grid for the experimental and numerical models. Indicated dimensions are in [m]. The numbers refer to the cross-sections in which velocity measurements were performed.

3 Hydrodynamic model

3.1 Model equations

The flow field is determined by the following Reynolds-averaged Navier-Stokes (RANS) and continuity equations, written in cartesian coordinates:

$$\frac{\partial u_i}{\partial x_i} = 0 \tag{1}$$

$$\frac{\partial u_i}{\partial t} + \frac{\partial (u_i u_j)}{\partial x_i} = -\frac{1}{\rho}\frac{\partial p}{\partial x_i} + \frac{1}{\rho}\frac{\partial \tau_{ij}}{\partial x_j} + F_i \tag{2}$$

where u_i (i = 1, 2, 3) are the velocity components; F_i is the gravity force per unit volume; ρ = fluid density and p = pressure. The effective shear stresses τ_{ij} are calculated with the k-ε turbulence model (Rodi [4]), which employs the eddy viscosity relation

$$\tau_{ij} = \rho(\nu + \nu_t)\left(\frac{\partial u_i}{\partial x_j} + \frac{\partial u_j}{\partial x_i}\right) - \frac{2}{3}\delta_{ij}k \tag{3}$$

with

$$\nu_t = c_\mu k^2/\varepsilon \tag{4}$$

where the turbulent kinetic energy k and its dissipation rate ε determining the eddy viscosity ν_t are obtained from the following model equations:

$$\frac{\partial k}{\partial t} + \frac{\partial (u_j k)}{\partial x_j} = \frac{\partial}{\partial x_j}\left(\frac{\nu_t}{\sigma_k}\frac{\partial k}{\partial x_j}\right) + G - \varepsilon \tag{5}$$

$$\frac{\partial \varepsilon}{\partial t} + \frac{\partial (\varepsilon)}{\partial x_j} = \frac{\partial}{\partial x_j}\left(\frac{\nu_t}{\sigma_\varepsilon}\frac{\partial \varepsilon}{\partial x_j}\right) + (c_{\varepsilon 1} G - c_{\varepsilon 2}\varepsilon)\frac{\varepsilon}{k} \tag{6}$$

with

$$G = \nu_t\left(\frac{\partial u_i}{\partial x_j} + \frac{\partial u_j}{\partial x_i}\right)\frac{\partial u_i}{\partial x_j} \tag{7}$$

the production of k. The following values of the model coefficients are used: c_μ = 0.09; $c_{\varepsilon 1}$ = 1.44; $c_{\varepsilon 2}$ = 1.9; σ_k = 1 and σ_ε = 1.2.

3.2 Water depth calculations

In this paper, the Volume of Fluid Technique (VOF, Hirt and Nichols [5]) has been incorporated into the solution of the Navier-Stokes equations in order to predict the water surface elevation, as opposed to a 'fixed lid approach'. For use of the latter, detailed knowledge of the river bathymetry is absolutely necessary, as any incorrect 'fixed lid' will affect the distribution of the mass and momentum of the fluid flow in the numerical simulation, leading to errors in the prediction of bed shear stress, and consequently, bed load transport (Ma et al [6]). Although the model presented in this paper does not yet include a sediment transport module, such a module will be implemented in the near future. Therefore, the VOF technique was selected for water depth calculations.

Using the VOF technique, the flow consists of two phases: water and air. The volume fraction of the water, F, is introduced in each computational cell and is defined as follows:

$$F = \frac{\delta\Omega_{water}}{\delta\Omega_{cell}} \tag{8}$$

where $\delta\Omega_{cell}$ is the volume of the computational cell and $\delta\Omega_{water}$ is the fraction of the cell filled with water. Thus, the following applies:

$$\begin{cases} F = 1, \quad cell\ is\ full\ of\ water \\ F = 0, \quad cell\ is\ full\ of\ air \\ 0 < F < 1, \quad cell\ is\ filled\ with\ water\ and\ air \end{cases} \tag{9}$$

The governing fluid flow equations for the water flow and the air flow above the water are expressed in a single form as given by eqns. (1) and (2), but the physical properties that appear in eqns. (1) and (2) are different and are defined by the volume-fraction-weighted average of physical properties of the air and water as follows:

$$\rho = F\rho_{water} + (1 - F)\rho_{air} \tag{10}$$

$$\mu = F\mu_{water} + (1 - F)\mu_{air} \tag{11}$$

According to the law of mass conservation of air and water, the volume fraction of the water satisfies

$$\frac{\partial F}{\partial t} + u_i \frac{\partial F}{\partial x_i} = 0 \tag{12}$$

By numerically solving the volume fraction eqn. (12), the volume fractions of water, F, and of air, 1-F, in a control volume cell may be obtained.

3.3 Boundary conditions

As upstream boundary condition, the velocity distribution for both phases and the water depth are given, consistent with the water discharge through the model. At the downstream end the water depth is specified, along with a zero gradient

boundary condition. At the river bed, the standard wall function (Launder and Spalding [7]) is employed, given by:

$$u^+ = \frac{1}{\kappa} ln(Ey^+) - \Delta B(K_s^+) \quad (13)$$

with $u^+ = u/u^*$, $y^+ = y/y^*$, $K_s^+ = K_s/y^*$,$y^* = \nu/u^*$ and $u^* = (\tau_w/\rho)^{1/2}$. In this, u is the fluid velocity parallel to the solid wall, y is the distance from the wall, u* is the wall friction velocity, K_s is the wall roughness height, E is a constant taking a value of 9.8, ΔB is an expression dealing with hydraulically rough beds, κ is Von Karman's constant which usually takes a value of 0.4187, ν is the dynamic viscosity of the fluid and τ_w is the shear stress at the solid wall boundaries. In the study reported in this paper, a smooth bed and vertical banks have been employed in the model, so that ΔB=0. The turbulent kinetic energy k and dissipation rate ε of the fluid flow at the upstream and downstream boundaries are determined by specifying the turbulent intensity of the fluid flow. In this paper a turbulent intensity of 10% was assumed for both upstream and downstream boundaries (Ma et al [6], Nallasamy [8]).

3.4 Solution strategy

Having set up the grid and specified the necessary boundary conditions, the governing fluid flow equations are solved by means of the control volume method. The Power Law scheme (Patankar [9]) is used for the space discretisation of the convection terms, while a second order implicit scheme is used for the discretisation of the transient terms. For pressure-velocity coupling, the PISO scheme is employed (Issa [10]). This scheme is part of the SIMPLE (Patankar [9]) family of algorithms and is based on the higher degree of the approximate relation between the corrections for pressure and velocity. The main idea of the PISO algorithm is to move the repeated calculations required by SIMPLE and SIMPLEC inside the solution stage of the pressure-correction equation. After one or more additional PISO loops, the corrected velocities satisfy the continuity and momentum equations more closely. The PISO algorithm takes a little more CPU time per solver iteration, but it can dramatically decrease the number of iterations required for convergence, especially for transient problems.

4 Results

In order to validate the numerical model, physical model experiments were conducted, along with several numerical experiments, in which the sensitivity of the computations to changes in model parameters was tested. The following section discusses the main results obtained from these experiments.

4.1 Water depth

A first experiment was conducted with the outlet height at 5 cm, and a steady discharge Q of 2 l/s. Measurements along the experimental channel length show that the numerically computed water depths are a very accurate representation of

the water depths in the physical model. Moreover, the water depth drops in the inner bends and rises in the outer bends, in agreement with the theory of flow through meander bends.

To investigate the influence of the discharge on the computed water depths, a second numerical experiment was conducted, with the discharge set at 2.5 l/s. Because the type of weir at the outlet remains the same in all experiments, the numerical results can be validated by means of the calibration formula for the outlet weir

$$Q = \frac{2}{3} C_d b h^{\frac{3}{2}} \sqrt{2g} \tag{14}$$

with Q the discharge, b the outlet width, h the water height above the outlet weir, g the gravitational acceleration and C_d the dimensionless discharge coefficient. For the same type of outlet, the value of C_d is a constant. For both experiments the value of h was calculated by subtracting the height of the outlet weir from the computed water depth, and was substituted in eqn. (14). This yielded a C_d of 0.822 for the first experiment and a C_d of 0.812 for the second experiment. Thus, it can be concluded that the numerical model accurately predicts the water depths for any value of the discharge Q.

In a third numerical experiment, the height of the outlet weir was changed from 5 cm to 6 cm, with a discharge of 2 l/s. According to eqn. (14), the value of the overflow height h should remain unaffected by this change. Calculation of h for the first experiment yielded a value of 2.64 cm, and a value of 2.58 cm for the third experiment. Thus, it can be concluded that the numerical model adapts very well to changes of the height of the outlet weir and calculates the water depths accordingly.

4.2 Velocity profiles

Velocity measurements were carried out in several cross sections along the experimental channel length, by means of an electromagnetic velocity meter. Each cross section consists of 12 measuring points. Analysis of the measurements shows that the streamwise velocity reaches its maximum value at the inner bank, right before the apex of the meander bend. For each cross-section, values of the streamwise velocity are higher at the inner bank than at the outer bank, and reach their minimum values at the bottom, as is to be expected. Fig. 2 shows the experimentally measured and numerically computed streamwise velocities for cross-section 17. Comparison shows that the computed velocities agree reasonably well with the measured velocities, only slightly underpredicting the higher values at the top of the section. The numerical velocity profiles are according to the theoretical profiles. Because of technical limitations, the measuring grid for the velocity measurements in this first set of experiments was too coarse to determine a full experimental velocity profile. In a next series of experiments, PIV measurements of the cross sections will be conducted, providing a more accurate representation of the physical velocity profiles. This will allow for a more detailed comparison of the measured and computed velocities, and a better evaluation of the overall accuracy of the numerical computations.

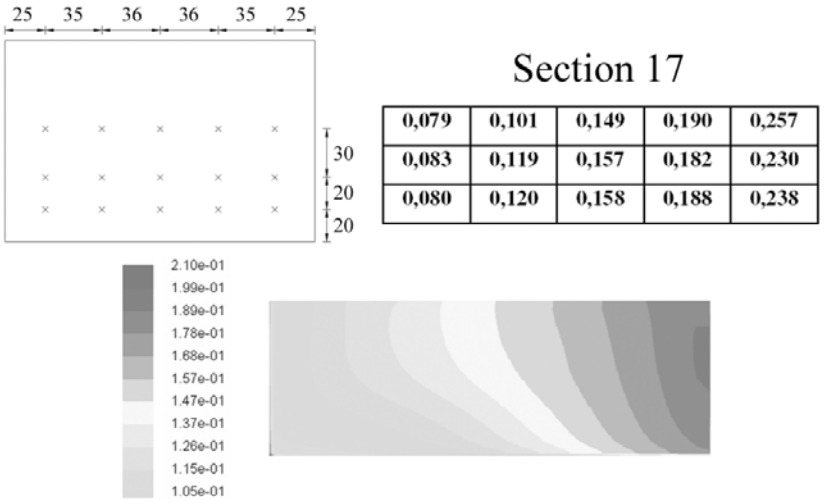

Figure 2: Comparison of experimentally measured and numerically modelled streamwise velocities at cross-section 17. Reported values are in [m/s]. Upper left frame: distribution of measuring points, dimensions are in [cm]; upper right frame: experimental streamwise velocities measured with the electromagnetic flow meter; bottom frame: contour plot of numerical results.

4.3 Secondary current

In order to see whether or not the numerical model captures the motion of the secondary current or transverse flow well, the experiment with Q = 2.5 l/s and an outlet height of 5 cm was repeated. In several sections of the experimental model, streamlines were visualized with pieces of very fine string, suspended near the bottom and near the water surface. This visualization could then be compared with the streamline visualization performed on the numerical output. Comparison yields that both the experimental and the numerical streamlines follow the same path, which is a good first indication that the numerical model captures the motion of the secondary current. The numerical model also allows for cross-sectional vector plots of the secondary current. This way, the output can be compared with the theoretical motion of the secondary current in meander bends, which indicates that the flow consists of a primary rotational cell, and alternates between a clockwise and counter-clockwise motion every other meander bend. Together with this rotational cell, a smaller, counter-rational cell appears near the outer bank (Blanckaert and Graf [11], Blanckaert and De Vriend [12]).

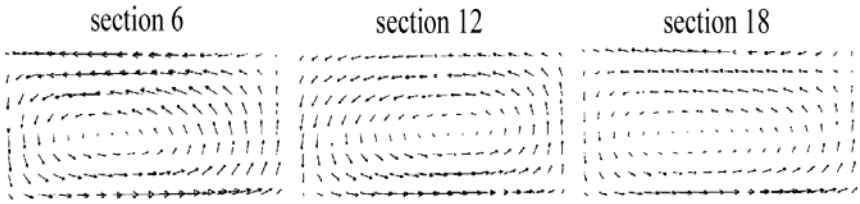

Figure 3: Vector plots of the secondary current. Primary flow direction is into the page. The numbers refer to the sections as defined in Fig. 1.

Fig. 3 shows vector plots of the secondary current in several cross-sections of the three meander bends. It can be seen that there is indeed only one rotational cell, but that the current does not alternate its direction. Moreover, extra numerical simulations with altered geometries show that the direction of the secondary current is dictated by the first meander bend the flow encounters, and that it keeps this direction along the entire model length. In reality, the bathymetry of the deformed river bed in between river bends dissipates the motion of the secondary current in such a way that but a fraction of its strength remains, if not completely disappears. Therefore, the secondary current has little or no 'motion history' when it reaches the next bend, and it takes on the natural rotation in this bend. However, in the experimental and numerical model, there is no dissipation due to a deformed river bed, neither is there a substantial influence of friction. The section in between the river bends is too short to account for a full dissipation, so that the secondary current still keeps the motion it was given

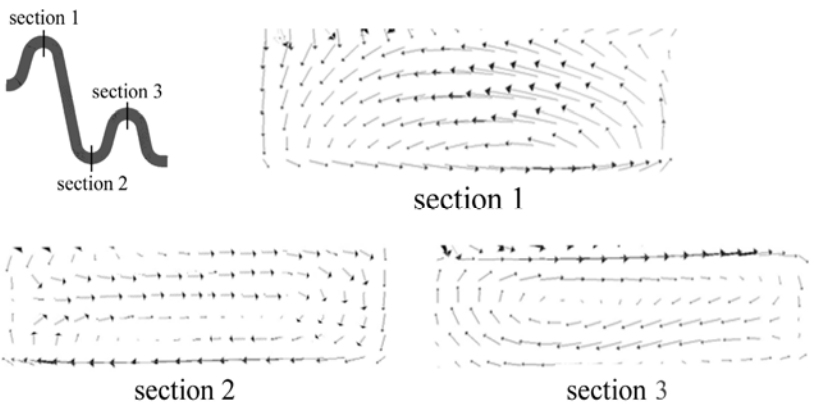

Figure 4: Upper left frame: geometry with lengthened straight section between the first and second meander bend; upper right frame: vector plot of the secondary current in section 1; bottom frame: vector plots of the secondary current in sections 2 and 3. Primary flow direction is into the page.

possible explanation, numerical simulations were performed in which the section in between the first and the second meander bend was lengthened to four times in the first bend and resists the natural counter-rotation in the following bends. The motion does however seem to weaken, as can be seen in Fig. 3. To test this the original size, as is displayed in Fig. 4. Also, vector plots are shown of the secondary current in cross sections in the three meander bends. It can be seen that the secondary current indeed switches direction from a counter-clockwise rotation in the first meander bend to a clockwise rotation in the second meander bend. The secondary current does not change rotation in the third meander bend, but keeps the rotation it had in the second bend. Thus, it can be concluded that the short straight sections and the according lack of frictional effects in between the meander bends of the experimental and numerical model are responsible for the described behavior of the secondary current. The appearance of only one rotational cell in the numerical results has two possible explanations: the counter-rotational cell near the outer bank does not exist in our specific experiments, or the numerical grid is too coarse to capture this weaker current. Future measurements should provide more insight into this matter.

5 Conclusions

Experimental and numerical models have been developed in order to predict the flow in a meandering river. The model represents two wavelengths of a regime channel. Results are presented for simulations with fixed cross-sections and steady discharge. The main conclusions are: (1) the numerical model accurately predicts the water depth along the channel length and at the outer and inner banks of the meander bends, (2) realistic simulations of the streamwise velocities are produced experimentally as well as numerically and the numerically computed velocities are in good agreement with the experimentally measured velocities, (3) streamline visualisation indicates that the numerical model captures the motion of the secondary current and that the secondary current does not alternate its rotation but maintains the rotation of the first meander bend. In a second set of experiments, the PIV measurement technique will be used to gather velocity data. This will allow for a more detailed comparison of the streamwise velocity patterns, and will enable the visualisation of the secondary current in the experimental model and comparison with the output of the numerical model. Also, a sediment transport module will be incorporated in the numerical model, and experiments with deformable beds will be performed.

Acknowledgements

This research is supported by research grants from the Flemish Fund of Scientific Research (project nr. G.0330.07). The authors wish to thank the technical staff of the laboratory for their assistance with the experimental test-setup, and Joost Cornelli for his assistance with the numerical computations.

References

[1] Olsen, N.R.B., Kjellesvig, H.M., Three-dimensional numerical modeling of bed changes in a sand trap. *Journal of hydraulic resources*, **37**, pp. 189–198, 1999

[2] Rajendran, V.P., Constantinescu, S.G., Patel, V.C., Experimental validation of a numerical model of flow in pump-intake bays. *Journal of hydraulic engineering*, **125**, pp. 1119–1125, 1999

[3] Williams, G.P., River meanders and channel size. *Journal of hydrology,* **88***,* pp. 147–164, 1986

[4] Rodi, W., *Turbulence models and their applications in hydraulics*, Balkema, Rotterdam, 1993

[5] Hirt, C. W., Nichols, B.D., Volume of Fluid (VOF) method for the dynamics of free boundaries. *Journal of Computational Physics,* pp**.** 201–225 , 1981

[6] Ma, L., Ashworth, P.J., Best, J.L., Elliot, L., Ingham, D.B., Whitcombe, L.J., Computational fluid dynamics and the physical modeling of an upland urban river. *Geomorphology,* **44**, pp**.** 375–391, 2002

[7] Launder, B.E., Spalding, D.B., The numerical computation of turbulent flows. *Computer Methods in Applied Mechanics and Engineering*, **3**, pp. 269–289, 1974

[8] Nallasamy, M., Turbulence models and their applications to the prediction of internal flows – a review. *Comput. Fluids.,* **15,** pp**.** 1183–1195 , 1987

[9] Patankar, S.V., *Numerical heat transfer and fluid flow*, Hemisphere, Washington, DC, 1980.

[10] Issa, R.I., Solution of the implicitly discretized fluid flow equations by operator-splitting. *Journal of Computational Physics*, **62** , pp. 40–65, 1985.

[11] Blanckaert K., Graf W.H., Mean flow and turbulence in open-channel bend. *Journal of Hydraulic Engineering*, **127**, pp. 835–847, 2001

[12] Blanckaert K., De Vriend H.J., Secondary flow in sharp open-channel bends. *Journal of Fluid Mechanics*, **498**, pp. 353–380, 2004

Integration of 3D incompressible free surface Navier-Stokes equations on unstructured tetrahedral grid using distributed computation on TCP/IP networks

N. Evstigneev
Doctor of Science, Department of Nonlinear Dynamic Systems, Institute of System Analysis, Academy of Science, Russia

Abstract

The incompressible system of Navier-Stokes equations for an Initial-Boundary Value Problem is solved on an unstructured tetrahedral grid using a finite volume method. Implementation of a free surface calculation is done by using a combination of Level Set and Volume Of Fluid methods. A numerical scheme utilizes the method of fractional steps based on the predictor-corrector method and the artificial compressibility method. Invariant features of a tetrahedron are used in order to calculate fluxes over a control volume with higher order. A high order approximation in Navier-Stokes and VOF level set advection equations is made by a TVD SuperBEE scheme. The turbulence model is based on LES methodology. In order to decrease the time of solution for a large geometry, a distributed computation routine is incorporated into the method. The distributed calculation is based on a TCP/IP network and can use personal computers under Windows or UNIX. The efficiency of the distributed calculation is shown. The method is verified by comparison of results with other calculations and experiments – cavity flow case, dam break free surface flow case, turbulent flow in a circular pipe case – Poiseuille flow (turbulent energy distribution). The method is successfully used for CFD simulation of water intake on Zagorskaya Hydraulic Power Plant (Russia). The results are close between laboratory experiments and CFD computations.

Keywords: unstructured grid, finite volume method, artificial compressibility method, predictor-corrector method, Navier-Stokes equations, distributed computation.

WIT Transactions on Engineering Sciences, Vol 59, © 2008 WIT Press
www.witpress.com, ISSN 1743-3533 (on-line)
doi:10.2495/AFM080071

1 Introduction

It is a common practice these days to use computational fluid dynamics for complex technical applications. Thus, computational methods must meet certain requirements: high order of space and time discretization, lesser time demands for integration, fair geometry approximation and exact representation of flow specific features. For this purpose, a numerical solution of incompressible viscous fluid equations with free surface, utilizing a weak form of Navier-Stokes equations is designed. The method incorporates a high order of approximation, a decrease in integration time by using distributed computation on cheap available PCs, unstructured mesh topology, allowing approximation of any arbitrary complex geometry.

2 Mathematical model and governing equations

2.1 Governing equations

In order to describe a fluid motion in E^4, the most basic system of governing equations is used, Temam [1]. Three dimensional evolutional equations of mass and momentum conservation for Newtonian incompressible fluid, Navier-Stokes equations, in dimensionless form for the turbulent flow in a weak form are used:

$$\frac{\partial}{\partial t}\int_{\Omega} q \cdot dW + \oint_{\partial\Omega} \vec{f}_i \cdot n \cdot ds - \oint_{\partial\Omega} \vec{f}_v \cdot n \cdot ds - F_s - Fr^{-1} g = 0\,; \tag{1}$$

$$q = [0;u;v;w]^T\ ;\ \vec{f}_i \cdot n = \left[(\Theta);(u\Theta + n_x \cdot P);(v\Theta + n_y \cdot P);(w\Theta + n_z \cdot P)\right]^T\ ;$$

$$\vec{f}_v \cdot n = [0;(n_x\tau_{xx} + n_y\tau_{xy} + n_z\tau_{xz} + m_{xu} + m_{xz});(n_x\tau_{yx} + n_y\tau_{yy} + n_z\tau_{yz} + m_{yx} + m_{yz});$$
$$(n_x\tau_{zx} + n_y\tau_{zy} + n_z\tau_{zz} + m_{zx} + m_{zy})]^T$$

here: velocity vector-function $V : \Omega \times [0,T] \to \Re^3$, scalar pressure function $P : \Omega \times [0,T] \to \Re$. We seek solution on an arbitrary bounded domain $\Omega \in E^3$; x_i – directions in E^3 (x,y,z – for Cartesian coordinate system); $\Theta = n_x u + n_y v + n_z w$; Re – Reynolds number; Fr – Froude number; g – gravity unit vector. $\tau_{ij} = \frac{1}{\mathrm{Re}}\left(\frac{\partial V_i}{\partial x_j} + \frac{\partial V_j}{\partial x_i}\right)$ - Viscous stress tensor for Newtonian fluid where i=1..3,j=1..3; m_{ij} – turbulent stress tensor, $m_{ij}^L = \overline{\overline{V}_j V_i} - \overline{V}_j \overline{V}_i - 0.5(V_j \partial_i \overline{V}_j - \overline{V}_j \partial_i V_j)$,see section 2.2. The integral form of (1) assumes that weak solutions exist in R^4 [1,2].

A free surface is described by a modified Volume of Fluid (VOF) method, Sussman et al. [5].; $F_s = \sigma \cdot k \nabla F$ - surface tension; k – free surface curvature; F – color set function, that indicates the level of free surface; σ - wetting coefficient. System of equations (1) is added to by the kinematic and dynamic conditions for

a free surface (continuity of normal stress vector on a free surface), described in the level set advection and gradient equations:

$$\frac{\partial F}{\partial t}+u\frac{\partial F}{\partial x}+v\frac{\partial F}{\partial x}+w\frac{\partial F}{\partial x}=0; F\in[0;1]; k=\nabla\cdot\left(\frac{\nabla F}{|\nabla F|}\right), \tag{2}$$

We assume that a color set function F equals 0 for air and 1 for liquid. It differs form general idea for F>0 for liquid and F<0 for air, as described in the general VOF approach, Sussman et al [5]. So the method can be called a Level Set method with a VOF procedure of calculating stress vectors on a free surface.

2.2 Boundary conditions

System of PDE equations (1) must be completed by initial-boundary values in order to have a well-posed problem in Ω. Boundary conditions in general form are Dirichlet and Neuman conditions for Boundary-value Navier-Stokes equations, Temam [1]. In the physical domain one can define the following boundary conditions: at the inlet, the values of all variables are prescribed. At the outlet, the streamwise gradient for each variable is prescribed to be equal to zero. At the walls, no slip and no penetration are assumed. The pressure gradient normal to the wall is calculated as $\frac{\partial P}{\partial n_i}=\mathrm{Re}^{-1}\nabla^2 u_i+m_{ij}$, and for turbulent flows is assumed to be $\frac{\partial P}{\partial n_i}=-0.5(\overline{V_j\partial_i\overline{V}_j-\overline{V}_j\partial_i V_j})$. Derivatives on the right side are small for the near wall velocities and can be assumed to be equal to 0.

2.3 Large eddy simulation model for turbulent flows

To represent turbulent flows one must recover all flow scales, thus closing a turbulent stress tensor m_{ij} in (1) one way or another. This can be done by four ways: recovering all flow scales directly from Navier-Stokes equations (Direct Numerical Simulation) and, hence, neglecting m_{ij}; imposing a complex turbulent model via additional equations for m_{ij} and averaging (1) by Reynolds averaging procedure, hence computing only mean flow properties; representing large flow scales (where the turbulent flow is anisotropic) directly from Navier-Stokes equations (1) and imposing a simple turbulent model (sub grid model) for small (isotropic) scale turbulence (Large Eddy Simulation); combining the latter two approaches (Detached Eddy Simulation). Here we shall use the LES model for turbulent flows. A detailed description for LES methods and applications can be found in Chunlei et al. [9]. In brief, the Large Eddy Simulation is conducted by averaging (1) in time and space with arbitrary scale L, related with mesh size of Ω discretization. Let's impose a general noncommutative averaging operator in $\Re^4$:

$$\overline{V}=L(V), \tag{3}$$

Thus there exists decomposition in $\Re^4$: $V = L^{-1}(\overline{V})$ with commutative properties for a differential operator:

$$\partial_t V_i = L^{-1}(\partial_t V_i) = \partial_t (L^{-1}(V_i)) \text{ etc for all } x_i. \quad (4)$$

Here we denote $\partial_t = \partial/\partial t$ for brevity.

In general m_{ij} is a nonsymmetrical tensor, which arises from averaging of the advective part in the momentum equation by applying (3) to (1). In general $m_{ij}^L = L(\overline{V}_j L^{-1}(\overline{V}_i)) - \overline{V}_j \overline{V}_i$, so closing the asymmetrical tensor on the selected small scale is done by the modified Leray model, Chunlei et al. [9]:

$$m_{ij}^L = \overline{\overline{V}_j V_i} - \overline{V}_j \overline{V}_i - 0.5(\overline{V_j \partial_i \overline{V}_j - \overline{V}_j \partial_i V_j}) . \quad (5)$$

Adding (5) to (1) closes the system of equations. Hence, the solution of evolutional PDE system (1) with tensor (5) on scales greater than L is conducted as a direct numerical simulation. For the flow scales less than L (for greater wave spectra numbers of turbulent kinetic energy, small scale turbulence Chunlei et al. [9]), the flow is represented by the modified Leray model (5). To have a well-posed problem for LES modeling initial conditions must be properly imposed. For technical problems initial conditions are derived from laminar flow calculations in the same geometry.

3 Numerical method

3.1 Meshing

In order to solve (1) on a given bounded domain, Ω in E^3 must be meshed. In the following method a tetrahedral gird that covers the domain is used. The grid generation is using a Delauny algorithm, Cignoniz et al. [7], that allows the creation of a space-adopted high quality mesh. The algorithm utilizes mesh refinement near given areas. Any arbitrary geometry can be discretized due to an unstructured mesh structure. An example of meshing a 3D power intake of Zagorskaya Hydraulic Power Plant is given in fig. 1.

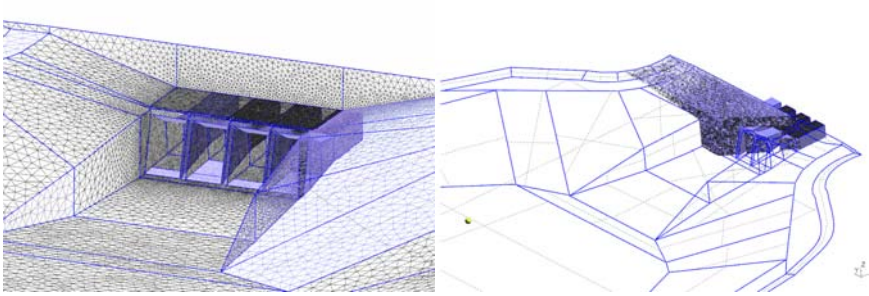

Figure 1: An example of meshing – a power intake of Zagorskaya Hydraulic Power Plant.

3.2 Numerical integration

In accordance with the PDE system (2) two methods are applied to integrate the system in space. A march algorithm similar to the method used in aerodynamics, Evstigneev [12], is used for a continuity equation in (1) is rewritten as $\frac{\partial}{\partial t}\int_{\Omega} P \cdot dW + \oint_{\partial\Omega} \beta \cdot \Theta \cdot ds = 0$, and a predictor-corrector method is used for classic system of Navier-Stokes equations (1). Here β is an artificial compressibility parameter, and equals 80-120, Chorin [6]. The march algorithm is more reliable and much faster due to the lack of Poisson correction equation for pressure function but the predictor-corrector algorithm is more accurate. So the combination of these two methods provides a fast and reliable procedure for flow calculation in complex conditions.

When the space integrals are found, time integration must be applied to the advance solution in time. So, the integration of PDE system (1) consists of two steps: finding space integrals (integral-differential operator in $\Re^3$) and applying the time advancing procedure (solution of ODE in $\Re^1$ with found integrals in $\Re^3$).

Considering a free surface flow, the solution of (1) is only done in the part of the domain where F>0. So the color function equation must be integrated as well.

3.2.1 March scheme

The march method is based on integration of a PDE system like a hyperbolic system of equations, thus flux solvers must be applied to find a solution. The idea of the method originates from Chorin's artificial compressibility solution methodology [6]. In this case a system of singular perturbed PDE is considered thus constructing a strictly hyperbolic system of equations for a void viscosity, i.e. Re equals eternity.

In this case a flux splitting scheme for the inviscid part of (2) on a tetrahedron boundary is used. Thus, the flux value on the boundary of a tetrahedral equals:

$$F = 0.5\left(f_r + f_l - |A| \cdot (q_r - q_l)\right), \tag{6}$$

where F is a flux value on the side of a tetrahedron; 'l' and 'r' letters stand for left and right side values of variables; $A = \partial F / \partial q$ -system Jacobean, which has the following decomposition $A = T\Lambda T^{-1}$, the same as the compressible flow equations with four real eigenvalues:

$$\lambda_{1,2} = \Theta, \lambda_{3,4} = \lambda_{1.2} \pm c, \tag{7}$$

where $c = \sqrt{\lambda_{1,2} + \beta}$ - artificial wave speed propagation. In accordance with the found Jacobean eigenvalues, a U-CUSP similar to the Evstigneev [12] scheme is constructed, thus solving an inviscid part of the Navier-Stokes equations. A detail description of the scheme can be found in Evstigneev [12]. In order to have a high accuracy in flux splitting scheme a high order reconstruction of variables is used. A diffusion equation is solved using a Finite Volume scheme,

described in [4,9]. Hence, a solution is found by integrating a singular perturbed system of hyperbolic PDEs in artificial compressibility methodology on a tetrahedral unstructured grid.

3.2.2 Predictor corrector scheme

Consider a classic system of Navier-Stokes equations (1) without singular perturbations. In this case a link between pressure and the solenoid velocity field must be found in an implicit way. There are many ways to do that, for example see [2,4] In the present work we use a predictor-corrector factual step scheme, based on Yanenko et al [2]. The semi-discrete steps are:

$$\text{Step 1. } V' - V^n = -\Delta t \cdot \nabla(V^n V^n) \text{ - explicit scheme.} \tag{8}$$

$$\text{Step 2. } \widetilde{V} - V' = \Delta t \cdot \mathrm{Re}^{-1} \nabla^2 \widetilde{V} + m_{ij} \text{ - implicit scheme.} \tag{9}$$

$$\text{Step 3. } \nabla^2 P = -\nabla \cdot \widetilde{V} / \Delta t \text{ - Poisson equation solution in assumption that } \nabla \cdot V^{n+1} = 0. \tag{10}$$

$$\text{Step 4. } V^{n+1} = \widetilde{V} - \Delta t \nabla P \text{ - correction of V solenoid field.} \tag{11}$$

Let's assume that a vector-function V and pressure function P values (i.e. from initial conditions) are known in $\Omega x T^n$, and vector-function V is solenoidal in Ω. Then on the first step a nonlinear advection equation (inviscid Burgers equation) is solved (8). On the second step a solution of diffusion equation (9) is found. Vector function field V is not solenoid in Ω if only two steps are applied – that's the predictor part. So the velocity field is corrected on the fourth step (11), that's the corrector part. In order to consider solenoidality of velocity vector-function a pressure function is calculated on the third step by the Poisson equation (10) with a right side as the divergence singular term. The convergence of fractional steps method (11) is proved in Yanenko et al. [2]. Numerical integration of fractional steps is done using a finite volume method.

3.2.3 High order variable reconstruction

In order to find a variable value on a boundary side of a tetrahedron with high accuracy, a high order interpolation is applied for both schemes. Unstructured grid solvers usually suffer from the main loss of accuracy due to the difficult topological interpolation of variables. In this work with the staged grid variable storage high accuracy approximation is achieved by applying Taylor series on the tetrahedron boundary side projection, i.e.:

$$q(x, y, z) = q(x_e, y_e, z_e) + \nabla q_e \cdot \Delta L + 0(\Delta L^2); \tag{12}$$

here ΔL – length in E^3 from centers of nearby tetrahedra; q_e – variable value in tetrahedron center; q – variable value in tetrahedron boundary side.

In the present work a geometrical invariance of a tetrahedron is used, for details see Evstigneev [12]. As the result a gradient would transfer in the following form:

$$\nabla q_e \cdot \Delta L = \partial q / \partial L \cdot \Delta L \cong 0.25 \cdot [1/3(q_B + q_C + q_D) - q_A] \cdot \Delta L / \Delta L,$$
$$\text{hence: } q_f = q_e + 0.25[(q_B + q_C + q_D)/3 - q_A], \quad (13)$$

so that the values of left and right variables on a tetrahedron side are found using (13). Here q_A etc are the values of the variable on the vertexes of a tetrahedron; q_f – variable value on a tetrahedron face. Values on tetrahedron vertexes are found using geometrical weighted interpolation.

Using high order in advection equations leads to instability due the existence of nonmonotonous solutions as described by the Godunov's theorem, see Fletcher [4]. To avoid numerical instability a nonlinear scheme must be applied. In the present work a TVD SuperBEE limiter is used as one of the least numerical diffusive. This limiter was tested on modal transport and inviscid Burgers equations [9,12] with very good results. In the author's recent works the limiter was applied to DNS and LES solutions [9–11] and good agreement found with experimental and numerical data.

3.2.4 Time integration

Time integration for the inviscid part of (1) in both schemes (predictor-corrector and march schemes) is done using the 4-th staged explicit Runge-Kutta method [3]. Time advancement of diffusion equation utilizes the implicit 2 staged Runge-Kutta scheme, Hairer et al. [3]. Both methods are described in [9,12] thoroughly. The time step limit in both methods is based on the limit for the advection Burgers equation, hence limited by the CFL [3] condition.

3.2.5 Color set function integration

After the numerical scheme to solve (1) is applied, a free surface must be considered, thus a PDE system (2) must be integrated. The level set equation for the color function (2) is solved using the finite volume method by converting it into appropriate hyperbolic form, using the same approach as for the advection equation in the predictor-corrector scheme, i.e. using finite volume with high order variable reconstruction. The equation (2) changed to:

$$\frac{\partial F}{\partial t} = -\nabla(V \cdot F) + F\nabla \cdot V \,. \quad (14)$$

If the velocity vector-function field is solenoid, thus $\nabla \cdot V = 0$, equations (14) and (3) are equivalent. But, since the numerical method uses singularity perturbation for artificial compressibility or the fractional steps predictor-corrector method, the divergence term in (14) must be considered to ensure solenoidal velocity vector-function behavior on a free surface.

The free surface tension Fs in (1) is calculated on every time step. Numerical integration of (1) is applied only in the part of the domain where $F>0$, thus decreasing computational time. The pressure and velocity are solved on the liquid side of the interface between air and liquid using the methods described in Sussman et al. [5]. For the edges that intersect the free surface, the pressure that would be calculated via the extrapolation to the control volume face is replaced by the hydrostatic pressure as the differences of distances where $0<F<1$ in the

direction of the gravity vector field. The free surface tension is applied by the Fs in (1) only for the liquid side of the interface between air and liquid, and only in regions where 0<F<1 that come from the equation for k in (3).

3.3 Distributed calculations

The numerical method for Navier-Stokes equations integration, presented in the following work, is developed for complex geometries and turbulent flows. Hence, as any CFD method, it is very resourceful on computer processor power and memory. In order to decrease computer resource dependence, a distributed computation routine is incorporated in the method for TCP-IP networks. Computations can be distributed on any PC network. Tests were made on PCs with MS Windows XP and RedHat Linux 7.0 operational systems. The algorithm is based on division of source domain Ω on separate parts with crosslink boundary tetrahedra. Each PC in the network has a client-sever application that connects to the neighbor computer in the network by the given IP address. Data exchange is done only for neighbor tetrahedra, thus decreasing network usage. Detailed description of the proposed method is given in Evstigneev [12]. Computation acceleration comparison for both schemes as given in fig. 2 was conducted for the lid driven cavity problem with Re=25 000. The grid consisted of 701 434 tetrahedral elements.

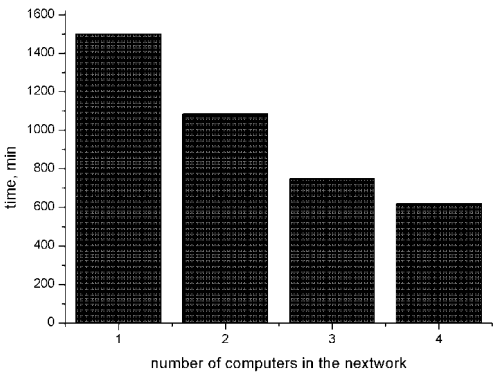

Figure 2: Calculation time for distributed computation.

4 Numerical experiments

4.1 Testing numerical scheme

Thorough tests of the numerical method for incompressible turbulent Navier-Stokes equations were carried out. Only few brief results are presented in the present paper.

4.1.1 Lid driven cavity problem

This test case is the classic task for numerical methods in 2D and 3D geometry for incompressible and compressible low Mach number viscous flows. The test was preformed by many authors for various Reynolds numbers, including fundamental results for nonlinear dynamics, Evstigneev [10]. As a result, this test case has became a main model task for all CFD codes since the end of the 60-th. The test case has a cubic geometry with solid wall boundary conditions. On one of the walls a tangent velocity is set to 1.

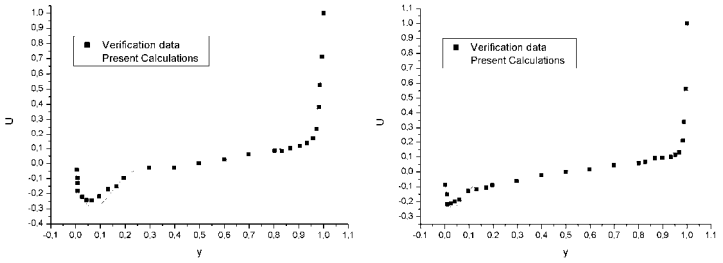

Figure 3: Data comparison form [11]. a – Re=1 000; b- Re=10 000.

Results for Re=1 000 and 10 000 are given in fig. 3 from [10]. For Re=10 000 the flow is turbulent, so averaged velocity profiles are compared. It can be seen that the results of different authors have a close fit. For more results see Evstigneev [10].

4.1.2 Broken dam problem

Broken dam problem is a good model test case for the free surface flow problem that has good experimental and numerical results.

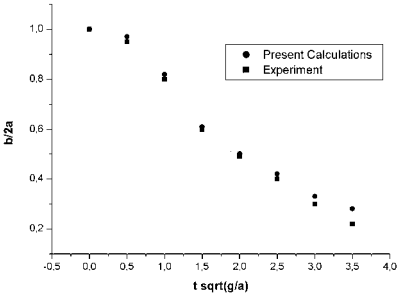

Figure 4: Comparison of numerical and experimental results for the dam break case, Re=500. 2a – initial liquid fraction height, b – current liquid fraction height; t – time in sec.

The test case has a rectangular geometry with ¼ volume filled with liquid. Experimental results were obtained for the same geometry from Sussman et al. [5], results are shown in fig. 4 for Re=500.

4.1.3 Turbulent flow in a circular pipe

This test case is a classic case study for turbulent flow verification for incompressible viscous flows. The test case has detailed data obtained from DNS laminar-turbulent Poiseuille flow transition studies as well as for the developed turbulent regimes, e.g. Chunlei et al. [9].

The case study has a circular geometry with solid wall boundary conditions and periodic boundary conditions on an outflow border. Inflow boundary conditions are laminar as well as initial conditions with no initial perturbations.

Results of turbulent energy distribution from numerical investigation with comparison to the other authors' results are shown in fig. 5. Energy spectrum comparison shows good data correlation with other results. For more information see Evstigneev [11].

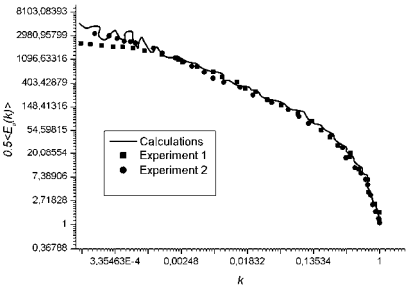

Figure 5: Kinetic turbulent energy spectrum comparison for turbulent Poiseuille flow in a circular pipe for Re=12 000. E – mean turbulent energy, k – wave number.

All tests of the numerical method presented in this paper showed good results and data fit.

4.2 Applications for technical hydrodynamics

The method was designed for technical application and has already been used for hydrodynamic investigation of complex hydraulic power plants. One example of its technical application is presented in the present work.

4.2.1 Investigation of turbulent free surface flow over a power intake of Zagorskaya hydraulic power plant

Input geometry was presented in AutgoCAD and translated to preprocessor format by a Visual Basic adaptive program. An adaptive tetrahedral grid was created automatically by the preprocessor; the fragment of surface is shown in fig. 1. Governing system of equations (1) was used with Carioles acceleration. Integration was conducted on 4 computers on a TCP-IP network using a combination of march and predictor-corrector algorithms.

Boundary conditions on the input boundary are given by the time changing discharge Q(t) through the intake. Other boundary conditions are standard. Free surface is given on a constant level with no perturbations.

The numerical experiment was carried out for 10 hours of working time for the power intake. Averaged vector function V on the surface is presented on fig. 7. A laboratory model scaled 1/50 was made for the given intake geometry for experimental hydrodynamic investigation. Velocities were measured by thermoanemometers. Data was presented to the author by the Hydroelectric Power Plant maintenance organization. Numerical and experimental data comparison for laboratory scaled model on twelve vertical sections is done with 5% mean results deviation. Two verticals for the first section (15sm from the power input in 1:50 scale) are presented in fig. 6.

Average and pulsation velocities and pressure functions, turbulent stress, free surface levels are calculated as the result of numerical investigation. Obtained data was used for power intake construction optimization for the second power plant construction queue.

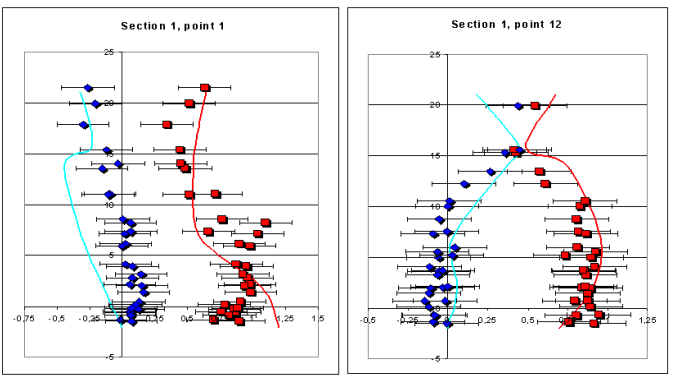

Figure 6: Comparison of computational (lines) and experimental data for averaged streamwise (right) and spanwise (left) averaged velocities.

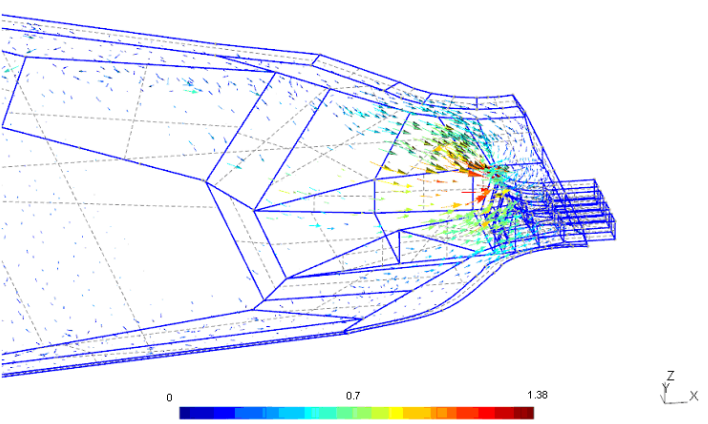

Figure 7: Averaged vector-function V in E^3 on the surface of the power-intake.

5 Conclusions

The purpose of this paper is to present a new numerical method for viscous incompressible flow calculation in R^4 with utilization of distributed computations and large eddy simulation methodology of free surface flows, governed by Navier-Stokes equations. The integration is conducted on a unstructured tetrahedral grid. This allows the use of the method for complex geometry of technical challenging tasks. A high order finite volume method for flux calculation is used. To maintain monotonous solutions a TVD SuperBEE flux limiter is applied. A large eddy simulation method is considered for almost any averaging scale. The distributed computation on cheap PC networks allows the use of any arbitrary network as a computational environment.

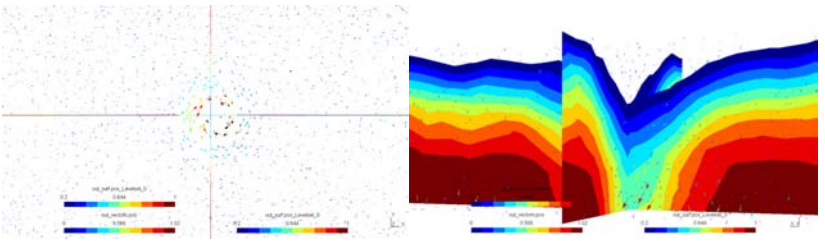

Figure 8: Zoomed velocity vectors (V) and free surface depression (F) near one of the vertexes.

Numerical results and data comparison for case studies demonstrated good performance. The method is used to calculate turbulent free surface flows on complex geometries. Two technical tasks are considered to demonstrate the ability of the method in handling complex turbulent regimes and geometries.

The numerical method, presented in the paper, is part of a complex CFD module that was developed by the author. Other parts of the complex, used for compressible viscous and inviscid flow computations, are presented in other papers [9,12].

References

[1] Temam R. Navier-Stokes equations – theory and numerical analysis.- North Holland Publishing Company, Oxford, 1981.

[2] Yanenko N.N., Kuznetsov B.G., Smagulov Sh. On the approximation of the Navier-Stokes equations for an incompressible fluid by evolutionary-type equations // Numerical Methods in Fluid Dynamics. - Moscow, 1984. - P.290–313.

[3] Hairer E.,Norsett S.P., Wanner G. Solving ordinary differentional equations. - V1., Springer-Verlag Berlin Heidelerg, 1987.

[4] Fletcher C.A.J., Computational Techniques for Fluid Dynamics - Springer-Verlag, 1056 p., 1988.

[5] Sussman M., Smereka P. and Osher S. A Level Set Approach for Computing Solutions to Incompressible Two-Phase Flow //, J. Comput. Phys. 114, pp.146–159, 1994.
[6] Chorin A., A Numberical Method for Solving Incompressible Viscous Flow Problems, // J. Comput. Phys. 2, pp.12–26, 1967.
[7] P. Cignoniz, C. Montaniz, R. Scopigno. DeWall: A Fast Divide & Conquer Delaunay Triangulation Algorithm in Ed. // The Computer J., 19(2):pp178–181, 2006.
[8] Roe P.L. Characteristic based schemes for the Euler equations. // Annual Review of Fluid Mechanics. Vol. 18, pp. 337–365., 1986.
[9] Chunlei Liang, Evstigneev N., A study of kinetic energy conserving scheme using finite volume collocated grid for LES of a channel flow. // Proceedings of the international conference on numerical methods in fluid dynamics. King's College London, Strand, WC2R 2LS, 2006.
[10] Evstigneev N.M. Lid driven cavity flow on various Reynolds numbers using 3D unstructured method for Navier-Stokes equations. // Moscow, Journal of Fundamental and technical science 1, 2006. (in russian)
[11] Evstigneev N.M. LES of Poiseuille flow in a circular pipe for transition and turbulent regimes. // Moscow, Journal of Fundamental and technical science №3, 2006г.
[12] Evstigneev N.M. Solution of 3D nonviscous compressible gas equations on unstructured meshes using the distributed computing approach. // J. of Comp. Math. and Math. Physics. V.8, pp. 252–264, 2007.

This page intentionally left blank

CFD modeling of turbulent boundary layer flow in passive drag-reducing applications

R. I. Bourisli[1] & A. A. Al-Sahhaf[2]
[1]*Department of Mechanical Engineering, Kuwait University, Kuwait*
[2]*School of Engineering and Design, Brunel University, UK*

Abstract

In this paper, the turbulence boundary layer, velocity and skin friction coefficient characteristics of grooved surfaces are studied. Flow over surfaces with transverse square, triangular and semicircular grooves are numerically modeled via the finite volume method. Comparisons are made on the basis of the grooved surfaces' skin-friction coefficient, normalized by that of a smooth surface, with Reynolds number in the vicinity of 2×10^6. Results show that square grooves are superior to the two other groove geometries in reducing the drag. Viscous damping in all grooves keeps skin friction inside them well below the surface above. However, the interior geometry of square grooves allows them to balance the net inward momentum due to the sudden absence of the wall in a way that minimizes disturbance of the main flow while taking advantage of the restart of the boundary layer. As a consequence to the separation of the boundary layer, an inevitable stagnation point within the groove must exist. Square grooves had the highest such stagnation point along the backward-facing side of the groove. The shortness of the resulting upward boundary layer from the stagnation point to the corner produces smaller near-wall secondary flow motion and more relaxed merger with the main flow. All this contributes to enhanced drag reduction for the described groove structure.
Keywords: viscous drag, skin-friction coefficient, grooved surfaces, turbulent boundary layer, momentum transfer.

1 Introduction

In the past, turbulence was thought to be totally random in terms of its microscopic flow behavior and initiation mechanisms. However, some sort of order was found in turbulent flows (Hama et al. [1] and Kline et al. [2]) which allowed engi-

WIT Transactions on Engineering Sciences, Vol 59, © 2008 WIT Press
www.witpress.com, ISSN 1743-3533 (on-line)
doi:10.2495/AFM080081

neers to begin work on trying to control them. The problem of reducing drag for external flows over surfaces is one such endeavor; it has been the subject of much research, off and on, for the past few decades. The basic methodology has been to delay laminar-to-turbulence transition, with the primary intention of reducing skin-friction drag. With recent energy and environmental concerns, improvement of the efficiency of transportation means has seen a renewed focus. The subject is relevant to a large number of areas as it relates to more than a few devices across many engineering applications, each with direct influence on energy consumption. For example, in civil or commercial transport aircraft, viscous or skin friction drag is responsible for about 40–50% of the total drag under typical cruise conditions [3]. Therefore, enhancing the drag-related hydrodynamic performance of these curved surfaces can lead directly to huge increase in fuel efficiency, even if the reductions are small. Since most of these vessels operate in the turbulent regime, understanding turbulent flow behavior at the surfaces and how it relates to the possibility of drag reduction becomes extremely important.

Various techniques have been proposed over the years with the aim of reducing the drag experienced by solid bodies moving in viscous fluids. Passive techniques have generally been concerned with using surface grooves and micro-grooves (riblets) to alter near-wall turbulence in a way that reduces wall shear stress. The suggestion that drag can be reduced using transverse square grooves was originally suggested by Tani et al. [4]. The plethora of subsequent heavily-investigated techniques included longitudinal (streamwise) and transverse grooves, with the shape of grooves frequently being square or triangular, with round and rectangular getting less attention.

However, it was discovered early that turbulent flow regime greatly influences the effectiveness of such techniques. Ching and Parsons [5] studied the drag characteristics of the turbulent boundary layer over flat plates with transverse square grooves using direct drag measurements in a tow tank. They reported little to no reduction in total drag for the cases tested. In fact, many of the configurations tested resulted in drag increase on the order of 1%. The large number of variables and flow settings involved gave rise to a large body of research in this area that is continually growing.

Viswanath [3] thoroughly reviewed the performance of the longitudinally-applied 3M riblets on airfoils, wings and wing-body configurations at different speed regimes. He reported drag reductions of 5–8% for airfoils and 2–3% for wing-body configurations. He also reported that riblets are more effective in adverse pressure gradients. Caram and Ahmed [6] also studied the near and intermediate wake region of the NACA 0012 airfoil and reported drag reduction as high as 13%, the non-monotonic variation of drag reduction with riblet height raised some doubts regarding measurements accuracy.

Use of compliant coating to reduce drag was first proposed by Kramer [7]. He observed that stability and transition characteristics of a boundary layer can be modified by hydroelastic-coupling to compliant coating. Various subsequent research in that field has met varying degree of success. Gad-el-Hak [8] provided an excellent review of progress in this field.

Katoh et al. [9] presented a theoretical analysis of potential heat transfer enhancement and the associated pressure loss as they relate to the roughness in turbulent channel flows. The use of roughness elements is a typical example of utilizing turbulence to increase heat transfer coefficient. They analytically confirm, however, that the enhancement in heat transfer is usually accompanied by an increase in drag, contrary to original desires. They also noted that, given the definition of Prandtl number as the ratio of effective diffusivity to heat transfer, the momentum transfer will always be more effective when the Prandtl number is less than or equal to the turbulent Prandtl number.

Another thermally-related drag question is whether varying the thermal gradient between the surface and fluid modify the surface shear stress distribution and the resulting skin-friction drag. Polidori et al. [10] investigated the effect in the context of underwater swimming. They tried to theoretically quantify the effect the integral formalism applied to the forced convection theory. It was demonstrated that, regardless of the flow Reynolds number, a 5% reduction in the skin-friction drag would occur by increasing average *laminar* boundary-layer temperature. For a turbulent flow analysis, which is more relevant to practical applications, the effect was less pronounced, with at most 1.5% reduction for medium to high Reynolds numbers. The authors correctly conclude that for turbulent flows the skin-friction drag is solely a function of Reynolds numbers.

While passive techniques are simple, easy to apply, and inexpensive, more recently, active feedback control with distributed micro sensors and actuators were the subject of much attention. The potential large modification of boundary layers and of the overall flow field with the small controlled input made such active devices attractive wherever their installation is feasible. In some Reynolds numbers ranges, drag reduction as high as 20% can be established, albeit after some time has elapsed, as reported by Endo et al. [11]. Despite their robustness in hostile environments and little fouling potential, however, complex construction, complex method of attachment, and difficulty of attachment to existing surfaces make their use less attractive. The high initial cost, the auxiliary power required to actuate the wall, and the extra space needed to host the hardware constitute additional constraints.

The two main variables to consider in such configurations are the groove spacing (s) and width (w). In general, a reduction in the wall shear stress (τ_w) is observed at the start of the groove where the boundary layer separates. The sudden temporary absence of the wall weakens the streamwise vorticity promoting the observed response by the near-wall flow. The observed drop in τ_w is followed by a sharp rise immediate downstream of the groove. The sharp rise in τ_w is commonly attributed to the local intense favorable pressure gradient emanating from the downstream edge of the groove. Research on exactly how the geometry of the grooves influence the flow dynamics and turbulent boundary layer structure is seldom found. This will be the primary focus of the current study.

This paper tries to address the following basic questions: 1) is the shape of the groove a factor in the amount of skin drag reduction? and if so, to what degree? 2) How does the shape of the groove influence the structure of the tur-

bulent boundary layer and flow outside the groove? Lastly, 3) what effect do modeling techniques have on any reported results? Some observation are also made on to what degree the performance of one groove strategy changes across ranges of Reynolds number. The first question determines the required type and range of surface treatments, while the second provides some insight on how future groove geometry modification might be geared toward enhancing drag reduction capabilities. The third question provides some guidelines regarding proper ways to model this effect for future applications and designs, at least in the Reynolds number range addressed. The observations made with regards to this last point will help specify the type of treatment most effective for multi-Reynolds number applications. To do this, the paper is organized as follows. Section 2 gives the formulation of the problem in terms of geometry, governing equations, and appropriate models used. Section 3 lists the results of the numerical simulations and discusses them from a physical as well as numerical point of view. Section 4 draws conclusions from the work presented and summarizes lessons learned for future use in similar simulations.

2 Formulation and numerical method

2.1 Geometry and governing equations

To give the problem practical dimensions, all the cases considered were modeled using a 2-D flat plate with a total length of 3 m, with treatment limited to the middle 1 m only. The physical structure can be encountered in numerous real-world applications, such as automobiles, ship hulls, aircraft wings, etc. The freestream velocity chosen for cases reported was 33 m/s which corresponding to a Reynolds number of 2×10^6 based on a characteristic length $L_c = 1$ m. The Reynolds number based on momentum thickness, Re_θ, is 4000 at the start of the grooved section. These values were specifically chosen to facilitate the necessary validation with the experimental data for a comparably grooved flat plate with square grooves done by Wahidi et al. [12].

Tested grooves were square, triangular and semicircular in shape. Various widths and depths were tested and comparison is presented for 2 mm wide, 2 mm deep grooves (1 mm radii semicircular) that are 20 mm apart. Comparisons are made between grooved middle sections and a comparable (middle 1 m) smooth section of the plate. Initial studies show that any pertinent effects of slight curvature can be neglected for purposes of this study. Deviation from true 3-D behavior is addressed in Section 4. The flow is governed by the steady, incompressible, Reynolds-averaged Navier-Stokes equations, shown below in dimensionless, primitive variable form,

$$\nabla \cdot u = 0 \tag{1}$$

$$(u \cdot \nabla)u = -\nabla p + \frac{1}{Re}\nabla^2 u \tag{2}$$

The k-ϵ model set of equations for eddy viscosity, turbulent kinetic energy, dissipation rate and closure coefficients can be found in any basic text on turbulence (see [13] for example). Double precision is used for all variables and a freestream velocity of 33 m/s and air were chosen as a base case.

Standard velocity inlet boundary condition was used for the inlet and standard pressure outlet was used for the exit. The plates were assumed stationary with a dimensionless roughness height of $k_s^+ = 0.5$. The boundary condition for the outer part of the flow for the rectangular domain is an important issue. The specification of the realistic pressure-far-field boundary condition is incompatible with the incompressibility assumption. Therefore, the symmetry boundary condition was specified at the top of the modeled region. This usually alters the physics of the flow because the presence of a solid surface is assumed at twice the height of the modeled region. To get around this artifact, the displacement thickness is precalculated using a generic 1/7 power law turbulent profile, $\delta^* = 0.046xRe_x^{-1/5}$, and the inlet velocity was corrected accordingly to give the desired Re and Re_θ values at the start of the grooved section.

2.2 Boundary layer resolution

The presence of solid surfaces greatly affects the behavior of turbulent flows, both in terms of velocity as well as turbulence variables. The solid surface is where the gradients are the largest, and, more importantly, it is where the flow turbulence kinetic energy and vorticity are produced. These vigorous fluctuations in momentum and other scalar transport variables have to be resolved accurately in order to have a faithful description of the secondary variables of interest. The turbulence model of choice (the k-ϵ model) is known to be primarily valid for turbulent core flow, away from solid surfaces. To ensure accurate prediction of variables throughout the boundary layer, particularly in the near-wall region, mesh resolution must be fine enough, but not finer.

In addition, the RNG (renormalization group theory) version of the standard k-ϵ turbulence model was used for this study. This model is similar to the standard model but includes an additional term that improves accuracy for rapidly strained flows.[1] While computationally more demanding, the convergence rate and solution quality of the RNG model justifies its use in such and similar flow simulations.

Numerous experiments have shown that turbulent boundary layers can largely be subdivided into three layers: the viscous sublayer, the log layer and the defect layer. Turbulence models are usually modified to enable the boundary to be resolved with a fine mesh from the outer edge of the boundary layer all the way to the wall, including the viscous sublayer. This approach was followed here for accurate prediction of wall shear stress, frictional drag, pressure drop, turbulence variables, and similar variables of interest. The complete resolution of the turbulent boundary layer usually imposes considerable computational load on the

[1]The RNG model also includes the effect of swirl on turbulence and an analytical formula for Pr_t which further enhances its accuracy.

solution algorithm. One would want to have a boundary layer formulation that is fine enough to resolve the turbulent sublayers, particularly the (laminar) viscous sublayer, and, at the same time, be coarse enough to facilitate realistic modeling turnaround times. To accomplish this goal, Fluent^{TM} two-layer model with enhanced wall functions is used [14].

To non-dimensionalize the velocity profile in the turbulent boundary layer, we use the dimensionless velocity, u^+, and distance, y^+, defined as,

$$u^+ \equiv \frac{\overline{u}}{u_\tau}, \tag{3}$$

$$\text{and} \quad y^+ \equiv \frac{u_\tau y}{\nu} \tag{4}$$

where $u_\tau \equiv \sqrt{\tau_w/\rho}$ is the friction velocity, τ_w is the shear stress at the surface, ρ is the density, and ν is the kinematic viscosity. As with the laminar boundary layer, close to the surface, the horizontal velocity varies linearly with distance, equation (5). For $y^+ \geq 7$ the velocity gradually asymptotes to the well-known *law of the wall*, obeying equation 6 between $y^+ = 30$ and $y = 0.1\delta$, where δ is the total boundary layer thickness. Further away from the surface, the velocity profile makes a noticeable departure from the law of the wall. A correlation of measurements, equation (7), combines the velocity behavior in the log and defect layers incorporating the Coles' wake-strength parameter, $\tilde{\Pi} \approx 0.6$.

$$u^+ = y^+ \quad \text{viscous sublayer} \tag{5}$$

$$u^+ = \frac{1}{\kappa} \ln y^+ + 5 \quad \text{log layer} \tag{6}$$

$$u^+ = \frac{1}{\kappa} \ln y^+ + 5 + \frac{2\tilde{\Pi}}{\kappa} \sin^2\left(\frac{\pi}{2}\frac{y}{\delta}\right) \quad \text{log + defect layers} \tag{7}$$

An effective accuracy test for the mesh suitability of any turbulent flow simulation is the reproduction of the three sublayers of the turbulent boundary layer. A base case representing a smooth plate was constructed, meshed, remeshed, and tweaked (mainly using the `Adapt` feature of Fluent for better targeted refinement) until a satisfactory mesh resolution is reached with respect to the experimentally-verified boundary layer relations above. Specifically, boundary layer mesh adaption was done based on the combined consideration of three quantities: grid iso-value, parallel velocity gradient, and y^+ iso-value. The bottom-right mesh of figures 1 shows a sample resultant adaption effect for part of the flat surface. The initial tuning of the boundary layer mesh produced the excellent agreement shown in figure 2. For subsequent (grooved) cases, only the small, comparably-meshed grooves (with different sizes and shapes) were added and attached to the flow domain. Similar adaption was also performed once the final grooved surface geometry is being solved. The top two and the bottom-left meshes of figure 1 show sample resultant adaption effects for the three types of grooves.

3 Results and discussion

3.1 Skin friction coefficient

Initial comparisons between grooves geometry are done by straightforward integration of the skin friction coefficient over the whole middle section of surfaces

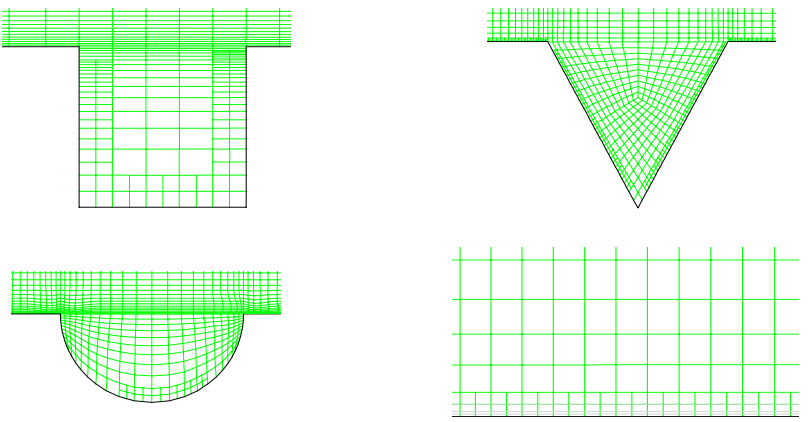

Figure 1: Adaption results for the geometry based on the combined consideration of velocity gradients, and grid and y^+ iso-values.

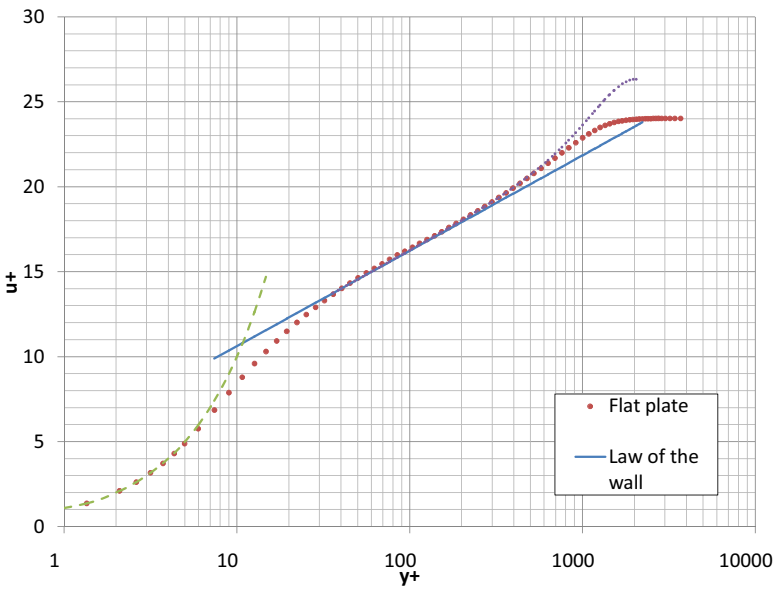

Figure 2: Velocity profile for the turbulent boundary layer flow compared experimental correlation.

including any horizontal components of interior groove surfaces. These comparisons clearly favor the square and semicircular grooves over the triangular ones. For the specified geometry and boundary conditions, reductions in skin friction were 8% for square grooves and 7.6% for semicircular ones. Triangular grooves provided little or no reduction at all. In fact, for the best square case, substituting triangular grooves resulted in a 3.6% drag increase. This finding is intriguing if one notices that triangle are far superior to other shapes when the grooves are placed longitudinally [3]. This point will be addressed when the dynamics of the flow inside the grooves are discussed further below.

One primary mechanism by which grooved surfaces are believed to reduce friction drag is delaying transition. One way of accomplishing a similar effect that is pertinent to the current type of treatment is "restarting" the boundary layer at a proper place in a way that takes advantage of the sudden drop in shear stress due to the sudden absence of the wall but does not let it grow thick enough to wipe out any benefit scored. The flow generally exhibits a drop in friction coefficient over the groove and a spike at the restart of the boundary layer over the next section downstream. The general picture and numbers compare well with experimental results reported by Wahidi [12].

Figure 4 shows the skin friction coefficient, normalized by the skin friction value of the same location for a smooth surface, upstream of, over and downstream of a typical (middle) groove. The dots are connected via simple smoothed lines for ease of viewing. Taking the grooves one by one, one can make the following obvious observations regarding the behavior of the friction coefficient. First, for the square groove, the friction coefficient drops suddenly over the groove, builds up gradually along the bottom of the groove, and then peaks slightly at the restart of the surface. The increase and decrease in friction is smooth and monotonic, with no kinks, mainly because of the simple geometry of the square groove. Additionally, one notices that upstream and downstream of the groove, the skin friction is not the lowest. This is a result of the gradual built-up modification of the boundary layer by grooves upstream of the groove shown. Finally, we see that the peak of the friction coefficient at the restart of the boundary layer is not very sharp. This is addressed further when the momentum of the flow is discussed in the next subsection for this and the two other groove geometry.

For the triangular groove, skin friction peaks just before the groove, drops suddenly, then fluctuates around the sharp bottom of the groove. It makes a noticeable jump before the level flat surface is reached, and spikes considerably at the restart of the boundary layer. We notice that despite the fluctuations, the triangular groove has the lowest friction coefficient inside the actual groove. The cumulative effect of such spikes, however, are seen in the higher than average skin friction far away from the triangular groove, explaining their poor performance as mentioned above.

Finally, for the semicircular groove, which has the lowest upstream and downstream skin friction levels, the behavior is relatively simpler. After the initial drop, the skin friction monotonically increases over the semicircular surface of the groove then quickly drops at separation and spikes again at the beginning of the boundary layer downstream of the groove. The skin friction values as well as the

spike at separation are comparable to the square groove's, which explains the close performance of these two geometries in the overall calculation of the skin friction presented in figure 4.

3.2 Cross-flow momentum transfer

To understand the mechanism of the turbulent flow in and around the flow and how the geometry might affect the separation and restart of the boundary layer, one must consider the interaction between the main flow and any small-scale flow emanating from the grooves. Figures 3 show velocity vector plots in and around the typical square, triangular and semicircular grooves. In general, turbulence rarely penetrates into the grooves, making the shear stress and thus skin friction much lower than that over the flat part of the surface. Moreover, inside the grooves, the large viscous damping reduces the tangential fluctuations in velocity , while kinematic blocking reduces the normal fluctuations. However, the dynamic behavior of the flow inside the grooves greatly affects their compound effect on the overall reduction or increase in drag over the whole surface.

Pound-for-pound, square transverse grooves are expected to induce lower shear stress in the direction of the flow than, say, triangular grooves, for two reasons: first, the vertical walls do not contribute directly to the surface shear stress parallel to the main flow direction. Secondly, the bottom walls of the grooves are well below the main flow in a way that deems the resultant friction much lower due to decreased velocity inside the grooves. Semicircular grooves, on the other hand, have smooth interiors but are relatively closer to the main flow than are the other two groove shapes. Detailed discussion of velocity vectors is presented below.

The symmetric, sharp geometry of the square groove sustains enough equilibrating pressure for the flow just above the groove so as to keep the disturbance of the main flow to a minimum after separation has taken place. The high point of reattachment on the opposite wall of the groove allows the boundary layer to make

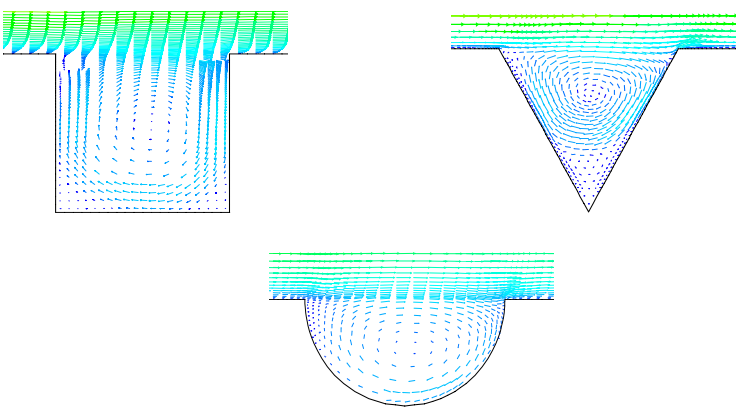

Figure 3: Velocity vectors in and around grooves.

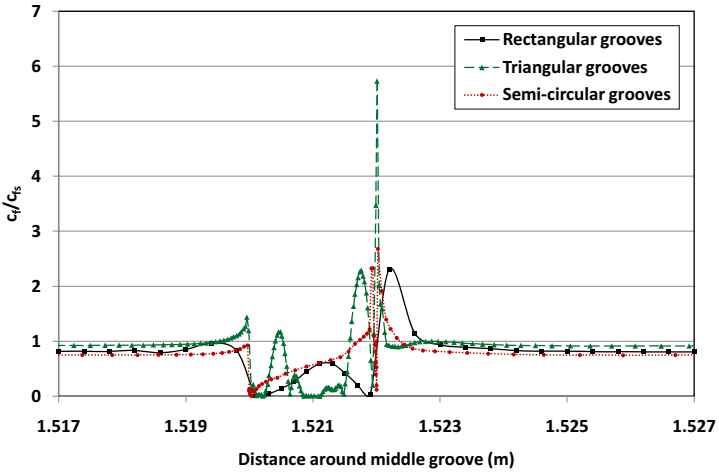

Figure 4: Normalized skin friction coefficient upstream of, inside and downstream of grooves.

a clear restart at the downstream flat surface, while the large area of the groove smoothly absorbs some longitudinal momentum into the crisp recirculating flow and prevents it from interfering with the remainder of the main flow crossing over. This explains the relatively small jump in friction coefficient downstream of the groove in figure 4. From preliminary runs done for this study, the structure of the detachment/reattachement does not change much when the inter-groove spacing of 2 mm is increased. However, the reduction in the friction coefficient starts to decrease, as they become smaller than the large-scale longitudinal vortices. This agrees well with experimental drag characteristic measurements done by Ching et al. on a tow tank but for comparable Reynolds numbers [5].

Figure 3 shows a velocity vector plot of the middle triangular groove discussed earlier. One immediately notices the lower stagnation point inside the inclined backward facing side of the groove. The boundary layer developed therein grows longer in this case, disturbing further the main flow over the groove. Greater near-wall secondary flow motion contributes to drag increase, as is evident by previous plots and integrals. Additionally, even more clear in this figure are the two sizeable recirculation zones inside the groove. The two ensuing stagnation points give rise to the ensuing fluctuations in friction coefficient noticed in figure 4, and the horizontal components of these clearly contribute to the deteriorated performance of these grooves in this study.

For the case of semicircular grooves the stagnation point is also high, similar to the square groove case. Thus the spike in skin friction at the restart of the boundary layer is much lower than the triangular groove. The comfortable, monotonic development of the boundary layer inside the groove, however, adds to the skin friction cost of these grooves.

4 Conclusions and future work

In this paper, the turbulent flow over transversely grooved surfaces was numerically studied. Three different groove geometries were constructed and compared on the basis of reduction in total skin friction coefficient. Skin friction values and behavior inside the grooves was a good indicator of how the flow exiting them would disturb the main flow and to what degree. The optimum groove was one that succeeds in terminating the boundary layer but does not introduce high cross flow at the beginning of the next straight section of the surface. In general, square grooves outperformed comparable triangular and semi-circular grooves in the medium turbulent Reynolds number ranges. It was found that the dynamics of the flow inside the grooves, the nature of separation and reattachment of the flow, and the location of the stagnation point influenced what happens downstream of the grooves greatly. For the studied groove sizes and spacings, the results favor square grooves for the Reynolds number range reported herein. Higher Reynolds number simulations would shed more light on the dynamics of interaction between the flow inside the grooves and the main parallel flow but then compressibility effects must be considered, which are not the subject of this paper.

The results validate the notion that optimally grooved surfaces might greatly benefit efforts to reduce viscous drag which will increase the efficiency and enhance the performance of many engineering devices in numerous applications across the industry. Future work in this area is to optimize the shape of the groove as to accomplish the above goal. This might be in the form of using jigsaw-shaped surfaces in a way that achieves the desired detachment and reattachment effect for maximum drag reduction. Another possibility to use *deep* grooves or completely open slits in the surface to accomplish the desired effect. Further optimization of inter-groove spacing is required, and different ranges of Reynolds number must also be studied to develop a more complete picture. The effect of the turbulent boundary layer modification on Nusselt number is also interesting. The question of whether heat transfer enhancement must come at the expense of drag (increase) is an interesting one. It is equally interesting to explore the possibility of existence of a pure hydrodynamic technique that alleviates the dependence of shear stress of Reynolds number as suggested by Polidori et al. [10] using temperature difference.

One final note about the numerics is that the solution tends to stagnate short of convergence when using single precision due to the large order of magnitude difference between the various equations. Even for moderate Reynolds numbers, the non-scaled residuals of turbulent dissipation rate and continuity equations are 10 orders of magnitude apart. That said, the prospects of using CFD as a valid tool to investigate such flows and geometry, in the opinion of the authors, still outshine many of the current experimental techniques due to the large number of data points required for the necessary measurements and the large fluctuations in quantities near rough surfaces. Nevertheless, CFD simulations will never replace experimental work. Only validated numerical models can give insight to the underlying physical aspects of such flows. This stipulates undertaking a thorough comparison

between the results obtained here and the experimental work conducted by Ching and Parsons [5], which agree favorably thus far.

References

[1] Hama, F.R., Long, J.D. & Hegarty, J.C., On transition from laminar to turbulent flow. *Journal of Applied Physics*, **28(4)**, pp. 388–394, 1957.

[2] Kline, S.J., Reynolds, W.C., Schraub, F.A. & Runstadler, P.W., The structure of turbulent boundary layers. *Journal of Fluid Mechanics*, **30**, pp. 741–773, 1967.

[3] Viswanath, P.R., Aircraft viscous drag reduction using riblets. *Progress in Aerospace Sciences*, **38**, pp. 571–600, 2002.

[4] Tani, I., Munakat, H., Matsumoto, A. & Abe, K., Turbulence management by groove roughness. *Turbulence Management and Relaminarization*, eds. H.W. Liepman & R. Narasimha, Springer-Verlag, pp. 161–172, 1987.

[5] Ching, C.Y. & Parsons, B.L., Drag characteristics of turbulent boundary layer over a flat plate with transverse square grooves. *Experiments in Fluids*, **26**, pp. 273–275, 1999.

[6] Caram, J.M. & Ahmed, A., Development on the wake of an airfoil with riblets. *AIAA Journal*, **30(12)**, pp. 2817–2818, 1992.

[7] Kramer, M.O., Boundary-layer stabilization by distributed damping. *Journal of the aeronautical sciences*, **24**, pp. 459–460, 1957.

[8] Gad-el-Hak, M., Compliant coatings for drag reduction. *Progress in Aerospace Sciences*, **38**, pp. 77–99, 2002.

[9] Katoh, K., Choi, K.S. & Azuma, T., Heat-transfer enhancement and pressure loss by surface roughness in turbulent channel flows. *International Journal of Heat and Mass Transfer*, **43**, pp. 4009–4017, 2000.

[10] Polidori, G., Taïar, R., Fohanno, S., Mai, T.H. & Lodini, A., Skin-friction drag analysis from the forced convection modeling in simplified underwater swimming. *Journal of Biomechanics*, **39(13)**, pp. 2535–2541, 2006.

[11] Endo, T., Kasagi, N. & Suzuki, Y., Feedback control of wall turbulence with wall deformation. *International Journal of Heat and Fluid Flow*, **21**, pp. 568–575, 2000.

[12] Wahidi, R., Chakroun, W. & Al-Fahed, S., The behavior of the skin-friction coefficient of a turbulent boundary layer flow over a flat plate with differently configured transverse square grooves. *Experimental Thermal and Fluid Science*, **30(2)**, pp. 141–152, 2005.

[13] Wilcox, D.C., *Turbulence Modelling for CFD*. DCW Industries Inc.: La Canada, CA, USA, 1993.

[14] Fluent Inc., Lebanon, NH, USA, *FLUENT 6.2 User's Guide*, 2005.

Section 2
Environmental fluid mechanics

This page intentionally left blank

Stability of meridionally-flowing grounded abyssal currents in the ocean

G. E. Swaters
Applied Mathematics Institute,
Department of Mathematical & Statistical Sciences and
Institute for Geophysical Research, University of Alberta, Edmonton, Canada

Abstract

Deep western boundary currents are an important component of the thermohaline circulation in the ocean, which plays a dominant role in Earth's evolving climate. By exploiting the underlying Hamiltonian structure, sufficient stability (and hence necessary instability) conditions are derived for meridionally-flowing grounded abyssal currents, based on a baroclinic model corresponding to a low frequency limit of the three-layer shallow water equations on a β-plane with variable topography.
Keywords: abyssal overflows, deep western boundary currents, meridional overturning circulation, baroclinic instability, climate dynamics.

1 Introduction

In a source region of deep water formation, the Sverdrup vorticity balance predicts equatorward abyssal flow (Stommel and Arons [1]). Away from the source region, Stommel-Arons theory cannot infer the flow direction of abyssal currents. However, many abyssal currents are characterized by the isopycnal field being grounded against sloping topography and the flow being in geostrophic balance. As shown by Nof [2], a fully grounded abyssal water mass lying over sloping topography flows, in the fully nonlinear but reduced gravity dynamical limit, nondispersively and steadily in the along slope direction, irrespective of the specific height or vorticity field within the abyssal water mass.

These two results provide a dynamical scenario for the initiation and maintenance of source-driven grounded abyssal flow. That is, in high latitude regions

WIT Transactions on Engineering Sciences, Vol 59, © 2008 WIT Press
www.witpress.com, ISSN 1743-3533 (on-line)
doi:10.2495/AFM080091

where deep water is produced (often over sloping topography), the Sverdrup vorticity balance initiates equatorward flow. Once produced, this water mass can become grounded and geostrophically adjusted, maintaining a Nof balance that permits sustained basin scale meridional quasi-steady and coherent abyssal flow. The principal purpose of the present contribution is to briefly present the stability properties associated with a baroclinic model that describes the dynamics of grounded abyssal currents as process that begins as a source-driven "Stommel-Arons flow" and then transitions to a "Nof flow" as the abyssal water mass flows equatorward. The report given here is part of a much larger study on the dynamics on grounded abyssal flow by Swaters [3, 4].

2 Governing equations

The model is a low frequency (sub-inertial) limit of the three-layer shallow-water equations on a β-plane with variable topography (for full details see Swaters [3]). In this limit, the primary dynamical variables are the geostrophic (leading order reduced) pressures in the upper two layers and the thickness of the bottom or abyssal layer (see Fig. 1). The nondimensional governing equations are given by

$$[\partial_t + J(\phi_1, \cdot)][\triangle\phi_1 - F_1(\phi_1 - \phi_2) + \beta y] = \frac{F_1 Q}{F_1 + F_2} + \frac{\triangle^2\phi_1}{R_e}, \tag{1}$$

$$\begin{aligned}[\partial_t + J(\phi_2, \cdot)][\triangle\phi_2 - F_2(\phi_2 - \phi_1) + h + h_B + \beta y] \\ = -r_2\triangle\phi_2 + \frac{F_1 Q}{F_1 + F_2} + \frac{\triangle^2\phi_2}{R_e},\end{aligned} \tag{2}$$

$$h_t + J\left(h + \phi_2 + h_B, \frac{h}{1 + s\beta y}\right) = Q + r_3\,\triangle(\phi_2 + h_B + h), \tag{3}$$

with the auxiliary diagnostic relations

$$\left.\begin{aligned}\mathbf{u}_{1,2} = \mathbf{e}_3 \times \nabla\phi_{1,2},\ \mathbf{u}_3 = \frac{\mathbf{e}_3 \times \nabla(\phi_2 + h_B + h)}{1 + s\beta y}, \\ p = \phi_2 + h_B + h,\ \eta = \phi_2 - \phi_1,\end{aligned}\right\} \tag{4}$$

with $J(A, B) = A_x B_y - A_y B_x$, and where the 1, 2 or 3 subscript on a *physical variable* refers to the upper, middle and abyssal layer, respectively, alphabetical subscripts (unless otherwise noted) indicate partial differentiation, $\mathbf{u}_{1,2,3} = (u_{1,2,3}, v_{1,2,3})$, $\nabla = (\partial_x, \partial_y)$, $\triangle = \nabla\cdot\nabla$, h_B is the height of the topography, h is the height of the abyssal layer relative to h_B, η is the deflection (measured positively upward) of the interface between the two upper layers from its equilibrium position and Q is the down or upwelling term, respectively. The dynamic pressures in the upper two layers is given by $\phi_{1,2}$, and in the abyssal layer by p, respectively. Equations (4c,d) express the continuity of total pressure across the deforming interfaces between the middle and abyssal layers and the upper

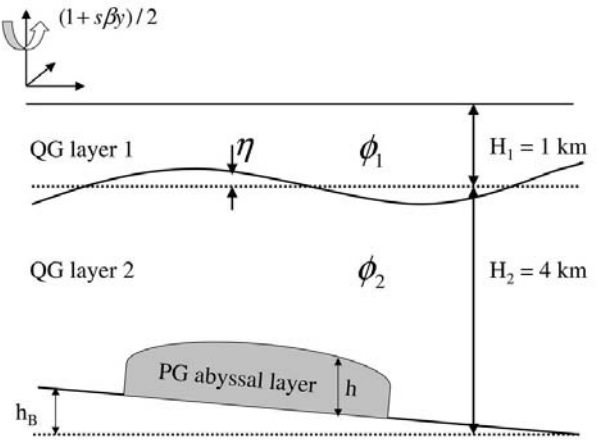

Figure 1: Model geometry used in this paper.

and middle layers, respectively. The model is a hybrid quasigeostrophic/planetary geostrophic (QG/PG) system in which (1) and (2) are the QG and (3) is the PG potential vorticity equations, respectively, for the individual layers.

The dynamical parameters are defined by

$$s = \frac{s^* L}{H_2},\ \beta = \frac{\beta^* L^2}{U_*},\ R_e = \frac{U_* L}{A_H},\ F_1 = \frac{g' H_2}{\widetilde{g} H_1},\ F_2 = \frac{g'}{\widetilde{g}},\ r_{2,3} = \frac{r^*_{2,3}}{s H_2}, \quad (5)$$

where $H_{1,2}$ are the constant reference layer thicknesses in the upper two layers, ρ_* is the reference Boussinesq density and $g' = (\rho_3 - \rho_2)g/\rho_* > 0$ and $\widetilde{g} = (\rho_2 - \rho_1)g/\rho_* > 0$ where $\rho_{1,2,3}$ correspond to the constant density in each individual layer with $0 < \rho_1 < \rho_2 < \rho_3$, $L = \sqrt{g' H_2}/f_0$ (the internal deformation radius for the middle layer), $U_* = s^* g'/f_0$ (the Nof speed), $s^* \approx O(\nabla^* h^*_B)$ (a representative value for the topographic slope), f_0 is the reference Coriolis parameter, β^* is the northward gradient of the Coriolis parameter, respectively. In addition, A_H is the horizontal eddy coefficient in the upper two layers and $r^*_{2,3}$ are "bottom friction coefficients" for the middle and abyssal layers, respectively. Ekman boundary layer theory implies that $r^*_{2,3} = H_{2,3}\sqrt{E^V_{2,3}}$, where $H_{2,3}$ are the vertical thickness scales and $E^V_{2,3}$ are the vertical Ekman numbers for, respectively, the middle and abyssal layers. Accordingly, $r^*_{2,3}$ are the scale vertical thicknesses of the Ekman bottom boundary layer in the middle and abyssal layers, respectively.

The unforced, inviscid dynamics of the model is purely baroclinic (i.e., the horizontal divergence of the barotropic mass flux is zero). Although there is no "thermodynamics" in the model *per se* (so that there is no genuine heat or salinity transport), $Q > 0$ can be heuristically interpreted as a cooling of the overlying water column that leads to a downward mass flux resulting in the depletion of the

overlying water mass and a corresponding increase in the volume of abyssal water. Similarly, $Q < 0$ can be heuristically interpreted as warming or freshening of the abyssal water mass that leads to an upward mass flux resulting in the depletion of the abyssal water mass and a corresponding increase in the volume of upper ocean water.

3 Stability problem

To examine the baroclinic instability problem in its simplest form, but still retain the most important features, the inviscid, rigid-lid and $2\frac{1}{2}$-layer approximation $F_{1,2} = \phi_1 = r_{2,3} = 0$, $R_e \to \infty$, is introduced into (1), (2) and (3), yielding

$$(\triangle\eta + h)_t + J(\eta,\ \triangle\eta + h + h_B + \beta y\ ) = 0, \tag{6}$$

$$h_t + J\left(h + \eta + h_B, \frac{h}{1 + s\beta y}\right) = Q, \tag{7}$$

where, for convenience, $\eta \equiv \phi_2$.

The area integrated energy for (6) and (7) is given by

$$\mathcal{E}(\eta, h) = \frac{1}{2}\iint_\Omega \nabla\eta \cdot \nabla\eta + (h + h_B)^2 - h_B^2\ dxdy, \tag{8}$$

which will be invariant in the inertial limit $Q = 0$. If $Q = 0$, (6) and (7) is a 2×2 infinite dimensional Hamiltonian dynamical system (Swaters [5, 6]), in which $\mathcal{E}$ will be the Hamiltonian functional and the Hamiltonian variables are given by $\triangle\eta + h$ and h, respectively. The *Casimirs* (i.e., the set of invariant functionals that span the Kernel of the Poisson bracket; see Swaters [5]), which are needed in the variational principle, may be written in the form

$$\mathcal{C}_1 = \iint_\Omega \left\{ \int_{h_B+\beta y}^{\triangle\eta+h+h_B+\beta y} F_1(\xi\ )\, d\xi \right\} dxdy, \tag{9}$$

$$\mathcal{C}_2 = \iint_\Omega (1 + s\beta y) \left\{ \int_0^{h/(1+s\beta y)} F_2(\xi\ )\, d\xi \right\} dxdy, \tag{10}$$

where $F_{1,2}$ are arbitrary functions of their arguments.

3.1 Steady solutions, variational principle and stability conditions

General *inertial* steady abyssal solutions to (6) and (7) of the form

$$\eta = \widetilde{\eta} = 0,\ h = \widetilde{h}(x, y),\ h_B = h_B(x, y),\ Q = 0, \tag{11}$$

must satisfy

$$J\left(\widetilde{h} + h_B, \frac{\widetilde{h}}{1 + s\beta y}\right) = 0 \Longrightarrow \widetilde{h} + h_B = F\left(\frac{\widetilde{h}}{1 + s\beta y}\right), \tag{12}$$

for some function F.

The solution (12) satisfies the first order conditions for an extremal of the invariant functional

$$\mathcal{I} \equiv \mathcal{E} + \mathcal{C}_1 + \mathcal{C}_2 = \mathcal{E} - \iint_\Omega (1 + s\beta y)\left\{ \int_0^{h/(1+s\beta y)} F(\xi)\, d\xi \right\} dxdy, \quad (13)$$

where $F_1 = 0$ and $F_2 = -F$. It follows (assuming $\eta = 0$ on the boundary of Ω) that

$$\begin{aligned} \delta\mathcal{I}(\eta, h) &= \iint_\Omega -\eta\triangle\delta\eta + \left[h + h_B - F\left(\frac{h}{1+s\beta y}\right)\right]\delta h \; dxdy \\ &= \iint_\Omega -\eta(\triangle\delta\eta + \delta h) + \left[h + \eta + h_B - F\left(\frac{h}{1+s\beta y}\right)\right]\delta h \; dxdy, \end{aligned} \quad (14)$$

so that $\delta\mathcal{I}(\widetilde{\eta}, \widetilde{h}) = 0$.

The second variation of $\mathcal{I}$ evaluated at the steady solution $(\widetilde{\eta}, \widetilde{h})$ is given by

$$\begin{aligned} \delta^2\mathcal{I}(\widetilde{\eta}, \widetilde{h}) &= \iint_\Omega \nabla\delta\eta \cdot \nabla\delta\eta + \left[1 - \frac{F'(\frac{\widetilde{h}}{1+s\beta y})}{(1+s\beta y)}\right](\delta h)^2 \; dxdy, \\ &= \iint_\Omega \nabla\delta\eta \cdot \nabla\delta\eta - \frac{h_{B_x}(x, y)}{\widetilde{h}_x(x, y)}(\delta h)^2 \; dxdy, \end{aligned} \quad (15)$$

where the "prime" means differentiation with respect to the argument and (12) has been used. It is *always* the case that $\delta^2\mathcal{I}(\widetilde{\eta}, \widetilde{h})$ is an invariant of the linear stability equations (Swaters [6]). Since the integrand of the functional $\delta^2\mathcal{I}(\widetilde{\eta}, \widetilde{h})$ is a diagonalized quadratic form with respect to $(\delta\eta, \delta h)$, if $\delta^2\mathcal{I}(\widetilde{\eta}, \widetilde{h})$ is definite in sign for all perturbations, then $(\widetilde{\eta}, \widetilde{h})$ is linearly stable (in the sense of Liapunov with respect to the norm $[|\delta^2\mathcal{I}(\widetilde{\eta}, \widetilde{h})|]^{\frac{1}{2}}$).

The case where $\delta^2\mathcal{I}(\widetilde{\eta}, \widetilde{h}) < 0$ is not considered. It requires certain mathematical properties to hold on the domain Ω and while these can occur this analysis is not pursued (see Swaters [5] for the f-plane Hamiltonian-based analysis). The case where $\delta^2\mathcal{I}(\widetilde{\eta}, \widetilde{h}) > 0$ is precisely analogous to Fjørtoft's stability theorem (Swaters [6]) and reduces to the f-plane results of Swaters [5, 7].

It follows from (15) that $\delta^2\mathcal{I}(\widetilde{\eta}, \widetilde{h}) > 0$ when

$$\frac{h_{B_x}(x, y)}{\widetilde{h}_x(x, y)} \leq 0, \quad (16)$$

This is a *sufficient* condition for stability. A *necessary* condition for instability is, therefore, that there exists at least one point $(x, y) \in \Omega$ for which

$$\frac{h_{B_x}(x, y)}{\widetilde{h}_x(x, y)} > 0. \quad (17)$$

Even though β has been fully retained, this stability condition is identical in form to that obtained by Swaters [7].

Consider the case where $h_{B_x}(x, y) < 0$ as would occur, on average, along the western shelf-slope region of an ocean basin (see Fig. 1). The necessary condition for instability is that there exists at least one point for which $\widetilde{h}_x(x, y) < 0$. For a parabolically shaped abyssal current with up slope and down slope groundings, this condition holds on the down slope flank but not on the up slope flank. This is why the instability preferentially amplifies on the down slope flank and the amplitude of the perturbations along the down slope grounding are much larger compared to those on the up slope grounding (see Swaters [4, 7, 8]). Physically, energy is required to move grounded abyssal fluid parcels located adjacent to the up slope grounding up the sloping bottom (against the force of gravity), while energy is released by the down slope movement of grounded abyssal fluid parcels located along the down slope grounding. The result is that there is a spatial asymmetry (even on an f-plane) in the destabilization of these grounded abyssal currents. This asymmetry is clearly seen in numerical simulations (Swaters [4, 8]).

4 Baroclinic instability characteristics for a constant velocity abyssal current

The *general* linear stability equations are analytically intractable. However, much can be learned from the constant velocity abyssal flow on the linearly sloping bottom, given by

$$h_0 = \widetilde{h} - \gamma x \geq 0, \; h_B = -x, \tag{18}$$

where $\widetilde{h} > 0$ is constant, and neglecting terms of $O(s\beta)$ but retaining β. The abyssal height (18) is the simplest profile for h_0 that satisfies the necessary condition for instability and for which the stability problem can be solved explicitly.

The linear stability problem associated with (18) can be written in the form

$$\triangle \eta_t + \beta \eta_x + (h + \eta)_y = 0, \; h_t - h_y + \gamma \eta_y = 0. \tag{19}$$

These equations will be solved in the meridional channel domain $x \in (0, L)$ so that the appropriate boundary condition is $\eta = 0$ on $x = 0, L$. It is convenient to write the solution in the form

$$(h, \eta) = A[\gamma/(1 + c), 1] \sin(n\pi x/L) \exp[ik(y - ct) - i\beta x/(2ck)] + c.c., \tag{20}$$

where $n \in \mathbb{Z}^+$, $c.c.$ means the complex conjugate of the preceding term, k is the meridional, or along slope, wavenumber, A is a free amplitude constant, and c is the complex-valued phase velocity that must satisfy the dispersion relationship

$$K^2 c^3 + (1 + K^2)c^2 + [1 + \gamma - (\beta/2k)^2]c - (\beta/2k)^2 = 0, \tag{21}$$

where $K \equiv \sqrt{k^2 + l^2}$ is the wavenumber modulus and $l \equiv n\pi/L$.

The three roots to the cubic dispersion relation (21) correspond to a barotropic and baroclinic topographic Rossby wave and to a planetary Rossby wave, respectively (Swaters [3]). The onset of instability corresponds to the coalescence of

the barotropic and baroclinic topographic Rossby modes. Mathematically, this coalescence occurs when the discriminate for the cubic (21) is zero and this condition defines the marginal stability boundary. Thus, the marginal stability boundary is given by

$$\varsigma_1^3 - (\varsigma_2\varsigma_1/2)^2 - 9\varsigma_1\varsigma_2\varsigma_3/2 + 27\varsigma_3^2/4 + \varsigma_2^3\varsigma_3 = 0, \tag{22}$$

where

$$\varsigma_1 \equiv [1 + \gamma - (\beta/2k)^2]/K^2,\ \varsigma_2 \equiv 1 + 1/K^2,\ \varsigma_3 \equiv -[\beta/(2kK)]^2. \tag{23}$$

Equation (22) is itself a cubic with respect to ς_1 (i.e., γ). It can be shown that the discriminate for (22) is strictly positive since $\varsigma_2 > 0$ and $\varsigma_3 < 0$ and is zero only if $\beta = 0$. Thus, there is only one real solution for γ, denoted as $\gamma_c(k, l, \beta)$, and this is the marginal stability boundary (or, equivalently, the critical equatorward abyssal velocity). That is, for a given k, l and β, instability only occurs if $\gamma > \gamma_c$, (neutral) stability occurs if $\gamma \leq \gamma_c$ and the marginal stability boundary is given by $\gamma = \gamma_c(k, l, \beta)$. The point of marginal stability will be the minimum $\gamma_c \geq 0$, with respect to k and l, for fixed β. In the limit $\beta = 0$, (22) reduces to $\gamma_c = (K^2 - 1)^2/(4K^2)$, which is the f-plane result of Mooney and Swaters [9]. Based on the nondimensionalizations introduced, it is possible to characterize the most unstable mode as having an along slope wavelength on the order of 94 km, an equatorward phase velocity on the order of 3 cm/s, a modal period on the order of 38 days and an e-folding amplification time on the order of 6 days (Swaters [3]).

5 Conclusions

A model has been presented capable of describing the meridional flow of source driven grounded abyssal flow in a stratified ocean. In the inviscid, unforced limit, the model can be written as an infinite-dimensional noncanonical Hamiltonian dynamical system and this formalism has been exploited to establish sufficient linear stability (and hence necessary instability) conditions for general steady bottom-intensified abyssal flow. The linear stability equations were explicitly solved in the case of an equatorward flowing abyssal current with constant velocity. The most unstable mode, which corresponds to a baroclinic topographic planetary wave, has a wavelength on the order of 94 km, an equatorward phase velocity on the order of 3 cm/s, a modal period on the order of 38 $days$ and an e-folding amplification time on the order of 6 $days$.

Acknowledgement

Preparation of this extended abstract was supported in part by the Natural Sciences and Engineering Research Council of Canada.

References

[1] Stommel, H., and Arons, A. B., On the abyssal circulation of the world ocean – I. Stationary flow patterns on a sphere. *Deep-Sea Res.*, 1960, **6**, 140–154.
[2] Nof, D., The translation of isolated cold eddies on a sloping bottom. *Deep-Sea Res.*, 1983, **30**, 171–182.
[3] Swaters, G. E., The meridional flow of source-driven abyssal currents in a stratified basin with topography. Part I. Model development and dynamical properties. *J. Phys. Oceanogr.*, 2006, **36**, 335–355.
[4] Swaters, G. E., The meridional flow of source-driven abyssal currents in a stratified basin with topography. Part II. Numerical Simulation. *J. Phys. Oceanogr.*, 2006, **36**, 356–375.
[5] Swaters, G. E., Nonlinear stability of intermediate baroclinic flow on a sloping bottom. *Proc. R. Soc. Lond. A*, 1993, **442**, 249–272.
[6] Swaters, G. E., *Introduction to Hamiltonian Fluid Dynamics and Stability Theory*, 2000 (Chapman&Hall/CRC Press: New York).
[7] Swaters, G. E., On the baroclinic instability of cold-core coupled density fronts on sloping continental shelf. *J. Fluid Mech.*, 1991, **224**, 361–382.
[8] Swaters, G. E., Numerical simulations of the baroclinic dynamics of density-driven coupled fronts and eddies on a sloping bottom. *J. Geophys. Res.*, 1998, **103**, 2945–2961.
[9] Mooney, C. J., and Swaters, G. E., Finite amplitude baroclinic instability of a mesoscale gravity current in a channel. *Geophys. Astrophys. Fluid Dyn.*, 1996, **82**, 173–205.

Experimental tests and Computational Fluid Dynamics (CFD) simulations of barriers installed around open storage piles of raw materials

I. Diego, J. Toraño, S. Torno & B. García
GIMOC, Mining Engineering and Civil Works Research Group, Oviedo School of Mines, University of Oviedo, Spain

Abstract

The international commerce of raw materials is growing every year at a high rate. Hugh amounts of granular materials are moved around the world and thus increase the need of storage space. Usually the stockage yards where the materials lay are installed in an open air, so the potential to create dust emissions due to wind blows is high, then generating operative and environmental problems. In order to quantify these emissions a series of scaled experiments to simulate air flows and dust emission around conical shaped piles of granulated materials stored in open areas have been developed. These experiments are then used to validate CFD models of the phenomena. In a first phase the experiments gave the possibility to effectively measure the flow patterns and the dust emission around conical material piles. A Lagrangian Multiphase model was implemented in CFD commercial code Ansys CFX 10.0, that successfully simulated the emission of dust as compared to experimental data. In the second phase, to be shown in this paper, metallic barriers are installed surrounding the piles, and flow characteristics and dust emission are measured through the use of hot-wire anemometers and light scattering instruments as well as simulated in the CFD package. The paper shows how k-epsilon turbulence models are accurate enough to simulate the air flow in affordable mesh resolutions and computing times. The superficial velocity contours over the cone face are also studied in order to obtain the degree of dust emission diminishing expected due to the barrier installation. These studies have been done in the framework of the Research Project CTM2005-00187/TECNO, "Prediction models and prevention systems in the particle atmospheric contamination in an industrial environment" of the Spanish National R+D Plan of the Ministry of Education and Science, 2004-2007 period.

Keywords: storage piles, wind tunnel, CFD Lagrangian methods, turbulence.

WIT Transactions on Engineering Sciences, Vol 59, © 2008 WIT Press
www.witpress.com, ISSN 1743-3533 (on-line)
doi:10.2495/AFM080101

1 Introduction

The research group of Mining Engineering and Civil Works of the University of Oviedo, based in the School of Mines of Oviedo (Spain) is developing a research project granted by the Spanish Ministry of Education and Science. One of the project goals is to develop and study dust emission factors in several industrial situations, from quarries blasts to ship unloading or loading facilities. The researches and simulations have been very successful in several fields obtaining interesting results in the case of dust coming from quarries blasts, both using CFD [1] and classical dispersion methods, [2], and comparing results for different pile shape configurations, [3] and [4]. Now the next step has been taken, trying to evaluate the mitigation of emissions using solid barriers that are installed surrounding the piles. These barriers can be porous or non-porous and there are several references where PIV (Particle Image Velocimetry) methods are used in order to evaluate flow around pile-shaped flow obstacles, [5] and [6].

Instead using PIV methods, indirect methods will be used to measure air velocities and dust concentrations in scaled tests. Light scattering instruments are used to measure dust clouds and hot wire anemometers in case of measuring air velocities.

1:10 scaled tests were conducted simulating a cone shaped pile surrounded by a solid barrier. In order to create the flow a mine ventilation fan is used, obtaining flows up to 16 m/s. Velocity values are measured in 64 points and dust concentrations are measured in two locations. A measured quantity of dust is homogeneously disseminated over the metallic cone surface, repeating the experiment in case of 3 different materials: coal, cement and limestone.

These measurements are then used to validate CFD (Computational Fluid Dynamics) models, in a first stage one phase models where air movements are simulated and in a second stage Lagrangian multiphase models where dust movement is represented. The main goal is to check the amounts of dust injected in the surrounding as compared to the calculations done by the North American standard EPA [7].

This paper will show how the CFD calculations can effectively simulate the air movement in these experimental setups. Later papers will use the dust concentration data to validate multiphase CFD simulations.

2 Measurements and 1:10 scaled tests

The scaled tests were conducted in the tailings dam area of the coal concentration plant installed in a coal mine in Asturias, northern Spain (see attached figure 1). The initial intention was to install the piles and the fans in one side of the dam and the dust sensors on the other side, 30 meters away, in order to evaluate just the dust floating in the air, as the dust falling to the dam will be trapped there. Unfortunately dust levels at a distance of 30 meters from the emission area were null, so all the experimental setup was changed and adjusted several times until dust concentration levels were correctly measured.

The final experimental setup is shown below: a metallic cone blown by air coming out of a 300 mm pipe where a 12 kW fan, compressed air powered, is connected. The cone is installed 50 cm apart from the pipe outlet, which its axes installed at the height of the cone apex. The cone surface is then homogeneously covered by dust and once the fan is started a dust cloud is created by the pick-up of the dust particles places in certain areas of the cone.

Figure 1: Coal stockage area and experimental setup.

The test is repeated for different materials over the cone and with and without barrier installed between the cone and the pipe. Photograph at the upper right corner of figure 1 shows the setup in case of barrier installed. This barrier has a height slightly lower than the cone height, as first tests conducted with barriers with the same height as the cone showed no dust clouds creation.

Once the dust measurement tests are done comes the second phase where the air velocities are measured. To do so a hot wire anemometer TSI Velocicalc Plus is used, shown in figure 2. During all the experiments a weather station (Met One Instruments) is measuring and recording wind speed and bearing and humidity, in order to evaluate possible changes in the results. The tests were conducted in moments were wind and humidity remained constant or wind was not present.

The air velocity was measured in 64 locations, shown below in figure 3, 22 of them over the cone and 44 in the developed flow area. As our goal is to define how the dust comes out of the pile surface the 22 measurement points are profusely measured with caution.

Figure 2: Instrumentation used in velocities studies.

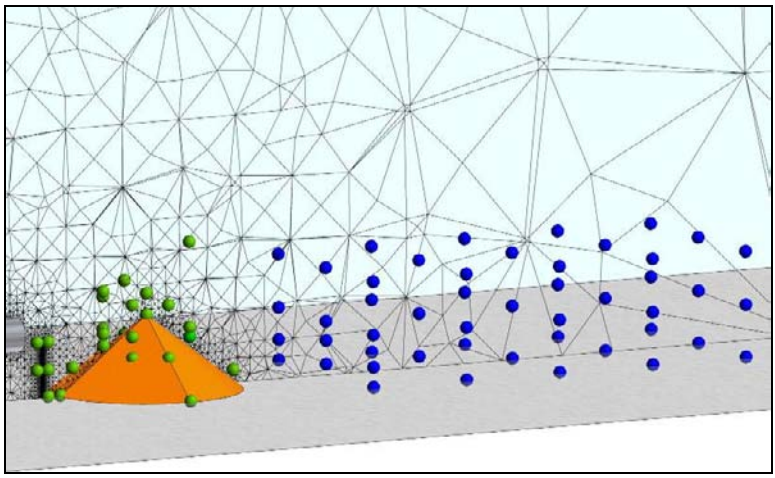

Figure 3: Measurement location.

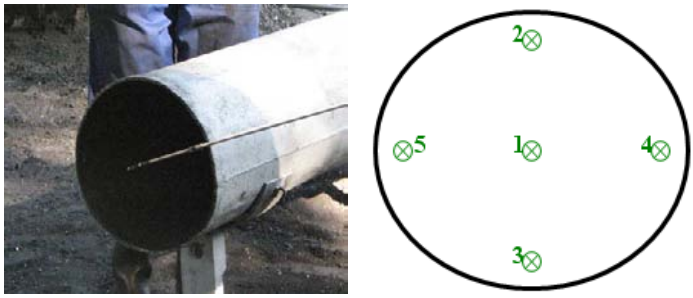

Figure 4: Measurement of inlet flow.

The air coming out of the pipe was also controlled (figure 4), observing a high difference between the several points of the pipe that were measured. Despite the expected difference between the points near the wall and the points in the axe of the pipe there are also quite big differences among opposite sides of the pipe. This is, the flow is not symmetrical, probably due to the swirl given to the air by the fan and by the fact that the pipe length is not long enough to stabilize this swirl caused by the fan blades. The velocity values in the pipe outlet are shown in table 1.

Table 1: Values of inlet flow.

Velocity values at Pipe outlet				
1	2	3	4	5
12.2 m/s	10.8 m/s	15.7 m/s	12.3 m/s	13.5 m/s

3 CFD simulation

The CFD commercial code Ansys CFX was used to develop a simulation model that allows the comparison of the experimental results and the simulated ones. The model considers a volume of 2000 m^3 surrounding the experimental setup.

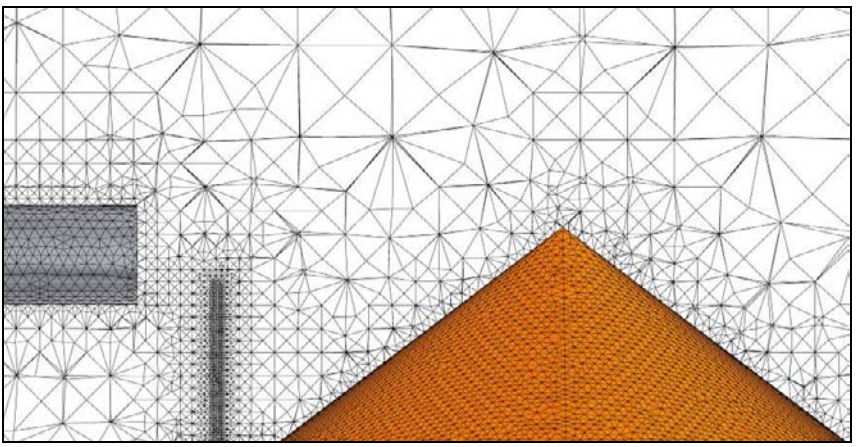

Figure 5: 3D mesh.

The meshing has been done using commercial software ANSYS ICEM CFD 10.0, importing the geometry from Solidworks parametric modelling tool through IGES format. First a geometry cleaning is done, deleting unnecessary geometry features and checking for physical incongruence. Figure 5 shows details of one of the developed meshes.

The physical characteristics of the problem are defined in CFX-Preprocessor. Three different simulations will be done, depending on the turbulence model used: Zero equation, K-epsilon, Spallart-Almaras and SST. CFX offers a wide

selection of turbulence models, from the quite simple Zero Equation models to LES and RANS, highly demanding in computing time and hardware requirements. The selection of these 4 more or less complex models is based on related bibliography, e.g. [8], [9], [10] and [11].

Despite the turbulence model selection and the problems associated to the mesh our main worries regarding the simulation were the ones associated with the inlet condition. As shown before an irregular flow pattern was obtained from the measurements and thus it should be considered in the simulation.
An inlet design sensitivity study was carried out, comparing plane inputs at the inlet condition, e.g. the same velocity and turbulence intensity values in the entire inlet surface, against curve-shaped inputs. This curve-shaped inputs were obtaining fitting a surface to the point velocity values shown in figure 4.

Figure 6 shows the adjusted curve data, obtained following method referred in [12]. Once this expression is used as the inlet velocity value there are not differences in the flow when comparing these results with the plain input ones. As this expression programming is very time-consuming it was decided to use plain inputs in all simulation cases.

$$81.7173 - 9.55898\,x - 4.83415\,x^2 - 0.566798\,x^3 + 0.325147\,x^4 + 304.339\,y - 39.8097\,x\,y - 19.4095\,x^2\,y - 2.37207\,x^3\,y + 1.21662\,x^4\,y + 703.734\,y^2 - 93.0891\,x\,y^2 - 45.2882\,x^2\,y^2 - 5.569\,x^3\,y^2 + 2.83453\,x^4\,y^2 + 1297.56\,y^3 - 167.578\,x\,y^3 - 82.2244\,x^2\,y^3 - 10.0406\,x^3\,y^3 + 5.24762\,x^4\,y^3 + 2159.8\,y^4 - 264.429\,x\,y^4 - 132.094\,x^2\,y^4 - 15.8337\,x^3\,y^4 + 8.74468\,x^4\,y^4$$

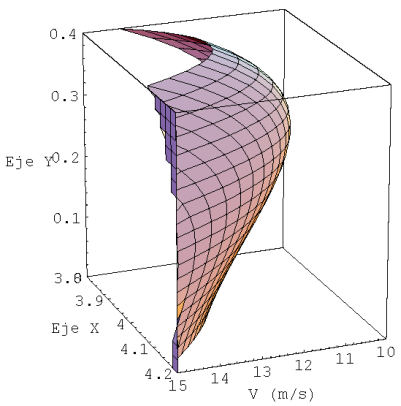

Figure 6: Inlet condition surface fitting.

Then taking into account all the factors explained above a series of simulations are repeated, with and without barrier installed, and considering 4 different turbulence model in each experimental setup. This means 8 different simulations.

Each one of these simulations is compared with the existent experimental data through a regression study.

A lineal regression is done between the pairs CFD-cfx values vs. field values. Below is shown (Figure 7) the best of the obtained comparisons, a k-epsilon model with the barrier present.

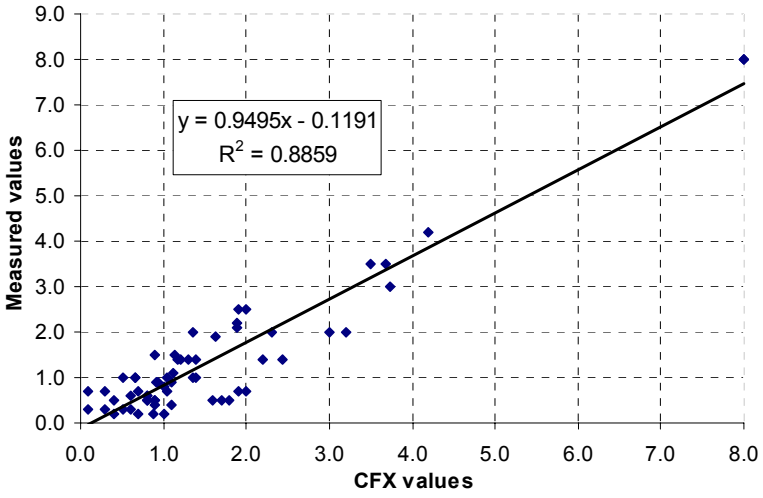

Figure 7: K-epsilon, barrier, model validation.

The following figure shows the results of this test in all analyzed cases. As can be seen the best fit, higher regression coefficient, is obtained in k-epsilon model. Generally speaking the fits are better where the barrier is not present.

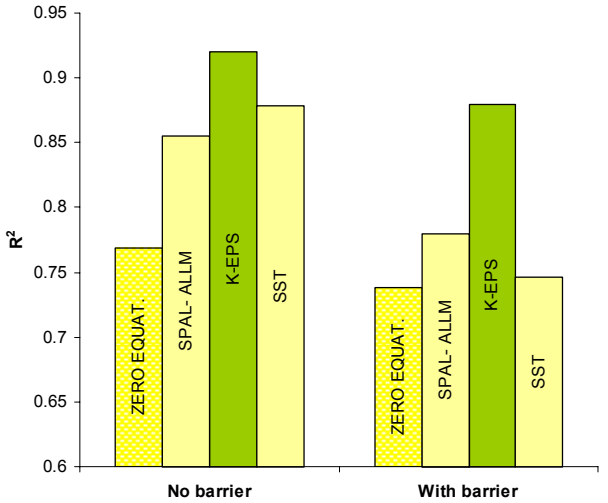

Figure 8: CFD vs. Experimental result comparison.

The great advantage of CFD, once its results have been thoroughly checked and validated, is the possibility of extreme powerful post processing. As an example found below, a comparison between the velocity distribution and streamlines of the situation with barrier and with no barrier present.

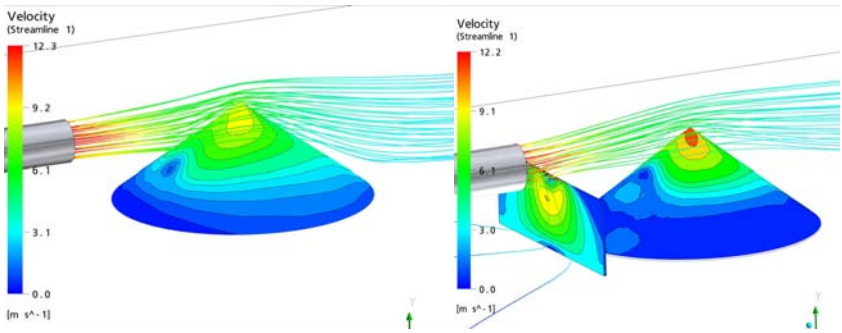

Figure 9: Results comparison.

As can be seen velocity values are lower in the vast majority of the surface of the barrier case, although velocity values in cone apex are higher in the barrier case. A post processing study must be done in order to evaluate which of the two cases will present more dust pick-up and emission over the cone surface, as is not so evident that the velocities values are higher in the no barrier case than in the barrier installed case.

4 Conclusions

Air flow around wall protected piles can be adequately simulated using CFD by means of quite simple turbulence models as k-epsilon and using meshes of medium size, around 160.000 nodes. Despite the quite simple instrumentation used, regression values obtained when comparing measured values and CFD values are surprisingly high, over 0.9 in some cases.

These results will be used to simulate the dust emission from the surface of the conical piles, and compared against the concentration measurements made with light scattering instrumentation.

Acknowledgements

We want to acknowledge the help and advices from the Ansys CFX Technical Support Team in the development of these studies.

We also want to acknowledge the support from the Spanish Ministry of Science and Education that granted these researches through the project CTM2005-00187/TECNO, “Prediction models and prevention systems in the particle atmospheric contamination in an industrial environment”.

Finally, we want to thank the help, wise advice and support of the management and staff at CARBONAR S.A., the coal mine where the scaled tests were conducted.

References

[1] J.Toraño et al - A CFD Lagrangian particle model to analyze the dust dispersion problem in quarries blasts. Capítulo del libro «Computational methods in Multiphse Flow IV». 2007. ISBN: 9781-84564-079-8.
[2] J. Toraño, R. Rodriguez, I. Diego and A. Pelegry, "Contamination by particulated material in blasts: analysis, application and adaptation of the existent calculation formulas and software". Environmental Health Risk III, pp. 209–219, (2004)Sd.
[3] I. Diego; R. Rodríguez; J.Toraño. ECCOMAS 2006. Capítulo de libro: Surface velocity contour analysis in the airborne dust generation due to open storage piles. Páginas, inicial: 1 final: 12Fecha: 2006. ISBN: 84-89925-70-4. Editorial (si libro): CIMNE (Centro Internacional de Métodos Numéricos en Ingeniería). España.Sd.
[4] J. Toraño, R. Rodríguez, I. Diego, A. Pelegry.Influence of the Pile Shape on Wind Erosion. CFD Emission Simulation. Applied Mathematical Modelling. ISSN: 0167-6105. Páginas, inicial: 1 final: 23. Fecha: 2006.Lugar de publicación: Reino Unido.Sd.
[5] Wind tunnel observations about the shelter effect of porous fences on the sand particle movements. Sang-Joon Lee, Ki-Chul Parkb, Cheol-Woo Parka. Atmospheric Environment 36 (2002) 1453–1463.
[6] Laboratory measurements of velocity and turbulence field behind porous fences. Sang-Joon Le*, Hyoung-Bum Kim. Journal of Wind Engineering and Industrial Aerodynamics 80 (1999) 311Ð326.
[7] Update Of Fugitive Dust Emissions Factors In AP-42 Section 11.2 — Wind Erosion, MRI No. 8985-K, Midwest Research Institute, Kansas City, MO, 1988.
[8] K. W. Moloney, I. S. Lowndes and G. K. Hargrave, "Analysis of flow patterns in drivages with auxiliary ventilation", Trans. Instn Min. Metall. 108, pp 17–26 (1999).
[9] A. Wala, J. Jacob, J. Brown and G. Huang, "New approaches to mine-face ventilation", Mining engineering, March 2003, pp 25-30. (2003).
[10] K.W. Moloney and I.S. Lowndes, "Comparison of measured underground air velocities and air flows simulated by computational fluid dynamics", Trans. Instn Min. Metall. 108, pp 105–114 (1999).
[11] S. A. Silvester, I. S. Lowndes and S. W. Kingman, "The ventilation of an underground crushing plant", Mining Technology (Trans. Inst. Min. Metall. A), Vol. 113, pp. 201–214 (2004).
[12] "Fitting a Surface to Scattered x-y-z Data Points". Web link http://amath.colorado.edu/computing/Mathematica/Fit/ accessed 15/11/07.

This page intentionally left blank

Evaluation of diffusion models for airborne nanoparticles transport and dispersion

F. Morency[1], S. Hallé[1], L. Dufresne[1] & C. Émond[2]
[1]*École de technologie supérieure, Département de génie mécanique, Montréal, Canada*
[2]*Université de Montréal, Département de santé environnementale et santé au travail, Montréal, Canada*

Abstract

The diffusion coefficient is a property that plays a significant role in the transport of airborne nanoparticles. However, there seems to be no general agreement in the literature on the most appropriate model to use for nanoparticle numerical simulations to be used in risk exposure assessments. This paper begins by presenting a brief review of some of the main models for small particles diffusion. A general dynamic equation for aerosol transport is briefly discussed next. Since the particle diffusion coefficient can be expressed in terms of a friction coefficient, three relationships are then presented and their influences on the friction and diffusion coefficients are considered for the particular case of TiO_2 nanoparticles. Although, all the models studied here predict a decrease in the value of the diffusion coefficient with increasing particle diameter, some significant variations can be observed between the models. A specific diffusion model, chosen between those studied, is finally applied to estimate the purge time of airborne TiO_2 nanoparticles in a simple closed space the size of a glovebox. It is shown that the sedimentation and the diffusion processes do not play a major role in the evaluation of the purge time.

Keywords: nanoparticles, diffusion, sedimentation, numerical simulations, titanium oxide, purge time.

1 Introduction

The evaluation of the potential risks associated with the inhalation of nanoparticles is a question which currently worries many researchers [1]. The

WIT Transactions on Engineering Sciences, Vol 59, © 2008 WIT Press
www.witpress.com, ISSN 1743-3533 (on-line)
doi:10.2495/AFM080111

phenomenal emergence of the nanotechnologies led government agencies to produce discussion papers on the secure use of particles in the nanometric scale. The international reports are unanimous to support proactive measures to ensure the safety of workers exposed to nanoparticles. One of the basic elements for the risk assessment evaluation in a work environment consists of an adequate characterization of the degree of exposure. Computer simulation could be used advantageously as a tool to predict the exposure levels. The development of reliable models will make it possible to predict the behaviour of nanoparticles in a workplace environment, to evaluate the risks of exposure and to contribute to the development of efficient ventilation systems which could make it possible to contain and, if required, to recover the airborne particles. In order to reach theses objectives, numerical models should be able to represent the dominant particles transport and agglomeration mechanisms. The objectives of this paper are to review the present models for small-particle diffusion and to select the most suitable one for nanoparticles transport modelling and risk assessment.

2 Literature review

The Brownian diffusion is a phenomenon of passive transport which results from the random movement of the particles subjected to the effect of the collisions with the surrounding molecules. In a macroscopic perspective, the average quadratic displacement of a nanoparticles cause by the Brownian motion can be characterized by a global diffusion coefficient D of the particle [2]. Hinds [2] used the Stokes-Einstein relation to express the diffusion coefficient in term of particule mobility. The resulting expression indicates that the coefficient D is proportional to the temperature of the medium and inversely proportional to the square of the particle diameter d_p. In spite of this dependence, the diffusion coefficient of a nanoparticle as small as 1 nm in diameter will be twenty times smaller than the equivalent coefficient for air (molecules). The diffusion of the nanoparticles in air is therefore unlikely to change the trajectory of the nanoparticles significantly compared the main flow streamlines [3]. This "passive scalar" behaviour implies that the nanoparticles can be transported directly by the convective movement of the fluid. However, the diffusion has a determining influence on the "particle-particle" collision probability and on the "particle-wall" collision probability. Therefore the diffusion coefficient may significantly affect the agglomeration of particles between themselves (the coagulation mechanism) or the filter efficiencies.

In a study relating to the theoretical bases of the analytical ultracentrifugation applied to nanoparticles, Lechner and Mächtle [4] make the assumption that the diffusion coefficient is independent of the mass of the particle, inversely proportional to the aerodynamic diameter, and proportional to the absolute temperature. In aerosol science, the aerodynamic diameter of a particle is usually defined as the equivalent diameter of a spherical particle of density equal to 1 g/cm³ having the same deposit rate or settling velocity as the measured particle [2].

Friedlander [5] proposed a correction factor in order to make the Stokes-Einstein relationship (see details below) applicable for small particles and large

mean free paths of the gas molecules. From the results of an analysis based on molecular dynamics, Rudyak *et al.* [6] developed, for their part, a diffusion model applicable to nanoparticles in dense medium. These latter authors compared their model with the diffusion coefficients obtained from the Einstein [7] and the Enskog kinetic theory of gases [8]. The numerical values of the diffusion coefficients differ considerably according to the model used.

Experimentally, Rudyak *et al.* [9] compared the results of measurements of the diffusion coefficients with the theoretical predictions of both the Einstein and Enskog theories. Two measuring devices were used for the determination of the D coefficient: a differential mobility analyzer (DMA) and electron microscopy (EM). Measurements obtained from the DMA made use of the Stokes law together with the Cunningham-Millikan-Davis correction. However, this measurement technique led to systematic variations when compared with the theory for very small particles ($d_p < 7$ nm). For aerodynamic diameters from 2 to 5 nm, the variations observed between the DMA measurements and the Stokes-Einstein relation can be as much as several tens of percent. On the other hand, the results obtained from the EM measurements follow very closely the theoretical Stokes-Einstein relation for diameters ranging between 2 and 9 nm. In this same paper, Rudyak *et al.* also presented a method for the determination of the coefficient D based on the kinetic theory of rarefied gases. This method takes into account the interactions between the surrounding ambient gas molecules and the nanoparticles. The application of this kinetic theory of rarefied gases approach was shown to give diffusion coefficient values between those obtained by DMA and EM measurements.

3 General dynamic equation

The transport of nanoscale particles dispersed throughout a fluid is governed by the aerosol general dynamic equation (GDE) [5]. For a discrete distribution function where k refers to the number of molecules in a particle, the GDE is written

$$\frac{\partial n_k}{\partial t} + \nabla \cdot n_k \mathbf{v} = \nabla \cdot D \nabla n_k + \left[\frac{\partial n_k}{\partial t}\right]_{growth} + \left[\frac{\partial n_k}{\partial t}\right]_{coag} - \nabla \cdot \mathbf{c} n_k . \qquad (1)$$

In this equation, n is the concentration, $\mathbf{v}$ is the velocity vector, D is the diffusion coefficient and $\mathbf{c}$ is the particle settling velocity vector resulting from gravity. Coagulation of particles leads to a reduction of the total number of particles, to an increase in the average particle diameter, and to an increase in the number of molecules in the particles. Growth of the particle occurs by gas-to-particle conversion by condensation or nucleation. It increases the particle mass concentration in air.

For particles with large number of molecules, it becomes convenient to pass from a discrete to a continuous distribution to carry out the calculations, but this is outside of the scope of the present paper. In any case, the diffusion coefficient must be determined before solving either the discrete or continuous GDE. The discrete GDE will be solved using classical CFD methods in a future work.

Classical theory relates the Brownian motion of small particles to the molecular motion of the gas molecules. The Stokes-Einstein expression for the diffusion coefficient is

$$D = \frac{KT}{f} \tag{2}$$

where K is the Boltzmann constant and T stands for the absolute temperature. The friction coefficient f furthermore depends on the particle size and on the fluid physical properties.

We will consider here three possible expressions to evaluate this nanoparticle friction coefficient. The appropriate equations depend on the Knudsen number, defined here as twice the ratio of the mean free path of the gas molecules, l_p, to the particle diameter d_p such that

$$\mathrm{Kn} = \frac{2l_p}{d_p}. \tag{3}$$

For a Kn lower than 1, the Stokes law may be applied. If the particle is considered as being rigid and spherical, the friction coefficient is thus written

$$f = 3\pi\mu d_p. \tag{4}$$

For a Kn much larger than 1, the friction coefficient can then be determined according to the Enskog kinetic theory [5, 10, 11] to be

$$f = \frac{2}{3} d_p^2 \rho \left(\frac{2\pi kT}{m} \right)^{1/2} \left(1 + \frac{\pi\alpha}{8} \right) \tag{5}$$

where ρ is the gas density, m is the molecular mass of the gas molecules, and the accommodation coefficient α is a constant parameter to be taken usually with a numerical value of 0.9.

A generalization of the above relations can be made to cover a more global range of Kn numbers by rewriting the Stokes law, eqn (4), with a correction factor C such that

$$f = \frac{3\pi\mu d_p}{C}. \tag{6}$$

The effects of the Knudsen number are then included in the coefficient C, the value of which can in turn be determined by more than one relation. Friedlander [5] and Rudyak *et al.* [9] suggest the following expression

$$C = 1 + \mathrm{Kn}\left(1.257 + 0.400 \exp \frac{-1.1}{\mathrm{Kn}} \right) \tag{7}$$

which has been derived from experimental data for oil droplets in air. Hinds [2] proposes a slightly different relation in the form of

$$C = 1 + \frac{\mathrm{Kn}}{2}\left(2.34 + 1.05 \exp \frac{-0.78}{\mathrm{Kn}} \right). \tag{8}$$

Finally, Gussman [12] suggests a relation applicable for different types of gas which reduces to

$$C = \left(1 + 0.615\,\mathrm{Kn}\right)^{-1} + 1.615\,\mathrm{Kn} \tag{9}$$

for air.

The friction coefficient values predicted by eqns (7)-(9) are shown in figure 1, for the particular case of TiO_2 particles in air at a standard atmospheric pressure of 101.3 kPa and at a temperature of 293 K. Typical TiO_2 nanoparticle diameters range from 10 to 100 nm. For reference, values predicted by the kinetic theory in eqn (5) are also plotted. As expected, the kinetic theory tends to over predict the friction coefficient with increasing particle size. Friedlander's eqn (7) and Hinds' eqn (8) give almost the same results and are thus equivalent for these specific conditions.

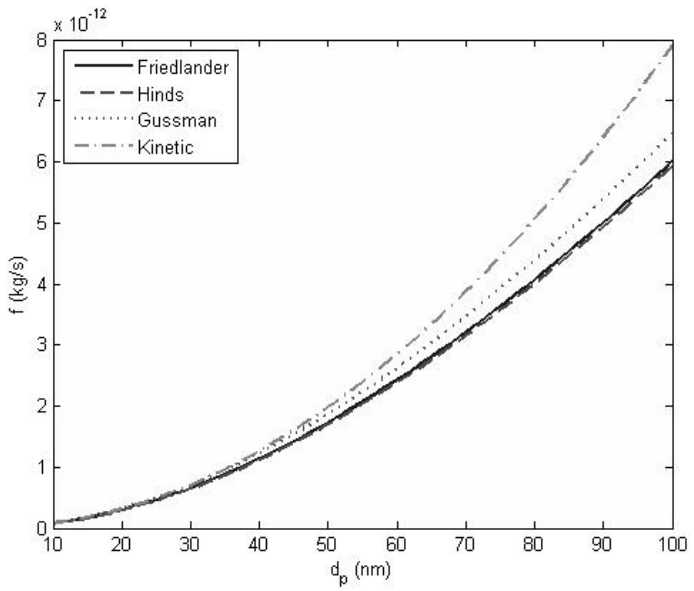

Figure 1: Friction coefficient for TiO_2 particle in air at atmospheric pressure.

Gussman's eqn (9) predicts slightly higher values than those of eqn (7) as particle diameter increases, reaching about 8 % difference at 100 nm. On the other hand, for particle diameters below 40 nm, all four relations give very similar results.

As previously mentioned, the numerical values of the diffusion coefficient predicted by eqn (2) depend on the particular expression used to determine the friction coefficient. Figure 2 compares the coefficient D predicted by i) Friedlander's eqn (7), ii) Gussman's eqn (9), iii) the kinetic theory of eqn (5), and iv) the Stokes law in eqn (4). The numerical values shown are obtained for airborne TiO_2 particles in air at standard ambient pressure and temperature. As can be seen on the figure, the diffusion coefficients decrease as particle size

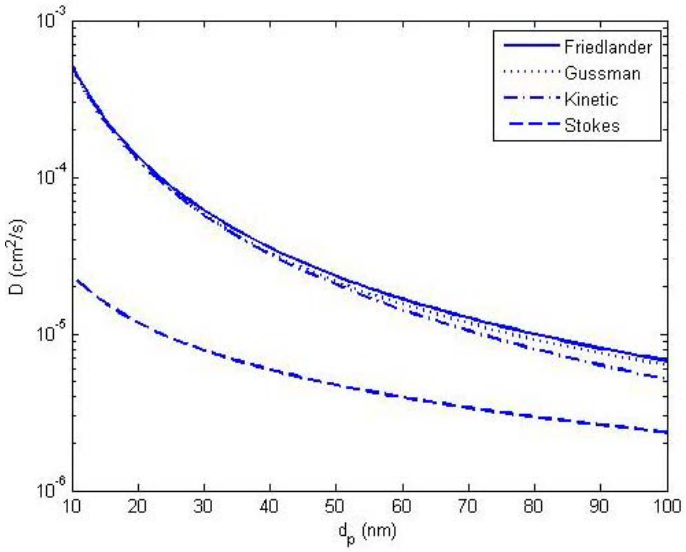

Figure 2: Diffusion coefficient for TiO_2 particle in air at atmospheric pressure.

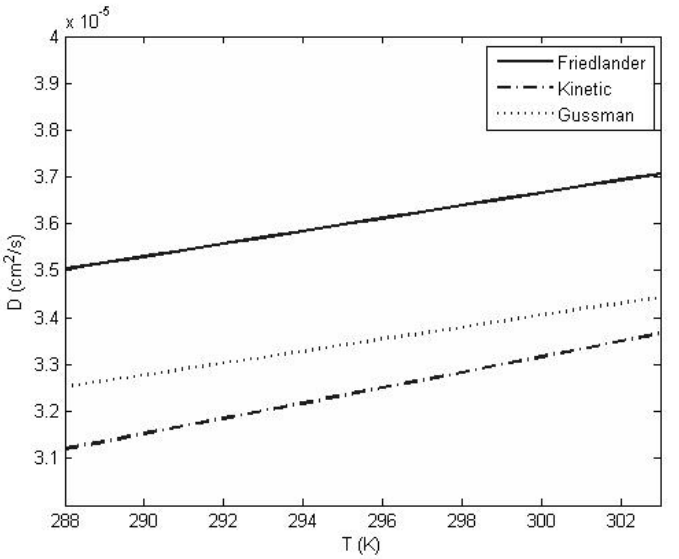

Figure 3: Evolution of the diffusion coefficient with temperature for 40 nm particles.

increases from 10 nm to 100 nm. As expected, the Stokes law under predicts the values of *D*. For particle diameters greater than about 40 nm (as for *f*), the kinetic

theory gives results different from those obtained from Friedlander's and Gussman's equations, which on the other hand agree quite well between themselves. Note that Hinds' equation results are not shown, as they are almost identical to those of Friedlander.

In figure 3, we show the effect of temperature on the diffusion. The curves are obtained for 40 nm particles in air, again at standard atmospheric pressure. The temperature value range is chosen to cover normal room conditions. The variation of the air viscosity in Stokes eqn is taking into account using Sutherland's correlation [2]. The three diffusion curves show once more the same trend, a nearly linear increase of the diffusion coefficient with temperature, a somewhat similar feature as for general gas behaviour. Friedlander's, the kinetic theory, and Gussman's equation results have about the same slope of a 5% augmentation for a 15 K temperature increase.

4 Particle extraction from a small room

In the eventuality of an airborne, possibly toxic, event involving nanoparticles in a workplace, it will certainly be critical to be able to estimate the time to completely purge the contaminated air from the room in which it took place, i.e., to remove as much as possible of the unwanted particles from that room. A first estimate of this purge time can be obtained knowing the volume of the room which could then divided by the volume flow rate Q of fresh air from the ventilation system. The time scale hence obtained represents the time taken by the ventilation system to achieve a single volume air exchange.

It may be important to note that for airborne nanoparticles, the diffusion effects close to the walls of the room and the sedimentation process may have a non negligible influence on the evolution in time of the particle concentration in that room. In order to take into account these additional effects, Hervé-Bazin [13] suggests the following exponential relation for the evolution of particle concentration C with time

$$C = C_o \cdot \exp(-t / T) \tag{10}$$

where C_o is the initial concentration, and T a constant time scale such that

$$\frac{1}{T} = \frac{Q}{V} + \beta \tag{11}$$

with β representing the deposition coefficient in turn obtained by the following relation

$$\beta = \frac{V_s}{h} + \frac{S \cdot D}{V \cdot \delta}. \tag{12}$$

In the last relation, eqn (12), V_S is the sedimentation or settling velocity of the particles, h is the room height, S is the room total wall surface, V is the room volume, and finally δ an estimate of the boundary layer thickness formed at the surface of the room's wall.

To give an idea of the purge time of a room, consider a set of TiO_2 nanoparticles uniformly distributed in a room with an initial, fairly low, concentration of 10^4 particles per cubic centimetre; at this concentration level, particle coagulation or agglomeration effects can reasonably be neglected [2]. If we now consider a rectangular closed space having the dimensions of a typical glovebox which could be used for nanoparticle experimentations, that is with a 1 m length, a 0.8 m width, and a 0.8 m height. The sedimentation velocity V_S, following Friedlander's general notation [5], depends on the particle density ρ_p, the air density ρ, and gravity g such that

$$V_s = \frac{\rho_P \cdot g \cdot d_p^2}{18\mu} C(1-\rho/\rho_p). \tag{13}$$

For TiO_2 particles (ρ_p = 4 g/cm^3) in air, one may readily note that the particle's buoyancy term, $(1 - \rho/\rho_p)$ is negligibly close to 1 and could thus be omitted.

In table 1, we show values of D, V_S, β, and T, for typical TiO_2 particles of 10 nm, 20 nm, 40 nm and 100 nm diameters. These results have been obtained assuming an air flow rate of $Q = 4.5\times10^{-3}$ m^3/s whence $Q/V = 7.0\times10^{-3}$ l/s. in eqn (11). Based on the quasi one dimensional (piston) flow hypothesis made above, we may estimate the particle purge time of the glovebox, T, to be at slightly more than 20 s. More specifically, for the smallest particles (10 nm) sedimentation effects are not significant and the purge time is thus the longest at 26.3 s. For 20 nm particles, Brownian motion and sedimentation are maximum hence giving the minimal time of 22.4 s. For 40 and 100 nm, the sedimentation velocity increases but the Brownian motion diminishes giving in this case purge time values a bit higher than for the 20 nm particles but still below the 10 nm value. One may also deduce from the table results that the sedimentation time scale h/V_S is significantly much larger (at least 4 orders of magnitude) than the global purge time T, confirming thus that the sedimentation or settling process plays a negligible role in the evolution of the particle concentration.

Table 1: Characteristics of TiO_2 particles dispersion in a rectangular closed space (see text for details).

d_p [nm]	D [cm^2/s]	V_S [cm/s]	β [1/s]	T [s]
10	5.2e-4	2.6e-5	3.7e-5	26.3
20	1.3e-4	5.4e-5	1.0e-5	22.4
40	3.5e-5	1.2e-4	3.9e-6	22.5
100	6.7e-6	3.4e-4	4.7e-6	22.7

5 Conclusion

The present paper is part of an ongoing work on the development of a numerical simulation model for the dispersion of airborne nanoparticles to be used in risk

exposure assessments. Our main concern at this stage has been on the evaluation of already existing diffusion models. More specifically, three models have been studied. These models are based on a generalization of the Stokes law for the dynamics of small spherical particles to which a correction factor is added to take into account the very small scale effects occurring at nanoscales. At given standard pressure and temperature, the diffusion coefficient is shown to decrease as the particle diameter increases from 10 to 100 nm. The diffusion models proposed by Friedlander and Hinds give almost identical results while the model proposed by Gussman gives slightly lower values. For particle diameters below 40 nm, the difference between the three models becomes very small though. All models are also shown to agree with the results obtained using a more classical kinetic theory approach for small particle diameters, but that latter theory tends to under predict diffusion for larger diameters. For a given particle diameter, diffusion is shown to increase with temperature, as it is the case in general for gases.

The Friedlander diffusion model was then applied to the evaluation of the time taken to extract a low-level concentration of TiO_2 nanoparticles from a small closed room the size of a glovebox. Assuming a certain air flow rate, we were then able to estimate a room purge time. From the values hence obtained, it was then shown that the sedimentation or settling of nanoparticles is negligible in the global dispersion process.

Future work includes the implementation of this diffusion model to more complete fluid dynamics simulation tools in order to be able to obtain more accurate estimations of the purge time in complex room geometries. The inclusion of particle agglomeration or coagulation dynamics will also be considered in order to be able to take higher and more realistic concentration of nanoparticles into account.

References

[1] Dawson, J., Nanotech risk research takes slow step forward, *Phys. Today*, **60**(11), pp. 29–30, 2007.

[2] Hinds, W. C., *Aerosol Technology: Properties, Behavior, and Measurement of Airborne Particles*, John Wiley & Sons, New York, 1999.

[3] Maynard, A.D. & Kuempel, E.D., Airborne nanostructured particles and occupational health, *J. Nanopart. Res.* **7**, pp. 587–614, 2005.

[4] Lechner, M.D. & Mächtle, W., Determination of the particle size distribution of 5-100 nm nanoparticles with the analytical ultracentrifuge: consideration and correction of diffusion effects. *Progr. Colloid. Polym. Sci.* **113,** pp. 37–43, 1999.

[5] Friedlander, S. K., *Smoke, Dust, and Haze. Fundamentals of Aerosol Dynamics,* Oxford Univ. Press, New York, 2000.

[6] Rudyak, V.Ya., Kharlamov, G.V. & Belkin, A.A., Diffusion of nanoparticles and macromolecules in dense gases and liquids. *High Temp.,* **39**(2), pp. 264–271, 2001.

[7] Einstein, A., *Investigation on the theory of Brownian movement*, R. Furth editor, Dover Publ., New-York, 1956.

[8] Ferziger, J.H. & Kaper, H.G., Mathematical theory of transport in gases. Amsterdam, North-Holland, 1972.
[9] Rudyak, V. Y., Krasnolutskii, S. L., Nasibulin, A.G. & Kauppinen, E.I., Methods of Measuring the Diffusion Coefficient and Sizes of Nanoparticles in a Rarefied Gas. *Dokl. Phys.,* **47**(10), pp. 758–761, 2002.
[10] Settumba, N. & Garrick, S. C., A comparison of diffusive transport in a moment method for nanoparticle coagulation. *Aerosol Sci.* **35**, pp. 93–101, 2004.
[11] Chan, T. L., Lin, J. Z., Zhou, K. & Chan, C.K., Simultaneous numerical simulation of nano and fine particle coagulation and dispersion in a round jet. *Aerosol Sci.* **37**, pp. 1545–1561, 2006.
[12] Gussman, R. A., On the Aerosol Particle Slip Correction Factor. *J. Appl. Meteorol.*, **8**, pp. 999–1001, 1969.
[13] Hervé-Bazin, B., *Les nanoparticules: Un enjeu majeur pour la santé au travail*, E.D.P. Sciences, Paris, 2007.

Numerical study of the effect of the type of fuel on pollutant emissions in a diesel engine

S. Kabar & M. Kadja
LEAP Laboratory, Département de Génie Mécanique,
Université Mentouri, 25000 Constantine, Algeria

Abstract

In order to minimise the planet heating observed during recent years, many studies have been undertaken on the different factors responsible for this atmospheric pollution, among which are the studies of the physical and chemical phenomena occurring in combustion. In order to diminish the polluting gases emanating from I.C. engines, the idea is to lower fuel consumption while maintaining engine performance. In this context, we numerically calculated the concentration of different polluting species (CO, CO_2, HC and NO) by using the commercial programme KIVA2 for four fuels (DF2, C_8H_{18}, C_7H_{16}, and $C_{14}H_{13}$) in a direct injection diesel engine of type CMT/FL912. The Zeldovich chemical reactions for the formation of NO, the global fuel oxidation reaction and the equilibrium reactions contributing to the formation of pollutants have been introduced. A comparison of polluting species of various fuels obtained after combustion is presented.
Keywords: KIVA2 code, diesel engine, turbulent combustion, polluting gases, fuels.

1 Introduction

During the last two decades, energy demand in the world has increased. The prices of fossil fuels have increased and the ecological repercussions due to the emissions of polluting gases CO, CO_2 and NO_X have become worrisome, particularly the rate of CO_2 in the atmosphere which is continuously increasing and which results in global heating. The shortage and the depletion of conventional energy resources are also one of the major concerns for western countries. This has incited scientists to develop alternate fuels such as bio fuels,

WIT Transactions on Engineering Sciences, Vol 59, © 2008 WIT Press
www.witpress.com, ISSN 1743-3533 (on-line)
doi:10.2495/AFM080121

LPG (liquid petroleum gas), GNV (vehicle natural gas) and finally synthesis liquid fuels.

The objective of our work is to numerically study the emissions of polluting gases CO, CO_2, HC (unburned hydrocarbons) and NO from a diesel engine. A comparison has been made between various fuels for the mass fractions of the polluting gases. The study was conducted using the code KIVA II. The latter solves simultaneously the equations governing the mechanics of fluids, the heat transfer, the mass transfer and the chemistry occurring during combustion inside an engine.

2 Mathematical formulation

The prediction of the properties of reactive flows due to the combustion of liquid fuel jets in diesel engines must take into account the liquid phase and the gaseous phase in the flow field. Several approaches have been suggested to model the discontinuity of the gas-liquid phases [1].

Among them, the statistical Eulerian-Lagrangian approach [2], which is used in the Kiva II code, and which consists of describing the field of flow of the gaseous phase in Eulerian coordinates by the averaged Navier-Stokes equations and the turbulent model equations. The liquid droplets field is described in a Lagrangian formulation, which has the advantage of being able to take into account the temperatures and the momentum of representative samples of all the different drops possessing the same characteristics (position, velocities, size, temperature, etc.) [4]; thereby avoiding the modelling of effective diffusion coefficients of mass, momentum and energy of the liquid.

The influence of the liquid phase on the gaseous phase is handled by introducing the source terms, due to the coupling of the liquid gas phases, in the balance equations of the Eulerian phase.

2.1 Chemical reactions

In the present study, four fuels have been chosen: these being $C_{14}H_{30}$ "n-tetradecane", the DF2 "diesel fuel 2" which is represented by the $C_{12}H_{26}$ "dodecane" in the chemical reaction, the C_7H_{16} "n-heptanes" and finally C_8H_{18} "iso-octane". Their global chemical reactions are:

$$\begin{aligned} 2\,C_{14}H_{30} + 43\,O_2 &\longrightarrow 28\,CO_2 + 30\,H_2O \\ 2\,C_{12}H_{26} + 37O_2 &\longrightarrow 24\,CO_2 + 26\,H_2O \\ 2\,C_8H_{18} + 25O_2 &\longrightarrow 16\,CO_2 + 18\,H_2O \\ C_7H_{16} + 7O_2 &\longrightarrow 7\,CO_2 + 8\,H_2O \end{aligned} \qquad (1)$$

2.2 Equilibrium reactions

$K_r(T)$ is the equilibrium constant of the n°r reaction, which is assumed to depend only on the temperature:

$$K_r = \exp\left(A_r \ln T_A + \frac{B_r}{T_A} + C_r + D_r T_A + E_r T_A^2 \right) \tag{2}$$

where A_r, B_r, C_r and D_r are constants, and $T_A=T/1000$.

We have considered the seven following reactions:

Table 1: Value of A_r, B_r, C_r and D_r.

Reaction n° r	A_r	B_r	C_r	D_r	E_r
$H_2 \leftrightarrow 2H^\circ$	0.990207	-51.7916	0.993074	-0.343428	0.0111668
$O_2 \leftrightarrow 2O^\circ$	0.431310	-59.6554	3.503350	-0.340016	0.0158715
$N_2 \leftrightarrow 2N^\circ$	0.7947009	-113.2080	3.168370	-0.443814	0.0269699
$O_2 + H_2 \leftrightarrow 2OH^\circ$	-0.652939	-9.8232	3.930330	0.163490	-0.0142865
$O_2 + 2H_2O \leftrightarrow 4OH^\circ$	1.158882	-76.8472	8.532155	-0.868320	0.0463471
$O_2 + 2CO \leftrightarrow 2CO_2$	0.980875	68.4453	-10.5938	0.574260	-0.0414570
$O_2 + N_2 \leftrightarrow 2NO$	0.000000	-10802	0.14	$7.2\ 10^{-5}$	0.0000000

2.3 Kinetic reactions

We take into account the kinetics of the reaction towards the equilibrium by a reaction rate given by the Arrhenius' law:

$$\dot{\omega}_r = k_{fr} \prod_{m=1}^{nsp} \left(\frac{\rho_m}{W_m} \right)^{a'_{mr}} - k_{br} \prod_{m=1}^{nsp} \left(\frac{\rho_m}{W_m} \right)^{b'_{mr}} \tag{3}$$

k_{fr} and k_{br} are the reaction rate constants respectively for both directions of reaction n°r.

Zeldovich's chemical mechanism for the formation of NO is taken into account by introducing the coefficients and the equilibrium constants of the following chemical reactions into the KIVA II code:

$O_2 + 2N_2 \rightleftharpoons NO + 2N$

$k_{fr} = 1.558.10^{14} \exp(6.76.10^4/T)$

$k_{br} = 7.500.10^{12}$

$N_2 + 2OH^\cdot \rightleftharpoons 2NO + 2H$

$k_{fr} = 2.648.10^{10} \exp(5.94.10^4/T)$

$k_{br} = 1.600.10^{9} \exp(1.96.10^4/T)$

$N_2 + 2O_2 \rightleftharpoons 2NO + 2O$

$k_{fr} = 2.132.10^{14} \exp(5.70.10^4/T)$

$k_{br} = 0.0$

3 Numerical methods

The temporal discretisation is a discrete sequence of times t^n ($n=0,1,2....$). The interval of time $\Delta t^n = t^{n+1} - t^n$ is the step of time and n is the number of cycles. In the KIVA II code, the cycle takes place in three stages or phases. Phase A and Phase B constitute the Lagrangian calculation where the grid nodes

move at the same speed as the fluid. There is thus no convection through the sides of the grid cells. So, during this first phase none of the convective terms of the aerodynamics equations are taken into account. In phase C, the field of flow is frozen and the grid nodes are returned to the new positions prescribed by the user with the aim of calculating the compression and the expansion. This remeshing is realized by transporting by convection the various quantities through the boundaries of the control volumes when these are moved to their new positions.

4 Results and discussion

The simulation has been applied to the combustion chamber of the diesel engine CMT FL912 that is mounted on the tractor CIRTA C6807 manufactured in Constantine, Algeria by the national company SONACOM. Its 68 KW power is reached through a rotation speed of 2300rpm. For the current work, we have used the engine regime which is 1600rpm rotation speed corresponding to the maximum couple. The walls are maintained at constant temperatures, the initial time step is dti = 10^{-7}s, the tolerances for the convergence of the method of conjugated residues for the implicit terms diffusion of pressure gradient epsp = 10^{-4}, chemical species epsy, momentum epsv, heat epst and kinetic energy epsk are all equal to 10^{-3}.

Table 2: Characteristics of the engine.

Cylinder diameter	100 mm
Piston course	120 mm
Distance between cylinder head and piston surface at TDC (squich)	1.8 mm
Length of the connecting rod	216 mm
Injector diameter	0.285 mm
Engine speed	1600 tr/min
Injection period	12°
Injection Mode	Injection according to a half sinusoid
Rate of injection	50 cm^3/s
Injection pressure	400 bars
Injection temperature	313°K (40°C)
Air temperature	400 K
Total number of injected particles	2000
Inclination angle of injector orifice	60°
Thickening angle of fuel jet	10°
Cylinder wall temperature	400K
Piston wall temperature	400K
Temperature of cylinder head	400K
Initial density of oxygen	2.4257×10^{-4} g/cm^3
Initial density of nitrogen	7.9851×10^{-4} g/cm^3

The numerical grid used in this study contains 25 cells in radial direction (NX=25), 1 cell in the azimuthal direction (NY=1) and 40 cells in the axial direction (NZ=40). At the beginning of the calculation (at -90°), the grid starts with 40 cells in the axial direction (NZ=40). During the compression phase, cells are compressed as the piston approaches the top of cylinder (top dead center TDC), until a minimal number of cells (which is two) between the cylinder head and the top surface of the piston is reached.

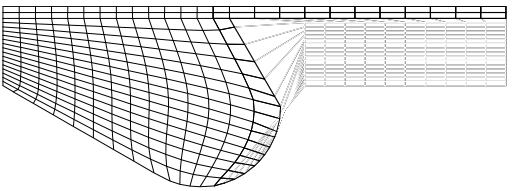

Figure 1: The grid mesh at 0.0068 degrees before the top of the cylinder.

4.1 Formation of pollutants

4.1.1 Unburned hydrocarbons

The curve of fuel consumption (Fig. 2) by the oxygen is the same for the various fuels. The fuel begins to evaporate as soon as the first injected drops in the combustion chamber from the advanced angle of injection until the evaporation of part of the fluid that corresponds to the maximum of the curve. From this point onwards the first free radicals start to form to provoke the immediate explosion of the fuel at around the top of the cylinder (TDC). At that moment, the curve decreases then becomes asymptotic to a value which corresponds to unburned hydrocarbons which are due to the short duration of the combustion at

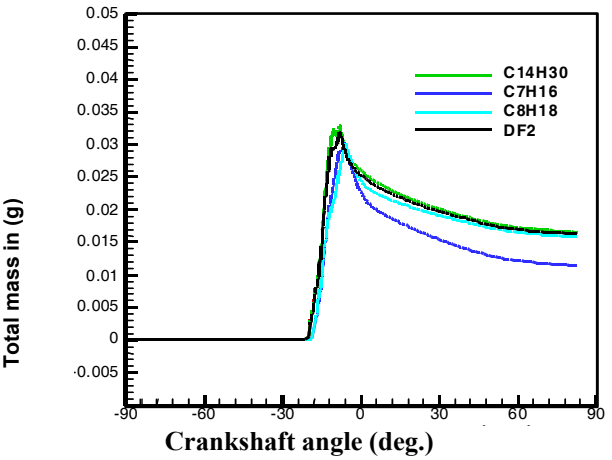

Figure 2: Evolution of total fuel mass as a function of Crankshaft angle for various fuels.

about 12° (Fig. 2), and which is shorter than the period of self-ignition necessary for the fuel to completely oxidize, and by the adhesion of droplets to the walls of the combustion chamber to evaporate which are at a lower temperature (Fig. 3). The unburned hydrocarbons are then chased away by exhaust gases.

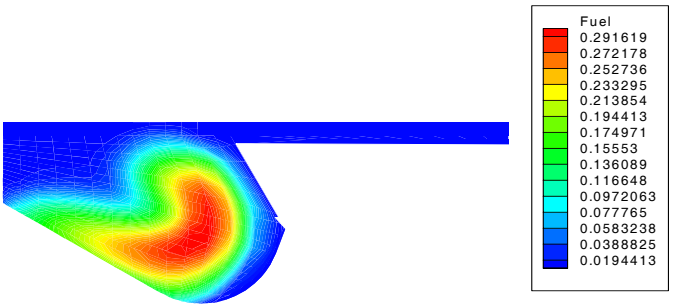

Figure 3: Contours of the mass fractions of the consumption of the fuel at the position (–5°) before the TDC for DF2.

4.1.2 Carbon dioxide

The carbon dioxide begins to form as soon as fuel ignition (Fig. 4) in the flame zone by the chemical kinetic mechanism of hydrocarbon oxidation at 12° before TDC (Fig. 5). The total mass of CO_2 increases quickly till the end of the ignition then continues to form in a slower way by the chemical mechanism of equilibrium of CO oxidation and of CO_2 dissociation into CO during the expansion phase up to a maximal value (Fig. 4).

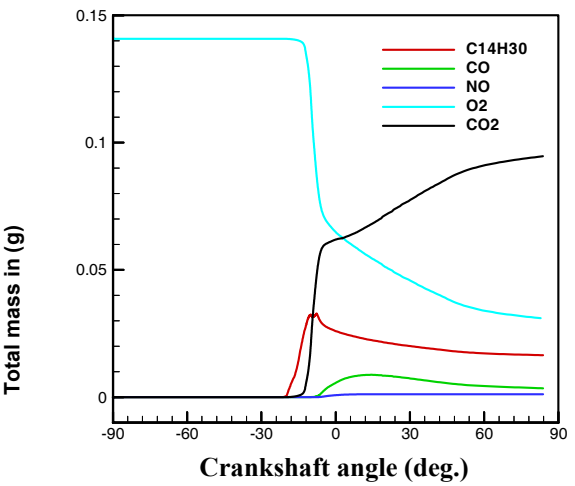

Figure 4: Evolution of total masses of polluting gases as a function of the crankshaft angle for the fuel $C_{14}H_{30}$.

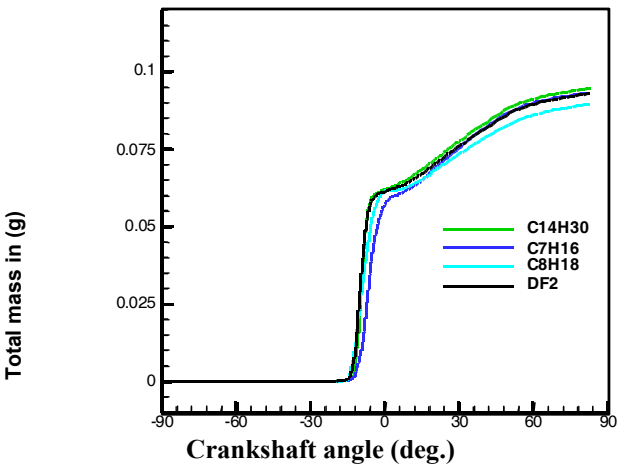

Figure 5: Evolution of CO_2 mass as a function of the crankshaft angle for various fuels.

4.1.3 Carbon monoxide

The carbon monoxide forms well far from the flame front (Fig. 4), by the fact of the lack of oxygen. The thermodynamic equilibrium of CO_2 dissociation and the reaction of CO_2 and H_2 will result in a mass that represents 20% of the mass of fuel at the maximum point at 15 ° after TDC (Fig. 6). This quantity will decrease during the expansion phase because of its transformation to CO_2 until a negligible value is reached (Fig. 4).

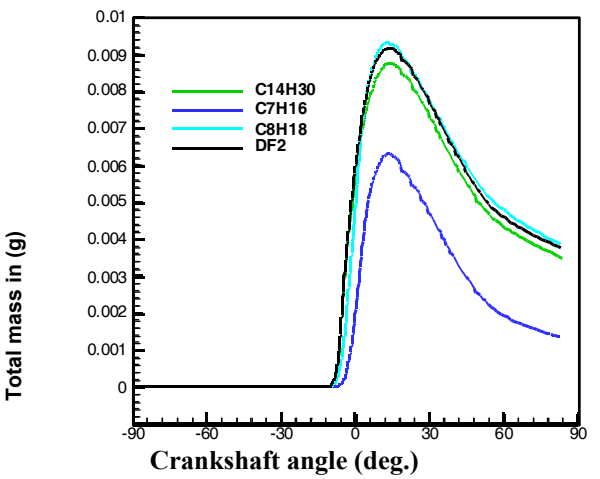

Figure 6: Evolution of the total masses of carbon monoxide according to the swing angle for the various fuels.

4.1.4 Nitrogen oxide

The formation of NO begins at 5 ° before TDC far from the flame front because of the lack of oxygen (Fig. 7). The curve undergoes an exponential jump, which confirms that the formation of NO essentially results from the chemical kinetics. NO then reaches a maximal value at the end of combustion, which will remain constant until the end of the expansion. We can deduce that the formation of NO takes place at high temperatures (fig. 7).

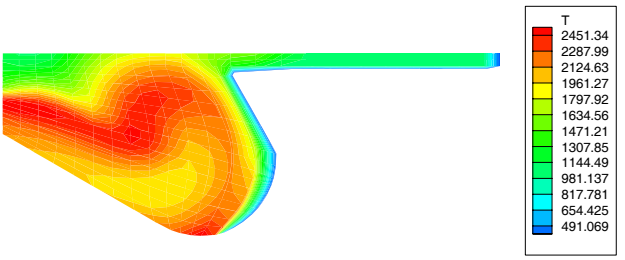

Figure 7: Isotherms at the position (–5°) before the TDC for C7H16.

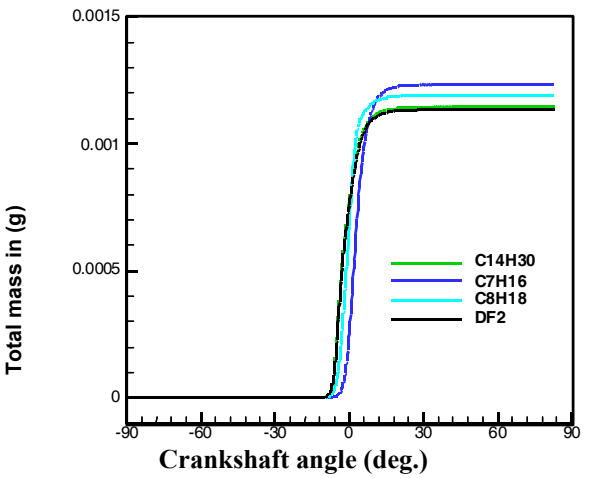

Figure 8: Evolution of nitrogen oxide mass as a function of the crankshaft angle for various fuels.

4.2 Comparison of the results for the various fuels

4.2.1 Unburned hydrocarbons

The C_7H_{16} (n-heptane) has the least unburned evaporated mass which is 0.011g, and which represents 36% of the evaporated mass, whereas $C_{14}H_{30}$ (n-tetradecane), DF2 and C_8H_{18} (isooctane) have almost the same unburned

hydrocarbons evaporated mass of 0.015g. Consequently C_7H_{16} (n-heptane) emits the least unburned hydrocarbons.

4.2.2 Carbon dioxide

The curve of CO_2 formation (Fig. 4) is the same for the four fuels. The mass of the carbon dioxide, CO_2 (Fig. 5) emitted by various fuels, is practically the same. The total mass of CO_2 is between 0.08g and 0.09g.

4.2.3 Carbon monoxide

The curve of CO (Fig. 6) is similar for the four fuels. The mass of the carbon monoxide CO emitted at the end of combustion by C7H16 (n-heptane) (Fig. 2) is 0.0013g and is sharply lower than those of the other fuels. We notice that the curves of CO for C14H30, Df2 and the C8H18 (isooctane) are identical. The mass emitted is 0.003g.

4.2.4 Nitrogen oxide

The curve of formation of NO is similar for the four fuels (Fig. 8). We notice in Fig. 5 that the combustion of $C_{14}H_{30}$ (n-tetradecane) and DF2 emits less nitrogen oxide NO gases, they have each a mass of 0.0114g at the end of the cycle whereas the combustion of the C_7H_{16} (n-heptane) produces more NO; its mass is 0.00122g.

5 Conclusion

The numerical bi-dimensional study of the type of fuel on the polluting emissions emanating from a diesel engine has been achieved by using the KIVA II code. The kinetic chemical mechanisms and the balance of the formation of various pollutants have been implemented in the code.

The results obtained for the four fuels give us the following comparative analysis:

- The four fuels produce at the end of the combustion the same density of carbon dioxide.
- The C_7H_{16} (n-heptane) emits less unburned hydrocarbons because of the weak number of the carbon atoms. The energy of atoms connection is less important than the other fuels.
- In spite of the lower number of carbon atoms, the emissions of C_8H_{18} (isooctane) polluting gases is the same as for the emissions of the DF2 and the $C_{14}H_{30}$ (n-tetradecane).
- The emissions of carbon dioxide for the four fuels are very close because of the temperature at the end of combustion, which is identical for all.
- The emissions of carbon monoxide are less important for C_7H_{16} (n-heptane) because the CO_2 residential time is shorter than the other fuels (ignition delay shorter).
- The emissions of nitrogen oxide are less important for $C_{14}H_{30}$ (n-tetradecane) and the DF2.

References

[1] R. Borghi et M. Champion, Modélisation et théorie des flammes: EDITION TECHNIP, Paris, 2000
[2] T. J. Chung, Computational fluid dynamics, Cambridge University Press, 2002
[3] Roland Borghi, Michel Destriau et Gérard De Soete, La combustion et les flammes: EDITION TECHNIP, Paris, 1995.
[4] A. A. Amsden, P. J. ÕRourke, T. D. Butler, KIVA-II: A Computer Program for Chemically. Reactive Flows with Sprays: LA-11560-MSUC-96, Los Almos, May 1989

Section 3
Experimental versus simulation methods

This page intentionally left blank

Macroscopic conservation equation based model for surface tension driven flow

T. M. Adams & A. R. White
Department of Mechanical Engineering,
Rose-Hulman Institute of Technology, USA

Abstract

Due to the small scales encountered in MEMS and microfluidic devices, surface tension can play a significant role in the device physics. As such, many microscale devices have exploited surface tension forces to serve as passive valves and to move fluids. Surprisingly, few models for surface tension driven flow seem to have been developed.

In this study a theoretical mathematical model for surface tension driven flow through a capillary of an arbitrary cross section is derived. The model is based on macroscopic mass and momentum balances, allowing for different physical insights to be drawn compared to approaches starting with the Navier-Stokes equations. Expressions for flow length and velocity are derived for both frictionless flow and for flow with wall friction. For frictionless flow the result of surface tension force is to increase the momentum of the fluid by constantly drawing mass into the capillary at a constant characteristic velocity. In the case of flow with wall friction, a characteristic time scale can be calculated. For times on the order of the characteristic time scale, the flow velocity exponentially decays from the characteristic velocity, whereas for larger times the velocity shows an inverse power law dependence. The model well predicts flow behaviour for previously published experiments in which the characteristic time is small. For systems in which the characteristic time is larger, the model may show improved performance over previous models.

Keywords: capillary, microchannel, microfluidics, surface tension.

1 Introduction

With the rapid development of microfluidic devices over the past decade, the favourable scaling of surface tension with small dimensions has been exploited

WIT Transactions on Engineering Sciences, Vol 59, © 2008 WIT Press
www.witpress.com, ISSN 1743-3533 (on-line)
doi:10.2495/AFM080131

for many purposes, including for use as passive valves [1], [2] and the seemingly ubiquitous capillary electrophoresis [3], [4] used as chemical and biological detection methods. Surprisingly, few models seem to be available to address the physics of liquid flows driven by surface tension.

Studies on the nature of interfacial surface tension and the dynamics of capillary wetting date back to over a century ago, including the early works by Young [5], Lucas [6], and Washburn [7]. More recently, the methods and equations developed by these early studies have been modified for use in parallel plate geometries by Schwiebert and Leong [8] and Jong *et al*. [9]. These recent studies have shown good agreement between predictions and experimentally obtained parameters.

The method of analysis in the above mentioned studies has typically started with a quasi-steady version of the Navier-Stokes equations and then introduced the non-steady effect of surface tension via manipulation of the applied pressure gradient term. Furthermore, the works focus on particular geometries and lack a general applicability to other capillary shapes.

The current study investigates surface tension driven flow in capillaries of arbitrary cross section. Rather than starting with differential equations of motion, the current study uses macroscopic conservation laws applied to the entire capillary in order to model the flow. The results of the model are compared to previous models, as well as the experimental predictions therein.

2 Frictionless flow model

As a starting point for modelling surface tension driven flow we begin with a frictionless flow model.

2.1 Conservation of mass

Figure 1 gives a schematic diagram of the open system used in the macroscopic mass conservation equation. A reservoir feeds flow into a capillary of arbitrary cross section with perimeter $\mathcal{P}$ and cross sectional area A_c. The leftmost boundary of the system remains stationary at the capillary inlet whereas the rightmost boundary moves with the liquid-gas interface at a distance L from the inlet.

Conservation of mass for this system requires

$$\frac{dm_{sys}}{dt} = \dot{m}_{in}, \tag{1}$$

where m_{sys} is the mass contained in the system at any time t and $\dot{m}_{in}$ is the rate of mass flow into the system. Eq. (1) reduces to

$$\frac{d(\rho A_c L)}{dt} = \rho A_c V, \tag{2}$$

where ρ is density and V is the average velocity of the fluid at the capillary inlet. For an incompressible fluid, ρ is constant and Eq. (2) reduces to

$$V = \frac{dL}{dt}. \tag{3}$$

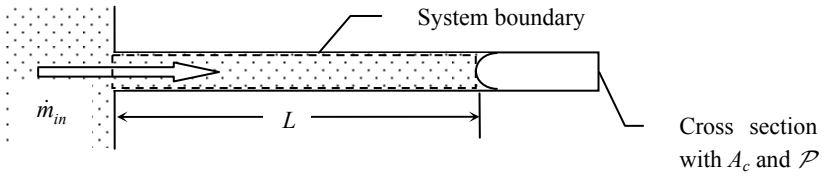

Figure 1: Schematic diagram of system used in macroscopic mass conservation.

The analysis would be identical for a system with a stationary inlet at any location along the capillary. Thus, at any point in time the entire fluid in the capillary moves with a single velocity equal to velocity of the liquid-gas interface.

2.2 Conservation of linear momentum

Figure 2 shows the open system used in the macroscopic momentum conservation equation. The leftmost boundary of the system extends just inside the reservoir where pressure is constant and the fluid velocity is approximately zero. The rightmost boundary coincides with the liquid-gas interface.

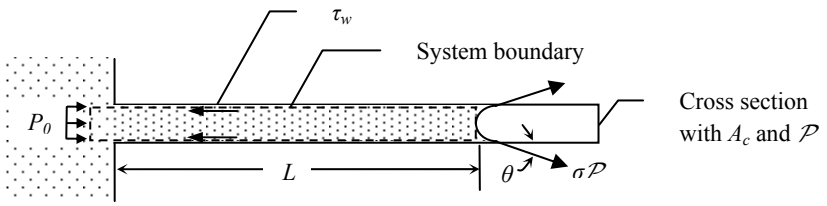

Figure 2: Schematic diagram of system used in macroscopic momentum conservation.

The flow direction component of linear momentum conservation requires that

$$\frac{d(mV)_{sys}}{dt} = \sum F_{external} \cdot \tag{4}$$

For frictionless flow the wall shear stress, τ_w in Fig.2 is zero and Eq. (4) becomes

$$\frac{d(mV)}{dt} = P_0 A_c + \sigma \cos\theta \mathcal{P} \,, \tag{5}$$

where P_0 is gage pressure in the reservoir, σ is surface tension and θ is the contact angle formed by the liquid-gas interface with the capillary wall. Integrating with respect to time yields

$$mV = (P_0 A_c + \sigma \cos\theta \mathcal{P})t + c_1 \,. \tag{6}$$

At t=0 the momentum of the system is zero, so that the constant of integration is c_1=0.

From the conservation of mass results, $V=dL/dt$. Substituting this along with $m=\rho A_c L$ into Eq. (6) gives

$$\rho A_c L \frac{dL}{dt} = (P_0 A_c + \sigma \cos\theta \mathcal{P})t \,. \tag{7}$$

Separating variables, integrating and solving for L,

$$L = \left(\left(\frac{P_0}{\rho} + \frac{\sigma \cos\theta \mathcal{P}}{\rho A_c} \right) t^2 + c_2 \right)^{1/2} . \tag{8}$$

At t=0, L=0, so that the constant of integration is c_2=0.

Eq. (8) can be differentiated with respect to t to find V; equivalently, Eq. (8) can be substituted into Eq. (7), which in turn can be solved for velocity. Either way the result is

$$V = \frac{dL}{dt} = \left(\frac{P_0}{\rho} + \frac{4\sigma \cos\theta}{\rho D_h} \right)^{1/2} \tag{9}$$

where P and A_c have been eliminated in favour of the hydraulic diameter,

$$D_h \equiv \frac{4A_c}{\mathcal{P}} \,. \tag{10}$$

For the case in which P_0=0, corresponding to a reservoir height of zero, the flow is driven completely by surface tension. Eq. (9) gives a characteristic velocity for this situation, one that represents a theoretical upper limit for flow velocity.

$$V_{chr} = \left(\frac{4\sigma \cos\theta}{\rho D_h} \right)^{1/2} \tag{11}$$

This velocity can also be found by setting the Weber number based on hydraulic diameter equal to 4cosθ:

$$We \equiv \frac{\rho V_{chr}^2 D_h}{\sigma} = 4\cos\theta \tag{12}$$

It is of interest to note that the flow velocity given by either Eq. (9) or Eq. (11) is constant. Therefore, the result of the surface tension force is to increase the system momentum, not by increasing its velocity, but by constantly drawing more mass into the capillary.

3 Flow model with wall friction

Due to the large surface area to volume ratios encountered in systems in which surface tension is important, the assumption of zero wall friction, a surface phenomenon, is not realistic. Though the frictionless model yielded a theoretical upper limit for flow velocity, in practice we would expect to see slower velocities due to the impeding effect of wall shear stress. Thus, a more accurate model should include the effects of wall friction.

3.1 Conservation of mass

As the presence of wall shear stress does not affect any of the terms appearing in the conservation of mass equation, the analysis of section 2.1 is still valid. At any point in time the entire fluid in the capillary again moves with a single velocity equal to velocity of the liquid-gas interface as given in Eq. (3).

3.2 Conservation of linear momentum

The flow direction component of linear momentum conservation given by Eq. (4) as applied to the system in Fig.2 including wall friction is

$$\frac{d(mV)}{dt} = P_0 A_c - \tau_w \mathcal{P} L + \sigma \cos\theta \mathcal{P} . \tag{13}$$

The wall shear stress, τ_w, is related to the Fanning friction factor, c_f, by

$$\tau_w = c_f \frac{1}{2} \rho V^2 . \tag{14}$$

Assuming that the flow is fully developed at any point in time, a reasonable assumption given the small entrance lengths encountered in microfluidics, the Fanning friction factor is given by

$$c_f = \frac{C}{Re} , \tag{15}$$

where Re is the Reynolds number based on the hydraulic diameter and C is a constant depending solely on the geometry of the cross section. Using Eqs. (14) and (15), along with the definition of Reynolds number,

$$Re = \frac{\rho V D_h}{\eta} , \tag{16}$$

Eq. (13) becomes

$$\frac{d(mV)}{dt} = P_0 A_c - \frac{C\eta}{\rho V D_h}\left(\frac{1}{2}\rho V^2\right)\mathcal{P} L + \sigma \cos\theta \mathcal{P} . \tag{17}$$

Recognizing that $m=\rho A_c L$ allows Eq. (17) to be rearranged as

$$\frac{d(mV)}{dt} = P_0 A_c - \frac{2C\eta}{\rho D_h^2}(mV) + \sigma \cos\theta \mathcal{P} . \tag{18}$$

Separating variables,

$$\frac{1}{P_0 A_c - \frac{2C\eta}{\rho D_h^2}(mV) + \sigma \cos\theta \mathcal{P}} d(mV) = dt . \tag{19}$$

Integrating and solving for mV,

$$mV = t_{chr}\left[P_0 A_c + \sigma \cos\theta \mathcal{P} - c_1 \exp(-t / t_{chr})\right], \tag{20}$$

where c_1 is a constant of integration and t_{chr} is a characteristic time of the system given by

$$t_{chr} = \frac{\rho D_h^2}{2C\eta} . \tag{21}$$

At t=0 the momentum of the system is zero, so that the constant of integration is found to be

$$c_1 = P_0 A_c + \sigma \cos\theta \mathcal{P} \,. \tag{22}$$

Eq. (20) is now

$$mV = t_{chr}\left(P_0 A_c + \sigma \cos\theta \mathcal{P}\right)\left[1 - \exp(-t/t_{chr})\right]. \tag{23}$$

As was the case with the frictionless flow model, the length L can be found by substituting V=dL/dt and m=$\rho A_c L$ into the expression above.

$$\rho A_c L \frac{dL}{dt} = t_{chr}\left(P_0 A_c + \sigma \cos\theta \mathcal{P}\right)\left[1 - \exp(-t/t_{chr})\right] \tag{24}$$

Separating variables, integrating and solving for L yields

$$L = \left\{2\left[t_{chr}\left(\frac{P_0}{\rho} + \frac{4\sigma\cos\theta}{\rho D_h}\right)\left(t + t_{chr}\exp(-t/t_{chr})\right) + c_2\right]\right\}^{1/2}, \tag{25}$$

where we have once again eliminated $\mathcal{P}$ and A_c for D_h. Requiring that L=0 at t=0 yields the constant of integration, c_2.

$$c_2 = -t_{chr}^2\left(\frac{P_0}{\rho} + \frac{4\sigma\cos\theta}{\rho D_h}\right) \tag{26}$$

Eq. (25) becomes

$$L = \left\{2t_{chr}\left(\frac{P_0}{\rho} + \frac{4\sigma\cos\theta}{\rho D_h}\right)\left(t - t_{chr}\left[1 - \exp(-t/t_{chr})\right]\right)\right\}^{1/2}. \tag{27}$$

If we again let P_0=0 and focus on surface tension driven flow only, this reduces to

$$L = \left\{\frac{4\sigma\cos\theta}{\rho D_h} 2t_{chr}\left(t - t_{chr}\left[1 - \exp(-t/t_{chr})\right]\right)\right\}^{1/2}. \tag{28}$$

The reader will recognize the characteristic velocity of Eq. (11) appearing in Eq. (28), which can be recast as

$$L = V_{chr}\left(2t_{chr}\left(t - t_{chr}\left[1 - \exp(-t/t_{chr})\right]\right)\right)^{1/2}. \tag{29}$$

As before the flow velocity can be found simply by differentiating the length with respect to time. The result is

$$V = V_{chr}\frac{\sqrt{2t_{chr}}}{2}\frac{1 - \exp(-t/t_{chr})}{\left[t - t_{chr}\left(1 - \exp(-t/t_{chr})\right)\right]^{1/2}}. \tag{30}$$

Both the length and velocity as given by Eqs. (29) and (30) initially show an exponential decay. For times much larger than the characteristic time scale t_{chr}, the exponential terms can be neglected, and Eqs. (29) and (30) respectively reduce to

$$L = V_{chr}\left(2t_{chr}t\right)^{1/2} \tag{31}$$

and

$$V = V_{chr}\left(\frac{t_{chr}}{2t}\right)^{1/2}. \tag{32}$$

And so for times larger than the characteristic time, both length and velocity show a power law dependence on time. Figures 3 and 4 illustrate these trends in dimensionless form.

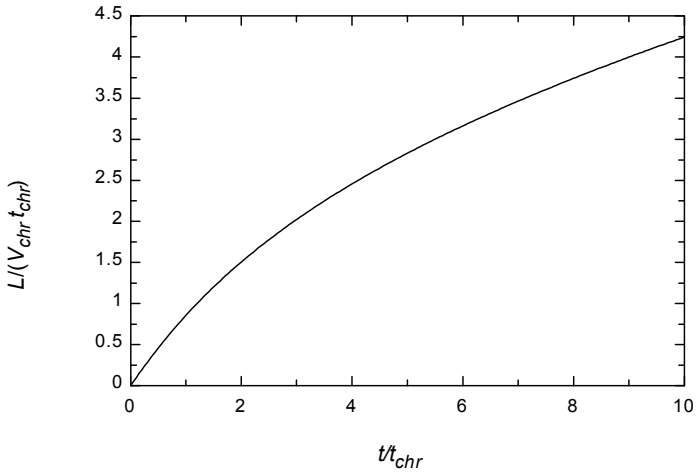

Figure 3: Variation of dimensionless penetration length as a function of dimensionless time.

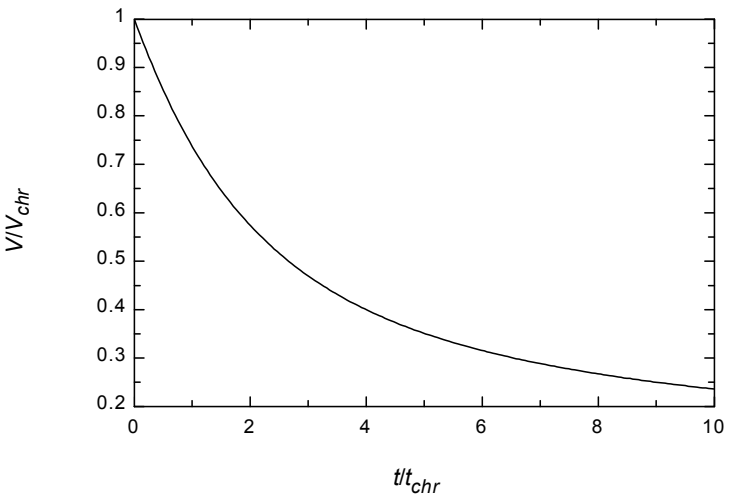

Figure 4: Variation of dimensionless velocity as a function of dimensionless time.

4 Comparisons with other models and experiments

For the frictionless flow model, the flow velocity is constant and the distance travelled by the fluid in the capillary increases linearly with time. In the model including wall friction, the velocity decreases with time and the fluid penetrates smaller and smaller distances into the capillary.

Both Schwiebert and Leong [8] and Jong *et al.* [9] derived expressions for surface tension driven flow between parallel plates. In both studies the length as a function of time can be given as

$$L = \left(\frac{a\sigma \cos\theta}{3\eta} t \right)^{1/2}, \tag{33}$$

where a is the separation distance between the plates. For parallel plates, the hydraulic diameter is D_h=2a and the constant appearing in the Fanning friction factor relation is C=24. This gives a characteristic velocity and characteristic time scale, respectively, of

$$V_{chr} = \left(\frac{2\sigma \cos\theta}{\rho a} \right)^{1/2} \tag{34}$$

and

$$t_{chr} = \frac{\rho a^2}{12\eta}. \tag{35}$$

Based on the material property values given in [8] and. [9], the time scales are on the order of 5×10^{-6} s, validating the use of the large time approximation of Eq. (31). Substituting Eqs. (34) and (35) into Eq. (31) yields

$$L = \left(\frac{a\sigma \cos\theta}{3\eta} t \right)^{1/2}, \tag{36}$$

which is identical to Eq. (33). As [8] and [9] both showed good agreement of Eq. (33) with experimental values of L, this serves as validation of the present model for times larger than the characteristic time scale t_{chr}.

For systems with larger hydraulic diameters, large fluid densities and/or small viscosities, however, the characteristic time scale may become a significant fraction of a second. As such, the approximations of Eqs. (31) and (32) to which previous models reduce may show significant deviations from measured values. This is especially evident in Eq. (32) in which the velocity approaches infinity as $t\rightarrow0$. Eq. (30), however, predicts V=V_{chr} at t=0, likely indicating a better model for small times and/or systems with large characteristic time scales. Physically this value makes sense as well, as V_{chr} represents a velocity characterized by zero wall friction. Since the fluid in the capillary initially makes contact with the wall over an infinitesimally small surface area, it should approximate frictionless flow at t=0. However, experimental values for velocity are needed as evidence for this claim. Further study is therefore warranted.

5 Conclusion

Models for surface tension driven flow in a capillary of arbitrary cross section have been developed using macroscopic conservation equations. Models for flow with and without wall friction were both investigated. For flow without friction, the flow velocity is constant and is a function of surface tension, contact angle, fluid density, and hydraulic diameter. For flows with wall friction, a characteristic time for the flow can be calculated. For flow times on the order the characteristic time scale, the flow velocity decays exponentially from the frictionless flow velocity. For larger times, both velocity and penetration length show a power law dependence on time.

For larger time scales, the derived equations for length and velocity reduce to expressions developed by earlier models. Previously obtained experimental values of penetration length validate the present model. However, experimentally measured values of flow velocity are needed to validate the model's accuracy for small times or systems with large characteristic time scales.

Acknowledgements

The authors wish to thank Drs. L. Olson and C. Lui for their generous comments and suggestions in regard to this work.

References

[1] Londe, G., Wesser, A., Cho, H.J., Zhai, L., Chunder, A. & Subbarao, S., Passive microfluidic valve using superhydrophobic/hydrophyilic nanostructures for lab-on-a-chip (LOC) systems. *Proc. 14th Annual international conference on solid state sensors, actuators and Microsystems* (*Transducers '07*), Lyon, pp. 1801-1804, June 10–14, 2007.

[2] Feng, Y., Zhou, Z., Ye, X., & Xiong, J., Passive valves based on hydrophobic microfluidics, *Sensors and Actuators A* **108**, pp 138–143, 2003.

[3] Vanifatova, N.G., Zavarzina, A.G., & Spivakov, B.Y., Potential of capillary zone electrophoresis for estimation of humate acid-base properties, *J. Chromatography A*, **1183(***1-2*, *7* pp 186–191, March 2008.

[4] Macka, M., Andersson, P., & Haddad, P.R., Changes in Electrolyte pH Due to Electrolysis during Capillary Zone Electrophoresis. *Anal. Chem.,* **70(743)**, 1998.

[5] T. Young, *Miscellaneous Works*, ed G. Peacock J., Murray: London, p. 418, 1885.

[6] Lucas, R., *Kolloid Z.,* **23(15)**, 1918.

[7] Washburn, E. W., The dynamics of capillary flow, *Phys. Rev.,* **17(273)**, pp 273–283, 1921.

[8] Schwiebert, M.K. & Leong, W.H., *IEEE Trans. Compon. Packag. Manuf. Technol.* **19(2)**, pp 133–137, 1996.

[9] Jong, W.R., Kuo, T.H., Ho, S.W., Chiu, H.H. & Peng, S.H., Flows in rectangular microchannels driven by capillary, *Int. Comm. in Heat and Mass Trans.,* **34**, pp 186–196, 2007.

This page intentionally left blank

Characteristics of the flow over a NACA 0012 airfoil at low Reynolds numbers

R. W. Derksen, M. Agelinchaab & M. Tachie
Department of Mechanical and Manufacturing Engineering, University of Manitoba, Winnipeg, Manitoba, Canada

Abstract

This paper presents our work of an experimental examination of the flow over a NACA 0012 Airfoil at low Reynolds numbers and large angle of attack using particle imaging velocimetry. The Reynolds numbers examined were 5,000, 30,000, and 60,000, while the angles of attack ranged from 8 to 12 degrees in 2 degree increments. This work was motivated by reports that lift and drag measurements for airfoils operating at Reynolds numbers less than roughly 40,000 could not be made due to flow unsteadiness. This is puzzling in that the flow should be laminar at these Reynolds numbers, which are an order of magnitude lower than the flat-plate transition Reynolds number of 500,000. To this end we examined a sequence of flow field measurements of the instantaneous velocity field. We observed mean streamline patterns that were very representative of those we would find for a strictly steady flow, however a random pattern of significant fluctuations in the velocity and vorticity were observed. The intensity of these fluctuations increased with Reynolds number and angle of attack.

Keywords: aerodynamics, low Reynolds number flow, particle imaging velocimetry.

1 Introduction

Historically, interest in low Reynolds number aerodynamics has been restricted to model radio controlled aircraft applications and did not garner a great deal of scientific interest. This situation is changing with the interest in small unmanned aerial vehicles, predominantly for military purposes. As such, our understanding of low Reynolds number flow over airfoils is limited to a few sources that are

WIT Transactions on Engineering Sciences, Vol 59, © 2008 WIT Press
www.witpress.com, ISSN 1743-3533 (on-line)
doi:10.2495/AFM080141

growing as time evolves. This naturally leads us to the outstanding work done by Selig *et al* [1–4] in the mid-nineties. This work details the results of a carefully constructed experimental program to produce a database of modern, low-Reynolds number airfoils. The measurements were exhaustively examined for their accuracy, for example drag was measured by the more accurate wake traverse method.

One observation made in the Selig work was that they could not reliably measure airfoil characteristics if the Reynolds number fell below 40,000 due to flow unsteadiness. Huang and Lin [5] clearly demonstrated vortex shedding and instability at low-Reynolds numbers using smoke-streak and hot-wire measurements of the flow over a NACA 0012 airfoil. Unfortunately, the smoke-streak method presents us with a time averaged view of the flow field and hot-wire only yields point observations. We suspected that this may be the result of a periodic bursting of a laminar separation bubble. In this process the separation bubble would develop to such a point that it would detach from the airfoil and move downstream. Once the remnant of the bubble was sufficiently far downstream the process would then repeat periodically. A computational study of unsteady boundary-layer separation over an Eppler 387 airfoil at low-Reynolds numbers done by Lin and Pauley [6] appears to support this view.

We felt that this was a sufficiently interesting possible phenomenon that deserved an in depth study which is described below. The main objective of this study was to determine the characteristics of the bubble growth, that triggered the detachment, to observe the movement of the detached bubble.

2 Experimental set-up and procedure

The experiments were based on the flow over a NACA 0012 symmetric airfoil, which is the same as that studied by Huang and Lin. This airfoil is often used in aerodynamic studies and forms a good base to work from.

2.1 Test section

The experiments were performed in a re-circulating open channel with a test section that is 2500 mm long, 200 mm wide and 200 mm deep. A provisional closed test section 2500 mm long with a 187 mm × 187 mm cross-section was inserted into the open channel to hold the airfoil in place. The airfoil is symmetric and has a chord length of 100 mm, a maximum thickness of 12 mm and a width of 187 mm that spans the entire width of the test section. The airfoil was tightly screwed to the side walls of the test section at 1000 mm downstream from the inlet of the channel to ensure uniform flow at the measurement section. Figure 1 is the schematic of the provisional closed test section with the laser and camera arrangement.

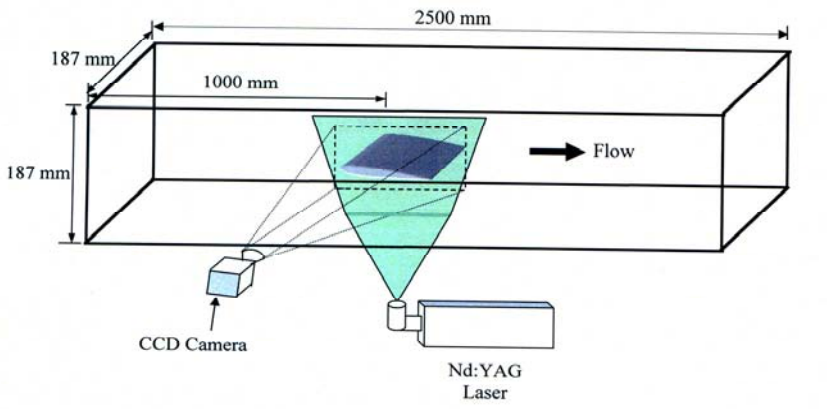

Figure 1: Experimental set-up of the test section, airfoil, CCD camera and laser arrangement.

2.2 Measurement procedure

A particle image velocimetry (PIV) technique was used for the velocity measurements. The flow was seeded with 5 μm polyamide seeding particles. An Nd-YAG, 120 mJ/pulse laser of 532 nm wavelength was used to illuminate the flow field. A 12-bit high-resolution CCD camera with 2048 pixels × 2048 pixels and a 7.4 μm pixel pitch was employed to image the flow field. The instantaneous images were processed using the adaptive correlation option of FlowManager (version 4.50.17) developed by Dantec Dynamics. A 32 pixels × 16 pixels interrogation window (IW) with 50% overlap and moving average validation was used. The adaptive correlation used a multi-pass FFT cross-correlation algorithm to determine the average particle displacement within the IW. A three-point Gaussian curve fit was employed to determine particle displacement with sub-pixel accuracy. The particle image diameter was estimated to be d_p = 2.1 pixels, a value that is very close to the recommended optimum value of $d_p \approx 2$ pixels required to minimize peak locking (Raffel *et al* [7]).

Whereas the vorticity contours are instantaneous, the mean streamlines, turbulent intensities, and Reynolds shear stress were obtained from a sample size of 250 images. A field of view was made large enough to capture the whole airfoil at once. The physical spacing between data points along the flow direction and normal to the flow direction were 1.2 mm and 0.6 mm, respectively.

The Reynolds numbers based on the chord length and the upstream velocities were Re = 5000, 30,000 and 60,000. For each Re, the angle of attack was varied from θ = 8°, 10° and 12° to investigate the effect of both Re and θ on the airfoil. The measurements were obtained at the mid-plane of the test section.

2.3 Measurement uncertainty

Uncertainty analysis was made following the AIAA standard derived and explained by Coleman and Steele [8]. In general, a complete uncertainty analysis involves identifying and quantifying both the bias and precision errors in each part of the measurement chain. In a PIV technique, the accuracy of velocity measurement is limited by the accuracy of the sub-pixel interpolation of the displacement correlation peak. Other sources of measurement uncertainties include particle response to fluid motion, light sheet positioning, light pulse timing and size of interrogation area. Detailed analyses of bias and precision errors inherent in the PIV technique are available in Prasad [9] and Forliti *et al* [10]. Forliti *et al* showed that a Gaussian peak-fitting algorithm has the lowest bias and precision errors. On the basis of the size of the interrogation area and the curve fitting algorithm used to calculate the instantaneous vector maps, the uncertainty in the mean velocities at a 95% confidence level was estimated to be ±2%, in turbulence intensities are estimated to be ±7%, and in Reynolds shear stress are estimated to be ±10%.

3 Results

A survey of the results will be given due to the volume of data that was produced and the limited space available in this document. The characteristics of the flow can be summarized as follows. The mean stream lines were as to be expected for a steady laminar flow for each angle of attack and for each of the three Reynolds numbers. The flow was attached to the airfoil for θ=8 and 10°, but a small separation bubble was evident for the 12° case. This bubble was most noticeable for Re=5,000 and diminished as the Reynolds number increased to the point that it was barely detectible for Re=60,000. Generally, the intensity of the disturbances, as indicated by the turbulence intensity, increased with Reynolds number for a fixed angle of attack. However there was a pronounced increase in both intensity and amount of the flow field affected by the disturbance for Re=60,000. A snap shot of the instantaneous vorticity field corresponds to this picture. It is interesting to note that the region that contains fluctuating vorticity is usually smaller and more dispersed than that indicated by the mean turbulence intensity field, indicating that the mean intensities indicate a greater influence of the disturbances that occurs at any given time. One would be tempted to think that this would indicate the presence of turbulence in the flow. However, with the exception of the Re=60,000 and θ=12° case, the mean Reynolds shear stresses were very small – virtually negligible. This would tend to indicate that an instability mechanism is at play generating random fluctuations, but that the flow has not developed a correlated turbulence region. We will focus on the Re=5,000 cases for our detailed discussion that follows.

3.1 Mean streamlines at Re=5,000

The mean streamlines for Re=5,000 are shown below, in Figure 2.

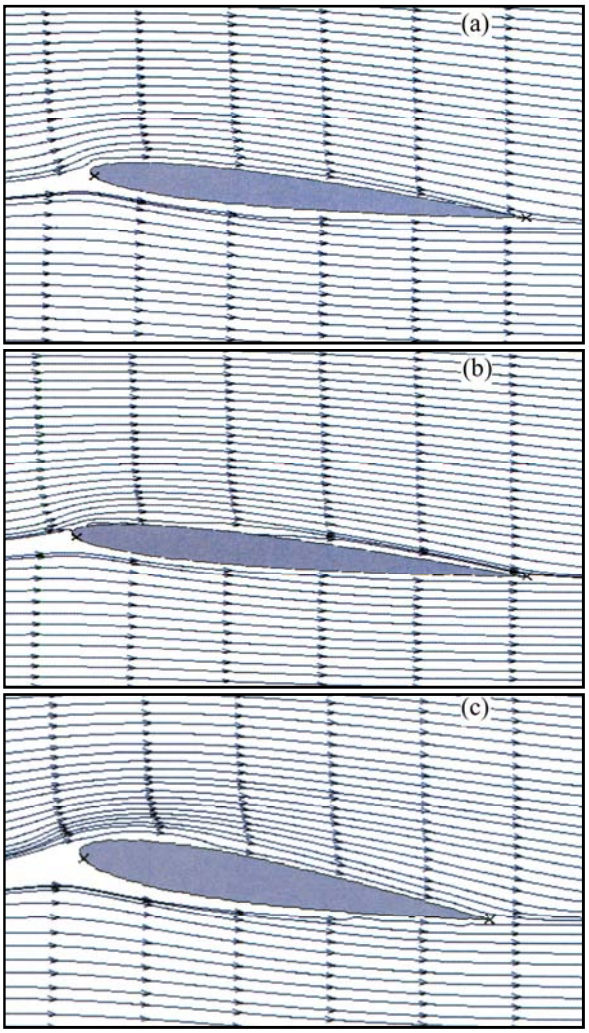

Figure 2: The mean streamlines at Re = 5,000; (a) $\theta = 8°$, (b) $\theta = 10°$, and (c) $\theta = 12°$.

This figure clearly demonstrates the characteristic streamline pattern that we would expect to see for a steady laminar flow. The flow is generally attached, but a separation bubble appears at θ=12° which corresponds to the known maximum lift angle of attack. This picture is consistent with the results for Re=30,000 and 60,000.

3.2 Turbulence intensities at Re=5,000

The measured turbulence intensities are shown below in Figure 3 for Re=5,000.

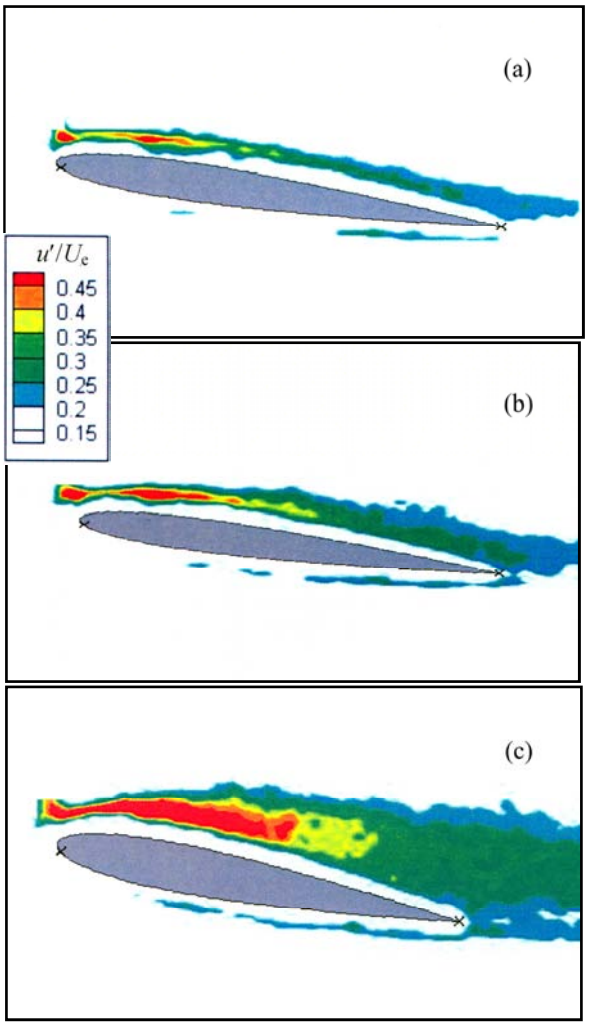

Figure 3: The turbulence intensities at Re = 5,000; (a) $\theta = 8°$, (b) $\theta = 10°$, and (c) $\theta = 12°$.

Figure 3 clearly demonstrates a zone of fluctuation that is most noticeable above the suction surface and in particular above the leading portions of the airfoil. This zone is physically separated from the surface of the airfoil at a distance approximately equal to its width. At the largest Reynolds number, 60,000, it appears that the affected zone grows dramatically in intensity and size.

3.3 Instantaneous vorticity distributions at Re=5,000

Instantaneous snapshots of the vorticity for Re=5,000 are shown below in Figure 4.

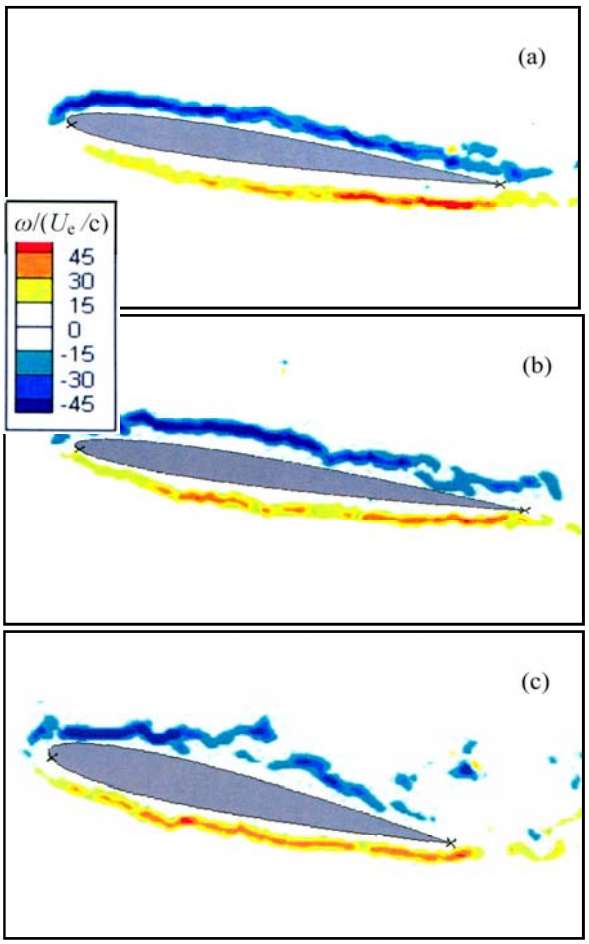

Figure 4: A snap shot of the instantaneous vorticity at Re = 5,000; (a) θ = 8°, (b) θ =10°, and (c) θ =12°.

Figure 4 clearly demonstrates the limited size of the zone affected by the disturbances at any given time. In all cases the size of the region is similar; however, the meander of the instantaneous vorticity clearly increases with Reynolds number. Notice that the size of the region of the flow that is affected by the disturbances is significantly smaller than that indicated by the size of the regions with notable turbulence intensity.

3.4 Reynolds shear stress at Re=5,000

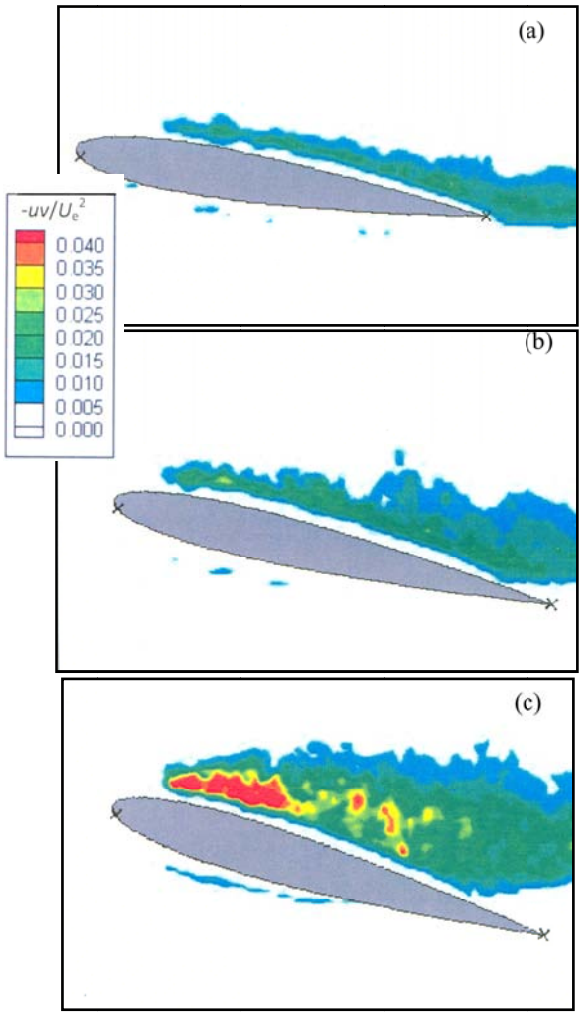

Figure 5: The Reynolds shear stresses at Re = 5,000; (a) θ = 8°, (b) θ = 10°, and (c) θ =12°.

Figure 5 is a flow field map of the mean Reynolds stresses for Re=5,000. Here we clearly see that the turbulence levels are negligible for the lower angles of attack, however at the higher angle of attack a significant degree of Reynolds stress is evident above the forward portion of the suction surface.

4 Discussion

An examination of the mean streamline patterns about the airfoils does not indicate any of the rich character of the flow. They are very similar to what we would expect if the flow was a strictly steady, laminar flow, as we would expect based on the low Reynolds numbers studies.

The results of this study clearly demonstrate that significant levels of fluctuations exist in the flow over a NACA 0012 airfoil at angles of attack between 8 and 12°. This is true even though the Reynolds numbers were very small, well below the typically turbulent transition Reynolds number of 500,000. Clearly, an instability mechanism is at play and we cannot assume that the flow is automatically steady. The magnitudes of the disturbances are too large to consider as minor background disturbances, which are not observed in the main body of the flow away from the airfoil.

The snapshots of the instantaneous vorticity distributions clearly indicate that similar zones are affected by the disturbances as indicated by the mean turbulence intensities in all cases. For Re=5,000 and 30,000 the instantaneously affected zones are very similar to that indicated by the mean turbulence intensity. However, at the highest Reynolds number the instantaneous vorticity affected zone meanders about the flow field considerably, causing the affected zone to appear much larger when we examine the mean turbulence intensities. The highest Reynolds number and angle of attack could result in transition as this angle of attack approximately corresponds to the maximum lift point.

The measured Reynolds stresses confirm the picture that the flow is not turbulent, at least for the lower angles of attack and Reynolds numbers. In general, we observe very low degrees of correlation between the stream wise and normal components of the velocity fluctuations. This is more indicative of a random, uncorrelated disturbance pattern that likely is the result of a flow instability mechanism. It also indicates that the mean streamline field would not be affected by these disturbances, as was observed.

The picture does appear to change somewhat at the highest angle of attack of 12°, particularly at Re=60,000. This may indicate that the transition Reynolds number for this airfoil at this angle of attack is about 60,000.

5 Conclusions

The results of this work present us with three interesting and somewhat unexpected observations.

First there is clear evidence of significant levels of flow disturbances in all cases examined, with some indication that there may be some turbulent flow at Re=60,000 and θ=12°. The consequences of this is that while our basic flow model of steady laminar flow will result in reasonably good predictions of mean behaviour, the flow is still highly unsteady, complicating measurements of the airfoil's characteristics.

The second observation is that the flow is not turbulent, except for the 12°, Re=60,000 case. The correlation between the stream-wise and normal velocity components is essentially negligible.

The third observation is that at low Reynolds numbers, the airfoil's characteristics will be unsteady, with fluctuations in lift, drag, and pitching moment. This will make measuring the mean characteristics more challenging.

It is interesting to note that these observations indicate that it will be easier to obtain an accurate estimate of the mean characteristics of an airfoil by computational methods than experimentally.

Acknowledgement

The authors would like to acknowledge the generous support of this work by the Natural Sciences and Engineering Research Council of Canada.

References

[1] Selig, M.S., Donovan, J.F., and Fraser, D.B., *Airfoils at Low Speeds*, Soartech 8, Soartech Publications, Virginia Beach, U.S.A, 1989.

[2] Selig, M.S., Guglielmo, J.J., Broeren, A.P. and Giguere, P., *Summary of Low Speeds Airfoil Data*, Volume 1, Soartech Publications, Virginia Beach, U.S.A., 1995.

[3] Selig, M.S., Lyon, C.A., Giguere, P., Ninham, C.P. and Guglielmo, J.J., *Summary of Low Speeds Airfoil Data*, Volume 2, Soartech Publications, Virginia Beach, U.S.A., 1996.

[4] Lyon, C.A., Broeren, A.P, Giguere, P., Gopalarathnam, A. and Selig, M.S., *Summary of Low Speeds Airfoil Data*, Volume 3, Soartech Publications, Virginia Beach, U.S.A., 1997.

[5] R.F. Huang, and C.L. Lin, Vortex Shedding and Shear-Layer Instabilities of Wing at Low-Reynolds Numbers, *AIAA Journal*, **33(8)**, pp. 1398-1403, 1995.

[6] J.C.M. Lin and L.L. Pauley, Low-Reynold-Number Separation on an Airfoi*l*, *AIAA Journa*l, **34(8)**, pp. 1570-1577, 1996

[7] M. Raffel, C.E. Willert, J. Kompenhaus, *Particle Image Velocimetry: A Practical Guide,* Springer, 1998.

[8] H.W. Coleman and W.G. Steele, Engineering Application of Experimental Uncertainty Analysis*, AIAA Journal*, **33**, pp. 1888-1896, 1995.

[9] A.K. Prasad, Particle Image Velocimetry*, Current Science* **79(1)**, pp. 51-60, 2000.

[10] D.J. Forliti, P.J. Strykowski and K. Debatin, Bias and Precision Errors of Digital Particle Image Velocimetry*, Experiments in Fluids*, **28(436)**, pp. 436-447, 2000.

An experimental investigation of the reduced frequency effects into pressure coefficients of a plunging airfoil

M. Mani[1], F. Ajalli[2] & M. R. Soltani[3]
[1]*Department of Aerospace Engineering, Amirkabir University of Technology, Iran*
[2]*Aerospace Research Institute, Iran*
[3]*Department of Aerospace Engineering, Sharif University of Technology, Iran*

Abstract

Aerodynamic coefficients on a two dimensional plunging airfoil, in a low-speed wind tunnel are presented. Dynamic motion was produced by plunging the model over a range of reduced frequencies, and mean angles of attack. The Reynolds number in the present test was held fixed ($\mathrm{Re} = 1.5 \times 10^5$), and the reduced frequency was varied in an almost wide range. Surface static pressure distribution was measured on the upper and lower sides of the model, during the oscillating motion. It was found that reduced frequency had strong effects on the pressure distribution, near the leading edge of the airfoil. For mean equivalent angles of attack of 0, 5 degrees, hysteresis loops on the upper surface of the airfoil near the leading edge were counter clockwise and for high mean equivalent angle they were clockwise. By increasing the reduced frequency the hysteresis loops became wider and larger.

Keywords: unsteady aerodynamic, hysteresis loops, plunging airfoil, reduced frequency.

1 Introduction

In many engineering applications, lifting surfaces experience unsteady motions or are perturbed by unsteady incoming flows. High level dynamic loading and noise generation are inherent problems, due to unsteadiness [1]. One of the basic

WIT Transactions on Engineering Sciences, Vol 59, © 2008 WIT Press
www.witpress.com, ISSN 1743-3533 (on-line)
doi:10.2495/AFM080151

problems of flight dynamics is the formulation of the aerodynamic forces and moments acting on a body in an arbitrary motion. For many years the aerodynamic functions were approximated by linear expressions leading to a concept of stability and control derivation but the addition of nonlinear terms are very important and should not be omitted in the control fields. These considerations were many time questioned base on the studies of aerodynamics, which go back to the twenties. Dynamic stall phenomenon appears on helicopters rotor blades, rapidly maneuvering aircraft, wind turbine and even insect wings. In many cases dynamic stall becomes the primary limiting factor in the performance of the associated vehicle or structure [2]. The mechanism of dynamic stall was first identified on helicopters. The importance of unsteady aerodynamics was considered by Harris and Pruyen [3] when helicopter designs were unable to predict the performance of high speed helicopters using conventional aerodynamics. Ham and Garelick [4] observed the extra lift due to vortex formation on the airfoil during the unsteady motion. Carta [5] was able to identify a pressure field on oscillating, two dimensional airfoils that was indicative of the passage of the vortex. Dynamic stall was then explored by McCroskey and Fisher [6] on a model of a rotor. Many of the aerodynamic phenomena governing the behavior of wind turbine blades and helicopter rotors are known, but the details of the flow are still poorly understood and need to be predicted accurately. As a result of this inaccuracy the actual loading are under predicted [7]. Due to the complicated behavior of unsteady forces during the plunging motion, numerical techniques are not able to predict accurately these variables yet, and relatively little experimental information is available about the precise fluid physics of oscillating airfoils. Also pure plunging airfoil motion has received relatively less attention than pitching motion. Therefore the main purpose of this experimental work is to study the pressure distributions at various locations of the Eppler-361 airfoil undergoing sinusoidal plunging oscillation at several angles of attack and different reduced frequencies. Fourteen pressure transducers and the on-line data acquisition system have significantly facilitated the study of the pressure distribution in the plunging airfoil.

2 Experimental facility and data processing

All experiments were performed in the subsonic wind tunnel of Amirkabir University of Technology, Department of Aerospace Engineering. The wind tunnel is closed return type, and has a test section of approximately 45 cm wide, 45 cm high, and 120cm long. The Maximum flow speed in the test section of this tunnel is approximately 45 m/s. The inlet of the tunnel has a 7.3:1 contraction ratio with four, anti-turbulence screens and honeycomb in settling chamber to reduced tunnel turbulence to less than 0.1% the test section at all speeds. The airfoil used in this study has an E-361 profile. A 15 cm constant chord airfoil model was designed and manufactured for the test program. To achieve two dimensionality of the flow, the airfoil span has been chosen the same size as the width of the tunnel. Figure 1 shows the airfoil section along with the 14 pressure taps located on upper and lower surfaces used for static pressure measurements.

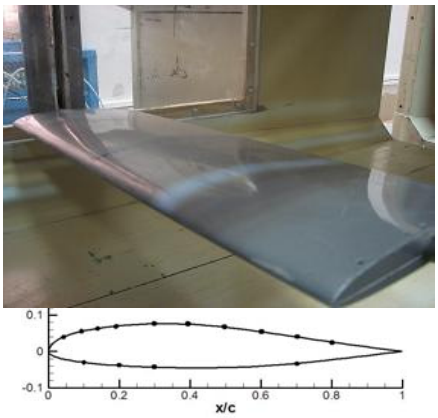

Figure 1: Airfoil section and location of pressure taps.

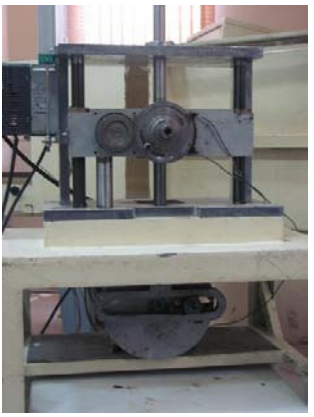

Figure 2: Oscillation mechanism.

Data are obtained by using differential pressure transducers with a quoted accuracy of 0.2% of full-scale pressure range. Due to the size of selected pressure transducers, we could not place the transducers inside the model. Therefore, the connections between pressure taps and Pressure Transducers are made by tubes. Extensive experiments were conducted to ensure that the time taken for the pressure to reach the transducers is much less than the frequency response of the transducers themselves [8]. The data was processed by using analog to digital board. Oscillatory data were then digitally filtered using various cut-off and transition frequencies to find the best frequencies to fit the original data. The filtering process is necessary to eliminate the electrical noise from the genuine data. The driving mechanism of the plunging airfoil has a simple and versatile design which consists of motor, gears, cam, and shaft. This mechanism can provide various frequencies (f), amplitudes (h) and mean angles of attack (α_0). The motor and gear combination develop a wide range of frequencies. The maximum frequency is 3 Hz. Figure 2 shows the picture of oscillation mechanism.

3 Results and discussions

Both static and oscillatory test were conducted at $\mathrm{Re} = 1.5 \times 10^5$, $\left(U_\infty = 15 m/s\right)$.The instantaneous displacement of the model was measured using a potentiometer. The static pressures at angles of attack 0, 2, 5, 10, 12, 15, 17 and 20 were measured. The surface pressure distribution at mean angles of attack (0, 5, 10 degrees) and different reduced frequencies for constant amplitude of oscillation $\tilde{h} = 8cm$ are presented in this paper. The effects of the amplitudes of oscillations on the static pressure distribution in dynamic motion are presented in [9].

Figure 3 shows the sinusoidal variation of displacement with non-dimensional time. Relative motions between pitching and plunging airfoils are compared by equivalent angle of attack [10]. The phase difference between two motions is 90degrees (Figures 3 and 4). The height of oscillation and its equivalent angle of attack are defined as:

$$h = \tilde{h}\sin(\omega t)$$

$$\alpha_{eq} = \tan^{-1}\left(\frac{\dot{h}}{U_\infty}\right) = k\bar{h}\cos(\omega t)$$

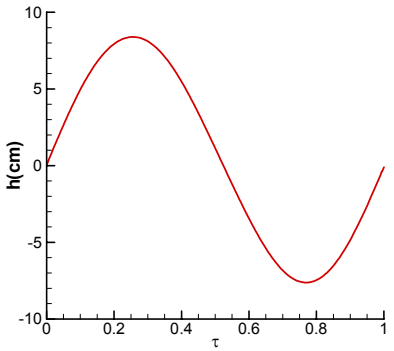

Figure 3: Sinusoidal variations of displacement ($\alpha_0 = 0$).

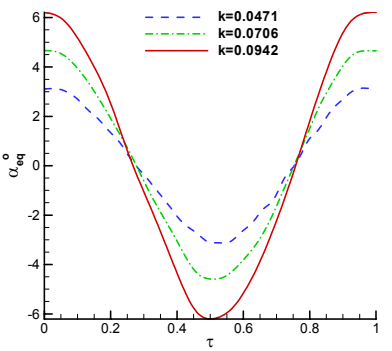

Figure 4: Variations of equivalent angle of attack vs. τ ($\alpha_0 = 0$).

There is a crossover point at which the value of pressure in upstroke and down stroke is the same, for specific angle of attack. For example as shown in (fig 5c) at k=0.0706 this angle is 1.8 degrees. By increasing the reduced frequency up to k=0.0942, the related equivalent angle to crossover point of the "8" shape is decreased to 1.4 degrees which shows an earlier separation of the flow in high frequencies. As mentioned before, the more the reduced frequency, the larger the variation ranges of equivalent angle of attack.

For example at $\alpha_{mean} = 0\,\text{deg}$ and k= 0.0942, the equivalent angle of attack is varied over the range of ($-5.8^\circ < \alpha_{eq} < 5.8^\circ$), that have noticeable effects in unsteady behavior of the flow. For the lower surface the direction of the hysteresis loops are clockwise (opposite direction of the upper surface), figure 5d. Variations of C_P vs. α in figure 5, shows that the hysteresis loops are larger and widen as reduced frequency increases from k=0.0471 to k=0.0942, because this parameter (k) make the flow more unsteady and reinforce the lag effects of the flow. In this figure, it is observed that, the maximum pressure suction

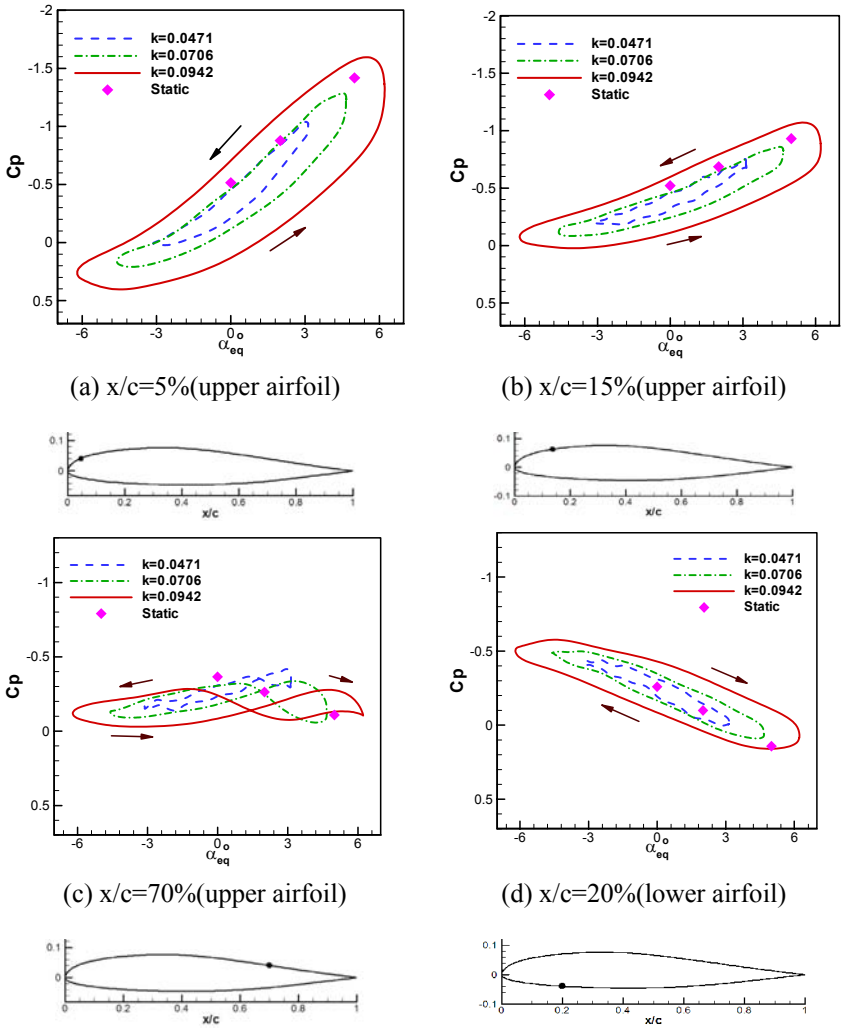

(a) x/c=5%(upper airfoil)

(b) x/c=15%(upper airfoil)

(c) x/c=70%(upper airfoil)

(d) x/c=20%(lower airfoil)

Figure 5: Dynamic variation of the pressure coefficients for α_{mean}=0 deg.

$|C_p|_{\max} = 1.7$ is near the leading edge at x/c=5% of the upper surface and occurs at an equivalent angle of attack about 5.5 degrees for k=0.0942. One could expected that the maximum pressure suction for k=0.0942 happens at maximum equivalent angle of attack (5.8 degrees), but it happens at $\alpha_{eq} = 5.5^\circ$. This is due to the lag effects and delay time of the flow in unsteady motions. At lower value of reduced frequency (for example k=0.0471) the delay time of the maximum pressure suction near the leading edge is negligible but it is much significant at higher reduced frequency (fig 5a). At the aft portions of the airfoil the dynamic variations of the pressure coefficient are lower regard to the forward portion.

This indicates that oscillation of the airfoil has no significant effect on the rear portion.

Figure 6 show the variation of pressure coefficients at several ports (x/c=5, 15, 60 and 70%) on the upper surface of the airfoil for $\alpha_{mean} = 5\deg$, meaning that the model was set to an angle of attack of 5 degrees and oscillated at amplitude of ±8cm. In this case, the suction pressure peak near the leading edges at x/c=5% and x/c=15% are increased. The maximum pressure peak at x/c=5% for k=0.0942 in comparison with figure (5a) is increased about $|\Delta C_p| = 0.8$. The direction of the hysteresis loops at the positions near the leading edge remains

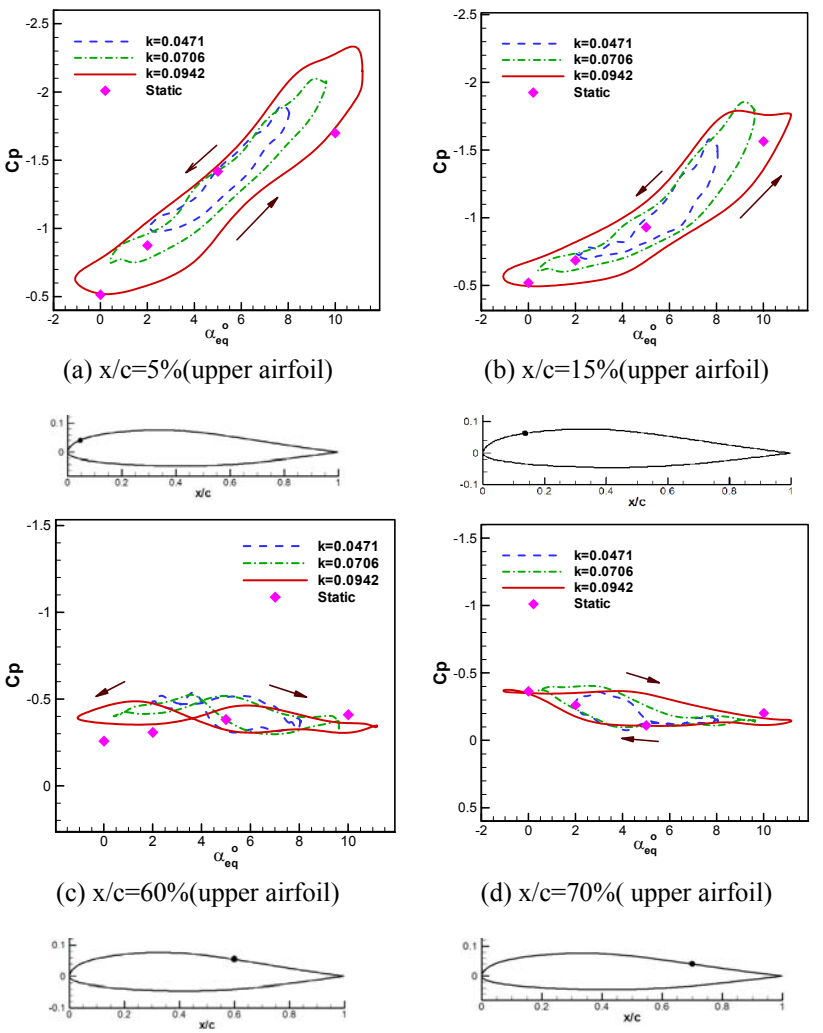

(a) x/c=5%(upper airfoil)

(b) x/c=15%(upper airfoil)

(c) x/c=60%(upper airfoil)

(d) x/c=70%(upper airfoil)

Figure 6: Dynamic variation of the pressure coefficients for α_{mean}=5 deg.

counter clockwise, that indicates the flow is attached yet, but at the aft portion x/c=60%, hysteresis loops become like "figure 8" shape which shows the separation has occurred in this position. In the pressure port x/c=70%, the direction of the hysteresis loops change to clockwise direction which is caused by the adverse pressure gradient near the trailing edge of the airfoil. Comparison the figures (5c, 6c), showed that the separation of the flow moved forward and happened at x/c=60%, because the model was oscillated at higher mean angle of attack. The effects of reduced frequency in this case are observed to be the same as the previous case.

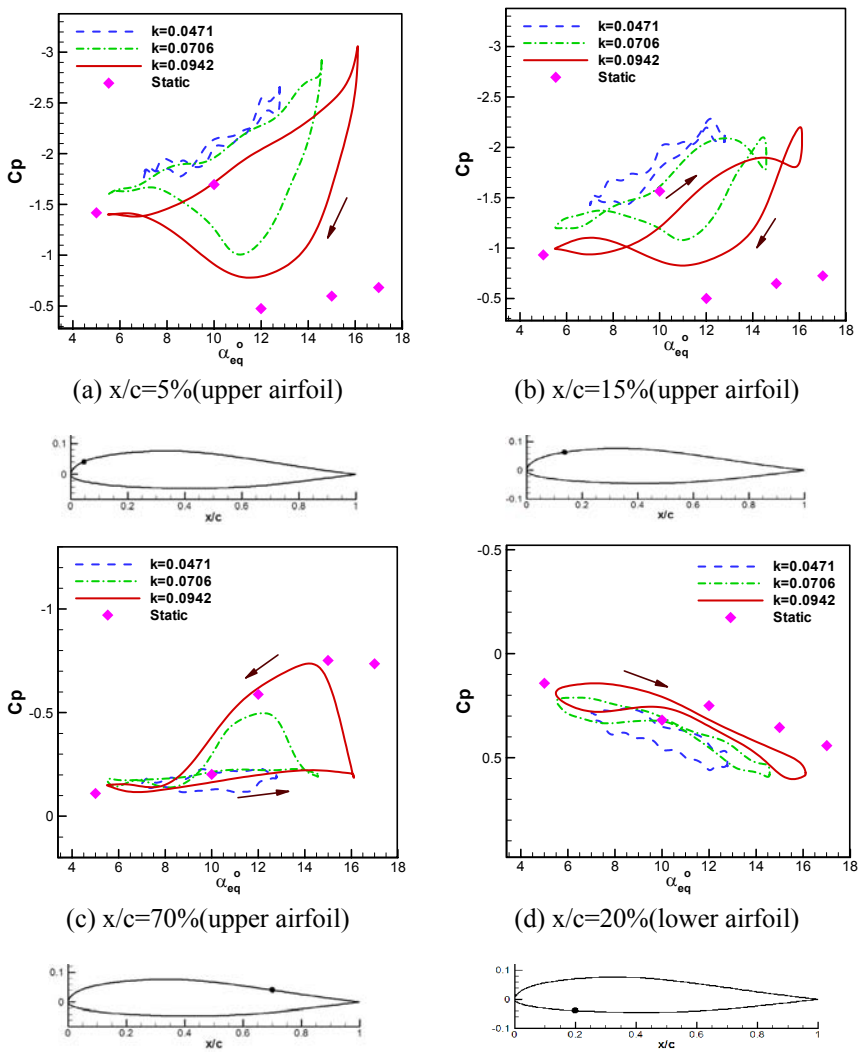

(a) x/c=5%(upper airfoil)

(b) x/c=15%(upper airfoil)

(c) x/c=70%(upper airfoil)

(d) x/c=20%(lower airfoil)

Figure 7: Dynamic variation of the pressure coefficients for α_{mean}=10 deg.

Figure 7 shows variations of Cp at higher mean angle of attack, (near static stall angle). Note that the static stall angle for this airfoil occurred at 12degrees. The directions of hysteresis loops at x/c=5% for the upper surface are clockwise which define that the motion has lead phase, figure 7a. When the mean angle of attack is increased up to 10 degrees, the width of the hysteresis loops in this pressure port increase drastically and also the maximum pressure suction is increased for the highest value.

For example the value of maximum pressure in figure (7a) for k=0.0942, is increased about $|\Delta C_p| = 1.4$ compared to figure 5a. It is observed that after the maximum suction a sudden undershoot of pressure coefficient happened which shows that dynamic starting vortex near the leading edge forms. This stating vortex as obvious in figure 7a, for k=0.0706 happens at $\alpha_{eq} = 16^\circ$ and for k=0.0942 it occurred at $\alpha_{eq} = 14^\circ$. The speed of starting vortex on the upper surface of the airfoil increases when the reduced frequency is increased.

When the plunging airfoil passes the static stall angle flow reverses near the surface at the rear part of the airfoil. By increasing equivalent angle of attack this reversal flow progresses up the leading edge of the airfoil; then at an angle of attack that depend on many parameters including frequency, airfoil shape, Reynolds number etc, the viscous flow no longer remains thin and attached, and a very strong vertical flow develops.

This vortex being near the leading edge of the airfoil, enlarges, and then moves down the airfoil then produces the phenomena known as dynamic stall. The vortex shedding process is the most obvious characteristic of dynamic stall [2]. In this case ($\alpha_{mean} = 10^\circ$), the variations range of the equivalent angle of attack was not enough large to cause deep stall and light stall [12] happened. In position x/c= 15%, three hysteresis loops are formed which the largest one is clockwise and lead phase. The maximum overshoot in figure 7c, (x/c=70% upper surface), shows the progressing of the starting vortex to trailing edge of the airfoil. Further from figure 7 note that, at the lower reduced frequency k=0.0471, there is no indication of the sudden undershoot and progressing of the starting vortex in the airfoil. On the lower surface, figures 7d, the directions of the hysteresis loops are clockwise. There is a lower pressure variations on the lower surface compared to the upper surface which is due to the shape of the airfoil. Hysteresis loops on the lower surface in this case in comparison with the figure 5d ($\alpha_{mean} = 0\,\text{deg}$), become narrower.

4 Conclusion

An extensive experimental study was conducted to investigate the flow phenomena over the plunging airfoil. Static pressure distributions at 14 positions over and under the model were measured. At mean angles of attack 0, 5 deg, hystresis loops in forward portion of the airfoil were counter clockwise and the flow was attached. Near the trailing edge of the airfoil where the flow was separated, hysteresis loops formed an "8" shape and at lower surface hysteresis

loops were clockwise. The directions of hysteresis loops for x/c=5% and α_{mean}=10deg on the upper surface were clockwise and the dynamic starting vortex was formed. The higher reduced frequency resulted larger hysteresis loop which was due to strong effects of unsteadiness. There was a lower pressure variations on the lower surface compared to the upper surface of the airfoil. In the aft portions of the airfoil the dynamic variations of the pressure coefficient were less regard to the forward portion.

References

[1] McCroskey, W. J., *Recent Developments in Dynamic Stall*, Symposium on Unsteady Aerodynamics, Vol. 1, Univ. of Arizona, March 1975, pp. 1–34

[2] Carr L. W., *Progress in Analysis and Prediction of Dynamic Stall*, Journal of Aircraft, Vol. 25, No.1, January 1988.

[3] Harris, F. D. and Pruyn, R. R., *Blade Stall-Half Fact, Half Fiction*, Journal of American Helicopter Society, Vol. 13, No. 2, April 1968, pp. 27-48.

[4] Ham, N. D. and Garelick, M. S., *Dynamic Stall Considerations in Helicopter Rotors*, Journal of American Helicopter Society, Vol.13, No.2, April 1968, pp. 49–55.

[5] Carta, F.O., *Experimental Investigation of the Unsteady Aerodynamic Characteristics of a NACA 0012 Airfoil*, Res.Rep. M-1283-1, United Aircraft Crop., July 1960.

[6] McCroskey, W. J., Fisher , R. K., *Detailed Aerodynamic Measurements on a Model Rotor in the Blade Stall Regime*, Journal of American Helicopter Society, Vol.17, No.1, Jan. 1972, pp. 20–30.

[7] Johansen, J. *Prediction of Laminar/Turbulent Transition in Airfoil flows,* Riso-R-987 (EN),Riso National Laboratory 1977.

[8] Mani, M. , Soltani M. R. and Tolouei E., *An Experimental Study of Time Lag Pressure Measurement in Different Tubes*, Amirkabir,Vol.16, No.61-B, Spring 2005.

[9] Ajalli F., Mani M., Soltani M. *An Experimental Investigation of Pressure Distribution around a Heaving Airfoil*, The 5th International conference on Heat Transfer, Fluid Mechanics and Thermodynamics, South Africa, Spring 2007.

[10] Carta, F.O. *A Comparison of the Pitching and Plunging Response of an Oscillating Airfoil*, NASA CR-3172, 1979.

[11] Lishman J.Gorden, *Principles of Helicopter Aerodynamics*, Cambridge University Press, 2000.

[12] McCroskey, W. J., *Unsteady Airfoils*, Annual Report of Fluid Mechanics, Vol. 14, pp. 285–311, 1982.

This page intentionally left blank

Semi-empirical formulas of drag/lift coefficients for high speed rigid body manoeuvring in water column

P. C. Chu[1], C. Fan[1] & P. R. Gefken[2]
[1]*Naval Ocean Analysis and Prediction Laboratory, Naval Postgraduate School, Monterey, California, USA*
[2]*Polter Laboratory, SRI International, Menlo Park, California, USA*

Abstract

Falling of rigid body through water column with high speed is investigated experimentally and theoretically. Several experiments were conducted to shoot rigid bodies with the density ratio higher than 1 into the hydrographical tank. During the experiments, we carefully observe the position and orientation of the bomb-like rigid bodies. Using the experimental data a semi-empirical formulas for the drag/lift coefficients were obtained. With the given drag/lift coefficients, the momentum and moment of momentum equations of a fast-moving rigid body can be integrated numerically. The numerical results are well compared by the experimental data.

Keywords: body-flow interaction, bomb manoeuvring, body trajectory and orientation, drag/lift coefficients, inverse modeling, bomb drop experiments.

1 Introduction

Study on falling rigid body through water column with high water entry speed has wide scientific significance and technical application. Scientific studies involve nonlinear dynamics, body and multi-phase fluid interaction, supercavitation, bubble dynamics, and instability theory. Technical application of the hydrodynamics of a rigid body moving fast in fluids includes aeronautics, navigation, and civil engineering.

The rigid-body dynamics allows one to set up six nonlinear equations for the most general motion (Chu et al., 2004, 2005a, b): three momentum equations and

WIT Transactions on Engineering Sciences, Vol 59, © 2008 WIT Press
www.witpress.com, ISSN 1743-3533 (on-line)
doi:10.2495/AFM080161

three moment-of-momentum equations. These equations are ready to solve if hydrodynamic coefficients (such as drag and lift coefficients) are given for computing hydrodynamic forces and torques. Unfortunately, these coefficients (usually Reynolds number dependent) are known only for bodies with some simple geometry such as cylindrical and spherical, not for bodies with more complicated geometry such as the Mk-84 general purpose bombs. Therefore, the key issue for solving the basic equations is to determine the hydrodynamic coefficients.

In this study, an inverse model is developed for determining the drag/lift coefficients from the rigid-body's trajectory and orientation. Then a bomb strike experiment is conducted to collect the data for the trajectory and orientation. Using the experimental data, semi-empirical formulas are derived for the drag/lift coefficients.

2 Hydrodynamic force and torque

Consider an axially symmetric rigid-body with length L such as bomb falling through water column with the centers of mass (c_m) and volume (c_v) on the main axis (Fig. 1a). The position of the body is represented by the position of c_m,

$$\mathbf{r}(t) = x\mathbf{i} + y\mathbf{j} + z\mathbf{k}, \tag{1a}$$

which is called the translation. The positions of the two end-points (such as head and tail points) are represented by $\mathbf{r}_h(t)$ and $\mathbf{r}_t(t)$. The difference between the two vectors in nondimensional form

$$\mathbf{e} = \frac{\mathbf{r}_h - \mathbf{r}_t}{\left|\mathbf{r}_h - \mathbf{r}_t\right|}, \tag{1b}$$

is the unit vector representing the body's main axis direction. The translation velocity is given by

$$\frac{d\mathbf{r}}{dt} = \mathbf{u}, \qquad \mathbf{u} = V\mathbf{e}_v. \tag{2a}$$

where V and $\mathbf{e}_v$ are the speed and unit vector of the rigid-body velocity.

Let $\mathbf{v}$ be the water-to-body relative velocity (called the relative velocity). If the water velocity is much smaller than the rigid-body velocity, the water-to-body relative velocity can be approximately given by

$$\mathbf{v} \approx -\mathbf{u} = -V\mathbf{e}_v \tag{2b}$$

Usually the two vectors ($\mathbf{e}$, $\mathbf{e}_v$) are not parallel and their vector product leads to a unit attack vector

$$\mathbf{e}_\alpha = \frac{\mathbf{e}_v \times \mathbf{e}}{\sin\alpha}, \tag{3}$$

where α is the angle between ($\mathbf{e}$, $\mathbf{e}_v$). For a two dimensional motion, if (β, γ) are the elevation angles of the rigid body and its velocity, the difference $\alpha = \beta - \gamma$, is the water attack angle (Fig. 1b).

Hydrodynamic force on a rigid body consists of a drag force ($\mathbf{F}_d$)

$$\mathbf{F}_d = f_d \mathbf{e}_d, \quad \mathbf{e}_d = -\mathbf{e}_v, \tag{4}$$

and a lift force ($\mathbf{F}_l$)

$$\mathbf{F}_l = f_l \mathbf{e}_l, \quad \mathbf{e}_l = \frac{(\mathbf{e}_v \times \mathbf{e}) \times \mathbf{e}_v}{|(\mathbf{e}_v \times \mathbf{e}) \times \mathbf{e}_v|}. \tag{5}$$

Their magnitudes are determined by the drag and lift laws,

$$f_d = \frac{1}{2} C_d \rho A_w V^2, \quad f_l = \frac{1}{2} C_l \rho A_w V, \tag{6}$$

where ρ is the water density; A_w is the under-water area of projection; and (C_d, C_l) are the drag and lift coefficients. Let $\boldsymbol{\sigma}$ be the vector from the center of mass (COM) to the center of volume (COV), or $\boldsymbol{\sigma} = \sigma \mathbf{e}$. The center of the hydrodynamic force (COF) is the location where the fulcrum is chosen with zero torque. In fact, the hydrodynamic torque is calculated from the resultant drag and lift force exerted on COF with COM as the fulcrum ($\mathbf{M}_h^*$). If we shift the exerted point of the resultant drag and lift force from COF to COV, the torque ($\mathbf{M}_h^*$) contains two parts

$$\mathbf{M}_h^* = \mathbf{M}_h + \mathbf{M}_t, \quad \mathbf{M}_h = \sigma \mathbf{e} \times (\mathbf{F}_d + \mathbf{F}_l), \quad \mathbf{M}_t = M_t \mathbf{e}_\alpha, \tag{7}$$

where $\mathbf{M}_h$ is the hydrodynamic torque with the resultant drag and lift force exerted on COV, and $\mathbf{M}_t$ is the torque caused by the shift of the exerting point from COF to COV. Here, the magnitude of $\mathbf{M}_t$ is calculated by the drag law

$$M_t = \frac{1}{2} C_m \rho A_w L_w V^2, \tag{8}$$

where C_m is the moment coefficient; and L_w is the under-water path length.

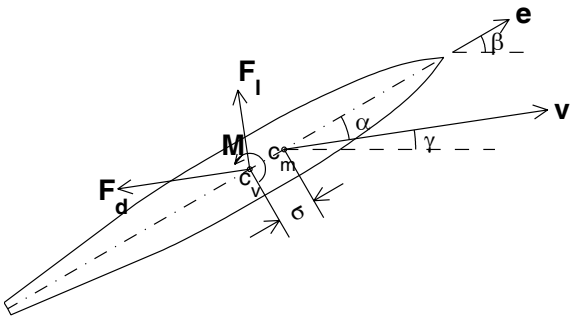

Figure 1: Shift of the exerted point of the drag/lift forces from COF to COV with an extra torque M_t. Here, (α, β, γ) are the attack angle, elevation angels of the body and its velocity.

3 Basic equations

Let (**i**, **j**, **k**) be the unit vectors of the Cartesian coordinate system fixed to the Earth with (**i**, **j**) in the horizontal plan and **k** in the vertical (positive upward). Time derivative of (2a) gives the acceleration of COM (Chu et al., 2006a, b),

$$\frac{d\mathbf{u}}{dt} = \frac{dV}{dt}\mathbf{e}_v + V\frac{d\mathbf{e}_v}{dt}. \tag{9}$$

If the translation velocity has an elevation angle γ and an azimuth angle ψ, the unit vector $\mathbf{e}_v$ is represented by

$$\mathbf{e}_v = \cos\gamma\cos\psi\mathbf{i} + \cos\gamma\sin\psi\mathbf{j} + \sin\gamma\mathbf{k}, \tag{10}$$

Substitution of (10) into (9) leads to

$$\frac{d\mathbf{e}_v}{dt} = \frac{d\gamma}{dt}\mathbf{e}_v^{\gamma} + \frac{d\psi}{dt}\mathbf{e}_v^{\psi}, \tag{11}$$

where

$$\mathbf{e}_v^{\gamma} = -\sin\gamma\cos\psi\mathbf{i} - \sin\gamma\sin\psi\mathbf{j} + \cos\gamma\mathbf{k}, \quad \mathbf{e}_v^{\psi} = -\cos\lambda\sin\psi\mathbf{i} + \cos\lambda\cos\psi\mathbf{j},$$

$$\mathbf{e}_v^{\gamma} \perp \mathbf{e}_v,\ \mathbf{e}_v^{\psi} \perp \mathbf{e}_v,\ \mathbf{e}_v^{\gamma} \perp \mathbf{e}_v^{\psi}. \tag{13}$$

The momentum equation is given by

$$m\frac{dV}{dt}\mathbf{e}_v + mV\left(\frac{d\gamma}{dt}\mathbf{e}_v^{\gamma} + \frac{d\psi}{dt}\mathbf{e}_v^{\psi}\right) = (\rho\Pi - m)g\mathbf{k} - f_d\mathbf{e}_v + f_l\mathbf{e}_l. \tag{14}$$

where (m, Π) are the mass and volume of the rigid body; (f_d, f_l) are the drag and lift forces.

Let $\mathbf{\Omega}^*$ be the body's angular velocity, which is decomposed into two parts with the one along the unit vector **e** (self-spinning or bank) and the other part $\mathbf{\Omega}$ (azimuth and elevation) perpendicular to **e**,

$$\mathbf{\Omega}^* = \Omega_s\mathbf{e} + \Omega\mathbf{e}_{\omega}, \qquad \mathbf{e}_{\omega}\bullet\mathbf{e} = 0, \tag{15}$$

where $\mathbf{e}_{\omega}$ is the unit vector of $\mathbf{\Omega}$ (perpendicular to **e**),

$$\mathbf{\Omega} = \Omega\mathbf{e}_{\omega} \qquad \Omega = |\mathbf{\Omega}|. \tag{16}$$

For axially symmetric body, **J** is a diagonal matrix

$$\mathbf{J} = \begin{bmatrix} J_1 & 0 & 0 \\ 0 & J_2 & 0 \\ 0 & 0 & J_3 \end{bmatrix}, \tag{17}$$

with J_1, J_2, and J_3 the moments of inertia. The moment of momentum equation for small self-spinning velocity is given by (Chu and Fan, 2007)

$$\mathbf{J}\cdot\frac{d\boldsymbol{\Omega}}{dt}\approx\sigma\rho\Pi g\mathbf{e}\times\mathbf{k}+\sigma\left(f_d\mathbf{e}\times\mathbf{e}_d+f_l\mathbf{e}\times\mathbf{e}_l\right)+\mathbf{M}_t+\mathbf{M}_{ae}. \tag{18}$$

where $\mathbf{M}_{az}$ is the torque due to the azimuth and elevation rotation,

$$\mathbf{M}_{ae}=\frac{1}{2}\mathbf{e}_\omega\int_{-\frac{L}{2}}^{\frac{L}{2}}C_r\rho D\left(V_r-x\Omega\right)^2xdx=-\frac{1}{12}C_r\rho DL^3V_r\Omega\mathbf{e}_\omega,\quad\text{for}\quad\frac{\Omega L}{2}\le V_r$$

$$\mathbf{M}_{ae}=\mathbf{e}_\omega\left[\int_{-\frac{L}{2}}^{\frac{V_r}{\Omega}}\frac{1}{2}C_r\rho D\left(V_r-x\Omega\right)^2xdx-\int_{\frac{V_r}{\Omega}}^{\frac{L}{2}}\frac{1}{2}C_r\rho D\left(V_r-x\Omega\right)^2xdx\right]$$

$$=-\frac{1}{2}C_r\rho DL^2\left[V_r^2\left(\frac{1}{4}-\left(\frac{V_r}{\Omega L}\right)^2\right)+\frac{4}{3}V_r\Omega L\left(\frac{V_r}{\Omega L}\right)^3+\frac{1}{2}\Omega^2L^2\left(\frac{1}{16}-\left(\frac{V_r}{\Omega L}\right)^4\right)\right]\mathbf{e}_\omega$$

$$\text{for}\quad\frac{\Omega L}{2}>V_r.$$

4 Hydrodynamic coefficients

Prediction of the rigid-body's orientation and COM location is to integrate the momentum equation (14) and moment of momentum equation (18) with known coefficients: C_d, C_l, and C_m. Inner products between equation (14) and the unit vectors ($\mathbf{e}_v$, $\mathbf{e}_v^\gamma$, $\mathbf{e}_v^\psi$) give

$$C_d=\frac{\left(\rho\Pi-m\right)g\mathbf{k}\cdot\mathbf{e}_v-m\dfrac{dV}{dt}}{\dfrac{1}{2}\rho A_w\left|V\right|V}, \tag{19}$$

$$C_l=\frac{mV\left(\mathbf{e}_v^\gamma d\gamma/dt+\mathbf{e}_v^\psi d\psi/dt\right)\bullet\mathbf{e}_l-\left(\rho\Pi-m\right)g\mathbf{k}\bullet\mathbf{e}_l}{\dfrac{1}{2}\rho A_w\left|V\right|V}. \tag{20}$$

Inner product of (18) by the vector $\mathbf{e}_r$ leads to

$$C_m=\frac{\mathbf{J}\bullet\dfrac{d\boldsymbol{\Omega}}{dt}\bullet\mathbf{e}_r-\sigma\rho\Pi g\left(\mathbf{e}\times\mathbf{k}\right)\bullet\mathbf{e}_r}{\dfrac{1}{2}\rho A_wL_wV^2}-\frac{\sigma}{L_w}\left(C_d\left(\mathbf{e}\times\mathbf{e}_d\right)\bullet\mathbf{e}_r+C_l\left(\mathbf{e}\times\mathbf{e}_l\right)\bullet\mathbf{e}_r\right), \tag{21}$$

where

$$\mathbf{e}_r=\mathbf{e}_\omega\times\mathbf{e},\quad V_r=\mathbf{V}\bullet\mathbf{e}_r. \tag{22}$$

The formulas (19)-(21) provide the basis for the experimental determination of (C_d, C_l, C_m) since each item in the right-hands of (19)-(21) can be measured by experiment.

5 Bomb drop experiment

Models of Mk-84 bombs with and without tail section are taken as examples to illustrate the methodology for determination of the bulk drag/lift coefficients, and in turn the prediction of location and orientation of a fast-moving rigid-body through the water column. The primary objective is to determine the Mk84 trajectory through the very shallow water zone to provide an estimate of the maximum bomb-to-target standoff and required fuse delay time for optimum target lethality. Because it is possible that a portion, or all, of the guidance tail section may become separated from the warhead during water entry, it is necessary to determine the Mk84 trajectory for a variety of different tail configurations ranging from a warhead with a completely intact tail section and four fins to a warhead with the tail section completely.

Using the Hopkinson scaling laws, 1/12-scale Mk84 bomb models were designed and constructed in SRI that matched the overall casing shape and mass inertial properties of the full-scale Mk84 prototype. To model the different possible damaged tail configurations, we fabricated models that consisted of the warhead section with a complete tail section and four fins, a complete tail section and two fins, a complete tail section and no fins, and with the tail section removed. The models were accelerated to velocities of up to about 454 m s^{-1} using a gas gun. The gun was positioned over a 6 m deep by 9 m diameter pool, located at SRI's Corral Hollow Experiment Site (CHES). Two orthogonal Phantom 7 high-speed video (HSV) cameras operating at 10,000 fps were used to record the water entry and underwater trajectory. The digital HSV data were used to generate depth versus horizontal trajectory, position-time history, velocity-time history, deceleration-time history, and drag coefficient-time history profiles. Typically, up to three experiments were performed for each model configuration to determine the overall reproducibility (Gefken, 2006).

A gas gun with 0.10 m (4 in.) diameter and 1.52 m (60-in.) long was positioned over a 6.10 m (20-ft) deep by 9.14 m (30-ft) diameter pool located at SRI's Corral Hollow Experiment Site (CHES). The gas gun barrel was evacuated before launching the scale model to prevent an air blast from disturbing the water surface prior to the model impacting the water surface. At the end of the gas gun there was a massive steel ring to strip the sabot from the scale model. At high velocities there is some deviation from the theoretical calibration curve, which may be attributed to gas blow by around the sabot or friction. For the maximum gun operating pressure of 2,500 psi, we were able to achieve a nominal water-entry velocity of about 304.80 m/s.

Two orthogonal periscope housings were positioned in the pool to allow simultaneous above-water and below-water visualization of the model trajectory. The housings supported Phantom 7 high-speed video (HSV) cameras, which were run at 10,000 fps. Five high-intensity, short duration (30 ms) flash bulbs were used to front-light the scale model as it entered the water and traveled under water. The HSV cameras and flash bulbs were triggered at the time the sabot was released within the gun.

A series of 19 experiments was performed with the different 1/12-scale Mk84 bomb models described in subsection 6.2 with nominal water-entry velocities ranging from 119.48 m/s to 308.83 m/s. Table 1 summarizes the overall experimental matrix and water-entry conditions. Typically, the water-impact angle of entry was between 88^o and 90^o. In Experiments 10, 11, and 12 the sabot failed to fully support the scale model within the gun during the launch phase, resulting in the scale model impacting the sabot stripper plate before impacting the water. All the experimental data have been converted to full-scale values.

Table 1: Summary of Mk84 underwater trajectory experimental matrix.

Experiment Number	Model Type	Water-Entry Velocity (m/s)	Water-Entry Impact Angle (^{o})
1	I	131.51	89.2
2	I	296.87	90.0
3	I	295.35	88.8
4	I	302.05	88.5
5	I	226.77	88.0
6	I	219.45	89.0
7	I	119.48	88.2
8	II Model	impacted sabot	stripper plate
9	II Model	impacted sabot	stripper plate
10	II	295.04	90.0
11	II	289.96	90.0
12	II Model	impacted sabot	stripper plate
13	IV	296.26	85.7
14	IV	300.53	90.0
15	IV	300.53	88.7
16	III	304.19	90.0
17	III	298.39	87.0
18	III	291.08	88.1
19	II	296.87	90.0

6 Semi-empirical formulas

Upon completion of the drop phase, the video from each camera was converted to digital format. For Mk84 warhead without tail section, vertical and horizontal locations of the two-end points (Fig. 2) versus time were recorded. From these data, the unit vector $\mathbf{e}$ can be directly determined using (1b). The translation velocity $\mathbf{u}$ and the angular velocity $\boldsymbol{\Omega}$ are measured and so as the fluid-to-body relative velocity $\mathbf{V}$ since it is assumed that the water velocity is much smaller than the bomb velocity [i.e., (2b) holds]. The unit vectors ($\mathbf{e}_v$, $\mathbf{e}_l$) are in turned determined since ($\mathbf{e}_v$, $\mathbf{e}_l$) represent the direction of $\mathbf{V}$ and its 90^o shift. When the orientation of the bomb is measured, the unit vector $\mathbf{e}$ is known and so as $\mathbf{e}_\omega$ using (22).

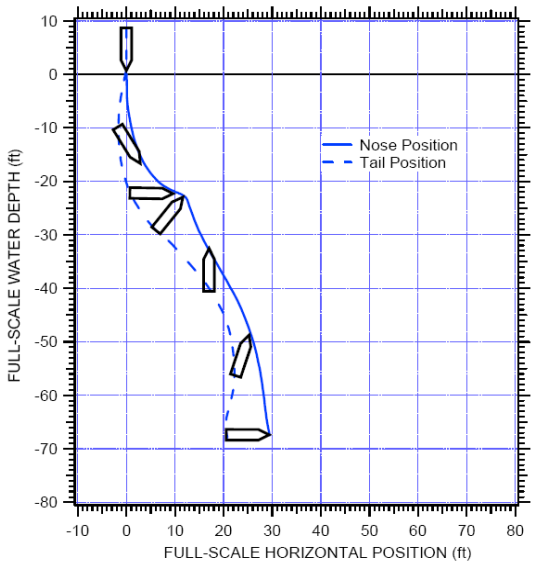

Figure 2: Trajectory of Mk84 with no tail section and water-entry velocity of 296 m/s (Exp-13) (from Gefken, 2006).

Using the unit vector $\mathbf{e}_v$, we determine the elevation angle γ and the azimuth angle ψ [see (10)] and the two other unit vectors ($\mathbf{e}_v^{\gamma}, \mathbf{e}_v^{\psi}$) [see (11)]. Using the unit vectors $\mathbf{e}$ and $\mathbf{e}_{\omega}$, we determine the unit vector $\mathbf{e}_r$ [see (22)]. With the calculated temporally varying (C_d, C_l, C_m) and (α, Re) data, we obtain the following semi-empirical formulas for calculating the hydrodynamic coefficients,

$$C_d(\mathrm{Re},\alpha) = \begin{cases} 8\sin(2\alpha)\left(\dfrac{\mathrm{Re}_{crit}}{\mathrm{Re}}\right)^2 + 0.02 & \text{if } \sin(2\alpha) \geq 0 \text{ and } \mathrm{Re} \geq \mathrm{Re}_{crit} \\ 0.34\left|\sin(2\alpha)\right|\left(\dfrac{\mathrm{Re}_{crit}}{\mathrm{Re}}\right) + 0.02 & \text{otherwise} \end{cases}, \tag{33}$$

$$C_l(\mathrm{Re},\alpha) = \begin{cases} 2.5\sin(2\alpha)\min\left[\left(\dfrac{\mathrm{Re}}{\mathrm{Re}_{crit}}\right)^{1.2}, \left(\dfrac{\mathrm{Re}_{crit}}{\mathrm{Re}}\right)^{1.2}\right] & \text{if } \sin(2\alpha) \geq 0 \\ 0.16\sin(2\alpha) & \text{if } \sin(2\alpha) < 0 \end{cases},$$

$$\mathrm{Re}_{crit} = 1.5 \times 10^7, \tag{34}$$

$$C_m = A\sin\theta - B\frac{d\alpha}{dt}, \quad A = \begin{cases} 0.06 & if\ \theta \le 180 \\ 0.006 & if\ \theta > 180 \end{cases}, \quad B = 0.00065. \tag{35}$$

7 Verification

The semi-empirical formulas of (C_d, C_l, C_m) were verified using the data collected from the experiments. We use the formulas (33)-(35) to compute the hydrodynamic coefficients (C_d, C_l, C_m), and then to predict the location and orientation of Mk-84 bomb in the water column by (14) and (18). Comparison between model predictions and experiments (Fig. 3) shows the validity of feasibility of the semi-empirical formulas (33)-(35).

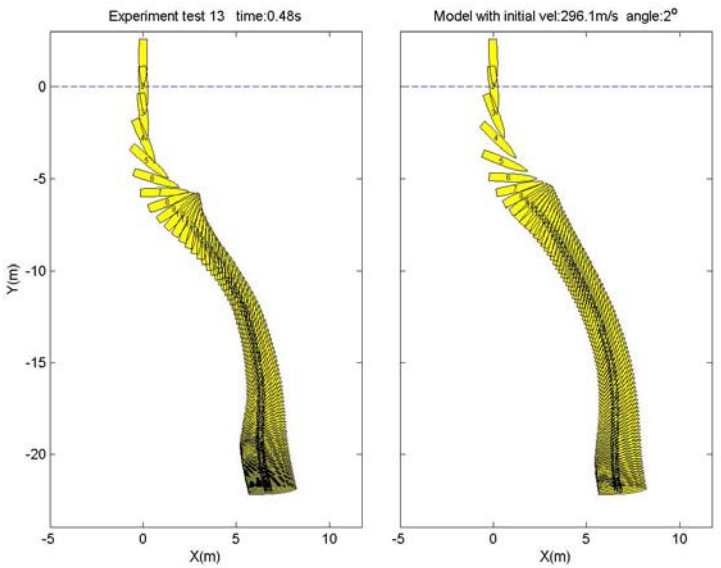

Figure 3: Comparison between modelled and observed bomb trajectories for the experiment shown in Fig. 2.

8 Conclusions

A new method has been developed to determine the hydrodynamic coefficients (C_d, C_l, C_m) of fast-moving rigid body in the water column. This method contains two parts: (1) establishment of the inverse relationship between (C_d, C_l, C_m) and the rigid-body's trajectory and orientation, and (2) experiments for collecting data of the rigid-body's trajectory and orientation. Using the experimental data, the inverse relationship leads to semi-empirical formulas of (C_d, C_l, C_m) versus Reynolds number and attack angle. This method is much cheaper than the

traditional one using the wind tunnel to determine (C_d, C_l, C_m). We also verify these formulas using the experimental data.

Acknowledgement

The Office of Naval Research Breaching Technology Program and Naval Oceanographic Office supported this study.

References

[1] Chu, P.C., C.W. Fan, A. D. Evans, and A. Gilles, 2004: Triple coordinate transforms for prediction of falling cylinder through the water column. Journal of Applied Mechanics, 71, 292–298.
[2] Chu, P.C., A. Gilles, and C.W. Fan, 2005a: Experiment of falling cylinder through the water column. Experimental and Thermal Fluid Sciences, 29, 555–568.
[3] Chu, P.C., and C.W. Fan, 2005b: Pseudo-cylinder parameterization for mine impact burial prediction. Journal of Fluids Engineering, 127, 1515–152.
[4] Chu, P.C., and C.W. Fan, 2006a: Prediction of falling cylinder through air-water-sediment columns. Journal of Applied Fluid Mechanics, 73, 300–314.
[5] Chu, P.C., and G. Ray, 2006b: Prediction of high speed rigid body maneuvering in air-water-sediment columns, Advances in Fluid Mechanics, 6, 123–132.
[6] Chu, P.C., and C.W. Fan, 2007: Mine impact burial model (IMPACT35) verification and improvement using sediment bearing factor method. IEEE Journal of Oceanic Engineering, 32 (1), 34–48.
[7] Gefken, P., 2006: Evaluation of precision-guided bomb trajectory through water using scaled-model experiments. SRI Final Technical Report-PYU-16600, Menlo Park, California, USA, 1–80.

Flow separation patterns in a 60-degree junction

K. Alhussan
Space Research Institute, King Abdulaziz City for Science and Technology, Saudi Arabia

Abstract

The work to be presented herein is a theoretical and numerical analysis of the complex fluid mechanism that occurs inside a 60^o-junction shape specifically with regard to the boundary layer separation, vortex shedding and generation of wake. The boundary layer separates from the surface, forms a free shear layer and is highly unstable. This shear layer will eventually roll into a discrete vortex and detach from the surface. A periodic flow motion will develop in the wake as a result of boundary layer vortices being shed from the solid boundary. The periodic nature of the vortex shedding phenomenon can sometimes lead to unwanted structural vibrations, especially when the shedding frequency matches one of the resonant frequencies of the structure.

A number of important conclusions follow from the current research. First, the study of the actual flow configuration inside 60^o-junction shape offers some insight into the complex flow phenomena. Second, the characteristics of the boundary layer separation, the vortex and wake change considerably with the divergent angle. This research shows that downstream, away from the junction, the boundary layer reattaches and normal flow occurs, i.e. the effect of the boundary layer separation is only local. Nevertheless fluid downstream of the junction will have lost energy. The results show that downstream, away from the junction, the boundary layer reattaches and normal flow occurs, i.e. the effect of the boundary layer separation is only local. Nevertheless fluid downstream of the junction will have lost energy. This research shows that when the velocity ratio is equal to unity the circulation and the vortex shedding phenomenon are maximized.

Keywords: flow separation, vortex flow, internal flow, boundary layer, numerical analysis, CFD.

WIT Transactions on Engineering Sciences, Vol 59, © 2008 WIT Press
www.witpress.com, ISSN 1743-3533 (on-line)
doi:10.2495/AFM080171

1 Introduction

Flow separation from the surface of a solid boundaries, and the determination of global changes in the flow field that develop as a result of the flow separation, are the most difficult and fundamental problems of fluid dynamics. Gases and water have extremely small viscosity and, therefore, most practical flows are characterized by very large values of the Reynolds number; both theory and experiment show that increasing Reynolds number almost invariably results in flow separation [1–3].

The difference between a separated flow and its theoretical unseparated flow concerns not only the form of trajectories of fluid particles, but also the value of aerodynamic forces acting on the body. For example, for blunt bodies in an incompressible flow, it is known from experimental studies that the drag force is not equal to zero. It does not approach zero as the Reynolds number becomes large. One of the most famous results of the inviscid flow theory is d'Alembert's paradox which says that solid bodies experience zero drag in incompressible flow. It is well known that this contradiction is associated with the assumption of a fully attached form of the flow; this case never happens in reality.

Separation imposes a considerable limitation and lead to a significant degradation of total performance. For example, separation is usually accompanied by a loss of the lift force and sharp increase of the drag at the reattachment region. The first attempts to describe flow separation past blunt bodies are due to Helmholtz (1868) and Kirchhoff (1869) in the analysis of the classical theory of inviscid fluid flows, but there was no adequate explanation as to why separation occurs. Prandtl (1904) was the first to recognize the physical cause of separation at high Reynolds numbers as being associated with the separation of boundary layers that must form on all solid surfaces [1–5].

In accordance with the Prandtl's theory, a high Reynolds number flow past a rigid body has to be subdivided into two characteristic regions. The main part of the flow field may be treated as inviscid. However, for all Reynolds numbers, no matter how large, there always exists a thin region near the wall where the flow is predominantly viscous. Prandtl termed this region the boundary layer, and suggested that it is because of the specific behaviour of this layer that flow separation takes place. Flow development in the boundary layer depends on the pressure distribution along the wall. If the pressure gradient is favourable then the boundary layer remains well attached to the wall. However with adverse pressure gradient the boundary layer tends to separate from the body surface. The reason for separation was explained by Prandtl in the following way. Since the velocity in the boundary layer drops towards the wall, the kinetic energy of fluid particles inside the boundary layer appears to be less than that at the outer edge of the boundary layer, in fact the closer a fluid particle is to the wall the smaller its kinetic energy. This means that while the pressure rise in the outer flow may be quite significant, the fluid particles inside the boundary layer may not be able to get over it. Even a small increase of pressure may cause the fluid particles near the wall to stop and then turn back to form a recirculating flow region, which is the characteristic of separated flows [2–6].

The work to be presented herein is a Computational Fluid Dynamics investigation of the complex fluid mechanisms that occur inside 60°-junction shape, specifically with regard to the boundary layer separation. This research shows a numerical simulation of mapping the flow inside a 60°-junction shape flow. The results show that downstream, away from the junction, the boundary layer reattaches and normal flow occurs i.e. the effect of the boundary layer separation is only local. This research shows that when the velocity ratio is equal to unity the circulation and the vortex shedding phenomenon are maximized.

A CFD analysis enables one to understand the complex flow structure inside this confined region. Through this computational analysis, a better interpretation and understanding of the physical phenomenon of the boundary layer separation that occurs in an internal flow; the 60°-junction shape, can be achieved. Figure 1 shows schematic view of a 60°-junction with two dimensional unstructured mesh.

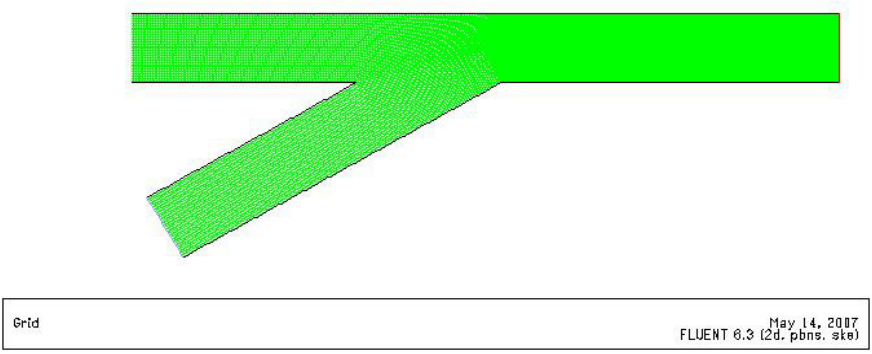

Figure 1: Schematic view of a 60°-junction showing a 2-D unstructured mesh.

2 Theoretical and numerical analysis

The governing equations are a set of coupled nonlinear, partial differential equations. In order to formulate or approximate a valid solution for these equations they must be solved using computational fluid dynamics techniques. To solve the equations numerically they must be discretized. That is, the continuous control volume equations must be applied to each discrete control volume that is formed by the computational grid. The integral equations are replaced with a set of linear algebraic equations solved at a discrete set of points.

Fluent is used in this current research to model the flow characteristics inside the two dimensional region. It should be possible to model the flow separation for internal flow inside a 60°-junction shape using the CFD analysis [7–14]. A numerical analysis must start with breaking the computational domain into discrete sub-domains, which is the grid generation process. A grid must be

provided in terms of the spatial coordinates of grid nodes distributed throughout the computational domain. At each node in the domain, the numerical analysis will determine values for all dependent variables such as pressure and velocity components. Creating the grid is the first step in calculating a flow. Two-dimensional Navier Stokes equations are solved using fully implicit scheme with K-epsilon turbulence model. The grid is refined near the solid boundary walls in order to model the large gradient.

3 Results and discussion

The work to be presented herein is a theoretical and numerical analysis of the complex fluid mechanism that occurs inside a 60°-junction shape specifically with regard to the boundary layer separation, vortex shedding and generation of wake.

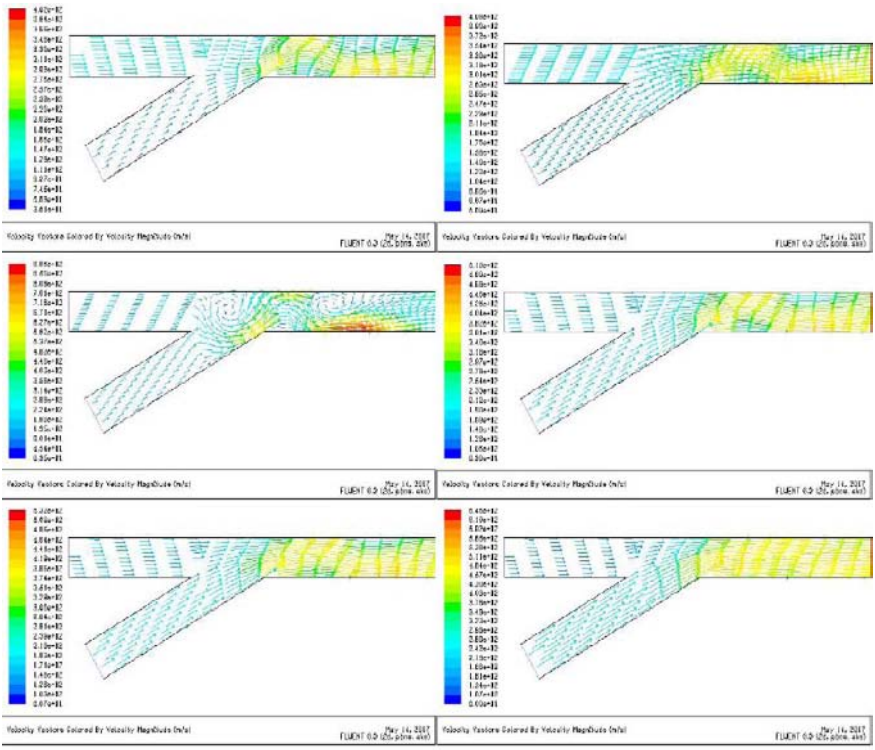

Figure 2: Velocity vectors for flow inside 60°-junction from top left to bottom right the velocity ratio is 0.5, 0.67, 1, 1.16, 1.3, and 2.

Figure 2 shows velocity vectors for internal flow of a 60°-junction shape. From top left to bottom right the velocity ratio is 0.5, 0.67, 1, 1.16, 1.3, and 2, respectively. The velocity ratio is defined as the velocity of the branched inlet to

the velocity of the main (straight) inlet. One can see in this figure that the circulation, wake generation and the vortex shedding phenomenon are evident when the velocity ratio is equal to 1. This figure shows that downstream, away from the junction, the boundary layer reattaches and normal flow occurs i.e. the effect of the boundary layer separation is only local. Nevertheless fluid downstream of the junction will have lost energy. The boundary layer separates from the surface forms a free shear layer and is highly unstable. This shear layer will eventually roll into a discrete vortex and separate from the surface. A periodic flow motion will develop in the wake as a result of boundary layer vortices being shed from the solid boundary. The periodic nature of the vortex shedding phenomenon can sometimes lead to unwanted structural vibrations, especially when the shedding frequency matches one of the resonant frequencies of the structure.

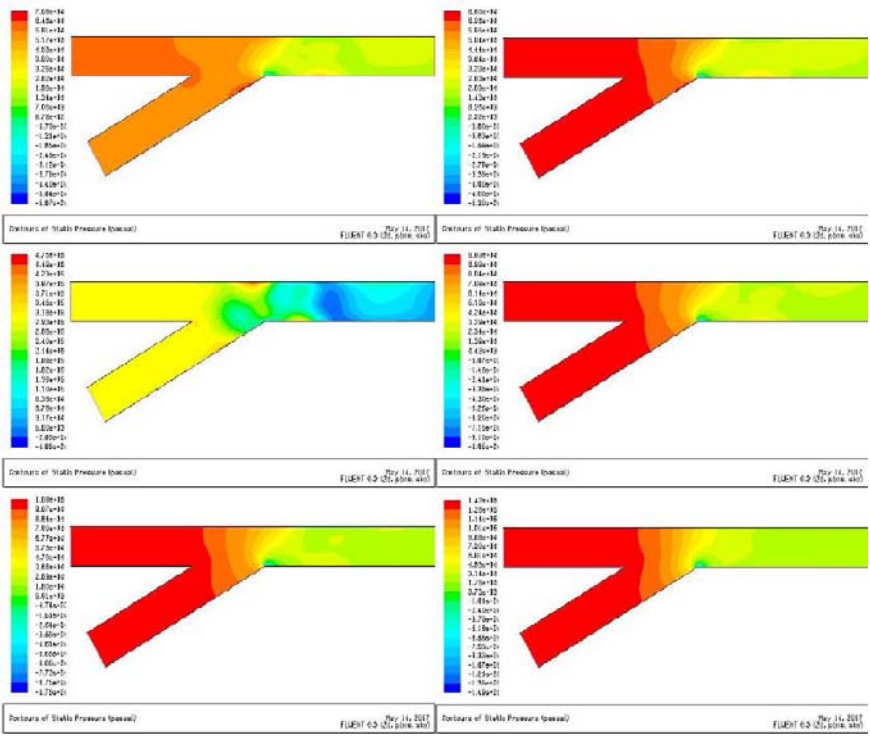

Figure 3: Contour plots of static pressure for flow inside 60°-junction from top left to bottom right the velocity ratio is 0.5, 0.67, 1, 1.16, 1.3, and 2.

Figure 3 shows contour plots of static pressure for internal flow of a 60°-junction shape. From top left to bottom right the velocity ratio is 0.5, 0.67, 1, 1.16, 1.3, and 2, respectively. One can see in this figure that the circulation is evident when the velocity ratio is equal to 1. The results show that downstream,

away from the junction, the boundary layer reattaches and normal flow occurs i.e. the effect of the boundary layer separation is only local. Nevertheless fluid downstream of the junction will have lost energy.

4 Concluding remarks

The work to be presented herein is a Computational Fluid Dynamics investigation of the complex fluid mechanisms that occur inside 60^o-junction shape, specifically with regard to the boundary layer separation, vortex shedding and generation of wake.

A number of important conclusions follow from the current research. First, study of the actual flow configuration inside the 60^o-junction shape offers some insight into the complex flow phenomena. Second, downstream, away from the junction, the boundary layer reattaches and normal flow occurs i.e. the effect of the boundary layer separation is only local. This research showed that when the velocity ratio is equal to unity the circulation and the vortex shedding phenomenon are maximized.

Acknowledgement

The author gratefully acknowledges sponsorship of this research from the Space Research Institute of the King Abdulaziz City for Science and Technology.

References

[1] Nesteruk I., "Can Shapes with Negative Pressure Gradients Prevent Cavitation", Proceedings of FEDSM'03,4Th ASME_JSME Joint Fluids Engineering Conference, Honolulu, USA, July 6-11, 2003, No. FEDSM2003-45323.

[2] Nesteruk I., "Experimental Investigation of Axisymmetric Bodies with Negative Pressure Gradients", Aeronautical Journ., v. 104: 439-443, 2000.

[3] Takahashi S., Washio S., Uemura K. and Okazaki A., "Experimental study on cavitation starting at and flow characteristics close to the point of separation", Fifth International Symposium on Cavitation (Cav2003), Osaka, Japan, No. Cav03-OS-3-003, pp. 1–8, 2003.

[4] Sahu, J. & Nietubicz, C."Navier-Stockes Computations of Projectile Base Flow with and without Mass Injection: AIAA Journal, Vol. 23, No. 9, pp.1348–1355, 1985.

[5] Bourdon, C. & Dutton, J. " Visualization of a Central Bleed Jet in an Axisymmetric Compressible Flow" Physics of Fluids, Vol. 15, No. 2 pp.499–510, 2003.

[6] Perkins, S. C.& Dillenius, M. " Supersonic Submunitions Aerodynamics during Dispense" Journal of Spacecraft and Rockets, Vol. 28, No.3 pp.276–283, 1991

[7] Lee, Y., Kim, H. & Raghunathan, S. “A Study of Base Drag Optimization using Mass Bleed” 15th Australian Fluid Mechanics Conference, Sydney, Australia, 2004.
[8] Lee, Y., Chang, S.Lee, J. & Kim, H.: A Study of the Aerodynamic Drag of a Blunt Body with an Air Bag” the 6th KSME-JSME Thermal and Fluids Engineering Conference, Jeju City, Korea, 2005.
[9] Alhussan, K., " Computational Analysis of High Speed Flow over a Double-Wedge for Air as Working Fluid", Proceedings of FEDSM2005 ASME Fluids Engineering Division Summer Meeting and Exhibition FEDSM2005-77441 June 19–23, 2005, Houston, TX, USA.
[10] Alhussan, K.," Study the Structure of Three Dimensional Oblique Shock Waves over conical rotor-Vane surfaces", Proceedings of FEDSM2005 ASME Fluids Engineering Division Summer Meeting and Exhibition FEDSM2005-77440 June 19–23, 2005, Houston, TX, USA.
[11] Alhussan, K. ," Oblique Shock Waves Interaction in a Non-Steady Three Dimensional Rotating Flow", Proceedings of FEDSM2005 ASME Fluids Engineering Division Summer Meeting and Exhibition FEDSM2005-77442 June 19–23, 2005, Houston, TX, USA.
[12] Alhussan, K. “Application of Computational Fluid Dynamics in Discontinuous Unsteady Flow with Large Amplitude Changes; The shock Tube Problem” IASME Transaction Issue 1 Volume 2, pp 98–104, January 2005.
[13] Alhussan, K. “Supersonic Flow over Blunt Body with a Decelerator” IASME Transaction ssue 3 Volume 1, pp 8–104, August 2005.
[14] Alhussan, K. “ The effect of the boundary layer separation in Y-junction shape” proceeding of the 5th joint ASME/JSME FEDSM2007, Fluid Engineering conference, paper number FEDSM2007-37461, San Diego, CA, USA, July 30–August 2, 2007.

This page intentionally left blank

A numerical and experimental study of a thin, high cambered airfoil at a low Reynolds number

A. Auletta[1], F. De Gregorio[1], D. Guida[1], M. Lupo[2] & M. Marrazzo[1]
[1]*Italian Aerospace Research Centre (CIRA), Italy*
[2]*University of Rome "La Sapienza", Italy*

Abstract

In the framework of the development of new aerodynamic design concepts, a joint numerical/experimental analysis has been performed on a 2D thin, high cambered airfoil at a low Reynolds number. The experimental investigation has been performed by means of the Pressure Sensitive Paint Technique (PSP) and Particle Image Velocimetry (PIV). These techniques have been selected for their characteristics of low-intrusivity and high spatial resolution. Details about the experimental set-up and results shall be reported. The experimental investigation has been intended to obtain detailed information about the pressure field and to detect flow characteristics on a non-conventional airfoil. Experimental data have been compared with numerical results obtained by FLUENT commercial code.

Results will be presented in terms of experimental and numerical velocity fields around the model and in terms of lift characteristics.

Keywords: PIV, PSP, endurance, non-planar wing, aerodynamic loads.

1 Introduction

In the framework of the Unmanned Aerial Vehicle (UAV) Project, which is aimed at designing a High Altitude Long Endurance (HALE) unmanned vehicle, some configurations have been tested. In more detail, a prerogative of HALE vehicles has the possibility of operating at high altitudes ranging between 20000–30000 metres, with an endurance of at least 48 hours. One of the considered configurations has been characterized by an inflatable leading edge so that an airfoil characterized by high curvature and small thickness has been produced, similar to a modern directional parachute (Figure 1). A wide

WIT Transactions on Engineering Sciences, Vol 59, © 2008 WIT Press
www.witpress.com, ISSN 1743-3533 (on-line)
doi:10.2495/AFM080181

numerical and experimental test campaign has been performed in order to analyse the aerodynamic behaviour of this configuration and to confirm the preliminary analysis carried out during the design phase.

2 Experimental set-up

2.1 Wind tunnel

Tests have been carried out in the Calibration Tunnel 1 (CT-1). CT-1 is an Eiffel type open circuit wind tunnel, with the following main characteristics:

- velocity range: 5-55 m/s
- nozzle contraction rate: 16:1
- maximum value of turbulence level at 50 m/s flow speed: <0.1%
- test section size (L×W×H): 600 × 305 × 305 mm^3.

The test section allows in the region of 100% optical access. It is equipped with a motorized turntable equipped with an angular decoder providing the geometric incidence angle of the model to the data acquisition system.

2.2 Test article

The investigated profile is thin like a modern directional parachute. It was designed in the framework of the project Non-Planar Wing (NPW) by CIRA researchers G. Andreutti and D. Quagliarella. A sketch of the geometry is shown in Figure 1. The main dimensions of the test model are as follows:

- span: 302 mm
- chord: 100 mm
- maximum thickness: 6.26 mm.

The test article is equipped with fifteen pressure taps, nine located on the upper surface and six located on the lower surface. The location of the pressure taps has been concentrated on the leading edge of the model in order to integrate the data coming from the PSP affected for some incidence angles by a lack of information.

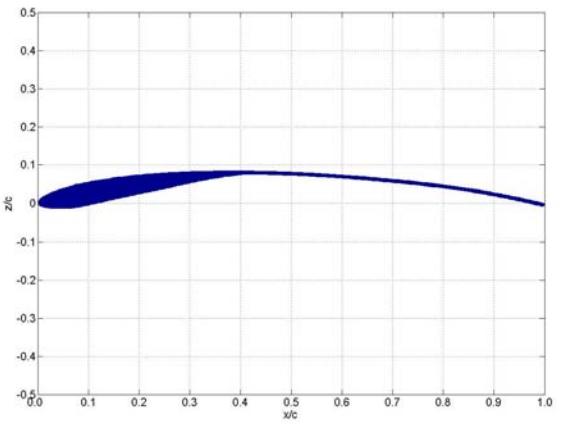

Figure 1: Investigated airfoil.

2.3 PIV system

The laser system is composed of two Nd-Yag resonator heads providing a laser beam of about 300 mJ each at 532 nm. The light sheet is delivered in the measurement area by means of two mechanical systems composed of a mechanical arm equipped with seven mirrors and which provides six freedom degrees. Measurements have been performed on the symmetry vertical plane of the test section in order to minimize possible wall effects and assure the bi-dimensionality of the phenomena.

A large seeding generator, equipped with twenty Laskin nozzles, has been used. A cyclone has been mounted in order to filter large droplets and avoid environmental contamination. DEHS oil has been adopted as the seeding material. In order to obtain a uniform concentration of particles the full wind tunnel room has been seeded.

Two CCD cameras equipped with 28 mm Zeiss lenses and mounted on a 2D linear traversing system have been used for measuring the flow field around the model and in the wake regions.

2.4 PSP system

The paint employed was the single component UniFIB, manufactured by ISSI. Paint luminescence was induced by three blue LED lamps (with a spike at 405 nm) equipped with a 10 deg. angle diffuser and supported by a X95 frame. Long-term stability is about 1.0% after 5 minutes, and 0.1% after 20 minutes of operation.

A Princeton Instruments 16–bit CCD back illuminated camera (model Pixis 1024B) equipped with a 50 mm, f1.8D Nikkor lens has been used for the images' acquisition. The camera is characterized by a 1024×1024 pixel resolution, a quantum efficiency of about 95% in the visible range and a full well capacity of 240ke$^-$. The camera position has been chosen in order to look at the entire model under the entire test campaign conditions.

3 Numerical flow solver algorithms

Numerical simulations have been carried out by means of Drela's MSES code and FLUENT commercial code.

MSES [3] is based on a finite-volume discretization of the Euler equations on a streamlined grid. Also in this case a compressible formulation has been used. The MSES code computes the viscous region by using an integral boundary layer formulation based on a multi-layer velocity profile representation. The inviscid and viscous regions are coupled by using the displacement thickness theory.

FLUENT™ solves the Navier-Stokes equations on hybrid grids by means of the Finite Volume method. A second order upwind scheme has been adopted for the spatial discretization whereas an incompressible formulation was chosen as the governing mathematical model. For such a flow model the continuity is

enforced by means of a Poisson equation for the pressure. The pressure-velocity coupling was ensured by means of the SIMPLEC algorithm and by using the pressure-staggering approach "PRESTO!". In some cases convergence problems occurred, therefore a collocated second order pressure interpolation scheme has been used instead. Moreover, due to the isothermal flow assumption, the energy equation was disregarded. In all cases the so called segregated implicit solution procedure was used, where each single flow equation is solved sequentially. Furthermore, the following boundary conditions types have been used in the computations.

The so called "velocity inlet" boundary condition was used to prescribe the velocity profile at the left boundary of the computational domain.

The classical no-slip boundary condition has been adopted on the lower side of the computational domain.

The "outflow" boundary condition has been adopted on both the upper and right sides of the computational domain. In such a case the normal derivative of all the flow variables is set to zero, except for pressure.

Finally, a RANS approach has been used in order to include turbulence effects on the flow solution. Further information can be found in [4].

4 Procedure for data reduction

With regards to the numerical analysis, an initial investigation by means of MSES has been carried out in order to get a preliminary estimation of the aerodynamic characteristics on the project conditions (low Reynolds number) and to have information about the transition location. This latter can have a great influence on the aerodynamic characteristics because of the airfoil's large curvature and low thickness. This information has been used as a starting point for the CFD analysis on the flow field carried out through FLUENT commercial code.

With regard to the experimental analysis, velocity profiles have been evaluated using two PIV cameras aligned vertically (one for the upper part of the test section, one for the lower part), scanning the entire flow region around and behind the model at different instants. The mean fields obtained for each region, partially overlapped with others, have been merged together to allow the necessary integration process for the aerodynamic coefficients evaluation.

The lift coefficient has been calculated applying the Kutta-Joukowski theorem on a circulation line surrounding the airfoil in the measurement plane. The drag coefficient, on the other side, has been evaluated using the momentum balance equation. All the results have been corrected taking into account the wall effects and compared with the numerical ones for different angles of attack.

The integration of pressure distributions obtained by PSP provided another criterion for an experimental measurement of the lift coefficient, as well as for the moment coefficient. The application of the PSP technique has been forced by the reduced dimensions of the test article that would not allow the insertion of a reasonable number of pressure taps, especially in the aft part of the model.

5 Results and discussion

In the scenario of experimental measurement technique for aerodynamics, PIV provides a unique tool in terms of data accuracy, test productivity and, at the same time, an understanding of the phenomena. PIV data give a clear general view of the flow field behaviour. Velocity field colormaps, around the model and in the wake region, for $\alpha = -4°$, 0° and +4° are reported in Figures 2–4 Plots give an insight into the aerodynamic behaviour at different angles of attack, showing a flow separation on the lower surface for the negative angle confirmed by the large wake left behind. Partial separation occurs at $\alpha = 0°$. For the positive angle of attack shown, the flow remains attached on the lower side of the model. The PIV analysis has shown that on the upper surface a trailing edge flow separation starts from about 11°. The flow field at 15° AoA is reported in Figure 5.

Figure 5 shows the velocity profile along the height of the test section (Z direction) two chords downstream from the model trailing edge for the highest investigated angles of attack ($\alpha = 11°$-15°). It can be seen that the wake at 11° and 12° shows quite the same extent whereas the momentum loss increases slightly starting from 14°. This is also highlighted by a soft stall starting from 12° AoA as presented in Figure 8.

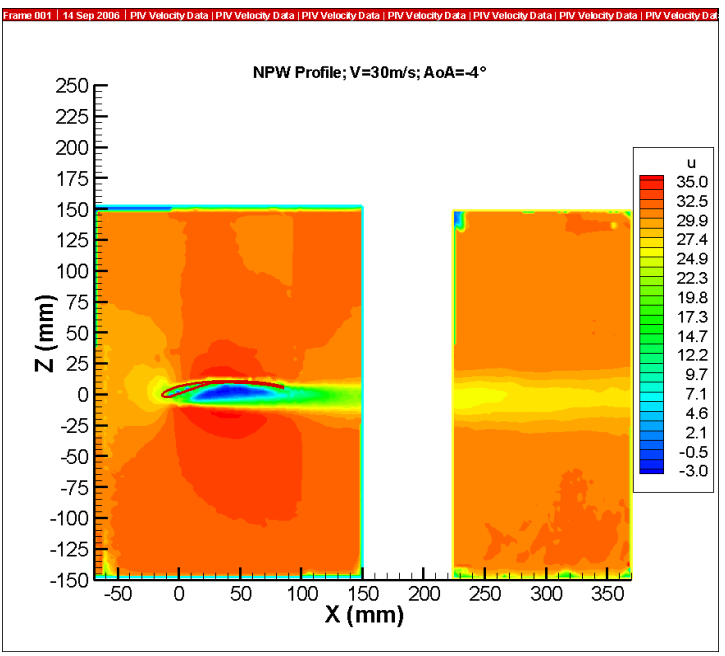

Figure 2: PIV flow field at –4° AoA.

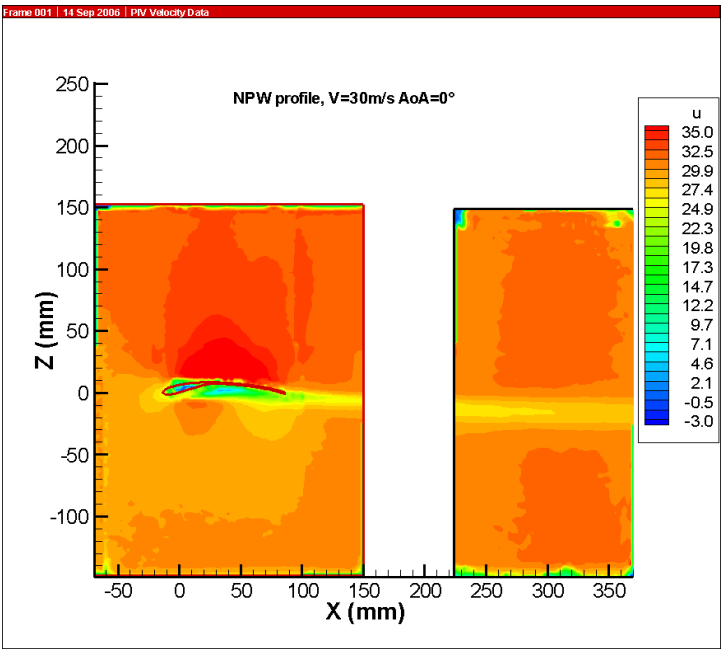

Figure 3: PIV flow field at 0° AoA.

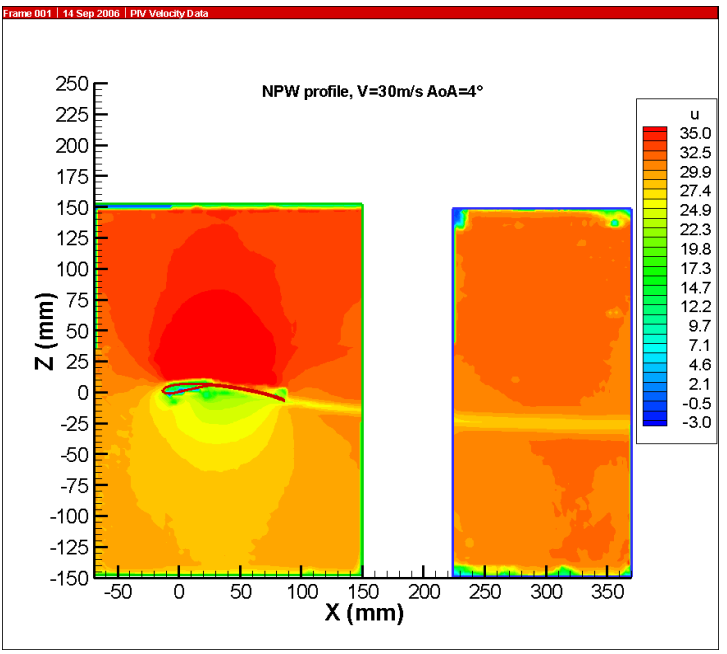

Figure 4: PIV flow field at 4° AoA.

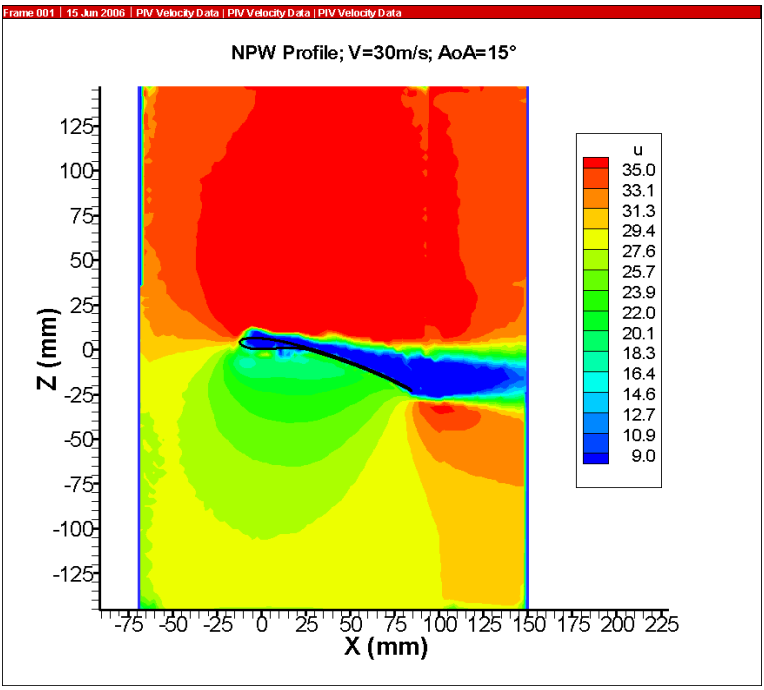

Figure 5: PIV flow field at 15° AoA.

Numerical simulations have highlighted that laminar-turbulent transition plays an important role on the flow field. In Figure 7, the flow field obtained considering a fully turbulent flow is compared with the free transition flow field at 0° AoA. It can be seen that flow characteristics are dramatically affected by transition position. The field predicted by a transition free criterion is confirmed by the experimental flow field shown in Figure 3, where a wide region of separated flow is evident in the lower part of the airfoil. The impact of the numerical algorithm chosen (fully turbulent or transition free) is also evident looking at the numerical/experimental comparison as reported in Figure 8 in terms of lift coefficient distribution. PIV and PSP integrated data are compared with results of RANS calculations for both fully turbulent and transition free conditions. It is noticeable that the experimental lift curves are close to each other whereas a sensible divergence is shown by the CFD fully turbulent curve. On the contrary, transition free simulations seem to provide lift values coherent with the experimental measurements. This suggests that the laminar-to-turbulent transition sensibly affects the flow field so that, the hypothesis of a fully turbulent flow on the entire model surface, eliminating the possibility of large separated regions, implies a wrong evaluation of normal strains and, in turn, of the lift coefficient.

A comparison of numerical and experimental results in terms of pressure coefficients is reported in Figure 9 for different angles of attack. Excluding the very critical case at $\alpha = 0°$, a good agreement is noticeable, although it can be

seen that experimental (PSP) pressure profiles are not closed on the model trailing edge. This is probably due to an inaccurate measurement in the last 5–10% of chord on the lower surface (a possible reason can be paint degradation or imperfection in the paint application due to the high curvature). In fact, pressure distribution on the lower surface, very close to the trailing edge, seems to show a smaller pressure recovery than the expected one, especially at low angles of attack.

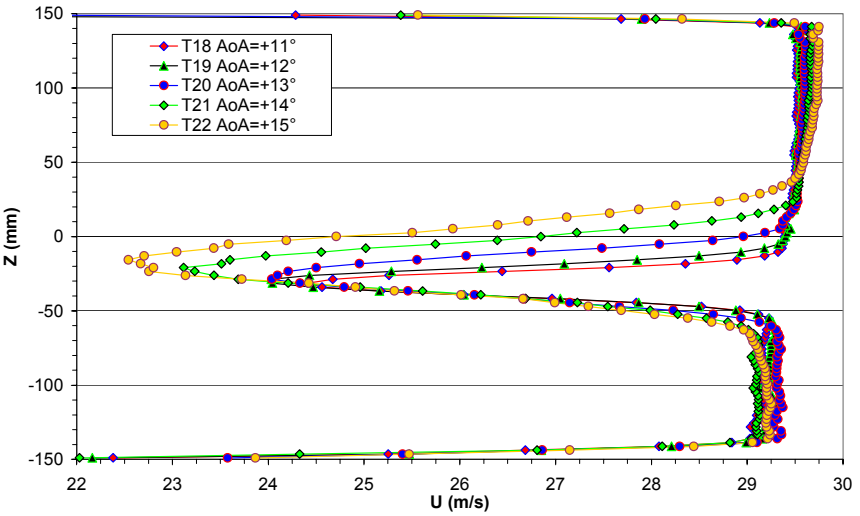

Figure 6: Wake velocity profiles (AoA between 11° and 15°).

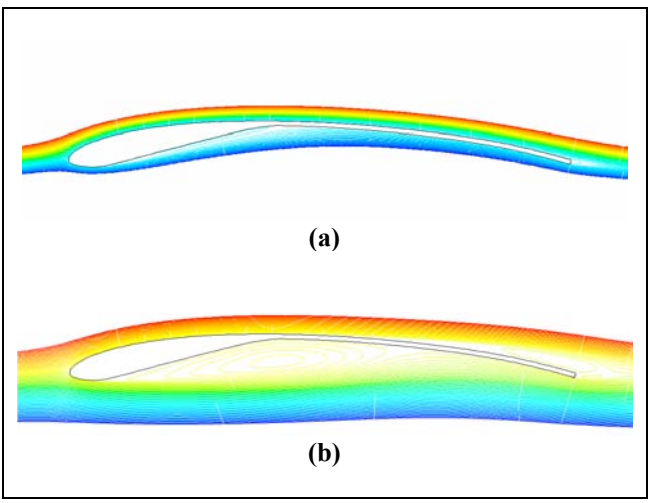

Figure 7: Numerical streamlines at 0° AoA (a: fully turbulent, b: transition free).

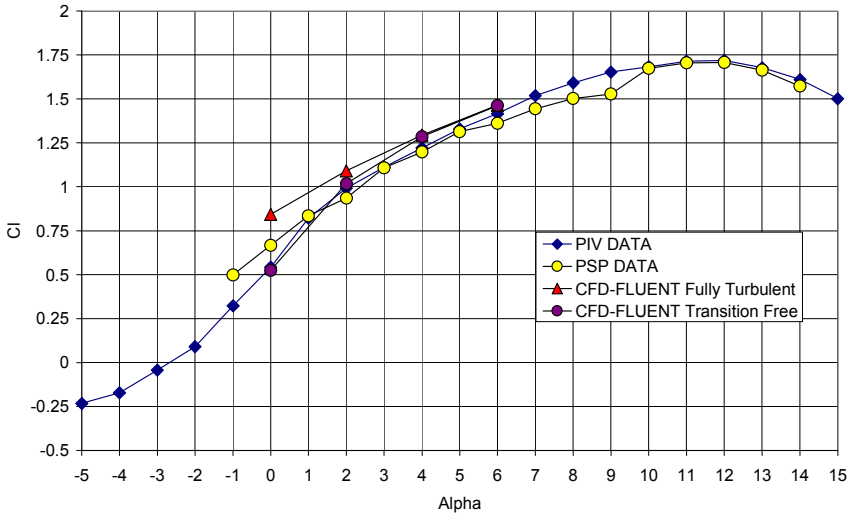

Figure 8: Comparison between numerical and experimental lift coefficient.

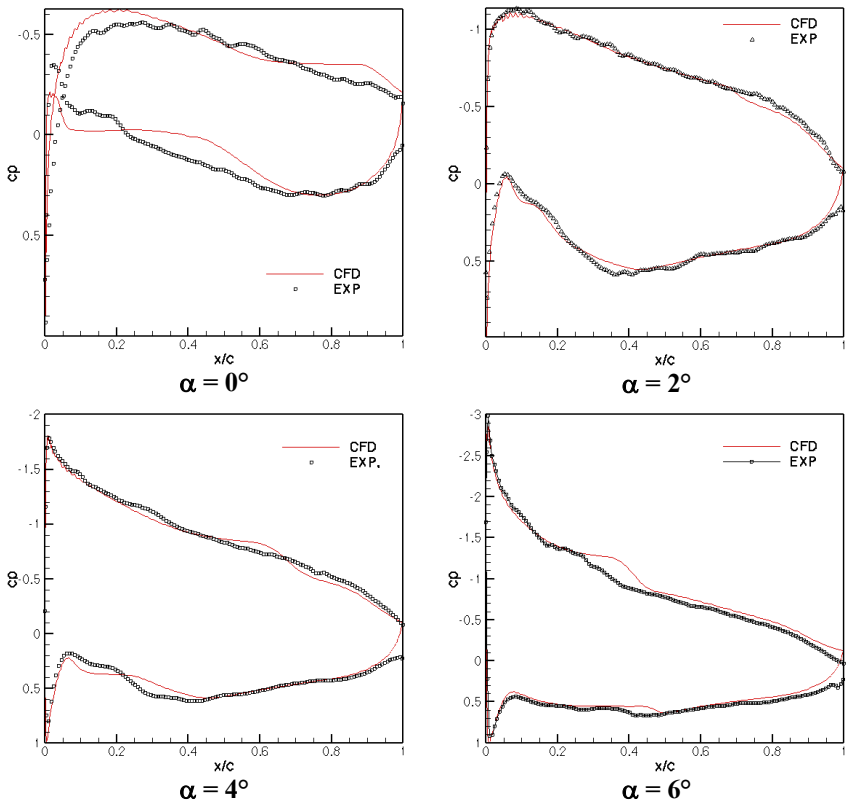

Figure 9: Comparison between CFD and PSP Cp distributions.

6 Conclusions

In the framework of the Non-Planar Wing Project, an accurate numerical and experimental analysis has been performed aiming to analyze the aerodynamic performance of a new airfoil.

The analysis has shown that the transition position strongly affects the airfoil performance. With regard to the experimental check, the agreement with numerical results is satisfying. In particular, if the laminar region is accurately predicted, the numerical/experimental comparison is quite good both in terms of local values (pressure and velocity distribution) and global parameters (lift coefficient).

References

[1] Barlow J. B., Rae W.H., Pope A. "Low Speed Wind Tunnel Testing" John Wiley &Son, Inc. Third Edition.
[2] Mosharov V., Radchenko V., Fonov S., Luminescent Pressure Sensors in Aerodynamic Experiments, Central Aerohydrodynamic Institute (TsAGI), 1997.
[3] M. Drela, "Newton solution of coupled viscous/inviscid multielement airfoil flows", in AIAA, Fluid Dynamics, Plasma Dynamics and Lasers Conference, AIAA Paper 90-1470, American Institute of Aeronautics and Astronautics (AIAA), Seattle, WA, June 1990.
[4] FLUENT™ 6.1, User's Guide, February 2003.

Numerical and experimental results for the warming of cylindrical timber segments

D. A. Gigliotti & P. J. Montgomery
Mathematics Program, University of Northern British Columbia, 3333 University Way, Prince George, B.C., Canada, V2N 4Z9

Abstract

As part of an industrial process in the forestry industry, pre-cut segments of debarked logs are *conditioned* by placing the wood segments in a warm water shower. For wood which is initially cold (or sometimes frozen) and has a relatively high moisture content, the conditioning process results in a net increase in temperature and change in moisture content. As a porous media, wood has a fairly complex structure due to the orientation and sizes of the cells which make up the fibers. In addition, the moisture content of the recently debarked log segments is relatively high, the moisture being almost completely composed of liquid water trapped by capillary forces. Simplistic models which assume a constant moisture content have previously been used to predict conditioning time. However, as is often the case in reality, the complexity of the problem is such that more accurate modelling is desired.

To learn more about the conditioning process, preliminary experiments were conducted using a data logger and an array of fifteen thermocouples placed radially at three points on a log segment which was then put through a full conditioning cycle. Theoretical model equations are presented, which take into account both the liquid and vapour components of the water, and spatial averaging is used to create a system of nonlinear partial differential equations. The problem is then simplified through some basic assumptions to pose a set of coupled differential equations for energy and moisture transport in one spatial dimension. A finite difference numerical method is used to solve the initial boundary value problem for the coupled system of nonlinear partial differential equations, and some numerical results are compared to experimental data for the one dimensional problem. Limitations of the model are identified and discussed.
Keywords: multiphase flow, porous media, water transport, finite differences.


WIT Transactions on Engineering Sciences, Vol 59, © 2008 WIT Press
www.witpress.com, ISSN 1743-3533 (on-line)
doi:10.2495/AFM080191

1 Introduction

The problem studied herein arises from an industrial application in the manufacturing of plywood. Of direct concern to industry is finding a quick and simple method to predict the amount of time required to warm pre-cut and debarked cylindrical wooden log segments from their ambient temperature outside to a desired production temperature. This process is known as *conditioning* and can be achieved in many ways, for example, submersing the segments in a hot water bath or exposure to hot steam. In this study, conditioning is achieved by placing the wood in a continuous shower of warm water, and waiting for a pre-determined time to move the wood onto the next stage in the production process. As a porous media, fluid within the cell structure can move from cell to cell under the influence of temperature and concentration gradients, and therefore the transport of water must be considered as an integral part of the conditioning process.

The specific problem considered is therefore to create a model for the reheating of a cylinder of wood through partial contact of its outer boundary with very humid air. In the next section, a set of governing equations are posed which describe the reheating of wood in this particular circumstance. The model takes into account the porous nature of wood, and the multiphase (liquid and gas) flow of water within the porous media in order to obtain a set of partial differential equations for the volume averaged temperature and moisture content. In section 3, the equations numerical solutions of the equations are compared to experimental data gathered on site. Some concluding remarks follow, and limitations of the model are discussed.

2 Model equations

A first attempt at modelling the heating of a homogeneous cylinder is typically achieved through the application of a linear form of the heat equation,

$$\frac{\partial T}{\partial t} = \nabla \cdot k_q \nabla T \tag{1}$$

where T is the temperature, t time, and k_q a heat conduction coefficient. Equation (1) has been well-studied [1], although there are several factors which are important when studying the warming of wood which require a more delicate and thoughtful approach. For example, the coefficient k_q can depend strongly on moisture content, and to a lesser extent, temperature, tree species, and spatial position within the wood [2]. Equation (1), coupled with an analogous moisture diffusion equation, has been used to model wood heating [3] and the non-isothermal drying of dimensional lumber [4]. Other limitations are imposed by assuming equation (1), particularly regarding moisture content. Heating and surface evaporation can result in the redistribution of fluid within the wood. Indeed, starting from the time of harvest, wood immediately begins to lose moisture, a process which is accelerated with de-barking. The humid environment employed during conditioning acts to reduce surface evaporation but still allows for the formation of pressure gradients which result in a nonhomogeneous moisture distribution.

Whitaker [5] completed a thorough characterization of the transport of energy and mass in general porous media, which was later applied to dimensional lumber drying by Spolek [4]. Whitaker's approach [5] considered the phases of water and the solid wood separately. The temperature T of the wood is modelled with a linear enthalpy approximation and Fourier's law of head conduction as a generalization of equation (1).

$$\rho_\sigma (c_p)_\sigma \left(\frac{\partial T_\sigma}{\partial t} \right) = k_\sigma \nabla^2 T_\sigma + \Phi_\sigma . \tag{2}$$

In equation (2), and in later equations, the standard symbols are used: ρ for density, c_p heat capacity, k thermal conductivity coefficient, and Φ for heat sources. The subscript σ is used for all of these variables to denote the properties within the solid wood.

The liquid phase obeys a similar continuity equation, with the added complication of transport, and can be stated (with subscripts β denoting liquid phase) as

$$\rho_\beta (c_p)_\beta \left(\frac{\partial T_\beta}{\partial t} + \mathbf{v}_\beta \cdot \nabla T_\beta \right) = k_\beta \nabla^2 T_\beta + \Phi_\beta . \tag{3}$$

In equation (3) a linear relationship between enthalpy and temperature is again used, as is Fourier's law of conduction within the liquid.

For the gas phase, the temperature of the water vapour and the existing inert gases (such as air) are taken into account to give a generalization for the gas phase, written with a subscript γ as

$$\rho_\gamma (c_p)_\gamma \left(\frac{\partial T_\gamma}{\partial t} + \mathbf{v}_\gamma \cdot \nabla T_\gamma \right) = k_\gamma \nabla^2 T_\gamma + \Phi_\gamma - \nabla \cdot \left(\sum_{i=1}^{i=N} \rho_i \mathbf{u}_i (c_p)_i T_\gamma \right), \tag{4}$$

where the last term represents the contribution due to the existence of N inert gases with diffusion velocity $\mathbf{u}_i$ and heat capacity $(c_p)_i$.

Equations (2), (3), and (4) are local in nature, and are standard expressions in the transport of fluids with the inclusion of diffusion and a source/sink term (Φ). To obtain relationships between the bulk properties of the wood, the equations must be averaged over a given volume. For example, for a volume element V, the average temperature of the solid phase is given by

$$\langle T_\sigma \rangle = \frac{1}{V} \iiint_V T_\sigma \, dV. \tag{5}$$

Each of equations (2), (3), and (4) are integrated to create volume averaged equations, which are subsequently manipulated using integration by parts theorems to bring in various phase boundary conditions into the problem. The individual equations are be then added together to create a total thermal energy equation, for the averaged temperature $\langle T \rangle$ [5]

$$\begin{aligned} &\langle \rho \rangle c_p \frac{\partial \langle T \rangle}{\partial t} + [\rho_\beta (c_p)_\beta \langle \mathbf{v}_\beta \rangle + \langle \rho_\gamma \rangle^\gamma \langle (c_p)_\gamma \rangle^\gamma \langle \mathbf{v}_\gamma \rangle] \cdot \nabla \langle T \rangle + \Delta h_{vap} \langle \dot{m} \rangle \\ &\quad = \nabla \cdot K_{eff}^T \nabla \langle T \rangle + \langle \Phi \rangle . \end{aligned} \tag{6}$$

The process leading to the derivation of equation (6) is quite detailed due to the consideration of all of the phases, and the details may be found elsewhere [5]. In equation (6) a few shorthand terms have been introduced: the superscript $^{\gamma}$ denotes an average over the portion of the volume element in relation to that phase, $\langle\Phi\rangle$ denotes a combined source term, and $\langle\dot{m}\rangle$ denotes the mass rate of vaporization per unit volume. In addition, the enthalpy of vaporization per unit mass at temperature $\langle T\rangle$ is given as Δh_{vap}, and being a non-homogeneous material, K^{T}_{eff} is a second order tensor which encompasses the thermal diffusivity in each of the three spatial dimensions.

A second equation can be created for the moisture content by applying an approach analogous to the derivation of equation (6). Again, the details are left to Whitaker [5], and the result is stated for the saturation, S, a quantity which represents the mass fraction of moisture in the form of liquid and vapour to the fully saturated mass.

$$\phi\frac{\partial\langle S\rangle}{\partial t}+\nabla\cdot\left(\langle\mathbf{v}_{\beta}\rangle+\frac{\langle\rho_1\rangle^{\gamma}\langle\mathbf{v}_{\gamma}\rangle}{\rho_{\beta}}\right)=\nabla\cdot\left[\frac{\langle\rho_{\gamma}\rangle^{\gamma}}{\rho_{\beta}}D^{(1)}_{eff}\nabla\left(\frac{\langle\rho_1\rangle^{\gamma}}{\langle\rho_{\gamma}\rangle^{\gamma}}\right)\right]. \tag{7}$$

In equation (7), the effective diffusivity $D^{(1)}_{eff}$, is a second order tensor which encompasses diffusivity of the vapour in each of three spatial dimensions, ρ_1 is the vapour density, and ϕ is the porosity or volume fraction of the void space in the wood.

To close the system, the momentum equations for the liquid and gas phases are used together with Darcy's law to relate the flow rate to the pressure gradient. The pressure P is then introduced in place of velocity, with the introduction of permeability constants K (with appropriate subscripts) The resulting two equations, neglecting heat sources and sinks $\langle\Phi\rangle$, are stated as

$$\langle\rho\rangle c_p\frac{\partial\langle T\rangle}{\partial t}-\left[\frac{K_{\beta}\rho_{\beta}(c_p)_{\beta}}{\mu_{\beta}}(\nabla\langle P_{\beta}\rangle^{\beta}-\rho_{\beta}\mathbf{g})+\frac{K_{\gamma}\langle\rho_{\gamma}\rangle^{\gamma}\langle(c_p)_{\gamma}\rangle^{\gamma}}{\mu_{\gamma}}\times(\nabla\langle P_{\gamma}\rangle^{\gamma}-\langle\rho_{\gamma}\rangle^{\gamma}\mathbf{g})\right]\cdot\nabla\langle T\rangle+\Delta h_{vap}\langle\dot{m}\rangle=\nabla\cdot K^{T}_{eff}\nabla\langle T\rangle, \tag{8}$$

and

$$\phi\frac{\partial\langle S\rangle}{\partial t}-\nabla\cdot\left[\frac{K_{\beta}}{\mu_{\beta}}(\nabla\langle P_{\beta}\rangle^{\beta}-\rho_{\beta}\mathbf{g})+\frac{\langle\rho_1\rangle^{\gamma}K_{\gamma}}{\rho_{\beta}\mu_{\gamma}}(\nabla\langle P_{\gamma}\rangle^{\gamma}-\langle\rho_{\gamma}\rangle^{\gamma}\mathbf{g})\right]=\nabla\cdot\left[\frac{\langle\rho_{\gamma}\rangle^{\gamma}}{\rho_{\beta}}D^{(1)}_{eff}\nabla\left(\frac{\langle\rho_1\rangle^{\gamma}}{\langle\rho_{\gamma}\rangle^{\gamma}}\right)\right]. \tag{9}$$

Equations (8) and (9) contain several coefficients which must be determined prior to solving the equations. By applying a mechanistic model of wood structure, the properties of wood may be used to develop theoretical relationships and values for many of the parameters to decrease the dependence on experimental parameters [2, 4]. As in the development of the equations, the technical details call

for a more thorough examination of their derivation; however, for brevity, only the impact of the simplifications will be used herein with the details referred to where appropriate. For example, the volume fraction ϕ can be determined by an analytic dependence on cell parameters [4].

The liquid and gas phase pressures remaining in equations (8) and (9) can be removed by assuming the gas phase acts as an ideal gas, and that the capillary pressure P_c is the difference between the gas phase pressure and liquid phase pressure, [5, 4]. The liquid phase pressure is therefore expressed as a function of the gas phase pressure and the capillary pressure, $\langle P_\beta \rangle^\beta = \langle P_\gamma \rangle^\gamma - \langle P_c \rangle^c$. The liquid pressure gradient can then be expressed by the following linear expansion,

$$\nabla \langle P_\beta \rangle^\beta = \left(\frac{\partial \langle P_1 \rangle^\gamma}{\partial T} + \frac{\partial \langle P_2 \rangle^\gamma}{\partial T} - \frac{\partial \langle P_c \rangle^c}{\partial T} \right) \nabla \langle T \rangle + \left(\frac{\partial \langle P_1 \rangle^\gamma}{\partial S} + \frac{\partial \langle P_2 \rangle^\gamma}{\partial S} - \frac{\partial \langle P_c \rangle^c}{\partial S} \right) \nabla S. \tag{10}$$

Analytic expressions for the partial pressures and capillary pressures in equation (10) are given by Spolek [4] as functions of temperature, saturation, and number of constants. In the interest of writing equation (10) in a more compact form, the following substitutions are made,

$$\nabla \langle P_\beta \rangle^\beta = -(C_{T,c} - C_{T,\gamma}) \nabla \langle T \rangle - (C_{S,c} - C_{S,\gamma}) \nabla \langle S \rangle. \tag{11}$$

In addition, a dimensionless temperature Q is used (M is already dimensionless definition) such that $Q = (T - T_0)/(T_\infty - T_0)$, where T_0 is the average initial internal temperature of the log, and T_∞ is the temperature of the bathing fluid. Since the saturation S does not include the hygroscopically bound water, it will be substituted for with the moisture content M through the relation $S = (M - M_{fsp})/(M_{max} - M_{fsp})$, where the subscript fsp denotes the fiber saturation point, and the subscript max refers to the maximum possible moisture content the wood can contain. The fiber saturation point is a species dependent parameter which is a measure of the moisture content due to hygroscopically bound water only.

In addition, as wood dries, surface tension forces the small valve-like openings which connect neighbouring cells, known as pits, to be forced shut. A chemical bond between the valve and pit opening forms, effectively sealing off the pit opening to gas transport, causing the gas phase to become trapped and permitting the assumption of a gas phase permeability very close to zero, ($K_\gamma = 0$) [2]. Although the bulk gas phase transport is neglected, vapour transport continues as a diffusive process which is captured in a diffusion coefficient denoted D_m, leading to the following simplification,

$$\langle \rho_\gamma \rangle^\gamma D_{eff}^{(1)} \nabla \left(\frac{\langle \rho_1 \rangle^\gamma}{\langle \rho_\gamma \rangle^\gamma} \right) = \rho_\beta D_m \nabla M, \tag{12}$$

where M is the moisture content, and D_m is a combined vapour and bound water moisture diffusion coefficient.

Employing the above simplifications, and neglecting transport due to gravity along with equations (12), and (10), permits equations (8) and (9) to be written as a more simplified set of transport equations,

$$\langle\rho\rangle c_p \frac{\partial\langle Q\rangle}{\partial t} + \left[\frac{\rho_\beta (c_p)_\beta K_\beta}{\mu_\beta}\Big((C_{T,c} - C_{T,\gamma})\Delta T\nabla\langle Q\rangle + (C_{S,c} - C_{S,\gamma})\frac{1}{\Delta M}\nabla\langle M\rangle\Big)\right]\cdot\nabla\langle Q\rangle = \nabla\cdot K_q\nabla\langle Q\rangle, \tag{13}$$

and

$$\frac{\phi}{\Delta M}\frac{\partial\langle M\rangle}{\partial t} + \nabla\cdot\left[\left(\frac{K_\beta}{\mu_\beta}(C_{T,c} - C_{T,\gamma})\right)\Delta T\nabla\langle Q\rangle + \left(\frac{K_\beta}{\mu_\beta}(C_{S,c} - C_{S,\gamma})\right)\frac{1}{\Delta M}\nabla\langle M\rangle\right] = \nabla\cdot D_m\nabla\langle M\rangle. \tag{14}$$

3 Results

the thermal conductivity can be reduced to a scalar quantity k_q, and A moisture diffusion coefficient, D_m, is introduced in an analogous way to the thermal conductivity derivation [4].

This section considers the restriction of equations (13) and (14) to cylindrical polar coordinates, with only the radial motion considered, such that $Q = Q(r, t)$ and $M = M(r, t)$. The equations are simplified further by suppressing the volume average bracket notation, and using the notation $C^T = (C_{T,c} - C_{T,\gamma})$ and $C^S = (C_{S,c} - C_{S,\gamma})$. In addition, the second order tensors K^T_{eff} and D_m can be reduced to scalar quantities k_q and d_m respectively, when considering only the radial direction. The resulting equations are expressed as

$$\rho c_p\frac{\partial Q}{\partial t} + \left[\frac{\rho_\beta (c_p)_\beta K_\beta}{\mu_\beta}\Big(C^T\Delta T\frac{\partial Q}{\partial r} + C^S\frac{1}{\Delta M}\frac{\partial M}{\partial r}\Big)\right]\frac{\partial Q}{\partial r} = \frac{1}{r}\frac{\partial}{\partial r}rk_q\frac{\partial Q}{\partial r}, \tag{15}$$

and

$$\frac{\phi}{\Delta M}\frac{\partial M}{\partial t} + \frac{1}{r}\frac{\partial}{\partial r}r\frac{K_\beta}{\mu_\beta}\left[C^T\Delta T\nabla Q + C^S\frac{1}{\Delta M}\nabla M\right] = \frac{1}{r}\frac{\partial}{\partial r}rd_m\frac{\partial M}{\partial r}. \tag{16}$$

Equations (13) and (14) are applied to model a symmetric simplification of log conditioning, considering only time-dependent radial transport of heat and moisture. The initial boundary value problem is solved in the domain $t > 0$ and $0 < r < R$. The boundary conditions at $r = 0$ are the standard symmetry conditions of zero flux. The outer boundary conditions at $r = R$ are somewhat more complex, as a balance of energy and mass must be maintained at this point causing the latent heat of evaporation to be included to derive a generalized Neumann boundary condition which couples moisture, temperature and the flux at the surface.

The thermal boundary can be approximated by the standard convective heat flux boundary condition, $\dot{q} = h_q(T(R,t) - T_\infty)$ [6], where h_q is the surface thermal transfer coefficient, and T_∞ is the temperature of the bathing fluid. The horizontal stacking of the cylindrical log segments in the conditioning tunnel give rise to horizontal voids between neighboring log segments. By approximating the voids as cylindrical, and the flow of the humid air in the voids to be in the laminar range, the surface heat transfer coefficient h_q can be expressed as $h_q = (k_\gamma/D)0.023Re_D^{0.80}Pr^{0.33}$, where k_γ is the thermal diffusion coefficient of humid air, D is the diameter of the void, Re is the Reynolds number of the flow, and Pr is the Prandtl number of the humid air.

The boundary condition for the moisture content should ideally be analogous to the thermal flux condition. Unfortunately, a mass flux boundary which does not result in an ill-posed problem has not yet been found and will therefore be approximated with a Dirichlet condition, $M(R,t) = M_0$, where M_0 is an appropriately chosen initial moisture content at the surface. Although a Dirichlet moisture boundary results in a somewhat unphysical moisture boundary condition, it will suffice as a first approximation until appropriate mass flux boundaries at the surface can be derived.

With the initial and boundary conditions specified, a finite difference numerical approach was taken to find numerical solutions. A forward in time central in space scheme was chosen, with some care employed to obtain second order spatial approximations for the Neumann boundary conditions. An exciting feature of this research program was the ability to conduct measurements of log conditioning, and data was collected for several experiments. Thermal sensors were placed in the log in a straight line along a ray outwards from the center with one at $r = 0$ cm (core), one at $r = R$ (surface), and three more positions between the core and the surface. The data from the temperature sensors was recorded over a period of several hours during conditioning. Moisture content was not measured during the experiment, however a rough estimate of initial and final moisture content was measured by removing samples for controlled measurement in the laboratory. The main sources of error were in the temperature measurement and placement of the thermocouples, and the lack of precision in moisture content measurements.

A selected result is displayed in Figure 1, which depicts temperature versus time giving a comparison of the model to experimental temperature data 30 cm from the end, and at both the core and 10 cm radially form the core. The thin dotted lines represent the placement error of the thermocouples.

4 Conclusion

The modelling of any industrial process can be plagued by oversimplification which causes the problem to be either trivial or too far removed from reality to be of much use. In this case, the modelling of log conditioning is a complicated process involving a consideration of the vapour and liquid phases of moisture moving within a the porous wooden cellular network. Through volume averaging, a system of differential equations, derived from a lumber drying model, were applied and

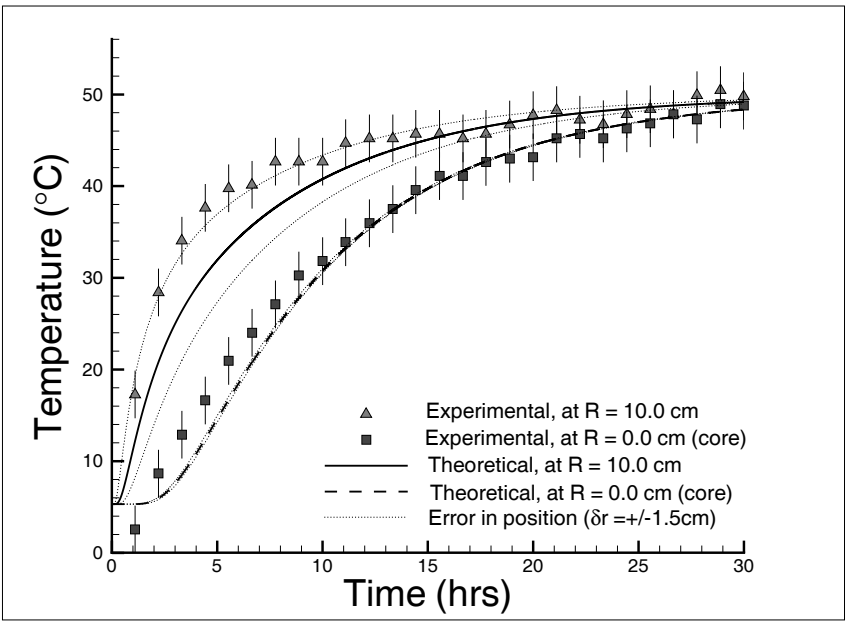

Figure 1: Comparison of theoretical model to experimental data for Douglas Fir, where $T_0 = 5.3°C$, $M_0 = 0.80$, $R = 15$ cm, $Z = 30$ cm.

found to model the experimental results relatively well within experimental error. Some underestimation of the temperature is seen which could be due to heating from the end of the log, which is neglected in the one dimensional problem. In addition, the Dirichlet boundary condition imposes a relatively unphysical moisture boundary which could cause the model to converge to an incorrect steady-state. Ongoing research will assist in probing the dependence of various types of boundary conditions, and generalizing the problem to more than one spatial dimension to account for these minor discrepancies.

Acknowledgements

PJM gratefully acknowledges UNBC for the assistance of a conference travel grant, and NSERC for a discovery grant to assist in research activity. DG thanks the Canfor Corporation and NSERC for an Industrial Postgraduate Scholarship. Both authors would also like to thank I. Hartley for his assistance.

References

[1] J. Crank, *The mathematics of diffusion*, Second Edition, Oxford University Press, Oxford, 1975.

[2] J. F. Siau, *Wood: Influence of Moisture on Physical Properties,* Virginia Polytechnic Institute and State University, 1995.
[3] H. P. Steinhagen, *Computerized Finite-Difference Method To Calculate Transient Heat Conduction With Thawing,* Wood and Fiber Science, 1986.
[4] G. A. Spolek, *A Model of Simultaneous Convective, Diffusive, and Capillary Heat and Mass Transport in Drying Wood,* Ph.D. thesis, Washington State University, 1981.
[5] S. Whitaker, *Simultaneous heat, mass, and momentum transfer in porous media: A theory of drying*, Advances in Heat Transfer, 13: 119-203, 1977.
[6] A. Bejan, *Heat Transfer,* John Wiley and Sons Inc., New York, 1993.

This page intentionally left blank

Experimental study on the oscillation of a separating shear layer in a cavity

Y. Inoue & S. Yamashita
Department of Mechanical and Systems Engineering,
Gifu University, Japan

Abstract

This study was performed to clarify the oscillation of a separating shear layer in a cavity formed peripherally on a cylinder in a uniform axial stream. Experiments were conducted on the cavity having the width-depth ratio of 4 and formed in a water channel. Firstly, the dynamic characteristics of the flow field were investigated by visualizing the flow, and a time-averaged flow field was measured with a particle imaging velocimetry (PIV). As a result, the typical three flow patterns were demonstrated. Secondly, spatiotemporal measurements were taken along and/or across the shear layer with a UVP monitor. Thirdly, the proper orthogonal decomposition was applied to the UVP dataset, and random coefficients at the low-order POD modes were examined. As a result, two dominant time scales of $f\,b/U_m = 0.1$ and 0.9 were found in the shear layer. These two-scale flow structures can be shown through filtration with discrete wavelet transformation.

Keywords: cavity flow, self-sustaining oscillation, ultrasonic Doppler method, wavelet analysis, POD.

1 Introduction

In many cases, the flow passing across an open cavity generates self-exited oscillation, causing two major problems: radiating noise and fluid induced oscillation. Although the characteristics of cavity oscillation have been studied in recent decades, there are still some problems that remain unsolved even today. The details of these problems were perused by Rockwell and Naudascher [1] and Grace [2] in their prospective papers and by Lin and Rockwell [3] and Howe [4].

WIT Transactions on Engineering Sciences, Vol 59, © 2008 WIT Press
www.witpress.com, ISSN 1743-3533 (on-line)
doi:10.2495/AFM080201

Rockwell and Naudascher [1] describe the self-excited oscillation by dividing it into three types, where the cavity oscillation under this study falls into a type caused by flow-specific instability according to their classification. Lin and Rockwell [3] describe the characteristics of the cavity oscillation in four steps: (i) interaction between a vorticity concentrated area and a downstream cavity edge, (ii) effects on a shear layer formed from an upstream edge, (iii) conversion to fluctuations in a separating shear layer, and (iv) amplification in the flow direction of this conversion. They comment that the sequence of these four steps is not stable in terms of time, and the instantaneous velocities in the direction along the shear layer should be measured. On the other hand, Grace [2] investigates the math calculation for cavity noise prediction, and Howe [4] treats the same subject theoretically.

This study is intended to experimentally clarify the flow field of an axisymmetric cavity on a cylinder placed in an axial flow. In this paper, a cylinder with a water channel of the aspect ratio of four is set up in a uniform water flow, instantaneous fluctuation velocities are measured with an ultrasonic velocity profiler (UVP monitor) [5], and the characteristics of the oscillation of the separating shear layer are studied from the results of the measurement.

The axisymmetric cavity was studied in detail by Sarohia [6], and the effects of the boundary layer thickness of the approaching flow, Reynolds number and the aspect ratio of the cavity on self-excited oscillation characteristics were clarified. Later, Gharib [7] studied the effects of periodic disturbance introduced into the approach flow, and Gharib and Roshko [8] studied the relationship between the drag acting on the cavity and the flow pattern. On the other hand, as to the instantaneous flow field, Rockwell and Knisely [9, 10] and Neary and Stephanoff [11] showed their experiments in the visualization of flow, and Lin and Rockwell [3] and Meganathan and Vakili [12] showed their experiments with a particle imaging velocimetry (PIV).

In this study, the basic flow patterns were studied through visualized flow observation by using the dye streak method, and then the mean velocity field was shown based on the results of measurement with the PIV. The spatiotemporal velocity information was measured with the UVP, and the low-order model of the separating shear layer in self-exited oscillation was identified through the mode analysis of the acquired data. The UVP method is detailed by Takeda [5].

2 Experimental apparatus and procedures

The experiment of this study was conducted by using a low-speed recirculating water channel. The measurement part of this channel was 0.7 m wide and 2.2 m long. The test body was an acrylic resin cylinder with the radius a = 100 mm having a streamlined head of aluminium alloy casting. The downstream end of the cylinder was fixed to a frame, which was independent of the tank. The posture of the cylinder toward the flow was adjusted with three wires located in the upstream part. The outline of the flow field and its coordinate system are shown in fig. 1. The main stream direction is taken to be the x-axis, the radial direction to be the z-axis and circumferential direction to be the y-axis. The

cavity was shaped with the width b = 100 mm and the depth h = 25 mm. Assuming that the reference velocity of the main stream outside the layer was expressed as U_m, the experiment was conducted as to the reference Reynolds number $Re = 0.6\times10^4$ and 1.0×10^4, where $Re = U_m\, b/\nu$. At this time, the boundary layer of the approach flow was laminar, and the momentum thickness was θ_0 = 1.38 mm (b/θ_0 = 71) at $Re = 1.0\times10^4$ and x = -10 mm.

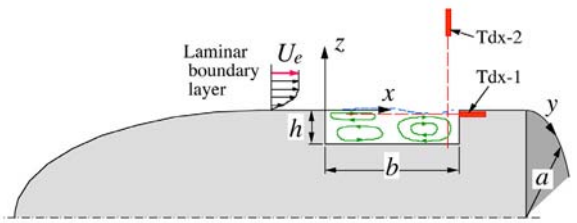

Figure 1: Flow field and coordinate system.

The flow visualization was realized by injecting fluorescence dye Rhodamine B from three small openings (ϕ1 mm) at x = -20 mm upstream from the cavity and x = 20 mm and 80 mm within the cavity, and illuminated by an Nd:Yag laser sheet light source. In the PIV method, Ar-ion laser was used for illumination, and a 1k×1k pixel digital camera SKC-100 and Digital Frame Grabber IPM-8540D were used for imaging at 15 frames/sec. Polymer spheres having the mean size of 180 μm were used as tracer particles, and the cross-correlation method was used for velocity analysis.

The data measured with the UVP is realized as the spatiotemporal distribution of instantaneous velocity components in the ultrasonic beam flying direction. In this experiment, as shown in fig. 1, ultrasonic transducers (frequency: 8MHz, beam diameter: 2.5 mm) were positioned axially (Tdx-1) and radially (Tdx-2), and $\tilde{u}(x,t)$ and $\tilde{w}(z,t)$ were measured respectively. The transducer Tdx-1 was embedded in the cylinder, and its center position was z = -7 mm. The transducer Tdx-2 was attached to the tip-end of the supporting rod having a wing cross-sectional profile, and moved axially within the range of x = 30 to 90 mm by using a traverser. For ultrasonic scattering particles, hydrogen bubbles generated from a Pt wire having the diameter of 30 mm were used. The velocity distribution sampling intervals of Tdx-1 and Tdx-2 were 32 ms and 50 ms, respectively, when these transducers were used independently. When a multiplexer was used and Tdx-1 and Tdx-2 were used concurrently and alternately while they were switched to each other, the switching time interval was 40 ms. As to the UVP data, the proper orthogonal decomposition (POD) method [13] was applied to the extraction of the spatial mode, and the Fourier transformation and the discrete wavelet transformation were applied to the analysis of the time fluctuation components. The details of this data processing are left out here (refer to [13]).

3 Experimental results and considerations

3.1 Visualization of flows

Figure 2 shows the visualized images of flows within the cavity, arranged for each of three typical flow patterns in four frames each as the time passes (from top to bottom). The main stream flows from left to right. In any flow pattern, the streakline from the upstream cavity edge to the downstream is broken almost in the middle of the cavity width, causing a large deformation in the downstream. The appearance of this deformation differs among the three patterns as shown. The tip of the streak collides with the downstream cavity edge in fig. 2(a), the streak tip is caught up in the cavity without break in fig. 2(b), and the streakline collides little with the downstream edge and flows off as it is downward in fig. 2(c). When it comes to the flow within the cavity, it is active in a comparatively compact area near the downstream in fig. 2(a), a large-scaled flow pattern occupying more than half of the cavity area is formed in fig. 2(b), and the degree of activity of flow is lower compared with the former and there is little flow recirculation within the cavity in fig. 2(c).

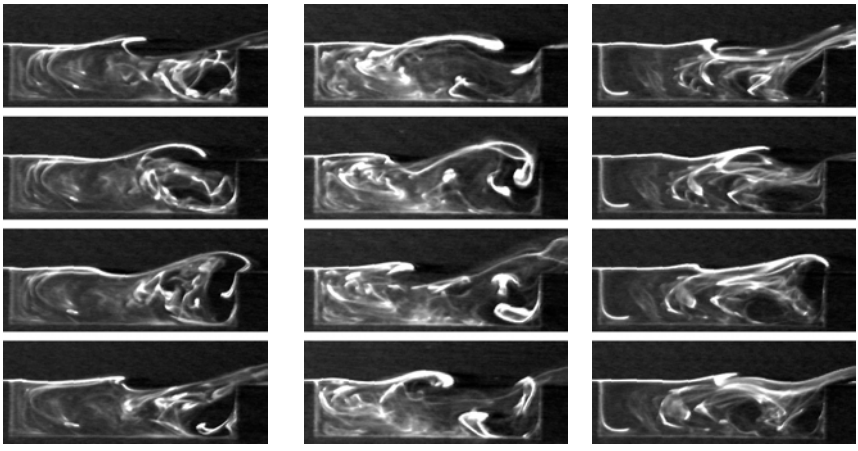

(a) pattern I (b) pattern II (c) pattern III

Figure 2: Typical flow patterns visualized by dye injection.

These integrated streaklines in fact represent certain realized flow patterns of all flow patterns existent numerously. As a result of observation, these three flow patterns were confirmed to be typical ones. As Lin and Rockwell [3] point out, the cause of the pattern fluctuation has not yet been identified clearly. While responsive jitters and relativity of three-dimensionality are thought of as possible causes, there have been few studies treating this subject actively (e.g. [10] and [11]).

3.2 Mean flow field

Figure 3 shows the mean behaviour in the x-z plane measured by the PIV method as $Re = 0.6 \times 10^4$. In fig. 3(a) showing the mean velocity vectors, a definite main vortex can be seen in an area occupying about half on the downstream side of the cavity width. The main vortex reaches the cavity bottom, and a boundary layer develops above the bottom. This boundary layer separates from the bottom and flows upward. Upon reaching the separating shear layer of the main stream, it forms a saddle point. In contrast with this, the flow on the upstream side of the saddle point is extremely weak, and the secondary vortex driven by the entrainment of the shear layer and another secondary vortex in reverse rotation to the main vortex are formed as shown schematically in fig. 3(b). Each letter in the figure indicates a singular point. N stands for node, S stands for saddle, N' stands for half-node and S' stands for half-saddle.

(a) velocity vector

(b) sketch of the streamline

(c) vorticity

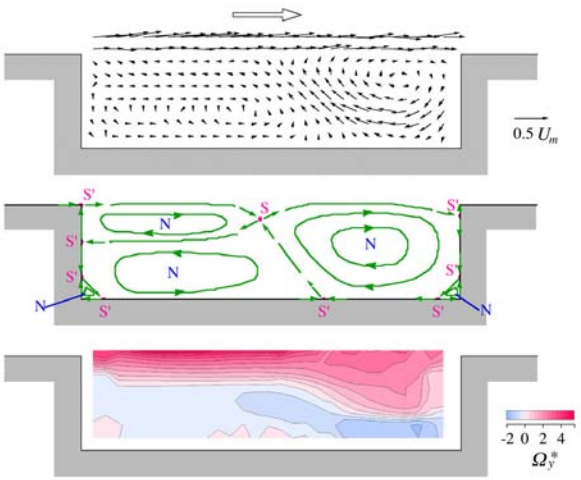

Figure 3: Time-averaged spatial maps measured with the PIV at Re = 0.6 $\times 10^4$.

Figure 3(c) shows the contour lines of the dimensionless vorticity component in the y-direction, Ω_y^*, defined as the following;

$$\Omega_y^* = \frac{\Omega_y}{U_m / b} = \frac{b}{U_m}\left(\frac{\partial U}{\partial z} - \frac{\partial W}{\partial x}\right). \quad (1)$$

It was calculated by numerical differentiation from the mean velocity field by using the least-square method of quintic polynomial. In the separating shear layer, there is an area showing positive vorticity corresponding to $\partial U/\partial z > 0$. The width of this area expands drastically at $x/b > 0.5$, filling most areas of the main vortex but without excessive concentration. The bottom boundary layer shows $\partial U/\partial z < 0$, generating negative vorticity. This area showing the negative vorticity is transferred into the cavity upon the separation of the bottom boundary layer.

3.3 Fluctuation energy

In this study, paying attention to the oscillation pattern of the shear layer, measurement was taken by the UVP method in the direction along the shear layer longitudinally (Tdx-1) and in the direction across the shear layer (Tdx-2), and the oscillation mode was analyzed. Figure 4 shows axial changes in the fluctuation velocity energy as u^2 quantified by Tdx-1, E_w quantified by Tdx-2 and w^2 at $z = 0$. Here, E_w expresses the total fluctuation energy within the measurement range defined by

$$E_w = \frac{1}{T}\iint w^2(z,t)\,dt\,dz = \sum_n \lambda_w^{(n)} \ , \tag{2}$$

and $\bar{E}_w$ is the spatial mean value of E_w. The distribution of u^2 increases gradually up to $x/b < 0.6$, and then increases rapidly toward the peak of $x/b \approx 0.85$. The distribution of the radial components shows almost the same trend, but the fluctuation energy at $x/b < 0.4$ is considerably smaller. $\lambda_w^{(n)}$ in eqn. (2) expresses the eigenvalue that can be obtained empirically by using the POD method [13]. When the eigenfunction corresponding to each mode is expressed as $\phi_w^{(n)}$, the original velocity data can be expressed by

$$w(z,t) = \sum_n w^{(n)}(t)\,\phi_w^{(n)}(z) \ . \tag{3}$$

Here, $w^{(n)}$ is the nth random coefficient. Since the norm of $\phi_w^{(n)}$ itself is normalized to 1, the square mean value of the random coefficient is equal to the eigenvalue $\lambda_w^{(n)}$. That is, even though there is an issue of the distribution profile of the eigenfunction, the spatiotemporal information of the UVP data can be contracted to the time change in the random coefficient.

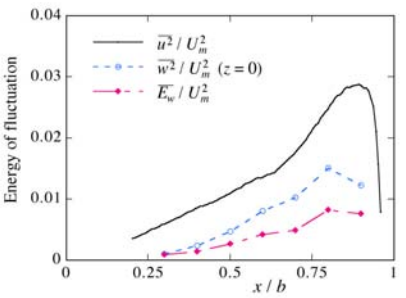

Figure 4: Axial change in the energy of velocity fluctuation.

The POD was applied to the data within the range of $x/b = 0.5$ to 1, and the estimated POD spectra are shown as to $Re = 0.6\times10^4$ and 1.0×10^4 in fig. 5(a). The spectra were normalized by the total fluctuation energy E_u. In both cases of Re, the spectra shown are almost the same. Only the first mode captures about 50% of the total fluctuation energy, and the first three modes contain over 80% of the total fluctuation energy. Here, due to limitations of space, the distribution

of the eigenfunction has to be omitted, but it should be noted here that the eigenfunction takes the sine-wave distribution with different wavelengths and phases depending on the mode. Also in the radial direction (fig. 5(b)), most fluctuation energy is captured in the lower-order modes, and the energy content rate of the first mode is slightly high at $x/b = 0.8$. The eigenfunction is expressed by the even and odd function taking the center of the shear layer as an axis of symmetry, whose distribution profile has no essential difference due to the axial position.

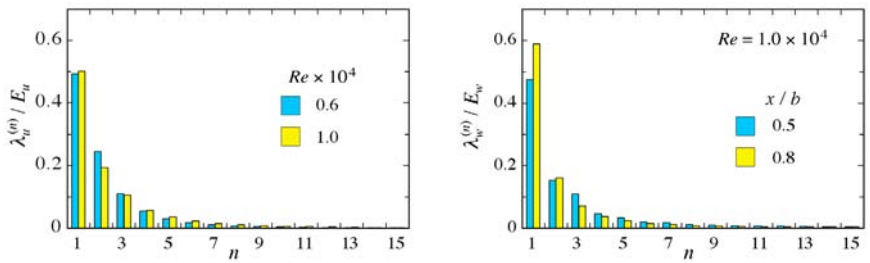

(a) *u*-component (b) *w*-component

Figure 5: POD spectra of velocity fluctuation.

The power spectra of the axial and radial random coefficients were normalized by U_m^2 as to $n = 1$ to 5 as shown in fig. 6. From these figures, it is understood that there are two typical time scales in the present flow and they coexist with a comparatively sharp peak of the dimensionless frequency of about 0.9 and the peak of the broad bandwidth centered about the dimensionless frequency of 0.1. The former peak corresponds to the self-excited oscillation and has its dominance in each spectrum excepting the axial spectrum of $Re = 1.0 \times 10^4$. In the radial direction, the spectral peak is sharper at $x/b = 0.5$. On the other hand, the long-period fluctuation of the dimensionless frequency of 0.1 is made apparent well in the spectra of $u^{(1)}$.

3.4 Oscillation pattern of shear layer

Here, to separate these two time scales and examine their oscillating modes, the random coefficient of the axial velocity distribution was subjected to discrete wavelet transformation. Daubechies with N = 4 was used for the mother wavelet. The wavelet spectrum was normalized by U_m^2 as shown in fig. 7. In the abscissa scale j, when $j = 0$ is the sampled signal level, the resolution degrades sequentially as j = -1, -2, … down to the lowest frequency at j = -10. As understood from this figure, the random coefficients of the POD mode $n = 1$ show their peaks at j = -5 and -8, while the random coefficients of the POD mode $n = 2$ and 3 show their peaks only at j = -5. Here, the dimensionless Nyquist frequency at j = -5 is about 0.8.

The random coefficients were inverse transformed by using j = -5 to -10 ($\bar{u}_{-4}^{(n)}$), j = -5 to -6 ($\tilde{u}_{-5}^{(n)} + \tilde{u}_{-6}^{(n)}$) and j = -7 to -10 ($\bar{u}_{-6}^{(n)}$) of all wavelet coefficients of each scale, and then the velocity field was reconstructed by using

the eigenfunction as shown in fig. 8. It is understood from this figure that the long and short scale flow structures are separated well (figs. 8(b) and 8(c)). That is, the long-period fluctuation can be captured by $\overline{u}_{-6}^{(1)}$, having the contribution of over 25% of the total fluctuation energy.

Lastly, correlation between the axial fluctuation and the radial fluctuation was studied. Figure 9 shows the random coefficients of the first mode and second mode as to the axial data and the radial data (x/b = 0.8). There is the lag of the dimensionless time of 0.04 between these two directional components due to a measurement problem. The positive and negative signs of the random coefficient are dependent on the eigenfunction. The time delay τ was varied and the correlation coefficient between the random coefficients was obtained as shown in fig. 10. The correlation between $u^{(1)}$ vs. ($w^{(1)}$ or $w^{(2)}$) is identical to the distribution of the time scale corresponding to the long-period fluctuation, where radial inflow and outflow repeats along with the repetition of the slow acceleration and deceleration of the axial velocity. Between $u^{(2)}$ vs. ($w^{(1)}$ or $w^{(2)}$), the correlation distribution is seen in response to the self-exited oscillation period but their correlation is weak.

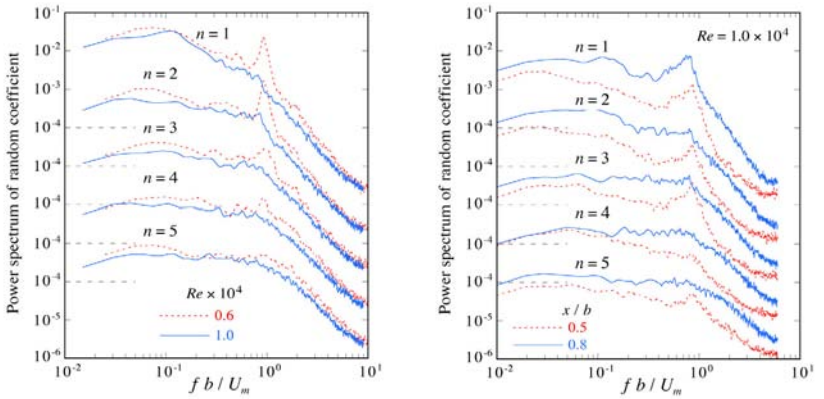

(a) the axial direction (b) the radial direction

Figure 6: Power spectra of the random coefficient.

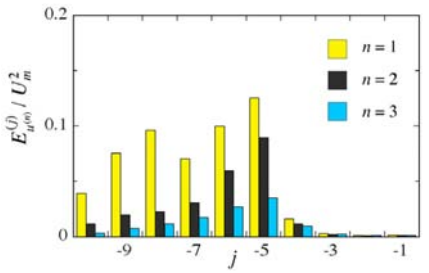

Figure 7: Wavelet spectrum of the random coefficient in the axial direction at $Re = 0.6 \times 10^4$.

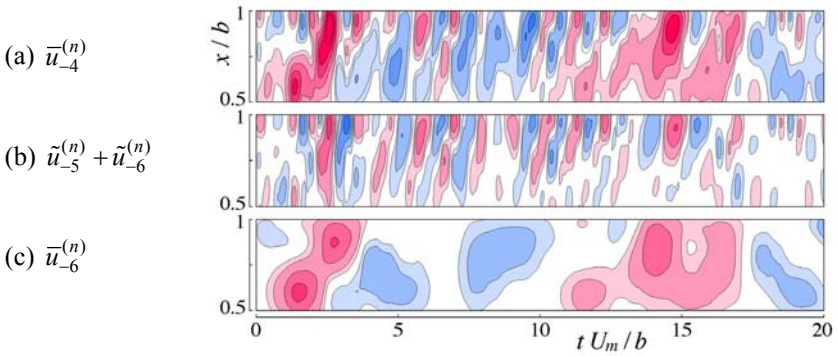

Figure 8: Velocity maps reconstructed with the first three modes.

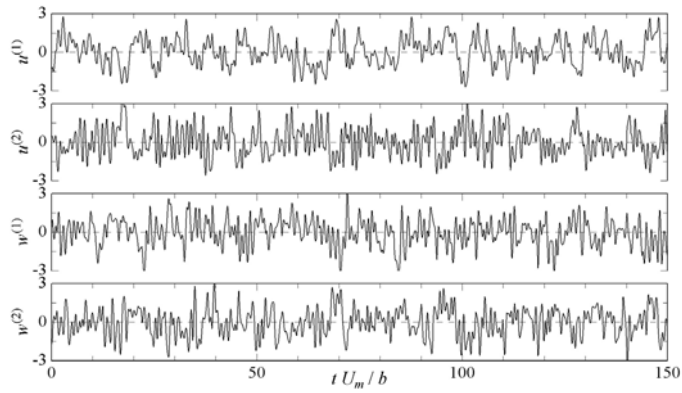

Figure 9: Traces of the random coefficients at the first two POD-modes for $u(x, t)$ and $w(z, t)$ at $x/b = 0.8$, which were simultaneously measured.

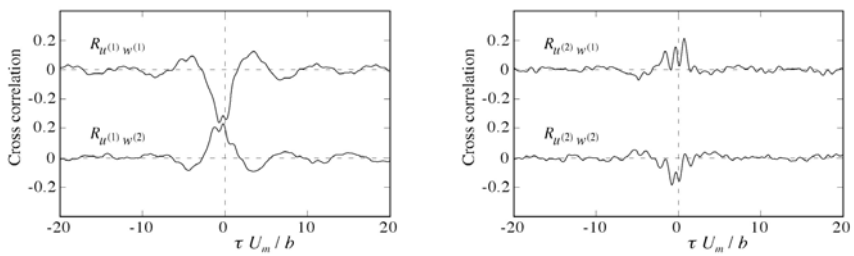

(a) $u^{(1)}w^{(1)}$ and $u^{(1)}w^{(2)}$ (b) $u^{(2)}w^{(1)}$ and $u^{(2)}w^{(2)}$

Figure 10: Correlation between the random coefficients at the two POD modes.

4 Conclusions

The results of this study are summarized as follows:

(1) Three patterns of flow fields were demonstrated according to the mode of interaction between the separating shear layer and the downstream cavity edge through visualized observation. Also, the mean velocity and vorticity within the water channel were defined through velocity measurement by the PIV, and streakline patterns were shown schematically.

(2) Axial and radial measurements were taken by the UVP, and the measurement results were analyzed by the POD. In both directions, fluctuation energy over 80% was captured in three low-order modes. From the power spectra of the random coefficients, the dominances of two time scales were demonstrated.

(3) When the time scales of the random coefficient were separated by using the discrete wavelet transformation and then reconstructed, the flow structures of the two scales could be separated and examined.

References

[1] Rockwell, D. & Naudascher, E., Review - self-sustaining oscillations of flow past cavities. *Trans. ASME: J. Fluids Eng.*, **100**, pp. 152-165, 1978.

[2] Grace, S.M., An overview of computational aeroacoustic techniques applied to cavity noise prediction. *AIAA Paper* 2001-0510, 2001.

[3] Lin, J.-C. & Rockwell, D., Organized oscillations of initially turbulent flow past a cavity. *AIAA J.*, **39**, pp. 1139-1151, 2001.

[4] Howe, M. S., Edge, cavity and aperture tones at very low mach numbers. *J. Fluid Mech*., **330**, pp. 61-84, 1997.

[5] Takeda, Y., Velocity profile measurement by ultrasonic Doppler method. *Exp. Thermal & Fluid Sci.*, **10**, pp. 444-453, 1995.

[6] Sarohia, V., Experimental investigation of oscillations in flows over shallow cavities. *AIAA J.*, **15**, pp. 984-991, 1977.

[7] Gharib, M., Response of the cavity shear layer oscillations to external forcing. *AIAA J.* **25**, pp. 43-47, 1987.

[8] Gharib, M. & Roshko, A., The effect of flow oscillations on cavity drag. *J. Fluid Mech.*, **177**, pp. 501-530, 1987.

[9] Rockwell, D. & Knisely, C., The organized nature of flow impingement upon a corner. *J. Fluid Mech.*, **93**, pp. 413-432, 1979.

[10] Rockwell, D. & Knisely, C., Observations of the three-dimensional nature of unstable flow past a cavity. *Phys. Fluids*, **23**, pp. 425-431, 1980.

[11] Neary, M.D. & Stephanoff, K.D., Shear-layer-driven transition in a rectangular cavity. *Phys. Fluids*, **30**, pp. 2936-2946, 1987.

[12] Meganathan, A.J. & Vakili, A.D., An experimental study of open cavity flows at low subsonic speeds. *AIAA Paper* 2002-0280, 2002.

[13] Inoue, Y., Yamashita, S. & Kondo, K., The ultrasonic velocity profile measurement of flow structure in the near field of a square free jet. *Exp. Fluids*, **32**, pp. 170-178, 2002.

Section 4
Multiphase flow

This page intentionally left blank

Study of bubbling fluidization dynamics via Digital Image Analysis Technique

A. Busciglio, G. Micale, L. Rizzuti & G. Vella
Dipartimento di Ingegneria Chimica, dei Processi e dei Materiali, Università degli Studi di Palermo, Italy

Abstract

In the area of chemical engineering, fluidization is a widely employed technology for a number of industrially important processes. A sound understanding of the mechanisms governing the complex flow phenomena involved in a fluidized bed still remains an open technical and scientific issue.

The principal difficulty in analysing fluidization quality and bubble dynamic is concerned with the possibility of measuring or predicting the physical and geometrical properties of gas bubbles chaotically rising in a solid granular medium.

In recent years the use of Computational Fluid Dynamics (CFD) has been significantly increasing to simulate multi-phase flows. It is invariably emphasized that a necessary step towards the development of reliable fully predictive CFD models is an extensive experimental validation of the simulation results.

On the above basis, the present work focuses on the statistical analysis of the behaviour of a 2-D fluidized bed operating under bubbling and slugging conditions. Experimental data are collected by the means of a purposely developed Digital Image Analysis Technique (DIAT). DIAT is capable of measuring several bubbles properties simultaneously. Moreover it could be used without any modification for computational data analysis, thus providing the answer to the need for close comparison between experimental and computational data. In fact, in many cases, direct experimental validation of CFD simulation is difficult and cumbersome, since different level of detail is available in experimental and computational investigations. In this work, the development of an image analysis technique available for both experimental and computational data does allow direct and effective quantitative comparison.

Keywords: multiphase flow, CFD, image analysis.

WIT Transactions on Engineering Sciences, Vol 59, © 2008 WIT Press
www.witpress.com, ISSN 1743-3533 (on-line)
doi:10.2495/AFM080211

1 Introduction

Many of the characteristic features of gas-fluidized beds, like the excellent solid mixing, heat and mass transfer properties, can be related to the presence of bubbles and are dominated by their behaviour. A deeper knowledge of the fluidized bed hydrodynamics and on how such hydrodynamics are affected by the operative conditions, especially geometry changes and plant scale-up, would provide the base for the development of a fully predictive model describing the gas solid flow in a fluidized bed.

The gas bubbles rising up through a typical fluidized bed ensure that the particles are circulated throughout the bed so that properties and process condition could be considered uniform, but at the same time could eventually allow gas bypass, depending on operative conditions. They have a considerable importance in the fluidized solid–gas systems because they govern hydrodynamics and efficiency of the operation for which the bed is used.

The recent development of mathematical modelling of particulate solids behaviour together with the increased computing power enables researchers to simulate the behaviour of fluidized powders and to link fundamental particle properties directly to the powder behaviour and predict the interaction between particles and gaseous or liquid fluids. In this regard, Computational Fluid Dynamics (CFD) modelling provides a fundamental tool to support engineering design and research in multiphase systems. Many Authors recognise that computational modelling in multi-phase systems has the potential to increase process efficiency and reduce the number of scale-up steps in the design of reliable commercial plants.

It is invariably emphasized that a necessary step towards the development of reliable fully predictive CFD models is an extensive experimental validation of the simulation results. In the first instance, the experimental validation will come to assess the CFD model chosen to simulate the investigated regimes.

On the above basis, the present work focuses on the simulation of a 2-D fluidized bed operating under bubbling and slugging conditions carried out with the use of the commercial CFD code Ansys CFX-10.0. Computational results are post-processed by a Digital Image Analysis Technique, [1], and compared with experimental data.

2 Literature review

Eulerian–Eulerian continuum modelling of multiphase flows, with the fluid and solid phases treated as interpenetrating continuum phases, is the most commonly used approach for fluidised bed simulations, [2]. The general idea in formulating the multi-fluid model is to treat each phase as an interpenetrating continuum, and therefore to construct integral balances of continuity, momentum and energy for both phases, with appropriate boundary conditions and jump conditions for phase interfaces. Since the resultant continuum approximation for the solid phase has no equation of state and lacks variables such as viscosity and normal stress [2], certain averaging techniques and assumptions are required to obtain a complete

momentum balance for the solids phase. In the last decades many investigators tried to develop a theory of particle collision based on the kinetic theory approach by [3]. The solid-phase momentum equation contains an additional term to account for momentum exchange due to particle–particle collisions. The absence of the stress term of the particle phase in the particulate momentum equation has led to different models adopting different closure methods, including the kinetic theory model [4-6]. The application of the kinetic theory to model the motion of a dense collection of nearly elastic spherical particles is based on an analogy to the kinetic theory of dense gases. A granular temperature, Θ, is defined to represent the specific kinetic energy of the velocity fluctuations or the translational fluctuation energy resulting from the particle velocity fluctuations. In granular flow, particle velocity fluctuations about the mean are assumed to result in collisions between particles being swept along together by the mean flow. The granular particle temperature equation can be expressed in terms of production of fluctuations by shear, dissipation by kinetic and collisional heat flow, dissipation due to inelastic collisions, production due to fluid turbulence or due to collisions with molecules, and dissipation due to interaction with the fluid [5].Numerous studies have shown the capability of the kinetic theory approach for modelling bubbling fluidized beds (e.g. [2, 4, 6, 7, 8]).

Once developed appropriate models for the explicit formulation of solid phase stress tensor, the inter-phase momentum transfer between gas and solid phases is still needed to mathematically close the problem. The momentum exchange (represented by a drag force) is one of the dominant forces in the gas- and solid-phase momentum balances. Numerous correlations for calculating the momentum exchange coefficient of gas–solid systems have been reported in the literature, including those of Syamlal and O'Brien [9], Gidaspow [5], and Wen and Yu [10].

3 Experimental set-up

The fluid-bed reactor purposely designed and built for the present investigation is made of Perspex® with dimensions equal to 800 (height) x 180 (width) x 15 (depth) mm. The whole experimental setup is shown in figure 1(a).

The reactor is therefore almost two-dimensional, thus allowing visual observations of bubble dynamics within the bed. A plastic porous distributor, whose thickness is equal to 10 mm, is placed at the bottom of the particle bed. Below the distributor a wind box allows to equalize the gas flow.

Glass ballotini in the size range 212-250 μm were used for the experimental runs with density equal to 2500 kg/m³. The particles were filled up to a bed height of 360mm, i.e. twice the bed width. The value of u_{mf} was experimentally determined and found equal to 5.24 cm/s. Also the value of gas voidage has been experimentally determined and found equal to 0.385. In these conditions the fluidized bed had a typical Geldart Group B system behaviour for both particulates. Air was used as fluidizing gas, at a velocity equal to 3.4 times the u_{mf}.

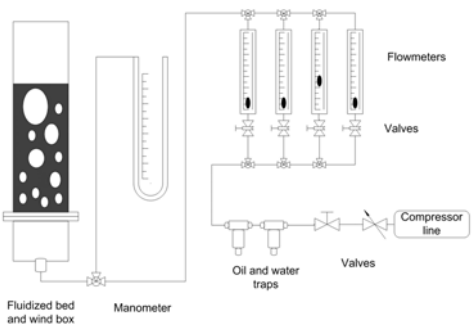

Figure 1: Experimental set-up.

The bubble-related flow structures were visualized with the aid of a continuous back-lighting device obtained by placing six fluorescent lamps at the back side of the bed, at approximately 10 cm, and recorded by a commercial digital camcorder (Sony, model DCRTRV530E PAL), placed opposite to the bed at a distance of 270cm. The digital visual acquisition system allowed to collect images of the bed at a frequency of 25 Hz. Each experimental acquisition provides at least 500 frames, equal to 20 seconds of real time experiment. Preliminarily, the measurement device was accurately calibrated by means of a purposely generated set of still images that included horizontal and vertical scales, with rectangular, circular and ellipsoid objects. The image processing routine was developed on Matlab 7.0 (The MathWorks inc.), using the Image Processing Toolbox. Thanks to the flexibility of the Matlab environment almost all steps in image processing, data acquiring and elaboration could be easily automated. The reader is referred to Busciglio et al., [1], for full details on the experimental set-up adopted and measurement techniques.

4 Computational models and methods

In this study the Eulerian-Eulerian Multi-phase Flow Model (MFM) coupled with the Granular Kinetic Theory (GKT) has been adopted to study the behaviour of gas-solid fluidized beds. This choice is a standard option of the presently adopted CFD code Ansys CFX-10.

Continuity and momentum balance equations are thus solved for each phase using a classical Eulerian–Eulerian description. The standard GKT model is adopted for estimating rheological properties of fluidized solid phase and standard Wen and Yu, [10], model is adopted for estimate the momentum exchange between phases at the phase boundaries.

Because of the similarities between particle-particle interactions and molecular interactions in a gas, the concepts from gas kinetic theory can be used to develop a model for the solids stress tensor. Complete details on the derivations and applications to dense phase flow can be found in Gidaspow [5].

The particulate phase is modelled as a population of identical, smooth and inelastic spheres. Particle-particle interactions are described as a binary instantaneous collisions, resembling those between gas molecules.

As far as the numerical aspects are concerned, CFD simulations were performed in a 2D fashion choosing a computational grid consisting of 5mm square cells, with 36(X) x 288(Y) cells. Thus the width of the computational domain exactly coincides with that of the real lab-scale bed previously detailed, conversely the height of the computational domain in fact is bigger than the real bed (i.e. 800mm) in order to apply a fully developed flow condition at the top of the freeboard. The lateral walls were modelled using the standard no-slip boundary condition. The upper section of the simulated geometry, or freeboard, was considered to be occupied by gas only. A simple pressure boundary condition was imposed at the top of freeboard (i.e. fully developed flow condition). A Dirichlet boundary condition was employed at the bottom of the bed to specify a uniform vertical gas inlet velocity throughout the distributor. Symmetry planes were imposed on the front and rear faces of the simulated bed.

The initial conditions specify only the distribution of solid volume fraction within the bed of solids which was set equal to 0.65.

Typical running CPU times for CFX10 simulations were equal to about 100 hrs for 10 seconds of real time simulated with a fixed time step interval $\Delta t = 10^{-4}$s on a Dell Dimension 8300 Personal Computer.

The simulated case is identical to that experimentally investigated.

5 Post-processing procedure via Digital Image Analysis Technique

The quantitative data on experimental and simulated bubble dynamics have been obtained by the means of an original Digital Image Analysis Technique, [1].

This is based on bed images, suitably obtained with backlighting in order to enhancing the contrast between the emulsion phase and the bubble phase. Bubbles in the bed are detected because they create transparent areas in the flat cross-sectional plane of the bed, through which light, emitted at the back of the bed can pass through and reach the camera.

The problem of phase separation enhancing in experiments does not exists in simulation. As a matter of fact, it is possible to obtain, by the mean of code post-processor, full coloured concentration maps. Images ready for Image Processing can be obtained by superimposing, as output of post-processor, black and white images, in which areas having solid concentration less than the conventional value of 0.15 are drawn as white areas and other areas are drawn as black ones.

By means of the DIAT, geometric properties of all bubbles found in the image are measured. The above mentioned Digital Images Analysis Technique (DIAT) can be easily used for both experimental images and computational volume fraction maps, without any adjustment. The data obtained can be used to rebuild some important statistical information about the bubble dynamics, such as:

i) Statistical probability density of bubble equivalent diameters in the whole bed and as function of bubble distance from the distributor;
ii) Average bubble number as function of the distance from the distributor;

The rising velocity distribution can be found by comparing bubble centroids positions in subsequent frames. Within the present work a Lagrangian Velocimetry Technique (LVT) has been adopted, [1], able to locally track each bubble in his chaotic rising motion along the bed.

The data processed through the use of the LVT allow to rebuild fundamental information on bubble dynamics, such as:
i) variation of bubble rise velocity with bubble diameter, as obtained by smoothing processing of raw data by means of a bisquare weight function ;
ii) Statistical probability density of bubbles rise angles;

The direct rigorous comparison between experimental and computational data on bubble dynamics so obtained will allow coherent validation of computer simulation of bubbling fluidized beds.

6 Results and discussions

In Figure 2.a and figure 2.b the experimental and computational distributions of bubble size distribution are reported. A characteristic positive skewed distributions are generally observed. This kind of distribution is in accordance with the relevant literature, [11].

It is worth noting that a single skewed distribution, such as Gamma distribution or Log-normal distributions are not able to correctly follow data trend. Theoretical analyses, [12], have shown that Gamma distribution can be obtained if a coalescence-driven bubble enlargement is considered.

On the other hand, complex nucleation and splitting phenomena generally give rise to significant amount of bubbles with smaller diameters at any distance from distributor, thus leading to a first (almost constant) peak at smaller diameter, and a moving peak typical of coalescence-enlarging bubbles.

This considerations lead us to consider, as fitting curves, the linear combination of Gamma distributions shown in Equations 1, that shows excellent fitting.

$$pdf(d_b) = \varphi \frac{1}{\gamma_2^{\gamma_1}\Gamma(\gamma_1)} d_b^{\gamma_1 - 1} e^{-\frac{d_b}{\gamma_2}} + (1-\varphi)\frac{1}{\gamma_4^{\gamma_1}\Gamma(\gamma_3)} d_b^{\gamma_3 - 1} e^{-\frac{d_b}{\gamma_4}} \tag{1}$$

where Γ is the integral Gamma function.

$$\Gamma(m) = \int_0^\infty e^t t^{m-1} \mathrm{dt} \tag{2}$$

The numerical predictions appear to qualitatively estimate the complex bimodal trend of bubbles size distribution, even if the quantitative agreement may still improve.

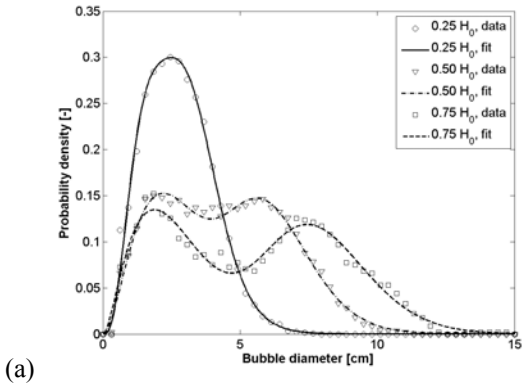

(a)

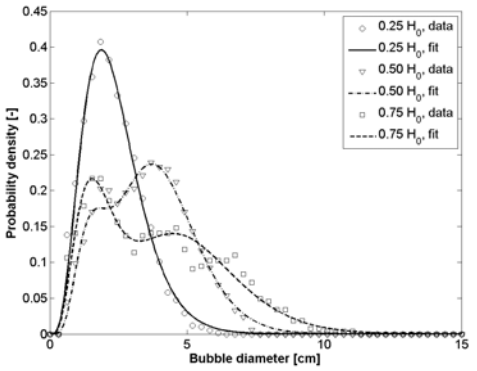

(b)

Figure 2: Experimental (a) and computational (b) probability density distributions of bubble diameter at different distances from distributor and relevant curve fitting.

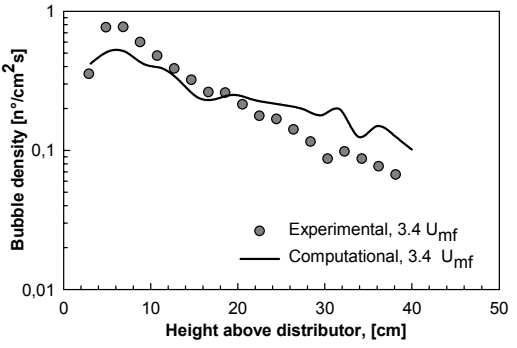

Figure 3: Bubble density along bed height.

Figure 3 reports the experimental and computational bubble density profiles along the bed height. It must be pointed out that a linear decay of bubble density in a logarithmic chart would characterize a constant bubble coalescence rate, while a constant value of bubble density would be that typical of fully developed slug flows.

The experimental data trend is characterized by a clear linear decay, related to a net constant decay rate of bubble density along bed height. Such trend appear to be sufficiently predicted by the code, even if somewhat lower decay rate is predicted.

As far as the experimental raw rise velocity data are concerned, a significant scattering has been observed. This is not surprising at all given the chaotic behaviour typical of bubbling fluidized beds. Therefore a choice was made to report in Figure 4 only the smoothed version of the rise velocity data. It can be noted that the numerical predictions are in satisfactory agreement with experimental data, particularly for the general trend. Moreover a comparison with the power law proposed by Davidson [13], $u_b=\varphi(gd_b)^{0.5}$ shows that the correlation acceptably predicts the trend of bubble rise velocity increase with increasing bubble diameter, although some general level of overestimation is found at all ranges.

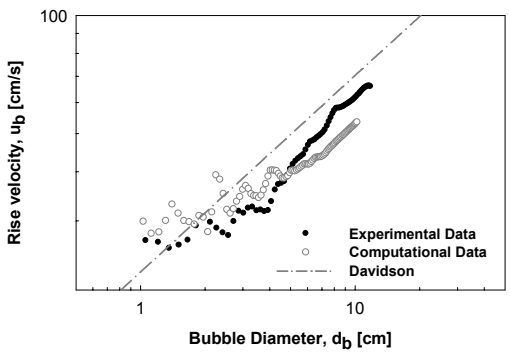

Figure 4: Smoothed distribution of bubble rise velocities.

In Figure 5 the probability distributions of rising angle for both experimental and computational data are reported. It must be noted that the rising angles always follow an almost symmetrical distribution, with the average value near the vertical rise angle, as physically expected.

Given the random lateral motion of bubbles a sort of Gaussian distribution may be expected to fit the data. However careful observation of the shape of the distribution, with respect to the relevant Gaussian fit curve, highlights a positive excess kurtosis. This can be principally due to the near wall bubbles, with limited random lateral motion. It is thus expected that fluidized beds with larger width could present rise angle distributions more similar to Gaussian distributions. The comparison of the computational distribution with the experimental one shows

an acceptable agreement along most of the distribution interval, while significant underestimation of the probability density is found around the mean value of the distribution.

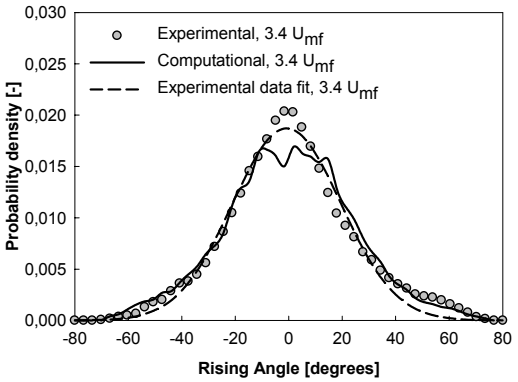

Figure 5: Probability density of bubble rise angle.

7 Conclusions

The direct comparison between experimental and computational data on bubble dynamics obtained by means of a Digital Image Analysis Technique allowed the validation of the predictive capability of the Ansys CFX 10.0 CFD code.

In particular the validation of CFD predictions with experimental data focused on the analysis of selected bubbles characteristics, namely the bubble diameter probability density function, bubble density, bubble rise velocity and bubble rise angle.

The statistical significance of the results, due to the substantial quantity of processed data, allowed to identify interesting features of fluidized bed dynamics, such as the bimodality of the local bubble size distribution or the positive excess kurtosis of rise angle distributions. In this regard the code capability in predicting such complex behaviours has been tested with encouraging results.

The present work draws the conclusion that the actual state of the art in mathematical modelling and computer simulation of bubbling fluidized beds allows the qualitative prediction of several phenomena, but major quantitative improvements are still an open task.

References

[1] Busciglio A., Vella G., Micale G., Rizzuti L., *Analysis of the bubbling behaviour of 2-D gas fluidized beds. Part I: Digital Image Analysis Technique*, Chemical Engineering Journal, doi:10.1016/j.cej.2007.11.015, 2007.

[2] Pain C.C., Mansoorzadeh S., de Oliveira C.R.E., *A study of bubbling and slugging fluidised bed s using the two-fluid granular temperature model*, International Journal of Multiphase Flow, 27, pp. 527–551, 2001.
[3] Chapman S., Cowling T.G., *The mathematical theory of non-uniform gases*, Cambridge University Press, Cambridge, UK, 3rd edition 1970.
[4] Sinclair J.L., Jackson R., *Gas–particle flow in a vertical pipe with particle–particle interactions*, AIChEJ, 35, pp. 1473–1486 1989.
[5] Gidaspow D., *Multiphase flow and fluidization*, Academic Press, San Diego, 1994.
[6] Hrenya C. M., Sinclair J. L., *Effects of particle–phase turbulence in gas–solid flows*, AIChE J., 43, pp. 853–869, 1997.
[7] Ding J., Gidaspow D., *A bubbling fluidization model using kinetic theory of granular flow*, AIChE Journal, 36, pp. 523–538 1990.
[8] Gelderbloom S.J., Gidaspow D., Lyczkowski R.W., *CFD simulations of bubbling/collapsing fluidized beds for three Geldart groups*, AIChE J., 49, pp. 844–858, 2003.
[9] Syamlal M., O'Brien T. J., *Computer simulation of bubbles in a fluidized bed*, AIChE Symposium Series, 85, pp. 22–31, 1989.
[10] Wen C.Y., Yu Y.H., *Mechanics of fluidization*, Chemical Engineering Progress Symposium Series, 62, pp. 100–111, 1966.
[11] Rowe P.N., Yacono C., *The distribution of bubble size in gas fluidised beds*, Trans. Instn. Chem. Engrs., 53, pp. 59–60 1975.
[12] Argyriou D.T., List H.L., Shinnar R., *Bubble growth by coalescence in gas fluidized beds*, AIChE J., 17, pp. 122, 1971.
[13] Davidson J.F., Harrison D., *Fluidised Particles*, Cambridge University Press, 1963.

New ways of fluidization in a centrifugal field

J. De Wilde
Department of Materials and Process Engineering,
Université catholique de Louvain, Belgium

Abstract

Both numerical and experimental observations on two novel technologies for fluidization in a centrifugal field are presented.

In the rotating fluidized bed in a static geometry, the rotating motion of the particle bed is generated by the tangential injection of the fluidization gas in the fluidization chamber via multiple gas inlet slots, so i.e. by the tangential fluidization of the particle bed. The fluidization gas is forced to leave the fluidization chamber via a centrally positioned chimney results in a combined tangential-radial motion of the fluidization gas through the particle bed. In case the radial gas-solid drag force balances the centrifugal force, radial fluidization of the particle bed can be obtained. As a result of the tangential fluidization of the particle bed in rotating fluidized beds in a static geometry, radial fluidization of the particle bed is, however, not necessary to take full advantage of the improved particle bed uniformity and the higher gas-solid slip velocities at which fluidized beds can be operated in a centrifugal field.

The rotating chimney can be combined with any rotating fluidized bed technology and allows increasing locally, i.e. in the vicinity of the chimney, the centrifugal force. The rotating chimney consists of multiple blades and rotates in the same sense than the rotating particle bed, but at higher rotational speeds. The fluidization gas is forced through the chimney blades to the chimney outlet. As a result of the centrifugal force generated by the rotating chimney, particles are not entrained by the fluidization gas, but remain rotating around the chimney in a fluidized state.

Keywords: fluidization, rotating fluidized bed, rotating chimney, process intensification, centrifugal force.

WIT Transactions on Engineering Sciences, Vol 59, © 2008 WIT Press
www.witpress.com, ISSN 1743-3533 (on-line)
doi:10.2495/AFM080221

1 Introduction

Fluidization in the earth gravitational field faces limitations in the gas-solid slip velocities and in the particle size that can be used. The limitation in the gas-solid slip velocity may induce external mass and heat transfer limitations, that is, in the gas-solid mass and heat transfer rates [1]. The limitation in the particle size may induce internal mass transfer limitations. Internal heat transfer limitations can usually be neglected by the large heat capacity of the particles.

Fluidization in a centrifugal field may allow to overcome the above mentioned limitations [2]. In the currently existing so-called rotating fluidized beds, the fluidization chamber is rotated fast around its axis of symmetry by means of a motor in order to generate a centrifugal field [2–6]. The particles form a cylindrically shaped particle bed against the outer cylindrical wall of the fluidization chamber. Radial fluidization of the particle bed is introduced by injecting the fluidization gas radially through perforations in the outer cylindrical wall of the fluidization chamber and by evacuating the fluidization gas via a centrally positioned chimney. It should be emphasized that in the current type of rotating fluidized beds, the particle bed is only radially fluidized by balancing the centrifugal force and the radial gas-solid drag force.

The current type of rotating fluidized beds has never been used on a large scale in the (petro)chemical industries. Major challenges encountered were related to the moving geometry, i.e. the rotating fluidization chamber, and include sealing, vibrations, particle feeding and removal, etc.

In the present work, two novel technologies for fluidization in a centrifugal field are presented and discussed: the rotating fluidized bed in a static geometry and the rotating chimney [7–9]. The present paper does not aim to give a detailed overview of experimental or simulation results, but rather summarizes the concept, the recent findings, and the potential of the novel technologies.

2 Rotating fluidized beds in a static geometry

2.1 The concept

In a rotating fluidized bed in a static geometry [7,9], the rotating motion of the particle bed is generated by the tangential injection of the fluidization gas in the fluidization chamber via multiple gas inlet slots in its outer cylindrical wall (Figure 1). The fluidization gas is forced to leave the fluidization chamber via a centrally positioned chimney. Whereas in the current rotating fluidized beds, the motion of the fluidization gas through the particle bed is mainly radial, in rotating fluidized beds in a static geometry, the fluidization gas is forced to move in a combined tangential-radial way through the particle bed. This is at the origin of the unique characteristics of rotating fluidized beds in a static geometry with respect to flexibility in the fluidization gas flow rate. Indeed, as can be theoretically shown [9] and as will be demonstrated in what follows, in rotating fluidized beds in a static geometry, the fluidization gas flow rate affects the centrifugal force and the counteracting radial gas-solid drag force in a similar

way. This allows to vary the fluidization gas flow rate while hardly affecting the radial bed expansion or the particle losses via the chimney.

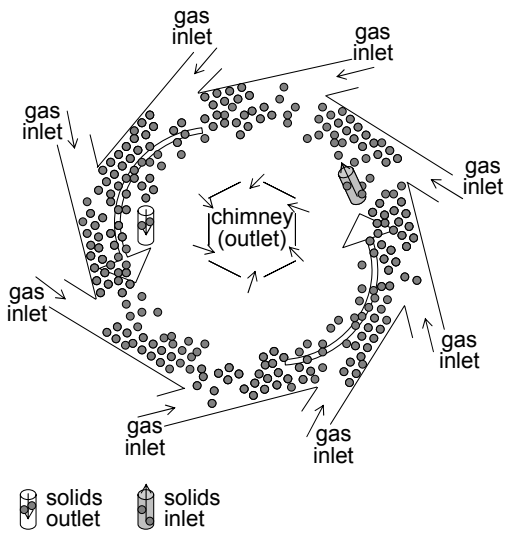

Figure 1: The concept of the rotating fluidized bed in a static geometry.

2.2 Basic experimental observations

Experiments were carried out using two different fluidization chamber designs and two different types of particles. The major fluidization chamber design parameters and particle characteristics are listed in Table 1. The first fluidization chamber has a cylindrical design and is 24 cm in diameter. The second fluidization chamber has a polygonal design and is 36 cm in diameter. The particles of the 1G-Geldart D-type are polymer pellets with an average size of 3.5 mm and a density of 950 kg m^{-3}. The particles of the 1G-Geldart B-type are alumina or salt particles with an average size of 350 μm and a density of about 2160 kg m^{-3}.

Independent of the fluidization chamber design, the particles fluidized, or the fluidization gas flow rate, the solids loading in the fluidization chamber was found to be crucial in obtaining a stable rotating fluidized bed in a static geometry (e.g. Figure 2 for the 24-cm diameter fluidization chamber and the polymer particles). At very low solids loadings, channelling is observed. In the case of channelling, a strongly non-uniform distribution of the particles and the fluidization gas in the axial direction of the fluidization chamber is observed. At somewhat higher solids loadings, slugging occurs (Figure 2). In the case of slugging, a strongly non-uniform distribution of the particles and the fluidization gas in the tangential direction occurs. A particle *slug* forms that rotates in the fluidization chamber and most of the fluidization gas enters the fluidization chamber via the gas inlet slots not facing the resistance of a particle bed [9]. At

sufficiently high solids loadings, a stable rotating fluidized bed is formed, rendering the gas-solid contact optimal (Figure 2). It should be emphasized that the fluidization gas flow rate has only a minor impact on the flow regime that is obtained in rotating fluidized beds in a static geometry (Figure 2).

This can be explained by the similar effect of the fluidization gas flow rate on the centrifugal force and the counteracting radial gas-solid drag force, a major feature of rotating fluidized beds in a static geometry.

Table 1: Fluidization chamber and particle characteristics.

	Unit	**Value**
Fluidization chamber diameter	[m]	(i) $24 \cdot 10^{-2}$, cylindrical (ii) $36 \cdot 10^{-2}$, polygonal
Fluidization chamber length	[m]	$13.5 \cdot 10^{-2}$ $11.5 \cdot 10^{-2}$ (rotating chimney)
Chimney diameter	[m]	(i) $15 \cdot 10^{-2}$ / $16 \cdot 10^{-2}$ (rotating chimney) (ii) $12 \cdot 10^{-2}$
Number of tangential gas inlet slots	[/]	(i) 12 or 24 (ii) 12
Gas inlet slot width	[m]	(i) $2.3 \cdot 10^{-3}$ (ii) $4 \cdot 10^{-3}$
Number of chimney outlet slots	[/]	1 32 (rotating chimney)
Chimney outlet slot width	[m]	(i) $8 \cdot 10^{-2}$ (ii) $9 \cdot 10^{-2}$
Number of solids inlets and outlets	[/]	1 / 1, via opposite end plates
Total gas flow rate	[$Nm^3\ h^{-1}$]	650-850
Outlet pressure	[Pa]	101300
Temperature	[K]	333
Particle material	[/]	a) polymer b) salt / alumina
Average particle size	[m]	a) $2 \cdot 10^{-3}$ (length)-$5 \cdot 10^{-3}$ (diameter) (cylinder pellets) b) $350 \cdot 10^{-6}$
Particle density	[$kg\ m^{-3}$]	a) 950 b) 2160

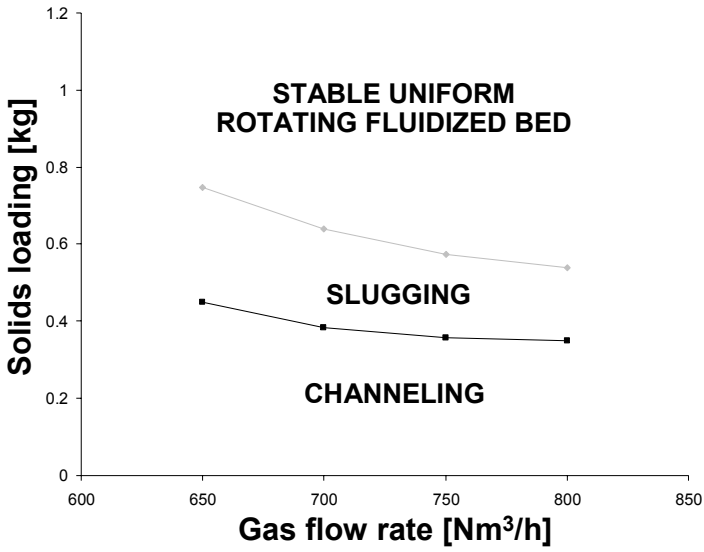

Figure 2: Different flow regimes as a function of the fluidization gas flow rate and the solids loading in the fluidization chamber. Fluidization chamber and particle characteristics: see Table 1, (i) and (a).

Figure 3 shows the typical experimentally observed behaviour at sufficiently high solids loadings with the two different types of particles using the same non-optimized 24-cm diameter fluidization chamber design. Similar observations were found with the 36-cm diameter fluidization chamber design [9]. The main difference in the behaviour of the two types of particles is found in the radial bed expansion, that is, the radial fluidization of the rotating particle bed. With the polymer particles, radial fluidization is nearly absent. As a result, an excellent separation of the particles and the fluidization gas leaving the fluidization chamber is obtained with minimal particle losses via the chimney. Despite the absence of radial fluidization of the particle bed, particle mixing is pronounced by the tangential fluidization that is introduced. The absence of radial fluidization indicates an unbalance between the centrifugal force and the radial gas-solid drag force. This implies that part of the centrifugal pressure generated by the rotating motion of the particle bed is supported by the outer cylindrical wall of the fluidization chamber, i.e. the rotating particle bed is pushed against the outer cylindrical wall of the fluidization chamber. The unbalance of the centrifugal force and the radial gas-solid drag force when using the polymer particles with the current fluidization chamber designs can be theoretically proven [9] and is confirmed by a comparison of the measured centrifugal pressure drop, derived from the measured particle bed rotational speed and solids loading in the fluidization chamber, and the measured radial pressure drop over the particle bed. With the alumina or salt particles, radial fluidization of the rotating particle bed is pronounced and bubble formation is observed (Figure 3).

Bubbles are transported in a combined tangential-radial motion through the particle bed [9]. Furthermore, most of the fluidization gas injected via one gas inlet slot is seen to leave the particle bed when approaching the next downstream gas inlet slot. This was confirmed by simulations (§ 2.3). As a result of the radial bed expansion, the separation between the particles and the fluidization gas leaving the fluidization chamber is somewhat less good than with the polymer particles and the particle losses via the chimney are pronounced. The balance between the centrifugal force and the radial gas-solid drag force can be theoretically calculated, confirming radial fluidization using the alumina or salt particles with the current fluidization chamber designs.

(a) polymer particles (b) salt particles

Figure 3: Rotating fluidized bed in a static geometry.(a): polymer particles (Table 1: (i), (a)); (b): salt particles (Table 1: (i), (b)).

2.3 Numerical investigation

Computational Fluid Dynamics (CFD) simulations were carried out to improve comprehension of the gas-solid flow behaviour in rotating fluidized beds in a static geometry. The Eulerian-Eulerian approach [10] was taken and the solid phase physico-chemical properties were calculated using the Kinetic Theory of Granular Flow (KTGF) [11]. Calculations were carried out using the *Fluent* code. Figure 4 shows some typical simulation results for a 36-cm diameter fluidization chamber and the salt particles. Whereas the simulation model or code fails to predict certain experimental observations, as for example bubble formation [9], other experimental observations are clearly confirmed. Upstream of each gas inlet slot, solids accumulation occurs (Figure 4(a)). The fluidization gas injected via a given gas inlet slot is seen to move radially inwards when approaching the next downstream gas inlet slot (Figure 4(b)). This results in a local tangential deceleration of the particle bed. The inertia of the solids prevents them from following the fluidization gas radially inwards (Figure 4(c)) and is at the origin of the solids accumulation upstream of the gas inlet slots.

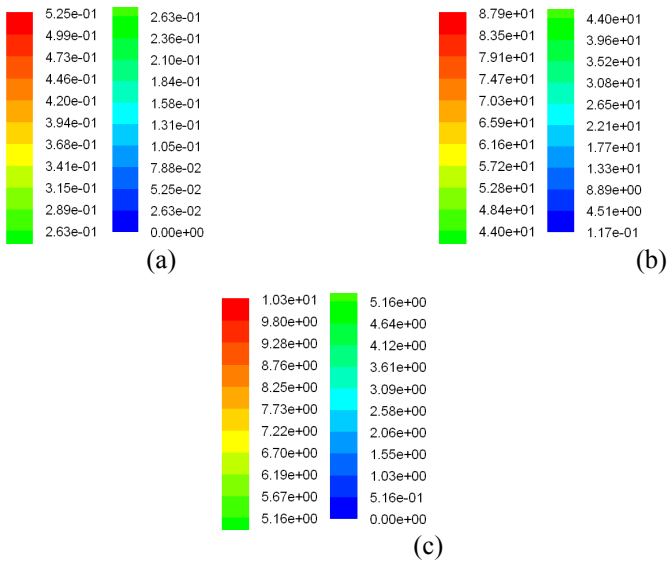

Figure 4: CFD simulation of a rotating fluidized bed in a static geometry.(a) solids volume fraction; (b) gas phase velocity vectors, coloured by the gas phase velocity magnitude; (c) solids velocity vectors coloured by the solids velocity magnitude. Focus on a region in the vicinity of a gas inlet slot.

2.4 Potential applications

Both the experimental observations (e.g. Figure 2) and the numerical simulations confirm the extreme flexibility in the fluidization gas flow rate when using rotating fluidized beds in a static geometry. In particular, this allows operating rotating fluidized beds in a static geometry at much higher, that is, one to several orders of magnitude higher gas-solid slip velocities than conventional fluidized beds. On the one hand, this implies that the residence time of the fluidization gas in the particle bed, i.e. the gas-solid contact time can be made very short. On the other hand, a higher gas-solid slip velocity implies a proportionally higher gas-solid mass and heat transfer coefficient. The possible combination of extremely short gas-solid contact times and extremely high gas-solid mass and heat transfer coefficients renders rotating fluidized beds in a static geometry potentially advantageous for use with extremely fast and highly endo- or exothermic reactions. For certain catalytic reactions, the removal of external mass or heat transfer limitations when using rotating fluidized beds in a static geometry will allow using a more active catalyst and the increase of the overall reaction rate. Internal mass transfer limitations could be removed by using smaller particles [1]. Indeed, even micro- and nano-scale particles were shown to fluidize uniformly in a sufficiently high centrifugal field [12,13]. Summarizing, by allowing operation at significantly higher gas-solid slip velocities and by a

similar impact of the fluidization gas flow rate on the centrifugal force and the counteracting radial gas-solid drag force, rotating fluidized beds in a static geometry pave the way for fluidized bed process intensification, i.e. the use of more compact reactors, and for an improved flexibility in fluidized bed operation.

3 Rotating chimney

3.1 The concept

When fluidizing small particles, in particular micro- and nano-size particles, in any type of rotating fluidized bed, particle entrainment by the fluidization gas to the chimney may be pronounced. To avoid excessive particle losses via the chimney, the chimney design can be modified or a rotating chimney [8] can be used.

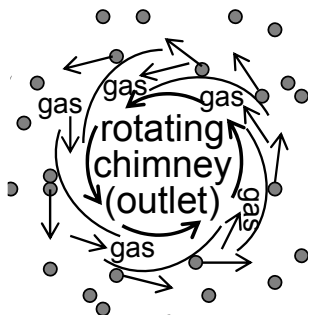

Figure 5: The concept of the rotating chimney.

The rotating chimney consists of multiple blades with inlets to the chimney in between them (previously called 'fluidization chamber outlets') and rotates fast around its axis of symmetry by means of a motor (Figure 5). The fluidization gas is forced to move from the region outside the chimney into the chimney by means of a compressor. Particles in the region outside the chimney cannot follow the fluidization gas into the chimney by the action of the centrifugal force generated by the chimney rotational motion. In case the centrifugal force by the chimney and the radial gas-solid drag force in the vicinity of the chimney are balanced, a rotating fluidized bed around a rotating chimney can be obtained, as will be confirmed by the simulations presented further in this work. In case the centrifugal force by the chimney is much stronger than the radial gas-solid drag force in the vicinity of the chimney, particles will, at contact with the chimney, be ejected more strongly. In such case and if the rotating chimney is used in combination with another rotating fluidized bed technology [2,5,7,9], the rotating chimney allows to build up more easily a high solids loading in the rotating fluidized bed against the outer cylindrical wall of the fluidization chamber. This has been experimentally demonstrated, as will be shown in the next paragraph.

3.2 Basic experimental observations

The action of the rotating chimney was experimentally investigated in combination with a rotating fluidized bed in a 24-cm diameter static fluidization chamber [7,9] and using polymer or salt particles. The fluidization chamber, chimney and particle characteristics are summarized in Table 1.

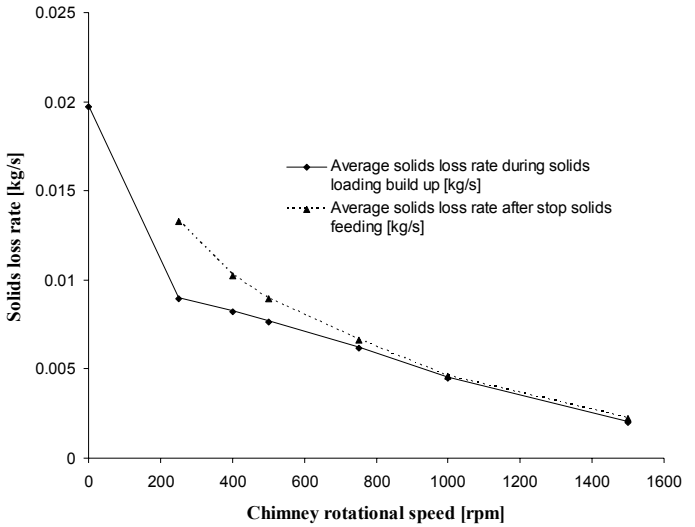

(a)

chimney: 250 rpm

chimney: 1000 rpm

(b)

Figure 6: (a) Solids loss rate via the chimney as a function of the chimney rotational speed; (b) maximum solids loading in the fluidization chamber for a chimney rotational speed of respectively 250 rpm and 1000 rpm. Fluidization chamber and particle characteristics: see Table 1 (i) and (a). Fluidization gas flow rate = 850 Nm^3/h; solids feeding rate = 0.0356 kg/s.

The typical experimentally observed behaviour is illustrated in Figure 6 using the polymer particles. For a given solids loading in the fluidization chamber and fluidization gas flow rate, the particle losses via the chimney decrease significantly with increasing chimney rotational speed (Figure 6(a)). For a given solids feeding rate and fluidization gas flow rate, on the other hand, a significantly higher solids loading in the fluidization chamber can be obtained with increasing chimney rotational speed (Figure 6(b)). These findings hold for the salt particles.

3.3 Numerical investigation

Numerical simulations were carried out to demonstrate the formation of a rotating fluidized bed of small size particles around a rotating chimney. The simulation model and method used are described in § 2.3. The rotating chimney in combination with the static outer cylindrical wall of the fluidization chamber requires the use of a rotating geometry. The mesh used for the simulations is split into two zones, one static and the other rotating together with the chimney. At the interface between the two mesh zones, an interpolation scheme is used for the exchange of information between the two mesh zones.

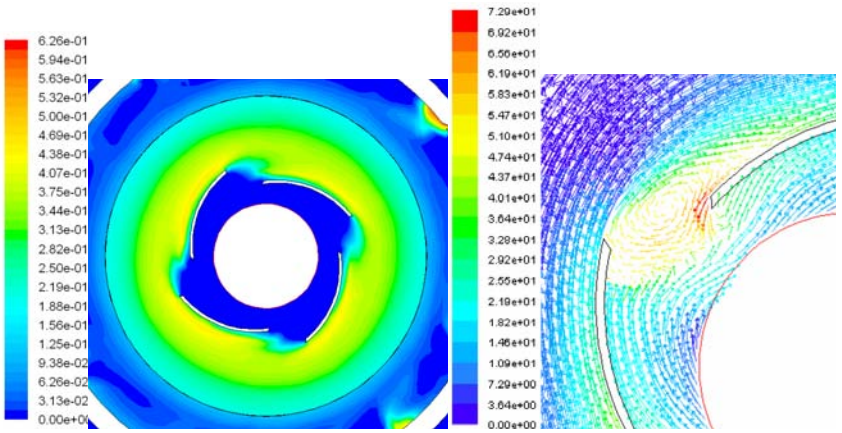

(a) (b)

Figure 7: Simulation of a rotating fluidized bed of 60 μm alumina particles around a rotating chimney. (a) Solids volume fraction; (b) Solids velocity vectors relative to the chimney rotational motion, coloured by the absolute solids velocity magnitude. Focus on a zone between two blades.

Figure 7(a) shows the simulated solids volume fraction profile in a 36-cm diameter fluidization chamber with a 4-blade, 12-cm diameter rotating chimney when fluidizing 60 μm alumina particles. The chimney rotational speed is 4000 rpm (rotations per minute). Figure 7(a) clearly demonstrates that, whereas the fluidization gas is forced to leave the fluidization chamber via the openings

between the chimney blades, the particles cannot follow the fluidization gas into the chimney and form a rotating fluidized bed around the rotating chimney.

Figure 7(b) shows the vectors of the solids velocity relative to the chimney rotational motion coloured by the absolute solids velocity magnitude, focusing on a region between two chimney blades. As seen from Figure 7(b), particles eventually entrained into the chimney by the fluidization gas can be returned to the rotating particle bed around the chimney by the rotating motion of the chimney. This is an important feature of rotating chimneys.

3.4 Potential applications

When used with other rotating fluidized bed technologies, rotating chimneys allow to increase locally, that is, in the vicinity of the chimney, the centrifugal force. As such, rotating chimneys can significantly reduce or even eliminate particle losses via the chimney. This may be of particular importance when fluidizing small, i.e. micro- or nano-scale, particles [12,13]. Furthermore, in certain applications, the particle size changes significantly during the residence time of the particles in the fluidization chamber. In such cases, the rotating chimney opens perspectives for multi-zone or multi-layer fluidized bed technology, with, for example, a rotating fluidized bed of the largest particles near the outer cylindrical wall of the fluidization chamber and a rotating fluidized bed of smaller particles near the chimney.

4 Conclusions

Two novel technologies for fluidization in a centrifugal field are presented and experimentally and numerically investigated. In rotating fluidized beds in a static geometry, the rotating motion of the particle bed and the centrifugal force are generated by the tangential injection of the fluidization gas via multiple gas inlet slots in the outer cylindrical wall of the fluidization chamber. The combined tangential-radial motion of the fluidization gas through the particle bed results in extreme flexibility with respect to the fluidization gas flow rate and, as such, with respect to the gas-solid mass and heat transfer coefficients. With rotating chimneys, the centrifugal force is generated by the rotational motion of the chimney. The radial gas-solid drag force resulting from the fluidization gas being forced into the chimney counteracts the centrifugal force generated by the chimney. In combination with conventional rotating fluidized beds or rotating fluidized beds in a static fluidization chamber, rotating chimneys allow to significantly reduce the particle losses via the chimney and to operate at higher solids loadings in the fluidization chamber. As such, rotating chimneys significantly increase the flexibility in operation of rotating fluidized beds. Rotating chimneys may be particularly advantageous when fluidizing small particles or mixtures of particles with different fluidization properties.

Acknowledgements

Axel de Broqueville is greatly acknowledged for the scientific collaboration and for the financial support of the research. Luc Wautier is greatly acknowledged

for the technical realization of the project and for the help with the experiments. I would like to thank CISM of the Université catholique de Louvain for the use of their computational facilities.

References

[1] Froment, G.F., Bischoff, K.B., *Chemical Reactor Analysis and Design*, Wiley Series in Chemical Engineering, Second Edition, 1990.
[2] Chen, Y.-M., Fundamentals of a centrifugal fluidized bed, *AIChE J.*, **33(5)**, pp. 722–728, 1987.
[3] Kroger, D.G., Levy, E.K., Chen, J.C., Flow characteristics in packed and fluidized rotating beds, *Powder Technol.*, **24(1)**, pp. 9–18, 1979.
[4] Fan, L.T., Chang, C.C., Yu, Y.S., Takahashi, T., Tanaka, Z., Incipient fluidization condition for a centrifugal fluidized bed, *AIChE J.*, **31(6)**, pp. 999–1009, 1985.
[5] Qian, G.-H., Bagyi, I., Burdick, I.W., Pfeffer, R., Shaw, H., Stevens, J.G., Gas-solid fluidization in a centrifugal field, *AIChE J.*, **47(5)**, pp. 1022–1034, 2001.
[6] Watano, S., Nakamura, H., Hamada, K., Wakamatsu, Y., Tanabe, Y., Dave, R.N., Pfeffer, R., Fine particle coating by a novel rotating fluidized bed coater, *Powder Technol.*, **141**, pp. 172–176, 2004.
[7] de Broqueville, Axel : Catalytic polymerization process in a vertical rotating fluidized bed : Belgian Patent 2004/0186, Internat. Classif. : B01J C08F B01F; publication number : 1015976A3.
[8] de Broqueville, A., De Wilde, J., Central rotating chimney apparatus for obtaining a rotating fluidized bed in a cylindrical fixed or rotating fluidization chamber and processes using this apparatus, April 23, 2007: PCT/EP2007/053941 (F-995-WO), European and United States of America patent application.
[9] De Wilde, J., de Broqueville, A., Rotating Fluidized Beds in a Static Geometry: Experimental Proof of Concept, *AIChE J.*, **53(4)**, pp. 793–810, 2007.
[10] Anderson, T., Jackson, R., A Fluid Mechanical Description of Fluidized Beds, *Industrial & Engineering Chemistry Fundamentals*, **6**, pp. 527–539, 1967.
[11] Gidaspow, D., *Multiphase Flow and Fluidization: Continuum and Kinetic Theory Descriptions*, Academic Press, 1994.
[12] Watano, S., Imada, Y., Hamada, K., Wakamatsu, Y., Tanabe, Y., Dave, R.N., Pfeffer, R., Microgranulation of fine powders by a novel rotating fluidized bed granulator, *Powder Technol.*, **131**, pp. 250–255, 2003.
[13] Quevedo, J., Pfeffer, R., Shen, Y., Dave, R., Nakamura, H., Watano, S., Fluidization of nanoagglomerates in a rotating fluidized bed, *AIChE J.*, **52(7)**, pp. 2401–2412, 2006.

Displacement of non-Newtonian compressible fluids in plane porous media flow

R. Ugarelli[1], M. Bottarelli[2] & V. Di Federico[1]
[1]*Dip. di Ingegneria delle Strutture, dei Trasporti, delle Acque, del Rilevamento, del Territorio (D.I.S.T.A.R.T.), Università di Bologna, Italy*
[2]*Dip. di Architettura, Università di Ferrara, Italy*

Abstract

Displacement of non-Newtonian fluid in porous media is of paramount importance in the flow modeling of oil reservoirs. Although numerical solutions are available, there exists a need for closed-form solutions in simple geometries. Here we revisit and expand the work of Pascal and Pascal [4], who analyzed the dynamics of a moving stable interface in a semi-infinite porous domain saturated by two fluids, displacing and displaced, both non-Newtonian of power-law behavior, assuming continuity of pressure and velocity at the interface, and constant initial pressure. The flow law for both fluids is a modified Darcy's law. Coupling the nonlinear flow law with the continuity equation considering the fluids compressibility, yields a set of nonlinear second-order PDEs. If the fluids have the same consistency index n, the equations can be transformed via a self-similar variable; incorporation of the conditions at the interface shows the existence of a compression front ahead of the moving interface. After some algebra, one obtains a set of nonlinear equations, whose solution yields the location of the moving interface and compression front, and the pressure distributions. The previous equations include integrals which can be expressed by analytical functions if n is of the form $k/(k+1)$ or $(2k-1)/(2k+1)$, with k a positive integer. Explicit expressions are provided for $k = 1, 2$; for other values, results are easily obtained via recursive formulae. All results are presented in dimensionless form; the pressure distribution and interface positions are studied and discussed as a function of the self-similar variable for different values of the mobility and compressibility ratios.

Keywords: porous media, non-Newtonian, compressible fluids, self-similar solution, immiscible displacement.

WIT Transactions on Engineering Sciences, Vol 59, © 2008 WIT Press
www.witpress.com, ISSN 1743-3533 (on-line)
doi:10.2495/AFM080231

1 Introduction

Displacement of non-Newtonian fluid in porous media is of paramount importance in the flow modeling of oil reservoirs, where often a power-law fluid of pseudo-plastic behavior (water thickened with polymer addictive) is used to minimize the instability effects [5]. A large bibliography exists on porous media flow of non-Newtonian fluids: see for example the papers by H. Pascal and coworkers and references therein [2,3]. Although numerical solutions are available [5], there exists a need for closed-form solutions in simple geometries. Pascal and Pascal [4] analyzed the dynamics of a moving stable interface in a semi-infinite porous domain saturated by two fluids, displacing and displaced, both non-Newtonian of power-law behavior. In this paper, we revisit and expand their work by providing: i) a dimensionless formulation of the problem; ii) explicit expressions for the variables of interest for special values of the flow law exponent; iii) a discussion of their behavior as functions of the problem parameters.

2 Problem formulation

We analyze the dynamics of a moving interface due to fluid injection of a non-Newtonian fluid in a semi-infinite porous domain of constant thickness m saturated by another non-Newtonian fluid (Figure 1); both fluids, displacing and displaced, are of power-law pseudo-plastic behavior with the same consistency index $n < 1$. The interface is stable, so that a piston-like displacement exists; the pressure and velocity fields are assumed to be continuous at the interface; the pressure is taken to be constant and equal to p_w in the domain occupied by the displaced fluid at time $t = 0$; the displacing fluid is injected at a constant pressure p_e greater than the ambient pressure p_w.

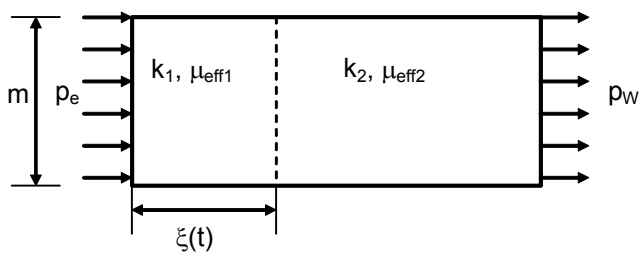

Figure 1: Definition sketch.

The flow law for both fluids is a modified Darcy's law taking into account the nonlinearity of the rheological equation [2–4]. Thus the flow and continuity equation for both fluids ($i = 1$ for the displacing, $i = 2$ for the displaced fluid) are:

$$v_i = \left(-\frac{k_i}{\mu_{efi}} \frac{\partial p_i}{\partial x} \right)^{1/n}, \quad \frac{\partial v_i}{\partial x} = -c_{0i} \phi \frac{\partial p_i}{\partial t}, \tag{1a,b}$$

where x denotes the spatial coordinate, t time, v Darcy velocity, p pressure, n fluid consistency index, c_0 compressibility coefficient, ϕ porosity, k permeability coefficient, μ_{ef} effective viscosity; in turn, the ratio between the latter two is a function of n, ϕ, k (see for example eqn 4 in [4]). Substituting eqn (1b) in eqn (1a) one obtains for the two fluids (i = 1, 2):

$$\frac{\partial^2 p_i}{\partial x^2} = nc_{0i}\phi\left(\frac{\mu_{efi}}{k_i}\right)^{1/n}\left(\frac{\partial p_i}{\partial x}\right)^{(n-1)/n}\frac{\partial p_i}{\partial t}, \tag{2}$$

where $p_i(x,t) = p_1(x,t)$ for $0 \le x \le \xi(t)$ and $p_i(x,t) = p_2(x,t)$ for $\xi(t) \le x < \infty$, with $\xi(t)$ interface position and $\xi(t=0) = 0$. The injection flowrate per unit width is $q(t) = v_1(0,t)m$. Initial and boundary conditions are:

$$p_1(x,0) = p_e;\ p_1(0,t) = p_e;\ \lim_{x\to\infty} p_2(x,t) = p_w. \tag{3a,b,c}$$

At the moving interface, the pressure and velocity fields are continuous; thus

$$p_1[\xi(t),t] = p_2[\xi(t),t];\ \left(-\frac{k_1}{\mu_{ef1}}\frac{\partial p_1}{\partial x}\right)^{1/n}_{x=\xi(t)} = \left(-\frac{k_2}{\mu_{ef2}}\frac{\partial p_1}{\partial x}\right)^{1/n}_{x=\xi(t)} = V, \tag{4a,b}$$

in which $V = \phi\, d\xi/dt$ is the common value of the Darcy velocity at the interface. We now define the following dimensionless variables (i = 1, 2):

$$(x',\xi',t',p_i',v_i',V',q') = \left(\frac{x}{m},\frac{\xi}{m},\frac{t}{T},c_{0i}p_i,\frac{v_iT}{\phi m},\frac{VT}{\phi m},\frac{qT}{\phi m^2}\right), \tag{5}$$

where $T = c_{01}^{1/n}\left(\mu_{ef1}/k_1\right)^{1/n}\phi m^{(n+1)/n}$ is a timescale. This recasts eqns (1a) and (2), respectively, in the following dimensionless forms, where primes are dropped for convenience:

$$v_1 = \left(-\frac{\partial p_1}{\partial x}\right)^{1/n};\ v_2 = \left(-M\frac{\partial p_2}{\partial x}\right)^{1/n}, \tag{6a,b}$$

$$\frac{\partial^2 p_1}{\partial x^2} = n\left(\frac{\partial p_1}{\partial x}\right)^{(n-1)/n}\frac{\partial p_1}{\partial t};\ \frac{\partial^2 p_2}{\partial x^2} = n\frac{\alpha}{M^{1/n}}\left(\frac{\partial p_2}{\partial x}\right)^{(n-1)/n}\frac{\partial p_2}{\partial t}, \tag{7a,b}$$

in which $M = \left(k_2/\mu_{ef2}\right)/\left(k_1/\mu_{ef1}\right)$ and $\alpha = c_{02}/c_{01}$ are respectively the mobility ratio and the compressibility ratio. Conditions at the interface (4a)-(4b) read in dimensionless form (primes omitted)

$$p_1[\xi(t),t] = p_2[\xi(t),t];\ \left(-\frac{\partial p_1}{\partial x}\right)^{1/n}_{x=\xi(t)} = \left(-M\frac{\partial p_2}{\partial x}\right)^{1/n}_{x=\xi(t)} = V = \frac{d\xi}{dt}, \tag{8a,b}$$

while initial and boundary conditions (3a)-(3c) remain unchanged.

3 Solution of the problem

Introducing the similarity variable

$$\eta = \frac{x}{t^{n/(n+1)}}, \tag{9}$$

eqns (6a)-(6b) and (7a)-(7b) take the form

$$v_1 = t^{-1/n+1}\left(-\frac{dp_1}{d\eta}\right)^{1/n}, \; v_2 = t^{-1/n+1}\left(-\frac{1}{M}\frac{dp_2}{d\eta}\right)^{1/n}, \tag{10a,b}$$

$$\frac{d^2p_1}{d\eta^2} - \frac{n^2}{n+1}\eta\left(-\frac{dp_1}{d\eta}\right)^{(2n-1)/n} = 0, \; \left(0 \le \eta \le \eta_1\right), \tag{11}$$

$$\frac{d^2p_2}{d\eta^2} - \frac{n^2}{n+1}\frac{\alpha}{M^{1/n}}\eta\left(-\frac{dp_2}{d\eta}\right)^{(2n-1)/n} = 0, \; \left(\eta_1 \le \eta < \infty\right), \tag{12}$$

where η_1 is linked to the position of the moving interface by

$$\xi(t) = \eta_1 t^{n/(n+1)}. \tag{13}$$

Initial and boundary conditions (3a)-(3c) coalesce into

$$p_1(0) = p_e, \; \lim_{\eta\to\infty} p_2(\eta) = p_w, \tag{14a,b}$$

while the conditions at the interface (8a)-(8b) become

$$p_1(\eta_1) = p_2(\eta_1) = p_{\text{int}}; \; \left(\frac{dp_1}{d\eta}\right)_{\eta=\eta_1} = M\left(\frac{dp_2}{d\eta}\right)_{\eta=\eta_1}, \tag{15a,b}$$

in which p_{int} is the pressure at the interface. The interface velocity becomes

$$V = \frac{d\xi}{dt} = t^{-1/(n+1)}\left(-\frac{dp_1}{d\eta}\right)^{1/n}_{\eta=\eta_1}. \tag{16}$$

Integrating eqn (16) with the initial condition $\xi(t=0) = 0$ yields

$$\xi(t) = \frac{n+1}{n}t^{n/(n+1)}\left(-\frac{dp_1}{d\eta}\right)^{1/n}_{\eta=\eta_1}. \tag{17}$$

Coupling eqns (13) and (17) leads to the following expression for η_1

$$\eta_1 = \xi(t)t^{-n/(n+1)} = \frac{1+n}{n}\left(-\frac{dp_1}{d\eta}\right)^{1/n}_{\eta=\eta_1}. \tag{18}$$

Now integrating once eqns (11)-(12) yields respectively

$$\frac{dp_1}{d\eta} = -\left[\left(-\frac{dp_1}{d\eta}\right)_{\eta=\eta_1}^{(1-n)/n} - \frac{n(1-n)}{2(1+n)}\left(\eta^2-\eta_1^2\right)\right]^{n/(1-n)} \quad (0\le\eta\le\eta_1), \tag{19}$$

$$\frac{dp_2}{d\eta} = -\left[\left(-\frac{dp_2}{d\eta}\right)_{\eta=\eta_1}^{(1-n)/n} - \frac{n(1-n)\alpha}{2(1+n)M^{1/n}}\left(\eta^2-\eta_1^2\right)\right]^{n/(1-n)} \quad (\eta_1\le\eta<\infty). \tag{20}$$

Note that eqn (19) is in variance with (18) of Pascal and Pascal [4]. From eqn (20) it is evident that $dp_2/d\eta = 0$ for

$$\eta^* = \left[\eta_1^2 + \frac{2(1+n)M^{1/n}}{n(1-n)\alpha}\left(-\frac{dp_2}{d\eta}\right)_{\eta=\eta_1}^{(1-n)/n}\right]^{1/2}. \tag{21}$$

Eqn (21) shows the existence of a compression front ahead of the moving interface, whose dimensionless position and velocity are defined by

$$\xi^*(t) = \eta^* t^{n/(n+1)};\ V^* = \frac{d\xi^*}{dt} = \frac{n}{n+1}\eta^* t^{-1/(n+1)}. \tag{22a,b}$$

At and beyond the compression front, the displaced fluid Darcy velocity v_2 is null; hence, the fluid remains at the constant pressure p_w for $\eta\ge\eta^*$. Therefore, the boundary condition (14b) is replaced by $p_2(\eta^*) = p_w$; taking this and eqn (14a) into account, the integration of eqns (19)-(20) yields

$$p_1(\eta) = p_e - \int_0^{\eta}\left[\left(-\frac{dp_1}{d\eta}\right)_{\eta=\eta_1}^{(1-n)/n} - \frac{n(1-n)}{2(1+n)}\left(\tau^2-\eta_1^2\right)\right]^{n/(1-n)} d\tau, \tag{23}$$

$$p_2(\eta) = p_w + \int_{\eta}^{\eta^*}\left[\left(-\frac{dp_2}{d\eta}\right)_{\eta=\eta_1}^{(1-n)/n} - \frac{n(1-n)\alpha}{2(1+n)M^{1/n}}\left(\tau^2-\eta_1^2\right)\right]^{n/(1-n)} d\tau. \tag{24}$$

On the other hand, subtracting eqn (24) from eqn (23) and taking into account the interface condition (15a) gives

$$\begin{aligned}\Delta p = p_e - p_w = &\int_0^{\eta_1}\left[\left(-\frac{dp_1}{d\eta}\right)_{\eta=\eta_1}^{(1-n)/n} - \frac{n(1-n)}{2(1+n)}\left(\tau^2-\eta_1^2\right)\right]^{n/(1-n)} d\tau + \\ &+\int_{\eta_1}^{\eta^*}\left[\left(-\frac{dp_2}{d\eta}\right)_{\eta=\eta_1}^{(1-n)/n} - \frac{n(1-n)\alpha}{2(1+n)M^{1/n}}\left(\tau^2-\eta_1^2\right)\right]^{n/(1-n)} d\tau\end{aligned} \tag{25}$$

The nonlinear algebraic system of equations (15b), (18), (21), and (25), for assigned pressure drop Δp, compressibility ratio α, and mobility ratio M, determines the pressure gradients at the interface, and the positions of the moving interface and of the compression fronts, i.e. $(dp_1/d\eta)_{\eta=\eta_1}$, $(dp_2/d\eta)_{\eta=\eta_1}$,

η_1, η^*; once these are known, the pressure distributions are easily determined. To solve the set of equations, we proceed as follows: first, we rewrite eqn (21), with the aid of eqs (15b) and (18), as

$$\eta^* = \eta_1 \left[1 + \frac{2(1+n)^n M}{n^n (1-n) \alpha \eta_1^{1+n}} \right]^{1/2} = \eta_1 c_1(\eta_1) . \tag{26}$$

Second, with the help of eqns (15b), (18), and (26), eqn (25) becomes

$$\Delta p = \int_0^{\eta_1} \left[\left(\frac{n}{1+n} \eta_1 \right)^{1-n} - \frac{n(1-n)}{2(1+n)} \left(\tau^2 - \eta_1^2 \right) \right]^{n/(1-n)} d\tau + \\ + \int_{\eta_1}^{\eta_1 c_1(\eta_1)} \left[\frac{1}{M^{(1-n)/n}} \left(\frac{n}{1+n} \eta_1 \right)^{1-n} - \frac{n(1-n)\alpha}{2(1+n) M^{1/n}} \left(\tau^2 - \eta_1^2 \right) \right]^{n/(1-n)} d\tau , \tag{27}$$

in which the only unknown is η_1; once η_1 is determined via eqn (27), η^* is then calculated through the function $c_1(\eta_1)$ defined in eqn (26). Finally, the pressure distributions behind and ahead the moving interface are given by eqns (23)-(24), which become, with the aid of eqns (15b), (18), and (21)

$$p_1(\eta) = p_e - \int_0^{\eta} \left[\left(\frac{n}{1+n} \eta_1 \right)^{1-n} - \frac{n(1-n)}{2(1+n)} \left(\tau^2 - \eta_1^2 \right) \right]^{n/(1-n)} d\tau , \tag{28}$$

$$p_2(\eta) = p_w + \int_{\eta}^{\eta_1 c_1(\eta_1)} \left[\frac{1}{M^{(1-n)/n}} \left(\frac{n}{1+n} \eta_1 \right)^{1-n} - \frac{n(1-n)\alpha}{2(1+n) M^{1/n}} \left(\tau^2 - \eta_1^2 \right) \right]^{n/(1-n)} d\tau . \tag{29}$$

The integrals in eqns (27)-(29) are of the type $\int (a - b\tau^2)^p d\tau$, with $a = a(\eta_1)$ and b positive quantities, and p a positive real number: hence, they can be expressed as analytical functions in two cases [1, p. 84]: i) $n = k/(1+k)$; ii) $n = (2k-1)/(2k+1)$, where k is a positive integer.

4 Closed-form results

In the following, explicit expressions for all variables of interest are provided for cases i) and ii) for $k = 1$ and $k = 2$, while for other values of k results are easily obtained via recursive formulae [1]; for each case, we report eqns (26)-(29), the expressions of the coefficients included therein, the position and velocity of the interface and of the compression front, and the dimensionless injection flowrate per unit width $q(t)$; for the sake of brevity, $c_1(\eta_1) = c_1$, $a_1(\eta_1) = a_1$, $a_2(\eta_1) = a_2$.

4.1 Case i) $n = k/(k+1)$; $k = 1$ ($n = 1/2$)

$$c_1 = \left[1 + \frac{4(3)^{1/2} M}{\alpha \eta_1^{3/2}} \right]^{1/2} , \tag{30}$$

$$\Delta p = \eta_1\left[a_1 + (c_1 - 1)a_2\right] - \frac{\eta_1^3}{3}\left[b_1 + \left(c_1^3 - 1\right)b_2\right], \tag{31}$$

$$p_1(\eta) = p_e - a_1\eta + \frac{b_1\eta^3}{3},\ p_2(\eta) = p_w + a_2(c_1\eta_1 - \eta) - \frac{b_2}{3}\left(c_1^3\eta_1^3 - \eta^3\right), \tag{32a,b}$$

$$a_1 = \left(\frac{\eta_1}{3}\right)^{1/2} + \frac{\eta_1^2}{12},\ b_1 = \frac{1}{12},\ a_2 = \frac{1}{M}\left(\frac{\eta_1}{3}\right)^{1/2} + \frac{\alpha\eta_1^2}{12M^2},\ b_2 = \frac{\alpha}{12M^2}, \tag{33a,b,c,d}$$

$$\xi(t) = \eta_1 t^{1/3},\ V(t) = \frac{\eta_1}{3}t^{-2/3},\ \xi^*(t) = c_1\eta_1 t^{1/3},\ V^*(t) = \frac{c_1\eta_1}{3}t^{-2/3}, \tag{34a,b,c,d}$$

$$q(t) = a_1^2 t^{-2/3}. \tag{35}$$

4.2 Case i) $n = k/(k+1)$; $k = 2$ ($n = 2/3$)

$$c_1 = \left[1 + \frac{3(50)^{1/3}M}{\alpha\eta_1^{5/3}}\right]^{1/2}, \tag{36}$$

$$\Delta p = \eta_1\left[a_1^2 + (c_1 - 1)a_2^2\right] - \frac{2\eta_1^3}{3}\left[a_1b_1 + \left(c_1^3 - 1\right)a_2b_2\right] + \frac{\eta_1^5}{5}\left[b_1^2 + \left(c_1^5 - 1\right)b_2^2\right], \tag{37}$$

$$p_1(\eta) = p_e - a_1\eta + \frac{2}{3}a_1b_1\eta^3 - \frac{1}{5}b_1^2\eta^5, \tag{38}$$

$$p_2(\eta) = p_w + a_2^2(c_1\eta_1 - \eta) - \frac{2}{3}a_2b_2\left(c_1^3\eta_1^3 - \eta^3\right) + \frac{1}{5}b_2^2\left(c_1^5\eta_1^5 - \eta^5\right), \tag{39}$$

$$a_1 = \left(\frac{2\eta_1}{5}\right)^{1/3} + \frac{\eta_1^2}{15},\ b_1 = \frac{1}{15}, \tag{40a,b}$$

$$a_2 = \frac{1}{M^{1/2}}\left(\frac{2\eta_1}{5}\right)^{1/3} + \frac{\alpha\eta_1^2}{15M^{3/2}},\ b_2 = \frac{\alpha}{15M^{3/2}}, \tag{41a,b}$$

$$\xi(t) = \eta_1 t^{2/5},\ V(t) = \frac{2\eta_1}{5}t^{-3/5},\ \xi^*(t) = c_1\eta_1 t^{2/5},\ V^*(t) = \frac{2c_1\eta_1}{5}t^{-3/5}, \tag{42a,b,c,d}$$

$$q(t) = a_1^3 t^{-3/5}. \tag{43}$$

4.3 Case ii) $n = (2k\text{-}1)/(2k+1)$; $k = 1$ ($n = 1/3$)

$$c_1 = \left[1 + \frac{3(4)^{1/3}M}{\alpha\eta_1^{4/3}}\right]^{1/2}, \tag{44}$$

$$\Delta p = \frac{\eta_1}{2}\left[\left(a_1 - b_1\eta_1^2\right)^{1/2} + c_1\left(a_2 - b_2c_1^2\eta_1^2\right)^{1/2} - \left(a_2 - b_2\eta_1^2\right)^{1/2}\right] +$$

$$+ \frac{a_1}{2b_1^{1/2}}\arcsin\left[\left(\frac{b_1}{a_1}\right)^{1/2}\eta_1\right] + \frac{a_2}{2b_2^{1/2}}\left\{\arcsin\left[\left(\frac{b_2}{a_2}\right)^{1/2}c_1\eta_1\right] - \arcsin\left[\left(\frac{b_2}{a_2}\right)^{1/2}\eta_1\right]\right\}, \tag{45}$$

$$p_1(\eta) = p_e - \frac{\eta}{2}\left(a_1 - b_1\eta^2\right)^{1/2} - \frac{a_1}{2b_1^{1/2}}\arcsin\left[\left(\frac{b_1}{a_1}\right)^{1/2}\eta\right], \tag{46}$$

$$p_2(\eta) = p_w + \frac{1}{2}\left[c_1\eta_1\left(a_2 - b_2c_1^2\eta_1^2\right)^{1/2} - \eta\left(a_2 - b_2\eta^2\right)^{1/2}\right] + \\ + \frac{a_2}{2b_2^{1/2}}\left\{\arcsin\left[\left(\frac{b_2}{a_2}\right)^{1/2}c_1\eta_1\right] - \arcsin\left[\left(\frac{b_2}{a_2}\right)^{1/2}\eta\right]\right\}, \tag{47}$$

$$a_1 = \left(\frac{\eta_1}{4}\right)^{2/3} + \frac{\eta_1^2}{12},\ b_1 = \frac{1}{12},\ a_2 = \frac{1}{M^2}\left(\frac{\eta_1}{4}\right)^{2/3} + \frac{\alpha\eta_1^2}{12M^3},\ b_2 = \frac{\alpha}{12M^3}, \tag{48a,b,c,d}$$

$$\xi(t) = \eta_1 t^{1/4},\ V(t) = \frac{\eta_1}{4}t^{-3/4},\ \xi^*(t) = c_1\eta_1 t^{2/5},\ V^*(t) = \frac{c_1\eta_1}{4}t^{-3/5}, \tag{49a,b,c,d}$$

$$q(t) = a_1^{3/2}t^{-3/4}. \tag{50}$$

4.4 Case ii) $n = (2k\text{-}1)/(2k\text{+}1)$; $k = 2$ ($n = 3/5$)

$$c_1 = \left[1 + 5\left(\frac{8}{3}\right)^{3/5}\frac{M}{\alpha\eta_1^{8/5}}\right]^{1/2}, \tag{51}$$

$$\Delta p = \frac{\eta_1}{4}\left[\left(a_1 - b_1\eta_1^2\right)^{3/2} + c_1\left(a_2 - b_2c_1^2\eta_1^2\right)^{3/2} - \left(a_2 - b_2\eta_1^2\right)^{3/2}\right] + \\ \frac{3\eta_1}{8}\left[a_1\left(a_1 - b_1\eta_1^2\right)^{1/2} + a_2c_1\left(a_2 - b_2c_1^2\eta_1^2\right)^{1/2} - a_2\left(a_2 - b_2\eta_1^2\right)^{1/2}\right] + \\ + \frac{3a_1^2}{8b_1^{1/2}}\arcsin\left[\left(\frac{b_1}{a_1}\right)^{1/2}\eta_1\right] + \frac{3a_2^2}{8b_2^{1/2}}\left\{\arcsin\left[\left(\frac{b_2}{a_2}\right)^{1/2}c_1\eta_1\right] - \arcsin\left[\left(\frac{b_2}{a_2}\right)^{1/2}\eta_1\right]\right\}, \tag{52}$$

$$p_1(\eta) = p_e - \frac{1}{4}\left(a_1 - b_1\eta^2\right)^{3/2} - \frac{3a_1\eta}{8}\left(a_1 - b_1\eta^2\right)^{1/2} - \frac{3a_1^2}{8b_1^{1/2}}\arcsin\left[\left(\frac{b_1}{a_1}\right)^{1/2}\eta\right], \tag{53}$$

$$p_2(\eta) = p_w + \frac{1}{4}\left[c_1\eta_1\left(a_2 - b_2c_1^2\eta_1^2\right)^{3/2} - \eta\left(a_2 - b_2\eta^2\right)^{3/2}\right] + \\ + \frac{3a_2}{8}\left[c_1\eta_1\left(a_2 - b_2c_1^2\eta_1^2\right)^{1/2} - \eta\left(a_2 - b_2\eta^2\right)^{1/2}\right] + \\ + \frac{3a_2^2}{8b_2^{1/2}}\left\{\arcsin\left[\left(\frac{b_2}{a_2}\right)^{1/2}c_1\eta_1\right] - \arcsin\left[\left(\frac{b_2}{a_2}\right)^{1/2}\eta\right]\right\}, \tag{54}$$

$$a_1 = \left(\frac{3\eta_1}{8}\right)^{2/5} + \frac{3\eta_1^2}{40},\ b_1 = \frac{3}{40}, \tag{55a,b}$$

$$a_2 = \frac{1}{M^{2/3}}\left(\frac{3\eta_1}{8}\right)^{2/5} + \frac{3\alpha\eta_1^2}{40M^{5/3}},\ b_2 = \frac{3\alpha}{40M^{5/3}}, \tag{56a,b}$$

$$\xi(t) = \eta_1 t^{3/8},\ V(t) = \frac{3\eta_1}{8}t^{-5/8},\ \xi^*(t) = c_1\eta_1 t^{3/8},\ V^*(t) = \frac{3c_1\eta_1}{8}t^{-5/8}, \tag{57a,b,c,d}$$

$$q(t) = a_1^{5/2}t^{-5/8}. \tag{58}$$

5 Discussion of results

In this section we discuss the behavior of the variables of interest as functions of the fluid properties. We do so for the reference case $p_e = 1$, $p_w = 0.5$; hence $\Delta p = 0.5$. We evaluate results for $n = 0.33, 0.50, 0.60, 0.67$; these values cover quite well the range of variation of n for pseudoplastic fluids in field cases. Finally, to grasp the influence of fluid mobility and compressibility, we consider the following cases for the mobility ratio M and compressibility ratio α: I) M = 0.2, α = 0.2; II) M = 0.2, α = 5; III) M = 5, α = 0.2; IV) M = 5, α = 5. In Figures 2a-d, the interface location $\xi(t)$ is illustrated as a function of time for the above values of n, M, and α.

When the displaced fluid is less compressible and less mobile than the displacing one (case I), the interface advances very slowly, more so for lesser values of n (Figure 2a); when the displaced fluid is more compressible and more mobile than the displacing one (case IV), the interface advances very fast, more so for larger values of n, even if the difference between results for different values of n is, relatively speaking, less marked than in the previous case (Figure 2d). When the displaced fluid is less mobile, but more compressible than the displacing one (case II), the interface advances almost as fast as for case I, and differences between results for different values of n are as marked as for case IV. Finally, when the displaced fluid is more mobile, but less compressible than the displacing one (case III), the interface advances faster than for case I, but less fast than for cases II and IV; this indicates, at least for the range of values of parameters examined here, that to achieve the maximum displacement, one needs not only large values of the power law model exponent n, but also of the compressibility and mobility ratio, the former more than the latter.

Figure 3a shows the compression front location $\xi^*(t)$ as a function of time in the four cases listed above for n = 0.50. As expected, the compression front advances fastest when the displaced fluid is more mobile, but less compressible than the displacing one (case III); the compression front is slower in cases I and IV, and becomes slowest for case II, when the displaced fluid is less mobile and more compressible than the displacing one.

On comparing Figure 3a with Figures 2a-d, it is noted that the compression front location is farther from the interface location when the displaced fluid is

less compressible than the displacing one (cases I and III); the reverse is true when the displaced fluid is more compressible than the displacing one (cases II and IV). The above conclusions hold true also for different values of n (not shown).

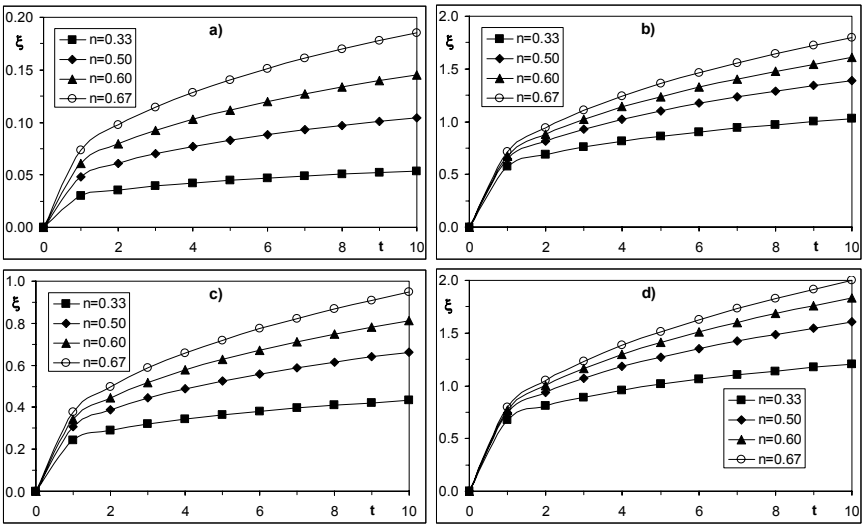

Figure 2: Interface location as a function of time for a) case I: $M = 0.2$, $\alpha = 0.2$; b) case II: $M = 0.2$, $\alpha = 5$; c) case III: $M = 5$, $\alpha = 0.2$; d) case IV: $M = 5$, $\alpha = 5$.

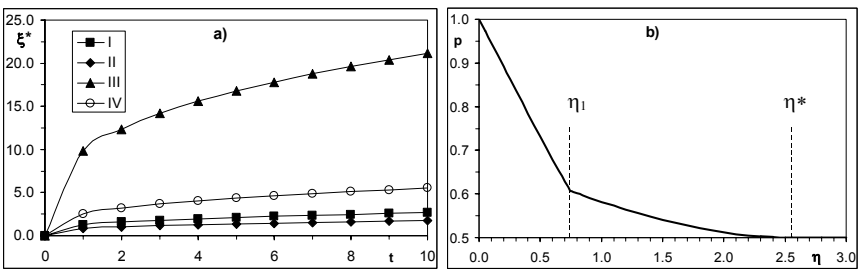

Figure 3: a) Compression front location as a function of time for Cases I-IV and $n = 0.50$; b) Pressure as a function of η for $n = 0.50$, Case IV.

Finally, Figure 3b shows the behavior of pressure in the displacing and displaced fluids, $p_1(\eta)$ and $p_2(\eta)$, as a function of η for $n = 0.50$ and case IV; note the discontinuity in the pressure derivative at the interface location $\eta_1 = 0.745$ and the pressure asymptote at the compression front location $\eta^* = 2.556$.

6 Conclusions

In this paper, we examined the dynamics of non-Newtonian interfaces when a fluid is injected at a constant pressure into a plane porous domain, revisiting and expanding the work of Pascal and Pascal [4]. Via the adoption of a self-similar variable, we obtained closed-form solutions for the pressure distribution, location and velocity of the moving interface and compression front for several values of the power law model exponent.

Expressing the model equations in dimensionless form, it was found that the variables of interest are functions of the imposed pressure difference, of the fluid consistency index (power law model exponent), and of the relative mobility and compressibility of the displacing and displaced fluids.

We confirmed the existence of a pressure front ahead of the moving interface, traveling with finite velocity. Evaluation of the interface location showed that, for a given power law model exponent, a large relative compressibility is comparatively more efficient than a large relative mobility ratio towards maximizing the resulting displacement.

Our results may help in better interpreting transient pressure response in polymer flooding projects in oil reservoir engineering.

References

[1] Gradshteyn, I.S., & Ryzhik, I.M., *Table of Integrals, Series, and Products*, edited by A. Jeffrey, Academic Press: San Diego, 1994.

[2] Pascal, H. & Pascal F., Flow of non-Newtonian fluid through porous media, *Int. J. Engng. Sci.*, **23(5)**, pp. 571–585, 1985.

[3] Pascal, H., On the existence of self-similar solutions of the equations governing unsteady flow through a porous medium, *Int. J. Heat and Fluid Flow*, **9(4)**, pp. 381–389, 1988.

[4] Pascal, H. & Pascal F., Displacement of non-Newtonian fluid interfaces in a porous medium: compressible fluid, *J. Non-Newt. Fluid Mech.*, **28**, pp. 227–238, 1988.

[5] Wu, Y.-S. & Pruess, K., A numerical method for simulating non-Newtonian fluid flow and displacement in porous media, *Adv. in Wat Res.*, **21**, pp. 351–362, 1998.

This page intentionally left blank

Rayleigh-Benard convection flow with liquid/solid phase transition in a low gravity field

D. Mansutti[1], E. Bucchignani[2] & M. M. Cerimele[1]
[1]*Istituto per le Applicazioni del Calcolo "M. Picone"/C.N.R., Rome, Italy*
[2]*Centro Italiano Ricerche Aerospaziali, Capua (CE), Italy*

Abstract

The presence of an icy crust covering several satellites of the solar system (e.g. Europa, the jovian satellite) suggested us to accomplish the numerical simulation of the Rayleigh-Benard convection flow of a horizontal layer of mushy water, covered at the top by its own ice and immersed in a low gravity field. The phase transition occurring at the ice/mushy water interface, with release/absorption of latent heat, is included in our study. Starting the simulation with ice and water at rest in a conductive temperature distribution, we pushed the computation forward enough to approach, possibly, the thermo-dynamical equilibrium. We adopt initial geometrical parameters resembling the present set-up of Europa's crust. As the changes undergoing on the satellite nowadays are imperceptible, the final computed configuration should recover the present dynamical and thermo-dynamical fields. We also provide the estimate of the amount of heat flowing up from the bottom of the domain that is from the inside of the planet, a quantity practically difficult to be measured even on Earth.

Keywords: continuum mechanics, phase transition, heat transfer, moving boundary, numerical simulation, natural convection, low gravity, front-fixing, finite differences.

1 Introduction

Due to the relevance to techniques in artificial crystal growth and metal manufacturing, in the last three decades specialists in CFD have devoted much

WIT Transactions on Engineering Sciences, Vol 59, © 2008 WIT Press
www.witpress.com, ISSN 1743-3533 (on-line)
doi:10.2495/AFM080241

attention and effort in developing numerical models and computational codes for the simulation of horizontal convection flows with liquid/solid (L/S) phase transition and a bunch of papers on this topic are available in the literature (see, for example [1–4]). Several issues have been deeply investigated, such as the impact of the convection flow of the liquid and of the deformations of the solid on the phase-change process and the dependence of the dynamical and thermal fields on gravity and on the physical and geometrical parameters.

The problem faced in this work, the Rayleigh-Benard convection flow with L/S phase change, is linked, as well, to interests of other scientific disciplines, in particular we mention planetology with its queries on the icy satellites of the solar system and geology and glaciology with the studies on the appearance and evolution of the Antarctic subglacial lakes. In both cases occurs the presence of a thick layer of ice with its water underneath, and either the ice or the water undergo a natural heating effect from below that induces vertical convection within both phases. For these applications, the description of the evolution of the icy crust (thickness and deformations), of the convection flow of the water and of heat transfer are, clearly, fundamental. Here, we propose the numerical simulation of the Rayleigh-Benard convection flow of a rectangular laterally open horizontal layer of mushy (freezing) water, covered at the top by its own ice, immersed in a low gravity environment, alike that one of Europa, the jovian satellite. In fig. 1 the geometrical setting is sketched (the phase boundary is drawn as a straight line in its initial shape; with time evolving, it is allowed to become curvilinear).

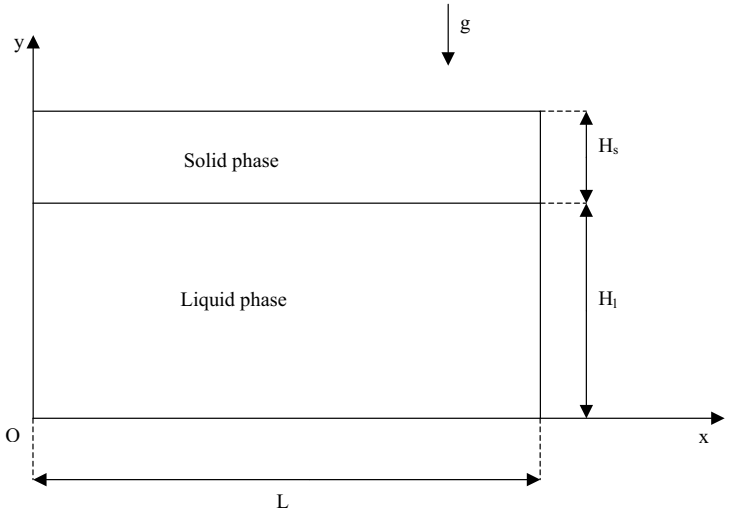

Figure 1: Initial geometrical setting.

In the next section the mathematical equations adopted and the numerical technique used are outlined and, in section 3, the numerical results are presented and discussed.

2 Mathematical and numerical modelling

2.1 Governing equations

The mathematical model governing the evolution of a continuum sample undergoing L/S phase transition has to include the equations for the conservation laws of momentum, of energy and of mass; for their structure we refer to the books on classical mechanics (e.g. [5]). So a set of equations for each single phase is obtained; they are coupled through the *jump conditions,* one for each balance equation. In the jump condition for the energy conservation law (so called *Stefan condition* [6]), most important is the contribution due to release or adsorption of latent heat corresponding respectively to the solidification or the melting processes.

In the model here adopted the liquid phase and the solid phase are respectively described as an incompressible viscous fluid and an isotropic linearly elastic material [5]. This choice allows one to keep average the level of difficulty of the final system of equations to be solved. Obviously, for the ice, a more appropriate model would be one describing correctly the specific material symmetry but, our aim, here, is to provide a first insight to the effects of the mechanical response of the solid phase within the transition process.

Additional simplifying assumptions are:
i) the density of the liquid phase and of the solid phase are assumed to be equal,
ii) the radiating heat is neglected,
iii) the material coefficients of the two phases are assumed to be constant.

Let t and (x,y) be, respectively, the time and the space Cartesian coordinates within a spatial reference frame with origin at the left lower corner of the sample and upward vertical axis. Let us call D_L, D_S and Γ the domains occupied respectively by the melt, the solid and the phase interface. Introducing the Boussinesq and Fourier approximations, the governing equations of the melt flow, holding in D_L result:

$$\rho_L \frac{d}{dt}\vec{v} = -\nabla p + \mu_L \nabla^2 \vec{v} - \rho_L \left[1 - \alpha_L \left(T_L - T_p\right)\right]\vec{g} \tag{1}$$

$$\nabla \cdot \vec{v} = 0 \tag{2}$$

$$\rho_L c_L \frac{dT_L}{dt} = k_L \nabla^2 T_L + \mu_L \left[\left(\frac{\partial u}{\partial x}\right)^2 + \frac{1}{2}\left(\frac{\partial u}{\partial y} + \frac{\partial v}{\partial x}\right)^2 + \left(\frac{\partial v}{\partial y}\right)^2\right] \tag{3}$$

p, T_L and ρ_L being $\vec{v}$=(u,v), respectively velocity, pressure, temperature and density of the melt.

These equations are coupled with the following ones for the solid phase holding in D_S:

$$\rho_S \frac{\partial^2 \vec{U}}{\partial t^2} = \mu_S \nabla^2 \vec{U} - \rho_S \left[1 - \alpha_S \left(T_S - T_p\right)\right]\vec{g} \tag{4}$$

$$\nabla \cdot \vec{U} = 0 \tag{5}$$

$$\rho_S c_S \frac{\partial T_S}{\partial t} = k_S \nabla^2 T_S \tag{6}$$

$\vec{U}$, T_S and ρ_S respectively being the displacement, the temperature and the density of the solid phase. The symbols *c, k* and α with the appropriate subscript (L or S) indicate respectively the specific heat, the conductivity and the thermal expansion coefficients for the liquid and the solid phases, whereas μ_L and μ_S are the viscosity coefficient of the melt and the second Lamé constant of the solid.

The jump conditions, that hold in $\Gamma(t)$, appear:

$$\vec{v}_L = \vec{v}_S \tag{7}$$

$$\left(-p\vec{I} + \mu_L\left(\nabla\vec{v}_L + \left(\nabla\vec{v}_L\right)^T\right)\right)\cdot\hat{n} = \mu_S\left(\nabla\vec{U} + \left(\nabla\vec{U}\right)^T\right)\cdot\hat{n} \tag{8}$$

$$-\rho\Lambda\left(v_L\cdot\hat{n} - u_n\right) - k_S\nabla T_S\cdot\hat{n} + k_L\nabla T_L\cdot\hat{n} = 0 \tag{9}$$

$\hat{n}$ being the normal unitary vector on $\Gamma(t)$ and Λ the latent heat. The set of equations (1) –(9) is completed by initial and boundary conditions according to the known requirements of the classical fluid and solid mechanics models (see [5] and further details in the next section).

Let us observe that equation (9) is the well-known Stefan condition; furthermore, let us focus on the fact that, at the phase front, the classical no-slip condition, holding for viscous fluids, within our model implies that interfacing fluid and solid particles are allowed to move sticking to each other with the same velocity. On the contrary in models for L/S phase change that neglect the solid deformations the no-slip condition implies that at the phase front the fluid particles have null relative velocity.

The Coriolis force is not included in the model; this choice is compatible with the application to the icy satellites as it has been shown by Cerimele et al. in [7].

By observing that the vectors $\vec{v}$ and $\vec{U}$ are both required to be solenoidal, we have reformulated the above model on the basis of the Helmoltz-Hodge decomposition in order to meet more accurately and easily such constrain.

This procedure is well known and experimented in fluid dynamics and leads to the scalar potential/streamfunction/vorticity formulation (ϕ, ψ, ω) [8]. In [9] we have proposed to extend this approach also to the treatment of the solid phase by introducing the new unknowns, ϕ_S, ψ_S and ω_S linked to $\vec{U}$ by these relations:

$$\vec{U} = \left(-\frac{\partial\psi_S}{\partial y} + \frac{\partial\phi_S}{\partial x}, \frac{\partial\psi_S}{\partial x} + \frac{\partial\phi_S}{\partial y}\right) \qquad \omega_S = \frac{\partial U_y}{\partial x} - \frac{\partial U_x}{\partial y}.$$

According to this, we transform the equation (4) by applying the curl operator and obtain a scalar equation for ω_S. In doing so, equation (5) reduces to a simple Laplace equation for ϕ_S and ψ_S results solution of the Poisson equation coming from the definition of ω_S.

2.2 Numerical method

Prior discretization, the mathematical model adopted has been written in nondimensional form by using the following reference quantities: H_L , $H_L{}^2 \ \rho_L \, c_L / k_L$ and $T_0 - T_m$ respectively for length, time and temperature.

Then a finite difference method has been applied, with the first order Euler scheme for first order time derivatives, the second order backward scheme for second order time derivatives and centred second order schemes for space derivatives.

Doing so, the unknowns ω_L , ω_S , T_L and, T_S result explicitly determined from the evolutive equations within a *time marching* algorithm. The Laplace equations for the scalar potentials and the Poisson equations for the stream-functions, one of each in both phases, are solved by a Bi-CGStab method [10], as linear system solver, supported by a pre-conditioner based on the ILU factorization [11].

In fact the first step in our solving procedure consists in the application of a front-fixing technique that overcomes the difficulties related to the moving boundary formulation: a coordinate transformation is adopted in order to transform the spatial domains, D_L and D_S, into the unitary square and make straightforward the finite difference discretization. Obviously, this transformation generates new factors to the differential operators of the model, which depend on the function of the unknown curve of the phase front. At each time step the discrete points of this curve are properly advanced according to the value of u_n obtained by the Stefan condition.

3 Numerical simulation test

3.1 The physical set-up

The simulation that we have developed is compatible, with respect to either the geometrical and the physical characteristics, with the evolution of a portion of Europa's icy crust, that is two adjacent infinite layers of ice, the conducting one laying above the convective (mushy) one.

Below and above the icy crust are supposed to be respectively the ocean and the atmosphere, not directly included in the simulation; at both boundaries free-slip and impermeability conditions are imposed together with the melting temperature T_m, at the ice/ocean interface, and the external temperature T_w, at the top.

At the phase interface, the temperature T_{top}, limiting the convecting ice, is imposed. At the left and right lateral open boundaries, where the infinite layer is artificially truncated, periodicity to 1^{st} order is imposed to the dynamical variables and to temperature. The remaining boundary value of the dynamical variables selects the solution with entire convecting cells.

The values of the geometrical, physical and material parameters, here, follow: H_S = 5 Km and H_L = 20 Km (initial thickness of ice and mush layers), L = 100 Km (length of the truncated layers), T_w = 95 K, T_{top} = 249.24 K, T_m = 270.5 K,

ρ_L = 1000 Kg/m^3, ρ_S = 917 Kg/m^3, k_L = 3.9 W/m K, $k_S = k_L$, c_L = 4.2 103 J/Kg K, c_S = 1925 J/Kg K, $\mu_L = 10^{14}$ Kg/m s, μ_S = 10 GPa, α_L = 1.6 10^{-4} K, $\alpha_L = \alpha_S$, $\Lambda = 3.34\ 10^5$ J/Kg, g = 1.3 m/s^2.

3.2 Results

In order to cope with the extremely long computing time required to accomplish the simulation, quite typical of any L/S phase transition computation, we have kept as low as possible the number of discrete unknowns and used time steps as large as possible. The space discretization grid used is (71 X 41) either in D_L and in D_S ; this choice is supported by the grid refinement analysis developed by two of the authors in [7] for a similar problem where the dynamical response of the conductive ice was neglected (eqs. (4-5) and (7-8) dropped). The larger non-dimensional time step allowed by numerical stability constrain has been Δt= ~10^{-2} (equivalent to 0.25 yr).

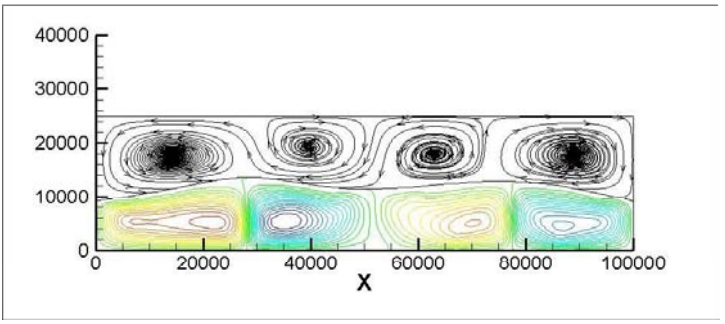

Figure 2: Particle track lines in the solid phase (above) and streamlines in the liquid phase (below) at t = 17 x 10^6 yr.

We have started the simulation with conducting temperature profile and both phases at rest and pushed the computation up to time t=17 x 10^6 yr, when symmetry establishes. In fig.2 we show the tangent lines to the deformation field of the solid phase (particle track lines) and the streamlines of the liquid phase. In fig. 3, the isothermal regions in the whole domain are displayed. We observe the formation of four cellular structures either in the liquid or in the solid phase. Although the elastic response of the solid to the tractive effort operated by the convecting liquid phase at the interface is clearly evident, it is not so important to influence sensibly heat transfer; actually, the thermal field within the solid phase exhibits a conducting behaviour. In the liquid phase two thermal plumes form. As far as that may be deduced by the plots of the thermal field, there is qualitative agreement with the results obtained by Mitri and Showman [12], based on a geology-purpose power-law/finite element code. By looking at the evolution of the phase front, we observe that, approaching the shot time, it still undergoes short oscillations that should be due to the linear elastic nature

imposed to the ice. So thermo-dynamical equilibrium, if there exists, is not reached yet.

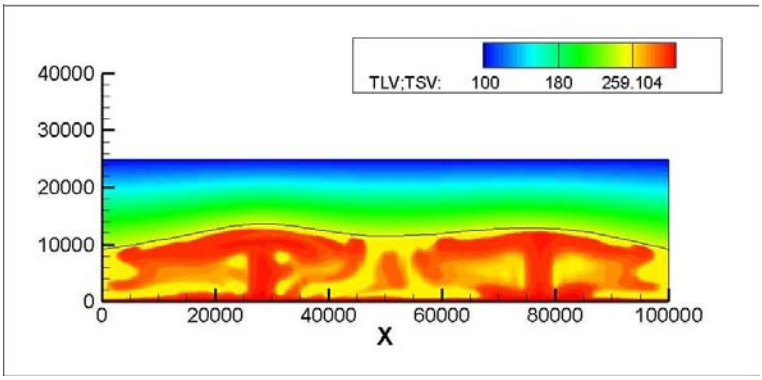

Figure 3: Isothermal regions at t= 17 x 10^6 yr.

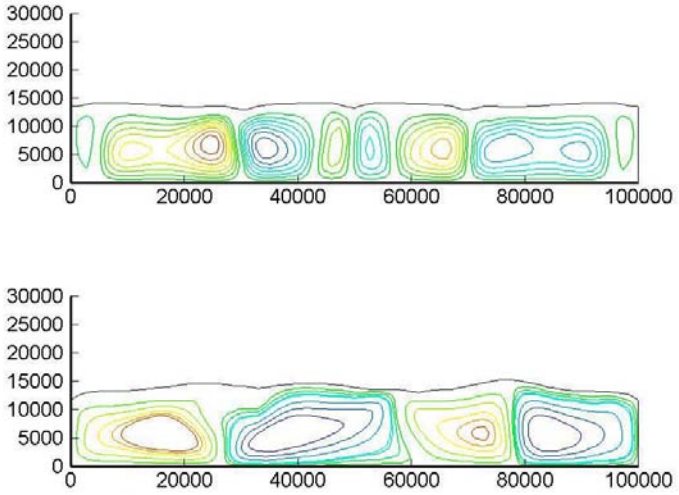

Figure 4: Streamlines in the liquid phase at t = 2 x 10^6 yr (above: solid mechanics not included; below: present model).

In fig. 4 it is possible to compare the streamlines obtained with the present model versus those computed by dropping the solid phase mechanical response: it is evident that this contribution is non-negligible (see the effect on the velocity of phase change) and has to be included in order to simulate correctly the phenomenon considered.

In fig. 5 the curve of the value of the heat flux, computed at the bottom of the liquid domain, is shown. Its shape is due to the gradients of the thermal field within the lower internal region and, in order to have an estimate of the heat flux coming from the inside of the satellite, it would be necessary to compute the average of the displayed values. We can say, however, that there is just a good match with the range of values extrapolated from the magnetic field data gathered by the Galileo and Voyager spacecrafts, that amounts to (0.02–0.07) W/m.

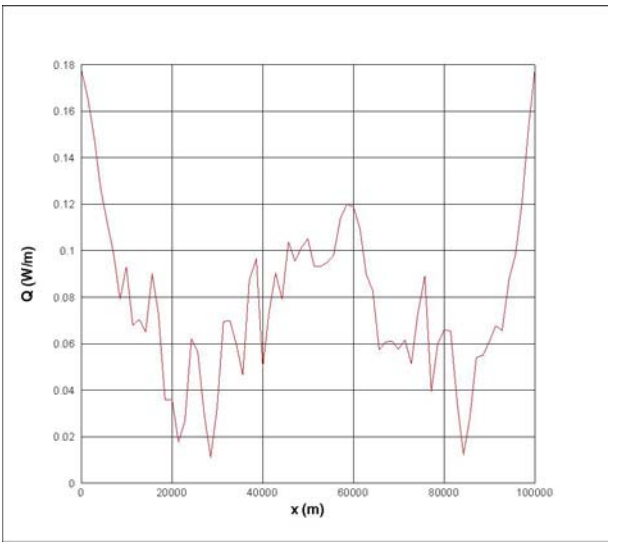

Figure 5: Estimate of the heat flux from the bottom of the domain.

We are aware that a mesh refinement analysis on the present model, at this time under development, is mandatory in order to increase the confidence in our numerical results.

The average CPU time required for running each time step was estimated to be about 0,4 sec.

The analysis of the transient regime and the dependence on the classical fluid dynamics non-dimensional parameters (Gr, Pr and Re) will be our next challenges.

Acknowledgement

We gratefully acknowledge Dr. Giuseppe Mitri at the Jet Propulsion Laboratory, Technology Institute of California, Pasadena, for introducing us to the world of the icy satellites of the solar system.

References

[1] Gau, C. and Viskanta, R., Melting and solidification of a pure metal on a vertical wall, *Transaction of the ASME, **108***, pp. 174–181, 1986.

[2] Bertrand, O., Binet, B., Combeau, H., Couturier, S., Delannoy, Y., Gobin, D., Lacroix, M., Le Quere, P., Medale, M., Mercinger, J., Sadat, H. and Vieira, G., Melting driven by natural convection. A comparison exercise: first results, *Int. J. Therm. Sci,* **38**, pp.5–26, 1999.

[3] Kumar, V., Durst, F. and Ray, S., Modelling moving-boundary problems of solidification and melting adopting an arbitrary lagrangian-eulerian approach, *Numerical Heat Transfer, Part B,* **49**, pp. 299–331, 2006.

[4] Mansutti, D. and Bucchignani, E., On the importance of solid deformations in convection-dominated liquid/solid phase change of pure materials, *IAC Reports n. 118(12/2006)*, 2006

[5] Slattery, J. C., *Momentum, energy and mass transfer in continua*, McGraw-Hill: New York, 1972.

[6] Crank, J., *Free and moving boundary problems*, Oxford Science Publication: Oxford, 1984.

[7] Cerimele, M. M., Mansutti, D. and Pistella, F., Study of Europa's crust via a Stefan model with convection, *Mathematics and Computers in Simulation,* doi:10.1016/j.matcom.2007.11.011, Elsevier Science, The Nederlands, 2007.

[8] Hirasaki, G. J. and Hellums, J. D., Boundary conditions on the vector and scalar potentials in viscous three-dimensional hydrodynamics, Quarterly *of Applied Mathematics*, **28**(2), pp. 163–178, 1970.

[9] Mansutti, D., Raffo, R. and Santi, R., Liquid/solid phase change with convection and deformations: 2D case, *Progress in Industrial Mathematics at E.C.M.I. 2004*, eds. A. Di Bucchianico, R.M.M. Mattheij, M.A. Peletier, Mathematics in Industry, **8**, pp. 268-272, Springer-Verlag, 2006.

[10] Van der Vorst, H., Bi-CGStab: a fast and smoothly converging variant of the Bi-CG for the solution of non-symmetric linear systems, *SIAM Jour.*, **13**(2), pp. 631–644, 1992.

[11] Golub, G. and van Loan, C., *Matrix computations*, The John Hopkins University Press, 1990.

[12] Mitri, G. and Showman, A. P., Convective-conductive transitions and sensitivity of a convective ice shell to perturbations in heat flux and tidal-heating rate: implications for Europa, *Icarus,* **177**, pp. 447–460, 2005.

This page intentionally left blank

A five-equation dissipative model for the simulation of two-phase flows

M. Labois[1], H. Guillard[2] & M. Grandotto[1]
[1]*DEN/DER/SSTH/LMDL, CEA Cadarache, France*
[2]*Projet SMASH, INRIA Sophia-Antipolis, France*

Abstract

This work deals with the design of a five-equation dissipative model for the simulation of two-phase flows and its numerical approximation. Two-phase flows are usually modeled using the well-known one-pressure two-velocity model, which is not hyperbolic, or using a two-pressure two-velocity model, whose complexity makes it costly. Finally, five-equation reduced models can be used, but they feature a unique velocity, which makes them unable to reproduce complex flows.

Our five-equation dissipative model is derived from the standard six-equation bifluid model using the Chapman-Enskog expansion technique. Developments to the first order lead to a hyperbolic system, and even if the model features only one velocity, dissipative second-order terms enable it to deal with velocity disequilibria.

A finite-volume numerical approximation of this model using a fractional step approach is proposed. After the convective step, which takes into account the hyperbolicity of the convective part, the solution of the dissipative step is evaluated. Numerical tests are presented, where the capability of the model to deal with flow featuring phenomena due to velocity disequilibria is shown.
Keywords: two-phase flows, velocity disequilibria, Chapman-Enskog expansion, finite-volume scheme.

1 Introduction

Two-phase flows arise in a large range of applications, and their numerical simulations are still an issue. Mixture models are often used for this purpose. But there are situations where velocity disequilibria between the phases have to be

WIT Transactions on Engineering Sciences, Vol 59, © 2008 WIT Press
www.witpress.com, ISSN 1743-3533 (on-line)
doi:10.2495/AFM080251

taken into account and for these cases, the most widespread model is the bifluid model based on the assumption of the phase pressure equality [1], which feature six equations in one dimension. This model is however basically non-hyperbolic, which can lead to numerical failures.

Thus, seven-equation models [2] have been proposed, with the addition of an equation on the volume fraction. This ensures the hyperbolicity, but it is seldom used because of its computational cost. Finally, five-equation models exist [3], which includes unique pressure and velocity for both phases, but this feature prevent them to model complex flows.

Here, we discuss a model that has been obtained using a Chapman-Enskog expansion [4] of the six-equation model. This gives us the five-equation model when the expansion is performed at the order zero, but expansion at the second order gives additional terms that can model the difference between phase velocities. The derivation of this model will be presented in the next section, then we will show some of its properties. Next, we will discuss its numerical approximation and present eventually some numerical results.

2 Derivation of a five-equation model with additional second-order terms

Our model is derived using a Chapman-Enskog expansion [4] of the classical bifluid model, which can be written

$$\begin{aligned}
&\partial_t \alpha_k \rho_k + \operatorname{div}(\alpha_k \rho_k \underline{u}_k) = 0 \\
&\partial_t \alpha_k \rho_k \underline{u}_k + \operatorname{div}(\alpha_k \rho_k \underline{u}_k \otimes \underline{u}_k) + \alpha_k \nabla p = \underline{M}_k^d + \alpha_k \rho_k \underline{g} \\
&\partial_t \alpha_k \rho_k e_k + \operatorname{div}(\alpha_k (\rho_k e_k + p) \underline{u}_k) = -p \partial_t \alpha_k + \underline{u}_I . \underline{M}_k^d + \alpha_k \rho_k \underline{u}_k . \underline{g}
\end{aligned} \tag{1}$$

where α_k are the phase volume fractions and verify $\alpha_1 + \alpha_2 = 1$, ρ_k are the phase densities, $\underline{u}_k$ the phase velocities, p the pressure and e_k the phase total specific energies, with $e_k = i_k + \underline{u}_k^2/2$, i_k being the phase internal specific energies. $\underline{g}$ stands for the gravity. The velocity at the interface is modeled by $\underline{u}_I = Y_1 \underline{u}_1 + Y_2 \underline{u}_2$, and the drag force terms are written $\underline{M}_k^d = (-1)^{k+1} \frac{\rho}{\varepsilon_u} (\underline{u}_2 - \underline{u}_1)$, where we have introduced the mixture density $\rho = \alpha_1 \rho_1 + \alpha_2 \rho_2$ and the mass fraction $Y_k = \frac{\alpha_k \rho_k}{\rho}$. ε_u denotes the characteristic time of the velocity relaxation, and is supposed to be small.

An expansion to the order zero in ε_u gives the five-equation model [3] that can be written

$$\begin{aligned}
&\partial_t (\alpha_1 \rho_1) + \operatorname{div}((\alpha_1 \rho_1) \underline{u}) = 0 \\
&\partial_t (\alpha_2 \rho_2) + \operatorname{div}((\alpha_2 \rho_2) \underline{u}) = 0 \\
&\partial_t \rho \underline{u} + \operatorname{div}(\rho \underline{u} \otimes \underline{u}) + \nabla p = \rho \underline{g} \\
&\partial_t \rho e + \operatorname{div}((\rho e + p) \underline{u}) = 0 \\
&(\alpha_1 C_2 + \alpha_2 C_1)(\partial_t \alpha_1 + \underline{u} . \partial_x \alpha_1) + \alpha_1 \alpha_2 (C_1 - C_2) \operatorname{div} \underline{u} = 0
\end{aligned} \tag{2}$$

where $\rho e = \rho i + \underline{u}^2/2$ is the total energy of the mixture, with $\rho i = \alpha_1\rho_1 i_1 + \alpha_2\rho_2 i_2$ the internal energy of the mixture and $C_k = \rho_k c_k^2$ is the adiabatic bulk modulus of phase k, with c_k the speed of sound.

If we now perform a first order expansion, we obtain an expression of the relative velocity between the phases as a function of the state variables. More precisely, it can be written $\underline{u}_r = (\underline{u}_1 - \underline{u}_2) = \varepsilon_u \frac{(Y_1-\alpha_1)}{\rho}\nabla p$. Introducing this expression in system (1), we obtain the following system with additional second-order terms

$$
\begin{aligned}
&\partial_t(\alpha_1\rho_1) + \operatorname{div}((\alpha_1\rho_1)\underline{u}) = -\operatorname{div}(\rho Y_1 Y_2 \underline{u}_r)\\
&\partial_t(\alpha_2\rho_2) + \operatorname{div}((\alpha_2\rho_2)\underline{u}) = \operatorname{div}(\rho Y_1 Y_2 \underline{u}_r)\\
&\partial_t \rho\underline{u} + \operatorname{div}(\rho\underline{u}\otimes\underline{u}) + \nabla p = \rho\underline{g}\\
&\partial_t \rho e + \operatorname{div}((\rho e + p)\underline{u}) = \operatorname{div}((h_2 - h_1)\rho Y_1 Y_2 \underline{u}_r) + \rho\underline{u}.\underline{g}\\
&(\alpha_1 C_2 + \alpha_2 C_1)(\partial_t\alpha_1 + \underline{u}.\partial_x\alpha_1) + \alpha_1\alpha_2(C_1 - C_2)\operatorname{div}\underline{u}\\
&\quad = (Y_1\alpha_1 C_2 - Y_2\alpha_2 C_1)\underline{u}_r.\nabla\alpha_1 - \alpha_1\alpha_2(C_1\operatorname{div}(Y_2\underline{u}_r) + C_2\operatorname{div}(Y_1\underline{u}_r))\\
&\qquad -\left(\alpha_1\alpha_2 + \left(\frac{\alpha_1 Y_1}{\rho_2\kappa_2} - \frac{\alpha_2 Y_2}{\rho_1\kappa_1}\right)(Y_1 - \alpha_1)\right)\underline{u}_r.\nabla p
\end{aligned}
\tag{3}
$$

where $h_k = i_k + p/\rho_k$ is the specific enthalpy of phase k and $\kappa_k = (\frac{\partial i_k}{\partial p})_k$. In the following, we will assume that this system of equations is completed with Stiffened gas equations of state for both phase, i.e. i_k is such that $i_k = \frac{p+\gamma_k p_{k,\infty}}{(\gamma_k-1)\rho_k} + i_{k,0}$, with γ_k, $p_{k,\infty}$ and $i_{k,0}$ are constants describing the thermodynamical properties of the material.

3 Properties of the model

The five-equation model (2), and therefore the model with second-order terms (3), is an unconditionally hyperbolic model, as shown by Murrone and Guillard [3]. Indeed, it features three distinct real eigenvalues, whose associated eigenvectors span $\mathbb{R}^5$. These eigenvalues are given by u, $u - \hat{c}$ and $u + \hat{c}$, where $\hat{c}$ is the well-known speed of sound in a multiphase flow given by the equation $1/(\rho\hat{c}^2) = \alpha_1/(\rho_1 c_1^2) + \alpha_2/(\rho_2 c_2^2)$ [5].

A second very interesting property of this model is the existence of two independent entropy-entropy flux pairs, one for each phase, which are consistent with the additional second-order terms. These pairs are $(-\alpha_k\rho_k s_k, -\alpha_k\rho_k s_k u)$, where s_k is the specific entropy of phase k.

Indeed, algebraic manipulations of the system (3) gives two equation on the phase entropies s_k

$$
\begin{aligned}
&-\partial_t(\alpha_k\rho_k s_k) - \operatorname{div}(\alpha_k\rho_k s_k\underline{u})\\
&\quad = \varepsilon_u \operatorname{div}((-1)^{k+1} Y_k Y_{k'} s_k (Y_1 - \alpha_1)\nabla p) - \varepsilon_u \frac{\rho Y_{k'}}{T_k}\left(\frac{(Y_1 - \alpha_1)}{\rho}\right)^2 \|\nabla p\|^2
\end{aligned}
\tag{4}
$$

where $k' = 3 - k$. Considering equation (4), it is therefore clear that dissipative terms due to velocity disequilibrium increase the phase entropies along the

trajectories. As a consequence, the mixture entropy $s = Y_1 s_1 + Y_2 s_2$ is also an increasing variable along the trajectories.

4 Numerical approximation

A fractional step is performed to solve numerically the system (3), as performed by Guillard and Duval [6]. This consists in first solving the convective step, i.e. solving the classical five-equation system (2), and then focusing on equations where only second-order dissipative terms appear.

4.1 Convective step

To solve the convective step, we use the Finite Volume method proposed by Murrone and Guillard [3]. This method is based on VFRoe-ncv methods [7], but characteristics on both sides of the discontinuity are linearized when using the approximate Riemann solver, which leads to a more robust solver than classical VFRoe-ncv methods.

It should be noted that the equation on the phase 1 volume fraction is not solved using the form given in system (2), because this form may cause numerical instabilities when cohesion pressures $p_{k,\infty}$ are very different, which is usually the case when dealing with gas-liquid flows. Indeed, when discretizing this equation, large rounding errors arise when evaluating the pressure. Thus, the volume fraction equation is transformed into

$$\partial_t \alpha_1 + \nabla.(\alpha_1 \underline{u}) - \frac{\alpha_1 C_2}{\alpha_1 C_2 + \alpha_2 C_1} \operatorname{div} \underline{u} = 0 \tag{5}$$

which prevents the propagation of large rounding errors.

4.2 Dissipative step

The dissipative step consists in solving the following equations, using the state vector ${}^t(\rho Y, \rho e, \alpha_1, \rho, \rho \underline{u})$

$$\partial_t \rho Y_1 = -\operatorname{div}(\rho Y_1 Y_2 \underline{u}_r) \tag{6.1}$$

$$\partial_t \rho e = \operatorname{div}((h_2 - h_1)\rho Y_1 Y_2 \underline{u}_r) \tag{6.2}$$

$$\begin{aligned}(\alpha_1 C_2 + \alpha_2 C_1)\partial_t \alpha_1 = {} & (Y_1 \alpha_1 C_2 - Y_2 \alpha_2 C_1)\underline{u}_r.\nabla \alpha_1 \\ & - \alpha_1 \alpha_2 (C_1 \operatorname{div}(Y_2 \underline{u}_r) + C_2 \operatorname{div}(Y_1 \underline{u}_r)) \\ & - \left(\alpha_1 \alpha_2 + \left(\frac{\alpha_1 Y_1}{\rho_2 \kappa_2} - \frac{\alpha_2 Y_2}{\rho_1 \kappa_1}\right)(Y_1 - \alpha_1)\right)\underline{u}_r.\nabla p\end{aligned} \tag{6.3}$$

$$\partial_t \rho = 0 \tag{6.4}$$

$$\partial_t \rho \underline{u} = 0 \tag{6.5}$$

Because the mixture density ρ and momentum $\rho\underline{u}$ are constant with respect to time during the dissipative step, the system can be simplified and written with the variables ${}^t(Y_1, i, \alpha_1)$

$$\rho\,\partial_t Y_1 = -\operatorname{div}(\rho Y_1 Y_2 \underline{u}_r) \tag{7.1}$$

$$\rho\,\partial_t i = \operatorname{div}((h_2 - h_1)\rho Y_1 Y_2 \underline{u}_r) \tag{7.2}$$

$$\begin{aligned}(\alpha_1 C_2 + \alpha_2 C_1)\partial_t \alpha_1 &= (Y_1\alpha_1 C_2 - Y_2\alpha_2 C_1)\underline{u}_r.\nabla\alpha_1 - \alpha_1\alpha_2(C_1 \operatorname{div}(Y_2\underline{u}_r) + C_2 \operatorname{div}(Y_1\underline{u}_r)) \\ &\quad - \left(\alpha_1\alpha_2 + \left(\frac{\alpha_1 Y_1}{\rho_2\kappa_2} - \frac{\alpha_2 Y_2}{\rho_1\kappa_1}\right)(Y_1 - \alpha_1)\right)\underline{u}_r.\nabla p\end{aligned} \tag{7.3}$$

We use again a fractional step method to solve this system. First, a "dissipative advection step" is performed, which consists in solving the following equation

$$\partial_t \alpha_1 \frac{Y_1\alpha_1 C_2 - Y_2\alpha_2 C_1}{\alpha_1 C_2 + \alpha_2 C_1}\underline{u}_r.\nabla\alpha_1 \tag{8}$$

Considering that $\underline{u}_a = \frac{Y_1\alpha_1 C_2 - Y_2\alpha_2 C_1}{\alpha_1 C_2 + \alpha_2 C_1}\underline{u}_r$ is a "dissipative advection velocity", we use a characteristic method to solve it, which ensures that the volume fraction α_1 remains between 0 and 1 if it was in this interval before, providing that the cfl condition $\Delta t \leq \min_{1\leq i\leq N} \frac{\Delta x}{|u_{ai}|}$ is verified, which is usually the case. If this is not the case, the time step is reduced and several "dissipative advection steps" are performed until the convective time step is reached.

Next, we focus on the term including the norm of the pressure gradient. We therefore want to solve the equation

$$\partial_t \alpha_1 = -\varepsilon_u \frac{\alpha_1\alpha_2(\rho_1 - \rho_2)}{\rho^2(\alpha_1 C_2 + \alpha_2 C_1)}\left(\alpha_1\alpha_2 + \left(\frac{\alpha_1 Y_1}{\rho_2\kappa_2} - \frac{\alpha_2 Y_2}{\rho_1\kappa_1}\right)(Y_1 - \alpha_1)\right)\|\nabla p\|^2 \tag{9}$$

In this step, we evaluate the pressure gradient explicitly, and then we solve this equation using a Newton method for each point.

Finally, we perform a "dissipative convection step", which consists in solving the system

$$\begin{aligned}\rho\partial_t Y_1 &= -\operatorname{div}(\rho Y_1 Y_2 \underline{u}_r) \\ \rho\partial_t i &= \operatorname{div}((h_2 - h_1)\rho Y_1 Y_2 \underline{u}_r) \\ \partial_t \alpha_1 &= -\frac{\alpha_1\alpha_2}{(\alpha_1 C_2 + \alpha_2 C_1)}(C_1 \operatorname{div}(Y_2\underline{u}_r) + C_2 \operatorname{div}(Y_1\underline{u}_r))\end{aligned} \tag{10}$$

which is done using a Newton method.

5 Numerical results

5.1 Air-water shock tube

We present the numerical results for a shock-tube problem, which consists in a tube of length 1.0 m, filled with air and water with a homogeneous volume fraction $\alpha_1 = 0.5$ through the tube. The tube is divided into a high-pressure room for $x < 0.7$ m, where the pressure is $p = 10^9$ Pa, and a low pressure room ($x > 0.7$ m) where $p = 10^5$ Pa. Water and air are both governed by Stiffened gas equations of state, with the following thermodynamical properties: $\gamma_G = 1.4$, $p_{G,\infty} = 0$ Pa, $\gamma_L = 4.4$, $p_{L,\infty} = 6.0\,10^8$ Pa. The velocity relaxation time is assumed to be a constant. To determine it, we require that the drag force we use must be equal to the drag force used in the Neptune code [1], which gives the equality

$$\underline{M}_1^d = \frac{\rho}{\varepsilon_u}(\underline{u}_2 - \underline{u}_1) = \frac{1}{8} S_V \rho_2 C_D |\underline{u}_2 - \underline{u}_1|(\underline{u}_2 - \underline{u}_1) \tag{11}$$

with $S_V = \frac{\alpha_1 S_{bubble}}{V_{bubble}} = \alpha_1 \frac{3}{R}$ is the interfacial area per volume unit and C_D is the drag coefficient, given by $\frac{24}{Re}(1 + 0.1925\, Re^{0.63})$ [8], with the Reynolds number $Re = \frac{\alpha_2 \rho_2 2R|\underline{u}_2 - \underline{u}_1|}{\mu_2}$. We take the dynamic viscosity of water $\mu_2 = 10^{-3}$ Pa.s, and we choose the bubble radius as $R = 5\,10^{-4}$ m, and the remaining variables are found by performing single-phase shock-tube test case for water and air, which give $\rho_{air} = 0.47$ kg.m^{-3}, $\rho_{water} = 1100$ kg.m^{-3}, $u_{air} = 25000$ m.s^{-1} and $u_{water} = 230$ m.s^{-1}. Thus, it is found that ε_u is equal to $2.4\ 10^{-5}$ s.

On Figure 1, we compare results obtained with the five-equation reduced model of [3], the seven-equation model and the present dissipative model. The solution consists in a rarefaction, a contact discontinuity and a shock traveling to the right: the initial pressure imbalance pushes a plug of water to the right (the front is the shock wave, the back is the contact discontinuity) and a low-pressure zone appears in the wake (the rarefaction wave). It is seen that the addition of dissipative terms allows to reproduce to a large extent the results of the seven equation one while the non-dissipative model is unable to introduce any velocity disequilibria between the two phases. We also note that the seven equation model predicts a change in the mass fraction inside the shock zone, this feature is reproduced by the dissipative model whereas the reduced model of [3] is unable to reproduce this feature.

5.2 Water-faucet problem

We now perform the water faucet test, which is a usual benchmark test for two-phase flows [9]. It consists in a vertical column of length 12 m, where a column of water is surrounded by air. Initially, the mixture is homogeneous along the tube, where the air volume fraction is $\alpha_1 = 0.2$, air density and velocity are $\rho_1 = 1$ kg.m^{-3} and $u_1 = 0$ m.s^{-1}, water density and velocity are $\rho_2 = 1000$ kg.m^{-3} and $u_2 = 10$ m.s^{-1}, and pressure is equal to $p = 10^5$ Pa. We again use the stiffened

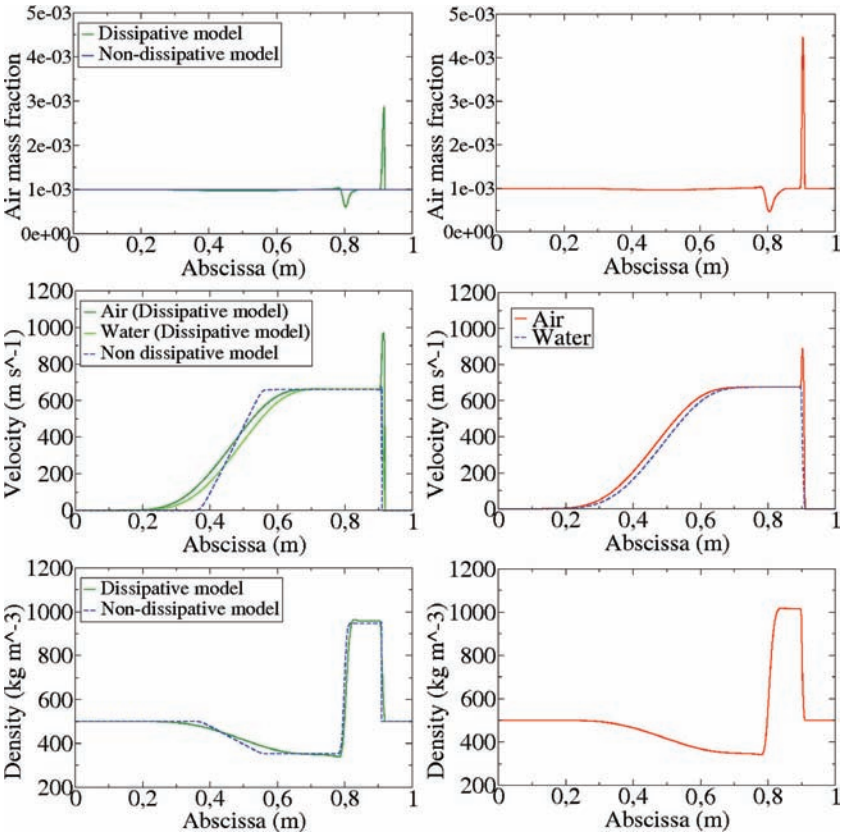

Figure 1: Comparison between the reduced model of [3] and the dissipative model (left) and the seven-equation model (right): air-water shock tube test after 150 μs. Mesh of 2001 nodes.

gas equation of state for both phase, with the same thermodynamic properties as in the previous test.

At time $t = 0\,\mathrm{s}$, a gravity field with $g = 9.81\,\mathrm{m.s}^{-2}$ is applied, which causes a lengthening of the water jet. This test is interesting because air and water have different velocities, and therefore the five-equation model completely fails to reproduce results given by the six- or seven-equation models. Figure 2 shows the results for the dissipative five-equation model and the seven-equation model on a mesh of 1001 nodes. The velocity relaxation time has been fixed to $\varepsilon_u = 10^3\,\mathrm{s}$, because this test is usually performed with no drag force, and although we cannot have zero drag in this five-equation model, such a value will reduce it dramatically. It should be noted that this values is also used for the seven-equation model. The pressure relaxation time is set to $\varepsilon_p = 10^{-12}\,\mathrm{s}$ for the latter model, which ensure an equality of the phase pressures.

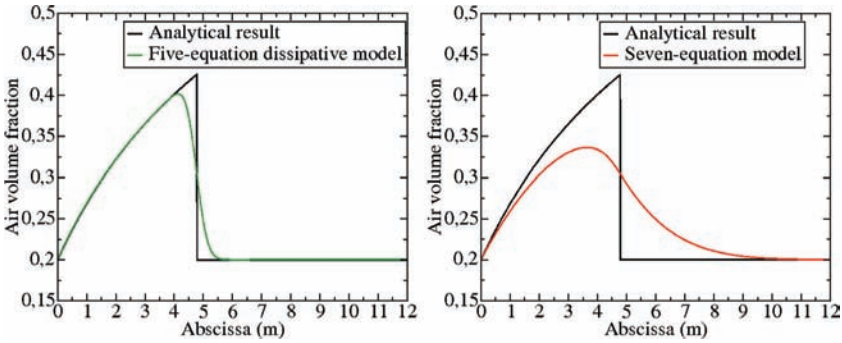

Figure 2: Comparison between the dissipative five-equation model (left) and the seven-equation model (right): Water-faucet test after 0.4 s. Mesh of 1001 nodes.

If we make the approximation of the incompressibility of the liquid and if we neglect the variations of the gas pressures, an analytic solution can be found. It can be seen on Figure 2 that the dissipative five-equation model reproduces in a large extent the variation of the air volume fraction. It can be even noticed that the scheme is less diffusive than the seven-equation model, because of the large number of waves of the latter. Thus, our model can deal with flow phenomena including large velocity differences between the phases, even if it is originally designed for small relative velocities.

6 Conclusion

We have derived a five-equation dissipative model from the standard bifluid six-equation model using first order Chapman-Enskog expansions. Thanks to these dissipative terms, this model can deal with flows featuring differences between phase velocities, although it features only one velocity. Numerical results are very promising, and show that the model can simulate flows with shocks or counter-currents in an accurate way, while being hyperbolic and less complex than the two-pressures two-velocity models.

Acknowledgements

The work of Mathieu Labois and Marc Grandotto has been achieved in the framework of the NEPTUNE project, financially supported by CEA (Commissariat à l'Énergie Atomique), EDF (Électricité de France), IRSN (Institut de Radioprotection et de Sûreté Nucléaire) and AREVA-NP.

References

[1] Guelfi, A., Bestion, D., Boucker, M., Boudier, P., Fillion, P., M., G., Hérard, J.M., Hervieu, E. & Péturaud, P., Neptune - a new software platform for advanced nuclear thermal-hydraulics. *Nuclear Science and Engineering*, **156(3)**, pp. 281–324, 2007.

[2] Baer, M. & Nunziato, J., A two-phase mixture theory for the deflagration-to-detonation transition in reactive granular materials. *Journal of Multiphase Flows*, **12**, pp. 861–889, 1986.

[3] Murrone, A. & Guillard, H., A five equation reduced model for compressible two-phase flow computations. *Journal of Computational Physics*, **202(2)**, pp. 664–698, 2005.

[4] Natalini, R., Recent mathematical results on hyperbolic relaxation problems. *Analysis of systems of conservation laws*, Chapman and Hall/CRC, Boca Raton, FL: Aachen, pp. 128–198, 1997.

[5] Drew, D. & Passman, S., *Theory of multicomponents fluids*. Springer: New York, 1998.

[6] Guillard, H. & Duval, F., A darcy law for the drift velocity in a two-phase flow model. *Journal of Computational Physics*, **224(1)**, pp. 288–313, 2007.

[7] Buffard, T., Gallouet, T. & Hérard, J.M., A sequel to a rough godunov scheme: Application to real gases. *Computers and fluids*, **29**, pp. 673–709, 2000.

[8] Clift, R., Grace, J. & Weber, M., *Bubble drops and particles*. Academic Press: New York, 1978.

[9] Saurel, R. & Abgrall, R., A multiphase godunov method for compressible multifluid and multiphase flows. *Journal of Computational Physics*, **150**, pp. 425–467, 1999.

This page intentionally left blank

Comparison of mixing between single- and bubbly two-phase systems in a Rushton stirred tank

J. S. Moghaddas[1], J. Revstedt[2,3], C. Trägårdh[2,4] & L. Fuchs[2,3]
[1]*Sahand University of Technology, P.O. Box 51335/1996, Tabriz, Iran*
[2]*Lund Institute of Technology at Lund University, Sweden*
[3]*Division of Fluid Mechanics, P.O. Box 118, SE-221 00 Lund, Sweden*
[4]*Division of Food Engineering, P.O. Box 124, SE-221 00 Lund, Sweden*

Abstract

Mixing is a widely practiced operation to effect distribution, intermingling and homogeneity of matter. Stirred tanks with different geometries (such as in main container tanks, impellers, baffles, etc.) are also widely used to mix different materials. The forces applied by impellers develop overall circulation or bulk flow. Superimposed on this flow pattern, there are turbulent eddies and also molecular diffusion of the fluids, which have a direct effect on the mixing phenomenon into the stirred tank reactors. In this work the mixing field in an aerated stirred reactor with two Rushton turbines was experimentally analysed using the particle image velocimetry technique (PIV). The mixing characteristics were measured at three different impeller rotational speeds: 225, 300 and 400 rpm, for both single- and bubbly two-phase mixing systems. The bubbles will, due to reflection and refraction of the laser light, cause an uneven and unknown distribution of light intensity in the measurement plane. This can be compensated for by introducing a second tracer with a known concentration. Based on this method the mixing of a determining tracer in liquid-phase in a double Rushton turbine stirred tank is studied. Using the PIV measurement technique and the flow structure of the liquid phase, the pumping capacity of those systems were calculated. The aerated-to-unaerated relative power was also calculated from the experimental results and compared with the theoretical values. Reasonable agreement between experimental and theoretical results was obtained.
Keywords: mixing, bubbly flow, two- phase flow, stirred reactor, Rushton, PIV.

WIT Transactions on Engineering Sciences, Vol 59, © 2008 WIT Press
www.witpress.com, ISSN 1743-3533 (on-line)
doi:10.2495/AFM080261

1 Introduction

Stirred tanks are widely used for the mixing of two miscible fluids in the chemical, food and process industries. Our understanding of the flow structure, the behaviour of stirred systems and the basic mixing mechanisms has improved over recent years, but there are still some problems associated with the mixing of fluids in bubbly gas-liquid stirred reactors.

The radial pumping flow rate of an impeller, Q_r, is defined as the volumetric flow rate leaving the turbine blades, for a chosen radial position, r, from the centre of the stirred tank, and can be expressed as:

$$Q_r = 2\pi \cdot r \int_{z_1}^{z_2} \overline{U_r} \mathrm{dz} \tag{1}$$

where $\overline{U}_r$ is the average velocity component in the radial direction. The integration is often performed over the blade height. Assuming $\overline{U}_r$ to be proportional to the blade tip speed, $\overline{U_r} \propto \pi ND$, then the pumping capacity near the blade can be expressed as in Eq. (2) (Holmes et al. [4]):

$$Q_p = N_q N D^3 \tag{2}$$

where N is the turbine rotational speed, N_q is called the pumping number and D is the impeller diameter. Comparing the results of different studies for single-phase flow in the stirred tanks with Rushton turbines, at the impeller tip where there is no fluid entrainment, the values of the pumping number varied between 0.75 and 1 (Wu and Patterson [7]). The value of Q_r can be assumed to be equal to Q_p near the blade tip. Therefore, by applying Eqs. (1) and (2) the value of the pumping number can be determined by extrapolating the data for the normalised pumping radial flow rate (Q_r / ND^3), as a function of the normalised radius (r / R), in a fully developed flow region of a discharging jet.

The stirring power input for the unaerated single-phase case, P_u, can be calculated using Eq. (3) (Guillard et al. [3]):

$$P_u = P_0 . (\rho N^3 D^5) . \left(\frac{NB_{imp}}{V_{Liq}} \right) \tag{3}$$

where P_0 is the power number and ρ is the density of the continuous phase, NB_{mp} is the number of impellers (two in this study) and V_{Liq} is the total volume of the liquid in the stirred tank. A value of $P_0 = 5.5$, determined by Guillard et al. [3] for the same stirred reactor, was used in the present study.

Trägårdh [6] used an extensive $k - \varepsilon$ numerical model to solve the equation of motion in order to calculate the gas void fraction, concentration, velocity and energy dissipation rate fields in an aerated stirred tank. He showed that the mass

transfer is higher in the regions of high shear stress, such as near the wall and the interface between the rapidly accelerating "jet" from the turbines and the slow rotating flow. He also stated that the gas void fraction is higher in the region closest to the turbine. In calculating the aerated power, P_a, he used the following equations:

$$P_a = P_u(1-12.6N_G) \qquad \mathrm{N_G} < 0.035 \tag{4}$$

$$P_a = P_u(0.62-1.85N_G) \qquad \mathrm{N_G} > 0.035 \tag{5}$$

where $N_G = Q_g / ND^3$ is the gas flow number and Q_g is the gas flow rate. It can be seen that the reduced aerated power is a function of the gas sparging flow rate, the geometry of the turbine, the rotational speed and the unaerated power, P_u.

At a constant rotational speed (N) the aerated turbine power (P_a) is lower than the unaerated power (P_u). The subscripts *a* and *u* denote the aerated bubbly two-phase and unaerated single-phase flow patterns, respectively. For a low gas void fraction, the ratio between aerated and unaerated pumping flow rates is equal to the ratio between their related powers (Bakker and van den Akker [1]):

$$\frac{(Q_r)_a}{(Q_r)_u} = \frac{P_a}{P_u} \tag{6}$$

Equation (6) shows that the mechanical agitation, which is a hydrodynamic generator, is affected by air dispersion through the efficiency factor $\frac{P_a}{P_u}$.

2 Materials and methods

The design and the dimensions of the stirred tank with two Rushton impellers of standard geometry, which were used in this work, are shown in Figure 1. The stirred tank consists of a flat-bottomed glass cylinder (refractive index 1.47 at a wavelength of 587 nm) an inner diameter *T* of 0.30 m. Four vertical baffles are symmetrically placed around the tank wall, each with a width of one-tenth of the tank diameter ($\ell_{baffle} = 0.1T$). The Rushton stirrer with two impellers, which is of standard design with a diameter (D) equal to one-third of the tank diameter (*D/T=1/3*), is located with a clearance from the tank bottom of about half of the tank diameter ($C_1=0.55T$). The upper impeller is placed $\Delta C=0.7T$ above the lower one. A pump drives the turbines and the stirring speed is measured using a calibrated digital oscilloscope. In order to reduce optical refractive index effects at the cylindrical surface of the tank, it is placed in a square glass vessel. The stirred tank is filled with tap water as the main continuous phase fluid, the surface of which is $C_2=0.55T$ above the upper impeller. The square vessel is also filled with water to reduce light refraction at the interface. For more details on the geometry of the stirred tank used in this study see Guillard et al. [3].

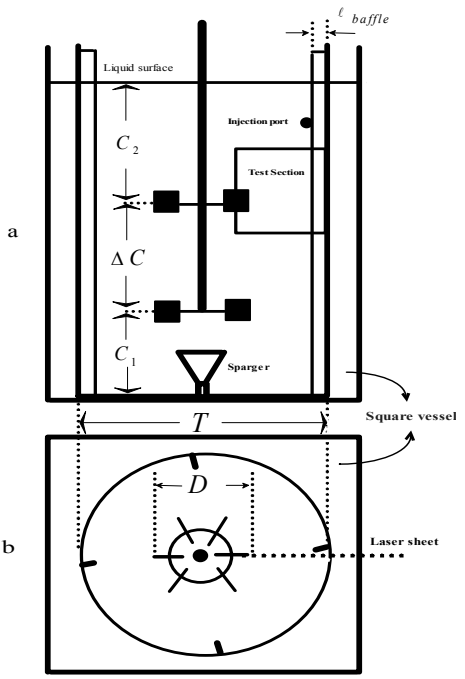

Figure 1: Stirred tank and impellers: a) side view, b) top view.

For the bubbly two-phase flow measurements, air bubbles are introduced, at a superficial gas velocity of 3.96×10^{-4} m/s 50 mm below the bottom impeller, through a sparger with a diameter of 3D/4 with 30 active orifices at the chosen gas flow rate.

A double-cavity 2 × 25 mJ Nd:Yag (Continuum) pulsed laser is used to produce a beam at a wavelength of 532 nm. The laser beam passes through a plano-concave lens to produce a two-dimensional vertical sheet of light (2 mm thick). Velocity measurements of the liquid phase using PIV were performed and 3 different rotational speeds of the impellers: 225, 300 and 400 rpm, were employed. For the determination of the average velocity a CCD camera captured 500 instantaneous images in each case.

In the measurements, the water in the tank was seeded with Rhodamine-B fluorescent tracer particles, 1-20 μm in diameter. The flow fields were measured at 23°, 30° and 37.5° angles behind the impeller blades for the three chosen rotational speeds of the impellers, i.e. 225, 300 and 400 rpm, respectively. A CCD camera with two long-pass filters, OG-550 and OG-570 (Melles Griot, Irvine, CA, USA) were used to capture the fluorescent signals from the particles. By masking the scattered signals from the bubbles using the two filters, only the signal from the seeding particles will be captured. The PIV image processing of the liquid continuous phase was performed using multipass interrogation windows decreasing from 32 × 32 to 16 × 16 pixels.

The aerated-to-unaerated relative power $\left[\frac{P_a}{P_u}\right]$ was determined experimentally using Eq. (6), and theoretical values were calculated by applying Eqs. (3) and (4).

3 Results and discussion

The flow pattern and the effects of aeration, for an impeller rotational speed of 300 rpm, are shown in more details in Figure 2. Figure 2a shows the normalised radial mean velocity profiles at a chosen streamwise location below the impeller as a function of the normalised distance from the blade's centreline, 2z/b = –2.36 for both single- and bubbly two-phase flow systems. It can be seen that the normalised radial velocities of the continuous liquid phase in the bubbly two-phase flow system are lower than those found in single-phase flow. Below the impeller region included higher volumetric gas void fraction according to the visualization, which discussed earlier. A comparison of the axial mean velocity results in a chosen normalised radius close to the wall, r/R = 2.8 is shown in Figure 2b. The bubbles enhance the axial velocity of the liquid continuous phase. Near the wall it could be expected that the influence of the impellers on the motion of the bubbles was less than in the central part of the tank.

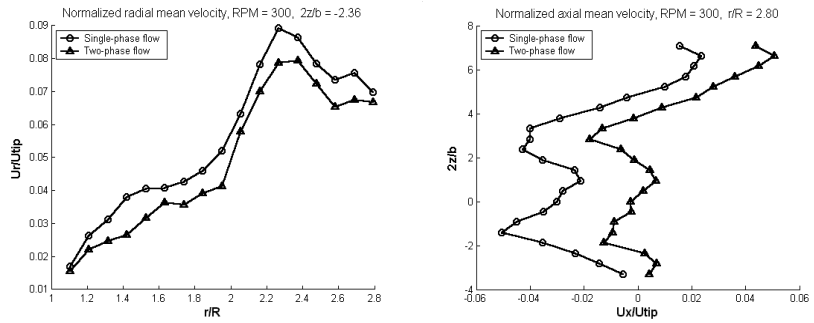

(a) (b)

Figure 2: Comparison of the normalised mean velocity profiles in single- and two-phase flow systems for an impeller speed of 300 rpm. a) Radial profiles, 2z/b = –2.36, b) axial profiles at r/R = 2.80.

Figure 3 shows the centreline radial mean velocity profiles for the three impeller rotational speeds investigated in both single- and bubbly two-phase flow systems. The velocity data are normalised by the tip velocities, $U_{tip} = \pi \cdot N \cdot D$, at each impeller speed. The non-random velocity fluctuation caused by the periodic passage of the impeller blades makes the flow structure in the region close to the impeller (1 < r/R < 1.5) more complicated. Stoots and

Calabrese [5] found that the extent of periodicity in the radial direction is from r/R = 0 to 1.7 and is controlled equally by the radial and tangential components of mean velocity, which shows very good agreement with the presented results in this study. The extent of periodicity in the mean velocity results was found for all three-impeller rotational speeds. However, as the flow field in this range is blade angle dependent, some differences for the mean velocities were noted between different impeller speeds. In this region an accurate measurement of the velocity field is very difficult due to the effect of strong out-of-plane motion due to the swirl. The influence of the bubbles on the centreline mean velocity profile was found to be more pronounced at the highest impeller speed (400 rpm) than at the others.

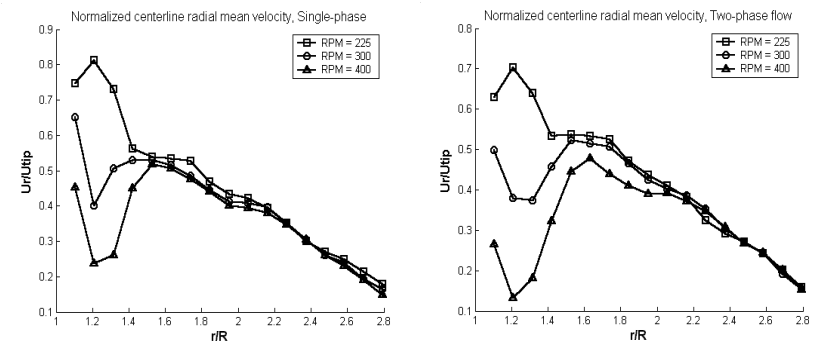

(a) (b)

Figure 3: Centreline radial mean velocity for three different rotational speeds, 225, 300 and 400 rpm. a) Single-phase flow, b) two-phase flow.

The normalised pumping flow rate at each speed of rotation for both single- and two-phase flow systems is presented in Figure 4. The results show that the normalised pumping flow rate is almost independent of the impeller speed in the single-phase flow system. The highest impeller speed (400 rpm) shows slightly different values than those for the other speeds. The values of normalised pumping flow rate for the bubbly two-phase flow system show some variation with the impeller speed and the distance from the blade. The effect of aeration on the pumping flow rate is the direct result of changes in the impeller hydrodynamics and the flow pattern.

Table 1 gives the calculated tip pumping numbers for all cases. In the case of single-phase flow it can be observed that the pumping number remains almost constant, with a mean value of 0.89, independent of the impeller rotational speed. These results are in very good agreement with the values obtained by Wu and Patterson [7]. The values of pumping number for the case of two-phase flow differ by the factor aerated-to-unaerated power ratio, which is the same effect as that on the normalised radial pumping flow rate.

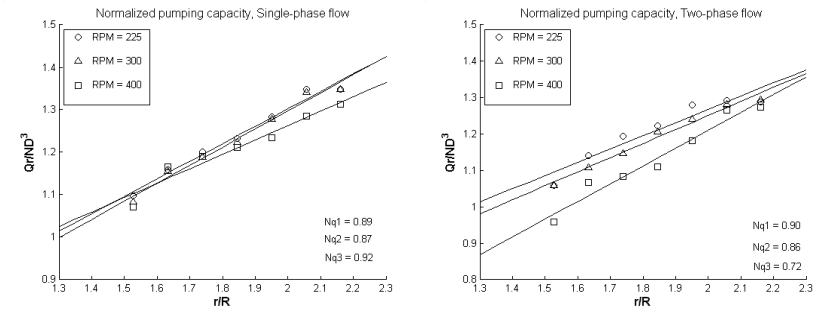

(a) (b)

Figure 4: Normalised pumping flow rate for 3 different rotational speeds, 225, 300 and 400 rpm. a) Single-phase flow, b) two-phase flow.

Table 1: Calculated tip pumping numbers for 3 different rotational speeds, 225, 300 and 400 rpm.

RPM	**225**	**300**	**400**
Single-phase flow	0.89	0.87	0.92
Two-phase flow	0.90	0.86	0.72

Table 2: Calculated mixing characteristics of single- and two-phase flow for three different rotational speeds, 225, 300 and 400 rpm.

RPM	**225**	**300**	**400**
N (s^{-1})	3.75	5	6.67
U_{tip} (m/s)	1.18	1.57	2.09
Re_{imp}	3.75×10^{4}	5.00×10^{4}	6.67×10^{4}
N_G	7.66×10^{-3}	5.67×10^{-3}	4.25×10^{-3}
Pu (W/kg)	0.12	0.30	0.72
Pa/Pu	0.90	0.93	0.95
Pa/Pu (Eq. 6)	0.97	0.96	0.93

Table 1 gives the calculated tip pumping numbers for all cases. In the case of single-phase flow it can be observed that the pumping number remains almost constant, with a mean value of 0.89, independent of the impeller rotational speed. These results are in very good agreement with the values obtained by Wu and Patterson [7]. The values of pumping number for the case of two-phase flow differ by the factor aerated-to-unaerated power ratio, which is the same effect as that on the normalised radial pumping flow rate.

At the aeration rate used the aerated stirring power in put (P_a) decreases with increasing impeller speed due to the decrease in the gas flow number (N_G), see Table 2. The relative power consumption was shown to be greater than 90% for all three impeller speeds without a strong drop, as was found by Bakker and van

den Akker [2], in the range of 0.02 < N_G < 0.04. Because in this study the values of gas flow numbers for every impeller speeds were less than the critical number of 0.02 found by them. A comparison between the theoretical and average experimental values of P_a/P_u shows quiet good agreement, spatially, for the two higher impeller speeds. Table 2 gives the calculated mixing characteristics of single- and bubbly two-phase flow for the three different rotational speeds.

4 Conclusions

The mixing field in an aerated stirred reactor with two Rushton turbines was experimentally analysed using the particle image velocimetry technique. The mixing characteristics were measured at three different impeller rotational speeds: 225, 300 and 400 rpm, for both single- and bubbly two-phase mixing systems. Based on PIV results, the pumping capacity of the systems was calculated. The aerated-to-unaerated relative power was also calculated from the experimental results and compared with the theoretical values. Reasonable agreement between experimental and theoretical results was obtained.

Acknowledgements

The authors are grateful for the partial financial support from Iranian Ministry of Science, Research and Technology and the Swedish Foundation for Strategic Research, program for Multiphase Flow.

References

[1] Bakker A; van den Akker HEA (1994a) A computational model for the gas-liquid flow in stirred reactors. Trans IChemE 72: 594–606.
[2] Bakker A; van den Akker HEA (1994b) Gas-liquid contacting with axial flow impellers. Trans IChemE 72: 573–582.
[3] Guillard F; Trägårdh C; Fuchs L (1999) A study of turbulent mixing in a turbine-agitated tank using a fluorescence technique. Experiments in Fluids 28: 225–235.
[4] Holmes DB; Voncken RM; Dekker JA (1964) Fluid flow in turbine-stirred, baffled tanks-I Circulation time. Chemical engineering Science 19: 201–208.
[5] Stoots CM; Calabrese RV (1995) Mean velocity field relative to a Rushton turbine blade. AIChE Journal 41: 1–11.
[6] Trägårdh Ch. (1988) A hydrodynamic model for the simulation of an aerated agitated fed-batch fermentor. Proceeding of the 2nd International Conference on Bioreactor Fluid Dynamics: 117–134.
[7] Wu H; Patterson GK (1989) Laser-Doppler measurements of turbulent-flow parameters in a stirred mixer. Chemical Engineering Science 44: 2207–2221.

Commercial scale slurry bubble column reactor optimization

W. Strasser & A. Wonders
Eastman Chemical Company, USA

Abstract

An in-depth numerical study has been carried out to investigate a high-pressure commercial scale (2–8 meter diameter) slurry bubble column reactor (SBCR). Typical superficial gas velocities are in the range of 0.5–3 m/s, and overall vapor hold-ups are in the range of 0.45–0.85. The study revealed that steady compartmental reaction models do not match plant data when reaction time constants are very fast. Also, off-the-shelf commercial CFD codes do not produce useful information about a reactive column of this scale and aeration without tuning to reconcile with vapor hold-up and reactant operating data "anchors" from in-plant units. Important measures include both transient and time-averaged profiles, integrals, and extrema of vapor hold-up and reactants. The present study proposes reactor designs that improve productivity and product quality.

Keywords: oxidation, staging, chaos, turbulence, pX, TPA.

1 Introduction

The liquid-phase partial oxidation of para-xylene (pX) to terephthalic acid (TPA) is conducted on a very large commercial scale (agitated vessels and bubble columns), principally for providing raw material for polyester fiber and packaging products. Huge oxidation reactors provide individual capacities presently ranging from 1,500 to 3,000 metric tons per day (TPD) of TPA for new construction. Although the partial oxidation of pX to TPA proceeds at very high yields and purities, further small improvements have a significant impact due to scale. The overall stoichiometry of TPA production is deceptively simple, as shown in equation (1).

$$pX + 3O_2 = TPA + 2H_2O \tag{1}$$

WIT Transactions on Engineering Sciences, Vol 59, © 2008 WIT Press
www.witpress.com, ISSN 1743-3533 (on-line)
doi:10.2495/AFM080271

Behind the seemingly simple overall reaction equation, there are at least four principle reaction steps; and each of those steps typically involves several elementary reaction sub-steps. In fact, the principal intermediates can even be reached by competing, alternative reaction pathways. In addition, there are literally hundreds of impurities formed at low to extremely low rates. Some of these impurities relate to impurities in the pX feedstock, and some derive from pX itself. The various impurities affect the TPA product's fitness for use differently, but some impurities are important at concentrations as low as 1 PPM by weight. Some of the particularly noxious impurities involve two or more aromatic rings coupled together.

Broadly speaking these undesirable reactions are suppressed by higher concentrations of dissolved oxygen and are promoted by higher concentrations of dissolved aromatic species. To elevate the concentration of dissolved oxygen, it is desirable to maximize aeration of the reaction medium, promoting mass transfer from gas to liquid phase. Notably, the reaction proceeds with such intensity that the average survival time of an oxygen molecule after dissolving is a very few seconds. Thus, the local concentration of oxygen in the gas phase varies greatly depending upon the agitation and location of gas feeding; and the concentration of dissolved oxygen involves a competition between dissolution rate and chemical demand. Similarly, the local concentration of pX will vary according to agitation and the location of pX addition. To lower the peak concentration of dissolved aromatics it is desirable to mix off the feed plume of pX quickly. However, the interplay of dissolved oxygen and dissolved aromatic is very complex. Different aromatic intermediate species react at different rates and with different stability while "searching" for an oxygen molecule. Important interactions exist when optimizing local oxygen and local aromatic concentrations. As a result, one of the goals in improving upon this rich, well-established method of making TPA is to optimize methods of gas and liquid feeding. A disclosure of the current invention can be found in US Patent Application # 20060116531.

Although the experimental and computational work for bubble columns has historically been fruitful, nothing exists for the conditions of the present work:

- High pressure (0.2 – 3 megapascal gauge), and
- High superficial gas velocity and holdup (0.5 – 3 m/s, 0.45 to 0.85), and
- High solids content (8% – 45% of the total slurry weight), and
- Strong evaporation (>30% of the gas fed by mass at operating temperatures as high as 250°C), and
- Large diameter (2 – 8 meters), and
- Fast reaction kinetics (pseudo half-lives of some species under 10 seconds).

The most recent work that comes near the conditions in the present work is that of Nottenkamper et al. [1] with superficial velocities approaching 1.5 m/s in a 1.0 meter diameter column at atmospheric pressure. They showed liquid centreline velocities near 2.0 m/s, with centreline hold-ups approaching 0.8. They found near-linear positively-sloped axial hold-up profiles, with the slope staying about the same (excluding the bottom transition region) with increasing superficial velocity. A near-linear hydrostatic pressure profile resulted from all

the column chaos. Since it is known that pressure strongly affects bubble size population (Letzel et al. [2] and many others), and since the other evaporative, chemical, and solids issues are removed, the results of this study can only be used as a guide. Other works will be discussed where pertinent in the upcoming discussions.

2 Method

2.1 Physics

Numerical methods for investing bubble columns have been a subject of intense study for years. An axial dispersion approach is employed by Xie and Li [3] to study pX oxidation. A 151-page review of various numerical approaches was given by Rafique et al. [4] in 2004. It was found through internal evaluations at Eastman Chemical Company that axial dispersion and compartmental approaches do not produce chemical species profiles for pX oxidation like those actually measured in a commercial scale unit. The results of a steady compartmental model (with the average of local fluctuations superimposed onto the mean) are superior to an axial dispersion model but still apparently distort the transient effects of correlated hydrodynamics and chemistry. As a result, a fully transient 3-D hydro-kinetic Eulerian-Eulerian three-phase CFD approach is sought. Each phase is allowed separate velocity, turbulence, thermal, and chemical fields, but share a common pressure. The liquid is assumed to be everywhere continuous, while the compressible gas and solid phases are assumed to be everywhere dispersed. Every computational cell is given some amount of all three phases.

Continuity for phase α

$$\frac{\partial r_\alpha \rho_\alpha}{\partial t} + \frac{\partial r_\alpha \rho_\alpha u_{\alpha j}}{\partial x_j} = 0 \tag{2}$$

The Reynolds averaged linear momentum balance in Cartesian coordinates for a compressible phase α is shown in equation (3) after invoking the Stokes assumption.

$$\begin{aligned} &\frac{\partial r_\alpha \rho_\alpha u_{\alpha i}}{\partial t} + \frac{\partial r_\alpha \rho_\alpha u_{\alpha i} u_{\alpha j}}{\partial x_j} = \\ &\frac{\partial}{\partial x_j} r_\alpha \left[\mu_\alpha \left(\frac{\partial u_{\alpha i}}{\partial x_j} + \frac{\partial u_{\alpha j}}{\partial x_i} - \frac{2}{3}\delta_{ij} \frac{\partial u_{\alpha k}}{\partial x_k} \right) - \rho_\alpha \left\langle u'_{\alpha i} u'_{\alpha j} \right\rangle \right] \\ &- r_\alpha \frac{\partial p}{\partial x_i} + r_\alpha \left(\rho_\alpha - \rho_{ref} \right) g_i + S_{\alpha i} + M_{\alpha i} \end{aligned} \tag{3}$$

Of course the liquid phase and solid phases are incompressible, so the div (normal stress) term drops out of the right hand side of equation (3) for these. $S_{\alpha i}$ involves momentum sources due to evaporation and condensation, while $M_{\alpha i}$ includes interfacial forces (drag and non-drag).

The shear stress transport (SST) two-equation linear eddy viscosity model of Menter [5] is used for computing the Reynolds stress terms for the continuous phase. This model involves a smooth blend between the standard k-ε model of Launder and Spalding [6] in the freestream and the k-ω model of Wilcox [7] near the wall. In the SST model, additional consideration is given to the transport of the principal turbulent shear stress via 1) an eddy viscosity limiting function and 2) a cross diffusion term in the transport equation for ω. Also, there is a turbulence production limiter, as discussed in [8], preventing the artificial build-up of fluctuating velocity in regions of irrotational strain. The local eddy viscosities of the dispersed phases are functions of the eddy viscosity of the continuous phase. "Scalable" wall functions, discussed in [8], are an alternative to standard wall functions of Launder and Spalding [6]. They have the advantage of being less sensitive to variation in near-wall grid resolution throughout the domain. The distance from the wall is computed via a Poisson equation with a uniform source value of -1. Additional compressibility effects and buoyancy-driven turbulence have been neglected in the present work. As with most Reynolds averaged turbulence models, the boundary layers are considered everywhere turbulent. The profiles in the near-wall region are topics of current debate. For example, Vitankar et al. [9] discusses boundary layer thinning by increased turbulence in two-phase flow, so there is not an obvious answer to the near-wall approach that is best. More complete discussions of turbulence models, advantages, and caveats are available in Pope [10]. It is well-known that eddy-viscosity turbulence computations are limited. For the purposes of industrial bubble column design optimization, it was decided that the use of a linear two-equation model for the liquid phase and a zero-equation model for the dispersed phases was an adequate starting point. As will be discussed in an upcoming section, the momentum balance (obviously includes phasic turbulence) is a result of many forces. It is the tuning of these to match experimental information that is the key. The results shown here represent a very small subset of the actual design work; time did not permit the use of a Reynolds stress model and certainly not a large eddy simulation approach.

The phasic chemical species balance is shown in equation (4):

$$\frac{\partial r_\alpha \rho_\alpha \phi_\alpha}{\partial t} + \frac{\partial r_\alpha \rho_\alpha u_{\alpha j} \phi_\alpha}{\partial x_j} = \frac{\partial}{\partial x_j} r_\alpha \left[\left(\rho_\alpha D_\alpha^\phi + \frac{\mu_{t,\alpha}}{Sc_{t,\alpha}} \right) \frac{\partial \phi_\alpha}{\partial x_j} \right] + R_\alpha^\phi \tag{4}$$

The gradient diffusion hypothesis has already been involved to separate out the molecular and turbulent diffusive effects on the right-hand-side. R_α^Φ is simply the reactive species volumetric source terms for species Φ in phase α. The basis for R_α^Φ is equation (1) plus enough competing, parallel reactions and species to account for the preponderance of oxidant consumption. When viscous heating

and compression work are ignored, the phasic energy equation looks very similar to equation (4) with the appropriate substitutions. Extremely large bulk evaporation rates are handled through appropriate sources and sinks shown above.

2.2 Drag, bubble size, and other forces

The momentum balance (holdup, backmixing, and velocity profiles) is directly related to a joint effect of drag coefficient (including swarm effects), bubble size distribution, bubble induced turbulence, turbulent dispersion, turbulence stress closure, and other non-drag forces such as lift and virtual mass. A given balance can be achieved from various combinations of these. Some of the most recent bubble swarm drag relationship work is given by Simonnet et al. [11], but deals with a situation unlike that of the current work. It is valid for atmospheric pressure, air/water, a maximum bubble diameter of 10 mm, and local void fractions less than 30%. A recent study of turbulence closure and interfacial forces is carried out by Zhang et al. [12]. They propose combinations of methods that produce more realistic validations, but all for homogenous flow. A new interfacial area transport equation has recently proposed by Ishii [13]. Interactions between the phases typically include bubble induced turbulence (Sato and Sekoguchi [16]) and turbulent dispersion (Lopez de Bertodano [17]). For further reference, Strasser [18] offers a study of turbulence interactions between continuous and dispersed phases. Commercial implementations of bubble population balance models for CFX and FLUENT are discussed in Olmos et al [14] and Chen et al. [15], respectively; however, application to pX oxidation proved ineffective at matching experimental hold-up and velocity distributions and pressure fluctuations. Therefore, the authors have developed a novel population balance method for realistic industrial pX oxidation conditions. Without matching experimental hydrodynamic information, there is little hope of ascertaining the overall operating quality of various design configurations. The particular choices of models and coefficients have not been disclosed for the present work due to the proprietary and unique nature of the liquid-phase oxidization at these conditions.

2.3 Solver

The ANSYS CFX Release 10 solver (details and individual references found in [8]) discretizes equations (2)–(4) using a vertex-based finite volume method. Each term is converted to mesh element volume integrals and element surface integrals. Advection terms are discretized using a high resolution algorithm similar to that of Barth and Jesperson. Time derivatives are discretized using a second-order transient scheme. Mass flows are discretized using a Rhie-Chow approach, modified by Majumdar, to avoid pressure decoupling on the co-located grid. The mass flow discretization also involves a Newton-Raphson linearization to handle compressibility effects. Viscous stresses, diffusion terms, and the pressure gradient are discretized using finite element shape functions, whose construction depends on the mesh element type. The solution algorithm is

fully implicit, with velocity and pressure coupled together in the same matrix. The resulting system of equations is solved using a coupled ILU algebraic multigrid technique.

2.4 Mesh

The computational mesh, involving prisms, tetrahedra, hexahedra, and pyramids, was built in Gambit and TGRID from Fluent, Inc. with the intent to balance computational load and accuracy. The smallest grid lengths scales were near the various feeds, such as the gas sparger holes. The expansion (in all three dimensions) of cells away from the feeds to areas with lesser gradients was carried out in such a way as to minimize cell aspect ratios, centroid shifts, and skewness. A "superblock" technique is used to ensure the cells at block boundaries (including boundary layer blocks) meet each other with nearly uniform mesh spacing. More on these concepts can be found in the transonic gas turbine blade passage research of Strasser et al. [19]. Also, the effects of gridding methods on the computational results are explored in Strasser [20]. Typical total cell counts ranged from 100,000 to 1,000,000 cells, depending on the complexity of the feeds. The particular cell length scales chosen for this work were arrived at through successive meshing numerical tests. The first grid built was referred to as 1X, and tests were performed to compare 1X, 2X, 4X, and 8X grids. It was found that increased resolution beyond 4X did not change the time-averaged radial velocity and gas hold-up profiles, so the 4X approach was employed for the model results shown in this work.

2.5 Convergence

The final mesh is partitioned to run on 8 to 16 CPUs. After months of tuning the model to match reality anchors for a particular geometry and set of operational conditions, a quasi-steady solution is sought. The model is then run typically 100 seconds of bubble column churn time, requiring two to four weeks of CPU time. The timestep and number of inner loops is chosen such that mass, energy, and chemical species mass imbalances are far less than 1%.

3 Results

3.1 Hydrodynamics

With superficial velocities in the range of 0.5 to 3 m/s, this column operates in well into the heterogeneous flow regime. At this high of a superficial velocity, Nedeltchev et al. [21] proposes a "coalesced bubble regime (3-region flow)". These 3 regions are central plume, vortical region, and descending region. The structures meander laterally and circumferentially, in both space and time. Figure 1 shows some un-related instantaneous views on a column mid-plane from one design of the present work. These are "partial" renderings in that they do not represent the entire height of the column. The colour represents low gas volume fraction (blue) to high gas volume fractions (red), while the black arrows

are liquid velocity vectors on that cutting plane. The ranges are purposely not disclosed, but it can be said that the gas volume fraction far exceeds 0.5, while the liquid velocity far exceeds 1m/s. The locations that show no vectors imply that the flow is aimed into the page and the likelihood of helical motion. It can be seen that, on average, there is no time-averaged flow present.

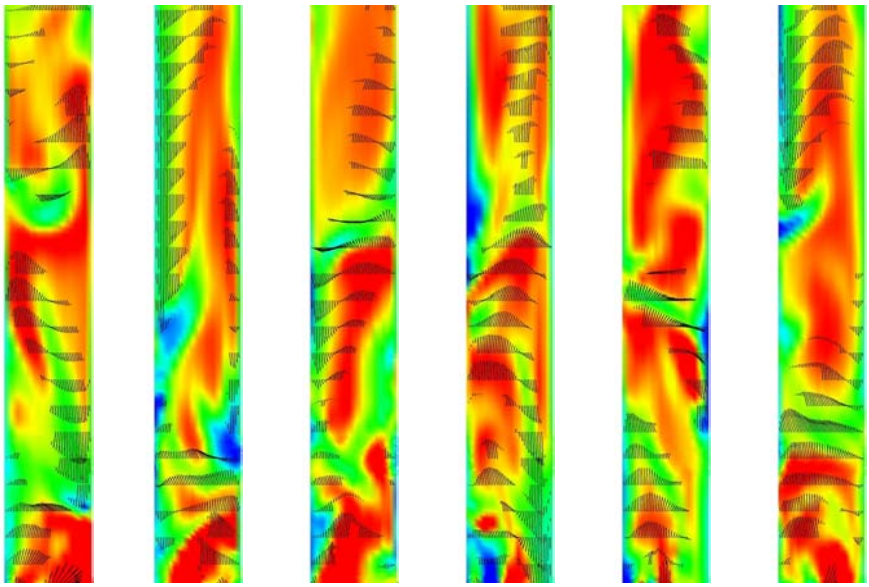

Figure 1: Instantaneous mid-plane volume fraction and liquid velocity vectors.

The flow is violent, sometimes moving up/down, radially inward/outward, and into/out of the page. The phase distribution gets slightly more uniform moving up the column, but, in general, a transition height is difficult to detect. The most unique aspect of the present work is not just the presentation of colourful pictures, but the fact that the radial and axial gas hold-up profiles have been compared and matched to experimental data from the same column in full, heated operation. Along with radial and axial hold-up profiles, CFD pressure pulses at the lower tangent line have been matched to experimental values in terms of both magnitude and frequency.

3.2 Hydro-kinetics

Key reactant concentration samples from various elevations in the numerical column have been compared to plant operating values. There was acceptable agreement for both the average concentration and temporal variation. Local

concentrations of the liquid and gas phase reactants within the column have a dramatic impact on product quality (see the Introduction section). Specifically, low values of a specific gas phase reactant and high values of some liquid phase reactants cause the production of colour-degrading contaminants. Steady models, that do not include the added effects of fluctuating velocities and fluctuating concentrations, do not detect all of the problematic locations within the column. Figures 2 and 3 show typical offending gas and liquid phase reactants, respectively, from one design of the present work. Again, these "partial" renderings do not represent the entire height of the column. The reader will see "isovolumes", which are depictions of the cells above or below a specified reactant threshold. The colours represent ranges of reactant concentration within the isovolume. For the purposes of the paper, the "offensive" gas phase involves any cell containing less reactant than the time-averaged concentration leaving the column top. That may not necessarily be a threshold for effective oxidizer operation. One will observe that the gas phase reactant (figure 2) is normally offensive down near the gas sparger, but can become offensive anywhere in the column. At some points in time, the total offensive gas phase volume amounts to 30% of the entire reaction mixture volume, while at other times it is as low as 1%. In other words, up to 30% of the reaction volume can contain a gas phase reactant level *lower* than the outlet value. The offensive volumes are typically not continuous in space. The volume of offensive liquid phase reactant (figure 3) is equally complex and is often offensive near the entry point. At a given sampling time, the volume of offensive gas phase reactant may or may not be the same shape or total volume as that of the offensive liquid phase reactant.

Similarly intriguing results are shown in figures 4 and 5. Here we explore mass flow-weighted area-averaged (MWFAA) values at various results cutting planes moving from the bottom to the top of the reaction mixture at four different un-related CFD sampling times. In general, it can be said that there is a trend from high to low values progressing up the column. Since both reactants are fed closer to the bottom, and since they jointly react, this behaviour is expected. Notice that the profiles, local minima and maxima, and the starting and ending values can be dramatically different within normal operation. Again, there is no time-averaged flow present on a regular basis. An optimized column design must be able to take into account the swings and peaks in both phasic reactants.

Figures 1–5 represent results of complex interactions between the spatio-temporal momentum balance, mass transfer effects, and interrelated kinetic relationships. Considering these figures, along with the time-averaged space occupancy of offensive volumes and their locations, the authors have designed an oxidizer that minimizes the offensive zones and produces a higher quality material at a higher rate. Ideally, reactants are "staged" properly in that phasic reactants' availabilities match their local reactive needs. This prevents the undesirable, colour-forming side reactions from occurring. The authors have found feed methods, feed locations, and column dimensions that meet this goal.

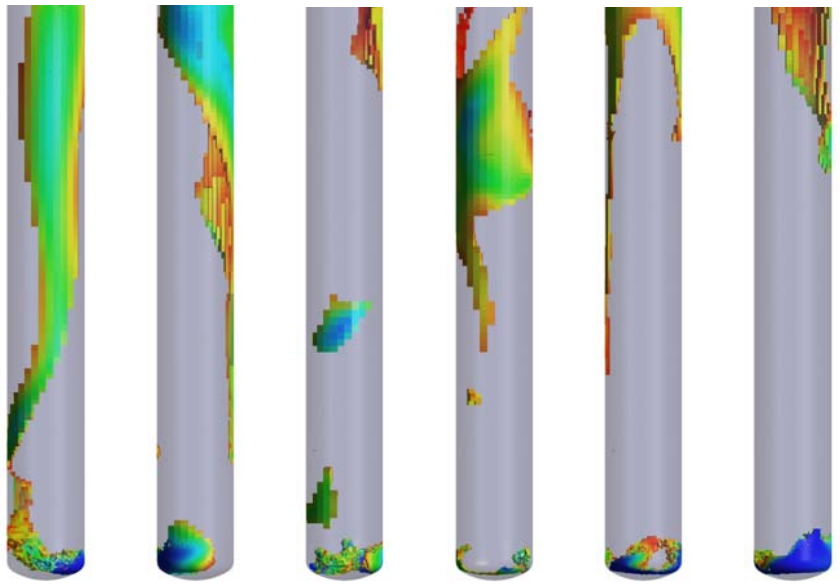

Figure 2: Partial renderings of instantaneous 3-D isovolumes of material having a gas phase reactant concentration less than the time-averaged outlet value.

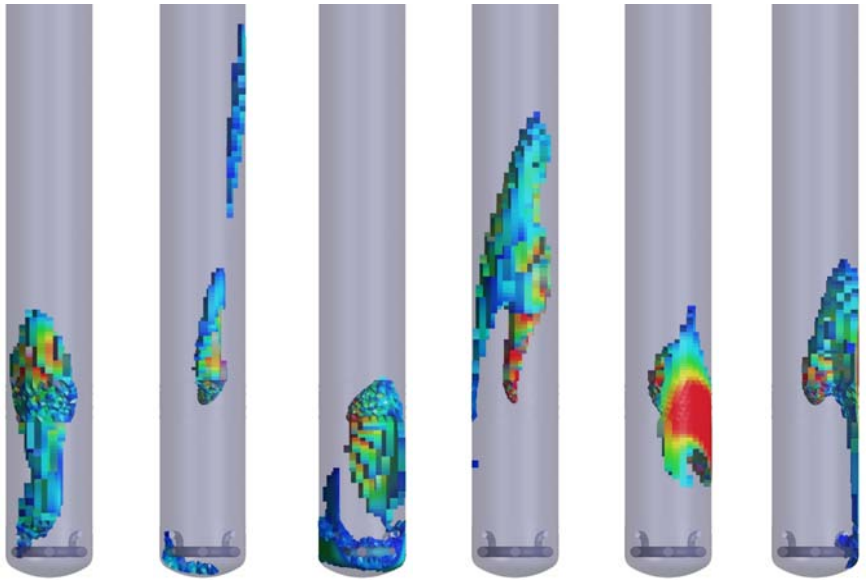

Figure 3: Partial renderings of instantaneous 3-D isovolumes of material having a liquid phase reactant above a critical value.

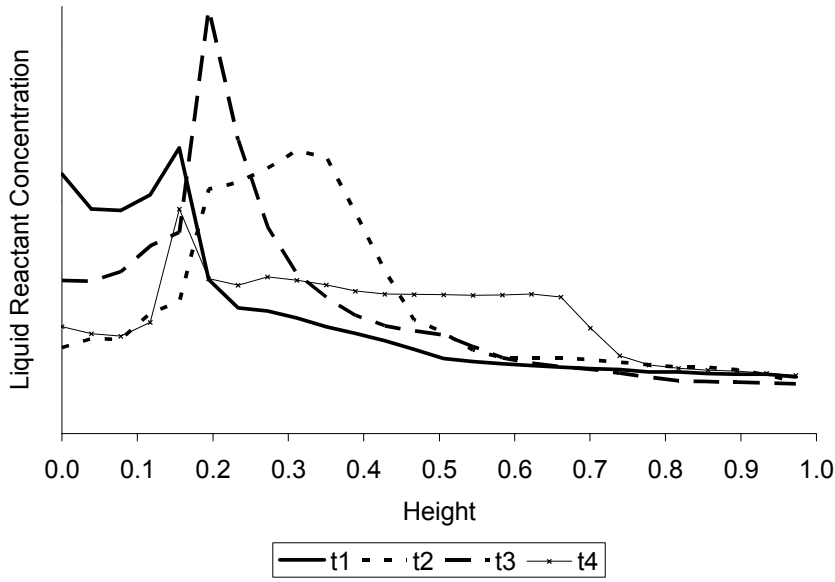

Figure 4: Planar MFWAA liquid reactant concentration versus normalized reaction mixture height for four random CFD time samplings.

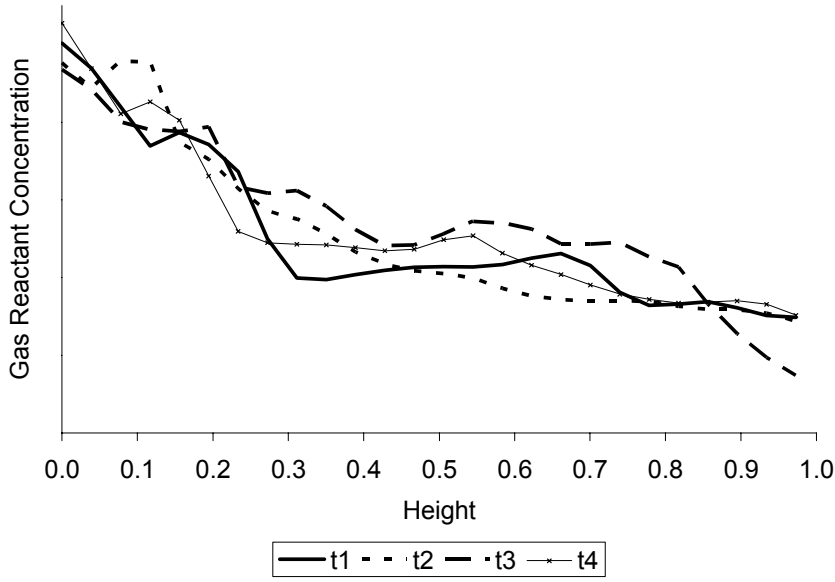

Figure 5: Planar MFWAA gas reactant concentration versus normalized reaction mixture height for four random CFD time samplings.

4 Conclusions

It was desired to study complex, coupled hydro-kinetics within a slurry bubble column at highly aerated, high pressure conditions. Steady 3-D compartmental models were shown in internal evaluations to miss the experimental results; therefore, a transient 3-D Eulerian-Eulerian Reynolds averaged approach was utilized. The various choices of models and bubble population approach were tuned with grid-independent solutions to match transient and time-averaged experimental information (hold-up, pressure fluctuation, and reactant concentrations). After tuning, various designs were considered in order to study methods of improved reactant feeding. The goal is to pair chemical availability with chemical reactivity for various species in each phase, locally throughout the column. Sample results were displayed for a particular design. Reactant concentrations that were above or below pre-determined thresholds were shown; these are responsible for off-quality material or the lowering of production rates. The shape and total volume of the offensive phase material were extremely variable (cumulative volume ranging from 1% to 30% of the total reaction volume) and were typically not continuous in space. Axial profiles of reactants were also shown, and proved that there was no apparent normal profile. The local maxima and minima shifted substantially in time. While time-averages are useful for making hydrodynamic CFD-experimental comparisons, fluctuating values of the chemical species in each phase are also considered in any optimized design.

Nomenclature

D	Diffusivity
g	Gravity
k	Turbulence kinetic energy
i-l	Tensor summation indices
M	Momentum source term
p	Pressure
r	Volume fraction
R	Reaction source term
S	Source through mass exchange
Sc_t	Turbulence Schmidt number
t	Time
u'	Fluctuating velocity component
x	Spatial coordinate
α	Phase designation
δ	Kronecker Delta
ε	Turbulence dissipation rate
Φ	Chemical species
ω	Specific dissipation rate
ρ	Density
μ_t	Turbulent (or eddy) viscosity

References

[1] Nottenkamper, R., Steiff, A., and Weinspach, P., "Experimental investigation of hydrodynamics of bubble columns," Ger. Chem. Eng., **6**, pp. 147–155, 1983.

[2] Letzel, M., Schouten, J., van den Bleek, C. and Krishna, R., "Effect of gas density on large-bubble holdup in bubble column reactors," AIChE Journal, **44**, pp. 2333–2336, 1998.

[3] Xie, G. and Li, X., "An axial dispersion model for evaporating bubble column reactor," Chinese J. Chem. Eng., **12**, pp. 214–220, 2004.

[4] Rafique, M., Chen, P., and Dudukovic, M., "Computational Modeling of Gas-Liquid Flow in Bubble Columns," **20**, pp. 225–375, 2004.

[5] Menter, F.R., "Two-equation eddy-viscosity turbulence models for engineering applications", AIAA-Journal, **32**(8), pp. 1598–1605, 1994.

[6] Launder, B. E. and Spalding, D. B., *Mathematical Models of Turbulence*, Academic Press, 1972.

[7] Wilcox, D.C., "Multiscale model for turbulent flows", In AIAA 24th Aerospace Sciences Meeting. American Institute of Aeronautics and Astronautics, 1986.

[8] ANSYS CFX Solver Documentation

[9] Vitankar, V., Dhotre, M., and Joshi, J., "A Low Reynolds Number k-ε Model For the Prediction of Flow Pattern and Pressure Drop in Bubble Column Reactors," Chemical Engineering Science, **57**, pp. 3235–3250, 2002.

[10] Pope, S., *Turbulent Flows*, Cambridge University Press, 2000.

[11] Simonnet, M., Gentric, C., Olmos, E., and Midoux, N., "Experimental Determination of the Drag Coefficient in a Swarm of Bubbles," Chemical Engineering Science, **62**, pp. 858–866, 2007.

[12] Zhang, D., Deen, N., and Kuipers, J., "Numerical Simulation of the Dynamic Flow Behavior in a Bubble Column: A Study of Closures for Turbulence and Interface Forces," Chemical Engineering Science, **61**, pp. 7593–7608, 2006.

[13] Ishii, M., "Two-fluid model based on interfacial area transport equation," 5th International Conference on Multiphase Flow, Paper No. PL4, 2004

[14] Olmos, E., Gentric, C., Vial, C., Wild, G., and Midoux, N., "Numerical simulation of multiphase flow in bubble column reactors. Influence of bubble coalescence and break-up," Chemical Engineering Science, **56**, pp. 6359–6365, 2001.

[15] Chen, P., Sanyal, J., and Dudukovic, M., "Three dimensional simulation of bubble column flows with bubble coalescence and breakup," AIChE Journal, **51**, pp. 696–712, 2005.

[16] Sato, Y. and Sekoguchi, K., "Liquid Velocity Distribution in Two-Phase Bubbly Flow", Int. J. Multiphase Flow, 2, p.79, 1975.

[17] Lopez de Bertodano, M., "Turbulent Bubbly Flow in a Triangular Duct", Ph. D. Thesis, Rensselaer Polytechnic Institute, Troy New York, 1991.

[18] Strasser, W., "Discrete Particle Study of Turbulence Coupling in a Confined Jet Gas-Liquid Separator," Journal of Fluids Engineering, Review in progress.
[19] Strasser, W., Feldman, G., Wilkins, C., and Leylek, J., "Transonic Passage Turbine Blade Tip Clearance with Scalloped Shroud: Part II – Losses with and without Scrubbing Effects in Engine Configuration," ASME Paper No. IMECE2004-59116.
[20] Strasser, W., "CFD Investigation of Gear Pump Mixing Using Deforming/ Agglomerating Mesh," Journal of Fluids Engineering, **129**, pp. 476–484, 2007.
[21] Nedeltchev, S., Shaikh, A, and Al-Dahhan, M., "Flow regime identification in a bubble column base on both statistical and chaotic parameters applied to computed tomography data," Chem. Eng. Technol., **29**, pp. 1054–1060, 2006.

This page intentionally left blank

An application of contact melting theory to skates sliding on ice

P. J. Montgomery
Mathematics Program, University of Northern British Columbia, 3333 University Way, Prince George, B.C., Canada

Abstract

The problem of a skate blade sliding over ice is a complex and classic problem, with an early form considered by Reynolds over a century ago. The problem is revisited herein: a thin layer of water in between the skate blade and the ice surface is assumed to exist, and acts as a lubricant for the sliding motion of the skate blade. The existence of the melt layer is caused by viscous friction in the liquid film itself, instead of pressure melting. Governing equations are considered for a Newtonian and inviscid fluid of constant density. These equations are reduced by considering some scaling analysis to determine the negligible terms, and a simpler planar flow is considered. Through some straightforward manipulations of the governing equations, the viscous stress on the surface of the skate blade is analytically expressed as a function of the depth of the melt layer. Other results are used to posit an approximate expression for the non-constant depth of the melt layer, and this is used to calculate the frictional force. The results are compared to others in the area, and limitations on the modelling are discussed.
Keywords: multiphase flow, fluid dynamics, stefan problem.

1 Introduction

Contact melting is an area of research in which two solids interact in such a way that one of the solids partially melts at the surface to create a thin melted layer between the two solids which acts to lubricate the motion between the two parts. A relatively recent review of the industrial and engineering applications of this theory has been completed by Bejan [1], although the area of focus of this manuscript is on the application of the contact melting theory to describe a skate blade sliding over ice. The classical mechanism of melting due to surface pressure has been

WIT Transactions on Engineering Sciences, Vol 59, © 2008 WIT Press
www.witpress.com, ISSN 1743-3533 (on-line)
doi:10.2495/AFM080281

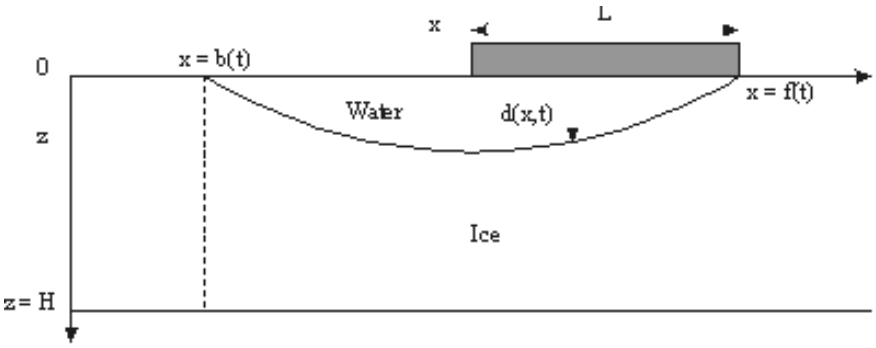

Figure 1: Geometry of the skate blade variables (not to scale).

shown to be essentially incorrect, and the melted layer is considered to be created due to the viscous friction of the motion (see [2] and the references therein.)

In a previous study, the concept of a thin lubricating layer of water was used to permit a study of the frictional drag on an object sliding over ice [3]. In Summers and Montgomery [3] the two main limitations on the theory were an assumption that the horizontal pressure gradient was negligible, and the depth of the melt layer was undetermined. In a more recent work Penny *et al* [4] posed a partial solution for the depth of the melt layer in the form of a nonlinear nonhomogeneous first order ordinary differential equation, thus partially removing one of the previous limitations.

In this study, the theory of contact melting is applied to determine the frictional force on a skate blade over ice. The theory follows that of Fowler and Bejan [5] and implements the results of Penny *et al* [4] to create an expression for the viscous drag force on the skate blade. In Section 2, the governing equations for the melt layer are derived fairly thoroughly as this seems to be something that is lacking in the standard literature. In two subsections, the equations are simplified by assuming a small aspect ration (vertical to horizontal) and a thin model layer is developed. The equations are used in Section 3 to create a solution for the pressure and velocity in the melt layer without any assumptions on the depth of the layer. By using an approximate solution similar to the numerical results of Penny *et al* [4] an expression for the viscous drag force is derived which is similar to previous results [6].

2 Model equations

A sketch of the initial skate blade geometry is depicted in Figure 1, where a solid metal blade of length L overlies a thin layer of liquid melted from the ice beneath. It is assumed that the start of the melt layer occurs coincidentally with the beginning of the skate blade, and that there are no asperities in the ice which would cause uneven contact [5].

To model the liquid layer, the fluid is assumed to be Newtonian, and therefore satisfies the Navier-Stokes equations [7] in a Cartesian coordinate frame of reference;

$$\frac{1}{\rho}\frac{D\rho}{Dt} + \nabla \cdot \vec{u} = 0, \tag{1}$$

for mass conservation, and the momentum equation

$$\rho\frac{D\vec{u}}{Dt} = -\nabla p + \rho\vec{g} + \mu\left[\nabla^2\vec{u} + \frac{1}{3}\nabla(\nabla \cdot \vec{u})\right]. \tag{2}$$

In equations (1) and (2), ρ and $\vec{u} = (u, v, w)$ denote the fluid density and velocity, p the pressure, μ the viscosity, and $\vec{g}$ the gravitational force per unit mass. The standard material derivative notation $\frac{D}{Dt} = \frac{\partial}{\partial t} + \vec{u} \cdot \nabla$ is also used. The viscosity is assumed to be a constant as the temperature of the liquid layer is expected to be very near the freezing point for the duration of the fluid motion.

To complete the description of the fluid and close the governing equations, a thermal energy equation is required from the first law of thermodynamics. If e denotes the specific internal energy, $\vec{q}$ the outward heat flux vector per unit area, and there is no internal heat generation, then energy conservation can be written in the form of a thermal energy equation (heat equation,) [7, 6]

$$\rho\frac{De}{Dt} = -\nabla \cdot \vec{q} - p(\nabla \cdot u) + \mu\phi. \tag{3}$$

The viscous dissipation function, ϕ, in equation (3) can be written in its full form as [6]

$$\begin{aligned}\phi = 2\left[\left(\frac{\partial u}{\partial x}\right)^2 + \left(\frac{\partial v}{\partial y}\right)^2 + \left(\frac{\partial w}{\partial z}\right)^2\right] - \frac{2}{3}\left[\frac{\partial u}{\partial x} + \frac{\partial v}{\partial y} + \frac{\partial w}{\partial z}\right]^2 \\ + \left[\left(\frac{\partial u}{\partial y} + \frac{\partial v}{\partial x}\right)^2 + \left(\frac{\partial v}{\partial z} + \frac{\partial w}{\partial y}\right)^2 + \left(\frac{\partial w}{\partial x} + \frac{\partial u}{\partial z}\right)^2\right]\end{aligned} \tag{4}$$

Equations (1) to (4) are simplified in the next subsection and adapted to the geometry of Figure 1.

2.1 Incompressibility and symmetry

To simplify the governing equations (1)–(4), some assumptions are of course necessary. Fortunately, these are well justified, and the resultant equations can be seen to capture the essential components of the model without making unjustified assumptions merely for the sake of simplicity. The first simplification arises from specifying a few standard properties of the fluid layer, and it is thus assumed that the fluid is of constant density and incompressible. The second assumption is to consider only planar motion in the horizontal and vertical plane, neglecting any variation across the skate blade (i.e. the y direction). Although the assumption of incompressibility is standard [6, 5] the assumption of a uniformly placed

skate blade is restrictive as often blades are subject to varying forces during an actual skating stroke [4]. However, in order to obtain an advancement of the theory, the variation of forces within the skate blade are assumed to average out, and the assumptions thus permit equation (1) to be written as the standard assumption of incompressibility in two spatial dimensions [7]

$$\frac{\partial u}{\partial x} + \frac{\partial w}{\partial z} = 0. \tag{5}$$

The restriction to planar motion simplifies the vector equation (2) by one component, and only the x and z components remain. Substitution of equation (5) into equation (2) gives these two components as

$$\rho \frac{Du}{Dt} = -\frac{\partial p}{\partial x} + \mu\left(\frac{\partial^2 u}{\partial x^2} + \frac{\partial^2 u}{\partial z^2}\right), \tag{6}$$

and

$$\rho \frac{Dw}{Dt} = -\frac{\partial p}{\partial z} - \rho g + \mu\left(\frac{\partial^2 w}{\partial x^2} + \frac{\partial^2 w}{\partial z^2}\right), \tag{7}$$

where the gravitational force is taken to be in the vertical direction, and the material derivative simplifies to $\frac{D}{Dt} = \frac{\partial}{\partial t} + u\frac{\partial}{\partial x} + w\frac{\partial}{\partial z}$.

The thermal energy equation (3) is rewritten by using the linear relation of internal energy e to temperature T, $e = c_w T$ where c_w is the specific heat capacity of water [6]. In addition, the constitutive relation given by Fourier's law of heat conduction [7],

$$\vec{q} = -k_w \nabla T, \tag{8}$$

is used where k_w is the thermal conductivity of water. These changes, together with the incompressibility assumption (5) give

$$\rho c_w \frac{DT}{Dt} = k_w\left(\frac{\partial^2 T}{\partial x^2} + \frac{\partial^2 T}{\partial z^2}\right) + \mu\phi, \tag{9}$$

where ϕ is simplified from (4) to

$$\phi = 2\left[\left(\frac{\partial u}{\partial x}\right)^2 + \left(\frac{\partial w}{\partial z}\right)^2\right] + \left(\frac{\partial w}{\partial x} + \frac{\partial u}{\partial z}\right)^2. \tag{10}$$

In the next subsection, the governing equations are further simplified to account for the specific geometry of thin layer flow.

2.2 Small aspect ratio

The second major simplification applied to the governing equations is to neglect those terms which may be extremely small compared to the other terms. To that

end nondimensional variables denoted with a tilde $\tilde{()}$ are introduced by factoring out dimensional constants according to

$$(u, w) = (U\tilde{u}, W\tilde{w}),\ (x, z) = (X\tilde{x}, Z\tilde{z}),\ t = \frac{X}{U}\tilde{t},\ T = \Lambda\tilde{T},\ p = -\rho g z + P\tilde{p}. \tag{11}$$

Substitution of the new variables (11) into the incompressibility equation (5) gives

$$\frac{U}{X}\frac{\partial\tilde{u}}{\partial\tilde{x}} + \frac{W}{Z}\frac{\partial\tilde{w}}{\partial\tilde{z}} = 0, \tag{12}$$

from which it is inferred that $W = \delta U$, where $\delta = Z/X$ is the aspect ratio of vertical to horizontal scales.

The momentum equations (6) and (7) are written in expanded form with the new variables (11) and use of the previous scaling notation as

$$\rho\frac{U^2}{X}\left(\frac{\partial\tilde{u}}{\partial\tilde{t}} + \tilde{u}\frac{\partial\tilde{u}}{\partial\tilde{x}} + \tilde{w}\frac{\partial\tilde{u}}{\partial\tilde{z}}\right) = -\frac{P}{X}\frac{\partial\tilde{p}}{\partial\tilde{x}} + \mu\frac{U}{\delta^2X^2}\left(\delta^2\frac{\partial^2\tilde{u}}{\partial\tilde{x}^2} + \frac{\partial^2\tilde{u}}{\partial\tilde{z}^2}\right), \tag{13}$$

and

$$\rho\frac{\delta U^2}{X}\left(\frac{\partial\tilde{w}}{\partial\tilde{t}} + \tilde{u}\frac{\partial\tilde{w}}{\partial\tilde{x}} + \tilde{w}\frac{\partial\tilde{w}}{\partial\tilde{z}}\right) = -\frac{P}{\delta X}\frac{\partial\tilde{p}}{\partial\tilde{z}} + \mu\frac{U}{\delta X^2}\left(\delta^2\frac{\partial^2\tilde{w}}{\partial\tilde{x}^2} + \frac{\partial^2\tilde{w}}{\partial\tilde{z}^2}\right). \tag{14}$$

Similarly, equations (9) and (10) become

$$\rho c_w\frac{\Lambda U}{X}\left(\frac{\partial\tilde{T}}{\partial\tilde{\tau}} + \tilde{u}\frac{\partial\tilde{T}}{\partial\tilde{x}} + \tilde{w}\frac{\partial\tilde{T}}{\partial\tilde{z}}\right) = k_w\frac{\Lambda}{\delta^2X^2}\left(\delta^2\frac{\partial^2\tilde{T}}{\partial\tilde{x}^2} + \frac{\partial^2\tilde{T}}{\partial\tilde{z}^2}\right) + \mu\phi, \tag{15}$$

and

$$\phi = \frac{U^2}{\delta^2X^2}\left[2\delta^2\left(\frac{\partial\tilde{u}}{\partial\tilde{x}}\right)^2 + 2\delta^2\left(\frac{\partial\tilde{w}}{\partial\tilde{z}}\right)^2 + \left(\delta^2\frac{\partial\tilde{w}}{\partial\tilde{x}} + \frac{\partial\tilde{u}}{\partial\tilde{z}}\right)^2\right]. \tag{16}$$

For a very thin layer, the aspect ratio is necessarily small, perhaps of the order of 10^{-6} [4]. If the terms which are of order δ^2 are neglected from equations (13) to (16) the resulting approximate equations are drastically reduced, and result in a problem similar to Couette flow. For the skate blade problem, the pressure scaling term P is unknown, but is expected to be relatively large and therefore all terms which are $O(\delta^2)$ are neglected except those which contain the scaling P. The resulting equations are stated as three results (since equations (15) and (16) are combined):

$$0 = -\frac{P\delta^2}{X}\frac{\partial\tilde{p}}{\partial\tilde{x}} + \mu\frac{U}{X^2}\frac{\partial^2\tilde{u}}{\partial\tilde{z}^2}, \quad 0 = -\frac{P}{X}\frac{\partial\tilde{p}}{\partial\tilde{z}} + \mu\frac{U}{X^2}\frac{\partial^2\tilde{w}}{\partial\tilde{z}^2}, \tag{17}$$

and

$$0 = k_w\frac{\Lambda}{X^2}\frac{\partial^2\tilde{T}}{\partial\tilde{z}^2} + \mu\frac{U^2}{X^2}\left(\frac{\partial\tilde{u}}{\partial\tilde{z}}\right)^2. \tag{18}$$

By using equation (17) scalings can be compared to finally deduce that the pressure scaling can be fixed as $P = \mu\frac{U}{\delta^2X}$, which then justifies the assumption of

a large pressure scaling and yields the approximate equations, now stated dimensionally (and neglecting the vertical hydrostatic part of the pressure term) as

$$0 = -\frac{\partial p}{\partial x} + \mu \frac{\partial^2 u}{\partial z^2}, \tag{19}$$

$$0 = -\frac{\partial p}{\partial z}, \tag{20}$$

and

$$0 = k_w \frac{\partial^2 T}{\partial z^2} + \mu \left(\frac{\partial u}{\partial z} \right)^2. \tag{21}$$

Equations (19), (20), and (21) are an extension of those used previously [3] as the temperature variation is included. They have been used previously [5] but with minimal justification as to their derivation, and it was felt by the author that a thorough exposition was warranted.

3 Thin layer solution

The approximate equations derived in the previous section are employed to give a first solution for the skate blade problem following the method of Fowler and Bejan [5]. An inertial frame of reference with the blade of the skate, and oriented such that the layer is of positive height in positive horizontal position is used (essentially a rotation of the geometry in Figure 1. As such, the steady state problem moving with the speed of the skate is considered, and transition effects to this steady state solution are not obtained. First, using equation (20) we note that $p = p(x)$ only, and therefore, equation (19) may be integrated over the vertical domain $0 \leq z \leq h$. Using the boundary conditions $u(x, 0) = 0$ and $u(x, h) = V$ the double integration of equation (19) yields the solution

$$u(x, z) = \frac{1}{2\mu} \frac{dp}{dx} (z - h) z + \frac{V}{h} z. \tag{22}$$

The solution (22) is not completely specified as the horizontal pressure gradient is still unknown. However, the incompressibility equation (5) may be used by substituting the expression (22). The result is

$$\frac{1}{2\mu} \left[\frac{d^2 p}{dx^2} (z - h) z - \frac{dp}{dx} \frac{dh}{dx} z \right] - \frac{V}{h^2} \frac{dh}{dx} z + \frac{\partial w}{\partial z} = 0. \tag{23}$$

Integrating equation (23) vertically and using the kinematic boundary condition $w = 0$ at $z = 0$ gives

$$\frac{1}{2\mu} \left[\frac{d^2 p}{dx^2} \left(\frac{1}{3} z - \frac{1}{2} h \right) z^2 - \frac{1}{2} \frac{dp}{dx} \frac{dh}{dx} z^2 \right] - \frac{1}{2} \frac{V}{h^2} \frac{dh}{dx} z^2 + w = 0. \tag{24}$$

Evaluating equation (24) along the contour $z = h$ where $w = 0$ is assumed gives a second order ODE for $p(x)$,

$$\frac{1}{2\mu}\left[\frac{d^2p}{dx^2}\left(-\frac{1}{3}h+\frac{1}{2}h\right)h^2+\frac{1}{2}\frac{dp}{dx}\frac{dh}{dx}h^2\right]-\frac{1}{2}\frac{V}{h^2}\frac{dh}{dx}h^2=0, \tag{25}$$

which can be rearranged to a simpler form via the chain rule,

$$\frac{d}{dx}\left(h^3\frac{dp}{dx}\right)=-6\mu V\frac{dh}{dx}. \tag{26}$$

The pressure gradient can now be expressed by integrating equation (26) and using a boundary condition at the end of the skate blade where it is assumed that the gradients vanish. This assumption yields

$$\frac{dp}{dx}=\frac{6\mu V(h_0-h)}{h^3}, \tag{27}$$

where h_0 is the maximum depth of the liquid layer.

Finally, substitution of equation (27) into equation (22) gives the solution

$$u(x,z)=\frac{Vz}{h}\left[\frac{3(h_0-h)(z-h)}{h^2}+1\right]. \tag{28}$$

4 Viscous drag on the skate blade

The velocity of the lubricating liquid layer given by equation (28)permits the viscous drag force, F, on the skate blade to be calculated by integrating of the shear stress along the length of the skate

$$F=\int_0^L \mu\left.\frac{\partial u}{\partial z}\right|_{z=0} dx. \tag{29}$$

Substitution of equation (28) into the above gives

$$F=\mu V\int_0^L \frac{(3h_0-2h)}{h^2}\,dx. \tag{30}$$

At this point, some expression for the depth $h(x)$ of the liquid layer is needed to complete the calculation for the drag on the skate blade. A separate analysis containing a discussion of this has been completed [4], however an analytic expression for $h(x)$ is not yet available. A graph obtained from the numerical approximation of the results of [4] is given in Figure 2, along with the approximate solution ($L = 40\,cm$ is used for the calculations in Figure 2)

$$h(x)=h_0\left(\frac{x}{L}\right)^{\frac{1}{3}}. \tag{31}$$

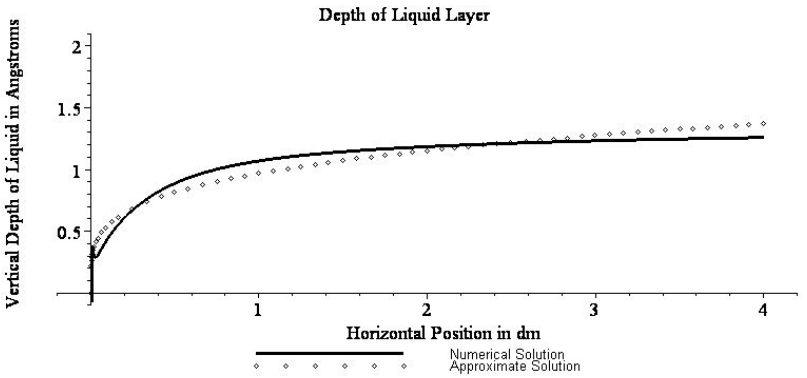

Figure 2: Numerical and approximate solutions of the depth, $h(x)$, of the liquid layer. A more complete description is given by Penny *et al* [4].

Substituting the assumption (31) into the integral (30) gives

$$F = \mu V \frac{3L}{h_0} 3L \left[3\left(\frac{x}{L}\right)^{\frac{1}{3}} - \left(\frac{x}{L}\right)^{\frac{2}{3}} \right] \Bigg|_{x=0}^{x=L} = \frac{6\mu V L}{h_0}. \tag{32}$$

The result (32) is similar in behaviour to a result obtained by Bejan [6] except for the factor of 6, where the layer was assumed to be of constant height, and knowledge of the depth $h(x)$ was not required. It is clear that there is a great degree of sensitivity to the expression used for the layer depth, and an approximation such as (31) will impact the tangential force heavily. Importantly, the Stefan problem [8] is not required to be solved, as long as an approximation for the depth of the melt layer is known.

5 Summary

The concept of a viscous lubricating melt layer was used to determine the frictional force on an idealised problem similar to that of a skate blade. By approximating the governing equations, explicit expressions for the pressure gradient and velocity were obtained as functions of the depth of the liquid layer. By using a power law to approximate the depth of the melt layer, the viscous shear stress was calculated directly to yield a result similar to previous results obtained elsewhere [6]. The results are limited by the accuracy of the assumptions and the expression used for the depth of the melt layer, which is an essential assumption.

Acknowledgements

The author PJM gratefully acknowledges UNBC for assistance in the form of a conference travel grant, and NSERC's essential support from a discovery grant.

References

[1] Bejan, A., *Contact melting heat transfer and lubrication,* Adv. Heat Transfer, **24**, pp. 129-155, 1994.
[2] Bejan, A., *The fundamentals of sliding contact melting and friction,* J. Heat Transfer, **111**, pp. 13-20, 1989.
[3] Summers, A.E. & Montgomery, P.J., Investigation of the motion of a fixed rotating solid body over ice with a thin fluid interface. *Advances in Fluid Mechanics V*, eds. C.A. Brebbia, A.C. Mendes & M. Rahman, WIT Press: Ashurst, pp. 247-256, 2004.
[4] Penny, A., Lozowski, E., Forest, T., Fong, C., Maw, S., Montgomery, P. & Sinha, N., Speedskate Ice Friction: Review and Numerical Model - FAST 1.0., *Proceedings of the 11th International Conference on the Physics and Chemistry of Ice (PCI 2006)*, Royal Society for Chemistry, in press, 2006.
[5] Fowler, A.J. & Bejan, A., *Contact melting during sliding on ice,* Int. J. Heat Mass Transfer, **36(5)**, pp. 1171-1179, 1993.
[6] Bejan, A. *Convection Heat Transfer,* 2^{nd} edn., John Wiley and Sons: New York, 1995.
[7] Kundu, P.K., *Fluid Mechanics,* Academic Press: San Diego, 1990.
[8] Crank, J.C., *Free and Moving Boundary Problems,* Clarendon Press: Oxford, 1984.

This page intentionally left blank

Subgrid particle method for porous media and suspension flow

R. G. M. van der Sman & G. Brans
Food and Bioprocess Engineering, Wageningen University, The Netherlands

Abstract

In this contribution we report on the initial steps in the development of a numerical scheme for flow through packed or suspended spheres. The spheres are semi-resolved, meaning that their diameter is smaller than the grid spacing, but their excluded volume is taken into account. Flow in the fluid phase is solved using the volume-averaged equations. Particle motion is solved via Newtons law, taking into account drag force and lubrication forces only. Despite the low resolution of the flow field, the particle trajectories of two spheres colliding in shear flow can be reasonable reproduced.
Keywords: Lattice Boltzmann, porous media, suspension flow, Euler-Lagrangian.

1 Subgrid particle method

The subgrid particle method is a Euler-Lagrangian method for modeling the multiphase flow problem of gas fluidised beds, cf. [1–3]. Here particles are underresolved, meaning that their radius is smaller than the grid spacing, but their volume is excluded for the fluid.

In this paper we present an extension of the subgrid particle method towards suspension flow, requiring that hydrodynamic interactions mediated via the liquid has to be included. Such a scheme for suspensions has been proposed by Schwarzer [4], but has been implemented in 2D. The model presented in this paper is 3D, and is implemented in Lattice Boltzmann. Lattice Boltzmann is chosen as it has shown to be a very versatile method capable of simulating a variety of complex fluids. Next to suspensions and fluidized beds, the subgrid particle method can also be applied to porous media. Governing equations for porous media flow and fluidized bed are identical if solid phase is assumed immobile.

WIT Transactions on Engineering Sciences, Vol 59, © 2008 WIT Press
www.witpress.com, ISSN 1743-3533 (on-line)
doi:10.2495/AFM080291

The validity of the method is shown via the simulation of several benchmark problems. We investigate the Beaver-Joseph problem of flow in a channel partially filled with a porous layer [5]. This problem is challenging due to the stepwise change in porosity, and poses for many numerical schemes serious problems [6, 12]. For the subgrid particle method for suspension flow it is important to handle the problems with changing porosity, i.e. solid fraction. Subsequently, we investigate the classical problem of two particle colliding in shear flow, as first investigated by Batchelor and Green [7]. This is a good problem for testing the validity of hydrodynamic interaction.

2 Governing equations for fluid phase

For the governing equations for the fluid phase we follow those of Feng and Yu [1].

$$\partial_t \rho\phi = \partial_\alpha \rho\phi u_\alpha \tag{1}$$
$$\partial_t \rho\phi u_\alpha + \partial_\beta \rho\phi u_\alpha u_\beta = -\partial_\alpha p + \partial_\beta \phi\mu(\partial_\beta u_\alpha + \partial_\alpha u_\beta) + F_{drag,\alpha}$$

Here ρ is the bulk density of the fluid, ϕ is the porosity, u_α is the component of the velocity field in the Cartesian direction x_α. p is the pressure, and μ is the dynamic viscosity of the fluid. We assume that particles are neutrally buoyant. We note that the superficial velocity field is $\tilde{u}_\alpha = \phi u_\alpha$. In suspension flow $F_{drag,\alpha}$ is the backflow induced by the drag of the fluid on the particles. Below we explain how this is computed in case of suspension flow. For porous media flow it follows from closure relations, such as the Ergun relations. In case of negligible inertia the above equation is equal to the Darcy-Forchheimer-Brinkman equation. The Ergun relation for a randomly packed bed of spheres in the Stokes flow regime is:

$$F_{drag,\alpha} = \frac{180\mu(1-\phi)^2}{\phi^2 d_p^2} u_\alpha \tag{2}$$

3 LB scheme for flow through inhomogeneous porous media

With the Lattice Boltzmann scheme [8] we simulate the above governing equations for the fluid phase. Via inverse Chapman-Enskog expansion we have derived this LB scheme. In order to model spatially varying porosity stability of the scheme requires that the speed of sound should be less than the regular value: $c_s^2 < c^2/3$, This induces however anisotropy in the viscosity μ [9]. This can be remediated via a modified MRT scheme [10]. We briefly present the resulting LB scheme. More details will be presented in a full length paper. In LB physical fields are represented by moments of particle distribution function f_i. These particles move over a simple cubic Bravais lattice with lattice spacing Δx with discrete set of velocities $c_{i,\alpha} = \Delta x_{i,\alpha}/\Delta t$ which brings them to nearest and next-nearest neighbouring lattice sites. Upon arrival the particles collide with each other, and after collision they

propagate with their new velocity. The collide and propagation steps are described by a discrete version of the Boltzmann equation:

$$f_i(\mathbf{x} + \Delta x_i, t + \Delta t) - f_i(\mathbf{x}, t) = -\Omega_{ij} f_j^{neq}(\mathbf{x}, t) \tag{3}$$

with $f_i^{neq} = f_i - f_i^{eq}$ the non-equilibrium part of the distribution function. The moments equilibrium part of the distribution function f_i^{eq} determines the governing physics, as shown by the inverse Chapman-Enskog expansion [9]. The collison rate is controlled by the scattering matrix Ω_{ij}. In the commonly used Lattice BGK scheme Ω_{ij} is linear with the unit matrix. But here we require the multiple relaxation scheme (MRT), which has a scattering matrix with different eigenvalues.

The moments of the equilibrium distribution, as follows from the inverse Chapman-Enskog expansion, are equal to:

$$M_0^{eq} = \sum_i f_i^{eq} = \phi\rho \tag{4}$$

$$M_{1,\alpha}^{eq} = \sum_i f_i^{eq} c_{i,\alpha} = \phi\rho u_\alpha$$

$$M_{2,\alpha\beta}^{eq} = \sum_i f_i^{eq} c_{i,\alpha} c_{i,\beta} = \rho c_s^2 \delta_{\alpha\beta} + \phi\rho u_\alpha u_\beta$$

$$M_{3,\alpha\beta\gamma}^{eq} = \sum_i f_i^{eq} c_{i,\alpha} c_{i,\beta} c_{i,\gamma} = \rho c_s^2 (u_\alpha \delta_{\beta\gamma} + u_\beta \delta_{\alpha\gamma} + u_\gamma \delta_{\alpha\beta})$$

Note that M_0^{eq} and $M_{1,\alpha}^{eq}$ are conserved quantities: density and momentum.

In the MRT scheme before collision the particle distribution function is projected on the set of eigenvector, which happen to be Hermite tensor polynomials [9]. Each moment of the distribution function is relaxed towards its equilibrium value, at a rate determined by its associated eigenvalue. After collision the moments are projected back to the particle distribution function, and are propagated to the adjacent lattice sites.

For the implementation of the drag body force, we have implemented the scheme of Ladd, who proposed to apply one half of the forcing before the collision step, and the other half after the collision.

3.1 Numerical tests

The above presented LB scheme is validated using the benchmark problem of flow in a flat channel partly filled with a porous layer. The porous layer has a height H, and the clear fluid layer has a height L_y. An analytical solution to this problem is by Beavers and Joseph [5]. Beavers and Joseph have treated the problem as a two domain problem, with different governing equations. Hence, at the interface of the two domains the boundary conditions have to be matched via a closure relations. Goyeau and coworkers have proposed a single domain approach, with one governing equation, namely Eq.(1) [12]. At the interface between fluid and porous medium they assumed continuity of the superficial velocity and the stress.

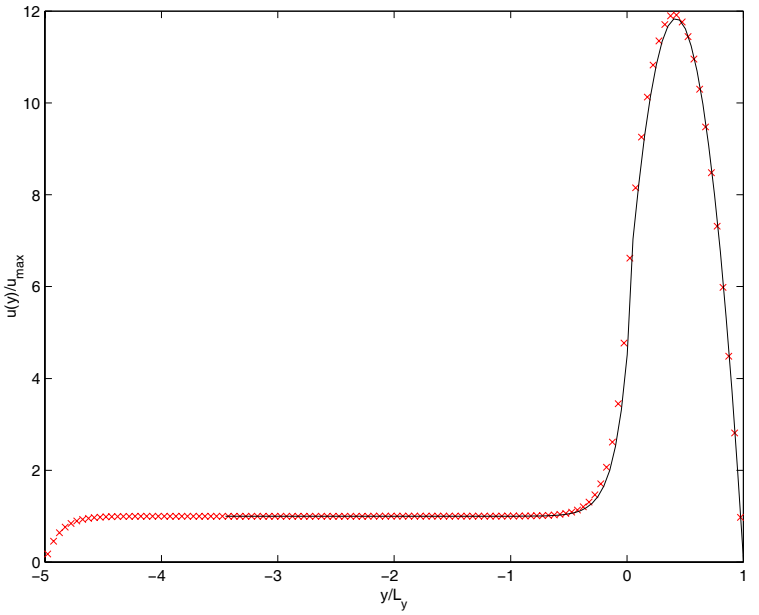

Figure 1: Analytical and numerical solution of flow in porous layer adjacent to fluid in a channel between parallel plates, with $Da = 0.08$, and $\phi_0 = 0.8$.

Their numerical solution agrees with the analytical solution of Beavers and Joseph, if a gradual change of porosity at the interface is assumed.

We have checked the results of Goyeau and coworkers. We have varied porosity as $\phi = \phi_0 + \frac{1}{2}(1 - \tanh(y/\zeta))(1 - \phi_0)$, with ϕ_0 the porosity of the porous layer. Simulations are performed with a 120 x 10 x 1 lattice, $\phi_0 = 0.8$, Darcy number $Da = 0.08$, $\zeta/\Delta x = 1$, porous layer height $H/L_y = 6$, and Reynolds number $Re = u_{max} L_y/\nu = 0.7$. Results are shown in figure 1, from which we observe that our model shows good agreement with the analytical solution.

4 Suspension flow

4.1 Lagrangian scheme

In this section we describe how the solid phase in suspension flow is treated in our scheme. Subsequently, we test the validity of this part using the benchmark problem of Green and Batchelor.

Subgrid particles have diameter $d_p \ll \Delta x_i$ and mass m_p. We solve their motion via Newtons law:

$$m_p \frac{d\mathbf{v}_p}{dt} = m_p \mathbf{a}_p = \mathbf{F}_{drag,p} + \mathbf{F}_{pq} + \mathbf{F}_{wall,p} \tag{5}$$

with $F_{drag,p}$ the drag force on the particle p, F_{pq} the force due to hydrodynamic interaction between particles p and q. Between particles and confining wall there is also hydrodynamic interaction. For other applications Newtons law is easily extended with gravity or Brownian forces.

The drag force on the particle follows the correlation of van der Hoef [13]:

$$\mathbf{F}_{drag,p} = \frac{G(\phi)}{\phi} 3\pi\mu d_p(\mathbf{u} - \mathbf{v}_p) \tag{6}$$

with the factor

$$G(\phi) = \frac{10(1-\phi)}{\phi^2} + \phi^2(1 + 1.5\sqrt{1-\phi}) \tag{7}$$

Note that in the limit of dilute suspensions, $G(\phi) \to 1$, and the drag force is equal to the Stokes drag force.

The drag force is coupled back to the fluid as backflow, following Newtons third law. If the boundaries of lattice cells intersect the volume of the particle, the force will be distributed over the lattice cells intersecting the particle, proportional to the volume fraction of the particle in the particular lattice cell, cf. [3]. In similar way, the solid volume fraction is distributed over the lattice cells. In this way the porosity field ϕ is computed.

The hydrodynamic interaction between particles with same diameter is given by the two-point lubrication force. As in regular Lattice Boltzmann part of the hydrodynamic interaction is already resolved. Hence, we take a modified lubrication force:

$$F_{pq,\alpha} = -6\pi\mu d_p^2(v_{p,\alpha} - v_{q,\alpha})\hat{e}_{r,\alpha}\left(\frac{1}{h} - \frac{1}{h_c}\right) \tag{8}$$

Note that r is the distance between the particles, which all have the same diameter d_p. The gap between particles is $h = r - d_p$. The lubrication force is proportional to the relative velocity between the particles. h_c is a cut off length where the lubrication force is zero.

If the gap between particles is smaller than $h_{\min}$ a spring force acts between particles p and q:

$$F_{spring,\alpha} = -k(h - h_{\min})\hat{e}_{r,\alpha} \tag{9}$$

The wall lubrication force acts only if the gap is within the cut off distance $h < h_c$:

$$\mathbf{F}_{wall,lub} = -6\pi d_p^2 \mu v_{p,n}\left(\frac{1}{h} - \frac{1}{h_c}\right)\hat{e}_n \tag{10}$$

Here $\hat{e}_n$ is the outward pointing normal vector to the confining plane. If the gap is even smaller $h < h_{\min}$ the spring force is acting on the particle, similar as above.

As common in molecular dynamics Newtons law is integrated via a velocity-Verlet scheme:

$$r_{p,\alpha}(t+\delta t) = r_{p,\alpha}(t) + v_{p,\alpha}\delta t + \tfrac{1}{2}a_{p,\alpha}\delta t^2 \qquad (11)$$
$$v_{p,\alpha}(t+\delta t) = v_{p,\alpha}(t) + a_{p,\alpha}\delta t$$

The timestep δt can vary during simulation, and will be determined by the smallest gap between particles, as shown below. Stability of the scheme set some requirements to the time scales involved. Below we list the time scales 1) convective time scale $\tau_\phi = d_p/v_p$, 2) time scale of drag force: $\tau_\beta = \rho_p d_p^2/18\rho_f \nu$, 3) kinematic time $\tau_\nu = d_p^2/\nu$, 4) spring force time scale: $\tau_k^2 = k_{spring}/m_p$ 5) lubrication force time scale $\tau_{lub} = \rho_p d_p h'/36\rho_f \nu$. with $1/h' = 1/h - 1/h_c$. Note that dimensionless numbers can be expressed in ratios of the above time scales, namely the Reynolds number: $Re = \tau_\nu/\tau_\phi$, and the Stokes number $St = \tau_\zeta/\tau_\phi$. Stability sets the following hierarchy of time scales: $\delta t \ll \tau_{lub} < \tau_\zeta < \tau_\nu \ll \tau_\phi$.

4.2 Numerical test

We compare the collision of two equal spheres in linear shear field with the solution of Batchelor and Green. Results are shown in figure 2. Results are obtain

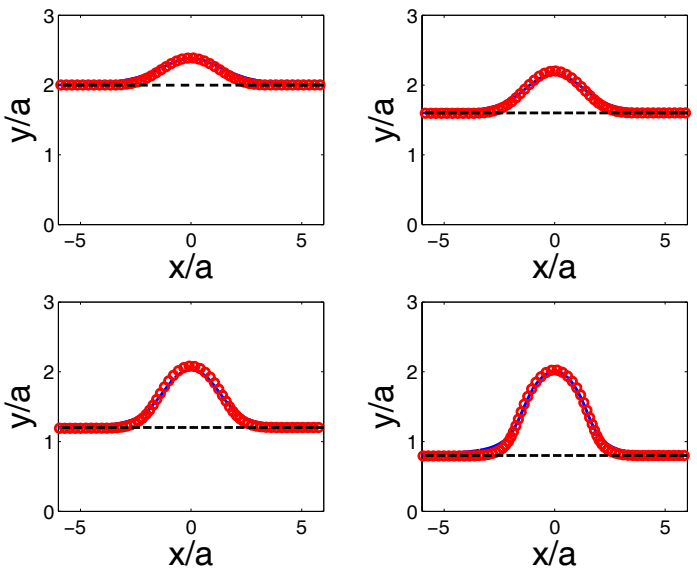

Figure 2: Normalised relative trajectory of a sphere colliding with a second sphere in a linear shear field. Solid lines indicate the solution given by Batchelor and Green, and symbols indicate our numerical solution. Dashed line indicates the base line to which the sphere should return after collision.

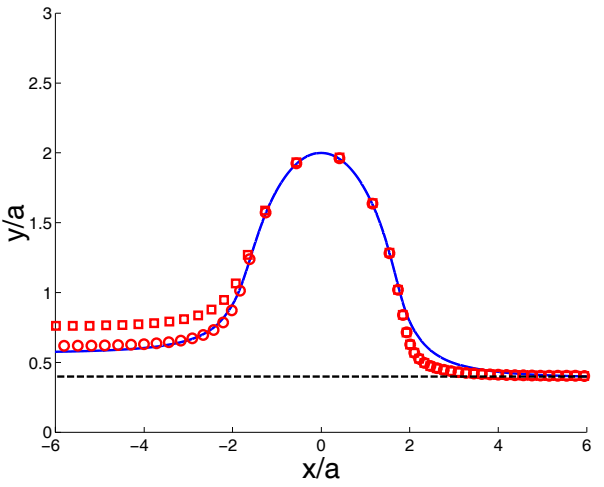

Figure 3: Normalised relative trajectory of a sphere colliding with a second sphere in a linear shear field, with initial vertical distance $y/a = 0.4$ and $h_{\min} = 0.01a$, and $h_{\min} = 0.004a$.

with cut off length for the lubrication $h_c = 2d_p$, $d_p = 0.2\Delta x$. Initial positions of the particles are at $x_0 = \pm 5d_p$, and $y_0 = \pm\frac{1}{2m}d_p$ with $m = \{1, 2, \ldots, 5\}$. In figure 2 we show the particle trajectory (with respect to the barycentre) for $m = 2, \ldots, 5$. Here we have set $h_{\min} = 0.01d_p$. Surprisingly we obtain very good agreement with the analytical solution of Batchelor and Green, although the flow is not fully resolved. In figure 3 we show results for $m = 1$, where the particle come very close in contact. In this case we have changed $h_{\min}$ to $h_{\min} = 0.005d_p$ and $h_{\min} = 0.002d_p$. We observe that the particles do not return to their initial streamlines. Still some asymmetry in the analytical solution. Might be due to the fact that tangential lubrication is not included [14].

This error improves if we take smaller $h_{\min}$, at the cost of a significant increase of computing time, as smaller gaps lead to smaller subgrid time steps δt. At $h_{\min} = 0.005d_p$ we obtain nearly the same solution as the integration of the analytical solution of the particle velocities given by Batchelor and Green.

5 Conclusions

In this paper we have given a first introduction to a numerical scheme describing flow through porous media and suspensions at a semi-resolved scale. We have obtained reasonable agreement with benchmark problems. Currently we are investigating problems of suspensions with a multitude of particles.

Acknowledgements

We thanks Prof. John Brady, Prof. Wim Briels, Prof. Mike Cates and dr. Kevin Stratford for useful discussions. The stay of Gerben Brans at the group of prof. Cates, Univ. Edinburgh is financially supported by HPC-Europe programme.

References

[1] Y.Q. Feng and A.B. Yu. Assessment of model formulations in the discrete particle simulation of gas-solid flow. *Ind. Chem. Res.* **43**: 8378–8390 (2004).
[2] Y.P. Tsuo and D. Gidaspow. Computation of flow pattern in circulating fluidized beds. *AIChE J.* **36**(6): 885–896 (1990).
[3] B.P.B. Hoomans, J.A.M. Kuipers, W.J. Briels, and W.P.M. van Swaaij. Discrete particle simulation of bubble and slug formation in a two dimensional gas-fluidised bed: a hard sphere approach. *Chem Eng. Sci.* **51**: 99–118 (1996).
[4] S. Schwarzer. Sedimentation and flow through porous media: simulating dynamically coupled discrete and continuum phases. *Phys. Rev. E* **52**(6): 6461–6475 (1995).
[5] G.S. Beavers, and D.D. Joseph. Boundary conditions at a naturally permeable wall. *J. Fluid Mech.* **30**: 197–207 (1967).
[6] J.A. Ochoa-Tapia, and S. Whitaker. Momentum-transfer at the boundary between a porous medium and a homogenous fluid .1. theoretical development. *Int. J. Heat Mass Transfer* **38**(14): 2635–2646 (1995).
[7] G.K. Batchelor, and J.T. Green. Hydrodynamic interaction of 2 small freely-moving spheres in a linear flow field. *J. Fluid Mech.* **56**: 375–400 (1972).
[8] S. Chen, and G.D. Doolen. Lattice Boltzmann method for fluid flows *Ann. Rev. Fluid Mech.* **30**: 329–364 (1998).
[9] R.G.M. van der Sman Galilean invariant lattice Boltzmann scheme for natural convection on square and rectangular lattices. *Phys. Rev. E* **74**(2): 026705 (2006).
[10] R.G.M. van der Sman, and S. Bogale. Porous media and suspension flow with modified MRT Lattice Boltzmann scheme. submitted to *J. Comput. Phys.* (2007).
[11] S. Whitaker. The Forchheimer equation: a theoretical development. *Transp. Porous Media* **25**: 27–61 (1996).
[12] B. Goyeau, D. Lluillier, D. Gobin, and M.G. Velarde. Momentum transport at a fluid-porous interface. *Int. J. Heat Mass transfer* **46**: 4071–4081 (2003).
[13] M.A. van der Hoef, R. Beetstra, and J.A.M. Kuipers. Lattice-Boltzmann simulations of low-Reynolds-number flow past mono- and bidisperse arrays of spheres: results for the permeability and drag force. *J. Fluid Mech.* **528**: 233–254 (2005).
[14] N.Q. Nguyen, and A.J.C. Ladd. Lubrication corrections for lattice-Boltzmann simulations of particle suspensions. *Phys. Rev. E* **66**(4): 046708 (2002).

Section 5
Hydraulics and hydrodynamics

This page intentionally left blank

Considering bottom curvature in depth-averaged open-channel flow modelling, based on curvilinear coordinates

B. J. Dewals[1,2], S. Erpicum[1] & M. Pirotton[1]
[1]*Department ArGEnCo, University of Liege, Belgium*
[2]*Fund for Scientific Research F.R.S.-FNRS, Belgium*

Abstract

Accurately modelling open-channel flows on strongly vertically curved bottoms, such as for instance over a spillway, is a challenge for any depth-averaged flow model. This type of computation requires the use of axes properly inclined along the mean flow direction in the vertical plane and a modelling of curvature effects. The present generalized model performs such computations by means of curvilinear coordinates in the vertical plane, enabling for instance one to simulate within one single computation domain the flows in the upstream reservoir, over the spillway, in the stilling basin and in the river reach downstream of a dam.

The frame of reference is chosen in such a way that one of the two curvilinear axes follows the local bottom curvature. Hence the set of generalized shallow water equations involves explicitly not only the channel bottom slope, but also the channel vertical curvature and its derivative. The velocity profile is generalized in comparison with the uniform one usually assumed in the conventional shallow-water equations. The pressure distribution is also modified as a function of the bottom curvature and is thus not purely hydrostatic but accounts for effects of centrifugal forces.

This enhanced mathematical modelling framework has been implemented in a 2D finite volume model. A specific flux vector splitting technique has been developed and demonstrated to be stable for any flow regime and any bottom curvature. The scheme offers the advantage of being dependent only on the sign of the bottom curvature. For a vanishing bottom curvature, the new model converges smoothly towards the conventional shallow-water equations.

Finally, two test cases are detailed and lead to satisfactory validation results for the new model.

Keywords: shallow-water equations, finite volume, bottom curvature.

WIT Transactions on Engineering Sciences, Vol 59, © 2008 WIT Press
www.witpress.com, ISSN 1743-3533 (on-line)
doi:10.2495/AFM080301

1 Introduction

In the conventional *shallow-water equations*, the main assumption states that velocities normal to a main flow direction are smaller than those in this main flow direction. As a consequence, the pressure field is found to be almost hydrostatic everywhere and a depth-averaging operation of the local conservation laws can be performed easily.

The large majority of flows occurring in rivers can reasonably be seen as shallow and are characterized by relatively small vertical velocity components everywhere, except near local singularities. Those singularities, such as weirs or spillways, can however play a major part in the flow behaviour in the vicinity of the structure, but also in the far field upstream and downstream. A key characteristic of most of those structures is the development of flows over *strongly vertically curved bottoms*.

While applying fully 3D flow models for large-scale real applications remains challenging in terms of computation cost and data requirements, modelling such flows over vertically curved bottoms is far from straightforward for any depth-averaged model. Indeed, such a computation requires the use of axes properly inclined along the *local* mean flow direction in the vertical plane. Since this local mean flow direction changes over the computation domain, a suitable modelling of the vertical *curvature effects* is needed.

Therefore, the present paper describes an extension of the shallow-water equations (SWE), based on a similar depth-averaging operation as in the development of the conventional SWE, but considering a frame of reference with curvilinear lines of coordinates following the main flow direction. As a consequence, the new set of equations includes terms involving not only the channel inclination θ [-], but also containing explicitly the bottom curvature κ [L^{-1}] and its rate of change κ' [L^{-2}]. The velocity profile is different from the uniform one usually assumed in the conventional shallow water equations. The pressure distribution is also modified to take into centrifugal forces. As a consequence, the mathematical and computational model described hereafter enables to achieve unified 2D modelling of the flows upstream, downstream and *over* river training structures (e.g. spillway) in *one single* simulation.

Besides a literature review, the present paper provides a description of the new depth-averaged model, covering the development of the mathematical model and a short overview of its computational implementation. Two validation test cases are also presented, demonstrating that the enhanced model provides more accurate water depth and bottom pressure results than the SWE.

2 Literature review

The first attempt to introduce vertical curvature effects in a shallow-water model was performed in a pioneering work by Dressler [13] in 1978. He developed a 1D model on a similar idea as in the present case, but without a proper depth-averaging operation. His mathematical formulation was thus non-conservative. Later he presented a modified friction term [14], taking into account the uneven

velocity profile. Experimental validations of this first model were performed by Sivakumaran *et al.* [21, 22] and later by Ilhan [18]. A 2D generalization, as well as a *finite element* computer code to solve the model, have been proposed by Berger and Carey [4, 5]. A *finite volume* numerical model for solving the 2D extended model, considering curvature along one direction, has been developed and validated by Dewals *et al.* [9]. Recently, Anh and Hosoda also derived a generalized formulation handling flows over an arbitrary 3D surface [1]. In parallel, 3D models were also applied to spillway overflows (e.g. Bürgisser and Rutschman [6]), while other authors [19, 20] have modelled flows over vertically curved beds by means of *vertically averaged and moment equations*. However, this later approach presents the drawback of involving 10 equations in 2D, in comparison with 3 equations in the present case.

3 Model development

In this section, the mathematical formulation of the model is described. Bed curvature is considered along one direction (x).

3.1 Curvilinear frame of reference

The fundamental idea of the extended model is to replace the Cartesian coordinates (x, z) in the vertical plane by *curvilinear coordinates* (ξ, η) selected in order that:

- the curvilinear abscissa ξ follows the local channel bottom;
- the second curvilinear axis (η) is normal to the local bed direction;
- the third axis of reference (y) is simply normal to the plane of curvature.

Figure 1 shows the new axes of reference and the main notations used.

In order to allow the evaluation of the space derivatives involved in the curvature expression and those present in the conservation equations, the

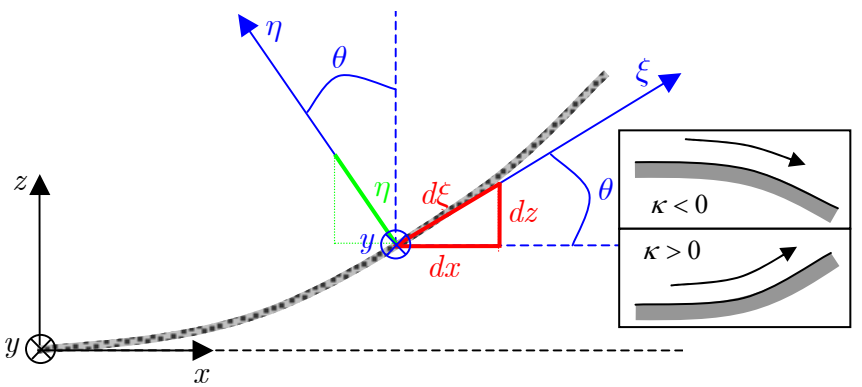

Figure 1: Symbols and axes of reference for the 2D extended model.

mathematical function describing the channel bed has to be continuous, have a continuous slope (θ) and a continuous curvature (κ). The curve representing the bottom must therefore be three times differentiable.

3.2 Change of variables

The correspondence between the Cartesian coordinates and their curvilinear counterparts is given by the following relations:

$$x = x(\xi,\eta) = x_{\text{bed}}(\xi) - \eta \sin\theta\,, \qquad y = y\,, \qquad z = z(\xi,\eta) = z_{\text{bed}}(\xi) + \eta\cos\theta\,. \quad (1)$$

The unit vector tangent to the channel bottom in a vertical plane and the bottom curvature are respectively defined as:

$$\vec{t} = \begin{pmatrix} dx_{\text{b}}/d\xi \\ dy_{\text{b}}/d\xi \\ dz_{\text{b}}/d\xi \end{pmatrix} = \begin{pmatrix} \cos\theta \\ 0 \\ \sin\theta \end{pmatrix} \qquad \text{and} \qquad \kappa = \left(\vec{t} \wedge \frac{d\vec{t}}{d\xi}\right)\cdot\vec{e}_y = \frac{d\theta}{d\xi}. \quad (2)$$

The Jacobian matrix can be deduced from relation (1), as well as the Jacobian of the change of variables, which is simply equal to the determinant of matrix J:

$$\mathrm{J} = \begin{bmatrix} \cos\theta(1-\kappa\eta) & 0 & -\sin\theta \\ 0 & 1 & 0 \\ \sin\theta(1-\kappa\eta) & 0 & \cos\theta \end{bmatrix}, \qquad \det(\mathrm{J}) = J = 1-\kappa\eta \quad (3)$$

The fundamental relation between derivatives in both systems of reference reads:

$$\begin{pmatrix} \frac{\partial}{\partial x} \\ \frac{\partial}{\partial y} \\ \frac{\partial}{\partial z} \end{pmatrix} = \begin{bmatrix} \cos\theta(1-\kappa\eta)^{-1} & 0 & -\sin\theta \\ 0 & 1 & 0 \\ \sin\theta(1-\kappa\eta)^{-1} & 0 & \cos\theta \end{bmatrix} \begin{pmatrix} \frac{\partial}{\partial \xi} \\ \frac{\partial}{\partial y} \\ \frac{\partial}{\partial \eta} \end{pmatrix}. \quad (4)$$

A change of variables is valid provided that the corresponding Jacobian remains positive. In the case of a negative bed curvature (convex), no special restriction needs to be introduced. On the contrary, if the bed curvature is positive (concave), the coordinate η must be limited to a value depending on the sharpness of the curvature. The Jacobian expression above remains positive as long as the water height verifies the following condition (with $\kappa > 0$ and R the radius of curvature): $H < 1/\kappa = R$.

3.3 Velocity transformation and velocity profile

The velocity vector $\vec{v}$ may be expressed in both frames of reference:

$$\vec{v} = U\,\vec{e}_\xi + V\,\vec{e}_y + W\,\vec{e}_\eta = u\,\vec{e}_x + v\,\vec{e}_y + w\,\vec{e}_z\,. \quad (5)$$

Those components are related by the simple transformation formula:

$$\begin{pmatrix} U \\ V \\ W \end{pmatrix} = \begin{bmatrix} \cos\theta & 0 & \sin\theta \\ 0 & 1 & 0 \\ -\sin\theta & 0 & \cos\theta \end{bmatrix} \begin{pmatrix} u \\ v \\ w \end{pmatrix}. \tag{6}$$

Following the work by Dressler [13], the most straightforward assumption concerning velocity distribution has been selected. This corresponds to a non-rotational flow in the vertical plane, expressed in curvilinear coordinates by:

$$\mathrm{rot}\vec{v} \cdot \vec{e}_y = 0 \qquad \Rightarrow \qquad \frac{\partial W}{\partial \xi} = J \frac{\partial U}{\partial \eta} - \kappa U. \tag{7}$$

Finally, heeding the shallowness of the flow, the corresponding ξ-velocity profile is given by: $U(\xi, y, \eta, t) = (1 - \kappa\eta)^{-1} C(\xi, y, t)$, with C representing the longitudinal velocity along the channel bottom. The profile of the velocity is hence completely determined by the condition of irrotationality and the bottom curvature, as shown in Figure 2(a).

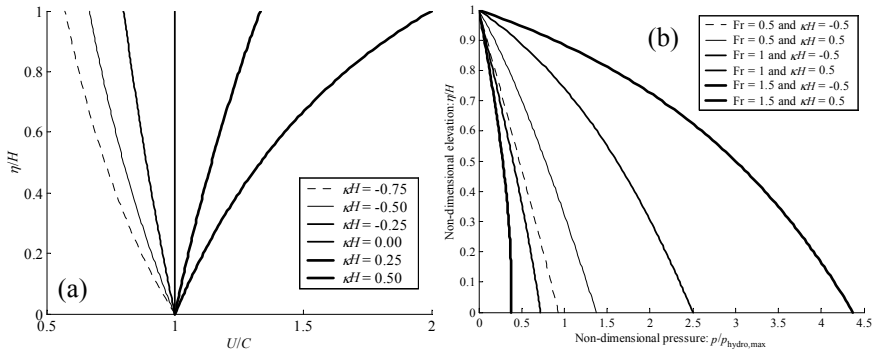

Figure 2: (a) Velocity profiles for different values of the non-dimensional curvature; (b) generalized pressure distributions for various Froude numbers and non-dimensional curvatures κH.

3.4 Local conservation laws for the flow

A general conservation law, such as

$$\frac{\partial s}{\partial t} + \frac{\partial f_x}{\partial x} + \frac{\partial f_y}{\partial y} + \frac{\partial f_z}{\partial z} = S, \tag{8}$$

may be transformed in the system of curvilinear coordinates by applying the fundamental relation (4). This operation leads to a new conservative law:

$$\frac{\partial (Js)}{\partial t} + \frac{\partial}{\partial \xi}\left(f_x \cos\theta + f_z \sin\theta\right) + \frac{\partial (J f_y)}{\partial y} + \frac{\partial}{\partial \eta}\left(f_z J \cos\theta - f_x J \sin\theta\right) = JS, \tag{9}$$

which can later on be used to transform the mass and momentum conservation equations for the flow. The local continuity equation can be easily deduced from its Cartesian form and the general relation (9):

$$\frac{\partial U}{\partial \xi}+\frac{\partial}{\partial y}(JV)+\frac{\partial}{\partial \eta}(JW)=0\,. \tag{10}$$

The same transformation performed for the momentum conservation equations leads to three new equations, which can be combined to provide the local momentum conservation laws expressed in curvilinear coordinates:

$$\frac{\partial}{\partial t}(JU)+\frac{\partial}{\partial \xi}\left(U^2+p/\rho\right)+\frac{\partial}{\partial y}\left(JUV\right)+\frac{\partial}{\partial \eta}\left(JUW\right)=-gJ\sin\theta+\kappa UW, \tag{11}$$

$$\frac{\partial}{\partial t}\left(JV\right)+\frac{\partial}{\partial \xi}\left(UV\right)+\frac{\partial}{\partial y}\left[J\left(V^2+p/\rho\right)\right]+\frac{\partial}{\partial \eta}\left(JVW\right)=0 \tag{12}$$

,

$$\frac{\partial\left(JW\right)}{\partial t}+\frac{\partial\left(UW\right)}{\partial \xi}+\frac{\partial\left(JVW\right)}{\partial y}+\frac{\partial}{\partial \eta}\left[J\left(W^2+\frac{p}{\rho}\right)\right]=-gJ\cos\theta-\kappa\left(U^2+\frac{p}{\rho}\right). \tag{13}$$

According to the conventional assumption regarding the shallowness of the flow ($W^2 \ll U^2+V^2$), the purely advective terms expressing an acceleration perpendicular to the bottom may be ignored in the latter equation. A complete non-dimensional analysis of orders of magnitude has been performed and demonstrates that this conclusion remains valid for the model expressed in curvilinear coordinates. As a result, the generalized pressure distribution can be deduced directly by integrating relation (13) along the η-axis:

$$p\left(\eta\right)/\rho=g\cos\theta\left(H-\eta\right)+C^2/2\left[\left(1-\kappa H\right)^{-2}-\left(1-\kappa\eta\right)^{-2}\right]. \tag{14}$$

It can be easily verified that in the case of a zero-curvature bed, the term in square brackets vanishes in relation (14) and hence the hydrostatic pressure distribution is restored. Figure 2(b) illustrates the effect of bed curvature on the pressure field as a function of a modified *Froude number*, defined as $\mathrm{Fr}=C/\sqrt{gH\cos\theta}$. The figure highlights a higher sensitivity of the pressure profile to positive curvatures, rather than to negative ones.

3.5 Boundary conditions

The interface between the studied liquid and the ambient air is defined by the impossibility for the fluid to cross this surface. This implies that the velocity of the fluid in the direction *normal* to the interface and the velocity of this interface in the same normal direction are equal. According to Whitham [23], and taking into consideration the specific velocity profile of the flow over a vertically curved bed, this equality of normal velocities can be expressed as follows:

$$W\left(t,\xi,y,H\right)=\frac{\partial H}{\partial t}+\frac{U\left(t,\xi,y,H\right)}{1-\kappa H}\frac{\partial H}{\partial \xi}+V\left(t,\xi,y,H\right)\frac{\partial H}{\partial y}. \tag{15}$$

The no-flow condition across the bottom is expressed by: $W\left(t,\xi,y,0\right)=0$.

Since the free surface position is not known *a priori*, its location constitutes an additional unknown and a second boundary condition is required. This dynamic boundary condition simply states that the pressure at the free surface is identical to the atmospheric pressure, selected as the reference: $p(\xi, y, H, t) = p_{\text{atm}} = 0$.

3.6 Depth-averaged equations for the flow

Integrating equation (10) from the bottom ($\eta = 0$) to the free surface ($\eta = H$) leads to the depth-averaged mass conservation equation:

$$\frac{\partial \mathcal{H}}{\partial t} + \frac{\partial q}{\partial \xi} + \frac{\partial}{\partial y}(\mathcal{H} V) = 0, \tag{16}$$

where $\mathcal{H}$ and q represent respectively the actual "volume" in a cell and the unit discharge, defined as:

$$\mathcal{H} \triangleq H\bar{J} = H\left(1 - \frac{\kappa H}{2}\right) \quad \text{and} \quad q(\xi, t) = H\bar{U} = \int_0^{H(\xi,t)} U(\xi, \eta, t)\, d\eta. \tag{17}$$

The previous expression can be evaluated for the particular velocity profile:

$$q = HC(-\kappa H)^{-1} \ln(1 - \kappa H). \tag{18}$$

A similar procedure applied to equations (11) and (12) leads to the momentum conservation along the ξ-axis:

$$\frac{\partial}{\partial t}(HC) + \frac{\partial}{\partial \xi}\left(\frac{HC^2}{1-\kappa H}\right) + \frac{\partial}{\partial y}(HCV) + \frac{\partial}{\partial \xi}\left[g\frac{H^2}{2}\cos\theta + \frac{HC^2}{2}\frac{\kappa H}{(1-\kappa H)^2}\right] = -g\mathcal{H}\sin\theta + \kappa H\overline{UW} \tag{19}$$

and the corresponding relation along the *y*-axis:

$$\frac{\partial}{\partial t}(\mathcal{H} V) + \frac{\partial}{\partial \xi}(Vq) + \frac{\partial}{\partial y}\left(\mathcal{H}V^2 + H\overline{J\frac{p}{\rho}}\right) = 0, \tag{20}$$

with the mean pressure term written out in full as follows:

$$H\overline{J\frac{p}{\rho}} = g\frac{H^2}{2}\cos\theta\left(1 - \frac{\kappa H}{3}\right) + \frac{HC^2}{2}\frac{1-\kappa H/2}{(1-\kappa H)^2} - \frac{HC^2}{2}\frac{\ln(1-\kappa H)}{-\kappa H}. \tag{21}$$

It can be easily verified that in the case of a zero curvature bed, equations (16), (19) and (20) become identical to the set of the conventional shallow-water equations. According to the non-dimensional analysis of orders of magnitude, the term $\kappa H\overline{UW}$ in (19) may not necessarily be ignored. It can be accounted for thanks to a proper assumption regarding the profile of the velocity component W (normal to the bottom), as detailed for instance by Dewals *et al.* [9].

A bottom friction term can be added on the right hand side of equations (20) and (21). Dressler and Yevjevich [14] suggest an adapted formulation of the conventional empirical friction laws (Chezy, Manning) for a 1D model including bed curvature. In addition, in further developments of the present research, the

velocity profile will be enhanced to take into account the corresponding bottom shear stress.

4 Computational model

The system of equations (16), (19) and (20) remains conservative, which is a crucial asset for numerical discretization. In the present case, a finite volume scheme is used for the space discretization of the system. An original Flux Vector Splitting (FVS) is used for the space discretization of the complete set of equations [7]. This second order upwind scheme is Froude independent and depends only on the sign of the bottom curvature. Its stability has been demonstrated by means of a theoretical study of the mathematical system [7, 9], as well as a von Neumann stability analysis [7]. The computational model deals with multiblock Cartesian grids. The multiblock organization of the computation code enables the activation of the extended model only in the vicinity of the spillway, while the simple SWE are solved in the rest of the computation domain. This feature leads to CPU time savings.

Several expressions in the additional terms of the extended model present a very stiff behaviour for low-value curvatures. For this reason, expressions, such as the specific discharge (18) or the mean pressure term (21), are replaced in the numerical model by a series expansion as soon as κH becomes very small.

The herein described model is integrated within the *modelling system WOLF*, developed at the University of Liege. This set of interconnected computational models enables the simulation of process-oriented hydrology [3], 1D [3, 15] and 2D hydrodynamics [2, 16, 17], sediment or pollutant transport [7, 10, 11], air entrainment [8], turbulence (incl. a k-ε closure) [15] … as well as optimisation processes (based on Genetic Algorithms) [15]. Other functionalities of WOLF include the use of moment of momentum equations [7] or the analysis of flow instabilities [12].

5 Validation

This section aims at demonstrating the improvements brought by the generalized SWE model in terms of results accuracy and realism. The section includes comparisons between the SWE and the extended model for idealized test cases. Full details can be found in the original reference cited for each example.

5.1 Symmetric profile

Sivakumaran *et al.* [22] studied the flow over a symmetric profile in a flume of 9.15 x 0.75 x 0.445 m. The flume roughness corresponds to a Manning coefficient $n \approx 0.01\ \mathrm{m}^{-1/3}\mathrm{s}$ and experiments were carried out with two different discharges: 0.11197 m²/s and 0.03599 m²/s.

In both cases, the present extended model with curvature leads to significantly more accurate predictions for the free surface location, as well as for the bed pressure. Results for the higher discharge are presented in Figures 3(a) and (b).

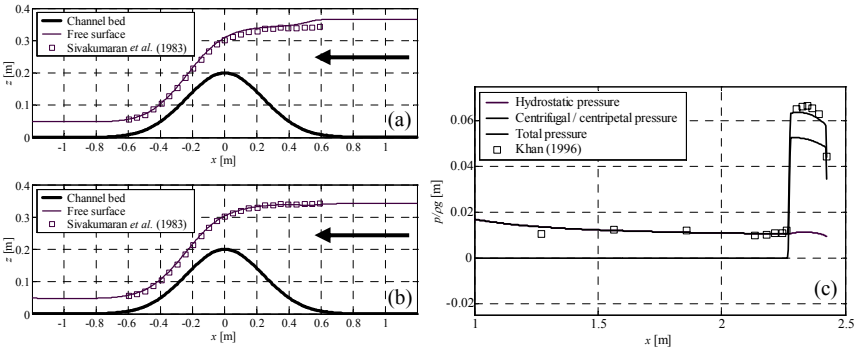

Figure 3: Water surface for the symmetric profile of Sivakumaran *et al.* [22], simulated with the SWE (a) and with the extended model (b); bed pressure on the flip-bucket spillway tested by Khan and Steffler [19] (c).

5.2 Flip-bucket spillway

Water profile and bed pressure measurements, conducted on a laboratory flip-bucket spillway, were presented by Khan and Steffler [19] in 1996. The slope of the chute was 20° and the idealized flip-bucket was represented by a circular arc of radius 15.4 cm. Two specific discharges were tested: 0.0187 m²/s and 0.0292 m²/s. Figure 3(c) shows a comparison between observed and computed pressures on the bottom of the spillway for the higher discharge. The pressure profile computed with the herein presented model agrees well with the measurements.

6 Conclusion

Since the shallow-water equations simply assume that both the bed curvature and its rate of change may be neglected, such an approach is valid only if no sharp changes in the bed inclination occur. Though these conditions are very widely met in waterways and rivers, experience in open channel flow modelling demonstrates the necessity for a better approximation for a wide range of applications, such as spillway overflows. Therefore, the herein presented 2D generalized model has been developed in order to handle correctly the effects induced by strong bottom curvatures, based on curvilinear coordinates in the vertical plane. The model presented generalizes the shallow water theory by incorporating effects of streamline vertical curvature. It leads to better estimations of particle velocity profiles and non-hydrostatic pressure distribution over curved surfaces. More accurate upstream water elevation and bottom pressure can thus be predicted.

Moreover, the approach enables simulations completely *integrating* the flow behaviour in the vicinity of large river structures, such as dams: the flows in the

upstream reservoir, on the spillway, in the stilling basin and in the downstream river reach can be treated in one single simulation.

The full development of the mathematical model has been presented and two successful test-cases have been described. Both cases lead to significant improvements in the numerical results compared to the conventional SWE.

References

[1] Anh, T.N. and T. Hosoda, Depth-averaged model of open-channel flows over an arbitrary 3D surface and its applications to analysis of water surface profile. J. Hydraul. Eng.-ASCE, 2007. **133**(4): pp. 350–360.

[2] Archambeau, P., B. Dewals, S. Detrembleur, S. Erpicum and M. Pirotton, A set of efficient numerical tools for floodplain modeling, in Shallow Flows, G.H. Jirka and W.S.J. Uijttewaal (eds). 2004, Balkema: Leiden, etc. pp. 549–557.

[3] Archambeau, P., Contribution à la modélisation de la genèse et de la propagation des crues et inondations. 2006, PhD thesis, University of Liege**.**

[4] Berger, R.C. and G.F. Carey, Free-surface flow over curved surfaces - Part I: perturbation analysis. Int. J. Numer. Meth. Fluids, 1998. **28**(2): pp. 191–200.

[5] Berger, R.C. and G.F. Carey, Free-surface flow over curved surfaces - Part II: computational model. Int. J. Numer. Meth. Fluids, 1998. **28**(2): pp. 201–213.

[6] Bürgisser, M.F. and P. Rutschmann. Numerical solution of viscous 2DV free surface flows: flow over spillway crests. in 28th IAHR Congress Graz. 1999.

[7] Dewals, B., Une approche unifiée pour la modélisation d'écoulements à surface libre, de leur effet érosif sur une structure et de leur interaction avec divers constituants. 2006, PhD thesis, University of Liege**:** 636 pp.

[8] Dewals, B.J., S. André, A. Schleiss and M. Pirotton. Validation of a quasi-2D model for aerated flows over stepped spillways for mild and steep slopes. in Proc. 6th Int. Conf. of Hydroinformatics. 2004. Singapore.

[9] Dewals, B.J., S. Erpicum, P. Archambeau, S. Detrembleur and M. Pirotton, Depth-integrated flow modelling taking into account bottom curvature. J. Hydraul. Res., 2006. **44**(6): pp. 787–795.

[10] Dewals, B.J., S. Erpicum, P. Archambeau, S. Detrembleur and M. Pirotton. Hétérogénéite des échèlles spatio-temporelles d'écoulements hydrosédimentaires et modélisation numerique. in Transports solides et gestion des sédiments en milieux naturels et urbains. 2007. Lyon, France: SHF.

[11] Dewals, B.J., P. Archambeau, S. Erpicum and M. Pirotton, A modelling system for open-channel flows with mobile bed - Application as a decision-support tool for sediment management in a hydropower project. Geophysical Research Abstracts, 2008. **10**.

[12] Dewals, B.J., S.A. Kantoush, S. Erpicum, M. Pirotton and A.J. Schleiss, Experimental and numerical analysis of flow instabilities in rectangular shallow basins. Environ. Fluid Mech., 2008 (accepted).
[13] Dressler, R.F., New Nonlinear Shallow Flow Equations with Curvature. J. Hydraul. Res., 1978. **16**(3): pp. 205–222.
[14] Dressler, R.F. and V. Yevjevich, Hydraulic-resistance terms modified for the Dressler curved-flow equations. J. Hydraul. Res., 1984. **22**(3): pp. 145–156.
[15] Erpicum, S., Optimisation objective de paramètres en écoulements turbulents à surface libre sur maillage multibloc. 2006, PhD thesis, University of Liege.
[16] Erpicum, S., P. Archambeau, S. Detrembleur, B. Dewals and M. Pirotton, A 2D finite volume multiblock flow solver applied to flood extension forecasting, in Numerical modelling of hydrodynamics for water ressources, P. García-Navarro and E. Playán (eds). 2007, Taylor & Francis: Londres. pp. 321–325.
[17] Erpicum, S., B.J. Dewals, P. Archambeau, S. Detrembleur and M. Pirotton. Detailed 2D numerical modeling for flood extension forecasting. in Proc. 4th Int. Conf. on Fluvial Hydraulics: River Flow 2008. 2008 (accepted).
[18] Ilhan, M.H., Computation of flow over vertically curved channels, in Gradual School of Natural and Applied Sciences. 1994, Master thesis, Middle East Technical University, Ankara.
[19] Khan, A.A. and P.M. Steffler, Vertically averaged and moment equations model for flow over curved beds. J. Hydraul. Eng.-ASCE, 1996. **122**(1): pp. 3–9.
[20] Khan, A.A. and P.M. Steffler, Modelling overfalls using vertically averaged and moment equations. J. Hydraul. Eng.-ASCE, 1996. **122**(7): pp. 397–402.
[21] Sivakumaran, N.S., R.J. Hosking and T. Tingsanchali, Steady shallow flow over a spillway. J. Fluid Mech., 1981. **111**: pp. 411–420.
[22] Sivakumaran, N.S., T. Tingsanchali and R.J. Hosking, Steady shallow flow over curved beds. J. Fluid Mech., 1983. **128**: pp. 469–487.
[23] Whitham, G.B., Linear and Nonlinear Waves. 1974, New York: Wiley, 636 pp.

This page intentionally left blank

Analytical investigation of ice floe drift in the marginal ice zone

R. M. Abid[1], S. H. Mousavizadegan[2] & M. Rahman[3]
[1]*Department of Information Technology, Schneider National, Inc., USA*
[2]*Faculty of Marine Technology, Amirkabir University of Technology, Iran*
[3]*Department of Engineering Mathematics, Dalhousie University, Canada*

Abstract

Analytical solutions were constructed to investigate the ice floe drift, velocity field, and trajectories. The mathematical model considers the balance of atmosphere and ocean drag forces on ice floe, including skin and body drag forces from wind, waves, and currents. We have obtained numerical solutions to our mathematical models of air-ice stress. Graphical solutions are presented for ice floe drift due to wind stress. Mathematical formulations are being developed for the ice floe drift due to Eulerian current, water-ice form stress, and wave radiation pressure. We systematically presented in this paper the classical solutions of the ice floe drift, velocity, and trajectories considering the effects of wind. Numerical solutions of the mathematical models developed here, have been computed and presented. The mathematical models will be tested with available experimental data.
Keywords: ice floe, marginal ice zone, MIZ, ice drift, ocean surface waves, energy balance equation, wave spectrum, ice floe velocity components, ice floe trajectories.

1 Introduction

An ice floe is a floating chunk of sea ice that is less than 10 kilometers in its greatest dimension. Marginal Ice Zone (MIZ) is an interfacial region of ice floes which forms at the boundary of open water and the continuous ice pack. Figure 1 depicts a typical MIZ situation including ice floes and wave induced ice fracture at the ice edge. This paper considers the mathematical model for the ice edge and ice floe trajectories which is based on a balance equation for forces due to wind, waves, and currents impinging on the ice, as described by Tang and Fissel [7], Steele et al. [6] and Jenkins [3].

WIT Transactions on Engineering Sciences, Vol 59, © 2008 WIT Press
www.witpress.com, ISSN 1743-3533 (on-line)
doi:10.2495/AFM080311

Figure 1: Marginal ice zone in the Antarctic, and wave induced ice fracture at the ice edge. *(Courtesy: National Science Foundation, USA, and Squire et al. [5]).*

The dominating physical processes that determine ocean surface waves are, input of energy due to wind S_{in}, nonlinear transfer between spectral components due to wave-wave interactions S_{nl}, and energy dissipation due to white capping and wave breaking S_{ds}. Operational wave models combine these processes in the energy balance equation, which may be written as

$$\frac{\partial E(f,\theta)}{\partial t} + \mathbf{C_g} \cdot \nabla E(f,\theta) = S_{in} + S_{ds} + S_{nl} \tag{1}$$

where the two dimensional wave spectrum $E(f,\theta)$ is a function of frequency f, direction θ, time t, and position $\mathbf{x}$ and where $\mathbf{C_g}$ is the group velocity. Following Hasselmann et al. [2] and Perrie and Hu [4], we parameterized S_{in}, S_{ds}, and S_{nl}. Figure 2 shows a JONSWAP Wave Energy Spectrum with peak frequency of 0.3 Hz, at 10 m/s wind speed developed over 3.25 hours.

We systematically illustrate the mathematical formulations of the ice floe drift velocity due to wind forcing effects. The ice floe trajectories and the ice floe velocity fields are illustrated in a clear cut way. Linearizing the governing equations with zero initial conditions and using the Laplace transform method, we have obtained solutions to simulate the real field conditions. Graphical solutions are displayed in case of the external wind stress which causes the ice floe drift from one place to another. These highly simplified results seem to agree quite well with real field data. Further analysis and detailed investigations of the Eulerian currents, water ice form stress and the wave radiation can be found in [1].

2 Mathematical formulation

The mathematical equation of motion for an ice floe in the marginal ice zone due to wind, waves, and current can be written as

$$m\left(\frac{\partial \mathbf{u}'}{\partial t} + \mathbf{f} \times \mathbf{u}'\right) = A(\boldsymbol{\tau}_{air}^{skin} + \boldsymbol{\tau}_{water}^{skin} + \boldsymbol{\tau}_{air}^{form} + \boldsymbol{\tau}_{water}^{form} + \boldsymbol{\tau}_{rad}^{wave}) - mg\nabla\xi + \mathbf{F} \tag{2}$$

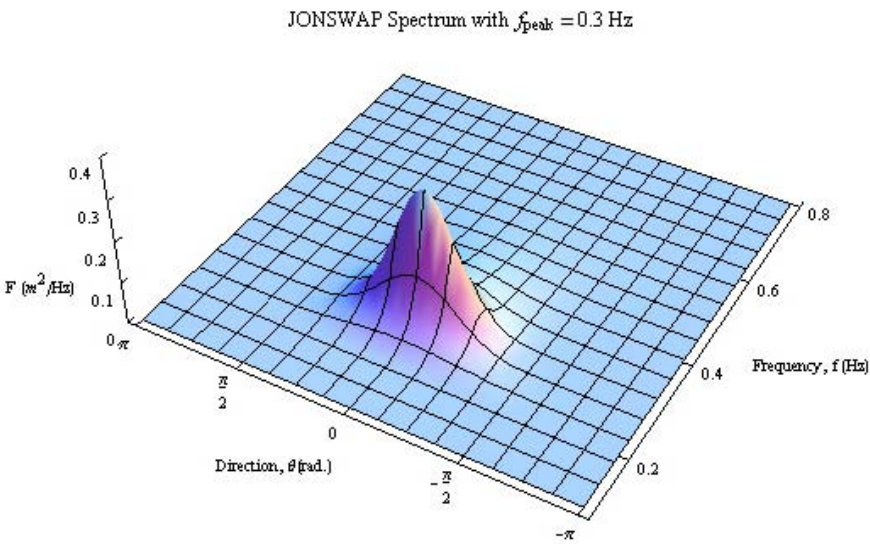

Figure 2: JONSWAP wave energy spectrum.

where g is the acceleration due to gravity, m is the ice mass, A is the ice floe surface area, ξ is the sea surface elevation, $\mathbf{F}$ is the ice internal stress gradient, $\mathbf{u}'$ is the absolute ice velocity, $\boldsymbol{\tau}_{air}^{skin}$ is the wind stress on the top surface of the ice floe, $\boldsymbol{\tau}_{water}^{skin}$ is the water stress on the bottom surface of the ice floe, $\boldsymbol{\tau}_{air}^{form}$ is the air-ice form stress, $\boldsymbol{\tau}_{water}^{form}$ is the water-ice form stress, and $\boldsymbol{\tau}_{rad}^{wave}$ is the wave radiation pressure.

If the ice concentration is low, the internal stress gradient $\mathbf{F}$ is essentially zero. Replacing $-mg\nabla\xi$ by the geostropic current $m\mathbf{f} \times \mathbf{U_g}$ and neglecting $\mathbf{F}$, equation (2) can be expressed as

$$m\left(\frac{\partial \mathbf{u}}{\partial t} + \mathbf{f} \times \mathbf{u}\right) = A(\boldsymbol{\tau}_{air}^{skin} + \boldsymbol{\tau}_{water}^{skin} + \boldsymbol{\tau}_{air}^{form} + \boldsymbol{\tau}_{water}^{form} + \boldsymbol{\tau}_{rad}^{wave}), \tag{3}$$

which gives the ice floe velocity, $\mathbf{u} = \mathbf{u}' - \mathbf{U_g}$, relative to the geostropic current $\mathbf{U_g}$.

The stresses $\boldsymbol{\tau}_{air}^{skin}$ and $\boldsymbol{\tau}_{water}^{skin}$ are caused by skin friction. It is assumed that $|\boldsymbol{\tau}_{air}^{form}| \ll |\boldsymbol{\tau}_{water}^{form}|$. Therefore, the final time-dependent equation of motion for an ice floe becomes

$$\left(\frac{\partial \mathbf{u}}{\partial t} + \mathbf{f} \times \mathbf{u}\right) = \frac{A}{m}(\boldsymbol{\tau}_{air}^{skin} + \boldsymbol{\tau}_{water}^{skin} + \boldsymbol{\tau}_{water}^{form} + \boldsymbol{\tau}_{rad}^{wave}). \tag{4}$$

Perrie and Hu [4] have described these expressions with various types of parameters effecting these stresses.

In a calm sea condition, the drift of the ice floe can be assumed to be only due to the effect of the wind. The air-ice-skin friction stress $\boldsymbol{\tau}_{air}^{skin}$, thus, is usually represented by a quadratic formula in terms of the wind speed $\mathbf{U_{10}}$,

$$\boldsymbol{\tau}_{air}^{skin} = \rho_a C_{ai}^{s} |\mathbf{U_{10}} - \mathbf{u}|(\mathbf{U_{10}} - \mathbf{u}) \tag{5}$$

where, ρ_a is the air density and C_{ai}^{s} is the air-ice-skin friction drag coefficient. Following Steele et al. [6], we used $C_{ai}^{s} \approx 3 \times 10^{-3}$.

3 Ice floe drift due to wind stress: model I

We simplify the governing partial differential equation with the initial condition and obtain,

$$\begin{aligned} \frac{\partial u}{\partial t} - fv &= \alpha U_{10} - \alpha u \\ \frac{\partial v}{\partial t} + fu &= -\alpha v \end{aligned} \tag{6}$$

where $\mathbf{u} = (u, v, 0)$ are the velocity components of the ice floe in a horizontal plane, $\mathbf{f} = (0, 0, f)$ are the Coriolis force components, and $\alpha = \frac{A}{m}\rho_a C_{ai}^{s} |\mathbf{U_{10}} - \mathbf{u}|$. Also, we have $(\mathbf{U_{10}} - \mathbf{u}) = (U_{10} - u, -v, 0)$. The wind velocity vector $\mathbf{U_{10}}$ is assumed to be parallel to the positive $x-$ direction. Here we assume that $U_{10} \gg |\mathbf{u}|$, i.e., the speed of wind is much greater than that of the ice drift and so we can safely assume that α is a constant parameter. The initial conditions at $t = 0$ are assumed as (when there is no wind):

$$u(0) = 0, \quad v(0) = 0. \tag{7}$$

Using Laplace transform $\mathcal{L}\{u\} = \int_0^\infty u(t)e^{-st}dt$ and $\mathcal{L}\{v\} = \int_0^\infty v(t)e^{-st}dt$ with the initial conditions (7), the simultaneous differential equations (6) can be transformed as

$$\begin{aligned} (s + \alpha)\mathcal{L}\{u\} - f\mathcal{L}\{v\} &= \frac{\alpha U_{10}}{s} \\ f\mathcal{L}\{u\} + (s + \alpha)\mathcal{L}\{v\} &= 0 \end{aligned}$$

Solving these two algebraic equations by Cramer's rule and using residue calculus, we obtain the non-dimensional forms of the solutions as:

$$U - a = e^{-\alpha t}\{b \sin ft - a \cos ft\} \tag{8}$$

$$V + b = e^{-\alpha t}\{b \cos ft + a \sin ft\} \tag{9}$$

where U, V, a, and b are given by

$$U = \frac{u}{U_{10}}, \quad V = \frac{v}{U_{10}}, \quad a = \frac{\alpha^2}{\alpha^2 + f^2} \quad \text{and} \quad b = \frac{\alpha f}{\alpha^2 + f^2}.$$

Thus, the velocity field of the ice floe, i.e., the $U - V$ plot, can be described by the following circular spiral type solution as a function of time

$$(U - a)^2 + (V + b)^2 = (a^2 + b^2)e^{-2\alpha t}. \tag{10}$$

The equation (10) reveals that the radius of the circle at $t = 0$ becomes simply $\sqrt{a^2 + b^2}$ but when the time progresses the radius starts to decrease exponentially and at very large time, i.e., when $t \to \infty$, the radius of the circle becomes zero implying that the circle shrinks to zero at the center $(a, -b)$. This simulated behavior of the drift of the ice floe is not unusual in a real field situation. The graphical representation of our mathematical model in Fig. 3 confirms this analytical conjecture of the velocity field of the ice floe. The computations were carried out by assuming a cylindrical shape for ice floe with diameter L and a thickness of T. The air-ice skin friction drag coefficient was set to $C_{ai}^{s} = 3 \times 10^{-3}$, following Steele et al. [6], the Coriolis parameter was set to $f = 1.07 \times 10^{-4}\text{s}^{-1}$, and the wind speeds at 10 m above the surface (U_{10}) were varied between 10 m/s and 25 m/s with 5 m/s increments.

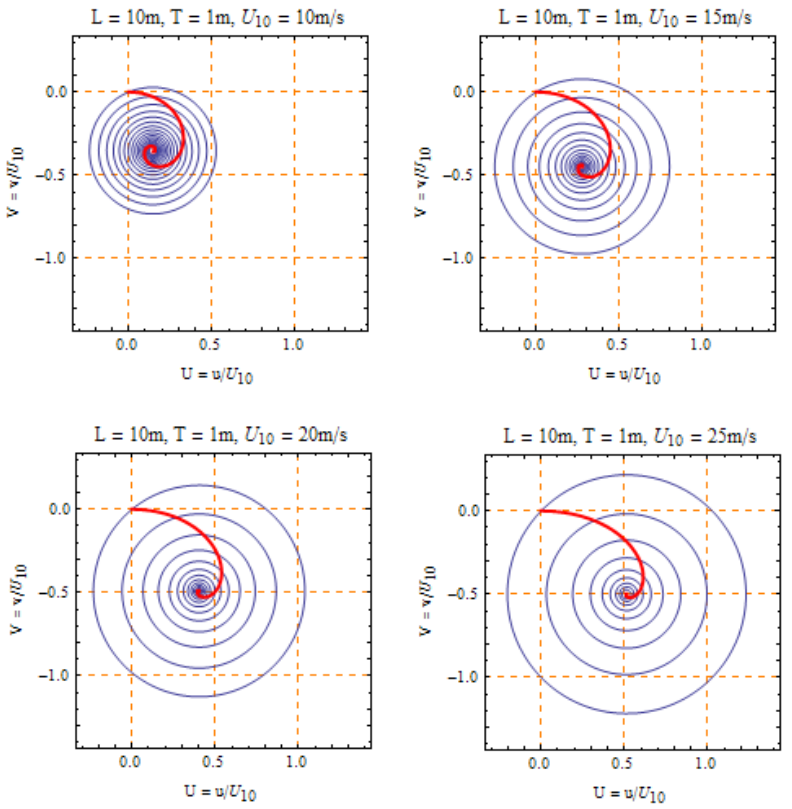

Figure 3: Non-dimensional ice floe velocity field in the phase plane.

To further verify this conjecture, we determine the ice floe trajectory. We replace u and v in terms of derivatives of x and y with respect to time, such that $u = \frac{\partial x}{\partial t}$ and $v = \frac{\partial y}{\partial t}$. Thus (6) will take the following form:

$$\frac{\partial^2 x}{\partial t^2} - f\frac{\partial y}{\partial t} = \alpha U_{10} - \alpha\frac{\partial x}{\partial t} \tag{11}$$

$$\frac{\partial^2 y}{\partial t^2} + f\frac{\partial x}{\partial t} = -\alpha\frac{\partial y}{\partial t} \tag{12}$$

The initial conditions are $x(0) = 0$, $\frac{\partial x}{\partial t}(0) = 0$. Also, $y(0) = 0$, $\frac{\partial y}{\partial t}(0) = 0$. The solutions can be obtained by using the Laplace transform method.

$$(s^2 + s\alpha)\mathcal{L}\{x\} - fs\mathcal{L}\{y\} = \frac{\alpha U_{10}}{s}$$

$$fs\mathcal{L}\{x\} + (s^2 + s\alpha)\mathcal{L}\{y\} = 0.$$

Solving these two equations by Cramer's rule and using the residue calculus, we obtain the solutions in non-dimensional forms as

$$X(t) = -\frac{\alpha^2 - f^2}{(\alpha^2 + f^2)} + \alpha t + e^{-\alpha t}\left\{\frac{(\alpha^2 - f^2)\cos ft - 2\alpha f \sin ft}{(\alpha^2 + f^2)}\right\} \tag{13}$$

$$Y(t) = \frac{2\alpha f}{(\alpha^2 + f^2)} - ft - e^{-\alpha t}\left\{\frac{(2\alpha f)\cos ft + (\alpha^2 - f^2)\sin ft}{(\alpha^2 + f^2)}\right\} \tag{14}$$

where $X(t)$ and $Y(t)$ are given by,

$$X(t) = \frac{x(t)}{\alpha U_{10}/(\alpha^2 + f^2)} \quad \text{and} \quad Y(t) = \frac{y(t)}{\alpha U_{10}/(\alpha^2 + f^2)}.$$

With these definitions, the ice floe trajectories can be obtained as

$$(X - c)^2 + (Y - d)^2 = e^{-2\alpha t} \tag{15}$$

where $c = -\frac{\alpha^2 - f^2}{\alpha^2 + f^2} + \alpha t$ and $d = \frac{2\alpha f}{\alpha^2 + f^2} - ft$, respectively. It can be easily seen that the ice floe path is a circle with the center (c, d) and radius $e^{-\alpha t}$. The parameters c, d and the radius are all dependent on time t. Thus the ice floe will move in a circular path with exponentially decreasing radius with respect to time. Further more, for large time, the floe trajectory will follow a linear path with the linearly dependent coordinates of the center of the circle with respect to time. At the initial stage, i.e., at $t = 0$, the trajectory will be a unit circle with center at $(-\frac{\alpha^2 - f^2}{\alpha^2 + f^2}, \frac{2\alpha f}{\alpha^2 + f^2})$. The $X-$ coordinate may be positive or negative according to $\alpha^2 < f^2$ or $\alpha^2 > f^2$, respectively. However, the $Y-$ coordinate is always a negative number. The graphical simulations of the non-dimensional trajectory of the ice floe with varying wind speeds and their corresponding phase diagrams following our derived mathematical formulations are shown in Fig. 4. The trajectories

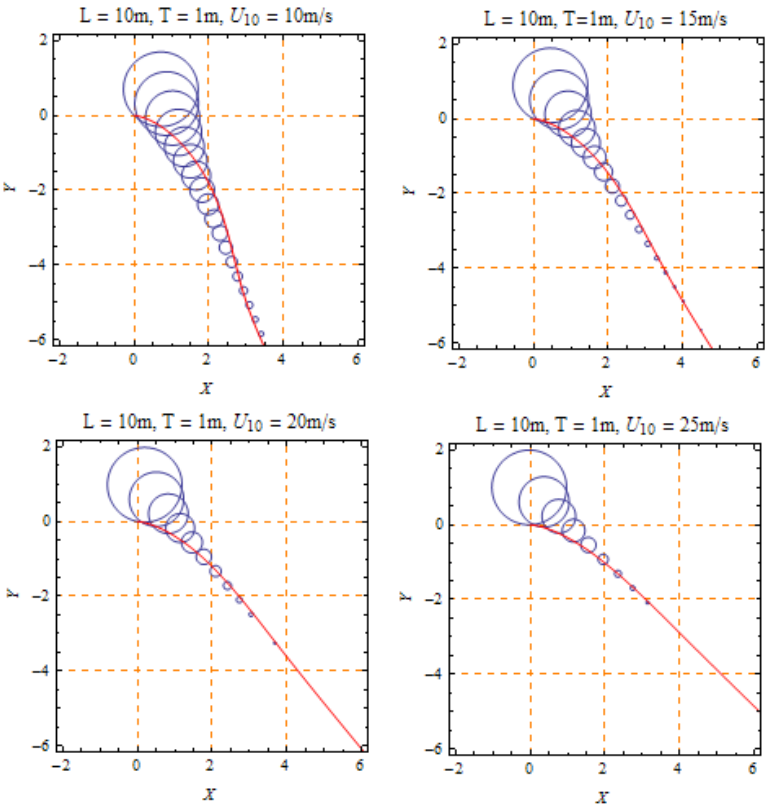

Figure 4: Non-dimensional ice floe trajectories in the phase plane.

are circular spirals starting with a unit circle at $t = 0$ and ending with a point circle at $t \to \infty$; but the center is moving according to law of order $O(\alpha t)$ such that $X \equiv \alpha t$ and $Y \equiv -ft$. Our computation shows that as time passes, the orbital motion of the ice floe, due to the earth's angular motion, gravitational pull, and the constant wind effect, eventually becomes linear. Also, the result of this simplified approach tends to display more displacement along the y-axis than that along the x-axis. However, this can be corrected with further mathematical computation. One such computation is given below.

4 Ice floe drift due to wind stress: model II

The equation of motion of an ice floe (5) can be rewritten in the form,

$$m \begin{bmatrix} \frac{\partial u}{\partial t} \\ \frac{\partial v}{\partial t} \\ 0 \end{bmatrix} + \begin{bmatrix} i & j & k \\ 0 & 0 & f \\ u & v & 0 \end{bmatrix} = A\rho_a C_{ai}^s \begin{bmatrix} \sqrt{(U_{10}-u)^2+v^2}(U_{10}-u) \\ -v\sqrt{(U_{10}-u)^2+v^2} \\ 0 \end{bmatrix} \tag{16}$$

We obtain,

$$\begin{cases} \dfrac{\partial u}{\partial t} - fv = \dfrac{A\rho_a C_{ai}^s}{m}(U_{10}-u)^2\sqrt{1+\dfrac{v^2}{(U_{10}-u)^2}} \\ \dfrac{\partial v}{\partial t} + fu = -\dfrac{A\rho_a C_{ai}^s}{m}v(U_{10}-u)\sqrt{1+\dfrac{v^2}{(U_{10}-u)^2}} \end{cases} \tag{17}$$

Using the binomial expansion, the above equations can be written as,

$$\begin{cases} \dfrac{\partial u}{\partial t} - fv = \dfrac{A\rho_a C_{ai}^s}{m}(U_{10}-u)^2 \\ \qquad \times\left[1+\dfrac{1}{2}\left(\dfrac{v}{U_{10}-u}\right)^2 - \dfrac{1}{8}\left(\dfrac{v}{U_{10}-u}\right)^4 + \dfrac{1}{16}\left(\dfrac{v}{U_{10}-u}\right)^6 + \cdots\right] \\ \dfrac{\partial v}{\partial t} + fu = -\dfrac{A\rho_a C_{ai}^s}{m}v(U_{10}-u) \\ \qquad \times\left[1+\dfrac{1}{2}\left(\dfrac{v}{U_{10}-u}\right)^2 - \dfrac{1}{8}\left(\dfrac{v}{U_{10}-u}\right)^4 + \dfrac{1}{16}\left(\dfrac{v}{U_{10}-u}\right)^6 + \cdots\right] \end{cases} \tag{18}$$

Considering wind speed is much greater than the ice floe drift, the above expansion can be linearized in the form,

$$\begin{cases} \dfrac{\partial u}{\partial t} - fv = \dfrac{A\rho_a C_{ai}^s U_{10}}{m}(U_{10}-2u) \\ \dfrac{\partial v}{\partial t} + fu = -\dfrac{A\rho_a C_{ai}^s U_{10}}{m}v \end{cases} \tag{19}$$

Proceeding as before, we represent equation (19) in non-dimensional form as follows:

$$\begin{cases} \dfrac{\partial U}{\partial t} - fV = \alpha(1-2U) \\ \dfrac{\partial V}{\partial t} + fU = -\alpha V \end{cases} \tag{20}$$

Using Laplace transform with initial conditions, equation (20) can be transformed as

$$\begin{cases} (s+2\alpha)\mathcal{L}(U) - f\mathcal{L}(V) = \dfrac{\alpha}{s} \\ f\mathcal{L}(U) + (s+\alpha)\mathcal{L}(V) = 0 \end{cases} \tag{21}$$

As before, solving these two equations, we obtain the solutions as,

$$\begin{cases} U = \dfrac{\alpha^2}{2\alpha^2+f^2} + \dfrac{e^{-3\alpha t/2}}{\beta}\left[-\dfrac{\beta\alpha^2}{2\alpha^2+f^2}\cos\left(\dfrac{\beta}{2}t\right) + \dfrac{\alpha(\alpha^2+2f^2)}{2\alpha^2+f^2}\sin\left(\dfrac{\beta}{2}t\right)\right] \\ V = -\dfrac{\alpha f}{2\alpha^2+f^2} + \dfrac{e^{-3\alpha t/2}}{\beta}\left[\dfrac{\alpha\beta f}{2\alpha^2+f^2}\cos\left(\dfrac{\beta}{2}t\right) + \dfrac{3\alpha^2 f}{2\alpha^2+f^2}\sin\left(\dfrac{\beta}{2}t\right)\right] \end{cases} \tag{22}$$

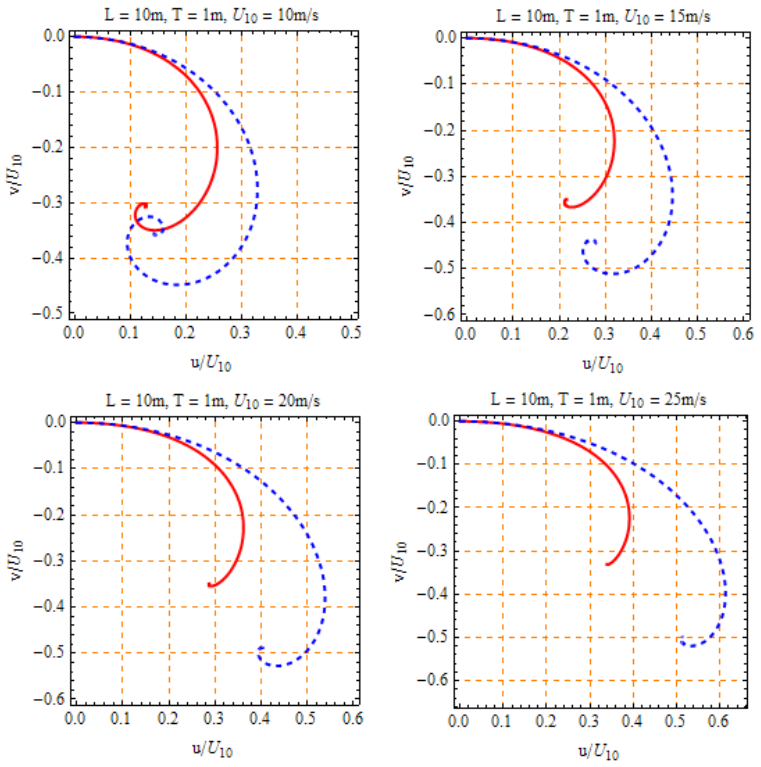

Figure 5: Non-dimensional velocity components of ice floes (dashed line: model I, solid line: model-II).

where $\alpha^2 - 4f^2 = -\beta^2 < 0$. The non-dimensional velocity components of the ice floe with the simplifications introduced in Model-I and Model-II have been computed and shown in Fig. 5. Interestingly, Model-II shows further improvements and its computational results tend to agree more closely with those of Perrie and Hu [4].

Acknowledgement

We are very grateful to Schneider National, Inc. and Natural Sciences and Engineering Research Council (NSERC) of Canada for financial support leading to this paper.

References

[1] Abid, R. M., S. H. Mousavizadegan, M. Rahman, Analytical and numerical estimation of ice floe drift in the marginal ice zone, to be published in *J. of Fluid Mech.*, 2008.

[2] Hasselmann, S., K. Hasselmann, G. K. Komen, P. Jenssen, J. A. Ewing, and V. Cardone, The WAM model-A third generation ocean wave prediction model, *J. Phys. Oceanogr.* **18**, 1775–1810, 1988.
[3] Jenkins, A., The use of wave prediction model for driving a near surface current model, *Drsch Hydrogr. Z*, **42**, 134–149, 1989.
[4] Perrie, W and Y. Hu, Air-ice-ocean momentum exchange. Part II: Ice drift, *J. Phys. Oceanogr.*, **27**, 1976–1996, 1997.
[5] Squire, Vernon A., John P. Dugan, P. Wadhams, Philip J. Rottier, and Antony J. Liu, Of Ocean Waves and Sea Ice, *Annu. Rev. Fluid Mech.*, **27**, 115–168, 1995.
[6] Steele, M., J. H. Morison, and N. Untersteiner,The partition of air-ice-ocean momentum exchange as a function of ice concentration, floe size, and draft . *J. Geophys. Res.* , **94**, 12739–12750, 1994.
[7] Tang, C., and D. Fissel, A simple ice-ocean coupled model for ice drift in marginal ice zones *J. Mar. Syst.*, **2**, 465–475, 1991.

Influence of vegetation on the propagation of flood waves

L. De Doncker[1], R. Verhoeven[1], P. Troch[1], N. Desmet[2,3], P. Meire[2] & P. Seuntjes[3]
[1]*Hydraulics Laboratory, Department of Civil Engineering, Ghent University, Belgium*
[2]*Ecosystem Management Research Group, University of Antwerp, Belgium*
[3]*Flemish Institute for technological Research, VITO, Mol, Belgium*

Abstract

Research on river ecosystems asks for a multidisciplinary approach. All components such as water, macrophytes, sediment, suspended solids, etc. play an important role. The presence of macrophytes in rivers has an influence on water levels and flow patterns since a wealthy vegetation growth causes back water effects and consequently higher upstream water levels. In view of this, flood risk increases in periods of higher flows and greater vegetation growth. So, river management also deals with the control of vegetation. Good management contributes not only to the quality of the water and the ecosystem, but also to flood protection.

Keywords: backwater effect, ecological modelling, vegetated rivers.

1 Introduction

In many lowland rivers in Flanders, a significant increase in macrophyte growth has been observed. This is due to eutrophication and a better water quality (Vereecken et al. [1]) of surface water, which is imposed by the European Union and laid down in the 'Water Framework Directive' (2000/60 EG). The directive aims at a better water quality by structural interventions in rivers. A better water quality influences the macrophytes (increasing growth) and so, the drainage of the river. Therefore, the ecological and hydraulic function of the macrophytes has to be understood. The vegetation influences the roughness of the channel bed

WIT Transactions on Engineering Sciences, Vol 59, © 2008 WIT Press
www.witpress.com, ISSN 1743-3533 (on-line)
doi:10.2495/AFM080321

and banks which, as a major modelling parameter, is important for the prediction of floods since aquatic plant growth can lead to a substantial rise of the water level (Aminal [2]), (NVVE [3]). The channel roughness can be expressed by the Manning coefficient.

By this, there is a relation between the amount of biomass in and the discharge capacity of the river. Good river management includes mowing of vegetation to avoid floods, with respect to the ecological functions of the river. Therefore, a well-considered choice of mowing patterns is essential to balance both requirements.

2 Study area and data set

2.1 The river Aa

Focus of the study is the downstream part of the river Aa. The catchment basin of the river Aa is situated in the region of Antwerp in Belgium and is hydrographically part of the Nete basin. The most important rivers of this basin are the Kleine Nete and the Grote Nete, both influenced by the tidal bore. More than 40% of the water in the Nete basin is carried by the river Aa, which is consequently the most important tributary of the Kleine Nete. It has a total length of 36.8 km and a drainage area of about 23 700 ha. The study area is focused on the downstream part of the Aa, on a 1.4 km reach controlled by two weirs at the up-and downstream end.

The river Aa is a typical lowland river with low velocities, a small fall and a strongly meandering character. Over the years, the river has been straightened and the section was enlarged. The water inflow originates from drainage of rain water and seepage of ground water. The water is rather acid, without chalk and a low amount of minerals, not suitable for organisms. Living conditions for them are caused by food supply in the way of organic drainage of fertilizers from the fields of agriculture along the banks of the river.

2.2 Hydraulic measurements

Discharge was monthly measured from a bridge and from a boat in different sections along the stretch under concern in the period from September 2004 to May 2007. The method used is the integration of the velocity field over the cross section as is explained in (Herschy [4]) Two devices are used for measuring the velocity of the water. In case of open water (no vegetation), hydrometric propellers (Type: OTT, C31 Universal Current Meter) are used, while in locations where vegetation might hinder the mechanical functioning of the propeller an electromagnetic instrument (Type OTT, Nautilus C2000/SENSA Z300 and Valeport, Type 801) is applied.

2.3 Biomass collection

In the river Aa, macrophytes found are various leaved water-starwort (*Callitriche platycarpa*), rigid hornwort (*Ceratohyllm demersum*) and floatingleaf pondweed (*Potamogeton natans*). Sampling is carried out upstream, downstream and half

way the stretch on a monthly base. In each of these cross-sections, the amount of macrophytes is determined by taking samples every meter, at the same position were the discharge measurements are carried out. First the fresh weight [g/m²] of the plants is defined, afterward also the dry weight [g/m²] is postulated. The sampling of the macrophytes is carried out with a sampler as described in (Marshall and Lee [5]). This instrument has no moving parts, its primary components are a cutting blade fixed to the base of a vertical shaft to shear off plant stems at the substrate surface, and a collection rake to allow retrieval of the freed vegetation. The sampler is well suited for the measurements in this study, because a large variety of macrophytes over a range of conditions can be sampled, while possessing the design features of prime importance: lightweight, low cost and easily used.

2.4 Femme environment

Calculation are performed making use of software developed in 'Femme' ('a Flexible Environment for Mathematically Modelling the Environment') is developed by NIOO (Netherlands Institute of Ecology) (Soetaert et al. [6]). It is a modelling environment for the development and application of ecological time dependent processes by use of numerical integration in the time of differential equations. The program is written in Fortran. 'Femme' consists of a wide range of numerical calculations and model manipulations (as integration functions, forcing functions, linking to observed data, calibration possibilities, etc.). These technical possibilities allow the user to focus on the scientific part of the model without the confrontation with real programming linked problems.

'Femme' is focused on ecosystem modelling, is open source (no black box) and has a modular hierarchical structure (implementation of different modules). What was missing up till now was the implementation of a hydrodynamic surface water model to couple ecology and surface water each timestep. For the study of the interaction of ecological processes and flow, a realistic modelling of the surface water flow is necessary. In this study, a one dimensional hydrodynamic model for surface water flow based on the solution of the Saint-Venant equations has been implemented in 'Femme'.

3 Biomass influence on the resistance coefficient

3.1 Manning roughness coefficient

The measured discharges and stages are used for the calculation of the roughness coefficient of the stretch, making use of the Bresse equation or the Manning equation. In steady state conditions (permanent flow) and assuming uniform flow, the energy slope is equal to the bottom slope and discharge, stage and Manning coefficient are linked directly by Manning's equation (Chow et al. [7]). In case of non-uniform permanent flow, Bresse equation is used to calculate the Manning coefficient.

3.2 Biomass distribution and the Manning coefficient

A positive correlation between the biomass and the Manning coefficient was found by (Brooker et al. [8]) and mentioned in (Viaene and Vereecken [9]). For all measurements carried out over almost three years, the amount of macrophytes was determined and the Manning coefficient was calculated from the Bresse equation. The relation between biomass and Manning coefficient is clear. Low values for both are seen during winter (November to April), high values during spring and summer (June to September). More biomass results in a higher Manning coefficient (De Doncker et al. [10]). An exponentional curve is fitted to the values of biomass and Manning coefficient in Figure 2. Presence of vegetation increases the roughness and decreases the section and by this raises also the water level for the same discharge value.

3.3 Relation between discharge and the Manning coefficient

As the vegetation only covers part of the cross section, it is clear that with increasing discharge, and by this increasing water level, the relative influence of the biomass will become smaller. Figure 2 depicts the link between discharge and Manning coefficient as calculated from the Bresse equation, based on the measured data in the Aa between September 2004 and May 2007.

3.4 Coaxial relation between the Manning coefficient, biomass and discharge

The Manning coefficient is linked to the discharge (Fig. 1) and related to the biomass (Fig. 2). The relation Manning coefficient – discharge has an R^2 value of 0.72, while the relation between biomass and Manning coefficient agrees with $R^2 = 0.77$. The relation between these three parameters is expressed by (Eq. (3)) (De Doncker et al. [11]).

$$n = 0.169 + \frac{0.1568}{Q} - 0.1593\exp(-0.0047 * biomass) \tag{3}$$

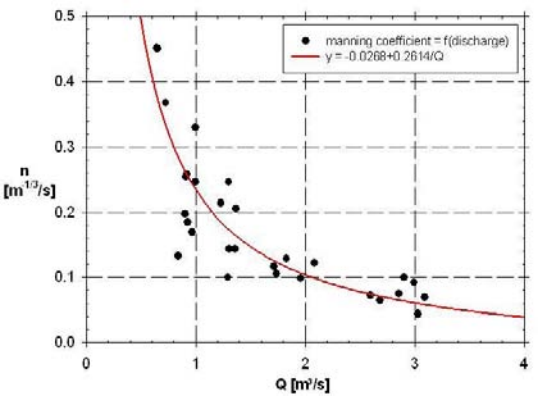

Figure 1: Correlation between discharge and the Manning coefficient in the river Aa from September 2004 to May 2007.

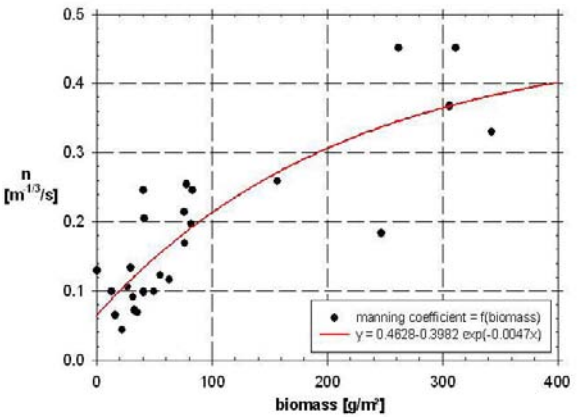

Figure 2: Exponentional correlation between biomass and the Manning coefficient in the river Aa from September 2004 to May 2007.

4 Calculation results

4.1 Steady state conditions

Due to vegetation and the consequential influence of backwater, the friction slope S_f of a river stretch can vary extremely, so the Manning coefficient has to be calculated using the Bresse equation. Figure 3 and Figure 4 show the situation in a theoretical stretch of 5000 m. The cross-section is rectangular and has a bottom width of 12.0 m. There is no slope along the stretch and the bottom level is 8.89 m. The accuracy of the 'Femme' model in both steady and unsteady conditions is checked by comparing some results with the Hec-Ras model (Hydrologic Engineering Center [12]), which is a one dimensional code, also based on the solution of the Saint-Venant equations. Both models give the same values and Hec-Ras has already proven his worth, it demonstrates that the 'Femme' model returns good and reliable results.

In Figure 3, two cases are considered, a Manning coefficient of 0.1 $m^{-1/3}/s$, which corresponds with the values in the winter for the river Aa and a Manning coefficient of 0.4 $m^{-1/3}/s$ (spring and summer values). The Manning coefficient is up to 9 times higher in spring when there is wealthy vegetation (De Doncker et al. [9]). Starting from the same downstream water level (10.20 m) and using a discharge of 1 m^3/s, the upstream water level is calculated for both values of n. In spring, a value of 11.25 m for the upstream water level is calculated, while 10.35 m is obtained in winter; this is a difference of 0.90 m due to the presence of vegetation.

Figure 4 shows the influence of the discharge on the energy slope S_f. For three different values of the discharge (0.5; 1 and 1.5 m^3/s), the water surface profile is calculated. The Manning coefficient is kept constant at 0.1 $m^{-1/3}s$. It is shown that tripling the discharge results in an increase of the water level of only 0.26 m (10.24 m for the lowest discharge, 10.35 m for Q = 1 m^3/s and 10.50 for

the highest value of Q). So, the impact of the vegetation on S_f is much bigger and explains why dangerous situations may occur with regard to inundation during summer floods.

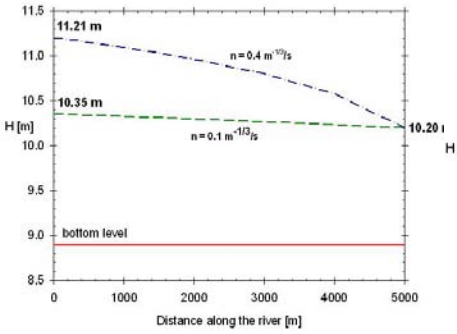

Figure 3: Backwater influence of the Manning coefficient on the water level for a given discharge.

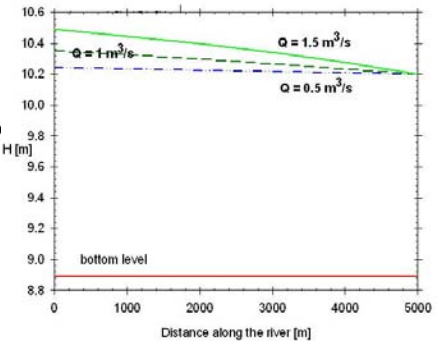

Figure 4: Backwater influence of the discharge on the water level for a given amount of vegetation.

4.2 Unsteady state conditions

Here, the impact of a variable resistance coefficient on the stream flow is illustrated. A flood wave, registered in the studied stretch of the river Aa, in the period from August 12th to August 19th (2005), is used as upstream boundary condition for the calculation (Qupstream). Downstream boundary condition is the registered water level at the downstream weir (Zdownstream). The studied stretch has a length of 5000 m, a rectangular cross section and a bottom width of 12.0 m. The bottom level is 8.89 m.

Fig. 5 and Fig. 6 depict the boundary conditions and the calculated results for Qdownstream and Zupstream for two values of the Manning coefficient: in winter conditions ($n = 0.1\ m^{-1/3}s$) and in summer conditions ($n = 0.4\ m^{-1/3}s$). The variation, with the Manning coefficient, of the downstream discharge is limited, but it is clear that the upstream water level (Zupstream) is strongly influenced by the dense vegetation growth during summer. With increasing values of the Manning coefficient, the downstream discharge peak shows a small time lag and a substantial attenuation.

The river banks are indicated in Figs. 6 and 7. For low vegetation growth, the peak discharge and corresponding water level cause no problems. For values of the Manning coefficient larger than $0.205\ m^{-1/3s}$ (Fig. 7), the river banks (11.6 m) will be too low for the peak discharge and neighbouring areas will inundate. Therefore, study of the roughness of the river, including all determining parameters, is important.

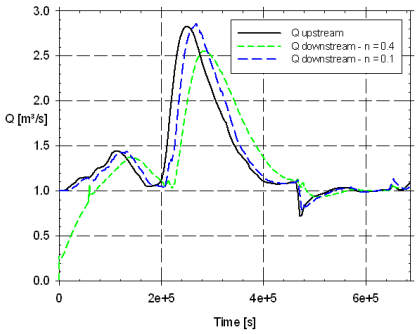

Figure 5: Boundary conditions Qupstream and calculated Qdownstream for n = 0.4 $m^{-1/3}$.s and n = 0.1 $m\text{-}^{1/3}$s.

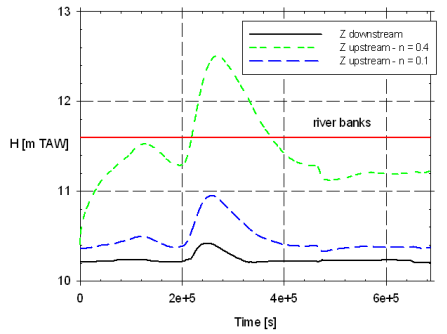

Figure 6: Boundary conditions Zdownstream and calculated Zupstream for n = 0.4 $m^{-1/3}$.s and n = 0.1 $m\text{-}^{1/3}$s.

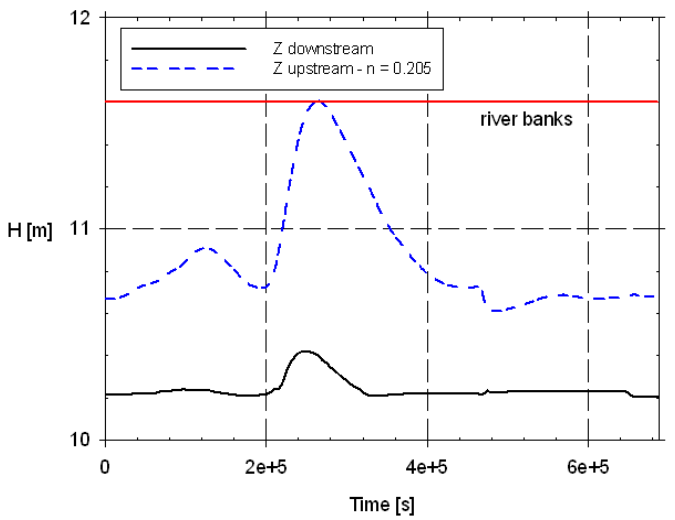

Figure 7: Upstream and downstream water level of the flood wave for n = 0.205 $m^{-1/3}$s, with indication of the river bank.

5 Conclusion

In this paper, the influence of aquatic vegetation on hydraulic characteristics in rivers is studied. Over the year, the amount of vegetation is linked to the seasonal cycle. The combination of a wealthy vegetation growth and summer storms can cause flood problems.

A well-considered integrated river management needs to balance the requirements from the ecosystem with regard to water quality and the need for a safe flood protection policy. For a stretch of the river Aa, the correlation between discharge, biomass in the river and the resistance coefficient is demonstrated based on field measurements and hydraulic modelling. Calculation results show the influence of the resistance on both flow and water levels. Taking into account the environmental conditions (living area, agricultural land, etc.), peak values of the discharge have to be reduced e.g. for safety reasons. Therefore, a sound vegetation control policy can contribute to control flood water levels while at the same time guaranteeing the quality of the ecosystem.

Acknowledgements

This research is funded by the FWO (Fund for Scientific Research) - Flanders (G.0306.04). It is part of the multidisciplinary research project 'A fundamental study on exchange processes in river ecosystems' (University of Antwerp, Vrije Universiteit Brussel, Ghent University, 2004 - 2007). The overall objective is to study the physical and biological exchange processes in margins and inundation areas of water courses and how their interactions determine the exchange of water, dissolved compounds and particulate matter.

Thanks to Mr. Martin Van Daele and Mr. Stefaan Bliki for their assistance with the discharge measurements.

Also thanks to the Hydrological Information Centre of Flanders Hydraulics Research (HIC, Mr. E. Cornet) for providing the discharge and water level data of the river Aa.

References

[1] Vereecken, H., Baetens, J., Viaene, P., Mostaert, F. and Meire, P., *Ecological management of aquatic plants: effects in lowland streams*, Hydrobiologia, 2006.

[2] Aminal, De Kleine Nete, computer modelling as a method, high water control as a target (in Dutch) - computermodellering als methode, hoogwaterbeheer als doel. Grontmij Belgroma nv, in order of Aminal, 2004.

[3] NVVE, Waterplanten als graadmeters voor de ecologische toestand van het water: doel, referentie en beoordeling. Nederlands-Vlaamse Vereniging voor Ecologie - Werkgroep Water-en Oeverplanten, 2003.

[4] Herschy, R. (Ed.), *Hydrometry: principles and practices*. Wiley Interscience Publication. ISBN 0471996491, 1978.

[5] Marshall, T. and Lee, P., *An inexpensive and lightweight sampler for the rapid collection of aquatic macrophytes*. Journal of Aquatic Plant Management (32), 77–79, 1994.

[6] Soetaert, K. et al., *Femme, a flexible environment for mathematically modeling the environment*. Manuals, 2004.

[7] Chow, VT., Maidment, DR. and Mays, LW., *Applied Hydrology*, 1988.

[8] Brooker, M., Morris, D. and Wilson, C., Plant flow relationships in the River Wye catchment. In *European Weed Research Society 5th International Symposium on Aquatic Weeds*, 63–70, 1978.
[9] Viaene, P. and Vereecken, H., *Stromingsweerstand tengevolge van waterplanten*. Technical report Flanders Hydraulics. Rapport Ministerie van de Vlaamse Gemeenschap, Departement Leefmilieu en Infrastructuur, Administratie Milieu, Land- en Waterbeheer, Afdeling Water, Model 566, 2001.
[10] De Doncker, L., Troch, P., Verhoeven, R. Determination of the Manning Roughness Coefficient influenced by Vegetation in the River Aa and Biebrza River. In review, 2007.
[11] De Doncker, L., Troch, P., Verhoeven, R., Desmet, N., Meire, P., Seuntjes, P. relation between resistance characteristics due to aquatic weed growth and the hydraulic capacity of the river Aa. In review, 2007.
[12] Hydrologic Engineering Center, HEC-RAS River Analysis System, Version 3.1.3, US Army Corps of Engineers, 2004, http://www.hec.usace.army.mil/.

This page intentionally left blank

Design of 'Smart' pebble for sediment entrainment study

A. Dwivedi[1], B. Melville[1], E. Akeila[2] & Z. Salcic[2]
[1]*Department of Civil & Environmental Engineering, The University of Auckland, Auckland, New Zealand*
[2]*Department of Electrical and Computer Engineering, The University of Auckland, Auckland, New Zealand*

Abstract

The 'Smart' pebble is a small self-equipped datalogger having a 40 mm outer diameter with a built-in sensor for acceleration and rotation measurements. This pebble has the capability to detect instantaneous acceleration due to turbulence in fluid, which is indicative of hydrodynamic forces acting on the pebble. The pebble stores the data continuously in its internal memory. These data can subsequently be transferred by serial port to a computer for detailed analysis. Test runs using the smart pebble have been carried out to validate accurate functioning of the acceleration and gyro sensor. The acceleration of the smart pebble was compared to the acceleration of the shake table. The results show the excellent capability of the pebble to record the instantaneous forces acting on the pebble during its entrainment.
Keywords: entrainment, hydrodynamic forces, accelerometer, gyroscope.

1 Introduction

In order to understand the processes causing particle entrainment, the stability of the separate particles must be evaluated. The hydrodynamic forces on the particles are very important for understanding this stability. Figure 1 (a) shows the hydrodynamic forces acting on the sediment particle. Figure 1 (b) shows the test arrangement of smart pebble.

This research has been aimed at improving the present level of understanding of the physical processes involved in the transport of individual sediment particles in the near bed region of a turbulent open channel flow by the use of smart pebble.

WIT Transactions on Engineering Sciences, Vol 59, © 2008 WIT Press
www.witpress.com, ISSN 1743-3533 (on-line)
doi:10.2495/AFM080331

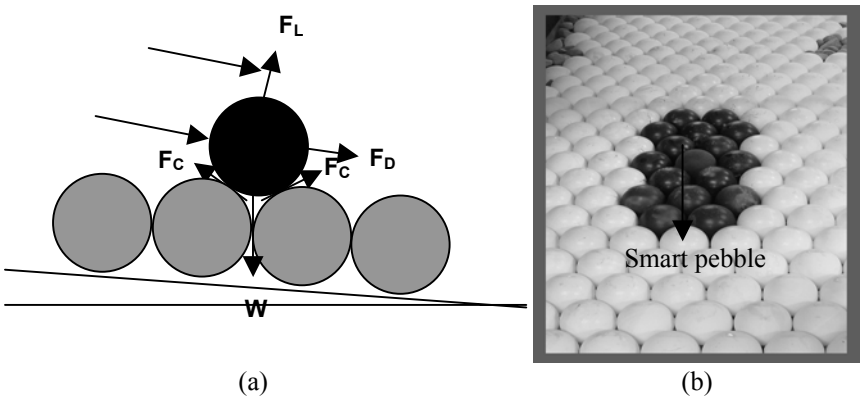

Figure 1: (a) Hydrodynamic forces on the particle where F_L is lift force, F_D is drag force, F_C contact force and W the weight of pebble. (b) Test arrangement using the smart pebble inside the flume.

2 Background

Inertial navigation system (INS) concepts (Titerron and Weston [3]) are used as the basis of this work. An INS is a system, which can determine its exact location in three-dimensional space, relative to a known starting location. The location is resolved by integrating the accelerations and rotations about the three axes. Three accelerometers and three gyroscopes measure the accelerations and angular rotations about the three axes, giving the particle six degrees of freedom. The reference frame consisting of three axes of the body of the pebble is known as the Body Frame. The set of sensor modules, organized in orthogonal form, measure the accelerations and gyrations with reference to the body frame. As the forces acting on the pebble need to be measured relative to a stationary frame of reference a conversion is necessary.

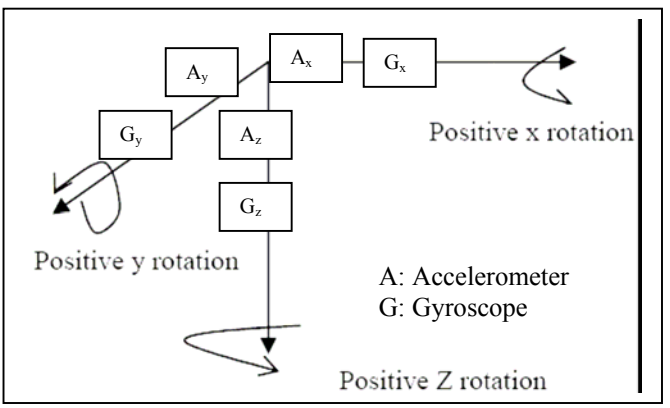

Figure 2: Axis conversion from body frame to reference frame.

There are several methods of performing a coordinate transformation (Titerron and Weston [3]). The Euler Angle method (Pio [4]) was chosen as the most appropriate method, given the processing and time constraints in this proof of concept project.

The Euler Angle method performs the coordinate transformation as three rotations about the three axes. To transform the body frame related motion parameters to the reference frame, three angular rotations, ψ, θ and φ are performed around the z, y and x axes respectively. When the three rotations are performed as per Figure 2, we get three matrices *C1, C2, C3*, representing the rotations as below:

Rotation ψ about the reference Z axis,

$$C_1 = \begin{bmatrix} Cos(\psi) & Sin(\psi) & 0 \\ -Sin(\psi) & Cos(\psi) & 0 \\ 0 & 0 & 1 \end{bmatrix} \tag{1}$$

Rotation θ about the new y-axis,

$$C_2 = \begin{bmatrix} Cos(\theta) & 0 & -Sin(\theta) \\ 0 & 1 & 0 \\ Sin(\theta) & 0 & Cos(\theta) \end{bmatrix} \tag{2}$$

Rotation φ about the new x-axis,

$$C_3 = \begin{bmatrix} 1 & 0 & 0 \\ 0 & Cos(\varphi) & Sin(\varphi) \\ 0 & -Sin(\varphi) & Cos(\varphi) \end{bmatrix} \tag{3}$$

The three individual matrices can be combined into one complete matrix as follows

$$C_n^b = C_3 \bullet C_2 \bullet C_1 \tag{4}$$

The complete matrix C_n^b is known as the rotation matrix

The conversion of any vector from the body frame to the reference frame is achieved by the multiplication of the body frame vector by the transpose of the rotation matrix. This is indicated in the following:

$$r^n = C_b^n \bullet r^b \tag{5}$$

r^n is the vector in reference frame,

C_b^n is the transpose of the rotation matrix C_n^b, and

r^b is the vector in the body frame

For the order of rotation in Equation (5) the transpose of the rotation matrix C_n^b is as follows.

$$C_b^n = \begin{bmatrix} Cos(\theta)Cos(\psi) & -Cos(\varphi)Sin(\psi)+Sin(\varphi)Sin(\theta)Cos(\psi) & Sin(\varphi)Sin(\psi)+Cos(\varphi)Sin(\theta)Cos(\psi) \\ Cos(\theta)Sin(\psi) & Cos(\varphi)Cos(\psi)+Sin(\varphi)Sin(\theta)Sin(\psi) & -Sin(\varphi)Cos(\psi)+Cos(\varphi)Sin(\theta)Sin(\psi) \\ -Sin(\theta) & Sin(\varphi)Cos(\theta) & Cos(\varphi)Cos(\theta) \end{bmatrix} \tag{6}$$

Between successive updates in the real time computation of body attitude there will be small change in angle rotations such that $\sin\phi \to \phi, \sin\theta \to \theta, \sin\psi \to \psi$ and the cosine of these angles approach unity. Making these substitutions in equation (6) and ignoring the product of angles, which also become small, the direction matrix expressed in terms of Euler rotations reduces approximately to the skew symmetric form

$$C_b^n = \begin{bmatrix} 1 & -\psi & \theta \\ \psi & 1 & -\phi \\ -\theta & \phi & 1 \end{bmatrix} \tag{7}$$

In such a situation, if commercial off the shelf (COTS) accelerometers and gyroscope ICs are used to monitor instantaneous motion parameters, r^b vector can be indicated as,

$$r^b = \begin{bmatrix} A_{x-b} \\ A_{y-b} \\ A_{z-b} \end{bmatrix} \tag{8}$$

where Ax_{-b}, A_{y-b} and A_{z-b} are the body frame accelerations in the corresponding axes.

This gives us the simplified relationship for the r^n vector in the reference frame as,

$$r^n = \begin{bmatrix} 1 & -\psi & \theta \\ \psi & 1 & -\phi \\ -\theta & \phi & 1 \end{bmatrix} \begin{bmatrix} A_{x-b} \\ A_{y-b} \\ A_{z-b} \end{bmatrix} \tag{9}$$

For the angular rotation parameters, the following relationships were used.

$$\psi = \int \omega_z dt\ ,\ \ \theta = \int \omega_y dt\ \ ,\ \ \phi = \int \omega_x dt$$

where ω_x, ωy and ω_z are the gyrations in respective axes.

3 Design considerations

Key design considerations for smart pebble are packaging, powering, relative physical placement of the MEMS, signal conditioning and providing a bare minimum digital subsystem and a compact and simple data communication

interface. Packaging has direct influence on the size of the pebble. Since roughness elements involved in the sediment entrainment study are 40mm diameter ping pong balls, the diameter of the pebble should not be more than 40mm, which is only possible with proper compact packaging of the electronics involved. Entrainment is a sporadic and instantaneous event. The time at which particle will be entrained can vary from few seconds to few minutes. This directly put constraint on powering the smart pebble for at least 15 minutes to capture the meaningful data before entrainment, during entrainment and after entrainment of the pebble. Physical placement of the sensors and electronics should be such that the centre of gravity is at the centre of the sphere (pebble) to avoid any abrupt motion due to eccentricity of the inside mass. Compact and simple data communication system was required to make the pebble user-friendly.

4 Sensors

In order to monitor the accelerations, commercial off the shelf (COTS) type accelerometers and gyroscope MEMS from Analog Devices were considered based on their sensitivity, accuracy, noise behaviour and the offset, etc (Brown et al [1]). ADXL202 dual axis accelerometers and ADXRS150 yaw rate gyroscopes were found suitable. These devices were placed in three orthogonal sensor modules with suitable signal conditioning circuitry.

The unit is powered by a 6V battery, which generally powers the circuit up to about 15 minutes continuously. A Texas Instruments TPS60132 charge pump has been utilized to regulate the supply voltage of the pebble at 5V. Additionally, it boosts up the battery voltage as it dips below 5V to maintain the accuracy of the sensor readings. The entire system works on 5V, except for the external flash memory, which requires 3V supplied through a REG102 3V regulator.

Since dual gang accelerometers were used, it was possible to take all the necessary measurements with two chips to keep the real estate of the PCBs to a minimum. Each sensor produces an analogue voltage proportional to the acceleration or gyration measured. These outputs are periodically scanned and averaged out to minimize noise, through the analogue-to-digital-converter channels of the Microchip PIC18F8520 microcontroller. The digitized sensor data is then stored in an external flash memory, SST25VF020. Since the data is collected at regular time intervals, this data is later processed to determine the accelerations of the pebble.

The smart pebble is a complete, battery powered unit equipped with two dual-axis accelerometers and three angular rate sensors, a microcontroller, non-volatile external memory and a user interface capable of communication with a PC. It has been packaged into a sphere of 40mm diameter as illustrated in Figure 3.

The stored data is transferred to a PC over the hyper terminal of the computer. This data is then processed in MATLAB to calculate the true accelerations along the reference axes. The MATLAB program takes in the raw digitized sensor data and converts them to the analogue voltage values measured originally. Since the fixed axis set of the sensor boards are subject to rotations, the accelerations

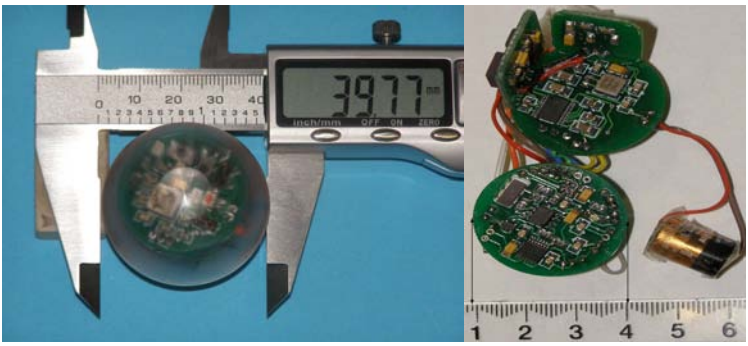

Figure 3: Final packaged 'smart pebble'. Right: Actual size of the PCBs. Left: The PCBs inside the shell of the smart pebble.

measured are in fact, not the true accelerations along a set of reference axes. Therefore the data needs some complex mathematical processing to extract the true acceleration data. The gyroscope measurements are integrated to obtain the rotation angles of the unit, about each axis. Next, the initial tilt of the unit and the gravity components along each axis are calculated. Then the direction cosine matrix and Euler angles are used to convert the data to obtain the true accelerations along each reference axis. Finally gravity is compensated for and the accelerations along the reference axes are plotted.

The sensors are mounted such that the accelerations along the three orthogonal axes and the gyrations about each axis are measured.

5 Operation of the smart pebble

There are two switches on the sensors, power switch and a Data protection switch (protection for the stored sensor data). Data protection switch is coupled with a push button, which triggers the interrupt to start reading the sensor data and storing them in the flash. Turn this switch on and push the button next to it. This should briefly light a blue LED. This means the processor will start reading the data off the sensors in one minute. Once the interrupt has been triggered (i.e. blue LED) turn the switch off.

This means that there will be no accidental triggering of the interrupts once we have set it out. The main reason for doing this is, each time we need to store data in the flash and retrieve data out to pc and then erase the chip for the next set of Data. So if the interrupt is triggered on the way all the data stored up until then will be lost. There is a second push button (also coupled to an LED) to retrieve data off the micro, into the PC

6 Calibration and testing

In developing a system of this nature, the designer has to be aware of the overall errors contributed by many sources. Some obvious errors are the accelerometer

offsets, OpAmp offsets, the analog calculation interface inaccuracies and offsets and noise from the sensors.

Calibration was performed in two steps. In the first step individual sensors were calibrated and in the second step complete smart pebble system was calibrated.

6.1 Individual sensor calibration

The accelerometer sensors were calibrated against the gravity by orienting the axes of the sensors towards the gravitational direction to get +g output and then opposite to that direction to get –g. After that, each sensor gain and offset is calculated using the following equations.

$$offset(V) = \frac{V_{+g} + V_{-g}}{2} \tag{10}$$

$$Gain(V/g) = V_{+g} - offset \tag{11}$$

The gyroscope calibration was carried out by placing each gyroscope on a servo motor. The motor moves in a controlled sequence ($\pm 180^0$). The rotational speed of the servo motor has been adjusted so that it does not exceed the gyroscope maximum sensitivity (150^0 /s). This was achieved by controlling the voltage level that supplies the motor (at 3V the speed is 83^0/s). The outputs of the gyroscopes are observed using an oscilloscope. When the motor rotates in the positive direction relative to the gyroscope sensitive axis, the output of the sensor gives a high pulse voltage with respect to the sensor's offset, and the opposite happens when the motor rotates in the reverse direction. The sensitivity (gain) of the gyroscope is calculated using equation 10.

$$Gain(V/^o/s) = \frac{(V_+ - V_{offset})\Delta t}{180} \tag{12}$$

6.2 Overall system calibration

Overall system calibration was done with shake table. For this set of calibration a hollow cube was made in which the sensors can be in housed. The advantage of using cube is that it can be placed on the shake table with the direction of the shaking coinciding with the direction of the acceleration sensors. The shake table is fitted with an accelerometer that records the acceleration of the table. After giving the sine wave motion to the shake table for 30 seconds, the accelerations were compared to the accelerations recorded by the smart pebble. This was done for all the three axis of the pebble coinciding with the motion of the shake table. Similar experiments were performed with the cube placed at 45 degrees to the shake table motion

The first step in the calibration process was testing the zero acceleration output (Null Offset). The total noise included in this version of the smart pebble has caused an accumulation error when implementing digital mathematical integration on the outputs of the gyroscopes. Figure 4 shows the output from the

smart pebble when it was left stationary for about 15 minutes while Figure 5 shows the accumulative angle calculation error.

The null offset output has been improved by filtering the data using some MATLAB built-in digital filters and taking the average of the first 5 seconds of each sensor output as reference value for calculating the accelerations and angles. Figure 5 shows the output data resulted from filtering and averaging.

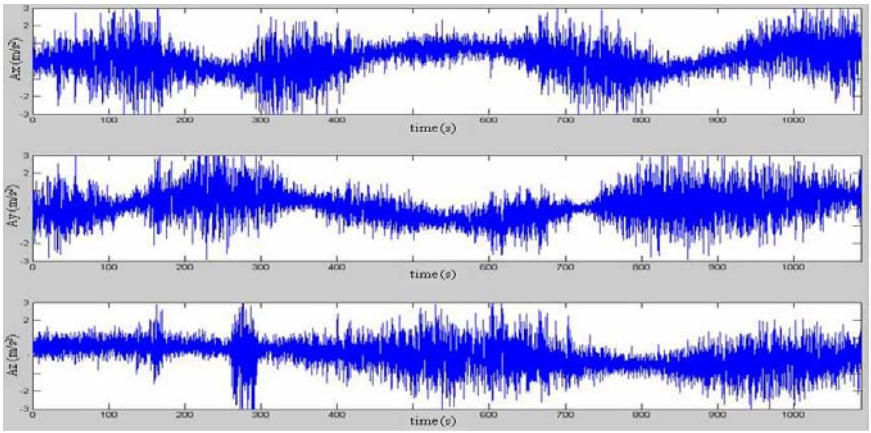

Figure 4: Acceleration resulted from the smart pebble when it is left stationary.

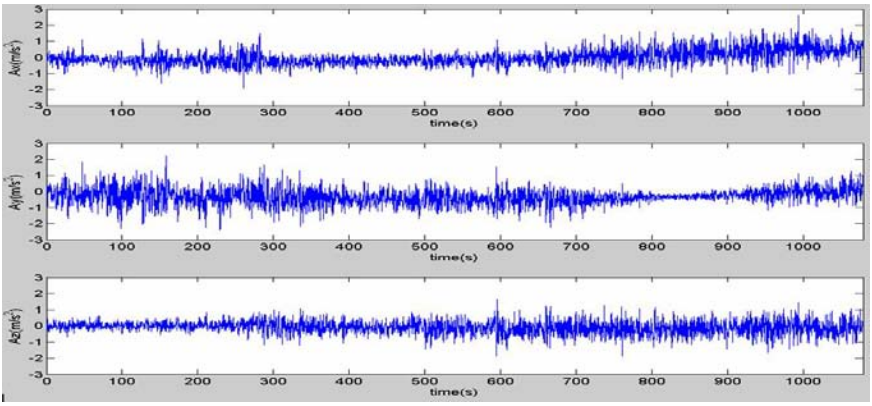

Figure 5: Smart pebble stationary output after filtering and averaging (acceleration).

Because of the low sampling rate (8.33 Hz), frequency of motions was selected to be less than 4 Hz to avoid signal aliasing. The preliminary results show that the pebble can accurately detect the frequency of the applied motions.

However, due to the noise and mainly the very low sampling frequency, the amplitude output error is very high (it ranges from 63% to more than 92% in some time intervals. To reduce the amplitude error we tested the smart pebble at different sampling frequency and found that the error can be reduced to almost 5% if sampling is done at more that ten times the required motion's frequency.

Figure 6 and 7 shows the affect of sampling frequency on smart pebbles output. It can be seen that the amplitude error is minimised by increasing the sampling frequency (Figure 7).

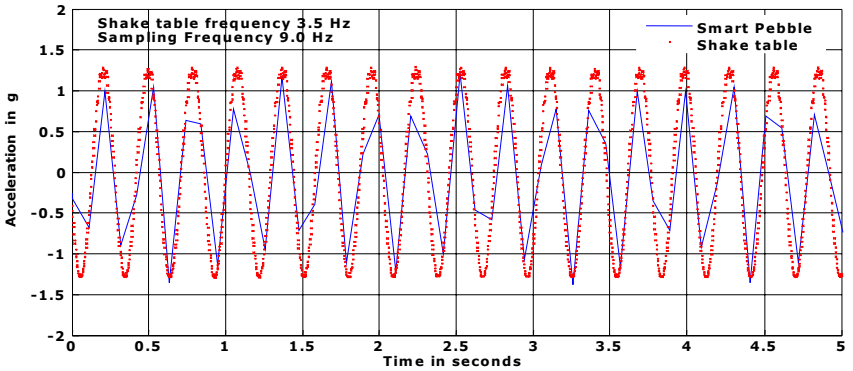

Figure 6: Smart pebble output versus the shake table (sampling frequency 9 Hz)

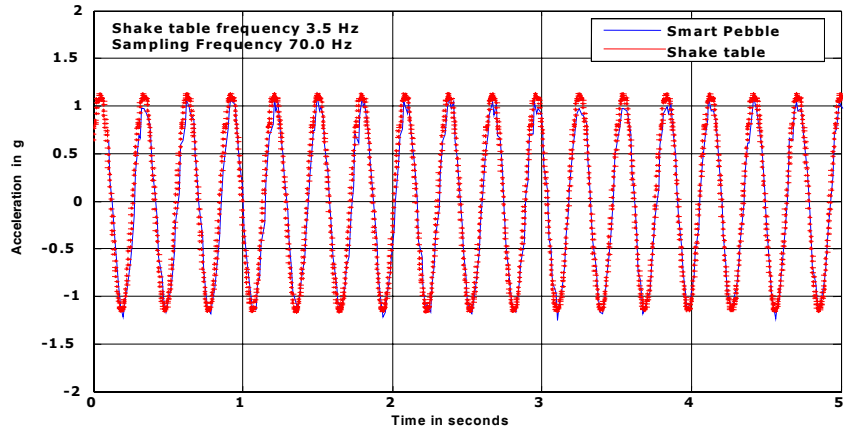

Figure 7: Smart pebble output versus the shake table (sampling frequency 70 Hz).

7 Conclusions

Initial testing and calibration of smart pebble shows the excellent functioning and its capabilities to log instantaneous accelerations. Few measurements of the smart pebble were done inside the flume with water and data analysis is in

progress. Further work in reducing the overall power consumption by selecting a lower power microcontroller is in progress, because the microcontroller in this version of the smart pebble is consuming more than 80% of the whole power. Work in reducing the noise to signal ratio is in progress. Work is in progress to reduce the size of the pebble by using three axis accelerometers e.g. (Tieman et al [2])

References

[1] Brown, T.G et al; " Strap-down micromechanical (MEMS) sensors for high-G ammunition applications"; *IEEE Trans on Magnetics*, Vol. 37, No 1, Jan 2001

[2] Tieman, J. et al; "Design of a MEMS based 3-axis accelerometer smart sensor"; *Proc of IEEE Sensors for Industry Conf, USA*, Nov 2002.

[3] Titerron, D.H. & Weston, J.L.: " *Strapdown inertial navigation technology*"; IEEE, 1997

[4] Pio, R**: "**Euler angle transformations**"**; *IEEE Transactions on Automatic Contro*l, Volume 11, Issue 4, Oct 1966.

An active controlling technique for a flow around a circular cylinder

H. Oualli[1], S. Hanchi[1] & A. Bouabdallah[2]
[1]*MDF, EMP, Bordj El Bahri, Algiers, Algeria*
[2]*LTSE, Université des Sciences et de la Technologie (USTHB), Algiers, Algeria*

Abstract

In this study we describe the near wake response and flow dynamics associated with experimentally simulated flows around a circular cylinder that is either stationary, superimposed to simple harmonic cross-section variation, or harmonic cross-section variation combined to steady rotation. Results are examined for a Reynolds number Re = 1000 and a fixed vibrating amplitude equal to 5% of the cylinder radius. A large domain of the forcing Strouhal number up to several times the natural shedding frequency of the cylinder in rest is considered.
Keywords: fluid-structure interaction, deforming-rotating cylinder, wake control, drag reduction.

1 Introduction

Bluff body wakes play an important role in the design of a diversity of engineering structures and industrial applications: aerodynamics, heat exchangers, offshore structures.

Control of vortex shedding leads to decreasing the unsteady forces acting on the body and can substantially reduce its vibrations. Flow control may be executed by controlling the boundary layer separation, the shear layers structures and / or the coherent structures dynamics in the body near wake.

Several techniques, such as blowing, suction, surface roughness elements, etc., have already been considered by researchers [1], [2] and [3] presented a fairly comprehensive overview of the various methods for suppressing vortex shedding.

WIT Transactions on Engineering Sciences, Vol 59, © 2008 WIT Press
www.witpress.com, ISSN 1743-3533 (on-line)
doi:10.2495/AFM080341

Smoke visualizations of the flow generated behind a circular cylinder, submitted to both steady rotation (inducing Magnus effect) and cross-section oscillation are performed. A detailed analysis of the resulting flow properties and involved mechanisms together with plausible explanations are addressed.

The main objective is to produce a first assessment as a first step to a reliable response about the possibility to optimize the lift to drag ratio using a combination of the Magnus effect (resulting from cylinder steady rotation) with a modulated near wake generated by harmonic cylinder cross-section variation.

2 Experimental set-up

These experiments were carried out in a Deltalab 38340 Voreppe open circuit channel facility EV 280 type. This consists of a low speed air turbine (0.3 - 3 m/s) with a large Plexiglas tunnel, approximately 1.5 m long, 0.35m height and 0.45 wide with optical access from all sides. The background streamwise disturbance level is less than 1% of the free stream velocity.

The cylinder made of PVC (Polyvinyl Chlorine) walls, figs.1 and 2, is mounted horizontally traversing the test section with the ends linked to two external motors destined to deliver rotating motion of the cylinder shaft and cylinder walls as well. The inside of the test cylinder, as shown by figs. 1 (b) and 2(b), consists of the cylinder shaft entrained in rotation motion (by means of the external motor), rotating cams appropriately transform the rotating motion into diameter variation movement of the test cylinder walls according the following law:

$$a = a_o\,(1 + As\,\sin\,(2\pi \times f \times t))$$

Where a is the variable cylinder radius, a_0 is the initial cylinder radius, As is the maximum deformation amplitude set equal to 5% of the cylinder diameter, f is the cylinder forcing frequency in Hertz and t is time in seconds.

Considering the cylinder dimensions, the above relation becomes:

$$a = 0.04\,(1 + 0.005\sin\,(2\pi \times f \times t)) \tag{1}$$

Flow is thus controlled by the sinusoidal variation of the radius a. The internal deforming system of the cylinder and the test section dimensions imposed an aspect ratio of 5.62.

The flow visualizations were carried out by releasing a horizontal smoke sheet in front of the cylinder created by injecting smoke through a tubing of a smoke generator enabling a steady leakage of smoke through the oncoming flow. The collection of flow visualization images was taken with a digital video camera in a rate of 24 images per second.

The rotating movement is generated by an electrical motor developing a rotation speed N varying from de 0 to 300 rpm. The cylinder axis is clamped to an electrical motor and constrained to move in a rotating motion to generate the

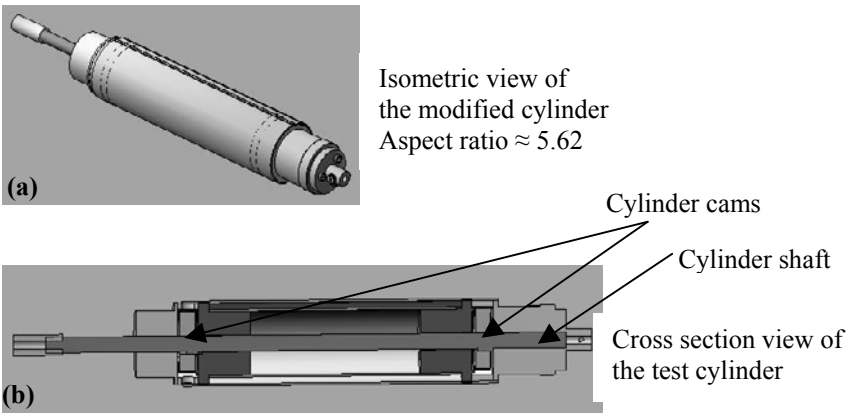

Figure 1: Operating set-up / cylinder deforming mechanism.

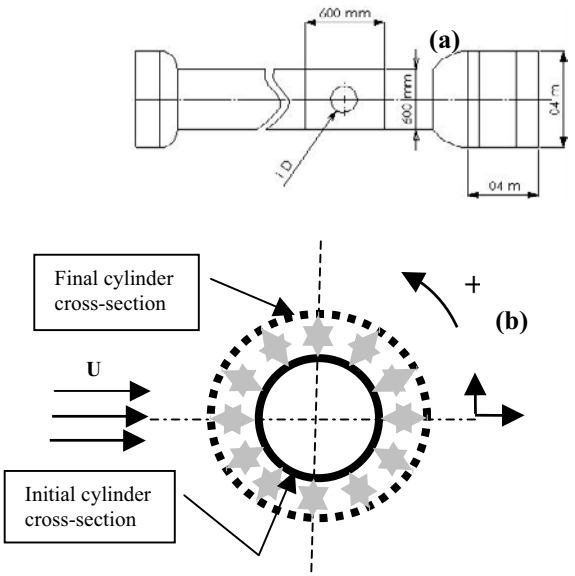

Figure 2: (a) The wind tunnel, (b) schematic diagram of the cylinder side view.

vibrating motion of the cylinder cross section via the integrated mechanism inside the cylinder. The rotating cams mechanism converts the rotary motion of the drive shaft into sinusoidal motion of cylinder walls by a mechanism reported elsewhere in [4] and [5].

The cylinder walls are entrained in a steady rotation by a second electrical motor. With this system, the corresponding forcing Strouhal number, $St_f = f D/U_\infty$, is between 0.7 and 15. D and U_∞ are respectively the cylinder diameter and the infinite flow velocity. The non dimensional steady rotating speed

considered in this study, $\alpha = \Omega a_0/U_\infty$, is in the wide range of 0 to 11.78, with Ω is the cylinder rotating speed in rpm and a_0 the cylinder radius.

The results are presented for Re=1000. Flow visualizations are carried out to study the behavior of the cylinder near wake in response to combined steady rotation and radial vibration controlling techniques.

The present investigation of the near wake of a circular cylinder superimposed simultaneously to steady rotation and diameter variation is an initial step towards understanding the intricate flow phenomena generated when such active controlling techniques (rotation and radial vibration) are coupled on the actuated flow around a circular cylinder.

3 Results and discussion

A first understanding of the visualization results is deduced from the digital video clips and the video tapes. Separation of the successive video frames into digital images enables compilation of time sequences showing evolution of the nascent vortices, vortices interactions and vortex shedding process. Dye streaks contours are detected and highlighted to interpret the results more clearly. These tracings scale-accurate representations of the near wake regions, showing the surrounding shear layers and the primary vortices in the cylinder vicinity.

The vortex shedding Strouhal number, St_0, for the non controlled cylinder at a freestream velocity of U_∞=3 m/s is determined to be 0.21. This value is in perfect agreement with the universal St-Re relation. The considered Reynolds number, Re=1000, coincides with the subcritical flow regime for which the Strouhal number fluctuates in the range of 0.18-0.22, [6] and [7]. The visualized near wake region for this nominal case at a time where the vortex formation is fully developed is shown in figure 3. The shear layers and the vortex roll-up surrounding the formation region are clearly illustrated on the figure. The shear layers roll-up and the Kàrman vortices are formed in a laminar fashion indicating the absence of Kelvin-Helmholtz instability vortices on the shear layers. [8] carried out experiments for an active control of a circular cylinder using a rotative-oscillating technique for Re=15000, corresponding to the same flow regime. This flow configuration is similar to the flow pattern found by [8] for the nominal case.

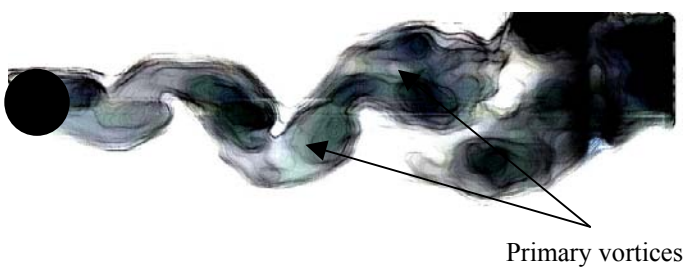

Figure 3: Von Kármán eddy-street behind the cylinder at rest.

The nominal case (without control) is presented as a reference flow situation for a comparison with visualization results for the formation region and the near wake behind the cylinder superimposed to both radial vibration and steady rotation.

When the cylinder is set into motion the flow developed various features and phenomena as a response to the applied actuating perturbations.

When examining the sequences of video pictures, several shedding modes are identified throughout these flow visualisations. Particularly, the four modes presented by [8] for a cylinder submitted to rotative oscillations and termed *dual shedding mode, global locking mode, local locking mode and the shear layer mode* are clearly identified but as partial modes in this study.

Flow configurations similar to these flow modes are previously observed by [9] for a cylinder subjected to transverse oscillations in a freestream.

An estimation of the drag coefficient is given by [8]. He showed that these shedding modes are accompanied by a substantial drag coefficient reduction (up to 80% of the non controlled case). This is in line with the goal researched through the elaboration of this work, namely lift to drag ratio optimization.

An interesting feature of this flow is the progressive and ordered way in which each mode evolves at the selected values of the frequency and steady rotation of the cylinder.

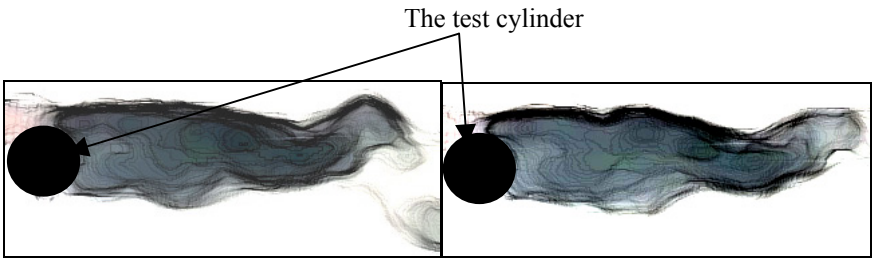

Figure 4: Instantaneous Von Kármán vortex suppression (St_f =0.51, α = 3.94).

In the images of fig. 4 (St_f =0.51 and α =3.94) the wake flow is parallel to the midspan plan (straight and without beating motion) the shear layers developed abrupt instabilities in the form of undulations and kinks without evolving to roll-ups vortices as this can be expected. In this configuration the shedding mechanism seems to be inhibited.

In the current experiments, the modification process (wake undulation) is not limited to the formation region but extends to farther wake behind the cylinder. This undulation phenomenon is thought to be caused by the cylinder walls acceleration during the radius increasing and decreasing motion. In fact, the Kelvin-Helmholtz instability settling in the flow shear layers is strongly enhanced. This tendency is immediately reversed by the steady rotation effect of the cylinder which attenuates the developing instability preventing, thus, roll-ups

vortices formation. The cylinder steady rotation seems forcing the cylinder wake to evolve in a straight and parallel direction.

The rotation of a circular cylinder in a viscous uniform flow is expected to deeply alter the wake flow pattern and vortex shedding mechanism. It may reduce the flow-induced oscillation or augment the lift force. The basic physical rationale behind the rotation effect is that as the cylinder rotates in the clockwise sense, the shear layer of the cylinder upper side is accelerated leading to separation delay or suppression. While the shear layer of the cylinder lower side is decelerated and easily separated. Hence, the pressure on the accelerated side becomes smaller than that of the decelerated side, resulting in a mean lift force (this effect is known as "Magnus effect") [10].

This parallel shedding mode may be explained by an unstable equilibrium state resulting from a non linear interaction of the effects induced by the radial vibration from one part and the steady rotation from the other. An evolution to more stable fashions is observed when the steady rotating speed is increased. The mode becomes more persistent accompanied by a largely narrower wake.

If the controlling parameters are maintained constant, the previous mode progressively shifts to a new mode in which the shedded structures rearrange into a more organized mode termed 2P mode following Williamson and Roshko [9] terminology, fig. 5.

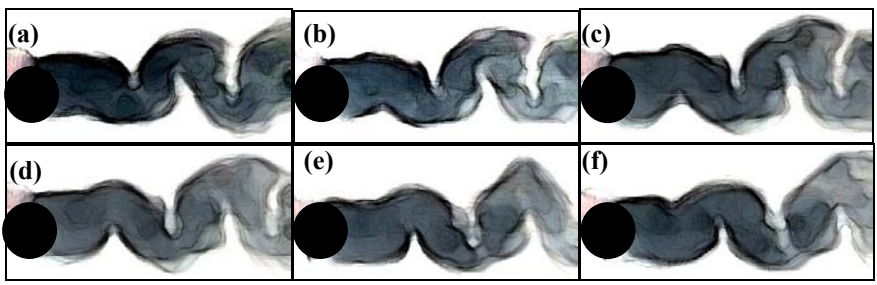

Figure 5: 2P shedding mode for α = 0.175 and St_f= 0.47/ wavelength variation.

The wake configuration is clearly seen to be of 2P-type in fig. 5. Two vortex pairs are shed per cycle of radial cylinder oscillation and the vortex pairs rapidly diverge away from the wake axis. The 2S-type wake pattern shown in fig. 3, where two vortices are shed from the circular cylinder per shedding cycle is markedly different from the 2P mode shown in fig. 5. In the former (2S mode), the vortices remain close to the wake axis as they convect downstream. The latter wake pattern (2P mode) is seen as indicating synchronisation with respect to cylinder motion as reported by [11] and [9].

The coherent synchronized wake patterns observed for the excitation regime frequencies within the synchronized regime is not preserved indefinitely over the oscillation cycles. Flow visualization results of the near wake and formation regions illustrating its evolution are given in fig. 6 corresponding to oscillation frequency St_f=0.87.

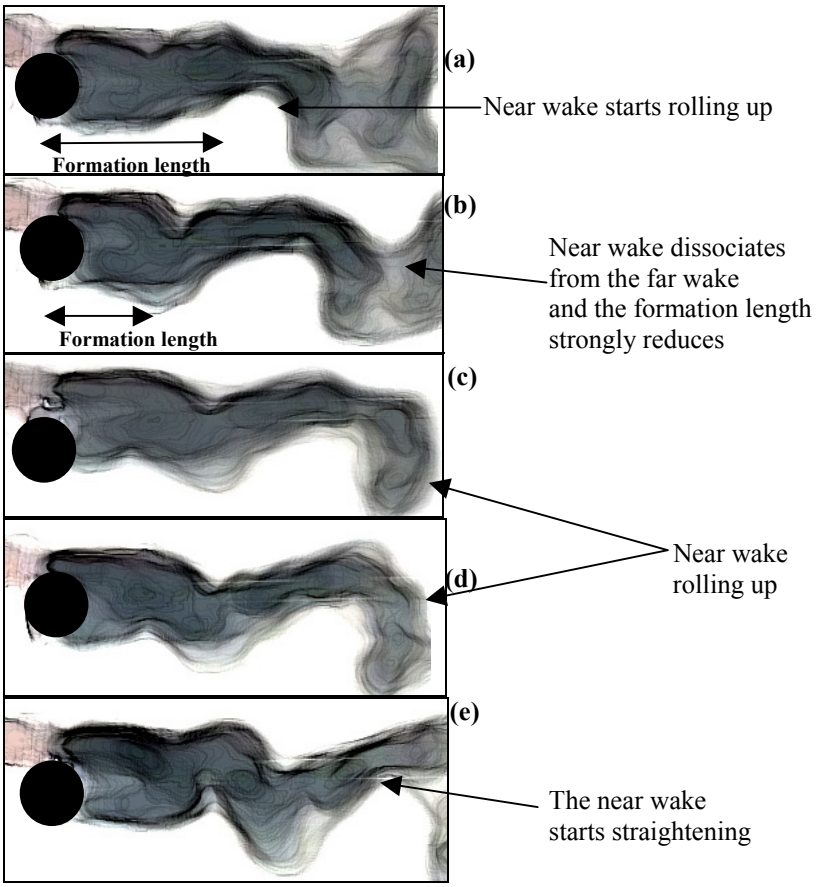

Figure 6: Near wake rolling up shedding mode, ($St_f = 0.87$ and $\alpha = 3.94$).

A comparison the images of this figure shows that the regular 2P mode shifts progressively to a new 2P wavy mode characterized by a horizontally beating wake and a variable wave number of the Von kàrman eddy street forming behind the cylinder with a rate of roughly 35% as estimated from the visualisations. The observed periodic variation of the instability wavenumber is seen in the current experiments to be accompanied by a substantial increasing and decreasing of the vortex formation length.

Though the excitation frequency, $St_f = 0.7$ (close to the 3-superharmonic synchronization value), is largely higher than those corresponding to the fundamental lock-in regime, $0.15 \leq St_f \leq 0.22$, the wake pattern persists in the 2P mode without relaxing to the usual Karmàn mode (2S) as this is reported by both [11] and [9]. On the other hand, for higher rotating speeds of the cylinder, $\Omega \geq 33$ rpm, the visualizations reveal appearances of the 2S mode as a subsidiary configuration considering its existence duration. This indicates that the steady rotating effect of the cylinder remains dominant throughout the whole spanned range.

An attempt to quantify vortex formation lengths for a cylinder vibrating frequencies in the range, $0.37 \leq St_f \leq 15$ and a constant steady rotation $\Omega_1 = 23$ rpm is now discussed.

While the vortex formation length is rather well defined for flows past a stationary cylinder, difficulties arise when the cylinder is forced to vibrate radially and rotate steadily around its axis, for the following reasons:

(i) The shear layers are subject to alternating repulsion and attraction movement induced by the cross-section increasing and decreasing respectively.

(ii) There are three vortex processes contributing to vortex formation: (a) those applicable to natural vortex formation from a stationary cylinder ([12], [3], and [13]), and (b) shear layers undulations in the form of roll-ups successions mainly induced by the radial acceleration of the cylinder walls with the cross-section variation. The vortex formation length is thus dependent on the process which gives rise to the vortices, [8] and the manner in which these formed vortices interact (before and after they are shed) is intricate and complex.

(iii) [11] reported that the more important effects of the steady rotation are: (a) Inducing of a continuous fluid layer that rotates with the cylinder in such a way that the stagnation and separation points around the cylinder are shifted from the wall within the stream. The thickness of this layer is found to increase with the rotating rate but decreases with Reynolds number increasing. (b) Destroying of the vorticity symmetry generated from the cylinder because of the difference between the relative fluid-to-wall velocity on each side of the cylinder (one side moving in the freestream direction and the other moving opposite to it). So, eddies with different size and strength are created. (c) Eddies detachment is accelerated and the vorticity evacuating process within the stream is likely to be modified.

Representative vortex formation lengths L_f are estimated as suggested by [10]. L_f is the streamwise distance from the axis of the cylinder to the core of fully formed vortex. It is determined for several vibrating frequencies with a fixed cylinder rotating speed were determined in the first case and for a fixed vibrating frequency and various rotating speeds in the second case.

These formation lengths are evaluated from images of the formation region in which a fully formed vortex was clearly seen when the shear layers were quasily straight. The results are plotted in figures 7(a) and 7(b). In the first case, the vortex formation length is evaluated for the fixed rotating nondimensional rate $\alpha = \Omega D/2U_\infty$ equal to 1.78.

As the forcing Strouhal number, St_f, is augmented the formation length increases with a jump of 73% and decreases in a rather sharp way until it reaches a minimum of L_f/D = 1.9-2 at St_f = 2.96. As the forcing Strouhal number is increased above 3.64 the formation length seems stabilizing around a constant value of L_f/D=3.

It comes out from the above results that an optimization of lift to drag coefficients ratio $(C_L/C_D)_{opt}$ can be obtained for an optimal vortex formation

length reduced by the right value of the rotation rate α_{opt} and maintained around this value by fixing the right value of the forcing Strouhal number St_{fopt}.

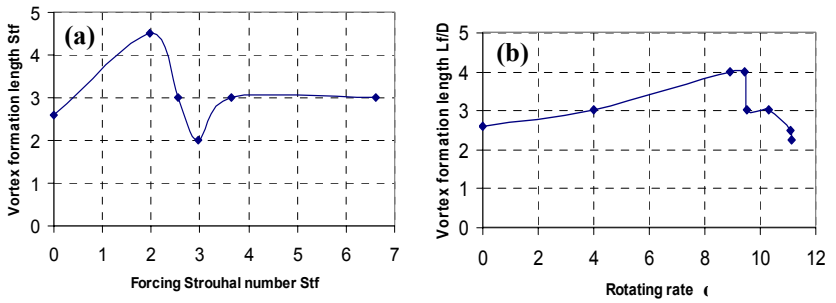

Figure 7: Vortex formation length L_f/D evolution.

4 Concluding remarks

It is noted that when the cylinder is actuated using cross-section variation and steady rotation the Von Kármán eddy street is re-arranged in such a way that four structure evolving modes prevail and become dominant in the flow dynamics.

Various features and phenomena are noticed. This illustrates a remarkable similarity with modes reported in several studies and devoted to rotative oscillation.

When the main controlling parameters, α and St_f are increased, the 2P mode seems to become dominant throughout the spanned ranges of the steady rotation rate and forcing Strouhal number.

To answer the central question related to an optimization of lift to drag coefficients ratio, it is established that the obtained results favourably encourage further quantitative exploration in order to be definitely fixed about the problem.

References

[1] M. Gad-el-hak and D. M. Bushnell: Separation control: Review, *ASME Journal of Fluids Engineering,* 113, 5–29 (1991).

[2] O.M. Griffin and M. S. Hall: Review-vortex shedding lock-on and flow control in bluff body wakes, *ASME Journal of Fluids Engineering* 113, 526–537 (1991).

[3] M. M. Zdravkovich: Review and classification of various aerodynamic and hydrodynamic means for suppressing vortex shedding, *Journal of fluid and Engineering and Industrial Aerodynamics* 7, 145–189 (1981).

[4] S. Hanchi, H. Oualli, A. Bouabdallah and R. Askoviç: Numerical Simulation and Experimental Visualization of the Influence of the Deformation Frequency of a Radially Deforming Circular Cylinder Impulsively Started on Cylinder Wake, Int. J. Num. Meth. Fluids. 41 (2003) 905–930.

[5] H. Oualli, S. Hanchi, A. Bouabdallah and R. Askoviç: Experimental investigation of the flow around a radially vibrating circular cylinder, Experiments in fluids 37, 789–801.
[6] A. Roshko: On the development of turbulent wakes from vortex streets, Ph. D thesis, California Institute of Technology, Pasadena, California (1952).
[7] M. M. Zdravkovich: Flow around circular cylinders, Vol. 1: Fundamentals. Oxford University Press, Oxford, England (1997).
[8] P. T. Tokumaru: Active control of the flow past a cylinder executing rotary motions, Ph.D thesis, California Institute of Technology, Pasadena, California (1991).
[9] C. H. K. Williamson and A. Roshko: Vortex formation in the wake of an oscillating cylinder, *Journal of Fluids and Structures* 2, 355–38 (1988).
[10] C. Homescu, I. M. Navon and Z. Li: Suppression of vortex shedding for flow around a circular cylinder using optimal control, *Int. J. Numer. Meth. Fluids*, 38, 43–69 (2002).
[11] S. Krishnamoorthy, S. J. Price and P. Païdoussis: Cross-flow past an oscillating circular cylinder: Synchronization phenomena in the near wake, *Journal of Fluids and Structures* 15, 955–980 (2001).
[12] J. H. Gerrard: The Mechanics of the Formation Region of Vortex Behind Bluff Bodies, *J. of fluid Mech.* 25, 401–413 (1996).
[13] M. Coutanceau, and C. Ménard: Influence of rotation on the near-wake development behind an impulsively started circular cylinder, *Journal of Fluid Mechanics* 158, 399–446 (1985).

Hydrodynamics of long jet impingement

M. M. Seraj & M. S. Gadala
Department of Mechanical Engineering, University of British Columbia, Canada

Abstract

A circular turbulent long jet has been assessed numerically using the volume-of-fluid method to examine the hydrodynamics of a long jet before impingement and to inspect the flow structure of a radial thin layer spreading over a flat plate after impingement. Typical steel mill industrial parameters are used in the model. Comparative results are shown for laminar and turbulent jets with different turbulence models. Model results showed good agreement with the analytical solution available for global parameters and jet behaviour. The film thickness of the water layer over the plate, for more than 27 jet diameter, was measured by tracking free-surface. A hydraulic jump was detected and occurred within the radial zone in different shapes in laminar and turbulent modelling, respectively.

Keywords: hydrodynamics, long jet, numerical simulation, hydraulic jump.

1 Introduction

Jet impingement is one of the effective means in cooling and heating applications. Water jet impingement has a distinguished ability to dissipate a large amount of heat fluxes and has attracted many studies over the past few decades. Recent reviews may be found in [1–3].

In an axisymmetric jet, the jet thickness decreases as the liquid radially travels outward. The thickness of the liquid sheet initially decreases with the radius but, because viscous drag slows the liquid sheet, its thickness begins to increase at larger radii. The rapid thickness decrease brings the growing boundary layer into contact with the free-surface of the liquid layer. If the Reynolds number is large enough, a shift to a turbulent regime could be expected for the radially spreading thin laminar liquid film. Layer thickening after thinning marks the radius of transition [3, 4].

WIT Transactions on Engineering Sciences, Vol 59, © 2008 WIT Press
www.witpress.com, ISSN 1743-3533 (on-line)
doi:10.2495/AFM080351

Far downstream, the impinging jet flow may be terminated by a hydraulic jump whose location depends on both upstream and downstream flow conditions. The liquid layer thickness upstream from the hydraulic jump is necessary in order to determine the location of the hydraulic jump. This thickness is also used to find the Fraud number of magnitude [5]. The effect of gravity in a long jet causes speeding up of the jet and contracting of the jet diameter. For the long jet, turbulence has enough time to develop and it derives surface jet disturbances and jet splattering.

This paper discusses the numerical simulation of the hydrodynamics of an axisymmetric long jet impingement with typical industrial parameters. The jet is considered fully developed turbulent. The FLUENT program is used for the numerical modelling [6].

1.1 Geometry and jet parameters

The parameters used are: nozzle radius, 19 mm, nozzle height above plate, 1.5 m, and jet flow rate, 15 lit/sec. The height of the issuing jet, H, at a given time, t, may be obtained from the following simple analytical equation:

$$H = \frac{1}{2} g t^2 + v_j t \tag{1}$$

where g is the gravitational acceleration and v_j is the jet issuing velocity (nozzle exit velocity). At a given time, the velocity of the jet, v, and the jet diameter, d, may be obtained from the following relations:

$$v = \sqrt{v_j^2 + 2gH}, \qquad d = d_j \sqrt{\frac{v_j}{v}} \tag{2}$$

where d_j is the nozzle diameter. Table 1 shows the jet parameters used in the simulation (note that suffix '*imp*' stands for the impingement instant).

2 Numerical simulation

The problem has two very different length scales, which make the numerical simulation quite difficult and time consuming to model in one simulation. Therefore, the domain was divided into two parts as shown in fig. 1. The upper part extends from the nozzle to just above the plate surface (1.2 m long) and the lower part covers the impingement area and the plate surface. Outputs of the upper domain such as velocity and VOF profiles at the outlets of the upper domain are used as the input conditions (inlet boundary conditions) for the lower domain.

The domains discretized based on the finite volume method. The volume-of-fluid method (VOF) was employed to analyze this two-phase flow problem and to track the interface between the water jet surface and the surrounding air. Numerical simulations were carried out using the FLUENT program.

The assessment of film flow structure travelling over the plate was carried out by examining the distribution of VOF and the velocity along lines parallel to the plate at different heights above the plate. These lines are termed 'parallel lines' and they are 0.5 mm apart, therefore, a '*1 mm parallel line*' indicates a line parallel to the plate at a distance 1 mm above the surface.

3 Results

Along a parallel line, a VOF value of zero means pure air and a VOF value of 1.0 denotes pure water. Hence, a map of the measured VOF along parallel lines represents how the water sheet evolves at the top of plate and one could resolve reasonably the free-surface. The velocity profile inside the water and at free-surface could be drawn from the velocity distribution along parallel lines.

3.1 Laminar modelling

An experimental facility has been established at The University of British Columbia for testing the heat transfer and hydrodynamic behaviour of jet impingement on hot plates (see fig. 2).

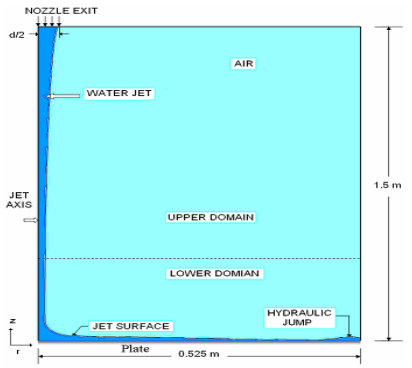

Figure 1: Problem geometry and jet parameters.

Table 1: Jet parameters.

r_j (mm)	19
V_j (lit/min)	15
V_j (m/s)	0.8817
V_{imp} (m/s)	5.5
r_{imp} (mm)	7.6
Re	33337
We	405

Experimental observations showed that the incoming jet is turbulent. Our simulation starts, however, with a laminar case just to establish some experience with the model. Table 2 shows the velocity and height data of the tip of the jet travelling downward until impingement in a laminar modelling. The subscript '*comp*' indicates FLUENT's results which is compared to results obtained from eqns. (1) and (2). Shortly after exiting the nozzle, the jet height resulted from the numerical simulation retarded by 10–20%. However, as time elapsed, the discrepancy decreased to less than 10%. In the lower domain the jet is generally off by less than 5% and the discrepancy is only about 2% near the plate surface. It should be noted that at a given time instant, the heights calculated analytically are larger than those calculated numerically indicating slightly faster velocities for the analytical solution. This is the case for both domains of analysis as indicated in table 2.

Fig. 3 shows the measured VOF distribution along a 0.5 mm parallel line. The measured VOF is 1.0 for the initial part of the line inside the stagnation zone. As the flow enters the radial zone, the water layer is thinned and the VOFs decreased. The assessment of VOF for a 0.2 mm parallel line shows that the film

has the thickness of 0.2–0.5 mm at the early region outside the stagnation zone (note that for the laminar simulation closer parallel lines are used just above the plate surface). A wavy free-surface was seen until a radius of more than 0.1 m was reached. Thereafter the film thickness was nearly unchanged but beyond the radius of 0.2 m the layer thickens. The parallel line is completely inside the water over the radius of 0.4 m.

Figure 2: Experimental testing of stationary and moving plates.

Table 2: Height and velocity of laminar jet before striking the plate (a) upper domain, (b) lower domain.

(a)

time (sec)	H (m)	$H_{com\,p}$ (m)	V (m/s)	V_{comp} (m/s)
0.05	0.056	0.047	1.3	1.23
0.12	0.176	0.16	1.98	1.9
0.2	0.373	0.34	2.73	2.6
0.275	0.613	0.58	3.49	3.26
0.344	0.884	0.805	4.07	3.9
0.4	1.138	1.038	4.6	4.43
0.425	1.261	1.151	4.83	4.66
0.433	1.3	1.19	4.91	4.74
0.435	1.31	1.2	4.93	4.76

(b)

time (sec)	H (m)	$H_{com\,p}$ (m)	V (m/s)	V_{comp} (m/s)
0.004	0.02	0.01	4.935	4.93
0.025	0.126	0.118	5.145	5.09
0.035	0.178	0.172	5.247	5.19
0.045	0.231	0.227	5.349	5.27
0.055	0.285	0.281	5.446	5.36
0.0575	0.299	0.295	5.472	5.374
0.0578	0.3	0.297	5.475	5.37
0.058	0.302	0.298	5.477	5.36
0.0585	0.304	0.3	5.481	0

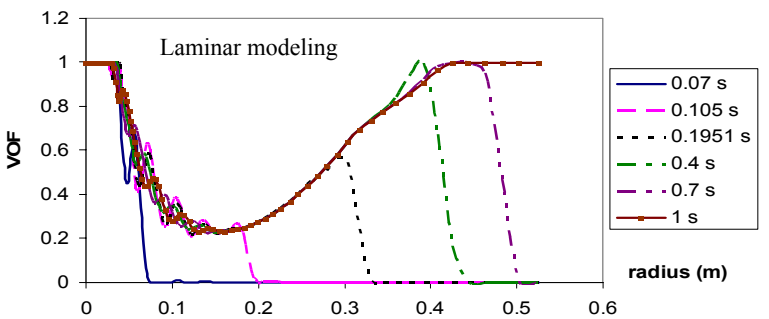

Figure 3: VOF distribution along a 0.5 mm parallel line.

A circular wave was seen at the leading edge of the water layer. The radial progress of the peak of the circular wave over the plate may be tracked by looking at the VOF variation along the higher parallel lines. At 0.4 sec the peak was well above 1 mm and thickness values become larger.

Fig. 4 shows the variation of radial velocity along a 0.5 mm parallel line. The velocities were decreasing monotonically as the fluid expanded radially downward. The numerically detected velocity fluctuations correspond to a wavy free-surface outside the stagnation zone as the liquid sheet thinned. The velocity ultimately became negligible at the plate border (over the radius of 0.5 m).

The assessment of radial velocity for lines parallel to the plate surface at different heights from the plate (up to 4 mm) revealed that the water film velocity has very similar variations along these lines, such as those shown in Figure 4. This result is quite reasonable and expected because of thinning of the water layer.

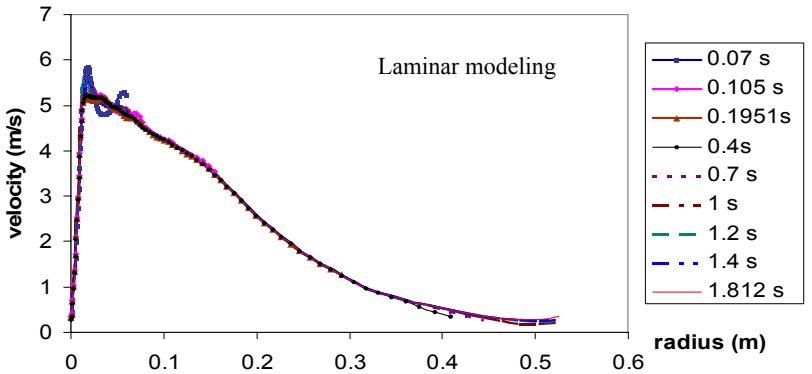

Figure 4: Velocity along a 0.5 mm parallel line.

3.2 Turbulent simulation

3.2.1 k-ε turbulent model

Table 3 shows the data of velocities and heights of the jet tip during impinging from the nozzle for different times until impingement on the plate using the k-ε turbulent model with wall functions. This model shows better performance for a radial jet with strong streamline curvature because it is adapted for wall bounded flows [6]. Analytical results could be determined as mentioned above in the laminar case. In the upper analysis domain, the differences between these results and the analytical ones are 5%. The difference in jet development in lower domains is about 10–20% showing a faster analytical jet from the analytical results by about 10%. The numerical simulation was continued until the jet passed the outlet of the lower domain and until striking the plate in the lower domain.

Fig. 5 shows the measured VOF along a 0.5 mm parallel line. Thinning of the water layer is evident as it exits the stagnation zone and free-surface disturbances have been determined for a radius of up to 0.1 m. Thereafter, the water layer

thickness starts to increase while the free-surface disturbances continue to more than 0.2 m radius. After 0.3 m the film thickness is more than 0.5 mm and parallel lines at larger distance from the plate are needed to assess the wavy free-surface. The VOF assessment for the parallel lines up to 5 mm show that the water layer thickness could rise up to 4.5 mm.

Radial velocity distribution along a 1 mm parallel line is shown in fig. 6. Also, each line shows how much the fluid is widening over the plate as time elapses until water covers the plate. The flow has velocity parallel to the plate after impinging almost equal to the incoming jet velocity. After exiting the

Table 3: Height and velocity of jet before striking the plate for k-ε model (a) upper domain, (b) lower domain.

(a)

time (sec)	H (m)	H_{comp} (m)	V (m/s)	V_{comp} (m/s)
0.05	0.056	0.049	1.32	1.28
0.12	0.176	0.166	2.0	1.95
0.2	0.373	0.349	2.76	2.64
0.275	0.61	0.571	3.46	3.34
0.35	0.91	0.845	4.166	4.05
0.395	1.11	1.036	4.6	4.46
0.413	1.2	1.119	4.77	4.64
0.42	1.24	1.149	4.83	4.69
0.424	1.26	1.166	4.86	4.74
0.431	1.29	1.2	4.93	4.82

(b)

time (sec)	H (m)	H_{comp} (m)	V (m/s)	V_{comp} (m/s)
0.004	0.0197	0.01	4.935	4.75
0.025	0.126	0.104	5.12	4.8
0.035	0.178	0.153	5.21	4.9
0.045	0.231	0.203	5.3	4.95
0.055	0.2852	0.253	5.4	5.08
0.0606	0.316	0.283	5.45	5.18
0.063	0.329	0.2953	5.47	5.1
0.064	0.333	0.3	5.48	0

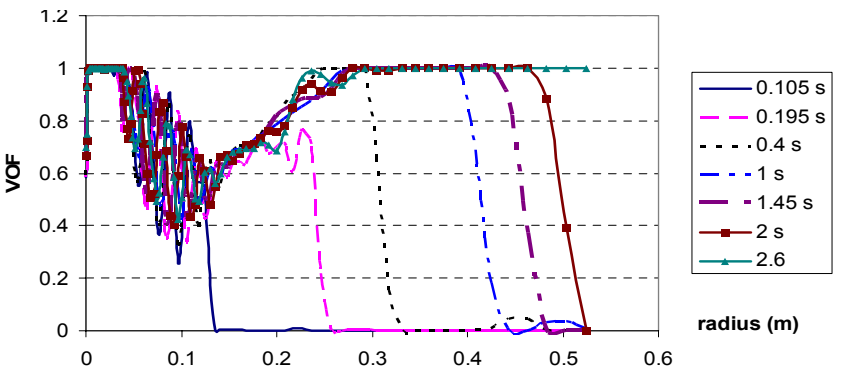

Figure 5: VOF distribution along a 0.5 mm parallel line.

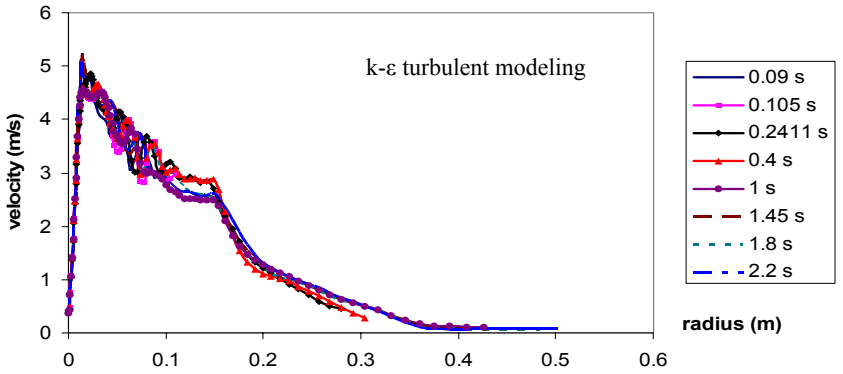

Figure 6: Velocity along 1 mm parallel line.

Table 4: Height and velocity of the jet before impacting the plate for the k-ω model: (a) upper domain (b) lower domain.

(a)

time (sec)	H (m)	H_{comp} (m)	V (m/s)	V_{comp} (m/s)
0.05	0.056	0.0472	1.32	1.19
0.107	0.151	0.132	1.835	1.77
0.2	0.373	0.337	2.76	2.6
0.275	0.614	0.557	3.47	3.27
0.35	0.91	0.825	4.119	4.0
0.4	1.137	1.0345	4.59	4.45
0.413	1.2	1.095	4.93	4.58
0.424	1.256	1.143	4.82	4.68
0.43	1.287	1.172	4.87	4.74
0.433	1.30	1.186	4.904	4.78
0.436	1.314	1.2	4.93	4.81

(b)

time (sec)	H (m)	H_{comp} (m)	V (m/s)	V_{comp} (m/s)
0.004	0.0197	0.01	4.94	4.79
0.015	0.0748	0.065	5.04	4.8
0.025	0.126	0.115	5.14	4.93
0.035	0.178	0.164	5.23	5.02
0.045	0.231	0.213	5.32	5.19
0.05	0.258	0.239	5.37	5.18
0.060	0.316	0.296	5.47	5.23
0.061	0.319	1.5	5.48	0

stagnation zone, the velocity is reduced while water expands in the radial zone downstream but has some fluctuations extending over a radius of 0.1 m. The velocity became flat thereafter and then dramatically decreased as the film thickness increased.

3.2.2 k-ω modelling

Table 4 shows the velocities and the heights of the jet tip during impinging from the nozzle exit and up to the impingement on the plate surface in the turbulent case using the shear stress transport (SST) k-ω model. This model has better performance than the standard k-ε model. The analytical results could be found as mentioned in the laminar case. The numerical results show jet delays from analytical one in the upper domain by 10% except for earlier times while the velocities are lower than the analytical results by less than 5%. In the lower domain, the comparison gives similar results as the upper domain.

Fig. 7 shows the development of water over the plate by the variation of measured VOF along a 0.5 mm parallel line. The peaks of VOFs were decreasing while the liquid spread beyond the radius of 0.1 m. However the trend turned over and the peaks began to increase. Enhanced water layer thickness reached the 1 mm parallel line at a time of around 0.4 sec and then passed it. The evaluation of other higher parallel lines reveals that the maximum height ultimately became larger than 3.5 mm. The evaluation of the velocity of the spreading water sheet at the top of the surface could also be discerned. In the stagnation zone downstream, as the thickness reduced the velocity fluctuations were seen to be monotonically decreasing.

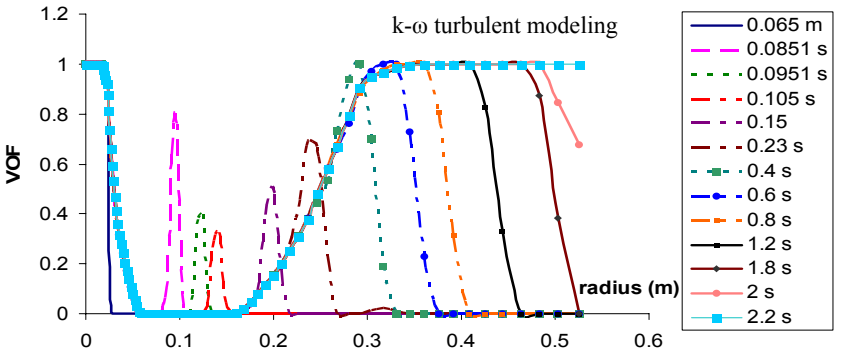

Figure 7: VOF distribution along a 0.5 mm parallel line.

4 Splashing

The exiting jet from the nozzle is fully developed turbulent which makes the jet surface rough on contact with the air and ultimately causes disturbances in the jet surface coming vertically toward the plate. A jet surface disturbance for turbulent modelling using k-e in the lower domain is shown in fig. 8. Any turbulence in the incoming axisymmetric jet can significantly disturb the free-surface of the thin liquid sheet, causing splattering of the liquid advancing parallel to the plate.

Bhunia and Lienhard [7] and Lienhard et al [8] developed a model for splattered fully developed turbulent jets. The onset of splattering where 5% of the incoming fluid is splattered is [7]:

$$\frac{S_0}{d_j} = \frac{130}{1 + 5 \times 10^{-7} We_d^2} \tag{3}$$

$$W_{e_d} = \rho v_j^2 d_j / \sigma \tag{4}$$

where W_e is Weber number.

This gives S0/dj ≈120 which is quite different from S/dj ≈ 40 obtained in this problem. Therefore, we expect to have less than 5% splashing while the jet travels downward. In the actual numerical simulation, we were able to capture a few ejecting drops from the jet tip in our turbulent simulation by reasonably fine mesh in the upper domain (fig. 8). This jet has a low Weber number. Therefore, the surface tension effect is dominant but it doesn't capillary break up [7].

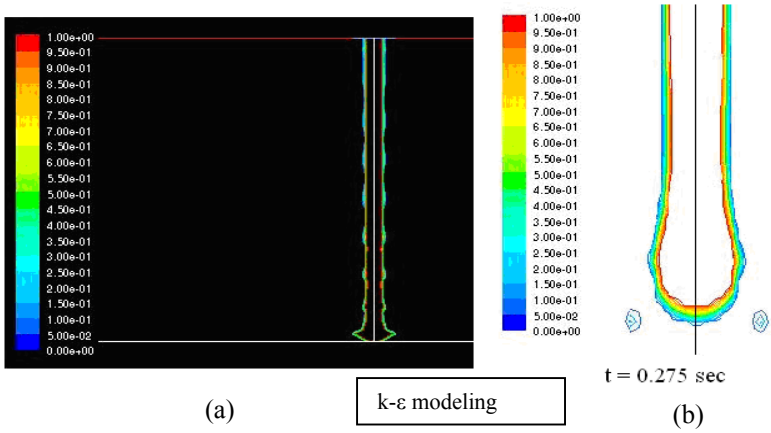

Figure 8: (a) jet surface disturbances; (b) drop splashing.

In k-ω turbulent modelling, the measured VOF of between 0 and 1 was found in some cells outside (above) the free-surface which may be an indication for splattering after impingement; tiny water drops in the air need highly refine mesh to confirm.

5 Discussion

In the laminar simulation case, the assessment of free-surface was carried out by measuring the VOF along the parallel lines up to 5 mm. The water film thickness covering a large area of the plate is extremely thin (0.2–0.5 mm). As the circular wave passes, the thickness h increases and then decreases again. The maximum thickness was detected with a value over 2 mm at the peak of the circular wave.

The radius of transition from laminar to turbulent was found to be around 0.2 m [2]. The wavy free-surface of this thin layer could be related to the eddies inside the layer [4]. It was not possible to measure the turbulent parameters in laminar modelling in FLUENT to confirm the position of transition to turbulent flow but increasing the thickness layer may be considered as an indication for this change [9]. The size of the plate is over 20 jet diameters and the flow has the Fraud number above 2, which are good indications for the occurrence of a hydraulic jump in a circular jet [4]. Therefore, considering the circular wave as a hydraulic jump, then it is a jump with a roller that could be unstable [5].

The free-surface was examined by measuring the VOF along the parallel lines up to 5 mm for k-e modelling. The free-surface disturbances were seen downstream of the stagnation zone which extend to around r = 0.1 m. The film became very thin and the height monotonically decreased to less than 0.5 mm. Thereafter, the thickness was increasing up to more than 4.5 mm.

The results for k- ω modelling are similar to k-ε but the maximum height is up to 4.5 mm. The water expanded over the target in a smoother layer than using k-ε model. Beyond 0.2 m in radius, the thickness of the front of the film started to increase with negligible radial velocity. This may be considered an indication

for the occurrence of a hydraulic jump. The shape of a hydraulic jump in turbulent modelling is a curve without a roller, which differs from the jump in the laminar case. The obtained results for turbulent modelling of a jet are better than those for the laminar one before impingement because higher order schemes for momentum equation and turbulent equations were chosen and finer mesh is used. However, in the laminar case the film was spreading faster than in the turbulent situations at the top of the plate and becoming thinner.

Watson [10] presented a model to determine the radius of the hydraulic jump for a radial spreading liquid layer without considering the jump width. Agreement with experimental data has been mixed [2]. Simple calculations reveal that the hydraulic jump could be occurring in laminar case [11]. Based on the assessment of the numerical results, a thickness of 1.5–2.5 mm was considered to have a crude estimate for the radius of the hydraulic jump using the Watson model in the laminar case. The jump radius was obtained in the range of 0.1–0.2 m, which is consistent with what has been shown in Figure 2. Free-surface disturbances need more mesh refining to be reasonably resolved, especially when a wavy surface is evident as is the case in the above simulations. Near the wall region, up to 4 mm for laminar and up to 6 mm for turbulent, should also be refined more.

References

[1] Viskanta, R., and Incropera, F. P., Quenching with liquid jet impingement. In Heat and Mass Transfer in Materials Processing, I. Tanasawa and N. Lior, eds., Hemisphere, New York, pp. 455–476, 1992.

[2] Lienhard, J.H., "Liquid jet impingement", in Annual Review of Heat Transfer, pp. 199–270, 1995.

[3] Webb, B.W. and Ma, C.-F., "Single-phase liquid jet impingement heat transfer", Advances in Heat Transfer, 26, pp. 105–217, 1995.

[4] T. Azuma and T. Hoshino, The Radial Flow of a Thin Liquid Film (Laminar Turbulent Transition), Bull. ISME, 27, pp. 2739–2746, 1984.

[5] X. Liu and J. H. Lienhard V, The Hydraulic Jump in Circular Jet Impinge-ment and in other Thin Liquid Films, Exp. Fluids, 15, pp.108–116, 1993.

[6] FLUENT 6.3 User's Guide

[7] S. K. Bhunia and J. H. Lienhard V, Splattering during Turbulent Liquid Jet Impingement on Solid Targets, J. Fluids Eng., 116, pp. 338–344, 1994.

[8] Lienhard, J. H. V., Liu, X., and Gabour, L. A., Splattering and heat transfer during impingement of a turbulent liquid jet. *J. Heat Transfer* 114, 362–372, 1992.

[9] T. Azuma and T. Hoshino, The Radial Flow of a Thin Liquid Film (2nd Report, Liquid Film Thickness), Bull. JSME, Vol. 27, pp. 2747–2754, 1984.

[10] B. J. Watson, The Radial Spread of a Liquid Jet over a Horizontal Plane, J. Fluid Mech., 20, pp. 481–99, 1964.

[11] M. Errico, A Study of the Interaction of Liquid Jets with Solid Surfaces, Ph.D. Dissertation, Univ. of California at San Diego, San Diego, CA, 1986.

Section 6
Heat and mass transfer

This page intentionally left blank

BEM for compressible convection flow in porous media

R. Jecl[1], L. Škerget[2] & J. Kramer[1]
[1]*Faculty of Civil Engineering, University of Maribor, Slovenija*
[2]*Faculty of Mechanical Engineering, University of Maribor, Slovenija*

Abstract

A boundary element method numerical scheme for simulation of compressible (density depended) fluid flow in porous media is presented. The fluid flow is modelled applying the Brinkman extended Darcy momentum equation, which is commonly used when it is important to satisfy the no-slip boundary condition on impermeable surfaces that bound the porous media domain. The model is applied to consider buoyancy driven flow in a closed porous cavity, differentially heated under large temperature gradients. The density is to be regarded as a dependent thermodynamic variable. The results in terms of velocity and temperature redistribution as well as the total heat transfer across the cavity are presented for different governing parameters.

Keywords: porous media, compressible fluid flow, boundary domain integral method, boundary element method, natural convection.

1 Introduction

Most of the studies dealing with transport phenomena in porous media are based on presuming the fluid is incompressible and viscous, where the mass density is a constant quantity the velocity does not depend on the mass density and pressure is simply a force in the linear momentum balance equation. However in numerous natural and engineering systems, density-dependent flow processes play an important role. Besides various applications in the dynamics of pure viscous fluids we find such phenomena also in subsurface hydrology, geophysics, reservoir mechanics, which are all the problems concerning a presence of a permeable solid-porous media. In this work, the boundary element method, which has been established for the viscous incompressible fluid motion

WIT Transactions on Engineering Sciences, Vol 59, © 2008 WIT Press
www.witpress.com, ISSN 1743-3533 (on-line)
doi:10.2495/AFM080361

in porous media [1], is modified and extended to capture the compressible fluid state with restriction to the subsonic flows. That means that the difference in mass density significantly changes the velocity field but there are no shock waves and no sudden sharp changes in the values of the field functions. Furthermore the pressure is a thermodynamic quantity which is temperature and mass density dependent.

2 Mathematical formulation

The fundamental processes of flow and transport in porous media are presented by the standard continuum approach. The physical properties such as velocity, pressure, temperature are continuously distributed in space and thus exist for any infinitely small material point. But in practical problems, of course, mass, motion and energy related quantities can't be measured and solved at microscopic level due to the geometric complexity of the real porous domain. Therefore the transformation to the macroscopic level by averaging over representative elementary volume is required. This procedure leads to measurable and solvable quantities for which the continuum approach is then invoked. The basis of density dependent flow and transport model is stated by the fundamental physical principles of conservation of mass, momentum and energy [2]:

$$\frac{\partial \phi \rho}{\partial t} + \frac{\partial \rho v_j}{\partial x_j} = 0\,, \tag{1}$$

$$\rho\left[\frac{\partial v_i}{\partial t} + v_j \frac{\partial}{\partial x_j}\left(\frac{v_i}{\phi}\right)\right] = -\phi\frac{\partial p}{\partial x_j} + \phi\rho g_i - \mu\frac{\partial^2 v_i}{\partial x_j \partial x_j} + (\mu + \hat{\mu})\frac{\partial^2 v_j}{\partial x_i \partial x_j} - \frac{\mu\phi}{K}v_j\,, \tag{2}$$

$$\frac{\partial}{\partial t}\left[\phi\left(\rho c_p\right)_f + (1-\phi)\left(\rho c_p\right)_s\right]T + \frac{\partial}{\partial x_j}\left[\phi\left(\rho c_p\right)_f \frac{v_j}{\phi}T\right] = \frac{\partial}{\partial x_j}\lambda_e \frac{\partial T}{\partial x_j}\,. \tag{3}$$

The parameters, used in equations are: v_i volume-averaged velocity, x_i the i-th coordinate, ϕ porosity, t time, ρ density, μ dynamic viscosity, $\partial p/\partial x_j$ the pressure gradient, g_i gravity, K permeability of porous media, $\hat{\mu}$ coefficient of bulk viscosity, T is temperature, λ_e the effective thermal conductivity of the porous media given as $\lambda_e = \phi\lambda_f + (1-\phi)\lambda_s$, where λ_f and λ_s are thermal conductivities for the fluid and solid phases, respectively. Furthermore $(\rho c_p)_f$ and $(\rho c_p)_s$ represent heat capacity for the fluid and solid phases. Introducing new variables $\rho' = \rho\phi$ and $v_j' = v_j/\phi$, and with the definition of Stokes

material derivative of the variable $(\cdot)$ as $D(\cdot)/Dt = \partial(\cdot)/\partial t + v_k\,\partial(\cdot)/\partial x_k$, continuity equation can be written as

$$\frac{\partial v_j'}{\partial x_j} = \mathsf{D}' = -\frac{1}{\rho'}\frac{D\rho'}{Dt}, \tag{4}$$

where D' represent a local expansion rate. According to Stokes hypothesis the second viscous coefficient can be taken as $\hat{\mu} = -2/3\,\mu$. Because of analytical reasons to develop velocity-vorticity formulation of governing equations, the momentum eq. (2) is worth writing in its extended form [3], [4]

$$\begin{aligned}\rho\frac{Dv_i'}{Dt} = &-e_{ijk}\frac{\partial \mu\omega_k'}{\partial x_j} + 2e_{ijk}\frac{\partial \mu}{\partial x_j}\omega_k' + 2\frac{\partial \mu}{\partial x_j}\frac{\partial v_i'}{\partial x_j} - \frac{2}{3}\frac{\partial \mu}{\partial x_i}\mathsf{D}' \\ &+ \frac{4}{3}\mu\frac{\partial \mathsf{D}'}{\partial x_i} - \frac{\partial p}{\partial x_j} + \rho g_i - \frac{\mu\phi}{K}v_j'\end{aligned}, \tag{5}$$

with the introduction of the vorticity vector ω, representing the curl of the velocity vector,

$$\omega_i = e_{ijk}\frac{\partial v_k}{\partial x_j}, \qquad \frac{\partial \omega_j}{\partial x_j} = 0, \tag{6}$$

and having in mind that in our case the original vorticity is replaced by the so-called compressible vorticity ω', $\omega' = (1/\phi)\omega$. It is important to stress out that porosity ϕ is taken to be constant over individual subdomain but changeable in respect to the whole computational domain.

Representing the material properties as a sum of a constant and variable part

$$\mu = \mu_0 + \tilde{\mu}, \quad \rho = \rho_0 + \tilde{\rho}, \quad \left(\rho' c_p\right)_f = c_0 + \tilde{c}, \quad \lambda_e = \lambda_{e0} + \tilde{\lambda}, \tag{7}$$

then the momentum and energy equations (3) and (5) can be written as

$$\frac{Dv_i'}{Dt} = -e_{ijk}\frac{\partial \mu_0\omega_k'}{\partial x_j} - \frac{1}{\rho_0}\frac{\partial p}{\partial x_j} + \frac{\rho}{\rho_0}g_i + \frac{1}{\rho_0}f_i^m - \frac{\mu\phi}{\rho_0 K}v_j', \tag{8}$$

$$\frac{DT}{Dt} = a\frac{\partial^2 T}{\partial x_j \partial x_j} + \frac{S_T^m}{c_0}, \tag{9}$$

where a is thermal diffusivity, and the pseudo body force f_i^m and pseudo heat source S_T^m terms including the effects of variable material properties, are given by

$$f_i^m = -e_{ijk}\frac{\partial \tilde{\mu}\omega_k'}{\partial x_j} + 2e_{ijk}\frac{\partial \mu}{\partial x_j}\omega_k' + 2\frac{\partial \mu}{\partial x_j}\frac{\partial v_i'}{\partial x_j} - \frac{2}{3}\frac{\partial \mu}{\partial x_i}\mathsf{D}' + \frac{4}{3}\mu\frac{\partial \mathsf{D}'}{\partial x_i} - \tilde{\rho}a_i, \tag{10}$$

$$S_T^m = \frac{1}{c_0}\left(\frac{\partial}{\partial x_j}\tilde{\lambda}_e \frac{\partial T}{\partial x_j} - T\rho' \frac{D(c_p)_f}{Dt} - \frac{\partial\left[(1-\phi)(\rho c_p)_s\right]T}{\partial t} - \tilde{c}\frac{DT}{Dt} \right). \qquad (11)$$

3 Numerical method

The numerical method chosen for this investigation is the Boundary Domain Integral Method based on the classical Boundary Element Method.
The kinematic is given by velocity vector Poisson's equation

$$\frac{\partial^2 v_i'}{\partial x_j \partial x_j} + e_{ijk}\frac{\partial \omega_k'}{\partial x_j} - \frac{\partial \mathsf{D}'}{\partial x_i} = 0\,, \qquad (12)$$

representing the mass conservation equation (1) and the vorticity definition (6), expressing the compatibility and restriction conditions between velocity, vorticity, and mass density field functions.

The vorticity kinetics is given by the vorticity transport equation obtained as a curl of the momentum equation (8) in the form

$$\frac{D\omega_i'}{Dt} = \nu_0 \frac{\partial^2 \omega_i'}{\partial x_j \partial x_j} + \omega_j' \frac{\partial v_i'}{\partial x_j} - \omega_i' \mathsf{D}' + \frac{1}{\rho_0} e_{ijk} \frac{\partial \rho g_k}{\partial x_j} + \frac{1}{\rho_0} e_{ijk} \frac{\partial f_i^m}{\partial x_j} - \frac{\mu\phi}{\rho_0 K}\omega_i' \,. \qquad (13)$$

The vorticity transport equation (13) is a highly nonlinear partial differential equation due to the products of velocity and vorticity having in mind that the velocity is kinematically dependent on vorticity. Due to the buoyancy force and variable material property terms, acting as additional temperature and pressure dependent vorticity source terms, the vorticity transport equation is coupled to the energy and pressure equations, making the numerical procedure very severe.

In the compressible fluid dynamics the pressure is a thermodynamic quantity which is temperature and mass density dependent. Writing the momentum equation (8) for the pressure gradient we have

$$\frac{\partial p}{\partial x_i} = f_{pi} = -\mu_0 e_{ij}\frac{\partial \omega'}{\partial x_j} - \rho_0 a_i + \rho g_i + f_i^m - \frac{\mu\phi}{K} v_j' \,. \qquad (14)$$

To derive the pressure equation, depending on known field and material functions, the divergence of equation (14) should be calculated, resulting in the elliptic Poisson pressure equation

$$\frac{\partial^2 p}{\partial x_i \partial x_i} - \frac{\partial f_{pi}}{\partial x_i} = 0\,. \qquad (15)$$

Equations (9), (12), (13) and (15) represent the leading non-linear set of coupled equations to which the weighted residual technique of the BDIM has to

be applied in establishing integral representations corresponding to original differential conservation equations. Each of those equations can be written following the general differential conservation equation where the linear differential operator can be either elliptic or parabolic. The velocity potential equation and a pressure equation are recognised as a nonhomogeneous elliptic vector Poisson equations, while the formulations of the integral representation for the vorticity kinetics and heat energy kinetics are based on a elliptic diffusion-convection character of the leading partial differential equations. For the numerical approximate solution of the field functions, namely the velocity, vorticity, pressure and temperature, the integral equations are written in a discretized manner in which the integrals over the boundary Γ and domain Ω are approximated by a sum of the integrals over all boundary elements and over all internal cells. In such a way we obtain the matrix form of the equations, which are solved by coupling kinetic and kinematic equations, considering the corresponding boundary and initial conditions. The integral formulation has been presented in detail previously by Jecl *et al*. [5], therefore only the resulting matrix form of the equations for kinematics, vorticity kinetics, heat energy kinetics and pressure are presented here. As the computational results of the present work are limited to the two-dimensional case, all the subsequent matrix equations are consequently written for the case of planar geometry only.

$$[\mathbf{H}]\{v_i'\} = e_{ij}[\mathbf{H}_t]\{v_j'\} - e_{ij}[\mathbf{D}_j]\{\omega'\} + [\mathbf{D}_i]\{\mathsf{D}'\}, \tag{16}$$

$$\begin{aligned}[\mathbf{H}]\{\omega'\} = {} & \frac{1}{\nu_0}[\mathbf{G}]\left\{\nu_0\frac{\partial\omega'}{\partial n} - \omega' v_n' - \frac{1}{\rho_0}e_{ij}\rho g_i n_j - \frac{1}{\rho_0}e_{ij}f_i^m n_j\right\} \\ & + \frac{1}{\nu_0}[\mathbf{D}_\mathbf{j}]\left\{\omega'\tilde{v}_j' + \frac{1}{\rho_0}e_{ij}\rho g_i + \frac{1}{\rho_0}e_{ij}f_i^m\right\} \\ & - \frac{\nu\phi}{\nu_0 K}[\mathbf{B}]\{\omega'\} + \frac{1}{\nu_0\Delta t}[\mathbf{B}]\{\omega'_{F-1}\}\end{aligned}, \tag{17}$$

$$\begin{aligned}[\mathbf{H}]\{T\} = {} & \frac{1}{\lambda_{e0}}[\mathbf{G}]\left\{\lambda_e\frac{\partial T}{\partial n} - 2c_f v_n' T\right\} \\ & - \frac{1}{\lambda_{e0}}[\mathbf{D}_\mathbf{j}]\left\{\tilde{\lambda}_e\frac{\partial T}{\partial x_j} - c_f v_j' T - \tilde{c}_f v_j' T - \bar{c}_f\tilde{v}_j' T\right\} \\ & + \frac{1}{\lambda_{e0}}[\mathbf{B}]\left\{T v_j'\frac{\partial\tilde{c}_f}{\partial x_j} + \tilde{c}_f T\mathsf{D}' - \tilde{c}_f\frac{\partial T}{\partial t} - (1-\phi)(\rho c)_s\frac{\partial T}{\partial t}\right\} + \frac{1}{\Delta t}[\mathbf{B}]\{T_{F-1}\}\end{aligned} \tag{18}$$

$$[\mathbf{H}]\{p\} = [\mathbf{D}_i]\{f_{pi}\}. \tag{19}$$

where kinematic viscosity ν_0 is defined as $\nu_0 = \mu_0/\rho_0$. In equations (16), (17), (18) and (19) the matrices $[\mathbf{H}]$, $[\mathbf{G}]$, $[\mathbf{D}_\mathbf{j}]$ and $[\mathbf{B}]$ are the influence matrices and

they are composed of integrals taken over the individual boundary elements and over the internal cells. In order to improve the economics of the computation, and thus widen the applicability of the proposed numerical algorithm, the subdomain technique is used, where the entire solution domain is partitioned into subdomains to which the same described numerical procedure can be applied. The final system of equations for the entire domain is then obtained by adding the sets of equations for each subdomain considering the compatibility and equilibrium conditions between their interfaces, resulting in a much sparse system matrix suitable to solve with iterative techniques. In our case each quadrilateral internal cell represents one subdomain bounded by four boundary elements. The geometrical singularities are overcome by using 3-node discontinuous quadratic boundary elements combined with 9-node corner continuous internal cells.

4 Test example

The extended numerical algorithm was tested on the problem of natural convection in a porous cavity heated from the side with the vertical walls held at different temperatures and the connecting horizontal walls considered adiabatic. The enclosure is filled with porous material, which is homogeneous and isotropic. The saturating density dependent fluid and the solid matrix are both in local thermodynamic equilibrium. The flow is assumed to be steady, laminar, and compressible. Detailed presentation of the geometry and boundary conditions are given in Fig. 1.

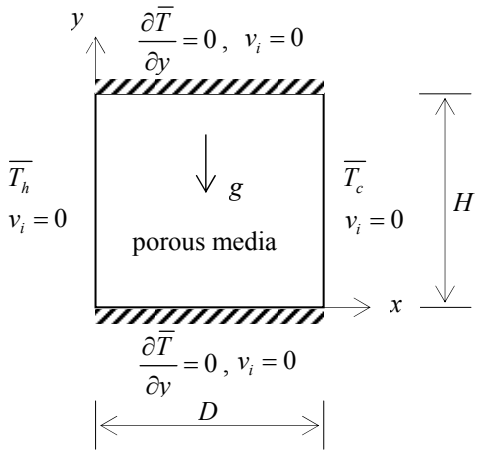

Figure 1: Geometry and boundary conditions for the cavity.

The governing parameters for the presented example are given in Table 1. An orthogonal 10 × 10 stretched grid in both dimensions was used for computations, where the grid aspect ratio was 6. The computations were performed for *Ra* =

1000, where the cold wall is imposed to temperature $T_c = 240\ K$ and the hot wall to temperature $T_h = 960\ K$. In the first case the value of porosity is $\phi = 1$, and in the second case $\phi = 0.1$, the values of permeability are $K = 10^{-6}, 10^{-7}, 10^{-8}\ m^2$.

Table 1: Parameters and boundary conditions for solved problem.

Dimension of the cavity	$L \times H = 0.01m \times 0.01m$
Porosity	$\phi = 1, 0.1$
Permeability	$K = 10^{-6}, 10^{-7}, 10^{-8}\ m^2$
Reference temperature	$T_0 = 600\ K$
Reference pressure	$p_0 = 101325\ Pa$
Reference density	$\rho_0 = 0.5884\ kg/m^3$
Dynamic viscosity	$\eta_0(T_0) = 0.295 \cdot 10^{-4}\ Pa \cdot s$
Specific heat (fluid phase)	$c_f = 1004.5\ J/kg\ K$
Specific heat (solid phase)	$c_s = 800\ J/kg\ K$
Temperature of cold wall	$T_c = 240\ K$
Temperature of hot wall	$T_h = 960\ K$
Rayleigh number	$Ra = 10^3$

Figures 2 and 3 show temperature and velocity fields respectively. The most evident difference in comparison to incompressible fluid flow is the asymmetry of both fields. The influence of permeability can be observed mainly in the

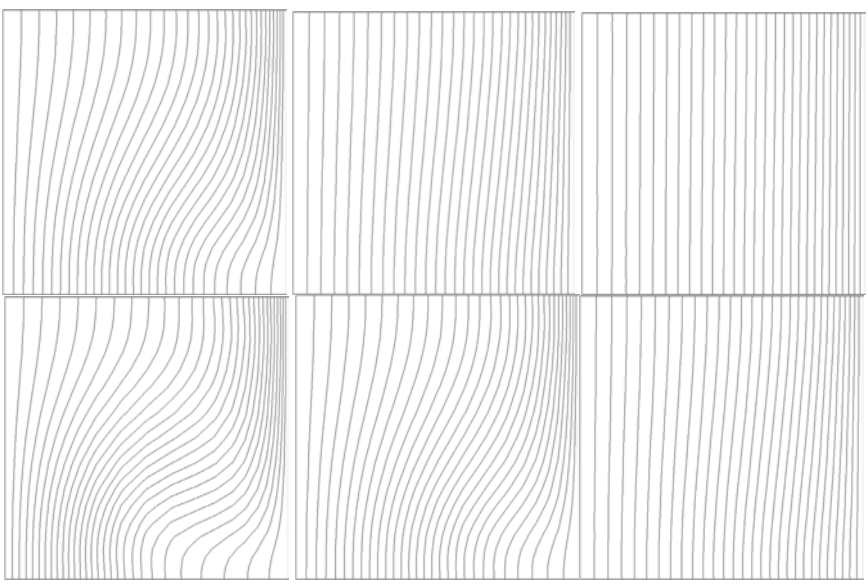

Figure 2: Temperature contours for $Ra=10^3$ and different values of porosity and permeability. Upper row $\phi=1$, bottom row $\phi=0.1$, left $K=10^{-6}\ m^2$, middle $K=10^{-7}\ m^2$, right $K=10^{-8}\ m^2$.

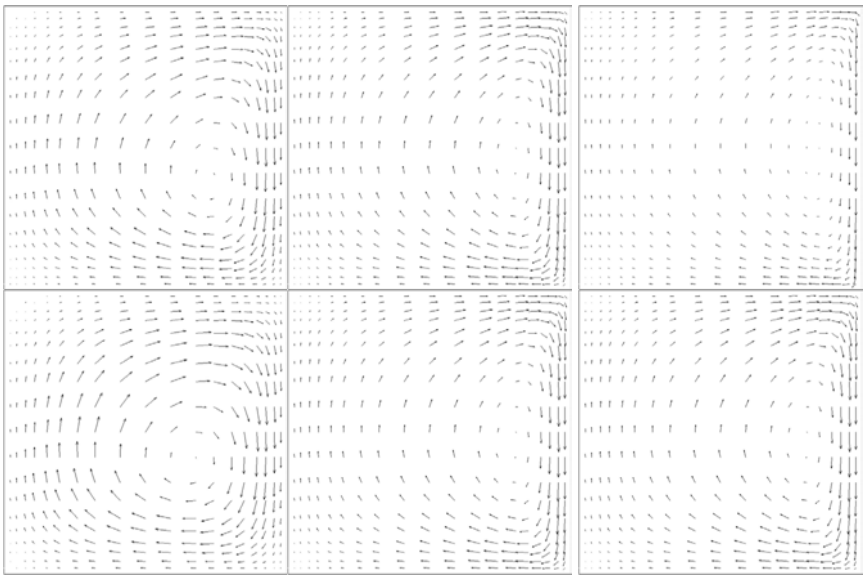

Figure 3: Velocity vectors for $Ra=10^3$ and different values of porosity and permeability. Upper row $\phi=1$, bottom row $\phi=0.1$, left $K=10^{-6}\ m^2$, middle $K=10^{-7}\ m^2$, right $K=10^{-8}\ m^2$.

Table 2: Values of Nusselt number at different values of parameters ϕ and K.

Nu	$K = 10^{-8}$	$K = 10^{-7}$	$K = 10^{-6}$
$\phi = 0.1$	1.817	1.487	1.299
$\phi = 1$	1.472	1.292	1.284

temperature field presentation. With the decrease of value K the heat transfer through cavity also decreases.

In Table 2 the results of overall Nusselt number Nu for different values of porosity and permeability are listed. The overall heat transfer is higher for the case of porosity $\phi = 0.1$ and for lower values of permeability, which is also evident from the temperature contours in Figure 2.

5 Conclusion

The boundary element integral approach for the numerical solution of compressible fluid motion in thermally driven porous cavity is presented. The derived numerical model is characterized by the decomposition of flow into its kinematics and kinetics, a result of the velocity-vorticity formulation of the modified (porous) Navier-Stokes equation for a compressible fluid. The described numerical algorithm leads to strong coupling between velocity, vorticity and mass density fields, resulting in a stable numerical scheme. The

proposed numerical procedure is studied for the case of natural convection in square porous cavity heated from the side. The characteristics of the flow and temperature fields in the cavity are analysed for different parameters. The results indicated that the BDIM as extended from BEM could be efficiently used for solving the convective heat transfer in porous media.

References

[1] Jecl, R., Škerget, L., Boundary element method for natural convection in non-Newtonian fluid saturated square porous cavity, *Eng. Anal. Bound. Elem.*, **27**, pp. 963–975, 2003.

[2] Bear, J., Bachmat, Y., *Introduction to Modeling of Transport Phenomena in Porous Media*, Kluwer Acad. Publ., Dordrecht, Boston & London, 1991.

[3] Škerget, L., Jecl, R., Compressible fluid dynamics in porous media by the Boundary Element Method (Chapter 6). *Emerging Technologies and Techniques in Porous Media*, eds.: D.B. Ingham, A. Bejan, E. Mamut, I. Pop, Kluwer Acad. Publ., Dordrecht, Boston & London, 93–117, 2004.

[4] Škerget, L., Samec, N., BEM for the two-dimensional plane compressible fluid dynamics, *Eng. Anal. Bound. Elem.*, **29**, pp. 1–17, 2005.

[5] Jecl, R., Škerget, L., Kramer, J., Numerical solution of compressible fluid flow in porous media with boundary element method., *Proc. of the Int. Conf. Fluid structure interaction and moving boundary problems IV*, eds. Chakrabarti, S. K., Brebbia, C. A.,WIT Transactions on the built environment, Vol. 92, Southampton: WIT Press, pp 143–151, 2007.

[6] Diersch H.-J.G., Kolditz O., Variable-density flow and transport in porous media: approaches and challenges, *Advances in Water Resources*., **25**, pp. 899–944, 2002.

This page intentionally left blank

Experimental study of heat transfer from in-line tube bundles to upward foam flow

J. Gylys[1], I. Gabrielaitiene[1], T. Zdankus[1], S. Sinkunas[2] & R. Maladauskas[2]
[1]*Energy Technology Institute, Kaunas University of Technology, Lithuania*
[2]*Department of Thermal and Nuclear Energy, Kaunas University of Technology, Lithuania*

Abstract

The heat transfer from the in-line tube bundle to the vertically upward directed laminar aqueous foam flow was investigated by means of experimental set-up, consisting of the foam generator, experimental channel, in-line tube bundle, measurement instrumentation and auxiliary equipment. Two in-line tube bundles with different geometries were used for the experiments. One bundle consisted of three rows with six tubes in each. Spacing between centres of the tubes across the experimental channel was s_1=0.06 m and spacing along the channel was s_2=0.03 m. The second in-line tube bundle consisted of five vertical rows with six tubes in each. Spacing between centres of the tubes was s_1=s_2=0.03 m. All tubes had an external diameter of 0.02 m. Statically stable foam was used for experiments. It was noticed that structure of foam varied while it passed the bundle: bubbles changed their size, liquid drainage from the foam appeared. Dependence of heat transfer intensity on flow velocity, volumetric void fraction of foam and liquid drainage was determined and described by empirical relationships. Moreover, density and the pattern of tubes location were estimated in experiments and the development of the heat transfer computation method.

Keywords: two-phase foam flow, in-line tube bundle, heat transfer, void fraction of foam.

1 Introduction

Development of heat exchangers with low consumption of primary energy resources and the enhanced heat transfer rates is the aim of this work. This issue

WIT Transactions on Engineering Sciences, Vol 59, © 2008 WIT Press
www.witpress.com, ISSN 1743-3533 (on-line)
doi:10.2495/AFM080371

is addressed by applying an advance heat transfer carrier, such as aqueous foam flow, consisting of gas bubbles separated by a thin liquid film. Foam coolant can be applied on heated surfaces only when bubbles of it don't collapses and retain their structure during transportation to heat transfer place and process of heat transfer. One type of aqueous foam – statically stable foam keeps initial dimensions and structure of bubbles within broad limits of time and velocity of motion; therefore it is suitable for heat transfer purpose [1]. To apply two phase foam flow in practice and to utilize effectively this type of coolant deep investigations of foam and heat exchanger interaction to be performed and influence of foam, flow and exchanger characteristics to heat transfer intensity are vitally needed. Drainage of liquid from foam [2, 3], diffusive transfer of gas between bubbles [3], division and collapse of foam bubbles [4, 5] take place in foam type heat exchangers. Those phenomena are closely linked between themselves what complicates very much application of analytical methods. Thus an experimental method was selected for our investigations as the most convenient and universal.

Heat transfer from single tube and tube line to statically stable foam flow was investigated in our previous works [6], therefore we have requires experience and necessary equipment. After these works an experimental series with in-line tube bundles in foam flow followed [7, 8]. The effect of tube bundles' geometries is the focus of this work, since bundles (behaving as obstacles in a flow) induce substantial changes of foam structure: bubbles are transformed by collapsing, dividing, appearing news bubbles. This, together with gravity and capillary forces, facilitates the liquid drainage from the foam and affects the thickness of liquid film, composing on the heated surfaces and channel walls. Such effects can significantly increase or decrease heat transfer rates. The results of our investigation are presented in this paper.

2 Experimental set-up

Experimental set-up consisted of the following elements [6, 7]: experimental channel, tube bundle, gas and liquid control valves, gas and liquid flow meters, liquid storage reservoir, liquid level control reservoir, air fan, electric current transformer and stabilizer. Cross section of the experimental channel had dimensions 0.14 x 0.14 m^2; height of it was 1.8 m.

Two in-line tube bundles with different spacing between tubes centres across the bundle were used during experimental investigation. A schematic view of the experimental channel with tube bundles is shown in the Fig. 1. The in-line tube bundle No.1 consisted of three vertical rows with six tubes in each. Spacing between centres of the tubes across the experimental channel was s_1=0.06 m and spacing along the channel was s_2=0.03 m. The in-line tube bundle No.2 consisted of five vertical rows with six tubes in each. Spacing between centres of the tubes was s_1=s_2=0.03 m. External diameter of all the tubes was equal to 0.02 m. An electrically heated tube – calorimeter had an external diameter equal to 0.02 m also. Endings of the calorimeter were sealed and insulated. During the experiments calorimeter was placed instead of one tube of the bundle. An

electric current value of heated tube was measured by an ammeter and voltage by a voltmeter. Temperature of the calorimeter surface was measured by eight calibrated thermocouples: six of them were placed around the central part of the tube and two of them were placed in both sides of the tube at a distance of 50 mm from the central part. Temperature of the foam flow was measured by two calibrated thermocouples: one in front of the bundle and one behind it.

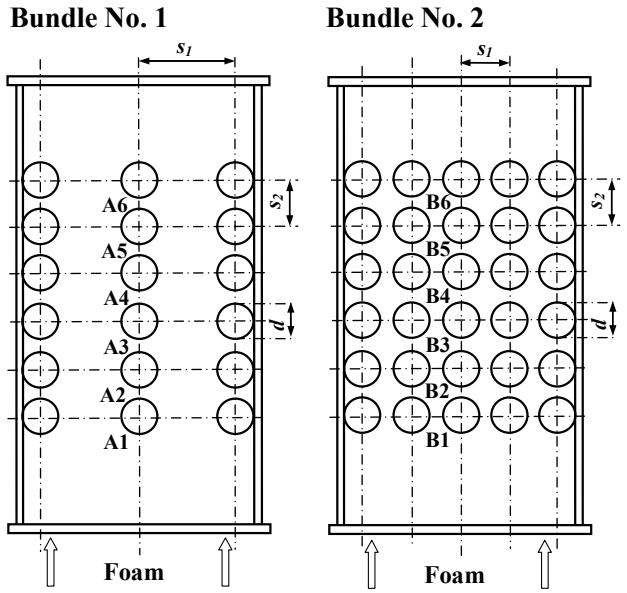

Figure 1: In-line tube bundle No. 1 and No. 2 in upward foam flow.

Statically stable foam flow was used for an experimental investigation. This type of foam was generated from water solution of detergents. Concentration of detergents (0.5%) was kept constant. Foam flow was produced by gas and liquid mixing on the riddle, which was installed at the bottom of the experimental channel. Liquid was delivered from the reservoir to the riddle from the upper side; gas was supplied to the riddle from below.

Measurement accuracies for flows, temperatures and heat fluxes were of range correspondingly 1.5%, 0.15–0.20% and 0.6–6.0%.

During the experimental investigation a relationship was obtained between an average heat transfer coefficient h from one side and foam flow volumetric void fraction β and gas flow Reynolds number Re_g from the other side:

$$Nu_f = f\left(\beta, \mathrm{Re}_g\right). \tag{1}$$

Nusselt number was computed by formula

$$Nu_f = \frac{hd}{\lambda_f}. \tag{2}$$

Here λ_f is the thermal conductivity of the statically stable foam flow, W/(m·K), computed by the equation

$$\lambda_f = \beta\lambda_g + (1-\beta)\lambda_l . \tag{3}$$

An average heat transfer coefficient we calculated as

$$h = \frac{q_w}{\Delta T} . \tag{4}$$

Gas Reynolds number of foam flow we computed by formula

$$\mathrm{Re}_g = \frac{G_g d}{A \nu_g} . \tag{5}$$

Foam flow volumetric void fraction we expressed by the equation

$$\beta = \frac{G_g}{G_g + G_l} . \tag{6}$$

Experiments we performed within limits of Reynolds number diapason for gas (Re_g): 190–410 (laminar flow regime) and foam volumetric void fraction (β): 0.996–0.998. Gas velocity for foam flow was changed from 0.14 to 0.32 m/s.

3 Results

The process of heat transfer from in-line tube bundle to upward foam flow was investigated experimentally. Tube bundle No.1 (see Fig. 1) was the subject of our research. The influences of foam flow gas Re_g numbers and tube position on heat transfer intensity Nu_f were evaluated for middle-line (A) tubes of tube bundle No.1 (Fig. 2). Heat transfer from the first tube (A1) to foam flow is more intensive than that of the other tubes for the entire interval of Re_g. Heat transfer of the second tube (A2) is lower than that of the third tube (A3). The heat transfer intensity of the third (A3), fourth (A4) and fifth (A5) tubes is almost the same – the difference is less than 5%. Heat transfer from the fifth (A5) tube to foam flow is slight higher than that of the third (A3) and fourth (A4) tubes. The exception is the last – the sixth (A6) tube. Heat transfer intensity of this tube is lower than that of the first (A1) tube and higher than that of the other tubes. This phenomenon can be explained by the fact that structure of foam flow changes while it passes the tube bundle. Passing the bundle the large bubbles of foam are divided into smaller ones, some of foam bubbles collapse. Therefore the real void fraction and the intensity of the liquid drainage process increases along the tube bundle. So, the heat transfer intensity from the last tubes to foam flow increases.

Average heat transfer intensity from the second (A2) tube to foam flow (β= 0.997) is equal to 63% of the first (A1) tube heat transfer intensity. The same of the third (A3) tube is equal to 81% of the second (A2) tube heat transfer intensity to foam flow. It is different in comparison with one-phase flow case, where the highest heat transfer intensity is of the third and furthered tubes and the heat transfer intensity of frontal (first) tubes are equal to about 60% of the third tubes

heat transfer intensity [8, 9]. Results showed that the heat transfer intensity from the bundles' third (A3) and further tubes varies insignificantly (except the last tube). It's the same in comparison with one-phase flow case.

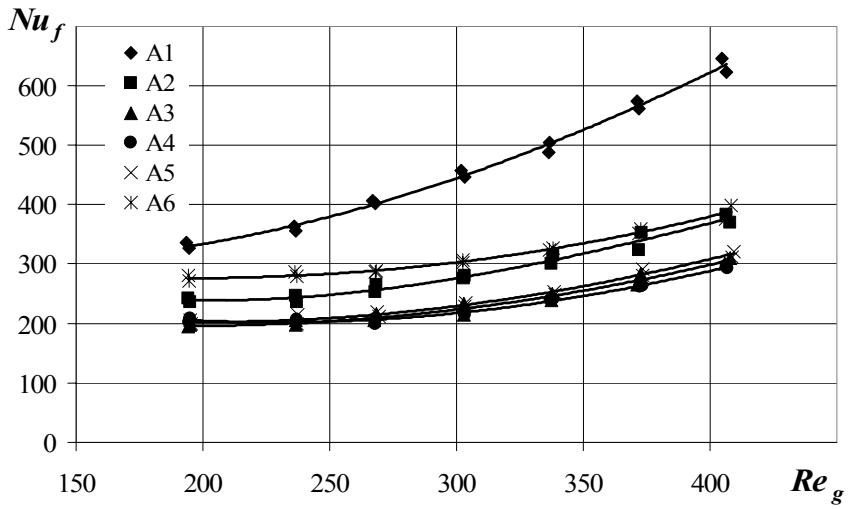

Figure 2: Heat transfer intensity from the tubes of the middle-line (A) to upward foam flow, β= 0.997.

Comparison of heat transfer intensity from both bundles' third tubes (A3 and B3) to upward foam flow is shown in the Fig. 3. Heat transfer from the tube A3 (tube bundle No.1) increased by 1.5 times for β=0.996, by 1.6 times for β=0.997, and by 1.4 times for β=0.998 for upward foam flow, when gas flow Reynolds numbers Re_g are changed from 190 to 410. For the B3 tube (tube bundle No.2), the heat transfer increased by 2.1 times for β=0.996, 1.9 times for β=0.997, and by 1.8 times for β=0.998.

Heat transfer intensity of the tube B3 is higher than that of the tube A3 on average by 58% for β=0.996 and 0.997 and by 50% for β=0.998, for Re_g=190–440.

An average heat transfer rate of middle-line tubes was calculated in order to compare the experimental results of in-line tube bundles No.1 and No.2. An average heat transfer intensity of the middle-line tubes (A and B) of the in-line bundle No.1 and No.2 to upward foam flow is shown in Fig. 4.

When foam is passing through the obstacle (the tube bundle) flow velocity increases, foam bubbles are intermixed, some bubbles collapsed or divided into smaller bubbles. These processes are more intensive in the case of tube bundle No.2, where five tubes are located across the channel in comparison with three tubes of the bundle No.1. Therefore average heat transfer intensity from the middle-line tubes (B) of the bundle No.2 to foam flow is higher than that of the middle-line tubes (A) of the bundle No.1.

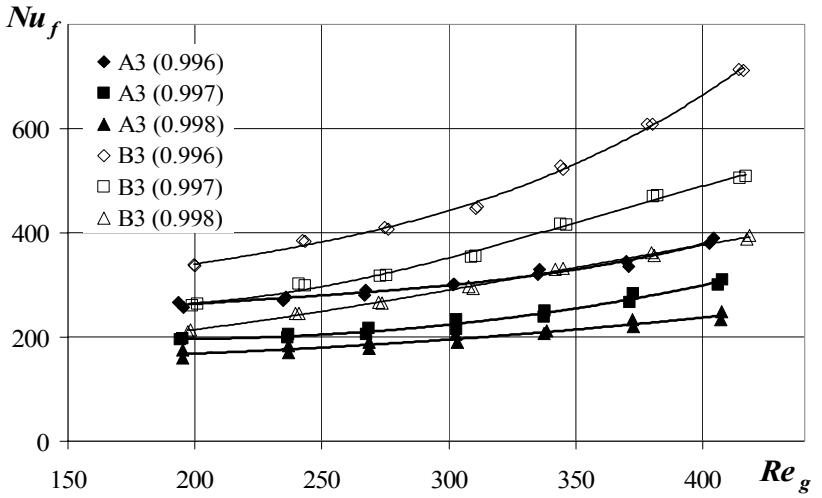

Figure 3: Heat transfer from the tubes A3 and B3 to upward foam flow, β=0.996, 0.997 and 0.998.

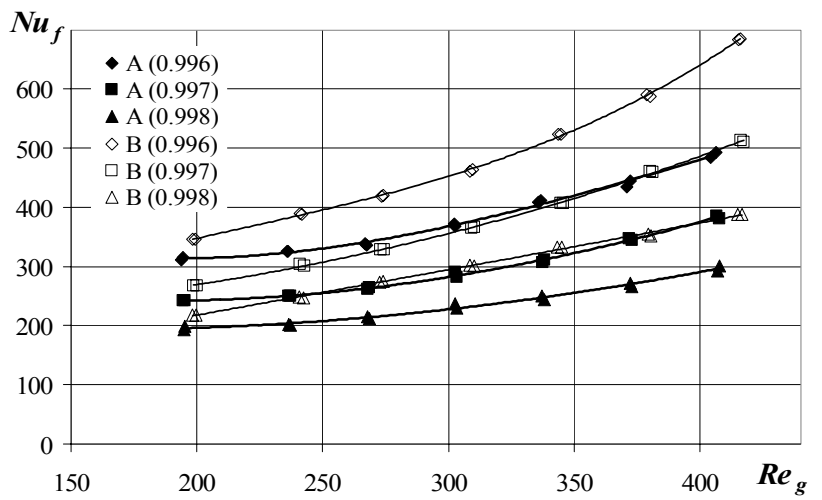

Figure 4: Average heat transfer intensity from the middle-line tubes of the in line bundle No. 1 and No. 2 to upward foam flow: β=0.996, 0.997 and 0.998.

Changing Re_g from 190 to 410, an average heat transfer intensity of the middle-line tubes of the in-line bundle No.1 to upward foam flow increases by 1.6 times for β=0.996 and 0.997, and by 1.5 times for β=0.998; and that for the tubes of the in-line bundle No.2 is twice for β=0.996; by 1.9 times for β=0.997, and by 1.8 times for β=0.998.

An average heat transfer intensity from the tubes of the tube bundle No.2 is higher than that of the tubes of the bundle No.1 on average by 27% for β=0.996–0.998, to upward foam flow for entire interval of Re_g (Re_g=190–440).

Experimental results of investigation of heat transfer from the in-line tube bundles to upward statically stable foam flow were generalized by criterion equation using dependence between Nusselt number Nu_f and gas Reynolds Re_g number. This dependence within the interval $190 < Re_g < 410$ for the in-line tube bundle in upward foam flow with the volumetric void fraction β=0.996, 0.997, and 0.998 can be expressed as follows:

$$Nu_f = c\beta^n \mathrm{Re}_g^m . \tag{7}$$

On average, for the whole middle-line tubes of bundle No.1 (s_1=0.06 and s_2=0.03 m) in the upward foam flow c=7.4, n= –111, m=22.8(1.023–β).

On average, for the whole middle-line tubes of bundle No.2 (s_1=s_2=0.03 m) in the upward foam flow c=5.7, n=340, m=102.1(1.006–β).

4 Conclusions

Heat transfer of two in-line tube bundles with different geometry to vertical laminar upward statically stable foam flow was investigated experimentally.

Heat transfer from the first tubes of the in-line bundle to foam flow moving in upward direction is higher than that of the next tubes, what is different in comparison with one-phase fluid flow case.

Heat transfer intensity from the third and the other (excluding the last) tubes are similar and close to that of one-phase flow case.

An average heat transfer intensity from the tubes of the tube bundle No.2 (s_1=s_2=0.03 m) is higher than that of the tubes of the bundle No.1 (s_1=0.06 and s_2=0.03 m) on average by 27% for β=0.996–0.998, to upward foam flow for entire interval of Re_g=190–440.

Criterion equation (7) may be applied for calculation and design of the statically stable foam heat exchangers with in-line tube bundles.

Nomenclature

A – cross section area of experimental channel, m^2; c, m, n – coefficients; d – outside diameter of tube, m; G – volumetric flow rate, m^3/s; Nu – Nusselt number; q – heat flux density, W/m^2; Re – Reynolds number; $\overline{T}$ – average temperature, K; h – average coefficient of heat transfer, W/(m^2·K); β – volumetric void fraction; λ – thermal conductivity, W/(m·K); ν – kinematic viscosity, m^2/s.

Indexes

f – foam;
g – gas;

l – liquid;
w – wall of heated tube.

Acknowledgement

The authors gratefully acknowledge the financial support of the Lithuanian Science Foundation.

References

[1] Gylys, J., Hydrodynamics and Heat Transfer Under the Cellular Foam Systems, Technologija: Kaunas, 1998.
[2] Nguyen A. V., Liquid Drainage in Single Plateau Borders of Foam. Journal of Colloid and Interface Science, **249(1)**, pp. 194–199, 2002.
[3] Tichomirov V., Foams. Theory and Practice of Foam Generation and Destruction, Chimija: Moscow, 1983.
[4] Vilkova N. G. and Kruglyakov P. M., Investigation of foam and emulsion destruction under the great pressure gradients. Advances in Colloid and Interface Science, **108–109**, pp. 159–165, 2004.
[5] Garrett P. R, Recent developments in the understanding of foam generation and stability. Chemical Engineering Science, **48(2)**, pp. 367–392, 1993.
[6] Gylys J., Giedraitis V., Sinkunas S., Zdankus T. and Gylys M., Study of in-line tube bundle heat transfer in upward vertical foam flow, Energy: production, distribution and conservation ASME conference, Milan, Italy, pp. 643–650, 2006.
[7] Gylys J., Zdankus T., Sinkunas S., Giedraitis V., Study of In–line Tube Bundle Cooling in Vertical Foam Flow. WSEAS Transactions on Heat and Mass Transfer, Iss. 6, **1**, pp. 632–637, 2006.
[8] Zukauskas A., Convectional Heat Transfer in Heat Exchangers, Nauka: Moscow, p. 472, 1982.
[9] Hewitt, G. F., Heat exchanger design handbook 2002, York, Begell House, 2002.

Flow patterns and heat transfer in square cavities with perfectly conducting horizontal walls: the case of high Rayleigh numbers (10^6–10^9)

R. L. Frederick & S. Courtin
Universidad de Chile, Departamento de Ingeniería Mecánica, Santiago, Chile

Abstract

Flow patterns and heat transfer in a square cavity with perfectly conducting horizontal walls are described by direct simulation for Rayleigh numbers of 10^6–10^9. The code uses second order time and space discretisations and non-uniform grids. For Ra = 10^6 or less a steady final state is found. Periodic characteristics are obtained at Ra = 10^7, and non periodic behaviour is found at higher Ra. Time averaged wall and mid plane Nusselt numbers (not previously known for this case) are reported and correlated. Their oscillation frequencies are determined to characterize the regime. The mid plane Nusselt number, $\overline{Nu}_{mid}$, always exceeds wall Nusselt numbers. $\overline{Nu}_{mid}$ represents the total heat moved by the cavity under the perfectly conducting condition. At Rayleigh numbers from 10^8 onwards, $\overline{Nu}_{mid}$ exceeds the corresponding value for the adiabatic problem.

Keywords: natural convection, enclosures, perfectly conducting walls.

1 Introduction

Natural convection in differentially heated square enclosures has received considerable attention in the CFD and Heat Transfer literature. Although the condition of perfectly conducting horizontal walls is more realistic when air is the test fluid, most studies use the adiabatic condition. In the present study, numerical simulations of the natural convection in a square cavity with perfectly conducting horizontal walls at high Rayleigh numbers are reported. Nusselt number values for some cases not previously treated in the literature are given.

WIT Transactions on Engineering Sciences, Vol 59, © 2008 WIT Press
www.witpress.com, ISSN 1743-3533 (on-line)
doi:10.2495/AFM080381

Attempts to simulate the flow in differentially heated cavities at very high Rayleigh numbers have been relatively scarce in the literature until very recently. A direct numerical simulation of cases with Rayleigh numbers in the turbulent range seems at first sight to be possible because the confined geometry limits the size of the largest turbulent structures. Even so, the need to describe in full detail even the smallest structures in the viscous layers near the walls is a very severe difficulty.

Very high Rayleigh numbers, above 10^9, are associated to turbulence or to the succession of chaotic flow patterns that result in turbulence. Successful simulation of flow and temperature fields must account for the extremely high temperature and velocity gradients at the walls, which require small grid steps. Time scales get shorter as *Ra* grows, requiring small time steps. However, simulation times must be long enough to get meaningful time averages of all quantities. The present study is restricted to a maximum Rayleigh number of 10^9.

Two-dimensional simulations of differentially heated cavities at high Rayleigh numbers, with adiabatic horizontal boundaries have been reported. Paolucci [1, 2] used the finite volume method to give detailed description of the flow dynamics. The first paper [1] dealt with the transition to turbulence, while [2] conducted a direct numerical simulation of turbulent flow for air, taken as a non-Boussinesq fluid, at $Ra = 10^{10}$. Le Quéré et al [3] used spectral methods to obtain numerical simulations at $Ra = 10^8$–10^{10}, using the Boussinesq assumption. The main goal in these contributions was to characterize the mechanisms governing the onset of unsteadiness, the transition to chaos and the turbulence. In the chaotic state, internal wave activity was not suppressed, as shown by high amplitude and low frequency oscillations in average Nusselt number at the vertical midline. High frequencies are observed in wall Nusselt number oscillations, which are associated to motion within the boundary layers.

Three-dimensional solutions for differentially heated, cubical enclosures with adiabatic walls were given by Fusegi et al [4], Janssen and Henkes [5], Tric et al [6] and others. In [5, 6] 2D results were also reported for Rayleigh numbers up to 10^8. From the 2D results in [6], the *Ra* exponent in the Nusselt –Rayleigh number relation is 0.3 at low *Ra* (10^3–10^6) and 0.2673 in the upper range (10^6-10^8). Le Quéré and Behnia [6] implies a 0.26 exponent in [4] for $Ra = 10^8$–10^{10}.

Information on Nusselt number values for the perfectly conducting square cavity is scarce, especially at high Rayleigh numbers (10^7–10^9). An experimental benchmark for cubical cavities up to $Ra = 10^8$ is available [7], and numerical simulations for the same situation have been performed [8]. In this paper direct numerical simulations are reported for a square cavity with perfectly conducting horizontal walls for $Ra = 10^5$–10^9. After a brief description of flow and heat transfer in this situation, the dependences of wall and central Nusselt number on Rayleigh number are described and explained. Then the results are generalized in the form of Nusselt number correlations.

2 Formulation and numerical method

Consider a square cavity of side L, filled with an incompressible Boussinesq fluid such as air ($Pr = 0.71$). From a uniform temperature, motionless state, a

difference ΔT between the hot left wall and the cold one is imposed at $t = 0$. The dimensionless governing equations of continuity, momentum and energy in terms of the Rayleigh number (Ra), based on L and ΔT are:

$$\frac{\partial U}{\partial X} + \frac{\partial V}{\partial Y} = 0$$

$$\frac{\partial U}{\partial t} + U\frac{\partial U}{\partial X} + V\frac{\partial U}{\partial Y} = -\frac{\partial P}{\partial X} + \Pr \nabla^2 U$$

$$\frac{\partial V}{\partial t} + U\frac{\partial V}{\partial X} + V\frac{\partial V}{\partial Y} = -\frac{\partial P}{\partial Y} + \Pr \nabla^2 V + Ra \Pr \Theta$$

$$\frac{\partial \Theta}{\partial t} + U\frac{\partial \Theta}{\partial X} + V\frac{\partial \Theta}{\partial Y} = \nabla^2 \Theta$$

Y and V are the vertical coordinate and velocity, respectively. The following boundary conditions apply:

$$X = 0,\ \Theta = 0.5;\ X = 1,\ \Theta = -0.5,\ Y = 0 \text{ and } Y = 1,\ \Theta = 0.5 - X$$
$$U = V = 0 \text{ on all walls}$$

Initial conditions for the interior points in the region are:

$$\Theta = 0,\ U = V = 0 \text{ at } t = 0.$$

A finite volume code based on the SIMPLER method with second order time and space discretisations and non-uniform grids in both directions was used. The coordinates of nodes in the deformed grid are expressed in terms of the coordinates in an equally spaced grid with the same number of nodes (X'), according to the rule of Janssen and Henkes [3]:

$$X = X' - \frac{1}{2\pi}\sin(2\pi X')$$

A grid sensitivity analysis showed that appropriate grids were of 252×252 nodes for $Ra \leq 10^8$ and 302×302 nodes for higher Rayleigh numbers. The latter grid gave 40 temperature nodes at the zone of high wall temperature gradient at $Ra = 10^9$. For validation the results of the code for a square cavity with adiabatic horizontal walls and $Pr = 0.71$ were compared with a benchmark for that problem [6]. For Rayleigh numbers up to 10^6, the maximum differences in horizontal and vertical peak velocities never exceed 0.2%. The Nusselt Numbers did not deviate from the benchmark by more than 0.1%. In addition, left and right average Nusselt numbers agreed to within 0.02% in our runs for the adiabatic case. Finally, our Nusselt number results for a perfectly conducting cavity agreed to within 0.1% with the results available in [8] at $Ra = 10^8$.

3 Results and discussion

Differences between the adiabatic and perfectly conducting cases will be briefly described. With perfectly conducting horizontal walls, heat transfer is

characterized by three average horizontal Nusselt numbers: the two wall Nusselt numbers, $\overline{Nu}_{hot}$, $\overline{Nu}_{cold}$, and the vertical midline average Nusselt number, $\overline{Nu}_{mid}$. While $\overline{Nu}_{hot} = \overline{Nu}_{cold}$, $\overline{Nu}_{mid}$ is higher than the other two. The difference is caused by heat flow across the horizontal walls.

The flow in the adiabatic case at $Ra = 10^6$ is in boundary layer regime, with a stratified core. A similar flow pattern occurs in the perfectly conducting case, but, as the horizontal walls are active, the velocities and circulation rate increase in comparison with the adiabatic case. However, the heat transfer at the vertical walls ($\overline{Nu}_{hot}$) is lower.

Fig. 1 shows the horizontal local Nusselt number profile at the hot (left) wall as a function of *Y*. In the adiabatic case (not shown) the local *Nu* in the vicinity of the arriving corner ($Y = 0$) is the highest. In the perfectly conducting case, *Nu* is unity at both corners due to the linear temperature on the horizontal walls. Buoyancy forces imposed by the lower wall at $0 < X < 0.5$ on the fluid coming from the cold wall, cause it to flow upwards, forming an inclined stream that moves toward the hot wall. These two facts result in a lower $\overline{Nu}_{hot}$ than in the adiabatic case at each *Ra*, in spite of the higher circulation rate.

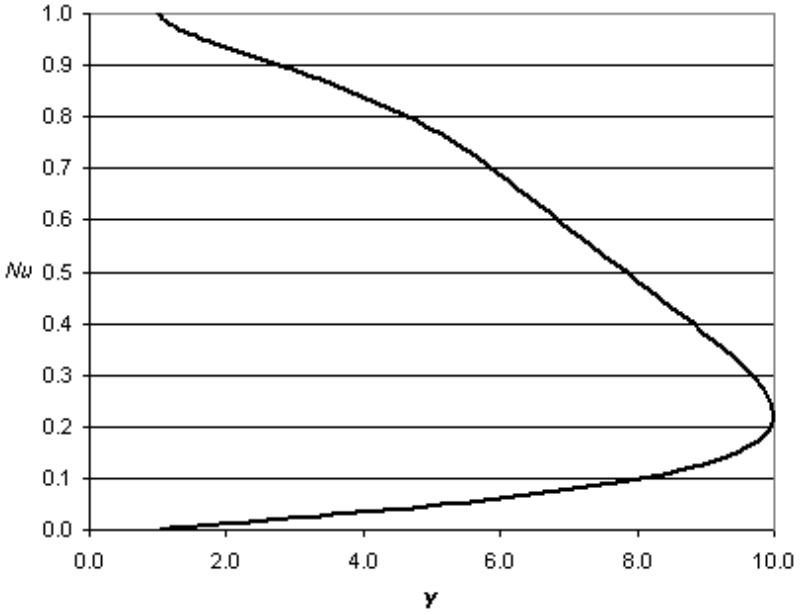

Figure 1: Horizontal Nusselt number profile at the hot wall, $Ra = 10^6$.

The vertical local Nusselt numbers across the perfectly conducting walls are zero at the corners, as vertical wall temperatures are uniform. A net vertical heat flow (fig. 2) enters the cavity in the interval $0 < X < 0.5$, and it is compensated by an equal heat output in the region $0.5 < X < 1$. As a result, the average horizontal Nusselt number varies with *X* and has a maximum at $X = 0.5$, which results from

the sum of the heat transferred through the hot wall and the contribution from the horizontal walls from $X = 0$ to 0.5. Therefore $\overline{Nu}_{mid}$ represents the total heat moved by the cavity under the perfectly conducting condition.

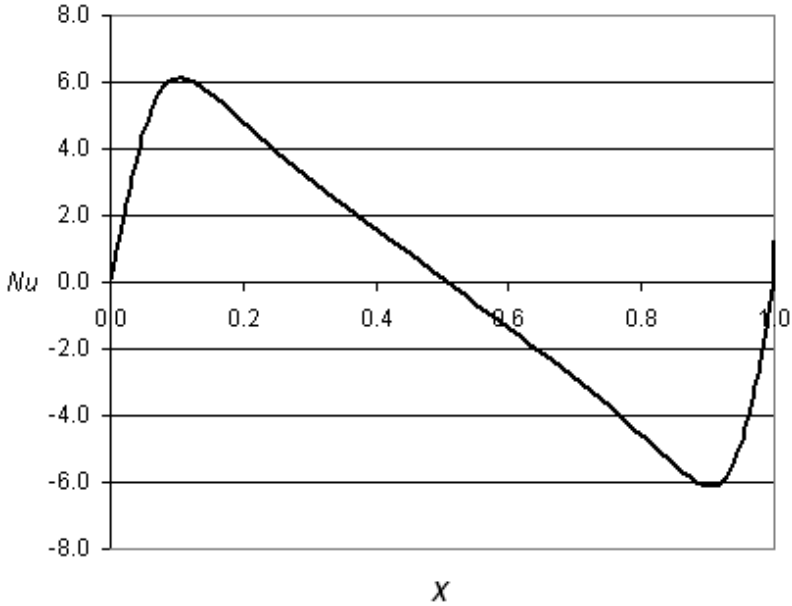

Figure 2: Net vertical heat flow across the horizontal walls of the cavity.

3.1 Cases $Ra = 10^7, 10^8$ and 10^9

The solutions for the two higher Rayleigh numbers were run from the uniform temperature motionless state, but the case 10^7 was run using the temperature, velocity and pressure fields for $Ra = 10^8$ as initial condition. In all these cases, the final regime is time dependent, with oscillations of great amplitude in $\overline{Nu}_{mid}$. At variance with $Ra = 10^6$, in which the final regime is permanent, at $Ra = 10^7$ the two wall Nusselt numbers are unequal at each time instant, and display roughly sinusoidal, out of phase oscillations (fig. 3).

From fig. 3, it is possible to identify the main oscillation frequencies. These are, for $\overline{Nu}_{mid}$, of 214.3 and for the wall Nusselt numbers, 785.7. A time averaged temperature field (fig. 4) shows complete stratification in the nucleus and full symmetry about the vertical axis. The boundary layer thickness is considerably reduced with respect to $Ra = 10^6$. Inclined fluid jets discharged by the active walls are visible. The similarity of this time- averaged temperature field with the steady one found at $Ra = 10^6$ shows that, although at $Ra = 10^7$ the regime is unsteady, it is fully laminar.

Non-periodic oscillations occur at $Ra = 10^8$. In a comparison of cold wall Nusselt number with the result of Janssen and Henkes (23.9), the percent differences are very low (0.1 %). Fig. 5 shows the evolution of Nusselt number

in the final regime at $Ra = 10^9$. $\overline{Nu}_{mid}$ displays complex oscillations in which its value at a given instant cannot be predicted from previous values. High amplitude oscillations are associated to internal wave motion that is not damped at this *Ra*. By Fourier analysis one main frequency was found for $\overline{Nu}_{mid}$ (1881.9), probably associated with internal wave motion. Oscillations of wall Nusselt number are of high complexity and show an additional frequency of 13174. As this frequency is not found in the central Nusselt number, it must be caused by near- wall motions. These frequencies agree in order of magnitude with the ones reported by Paolucci [1] for the adiabatic case. The behaviour at this *Ra* can be considered as chaotic. Fig. 6 shows a time- averaged temperature field. It is very complex compared to the one at $Ra = 10^7$. Local circulations appear at different heights in the vicinity of the hot wall. Thermal plumes are generated by interaction of hot fluid with the cold part of the upper wall, (also ascending plumes are generated in the hot part of the lower wall). This local behaviour is similar to a Rayleigh-Bénard situation. These plumes and the incidence of cold and hot fluids on the hot and cold walls respectively produce many local circulations (of a spatial scale smaller than the overall motion). This seems to be the cause of the instability of the final regime, which is transient at high *Ra*.

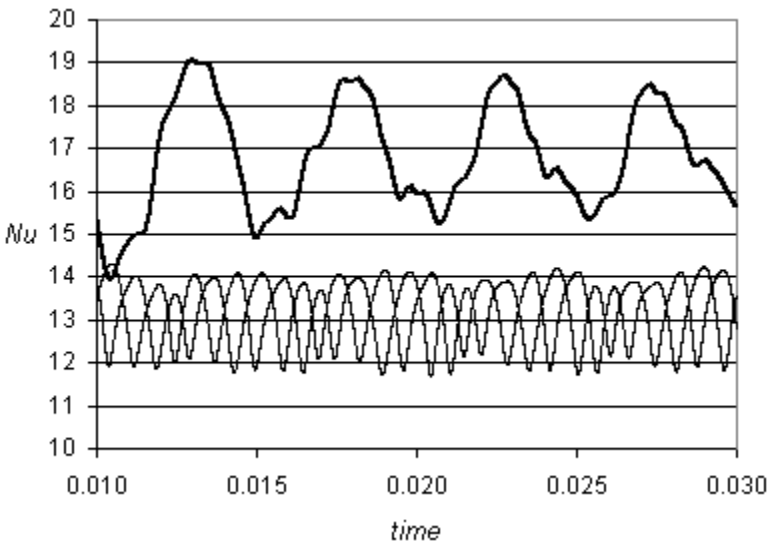

Figure 3: Evolution of mid plane (bold line) and wall Nusselt numbers at $Ra = 10^7$.

3.2 Heat transfer

Characteristic values of the solutions are given in Table 1. Maximum velocities at the cavity axes and Nusselt numbers are steady state values for *Ra* up to 10^6 and time averages for higher *Ra*.

Table 1: Maximum velocities and overall Nusselt numbers.

Ra	U_{max}	V_{max}	$\overline{Nu}_{mid}$	$\overline{Nu}_{cold}$
10^5	55.699	81.286	4.118	3.359
10^6	124.271	256.319	8.241	6.601
10^7	460.31	861.77	16.75	13.16
10^8	1358.32	2592.63	31.07	23.91
10^9	4501.25	7839.38	56.98	42.98

All velocities are a 15–20% higher than the corresponding values for the adiabatic problem. Nusselt numbers are in general lower than their adiabatic counterparts are. This holds for wall Nusselt numbers at all Ra, but at $Ra = 10^8$ and 10^9, $\overline{Nu}_{mid}$ exceeds the adiabatic value. The results in Table 1 can be expressed by the following equations:

$$Nu_{mid} = 0.16Ra^{0.282} \qquad Nu_{cold} \equiv 0.15Ra^{0.273}$$

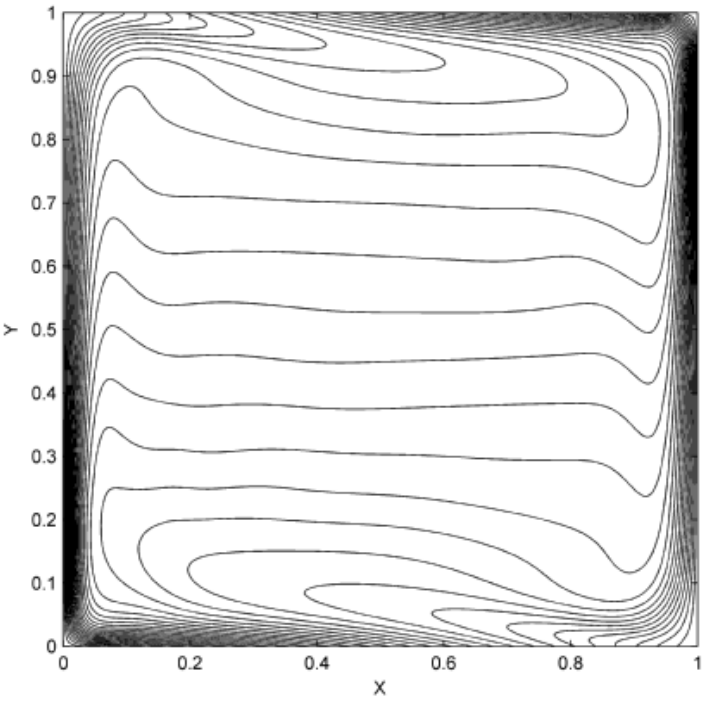

Figure 4: Time averaged temperature field, $Ra = 10^7$.

According to these trends the midline Nusselt numbers would progressively exceed the ones for adiabatic cavities (in which the Rayleigh number exponent is lower) as Ra grows.

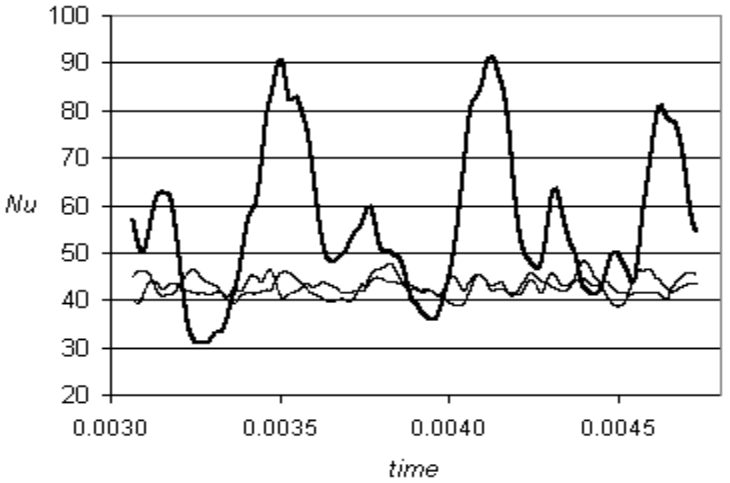

Figure 5: Evolution of mid plane (bold line) and wall Nusselt numbers at $Ra = 10^9$.

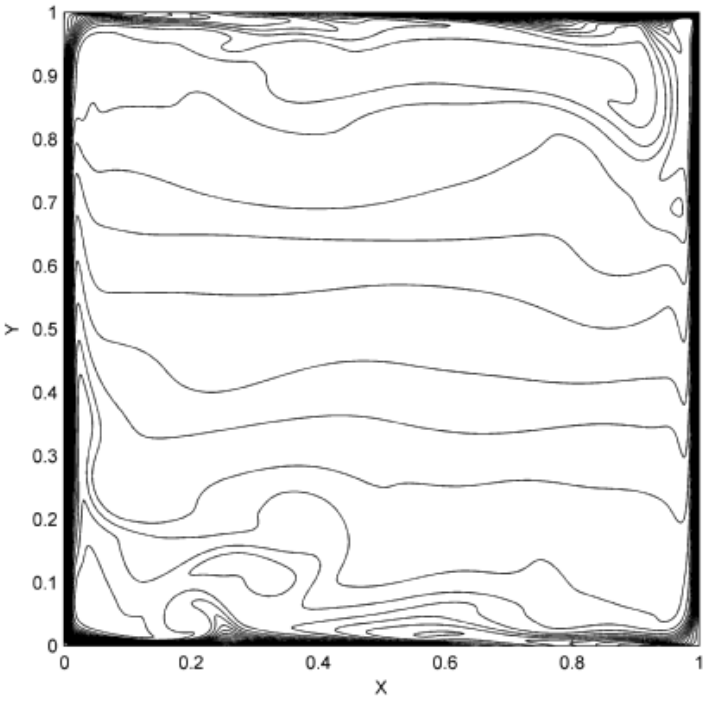

Figure 6: Time averaged temperature field, $Ra = 10^9$.

4 Conclusions

The simulation of the high Rayleigh number cases (up to $Ra = 10^9$) has been done successfully. The phenomenon is characterized by the generation of boundary layers on vertical walls with thickness that decrease as Ra grows. These boundary layers are extended to the adjacent horizontal walls. The internal wave regime characteristic of this phenomenon at all Rayleigh numbers is suppressed in the final regime up to $Ra = 10^6$. At higher Rayleigh numbers internal wave motion remains, with oscillation of high amplitude.

The wall Nusselt numbers, up to $Ra = 10^6$ are equal at all times, during the transient and final regimes. For $Ra = 10^7$ or higher, both wall Nusselt numbers oscillate out of phase.

At $Ra = 10^9$, the oscillations of the two wall Nusselt numbers are completely independent. The Nusselt number behaviour in the present situation had not been described previously. New results of wall and mid plane Nusselt number are the main contribution of this work. At Rayleigh numbers from 10^8 on, the total heat moved by the cavity under the perfectly conducting condition (Nu_{mid}) exceeds the corresponding value for the adiabatic problem.

References

[1] Paolucci, S. & Chenoweth, D.R., Transition to chaos in a differentially heated vertical cavity, *J. Fluid Mechanics*, **201**, pp. 379–410, 1989.

[2] Paolucci, S., Direct numerical simulation of two-dimensional turbulent natural convection in an enclosed cavity. *J. Fluid Mechanics*, **215**, pp. 229–262 1990.

[3] Le Quéré, P. & Behnia, M., From onset of unsteadiness to chaos in a differentially heated square cavity, *J. Fluid Mechanics*, **359**, pp 81–107, 1998.

[4] Fusegi, T., Hyun, J.M., Kuwahara, K. & B. Farouk, B., A Numerical Study of Three-dimensional Natural Convection in a Differentially Heated Cubical Enclosure, *Int. J. Heat Mass Transfer*, **34**, pp. 1543–1557, 1991.

[5] Janssen, R.J.A. & Henkes, R.A.W., Instabilities in three-dimensional differentially heated cavities with adiabatic horizontal walls, *Phys. Fluids*, **8**, pp 62–74, 1996.

[6] Tric, E., Labrosse, G. & Betrouni, M., A first incursion into the 3D structure of natural convection of air in a differentially heated cubic cavity, from accurate numerical solutions, *Int. J. Heat Mass Transfer*, **43**, pp. 4043–4056, 2000.

[7] Leong, W.H., Hollands, K.G.T. & Brunger, A.P., Experimental Nusselt numbers for a cubical cavity benchmark problem in natural convection, *Int. J. Heat Mass Transfer*, **42**, pp. 1979–1989, 1999.

[8] Henkes, R.A.W. & Le Quéré, P., Three dimensional transitions of natural convection flows, *J. Fluid Mech.*, **319**, pp. 281–303, 1996.

This page intentionally left blank

Natural convection in tubes – a solar water heating application

V. M. Kriplani[1] & M. P. Nimkar[2]
[1]*Department of Mechanical Eng., G.H.R.C.E., Nagpur, India*
[2]*Department of Mechanical Eng., PIET, Nagpur, India*

Abstract

The present work deals with experimental studies on heat transfer and flow characteristic for buoyancy induced flow through inclined tubes. The parameters that were varied during the experimentation are tube inclination and heat supply. It was found that the mass flow rate and the heat transfer coefficient increase with an increase in heat flux. The flow rate decreases for an increase in the tube inclination.

Keywords: thermo siphon, natural convection, buoyancy induced flow, solar water heating system, uniform wall heat flux, renewable energy.

1 Introduction

Heat transfer by natural convection inside the tube (circular or square) has a large number of applications in industries. These include solar water heating systems, cooling of gas turbine blades, heat exchangers etc. The heat transfer and flow characteristics with respect to various parameters play a vital role for the design of such systems .The present work is carried out with a specific application in mind, i.e. domestic solar water heating systems.

Presently most of the dimensions of solar water heaters are standardized from some other commercial consideration and not necessarily giving the best thermo-siphon results. Little information is available in the literature on the heat transfer characteristics for buoyancy-induced flow through inclined tubes [1–4]. The present work aims to study the effect of tube inclination and heat flux on heat transfer and flow characteristics for buoyancy induced flow through inclined tubes, and to develop an experimental model. Hence this work is undertaken.

WIT Transactions on Engineering Sciences, Vol 59, © 2008 WIT Press
www.witpress.com, ISSN 1743-3533 (on-line)
doi:10.2495/AFM080391

2 Nomenclature

a = Side of the square tube (m)
h= Heat transfer coefficient ($W/m^2\,^oC$)
q = Heat flux (W/m^2)
m' = Mass flow rate (ml/min)
g = Acceleration due to gravity (m/sec^2)
t = Temperature, (^oC)
k = Thermal conductivity (W/m^oC)
C_p = Specific heat at constant pressure, (kJ / kg K)
DIMENSIONLESS NUMBER
Gr = Grashof Number ($\beta\, g\, \Delta T\, a^3 / \nu^2$)
Nu = Nusselt Number ($h\, a / k$)
Pr = Prandtl Number ($\mu\, C_p / k$)
Ra = Rayleigh Number (Gr Pr)
Re =Reynolds Number ($4\, m' / (\prod a \mu)$)
GREEK SYMBOLS
θ = Angle of Inclination (degree)
β = Coefficient of Thermal Expansion, K^{-1}
ν = Kinematic Viscosity, (m^2 / sec)
μ = Dynamic Viscosity, (N-s /m^2)

3 Experimental set-up

A schematic of the test set up is shown in Fig.1. It consists of a long aluminum tube. The tube is wound uniformly with a 90-gauge Nichrome wire to provide a uniform heat flux condition on the tube surface. The power supplied is measured directly with the help of a pre-calibrated digital wattmeter. The tube was insulated to reduce the external heat loss. The tube is connected to a constant headwater tank and the flow is measured with the help of a calibrated measuring jar. Thermocouples were used to measure the wall and water inlet and outlet temperatures. The arrangement and methodology suggested by Prayagi and Thombre [4] was adopted for this purpose. Thermocouples were used to measure the wall temperature.

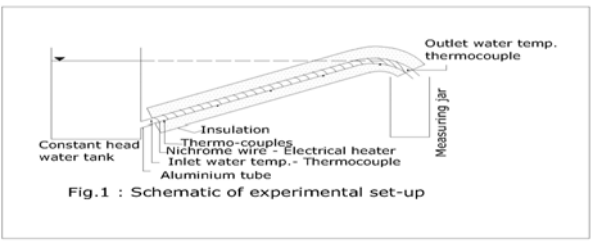

Figure 1: Schematic of experimental set-up.

Thermocouples were used to measure the inlet and outlet temperature of water flowing through the tube. A linear temperature variation was assumed from the inlet to the exit of the flowing water. It is well justified since the boundary condition created at the tube surface is a uniform heat flux boundary condition. The dimensional details of the experimental set-up and the parameters varied during the experimentation are given in table 1.

Table 1: Details of the experimental set-up.

Sr.No.	Parameter	Range
1	Tube length	1.5m
2	Square tube side	0.012 m
3	Tube inclination (θ)	20^0, 30^0, 45^0 and 60^0
4	Heat flux supplied (q)	200 W/m^2 to 7000 W/m^2
5	Insulation used	Asbestos
6	Fluid used	Water

4 Results

The steady state data generated in the experimental set-up for different values of tube inclination and heat flux where correlated for heat transfer and flow characteristics as described below.

4.1 Heat transfer characteristics

The increase in the heat transfer coefficient for different values of tube inclination with respect to heat flux is shown in fig.2. It represents the effect of heat supplied on the fully developed heat transfer coefficient for the test section of 20 degree inclination, 12mm side square tube and 1.5 m length.

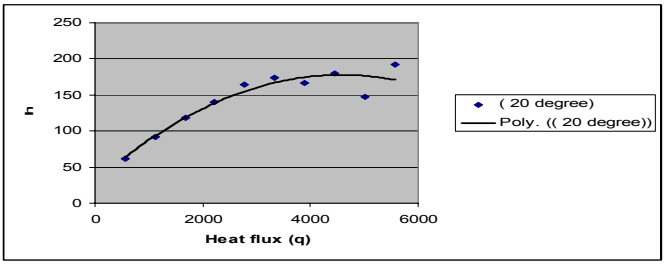

Figure 2: Heat transfer characteristics.

It can be seen from the fig.2 that with an increase in the value of heat supplied, the heat transfer coefficient tends to increase. This is due to the fact that with an increase in heat supplied the buoyancy force tends to increase. The net effect of this is to increase the mass flow rate of liquid through the tube. The same trend was observed for the other configurations.

Conventionally the heat supplied (the main driving force) is represented by the Rayleigh number, whereas the heat transfer coefficient is represented by the Nusselt number. Hence in the present study the heat transfer characteristics are obtained by correlating the Nusselt number with the Rayleigh number.

Fig. 3 shows the plot between the Nusselt number and the Rayleigh number for all configurations investigated.

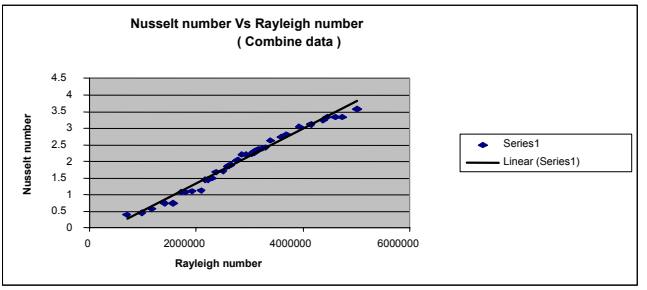

Figure 3: Nusselt number versus Rayleigh number.

It can be seen from this figure that the Nusselt number increases with an increase in the Rayleigh number. This is an expected result, since an increase in the Rayleigh number increases the buoyancy force and hence the flow rate and the Nusselt number. Typically for an increase in the Rayleigh number of about 50%, the increase in the Nusselt number is around 30%. This is attributed to the fact that if heat supplied is increased, the corresponding system equilibrium temperature will also increase, thereby leading to more heat loss from the system. Furthermore, the increase in heat loss depends upon the heat capacity of the liquid. The higher the heat capacity, the lower will be the heat loss and vice versa. The correlation (best fit curve) obtained from the fig.3 is as follows.

$$Nu=1*10^{-9}Ra^{1.442} \quad (1)$$

This equation is valid for Rayleigh numbers ranging from 7×10^5 to 5×10^6 and Reynolds numbers ranging from 0.3658×10^2.

4.2 Flow characteristics

Figure 4 represents the effect of heat flux on the flow rate for the test section with 20 degree inclination, 12mm side tube and 1.5m length. The following observations were made:

a. The induced flow rate increases with the heat supplied and the variation is nearly parabolic.
b. The same trend was also observed for other configurations investigated.

Conventionally the heat supplied for the buoyancy force is represented by the Rayleigh number, whereas the induced flow rate established is represented by Reynolds number. Hence to obtain mass flow characteristics, the Reynolds number is correlated with the Rayleigh number. The relevant data is plotted in the fig.5. It can be seen from the figure that the Reynolds number increases with an increase in the value of the Rayleigh number.

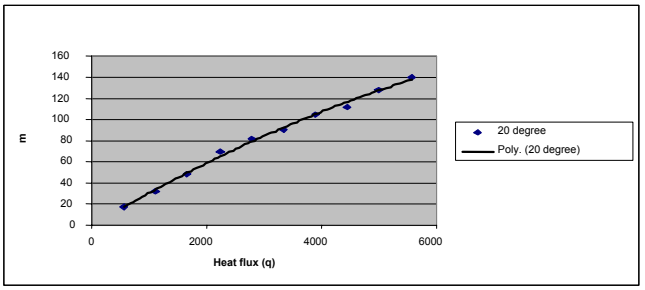

Figure 4: Flow characteristics.

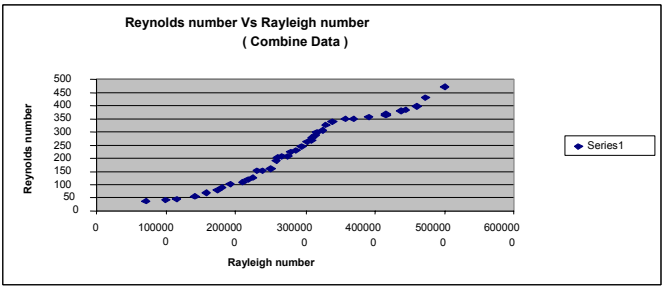

Figure 5: Reynolds number versus Rayleigh number.

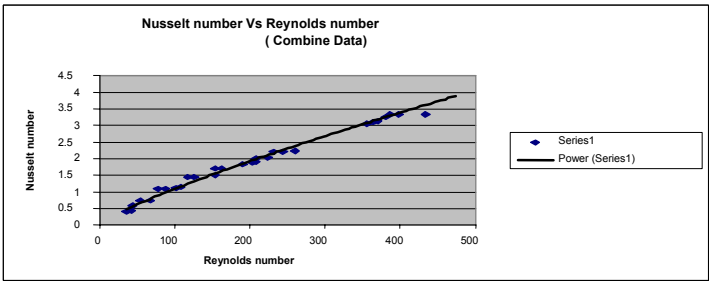

Figure 6: Nusselt number versus Reynolds number.

The Reynolds number increases with an increase in the value of the Rayleigh number. Typically it was observed that for an increase in the Rayleigh number from 3 x 10^5 to 4 x 10^5, the percentage increase in the value of the Reynolds number was around 30-35%. This is an expected variation as an increase in the Rayleigh number increases the buoyancy force, which results in a higher mass flow rate. Thus from the above analysis it can be concluded that the Reynolds number is dependent upon the Rayleigh number.

The correlation (best fit curve) obtained from the fig.6 is as follows.

$$Nu = 0.029 * Re^{0.7864} \quad (2)$$

This correlation is valid for Reynolds numbers ranging from 0.3658 x 10^2.

5 Validation

The present experimentation was validated against the laminar forced convection, which is available in the literature i.e.

$$Nu = ha/k = 4.36$$

6 Conclusions

Experiments were performed to study heat transfer and flow characteristics for buoyancy induced flow through inclined square tubes with different inclinations and variations in heat flux. The following observations were made.

6.1 Heat transfer characteristics

- The heat transfer coefficient is strongly influenced by heat flux.
- When the heat flux increases, the heat transfer coefficient also increases.
- The heat transfer coefficient is found to be the weak function of the tube inclination.

The correlation obtained is as follows:

$$Nu = 1 * 10^{-9} Ra^{1.442}$$

This equation is valid for Rayleigh numbers ranging from 7 x 10^5 to 5 x 10^6 and Reynolds numbers ranging from 0.3658 x 10^2.

6.2 Mass flow rate characteristics

- The mass flow rate increases with the heat supplied and the variation is parabolic.
- The mass flow rate is strongly influenced by heat flux.
- The mass flow rate is found to be practically independent of the tube inclination and tube length.

The correlation obtained is as follows:

$$Nu = 0.029 * Re^{0.7864}$$

This equation is valid for Reynolds numbers ranging from 0.3658 x 10^2.

7 Scope for future work

The present study needs to be extended further as suggested below.

- The experimental data should be generated for air as in the case of air heaters operating under natural convection.

- It is also proposed to change the fluid inlet temperature by placing the heater in between the inlet fluid tank and the test section, in order to study the effect of a change in the inlet temperature of fluid on the heat and mass transfer characteristics.
- Insertion of twisted strip or fins on the test section in order to enhance the heat transfer.
- It is also proposed that using a different aspect ratio (i.e. length to diameter ratio), an experiment should be performed to study the effect of diameter and length on heat and mass transfer characteristics.
- Mathematical models should be developed for heat transfer as well as for mass-flow rate and must be compared with the experimental data generated. This mathematical model will be helpful for an optimum design of the solar water collector system.
- Extensive experimental data should be generated to study the effect of twisted strip insertion inside the tube on the heat and mass flow characteristics. A mathematical correlation should be developed, in order to strike a balance between the parameters mentioned above for an optimum design.

References

[1] Akhtar N.A., Ali S.S., Siddiqui M.A., *Heat transfer and fluid flow in open loop thermo siphon with a inclined tube,* Journal of Heat & Mass Transfer, PP. 313–317, 1995.

[2] Agrawal C.P. Alam S.S., & Gopalkrishna N.: *Heat transfer studies in a vertical tube of a closed loop,* Indian Chemical Engineers XXI (3), PP.37–39, 1979.

[3] Ozoe, H. Sayama, Churchill S.W.: *Natural convection in an inclined rectangular Channel at various aspect ratios and angles –Experimental measurements,* International Journal Heat & Mass Transfer Vol.18, PP 1425–1431.

[4] Prayagi S.V. and Thombre S.B.: *Heat Transfer and Fluid Flow Characteristics for Buoyancy Induced Flow through Circular Ducts*, Proceedings, 6th ISHMT/ASME & 17th National HMT conference, Kalpakkam, 2004

[5] Prayagi S.V. and Thombre S.B.*: Effect of Inlet temperature on Buoyancy Induced Flow in a Circular Ducts Fitted with Twisted strip,* Proceedings of IMECE 2005. ASME International Mechanical Engineering Congress and Exposition, Orlando, Florida, 2005.

[6] Randy Clarksean, Greg Philips (Idaho) *A Parametric study of heat transfer with in a planar thermo siphon,* National Heat Transfer Conference Atlanta Aug 8-11, 1993.

[7] Kuan-Tzong,: *Laminar natural convection heat & mass transfer in vertical rectangular*, International Journal of Heat & Mass Transfer, Vol - 42, Issue - 24, 4523–4534. 1999.

[8] Dyer J.R., *The development of laminar natural convective flow in a vertical uniform heat flux duct,* International Journal of Heat & Mass Transfer, Vol-18, Issue -12, 1455–1465, 1975.
[9] Abdul-Wahed R.M: *Experiments on laminar flow and heat transfer in an elliptical duct,* International Journal of Heat & Mass Transfer, Vol- 27, Issue-12, 2397–2413, 1984.
[10] Siegwarth D.P.: *Effect of secondary flow on the temperature field and primary flow in a heated horizontal tube*, International Journal of Heat & Mass Transfer, Vol-12, Issue-12, 1535–1552, 1969.
[11] Ozoe Hiroyuki, *Natural convection in an inclined rectangular channel at various aspect ratios and angles*, International Journal of Heat & Mass Transfer, Vol-18, Issue-12, 1425–1431, 1975.
[12] Sukhatme S. P.: *A Text Book on Heat Transfer* 3rd ed., Orient Longman Ltd., Bombay 1989.
[13] Ozisik M.N.: *Heat Transfer: A basic approach*, McGraw Hill, New York.
[14] Sharma P.C.: *Power Plant Engineering* 6th Edition, 1988.
[15] S.B. Thombare, *A Data Book on Thermal Engineering.*
[16] *Engineering Index*, VNIT, Nagpur.

Numerical simulations of variable density starting jets

S. Benteboula[1,2] & G. Lauriat[3]
[1]*UPMC Univ Paris 06, UMR 7598, Laboratoire Jacques-Louis Lions F-75005, Paris, France*
[2]*CEA Saclay, DM2S/SFME/LTMF, 91191 Gif sur Yvette Cedex, France*
[3]*Université Paris-Est, Laboratoire de Modélisation et Simulation Multiéchelle FRE 3160 CNRS, 77454 Marne-la-Vallee, France*

Abstract

This work aims at developing computing tools for the numerical simulation of impulsively started jets with variable physical properties due to large thermal gradients. The fluid is injected at temperature T_j and density ρ_j in a quiescent surroundings at different temperature and density T_a, ρ_a. The 3D-time dependent Navier–Stokes equations, formulated in the low Mach number approximation, were numerically integrated by using a non divergence-free projection method. The computations were performed for 3D and axisymmetric jets, and for a wide range of the jet-to-ambient density ratio, $\alpha = \rho_j/\rho_a$, providing the expected flow features. Except the formation of a leading vortex in the head of the flow followed by a jet stem, the results show that the behaviour and the dynamics are quite different for hot and cold jets. The hot jet is indeed characterised by a leading vortex in which the hotter fluid is concentrated, while the vortex ring is a region of intermediate temperature and density for a cold jet. Particular attention is given to the influence of α on the integral characteristics of vortex rings such as circulation and impulse.
Keywords: numerical simulation, anisothermal vortex ring, low mach number flow, variable density.

1 Introduction

The fluid injection through an orifice or a nozzle in a stagnant atmosphere leads to the generation of a vortex ring followed by a tail. Vortex rings are encountered


WIT Transactions on Engineering Sciences, Vol 59, © 2008 WIT Press
www.witpress.com, ISSN 1743-3533 (on-line)
doi:10.2495/AFM080401

in nature, cyclones, human heart, and in several industrial applications such as internal combustion engines. Experimentally, the vortex ring is obtained with a piston-cylinder mechanism by pushing a column of fluid. The boundary layers at the orifice edge separate and roll up into a vortex ring which detaches from the rear flow and travels downstream induced by its own momentum. During its evolution, the vortex grows by viscous diffusion and entrainment of the surrounding fluid. For long-time injections, Kelvin–Helmholtz instabilities may develop in the trailing layer with more vortex interactions.

Vortex rings were the subject of numerous studies based on the constant density assumption. For a general review on the generation, formation, evolution and interaction of vortex rings, the reader could refer to Shariff and Leonard [1].

Theoretically, there are two models that predict evolution laws of the vortex characteristics. The first one (Saffman [2]) relies on the similarity theory while the 'slug-flow' model estimates the circulation, impulse and energy, using the injection program only.

In the present work, started jets with large density and temperature differences are investigated to get an insight into more complicated flows such as combustion which involves vortex ring dynamics. The flow is assumed to be laminar and the injection velocity small enough to consider applicable the formulation of the 3D Navier–Stokes equations derived in the low Mach number approximation. This model, proposed by Majda and Sethian [3] for combustion problems with premixed flames, is intermediate between the compressible and incompressible Navier–Stokes equations. Few results are available in the open literature about the variable density vortex rings, in particular the influences of the jet-to-ambient density ratio on the vortex characteristics. To our best knowledge, there is only a brief recent communication of Iglesias *et al.* [4] in which the authors suggest an extension of the 'slug-flow' model to estimate circulation of variable density vortex rings.

Computations of variable density flows at low Mach number by using fully compressible Navier–Stokes equations solvers are not well adapted for industrial flows. This is due to the large differences between the acoustic and the advective scales. Thus, very small time steps are required for stability conditions.

In this study, an incompressible algorithm [5] was extended to handle non divergence-free velocity flows ($\nabla \cdot \mathbf{v} \neq 0$). This approach is used in different ways by several authors (see Nicoud [6], Cook and Riley [7], Najm *et al.* [8]). By applying the low Mach number approximation to the Navier–Stokes equations, acoustic waves are removed while the convective modes are described. In these conditions, large density variations due to thermal effects are allowed irrespective of pressure fluctuations, for instance, in combustion.

In what follows, the mathematical model of the Navier–Stokes equations is first introduced within the framework of the low Mach number approximation. We describe then the numerical procedure used to integrate the governing equations. Results for variable density vortex rings simulations with different ratios α are discussed for both cases of hot and cold jets. The simulations are compared to the reference case of an incompressible vortex ring ($\alpha = 1$).

2 Governing equations

The fully compressible Navier–Stokes equations are nondimensionalized by using the reference quantities associated to the injected fluid. Let D_j^*, V_j^*, ρ_j^*, T_j^* be the orifice diameter, velocity, density and temperature, respectively. The buoyancy forces are neglected. We define the Mach, Reynolds and Prandtl numbers as:

$$Ma = V_j^*/\sqrt{\gamma r T_j^*}, Re = \rho_j^* V_j^* D_j^*/\mu_j^*, Pr = \mu_j^* C_p^*/\lambda_j^*.$$

All the primitive variables of the flow are then expanded in power series law of the small parameter ϵ ($\epsilon = \gamma Ma^2 \ll 1$). Under the hypothesis that the flow is fully described by the advective space and time scales, the single scale asymptotic analysis (Müller [9]) leads to the following Navier–Stokes equations of zero order.

– continuity equation

$$\frac{\partial \rho_0}{\partial t} + \nabla \cdot (\rho_0 \mathbf{v}_0) = 0 \tag{1}$$

– momentum equations

$$\frac{\partial (\rho_0 \mathbf{v}_0)}{\partial t} + \nabla \cdot (\rho_0 \, \mathbf{v}_0 \otimes \mathbf{v}_0) = -\nabla p_1 + \frac{1}{Re} \nabla \cdot \overline{\overline{\tau}}_0 \tag{2}$$

The shear stress tensor $\overline{\overline{\tau}}_0$ for a Newtonian fluid is given by

$$\overline{\overline{\tau}}_0 = -\frac{2}{3} \mu (\nabla \cdot \mathbf{v}_0) \cdot \overline{\overline{I}} + \mu (\nabla \mathbf{v}_0 + \nabla^t \mathbf{v}_0)$$

The viscosity variation is approximated by the following power law

$$\mu = T_0^\sigma \quad \text{with} \quad \sigma \approx 0.5 \tag{3}$$

– energy equation in term of density

$$\frac{\partial \rho_0}{\partial t} + \mathbf{v}_0 \cdot \nabla \rho_0 = -\frac{1}{T_0} \left[\frac{1}{RePr} \nabla \cdot (\mu \nabla T_0) \right] \tag{4}$$

Eq. (4) is obtained by combining the energy, the continuity equations and the equation of state (see Cook and Riley [7]). Another form of the energy equation can be derived in term of temperature (see Najm *et al.* [8]).

At the order -1, the momentum equations reduce to

$$\nabla p_0 = 0. \tag{5}$$

The most important outcome of the low Mach number approximation is the splitting of the pressure into two components: a thermodynamic pressure p_0 constant in space and allowed to vary in time according to Eq. (5), and a dynamic pressure p_1 decoupled from density and temperature fluctuations. Since we are considering an open computational domain, the thermodynamic pressure p_0 is also

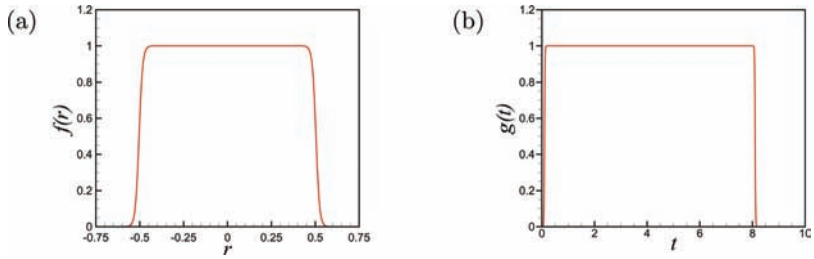

Figure 1: (a) Radial profile at the orifice exit, (b) velocity injection program.

constant in time and is given by the equation of state for an ideal gas

$$p_0 = \rho_0 T_0 = 1 \tag{6}$$

The equations are formulated in cylindrical coordinates (r, θ, z) for the set of conservative variables $(\rho, \rho q_r, \rho v_\theta, \rho v_z, p)$, where $q_r = r v_r$.

Initial and boundary conditions

At $t = 0$, the density and temperature fields are assumed uniform within the computational domain, $\rho = \rho_a = 1/\alpha, T = T_a = \alpha$. Moreover, the dynamic pressure and all the velocities are set equal to zero.

At $z = 0$, injection conditions are applied: $\rho v_z(r, t) = f(r)g(t)$, $\rho q_r = \rho v_\theta = 0$, where $f(r)$ is the top hat jet profile proposed by Michalke [10] (Fig. 1(a)). The impulsive and longtime injection program $g(t)$ in Fig. 1(b) controls the inflow velocity (see James and Madnia [11]). The density at the orifice $z = 0$ and $0 \leq r < 0.5$ is parameterised by the ratio α, $\rho(r, t) = \rho_a[1 + (\alpha - 1) f(r)g(t)]$. At the exit $z = L_z$, the dependent variables ρq_r, ρv_θ and ρv_z in the momentum equations satisfy the convection equation $\partial X/\partial t + C\partial X/\partial z = 0$. Note that the value of the phase speed $C = 0.5$ does not affect the solution because the velocities at the outlet are corrected at each time step to insure mass conservation. For the density, Neumann condition $\partial\rho/\partial z = 0$ is used. At the axis $r = 0$, symmetry conditions are applied, except for the radial component ρq_r which is set equal zero ($\partial\rho/\partial r = \partial\rho v_\theta/\partial r = \partial\rho v_z/\partial r = \rho q_r = 0$). At the lateral boundary $r = L_r$, Neumann conditions for the density and fluxes are applied ($\partial\rho/\partial r = \partial\rho v_\theta/\partial r = \partial\rho q_r/\partial r = \partial\rho v_z/\partial r = 0$). These conditions allow the entrainment of fluid through the lateral boundary. In the θ direction, periodicity is imposed on all variables.

3 Numerical procedure

The cylindrical computational domain was covered with a staggered grid, the fluxes and velocities being located at the centers of the faces and the scalar variables ρ, T, p at the center of the cells. A centered finite-difference scheme with a second-order accuracy was used for the spatial discretization. A total variation diminishing scheme (TVD) was employed for the conservative part $\nabla \cdot (\rho \mathbf{v})$

of the convective terms in the energy equation Eq. (4), as in Vreugenhil and Koren [12] in order to damp spurious oscillations for high density ratios. The time integration method employed is an extension of the fractional-step method to the low Mach number regime with $\nabla \cdot v \neq 0$. Different schemes (Benteboula [13]) were implemented and tested. The most efficient version in terms of CPU time is described here.

The energy equation was firstly integrated with a first-order Euler scheme

$$\frac{\rho^{n+1} - \rho^n}{\Delta t} = (-A_\rho + D_\rho)^n$$

where A_ρ and D_ρ are the convective and diffusive terms, respectively.

$$A_\rho = \nabla \cdot (\rho \mathbf{v}) - \rho \cdot \nabla \mathbf{v}, \qquad D_\rho = -\frac{1}{T}\left[\frac{1}{RePr}\nabla \cdot (\mu \nabla T)\right]$$

Next, the conservative momentum equations are advanced in time with a fractional-step method by using a second-order explicit Adams-Bashforth scheme. The resolution consists in two main steps:

1– Prediction: in this step, an intermediate solution $\widehat{\rho \mathbf{v}}_c$ is computed as

$$\frac{\widehat{\rho \mathbf{v}}_c - \rho^n \mathbf{v}_c^n}{\Delta t} = -\nabla p^n + \frac{3}{2}(-A_c + C_c + D_c)^n - \frac{1}{2}(-A_c + C_c + D_c)^{n-1}$$

where $\mathbf{v}_c = (rv_r, v_\theta, v_z)$ and A_c, C_c, D_c are the advective terms, coupled viscous terms and second-order derivatives viscous terms, respectively.

2– Projection: in order to satisfy the mass conservation, the following Poisson equation for the variable Φ related to the pressure was solved

$$\Delta \Phi^{n+1} = \frac{1}{\Delta t}\left[\nabla \cdot \widehat{\rho \mathbf{v}}_c + \left(\frac{\partial \rho}{\partial t}\right)^{n+1}\right], \quad \text{where } \left(\frac{\partial \rho}{\partial t}\right)^{n+1} = \frac{3\rho^{n+1} - 4\rho^n + \rho^{n-1}}{2\Delta t}$$

A second-order backward scheme seemed to be well adapted to approximate $\partial \rho / \partial t$ which is generally a source of instability, as reported in Nicoud [6]. The corrected velocity fields are then obtained from the following equation

$$(\rho \mathbf{v}_c)^{n+1} - \widehat{\rho \mathbf{v}}_c = -\Delta t \nabla \Phi^{n+1}$$

The pressure gradient is next updated with $\nabla p^{n+1} = \nabla p^n + \nabla \Phi^{n+1}$.

Finally, the temperature distribution is deduced from the equation of state, $T^{n+1} = 1/\rho^{n+1}$, and the viscosity field from the power law $\mu^{n+1} = (T^{n+1})^\sigma$.

4 Results and discussion

The computational domain is a cylinder of radius $L_r = 3$ and length $L_z = 7$, in which the fluid is injected through an orifice of radius $r_j = 0.5$ located at the center of the cylinder. The cylinder was discretized with a grid of $N_\theta \times N_r \times$

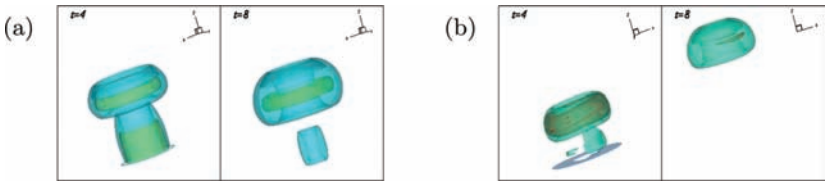

Figure 2: Surfaces of constant vorticity (a) axisymmetric cold jet $\alpha = 2$, $\omega_\theta = -0.5, 2, 5$, (b) disturbed hot jet $\alpha = 1/2$, $\omega_\theta = -3, 1.8, 3.5$.

$N_z = 32 \times 200 \times 500$ cells. For axisymmetric simulations $N_\theta = 1$. We consider $Re = 1000, 2000$ and $Pr = 0.71$ is kept constant. The effect of the jet-to-ambient density ratio is analysed for cold jets $1 < \alpha \leq 8$, isothermal jet $\alpha = 1$ and for hot jets $1/8 < \alpha \leq 1$.

3D simulations of a vortex ring produced by impulsively started jets are shown in Figure 2(a) for axisymmetric cold jet and in Figure 2(b) for disturbed hot jet. It can be seen a roll up of the sheet of vorticity that leads to the formation of a toroidal vortex ring at the head of the flow, followed by a symmetric annular layer. The vortex ring moves downstream by inertial effects and grows by diffusion and entrainment of the surrounding fluid. 3D effects are highlighted in Figure 2(b) by applying a random azimutal perturbation to the spatial profile $f(r)$. The surfaces of constant vorticity demonstrate how the resulting vortex ring is distorted by this perturbation which is shed in the trailing jet.

In the following, the analysis is restricted to axisymmetric flow. The plots in Fig. 3 show the azimuthal vorticity $\omega_\theta = \partial v_r/\partial z - \partial v_z/\partial r$ in the plane (r, z) at the same time $t = 10$. For hot jets, the roll-up of vorticity sheets is more intense and the core diameter of the leading vortex becomes smaller as the injected fluid is hotter. Furthermore, we observe the development of a negative vorticity layer at the head of the vortex as well as in the jet stem. This counter-rotation is due to the baroclinic torque that acts in regions of non-uniform density. On the other hand,

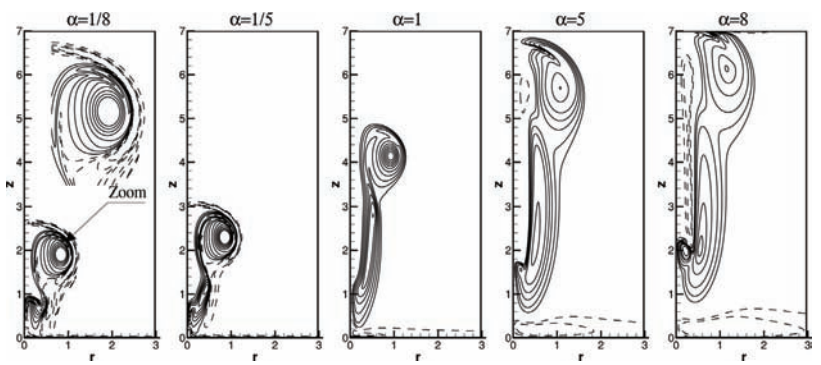

Figure 3: Instantaneous vorticity contours, $t = 10$, $Re = 1000$, for different density ratios, - - - negative vorticity.

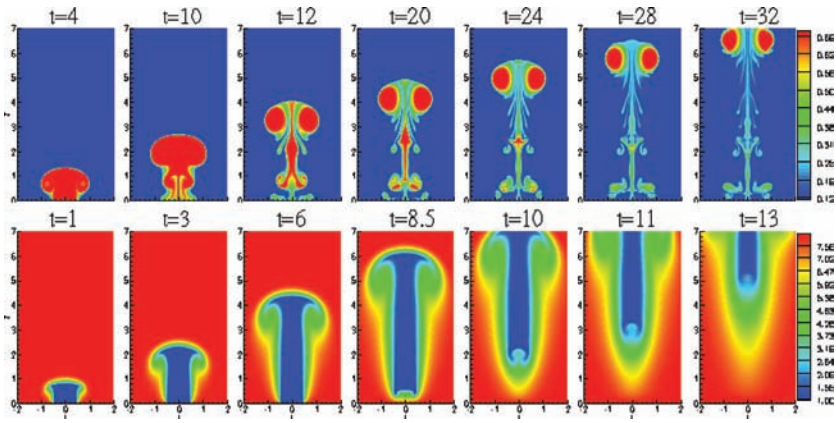

Figure 4: Instantaneous temperature fields: hot jet $\alpha = 1/8$, $Re = 2000$ (up), cold jet $\alpha = 8$, $Re = 1000$ (down).

the cold jet has a more voluminous and more inertial leading vortex which makes its penetration easier. Therefore, the vortex ring grows considerably by thermal diffusion when its vorticity decreases, as can be seen for $\alpha = 8$. It should be noted that the negative vorticity near the inlet section is due to the formation of the stopping vortex.

The temperature fields are shown in Fig. 4, during and after the injection, for both hot and cold jets with strong density contrasts. It is worth noting that the Reynolds number being based on the jet properties, the kinematic viscosity of the surrounding flow is smaller than the hot jet one by a factor $\alpha^{1+\sigma}$. The high temperature fluid, initially distributed at the orifice section, is progressively conveyed toward the vortex ring. At time $t = 12$, the hot fluid is trapped into the vortex core while the ambient fluid is led into the axis region for $t > 12$. Moreover, a sort of wake appears in the trailing flow with vortex pairing near the orifice exit. The maps in Fig. 4 (down) show that the colder fluid remains concentrated around the axis while the outer layer in contact with the surroundings is heated. Unlike the hot jet, the temperature values in the vortex core are now intermediate between those of the injected fluid and ambience. This outcome is due to the increase in thermal diffusivity with the temperature for constant Pr.

The jet front, z_f, is defined as the position on the axis where the scaled density $(\rho - \rho_a)/(\rho_j - \rho_a)$ is equal to 0.5. Except during the initial time development, the curves in Fig. 5(a) display a linear evolution with an increase in the slope with α. As expected, the cold jet having more inertia and evolving into a surroundings of lower density, travels much faster and spreads all the more quickly as α increases. While, the more viscous heated jets penetrate into the ambience more slowly. The corresponding front velocity, $U_v = dz_f/dt$, is shown in Fig. 5(b). Irrespective to the ratio α, the velocities considerably drop at the beginning of the vortex generation ($t < 2$). They reach then an almost constant value, mainly for cold jets. The hot jets velocities exhibit a drop at the end of the injection program ($t = 8$).

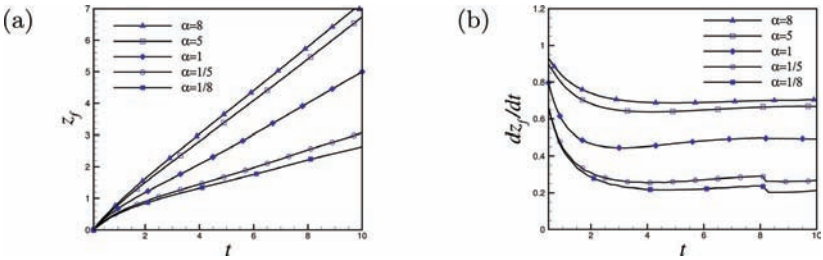

Figure 5: Time evolution (a) jet front, (b) front velocity for different α.

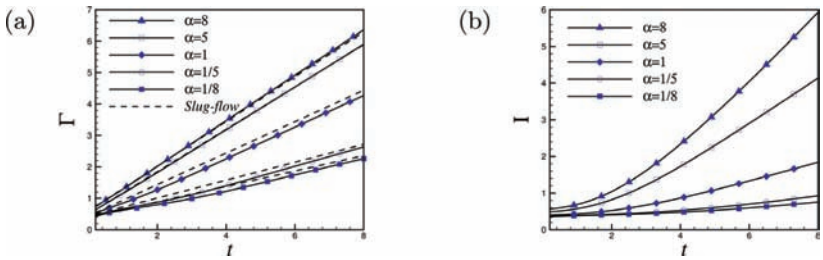

Figure 6: Time evolution : (a) —- total circulation, - - - Slug-flow circulation, (b) impulse.

The time evolution of the total circulation, $\Gamma = \int_0^{L_z} \int_0^{L_r} \omega_\theta dr dz$, is compared to the circulation, $\Gamma = \frac{1}{2} + \frac{t}{2}[1 + U_v^2(1-\alpha)]$, predicted by the slug-flow model (Iglesias *et al.* [4]) for different ratios α in Fig. 6. This model assumes a constant velocity at the orifice equal to the piston one and requires a prior knowledge of the vortex velocity U_v which is computed in a post-processing (Fig. 5(b)). The circulation presents an almost linear evolution, in particular, for cold jets. The growth rate of the circulation is larger when increasing values of α. The comparison with the slug-flow model shows a rather good agreement although this model overestimates the circulation for hot and isothermal jets. The discrepancies are partly due to non-constant hot jets velocities and to the contribution of the radial component of the velocity which is neglected in the slug-flow model.

The hydrodynamic impulse $I = \pi \int_0^{L_z} \int_0^{L_r} \omega_\theta r^2 dr dz$ delivered in the streamwise direction by the vortex is more important for cold jets compared to hot jets. Significant growth during the fluid discharge is noticed for $\alpha = 8$. The large differences between the impulse curves are mainly due to the influence of the vortex sizes in the crosswise direction r. To account for the smaller values of circulation and impulse for hot jets, we can examine the plots of the vorticity in Fig. 3. Indeed, the vorticity is considerably higher compared to that of the cold jet but at the same time it is in part balanced by the negative one in the integration. Furthermore, the vortices are confined in a narrow region in the vicinity of the orifice rim. On the other hand, even if the vorticity of the cold jet is small, the vortex is shed on much broader region.

5 Conclusion

A computational code for simulating variable density jets and appropriate for dealing with strong density and temperature contrasts was developed. Simulations performed for different injection cases of hot or cold fluid allow to describe the jet flow dynamics and thermals. The influences of the jet-to-ambient density ratio on the vorticity and temperature distributions as well as on the characteristics of the leading vortex ring (circulation, jet front and impulse) are discussed. These effects are found to amplify when increasing the density ratio α. Our results are in a good agreement with the theoretical slug-flow model.

References

[1] Shariff, K. & Leonard, A., Vortex rings. *Ann Rev Fluid Mech*, **24**, pp. 235–279, 1992.
[2] Saffman, P.G., The number of waves on unstable vortex rings. *J Fluid Mech*, **84**, p. 625, 1978.
[3] Majda, A. & Sethian, J., The derivation and numerical solution of the equation for zero mach number combustion. *Combust Sci Technol*, **42**, p. 185, 1985.
[4] Iglesias, I., Vera, M. & Antonio, L.S., Simulations of starting gas jets at low mach numbers. *Phys Fluids*, **17**, p. 038105, 2005.
[5] Danaila, I. & Benteboula, S., Etude numérique et théorique des structures tourbillonnaires dans une injection gaz-gaz. simulations numériques directes avec les codes jetles et avbp. Technical report, Paris 6 et Institut Français du Pétrole, 2004.
[6] Nicoud, F., Conservative high-order finite-difference scheme for low-mach number flows. *J Comput Physics*, **158**, pp. 71–97, 2000.
[7] Cook, A.W. & Riley, J.J., Direct numerical simulation of a turbulent reactive plume on a parallel computer. *J Comput Physics*, **129**, pp. 263–283, 1996.
[8] Najm, H.N., Wyckoff, P. & Knio, O.M., A semi-implicite numerical scheme for reacting flow. *J Comput Physics*, **143**, p. 381, 1998.
[9] Müller, B., Low mach number asymptotics of the navier-stokes equations. *Journal of Ingineering Mathematics*, **34**, pp. 97–109, 1998.
[10] Michalke, A., Survey on jet instability theory. *Prog Aerospace Sci*, **21**, p. 159, 1984.
[11] James, S. & Madnia, C.K., Direct numerical simulation of a laminar vortex ring. *Phys Fluids*, **8**, p. 2400, 1996.
[12] Vreugenhil, C.B. & Koren, B., *Numerical methods for advection-diffusion problems*, volume 45. Vieweg, Braunschweig, 1993.
[13] Benteboula, S., *Résolution des équations de Navier–Stokes à faible nombre Mach-Application à l'anneau de vorticité à masse volumique variable.* Ph.D. thesis, Université Paris-Est de Marne-la-Vallée, 2006.

This page intentionally left blank

Modelling the hot rolling process using a finite volume approach

J. A. de Castro & L. P. Moreira
Metallurgical Engineering Post Graduate Program,
Federal Fluminense University, UFF, Brazil

Abstract

A finite volume model for the hot rolling process is proposed to determine useful parameters in the hot rolling such as the loads, temperature, stress and strain fields and the microstructure. A non-Newtonian formulation and a Eulerian description are adopted with the finite volume method. The strain-rate field is firstly obtained from the pressure and velocities solutions. Then, the temperature field together with a constitutive equation provides the apparent viscosity of the material and thus the stress field. The adopted constitutive equations describe the microstructural phenomena occurring in the hot rolling, i.e., work-hardening, recovery and recrystallisation. The predictions obtained with the proposed finite volume model are in good agreement with the industrial measured rolling loads and surface temperatures for the 7-stand finishing mill of a C-Mn steel strip.
Keywords: transport equations, finite volume method, hot rolling.

1 Introduction

The mathematical modelling of the hot rolling process is an extremely hard task because of the deformation coupled to the temperature, the microstructure phenomena as well as the range of temperatures, strains and strain-rates which, in turn, cannot be well reproduced or even monitored under laboratory conditions. The mathematical models for describing the hot rolling process in the literature can vary from roll force and torque models based upon the works of Orowan [1] and Sims [2] up to integrated and stand alone Finite Element (FE) models, e.g., Zhou [3] and Mukhopadhyay et al. [4]. In bulk metal forming processes such as the hot slab or strip rolling, the elastic strains are usually very small in comparison to the high plastic strain levels and then can be neglected.

WIT Transactions on Engineering Sciences, Vol 59, © 2008 WIT Press
www.witpress.com, ISSN 1743-3533 (on-line)
doi:10.2495/AFM080411

This assumption makes possible to consider the deformation process by means of a flow formulation together with the finite volume (FV) method. This approach is adopted in this work where the basic constitutive equations are first presented. Then, the transport equations are detailed for the 3D case in a Eulerian frame. The microstructural changes taking place during the hot rolling process are also taken into account with the flow-stress model used in the commercial software SLIMMER [5]. The predictions forecasted with the proposed FV model are compared to the measured surface temperatures and rolling loads obtained from the hot strip rolling of a low C-Mn steel in an industrial 7-stand finishing mill.

2 Mathematical model

2.1 Viscoplastic finite volume model

In bulk metal forming such as the hot rolling process, the final material properties depend essentially upon the strain, strain-rate and temperature fields. Considering firstly the assumption of small elastic strains, the total strain rate tensor can be decomposed into an elastic part and a viscoplastic part:

$$\dot{\varepsilon}_{ij} = \dot{\varepsilon}_{ij}^{e} + \dot{\varepsilon}_{ij}^{vp} \tag{1}$$

Then, the elastic strains are usually very small in comparison to the plastic or viscoplastic strain levels in the hot rolling process and can, thus, be neglected. The total strain-rate is defined by the viscoplastic model of Perzyna [6]:

$$\dot{\varepsilon}_{ij}^{vp} = \gamma \left\langle \phi(F) \right\rangle \frac{\partial F}{\partial \sigma_{ij}} \tag{2}$$

In eq (1) γ is a fluidity parameter, σ_{ij} is the Cauchy stress tensor, $\langle \phi(F) \rangle = 0$ when $F < 0$ and $\phi(F)$ for $F \geq 0$ where F is the von Mises yield function given by:

$$F = \sqrt{(3/2) S_{ij} S_{ij}} - \bar{\sigma} \tag{3}$$

in which $\bar{\sigma}$ is a scalar measure of the material flow-stress and $S_{ij} = \sigma_{ij} - p\,\delta_{ij}$ is the deviatoric stress tensor where p is the pressure On the other hand, the behaviour of a linear isotropic Newtonian fluid relates the deviatoric stress and the total or the viscoplastic strain-rate tensors through the viscosity μ, that is,

$$S_{ij} = 2\mu\,\dot{\varepsilon}_{ij} \tag{4}$$

The strain-rates are obtained from the velocity field v_i in a Cartesian coordinate system x_i (i = 1,2,3) by:

$$\dot{\varepsilon}_{ij} = \frac{1}{2}\left(\frac{\partial v_i}{\partial x_j} + \frac{\partial v_j}{\partial x_i} \right) \tag{5}$$

Afterwards by introducing firstly the definition of the effective strain-rate conjugated of the von Mises effective stress, Eq. (3),

$$\dot{\bar{\varepsilon}} = \sqrt{(2/3)\dot{\varepsilon}_{ij}\,\dot{\varepsilon}_{ij}} \tag{6}$$

and assuming $\phi(F)$ as an exponential function $(F)^n$ and a viscoplastic loading stable condition of, $(F)^n > 0$, one obtains the viscosity from Eqs. (2)-(4) and (6):

$$\mu = \frac{\bar{\sigma}}{3\dot{\bar{\varepsilon}}} \tag{7}$$

The viscosity nonlinearity is accounted for through the flow stress definition that, in turn, depends upon the accumulated effective strains and strain-rates, the temperature and some internal variables defining the material microstructure. Thus, the material behaviour in bulk metal forming can be considered as rigid-viscoplastic likewise an incompressible non-Newtonian fluid. Furthermore, it should be noted that eq. (7) is only valid for a non-zero effective plastic strain-rate otherwise the material is a rigid body. For numerical purposes of stability, a small cut-off value is set equal to 0.01 s^{-1}.

The material behaviour during the hot rolling process is highly coupled to the temperature and the strain-rate fields. Thus, the solution of the hot deformation is achieved by solving the temperature, velocity and pressure fields simultaneously. For a steady-state flow condition and assuming plastic strain incompressibility, the hot strip motion and temperature are obtained from the transport equations of conservation of energy, momentum and mass. These equations are described in a Eulerian or spatial reference frame. Firstly, the temperature T is calculated from the solution of the energy balance equation:

$$\rho C_p \left(v_i \frac{\partial T}{\partial x_j} \right) = \frac{\partial}{\partial x_j} \left(\frac{K}{C_p} \frac{\partial T}{\partial x_j} \right) + S_P + S_F \tag{8}$$

where ρ, C_p and K are the material density, specific heat per unit volume and conductivity respectively. The first source term S_P in eq. (7) is the rate of energy dissipation per unit volume resulting from the plastic deformation process:

$$S_P = (\eta / J) \int_V \sigma_{ij} \dot{\varepsilon}_{ij} \, dV \tag{9}$$

where η is the fraction of the plastic work, which is transformed into heat and J is the mechanical equivalent of heat. The second source term S_F in Eq. (7) is the rate of energy dissipation due to the friction between the strip and the roll:

$$S_F = \int_S \tau \|\Delta v\| \, dS \tag{10}$$

In eq (10) $\tau = f(\bar{\sigma}/\sqrt{3})$ is the shear stress at roll-strip interface where f is friction factor and $\|\Delta v\|$ is the norm of the velocity discontinuity [7].

Then, the velocity **v** and the pressure p are determined from the solution of the conservation of momentum given by:

$$\frac{\partial}{\partial x_j} (\rho v_j v_i) = \frac{\partial}{\partial x_j} \left(\mu \frac{\partial v_j}{\partial x_i} \right) - \frac{\partial p}{\partial x_i} \tag{11}$$

together with the conservation of mass or continuity equation:

$$\frac{\partial v_i}{\partial x_i} = 0 \tag{12}$$

The transport equations are discretized using the finite volume method for the 3D case of an arbitrary domain, that is, a non-orthogonal domain, together with the "Body Fitted Coordinate" grid generation technique [8].

2.2 Flow-stress model

Figure 1 illustrates the typical flow-stress of low carbon steels deformed at high temperatures, where the mechanisms of work-hardening and restoration can be observed during the hot deformation process. The restoration events are respectively denoted as dynamic and static depending whether they take place concomitantly or not with the loading. At the onset of the deformation process, the material work hardens due to the increase of the density of dislocations, which are arranged into subgrains boundaries. As the plastic strain level rises, the annihilation and generation rates of dislocations are counteracted producing, consequently, a steady-state flow-stress shown by the plateau (a) in this figure. This restoration mechanism is known as dynamic recovery and its resulting microstructure, consisted of well-defined subgrains, is the source of the static recrystallisation nuclei.

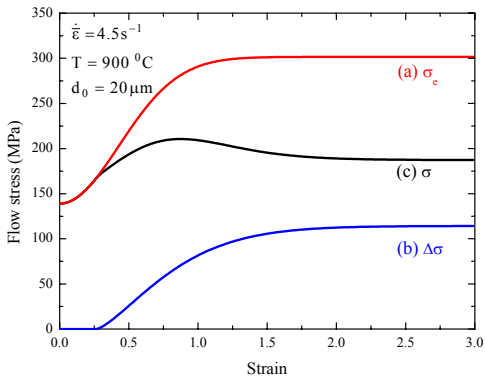

Figure 1: Flow-stress curve of low carbon steels [9].

When the dynamic recovery is the only active restoration mechanism, the flow-stress can be described as [9]:

$$\sigma_e = \sigma_0 + (\sigma_{SS} - \sigma_0)\left[1 - \exp(-C\varepsilon)^m\right] \tag{13}$$

where σ_0 is the flow-stress at zero plastic strain, σ_{ss} is the steady-state flow-stress and m is the work-hardening exponent. C depends upon the Zener-Hollomon parameter, which is defined by $Z = \dot{\varepsilon}\exp[Q/(RT)]$, where Q is the apparent activation energy for deformation, R is the gas constant (8.31 J/K mol) and T is the absolute temperature of deformation. Likewise, the flow stresses σ_0 and σ_{ss} depend upon the deformation conditions and can be generally defined in the form of $\sigma_{FS} = A_1 \sinh^{-1}(Z/A_2)^{A3}$ where A_k are material parameters determined from experimental tests, such as hot plane-strain compression or torsion tests.

Moreover, when the recovery process is insufficient so as to decrease the activation energy of deformation, the multiplication of dislocations may produce the nucleation and growth of recrystallised grains during the hot deformation. In such a case, the flow-stress curve increases up to a maximum value, namely, the peak stress, accompanied by an additional softening reaching a steady-state

value as shown by the plateau in curve (c), see Fig. 1. The onset of dynamic recrystallisation is characterized by a critical strain $\varepsilon_c = a\,\varepsilon_p$ which is estimated from the strain related to the peak in the flow-stress given by:

$$\varepsilon_p = A\, d_0^{p}\; Z^{q} \tag{14}$$

where d_0 is the initial grain size whereas *a*, *A*, *p* and *q* are material parameters.

The softening due to the dynamic recrystallisation, see curve (b) in Fig. 1, can be accounted for as [9]:

$$\Delta\sigma = (\sigma_{SS} - \sigma'_{SS}) \left\{ 1 - \exp\left[-k' \left(\frac{\bar{\varepsilon} - a\,\varepsilon_p}{\varepsilon_p} \right)^{m'} \right] \right\} \tag{15}$$

where σ'_{SS} is the current steady-state flow-stress at large strains whereas k' and m' are material parameters respectively. The curve (c) in Fig. 1 is then obtained by superposing the effects of dynamic recovery and dynamic recrystallisation, namely, $\bar{\sigma} = \sigma_e$ if $\bar{\varepsilon} < \varepsilon_c$ and $\bar{\sigma} = \sigma_e - \Delta\sigma$ if $\bar{\varepsilon} \geq \varepsilon_c$.

It should be noted that for a general state of stress the effective strain $\bar{\varepsilon}$ must be calculated from the deformation strain-history. An appropriate procedure for obtaining the effective strain is achieved from the material derivative in a Eulerian reference frame written in terms of the velocity field and its gradient as:

$$\dot{\bar{\varepsilon}} = \frac{D\bar{\varepsilon}}{Dt} = \frac{\partial\bar{\varepsilon}}{\partial t} + v \cdot \nabla\bar{\varepsilon} \tag{16}$$

where the term referring to the time derivative vanishes for a steady-state flow. Thus, Eq. (15) can be rewritten as a 1st linear, hyperbolic differential equation with a source term to obtain the effective strain, that is, $\rho\,\dot{\bar{\varepsilon}} = \nabla \cdot (\rho\, v\, \bar{\varepsilon})$.

The stored energy resulting from the deformation of dislocations also promotes additional microstructure changes immediately after the unloading. These static restoration mechanisms can also be followed by grain growth if there is enough time between the deformation intervals, as is the case for plate and roughing mills. On the other hand, the hot strip or finishing process is characterized by decreasing time intervals and increasing strain-rates per pass and may, therefore, lead to dynamic recrystallisation followed by metadynamic recrystallisation. The latter starts from the partly or steadily recrystallised structure resulting from the dynamic recrystallisation after a deformation above the critical strain [9]. In order to take into account the partially recrystallised regions that may receive further deformation, the following correction for the effective strain is made:

$$\bar{\varepsilon} = \bar{\varepsilon}_N + (1 - X)\,\bar{\varepsilon}_{N-1} \tag{17}$$

where *N* is the current pass or stand and *X* is the static recrystallised volume fraction after the time *t* and is described by the JMKA model [10]:

$$X = 1 - \exp\left[-0.693\,(t/t_{0.5})^{k} \right] \tag{18}$$

where $t_{0.5}$ is the time needed for half recrystallisation. In plain C-Mn steels the exponent *k* is equal to 1.0 and 1.5 for static recrystallisation and metadynamic recrystallisation mechanisms respectively [10].

The corresponding C-Mn times for half recrystallisation and recrystallised grain sizes *d* for the recrystallisation events are predicted by the equations

proposed in [10]. Also, once recrystallisation is completed, the austenite grain may continue to growth as a function of the available time between the deformation intervals. This further grain growth dependence upon the time for the hot strip rolling of C-Mn steels is described in [10].

2.3 Initial and boundary conditions

Figure 2 illustrates in a Cartesian coordinate system X_i (i = 1,2,3) the mesh used in the numerical simulations of the hot strip rolling. Due to the symmetry, only the half strip thickness is considered.

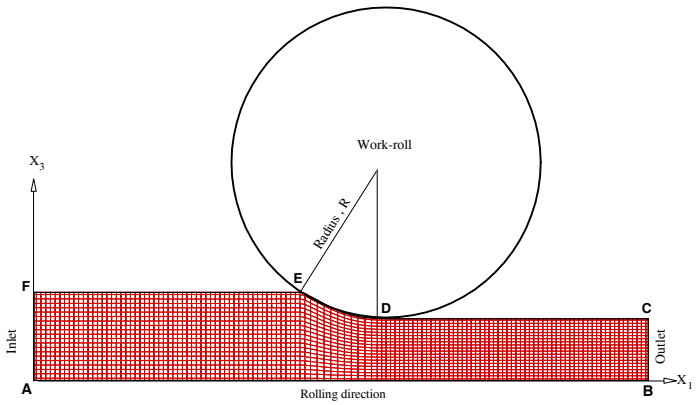

Figure 2: Finite-volume mesh of the hot strip rolling process.

At the free surfaces E-F and C-D, before and after the deformation zone, the dominant heat transfer mechanisms are convection and radiation defined by:

$$-K\left(\frac{\partial T}{\partial X_3}\right) = h\,(T - T_\infty) + \sigma\,\varepsilon\,(T^4 - T_\infty^4) \tag{19}$$

where T_∞ is the surrounding temperature, σ is the Stephan-Boltzmann constant whereas the convection heat transfer coefficient *h* and the emissivity factor ε has been taken equal to 12,5 kW/m^2 K and 0.8 respectively. In the roll-gap, that is, at the contact region D-E between the strip and the work-roll, the heat transfer is mainly by conduction:

$$-K\left(\frac{\partial T}{\partial n}\right) = h_{con}\,(T - T_{WR}) \tag{20}$$

where n stands for the normal direction vector along the arc contact, h_{con} is the roll-gap heat transfer coefficient and T_{WR} is the work-roll temperature.

At the symmetry plane A-B there is no heat flux along the direction X_3, i.e.:

$$\frac{\partial T}{\partial X_3} = 0 \tag{21}$$

as well as for the outlet section B-C along the normal direction X_1, see Fig. 2. The inlet temperature and the velocity field at the inlet section F-A for the first

stand are assumed to be constant whereas the corresponding values at the outlet section B-C are computed from the transport equations described in § 2.1.

3 Material and finishing mill data

The material analyzed has been processed at the CSN steel plant at Brazil and is a C-Mn steel for which the typical chemical composition is shown in Table 1. The plate thickness is equal to 35.4 mm with an average surface temperature of 984.7 ^{0}C and is reduced to 3.90 mm in a 7-stand finishing mill. The strip surface temperatures were measured with the help of an optical pyrometer [11].

Table 2 shows the constitutive parameters describing the typical behaviour of C-Mn steels during hot strip rolling, Eqs. (16)-(21), which have been taken as the values available in the material database of the commercial code SLIMMER [5]. The initial austenite grain size d_0 at the first stand was assumed to be equal to 120 μm. The apparent activation energy Q for the Zener-Hollomon parameter has set equal to 300 kJ/mol whereas the parameter *C* in eq (14) is defined as:

$$C = 10\left[(\sigma_{01} - \sigma_0) \Big/ (\sigma_{SS} - \sigma_0) \right]^2 \tag{22}$$

Table 1: CSN C-Mn steel chemical composition (% of weight).

C	Mn	P	S	Al	Si	N	Nb
0.03	0.25	0.02	0.025	0.025	0.025	0.007	0.005

Table 2: Constitutive material data for C-Mn steels [5].

	σ_0			σ_{SS}	
A_1	A_2	A_3	A_4	A_5	A_6
103.84	4.92×10^{13}	0.13	103.41	1.77×10^{11}	0.217
	σ_{01}			σ'_{SS}	
A_7	A_8	A_9	A_{10}	A_{11}	A_{12}
89.29	2.55×10^{11}	0.182	106.72	3.88×10^{12}	0.146
	$\Delta\sigma$			ε_p	
k'	m'	a	A	p	q
0.49	1.4	0.7	5.6×10^{-4}	0.3	0.17

Table 3 presents the CSN 7-stand finishing mill data and the adopted values for the roll-gap heat transfer coefficient at each stand where the work-roll temperature T_{WR} and the f is friction factor f are assumed to be constant and equal to 200 ^{0}C and 0.25 respectively.

4 Numerical predictions

Figure 3 shows the predicted temperature and flow stress distributions obtained for the first stand where a temperature increase is observed near to the strip central region up to the exit due to the conduction heat and generation from the plastic-work. In the roll bite region a strong variation of the flow stress is

observed as consequence of high deformation rate and deformation. The flow stress increases to about 200 MPa due to the temperature decrease in the contact region with the work-roll.

Table 3: CSN plant 7-stand finishing mill and heat transfer data [11].

Stand	F1	F2	F3	F4	F5	F6	F7
Work-roll radius (mm)	366	366	356	343.5	358.5	366	358.5
Initial thickness (mm)	35.40	24.8	17.13	11.68	8.37	6.12	4.70
Thickness reduction (%)	30	30.9	31.8	28.4	26.8	23.2	15.2
h_{con} (kW/m^2 K)	5	6	8.4	9.5	12.1	15.5	16.7

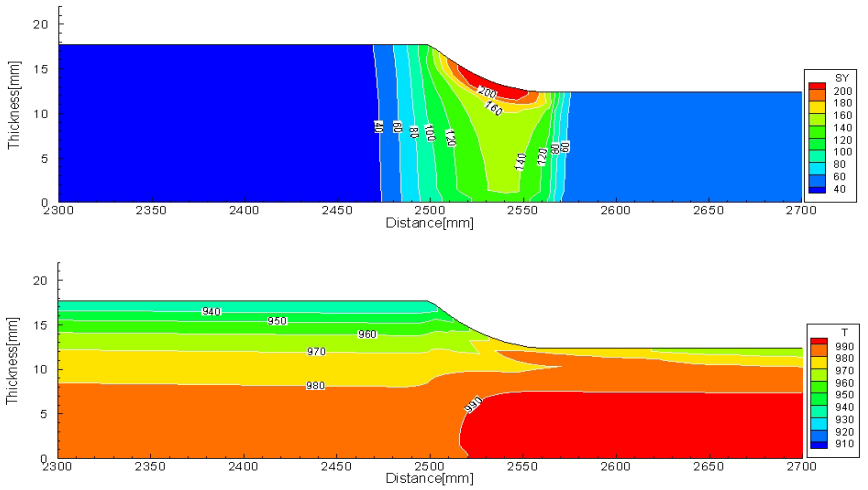

Figure 3: Predicted temperature (^{0}C) and flow stress (MPa) distributions obtained for the first stand of the hot rolling of a C-Mn steel strip.

Table 4 compares the numerical predictions with the measured rolling load data determined from the industrial rolling of a C-Mn steel strip. First of all, the FV model proposed in this work provides a very good prediction for the rolling loads. Secondly, since the deformation zone is strongly non-uniform, as can be observed from Fig. 3, the models which take into account uniform variables in this region, for instance, based upon Orowan's or Sim's works [1,2], usually furnish poor predictions of the rolling loads.

On the other hand, Fig. 4 compares the predicted temperature evolution with the interstand measured strip surface temperature. Strong variations of the temperature are observed during the hot strip rolling process. These variations strongly affect the materials properties and hence the rolling load prediction. Consequently, accurate computations of the local temperature are of fundamental importance for the description of the material flow stress and the prediction of material properties during the hot rolling process.

Figure 5 shows the average austenite grain size evolution during the 7-stand finishing mill of a C-Mn. One can observe that the grain growth is stronger in the five first passes due to the longer interpass times and the temperature conditions. Moreover, the range of the predicted grain sizes are in agreement with the expected grain refinement during the hot strip rolling process and with the numerical results obtained by the model proposed in [10].

Table 4: Measured and predicted rolling loads.

Stand	F1	F2	F3	F4	F5	F6	F7
Measured (MN)	12.69	13.07	13.40	10.65	10.50	9.09	5.79
Predicted (MN)	12.68	13.09	13.40	10.56	10.38	9.08	5.68
Error (%)	0.07	0.15	0.00	0.84	1.10	0.11	1.89

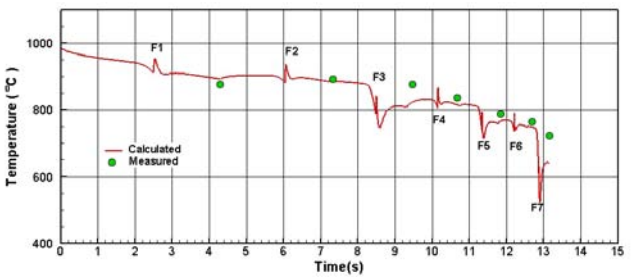

Figure 4: Predicted and measured temperature evolution during the hot strip rolling of a C-Mn steel in a 7-stand finishing mill.

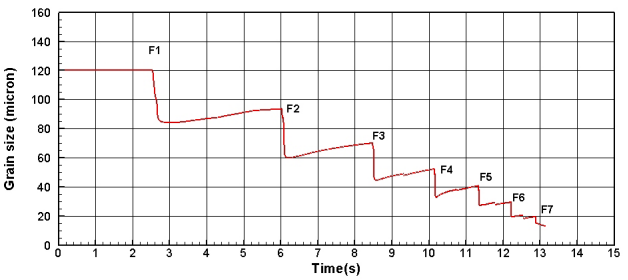

Figure 5: Predicted average austenite grain size evolution during the hot strip rolling of a C-Mn steel in a 7-stand finishing mill.

5 Conclusions

In the present work, a finite volume based model has been developed which takes into account the heat transfer phenomena of the contact region and the combined convective and radiation heat transfer. The microstructural evolution during the hot deformation and interpass processes were also taken into consideration. A constitutive law for low C-Mn steels was used in a local frame in order to consider the simultaneous effects of temperature, strain rates,

deformation and microstructural evolution. The numerical predictions obtained for the temperature evolution and the rolling loads showed good agreement with the measured data from an industrial 7-stand hot strip finishing mill. Moreover, the predicted austenite grain size evolution indicates the typical grain refinement that can be achieved from the thermomechanical processing of low carbon-manganese steels.

Acknowledgement

JAC is grateful to CNPq/Brazil for the research grant.

References

[1] Orowan, E., The calculation of roll pressure in hot and cold flat rolling. *Proceedings of the Institution of Mechanical Engineers*, **150**, pp. 140–167, 1943.
[2] Sims, E., The calculation of roll force and torque in hot rolling mills. *Proceedings of the Institution of Mechanical Engineers*, **168**, pp. 191–200, 1954.
[3] Zhou, S. X., An integrated model for hot rolling of steel strips. *Journal of Materials Processing Technology*, **134(3)**, pp. 338–351, 2003.
[4] Mukhopadhyay, A., Howard, I.C. and Sellars, C.M., Development and validation of a finite element model for hot rolling using ABAQUS/ STANDARD. *Materials Science and Technology*, **20(9)**, pp. 1123–1133, 2004.
[5] SLIMMER, Sheffield Leicester Integrated Model for Microstructural Evolution in Rolling, Pro Technology, University of Leicester, Leicester, United of Kingdom, 1992.
[6] Zienkiewicz, O.C., Jain, P.C. and Oñate, E., Flow of Solids During Forming and Extrusion: Some Aspects of Numerical Solutions. *International Journal of Solids and Structures*, **14(1)**, pp. 15–38, 1978.
[7] Lenard, J.G., Pietrzyk, M. and Cser, L., *Mathematical and Physical Simulation of the Properties of Hot Rolled Products*, Elsevier: Oxford and New York, pp. 105–150, 1999.
[8] Thompson, J. F., Warsi, Z. U. A. and Mastin, C.W., Numerical Grid Generation. North Holland: New York, Appendix C-3, p. 454, 1985.
[9] Beynon, J. H. and Sellars, C. M., Modelling microstructure and its effects during multipass hot rolling, *The Iron and Steel Institute of Japan*, **32(3)**, pp. 359–367, 1992.
[10] Siciliano Jr., F., Minami, K., Maccagno, T. M. and Jonas, J. J., Mathematical Modeling of the Mean Flow Stress, Fractional Softening and Grain Size During the Hot Strip Rolling of C-Mn Steels. *The Iron and Steel Institute of Japan*, **36(12)**, pp. 1500–1506, 1996.
[11] Radespiel, E. S., Silva, A. J., Reick, W. and Silva, M.A.C., Mathematical modelling and numerical simulation of thermomechanical and microstructural evolution of steels during hot-rolling, THERMEC'97, ed. T. Chandra, TMS, pp. 217–223, 1997.

Section 7
Industrial applications

This page intentionally left blank

Air flow induced vibration of the head carriage arm in a simulated hard disk drive using a large eddy simulation

K. Sundaravadivelu & Z. Qide
Mechatronics & Recording Channel Division,
Data Storage Institute, 5 Engineering Drive 1,
Singapore 117608

Abstract

Air-flow induced vibration of the simplified head carriage arm (HCA) in a simulated hard disk drive (HDD) is carried out using the large eddy simulation (LES). The dynamic Smagorinsky-Lily sub-scale model is employed to predict the turbulent air flow characteristics between two co-rotating magnetic disks of a simplified 3.5inch HDD model. The HCA is assumed to fly in between the two disks at two different positions viz., inner (ID) and middle (MD) disk diameters, while the disks are rotating at 10000 rpm. Predicted airflow characteristics are found to be in good agreement with the measurements. A large turbulent eddy is formed near the leading edge of the HCA, which in turn amplifies the unsteady aerodynamic forces acting on the HCA. The resulting aerodynamic forces are used as input for the structural analysis to predict the air flow induced HCA vibrations. The magnitudes of the in-plane and the out of plane vibrations when the HCA is positioned at ID are found to be 0.26nm and 4.8 nm respectively. In the case of HCA positioned at MD they are found to be 0.35nm and 11 nm respectively. Therefore it is inferred that in this simulated HDD model study the out-of-plane vibration is stronger than its corresponding in-plane vibration. This may in turn affect the flying height of the magnetic head. The numerical predictions are verified with observations and found to be in better agreement.

Keywords: air flow, hard disk drives, large eddy simulation, vibration, HGA, HCA.

WIT Transactions on Engineering Sciences, Vol 59, © 2008 WIT Press
www.witpress.com, ISSN 1743-3533 (on-line)
doi:10.2495/AFM080421

1 Introduction

The recording density of hard disk drives (HDDs) is increasing 60% every year targeting 1 Tb per square inch by 2012 [1]. In order to meet up with this increasing trend, the positioning accuracy of the magnetic head must be significantly improved. For instance, the fly height of the magnetic head above or beneath a rotating magnetic disk should be less than 20 nm and similarly the tolerance of the in-plane vibration should be within ± 10nm. But one of the major issues in the HDD positioning is the air flow-induced vibration of the head gimbals assembly (HGA) coupled with the vibration of the head carriage arm (HCA) caused by spinning of the magnetic disks. The resulting airflow is turbulent and hence generates unsteady pressure fluctuation that promotes the structural vibration. Hence it is very critical to overcome this issue for increasing the recording density in future HDDs.

Tsuda et al. [2] using direct numerical simulations (DNS) studied the effect of weight saving holes on the actuator arm flying above a magnetic disk rotating at 10000 rad/s. They observed that a three-dimensional spiral vortex in the wake region of the arm and the flow spilled from the weight saving hole. They explained that this type of flows could be the excitation source for the actuator arm vibration. Their predictions were found to be in good agreement with the measured wind disturbance.

Nakamura et al. [3] experimentally examined the characteristics of windage with the goal of enabling the development of smaller-windage HGA's. They conducted experiments under various conditions such a different slider radius locations, disk-rotational speeds, different fly heights, etc. They predicted that when the slider was positioned at a fixed location, the windage was proportional to the square of the disk rotational speed. Further they observed that at high temperatures, the resonant frequencies decreased and their amplitudes increased. Also they inferred that for some resonance modes there was an optimal fly height.

Aruga and Sugawa [4] conducted experimental and numerical studies on 10000 and 15000 rpm drives and found that most of the structural disturbances on the HGA/HCA are caused by air-flow induced vibration. In addition, they concluded that the flow-induced vibration becomes severe in the region between two rotating disks than between a rotating disk and a stationary cover. They performed LES and observed a similar trend.

Recently Ikegawa et al. [5] reported numerically (LES) that the air flow pattern changes in a HDD with the introduction of a bypass and a spoiler and the confirmed the same with the help of particle image velocimetry (PIV) observations. Their analyses reveal that the introduction of spoiler decreases the flow velocity near the arm by decreasing average flow velocity between the disks such as diverting the flow into the bypass channel, and by moving the high-speed-flow area toward the inner-radius area of the disks. They concluded that the arm vibration reduced by 30% with these modifications. In continuation to these investigations a numerical attempt has been made in this paper to predict the air flow induced vibration of the HCA in a HDD model using the large eddy simulation (LES).

2 Physical model

A real hard disk drive is shown in figure 1. The actuator arm (also called as HCA) together with the other important mechanical components are shown here for a better understanding. Whereas figures 2a and b depict the simplified HDD models used in this study with the HCA positioned at disk inner (ID) and middle diameters (MD) respectively. Although the present model is more simplified outside the disk region it is still useful to obtain fundamental understanding of the turbulent flow characteristics in a HDD. Note that we have also carried out LES on a more realistic HDD model and some of those results will be discussed in the conference. The current model consists of two co-rotating plexi-glass disks (95 mm diameter and 2 mm thickness) with an inter-disk spacing of 4.9 mm.

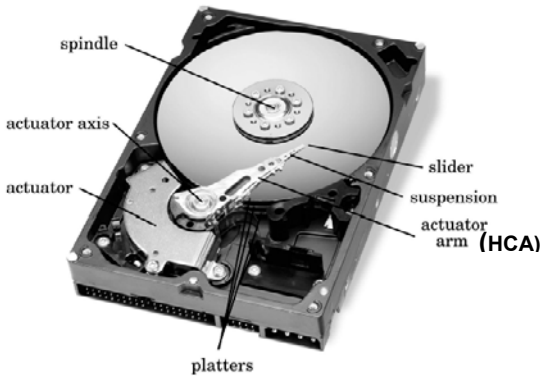

Figure 1: Schematic of a real HDD.

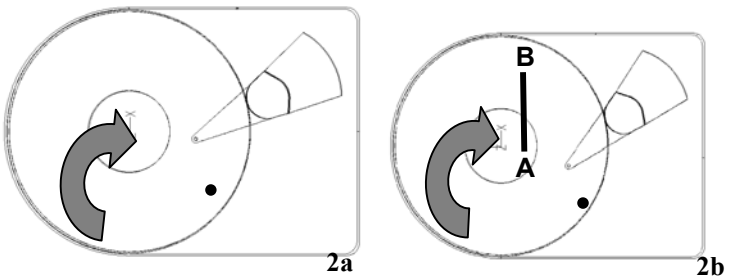

Figure 2: Simulated HDD models with the HCA positioned at a) inner disk diameter and b) middle disk diameter.

Three aluminum HCA's of 2 mm thickness are introduced in the middle of the gap formed between i) two co-rotating disks ii) top cover and first disk and iii) bottom cover and second disk respectively.

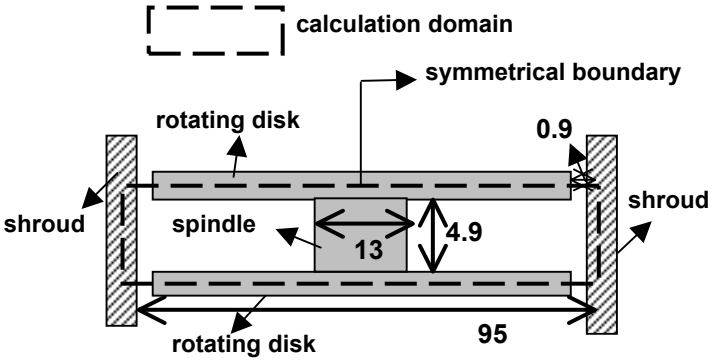

Figure 3: LES calculation domain between the disks (HCA not shown here, all dimensions are in mm).

However, for the present study only the region between two co-rotating disks as shown in figure 3 is considered. The disk rotational speed is set at 10000 rpm and rotated in clockwise direction.

3 Numerical model

The unsteady turbulent flow analysis is carried out using LES with the help of finite volume method. The equations governing the turbulent air flow are the filter-averaged grid-scale Navier-Stokes equations,

$$\frac{\partial}{\partial t}u_i + \frac{\partial}{\partial x_j}(u_i u_j) = -\frac{1}{\rho}\frac{\partial}{\partial x_i}p + \frac{\partial}{\partial x_j}(\nu\sigma_{ij} - u_i' u_j'),$$

and the equation of continuity,

$$\frac{\partial}{\partial x_i}(u_i) = 0,$$

where $u_i (\mathrm{i} = 1,2,3)$ are the velocity components, σ_{ij} are the components of stress tensor, p is the pressure, ρ is the density and ν is the kinematic viscosity. The subscripts indicate each direction in Cartesian coordinate and they comply with the summation law. The primed quantities are the fluctuation components of the sub grid scale and are modeled by using Dynamic Smagorinsky-Lily model, [5]. These equations are solved together with the well-defined boundary conditions. That is, all the flow variables are assumed to be symmetric with respect to symmetrical boundaries shown in figure 3. For the rotating spindle and disks, we applied velocity boundary condition of the rotational speed associated with the revolution of the disks. The no-slip boundary condition is applied on all other stationary walls namely on the arm, shroud, etc.

4 Method of simulation

The rotational Reynolds number based on the disk radius is first calculated and found to be 3.5×10^5. Based on the rotational Reynolds number different Kolomogrov scales viz. the length, time and velocity scales are then estimated. With reference to the length scales a structured mesh is constructed using GAMBIT [6] in such a way that 80% of the total energy scales is resolved thus ensuring that the present LES calculations are carried out on a sufficiently fine mesh. This amounted to a total number of 2 million grid cells in the whole calculation domain. The first computational cell next to each of the walls is found at $y^+<1$, where y^+ is the non-dimensional wall distance. The commercial CFD code FLUENT [7] is then used to solve the governing equations using the segregated approach. The spatial and time derivatives are approximated using bounded central-differencing and second order upwind discretization schemes. The time step used in this study is 10 μs, which is twice higher than the calculated Kolomogrov time scale. Thus to simulate one complete disk revolution, 600 time steps are required. The initial condition to start the LES is obtained by perturbing a converged RANS model solution. Thereafter transient computations were carried out for about 60ms (10 revolutions) so as to allow the flow become statistically steady. After the flow became statistically steady transient data in terms of the fluid forces and fluid flow variables were collected for about 18ms, at 10 μs time step, for performing the statistical analysis and generating input conditions (through a in-house developed code) to the structural code. Subsequently the input conditions were fed into the commercial FEM code ANSYS [8] for calculating the HCA vibration. The FEM model constructed consists of 46272 solid elements. The fluid forces acting on the HCA's surface nodes were extracted from the CFD solver and then mapped onto the surface nodes of the respective solid elements using an in-house developed code. The solid material assigned to the HCA is aluminum with the density 2700kg/m^3; the Poisson's ratio 0.33 and the Young's Modulus 6.9×10^{10} kg/m.s^2. Full transient structural analysis using the HHT time integration method [8] is performed to obtain the displacement of the HCA.

5 Results and discussion

Numerical simulations of turbulent air flow characteristics in a simulated HDD model is carried out using LES in order to understand the head carriage arm vibration due to air turbulence. Firstly we validate the LES calculations using the in-house LDA measurements. Comparison of the mean velocity magnitude on the mid-plane between co-rotating disks along the line AB (see figure 2b) is shown in figure 4. It is found that the predicted mean velocity compare well with the measurements. Hereafter the two different cases namely the HCA at ID and MD cases will be referred as ID and MD in short.

Figures 5a and b depict the velocity magnitude contours on the whole mid plane for the ID and MD cases. Also superimposed on the same figures are their respective in-plane path lines. A large turbulent eddy is seen near the upstream

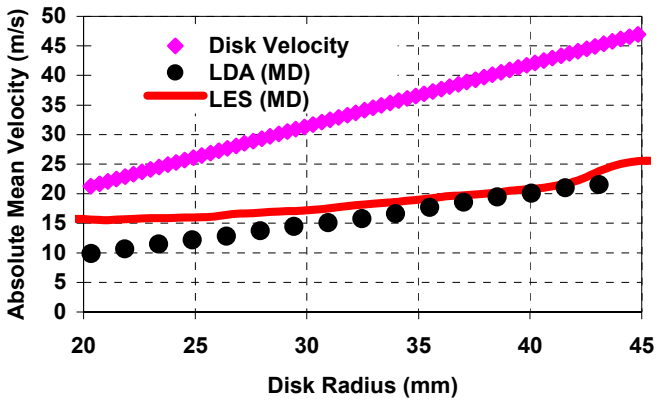

Figure 4: Comparison of predicted mean velocity against the LDA measurements for the case where HCA is positioned at MD and disks spinning at 10000 rpm.

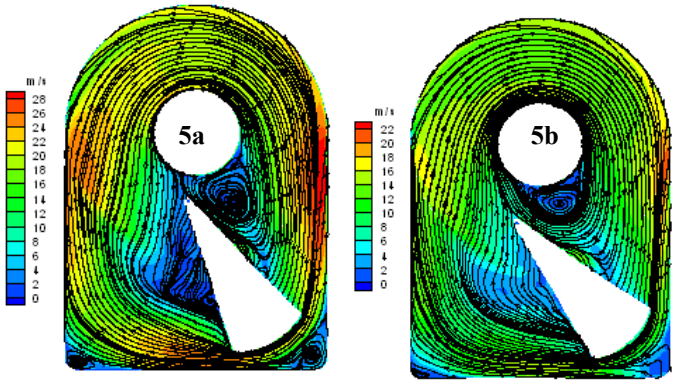

Figure 5: Mean velocity magnitude and streamlines on the mid-plane between two rotating disks for a) HCA at ID and b) HCA at MD.

surface of the HCA in both the cases. However the size is found reduced in MD than in ID. Furthermore the mean kinetic energy of this turbulent eddy in ID is found to be higher than that of in MD. This implies the turbulent activity is more pronounced in MD than in ID. The presence of large size eddy in the ID case allows only a small amount of air to strip through the gap between the HCA edge and the spindle. Hence large amount of air flows through the backside of the arm on this mid-plane. This is not the same in MD (see figure 4b).

The intensity of the turbulent activity around the HCA region for ID and MD case are shown in figures 6a and 6b. In general it is found that the air blowing on the arm surfaces in the case of MD is more violent than in the case of ID. Specifically, as explained earlier, the eddy formed near the upstream surface of the HCA in MD is more turbulent than in the case of ID.

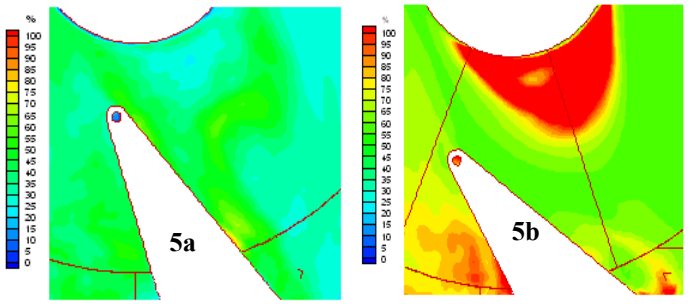

Figure 6: Turbulence intensity ($u'/\bar{u}$) around the HCA region on the mid-plane for the cases a) HCA at ID and b) HCA at MD, disks spinning at 10000 rpm.

That is the turbulent kinetic energy of this unsteady vortex is found to very high than the mean flow energy. Also observed is that the flow re-entering the disk region from backside of the HCA is more turbulent in MD than in ID (see the downstream region of the HCA in figures 6a and 6b). Thus it is inferred from figures 5 and 6 that the head carriage located at the middle disk diameter amplifies air turbulence and hence generating unsteady pressure fluctuation around the HCA region. This unsteady pressure fluctuation in terms of the form drag induces HCA vibration. The presence of the unsteady fluid vortex in the HCA upstream region also aids in generating unsteady pressure fluctuation. Hence by avoiding the formation of any turbulent vortices around the HCA region may help in reducing the vibration magnitude to a large extent. The dynamic pressure distribution around the HCA region is shown in figures 7a and b for both ID and MD cases. It is very clear from these figures that the unsteady pressure fluctuations are stronger around the HCA region in MD than in ID.

Having collected the transient forces for a period of 18 ms (~3 disk revolutions) after the flow became statistically steady the in house code was used to map the fluid forces on to the respective surface nodes of the FEM model. After mapping the forces acquired at all time-steps are combined together as one single input file and fed into the structural code to calculate the HCA displacement. Having calculated the displacement of all the nodes in the FEM model, only a few nodes on the HCA surfaces were selected to understand the HCA displacement. However, herewith we present the results of only one particular node located at the leading edge of the HCA (indicated by a black dot in figure 2).

A modal analysis is performed prior to the displacement calculation to confirm the correctness of the constraints by calculating the first four natural frequencies of the HCA. These four frequencies correspond to 1st bend, 2nd bend, 1st torsion and 1st sway type of modes respectively and their values are provided in table 1.

Figures 8–10 show the leading edge node displacements in the frequency domain along different axis for both the ID and MD cases. Specifically figures 8 and 9 show the frequency spectrum of the in-plane (x-y plane) displacement of the HCA positioned at both inner and middle disk diameters.

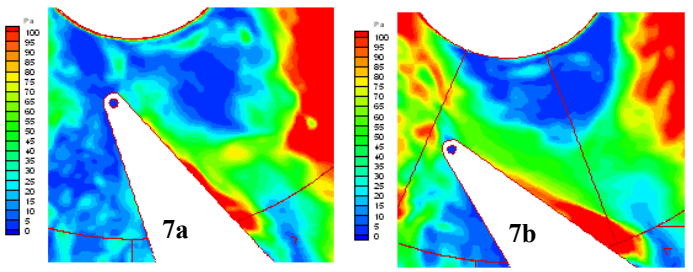

Figure 7: Dynamic pressure distributions around the HCA region on the mid-plane for the cases a) HCA at ID and b) HCA at MD, disks spinning at 10000 rpm.

Table 1: Modal analysis of the first four natural frequencies (Hz).

Natural Freq.	1st	2nd	3rd	4th
Solid Arm	2336	2590	5019	6733
Mode	1st bend	2nd bend	1st torsion	1st sway

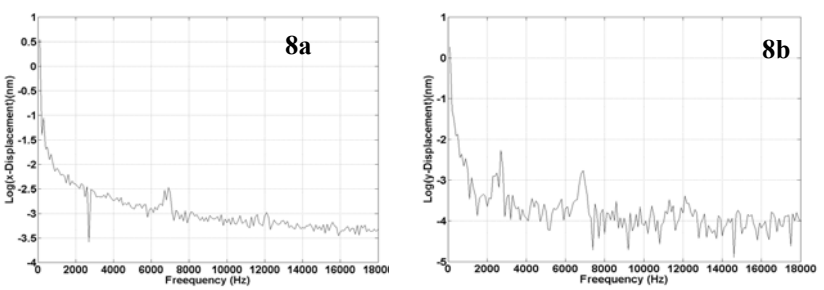

Figure 8: FFT of HCA leading edge node for the ID case with the disks spinning at 10000 rpm. a) x-displacement, b) y-displacement.

It is found from these figures that the air turbulence is more pronounced in the MD case and hence resulting in larger in-plane displacement namely 3.5 nm when compared to that of the ID case (0.26 nm). In both cases the second bend (2.8 kHz) and the sway natural modes (6.8 kHz) of the HCA appear to have the largest spikes in the spectrum. Air flow induced vibration magnitude of the head carriage arm is found to have an absolute mean of 6.95 nm and 8.4 nm and peak-to-peak range of about 3.2 nm and 2.5 nm respectively in the ID and MD cases.

The out-of-plane displacement (z-displacement) of the HCA in the frequency domain is shown in figure 10a and b for both the cases. As expected from the air flow behavior, the out-of-plane vibration is larger in the case of MD than in the case of ID. The peak-to-peak range in the ID and MD cases is about 18 and 60 nm respectively, whereas their mean values are not found to be altered largely.

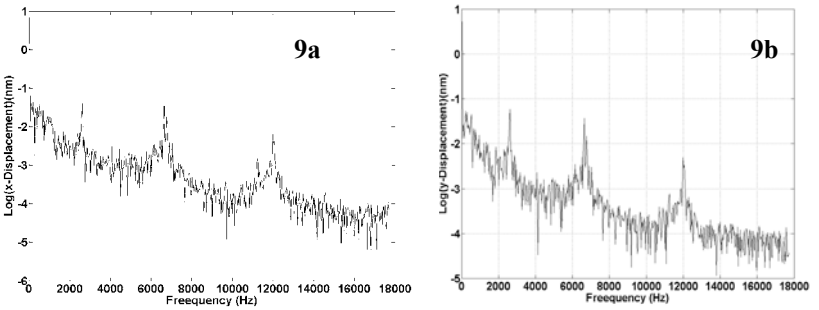

Figure 9: FFT of HCA leading edge node for the MD case with the disks spinning at 10000 rpm. a) x-displacement, b) y-displacement.

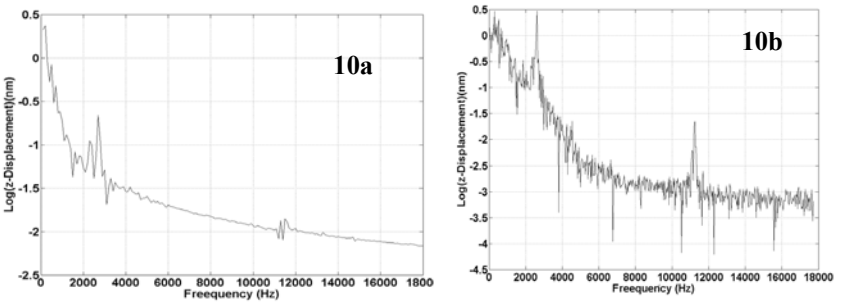

Figure 10: FFT of HCA leading edge node z-displacement with the disks spinning at 10000 rpm. a) ID case, b) MD case.

6 Summary

Large eddy simulations are carried out in a simulated HDD model to understand the turbulent air flow behavior and the flow induced vibration of the head carriage arm. It is inferred that the air flow becomes highly turbulent especially when the HCA is positioned at middle disk diameter and hence the resulting flow induced vibration is very significant. This in turn explain that in a real HDD model the turbulent activity of the air flow may be even more vigorous and complex because the real models are fully shrouded unlike the present model and hence may result in strong vibrations of the magnetic head. But in order to confirm the above conclusion we need to further study this problem in real HDD

model by accounting for various real time parameters, accurate shape and dimensions of the entire head assembly. This is expected to be a very challenging task in terms of the model complexity, numerical modeling and computational cost.

Acknowledgement

We thank Dr. T.H. Yip for providing us with the LDV measurements.

References

[1] P Frank, R Wood, APMRC 2006, Singapore.
[2] N Tsuda, H Kubotera, M Tatewaki, S Noda, M Hashiguchi and T Maruyama, IEEE Trans. Magn., 39(2), 819–825, 2003.
[3] S Nakamura, R Aduma, H Takahashi, K Wakatsuki, S Hagiya, IEEE Trans. Magn., 41(2), 769–773, 2005.
[4] K. Aruga, M. Sugawa, *A Study on Position Error Caused by FIV using Helium Filled Hard Drives*, APMRC 2006, Singapore.
[5] M Ikegawa, Y Hirono, H Mukai, M Kaiho, IEEE Trans. Magn., 42(10), 2594–2596, 2006.
[6] D. K. Lilly, *Physics of Fluids*, 4:633–635, 1992.
[7] GAMBIT Release 2.1 Documentation, 2005.
[8] FLUENT Release 6.3 Documentation, 2007.
[9] ANSYS Release 10.0 Documentation, 2005.

Boiler safety improvement for safety controls utilizing flow measurement for input

D. F. Dyer
Department of Mechanical Engineering, Auburn University, Auburn, Alabama 36849, USA

Abstract

This paper describes a very interesting industrial safety problem and its solutions. Currently, boiler safety controls utilize pressure drop across various boiler elements in an attempt to guarantee adequate combustion air flow, purge air flow, and atomizing media flow. This paper describes various practical situations where these flow measurements are inadequate. Various alternative measures are described to mitigate the problems presented. The paper should serve as a basis for complete re-thinking on these safety controls on both power, industrial, and commercial boilers.
Keywords: boiler, safety control, flow measurement.

1 Introduction

A typical industrial or steam boiler utilizes approximately 50 different alarms and interlocks to satisfy safety for automatic operation. Some of these interlocks require that flow rate be measured and compared to a minimum requirement. There are two kinds of interlocks that are used in the boiler safety control system: 1. pre-ignition or start-up interlocks and 2. running interlocks.

The start-up interlock monitors the pertinent parameter only during start-up and once that parameter is satisfied it allows the boiler to continue in the start-up sequence. Running interlocks are active once the boiler begins firing. These interlocks use a continuously measured signal to shut the boiler down if the pertinent measured parameter does not meet its requirement. A running interlock interrupts boiler operation by causing the closure of two automatic fuel shut off valves. A pre-ignition interlock causes the safety control system to return the boiler to its initial start-up position. Three of these controls are considered in this paper. For each of these controls, the system is described, the problems are

WIT Transactions on Engineering Sciences, Vol 59, © 2008 WIT Press
www.witpress.com, ISSN 1743-3533 (on-line)
doi:10.2495/AFM080431

presented, and solutions are discussed. A much more detailed discussion of boiler safety controls is given in references Dyer [1] and ASME [2] although neither references discusses the problems considered in this paper.

2 Combustion air flow interlock

2.1 Typical system requirements, design, and operation

There is an interlock control which continually monitors flow of combustion air while the boiler is firing. (In other words this is a running interlock as opposed to a start-up interlock). The purpose of this interlock is to guarantee as much as possible that adequate air flow is present at all firing rates for the boiler. The flow rate through the boiler varies dramatically with load-typically the flow rate at minimum firing rate would be 20% of that at maximum firing rate. To guarantee adequate flow rate one would want the signal coming to the interlock to be approximately the same at all firing rates. Another desirable characteristic is that the signal be as large as possible to make the control sensitive and accurate. This interlock typically works by measuring the pressure rise across the combustion air supply fan because the head/flow characteristic for centrifugal fans used is usually fairly "flat" over the operating range of flow rates typically used. A schematic diagram of a boiler showing the flow circuits and safety controls considered in this paper are shown in Figure 1.

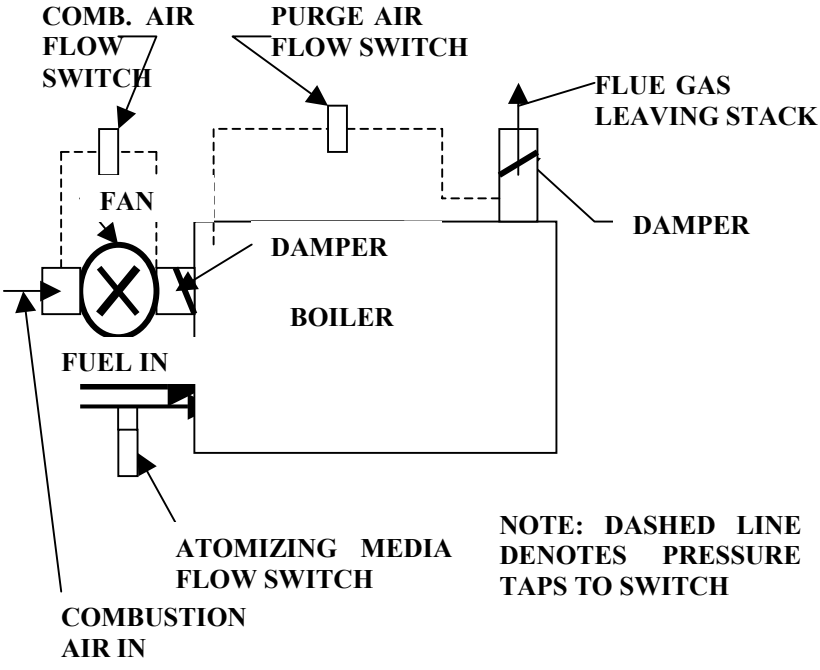

Figure 1: Schematic of boiler and safety system.

2.2 Problems with combustion air interlock arising in applications

Because of rising fuel prices, increasing emphasis is being placed on reducing energy use in boilers. Savings can be obtained by using "O_2 control" by adjusting automatically the relationship between the fuel and air supply rates. This is done by biasing the ratio between the air and fuel supplied to the boiler by continually measuring the $\%O_2$ in stack gases and using this signal in a feedback control system. Probably the best way to accomplish the required bias is to use variable speed control of the combustion fan. Variable speed control produces a linear relationship between speed and flow as opposed to a highly non-linear relationship when dampers or valves are used. In addition, considerable energy savings result from variable speed control. Use of variable speed control introduces a new problem for the combustion air switch because the pressure falls off as the square of the flow rather than remaining essentially linear.

A second problem that occurs is that for some boilers the pressure drop across the boiler system is very low. Hence, the pressure signal generated across the combustion air supply fan is low. This results in a low sensitivity for the control that in turn limits its effectiveness.

2.3 Solutions to problems with combustion air flow interlock

Inadequate flow of combustion air can be sensed by a decrease in $\%O_2$ and increase in combustibles in the stack gas. Reliable, self-checking sensors are now available for continually monitoring these two parameters. The use of one or both of these signals to replace the combustion air flow switch would eliminate the deficiencies of the flow switch. However, the relative costs would be dramatically different. A typical flow switch costs approximately one hundred US dollars while sensors to measure the two stack gas parameters and their inclusion into a control system would cost fifty times that much.

An alternative solution for solving the problem introduced by variable speed control would be to use fan speed to set the limit on pressure at which the safety control shuts down the boiler rather than use a fixed limit. However, at low fan speed the pressure rise produced will be low resulting in low sensitivity. If that is the case one would best resort to the use of $\%O_2$ and combustibles in the stack gas as described above.

3 Purge air flow interlock

3.1 Typical system requirements, design, and operation

The purge air flow interlock system functions as a pre-ignition control to guarantee that adequate purge air has been supplied to the boiler to eliminate combustible gases that would cause a boiler explosion if present at light off of the boiler. Actually, there are several elements in the safety control system to guarantee adequate purge air including a position switch(s) to guarantee that the damper(s) (see Figure 1) are open and an electrical switch to guarantee that

power is being supplied to the combustion fan. However, the purge air flow switch is the most important of this system of interlocks because if it is properly satisfied adequate purge air is being provided. The purge air switch normally utilizes the pressure drop across the "boiler bank" which is the pressure drop from furnace inlet to boiler outlet stack (see Figure 1). To be an effective control the pressure difference employed must be small when the boiler controls are at low fire condition and large at high fire (purge) condition. The interlock functions by requiring the purge air flow switch be "made" in the start up cycle by sensing a pressure that exceeds the required set point.

3.2 Problems with purge air flow interlock arising from applications

The biggest problem encountered in using pressure drop to operate the purge air flow control is that some boilers exhibit almost no pressure drop resulting in a lack of sensitivity for the control. Thus, flow control is not a viable means for guaranteeing that purge air flow requirements are met.

3.3 Solutions to problems with purge air flow interlock

In cases where the purge air flow interlock can not be effective, it is doubly important that the position switch(s) for dampers be in place and operable and that power going to the combustion air fan be monitored. Hence, both of these interlocks should be operable and functioning continuously during the pre-ignition phase (typically they are operable only during the running phase). In addition several different means are used to monitor power to the combustion air fan that includes an auxiliary contact, phase monitors, and current relays. The auxiliary contact and phase monitors do not guarantee that power is being supplied to the fan and, hence, should not be used (over 90% of the systems currently use an auxiliary contact). Current relays measure current in each of the phases feeding power to the fan motor. If no power is being supplied to the motor, no current will be sensed and the safety control system will shut down the boiler.

An alternative approach to the problem would be to use a combustible sensor in the stack to indicate the presence of combustibles and to prevent firing of the boiler. The same sensor that could be used in the running sequence as described in section 2.3 could be used for this purpose.

4 Atomizing media flow interlock

4.1 Typical system requirements, design, and operation

For oil fired boilers, a secondary fluid (atomizing media) is supplied to the burner to atomize (break up) the oil into droplets and distribute it into the combustion air stream. The fluids used are either steam or compressed air. If inadequate flow of the atomizing fluid is delivered to the burner, unstable, incomplete combustion will result. This condition could lead to flame out and potential combustion explosions as well as poor efficiency. The usual setup to

eliminate this problem is to use a differential pressure switch to monitor the pressure difference between the atomizing media and oil. On some boilers there is a "crossover" of pressure with the atomizing media pressure being greater than the oil pressure at low firing condition and lower at high firing condition. A differential switch will not work under this condition because there is no minimum pressure set point that can be used (the pressure difference goes negative at high fire). In this case, a flow switch has been proposed that would measure the flow of atomizing media.

4.2 Problems with an atomizing media flow interlock arising from applications

Although this switch has been proposed and used it provides little protection for the simple fact that the atomizing media flow requirement varies tremendously from the low to high firing condition. Thus, the switch can provide some protection at low fire but virtually no protection at higher firing rates.

4.3 Solutions to problems with atomizing media flow interlock

Since a flow switch can not work, the alternative solutions require a different approach. Probably the best protection is the use of an interlock based on measuring $\%O_2$ in the stack gas as described in section 2.3. The reason why this type interlock will work is interesting. If the atomizing flow decreases, less pressure will exist at the burner nozzle. This reduced pressure will decrease the flow resistance seen by the oil stream. Hence, the oil flow rate will increase which, in turn, will decrease the $\%O_2$ in the stack gas. Obviously, the combustible sensor will also be important in this situation because a high fuel to air ratio will produce combustibles. Therefore, the combustible sensor could become an important part of the solution.

A second solution to the problem, when compressed air is being used, is to use current relays on the power supply to the compressor motor to insure that the compressor is running (see section 3.3). While this is not as fail safe as using combustibles or $\%O_2$ in the stack gas, it does provide a considerable measure of safety.

5 Conclusions

Three safety controls for boilers based on flow measurement are described. Problems in applying these controls in certain situations are discussed. Alternative means to satisfy safety requirements are presented. These solutions are new and are not generally practiced in industry today. The results presented serve as a basis for upgrading existing safety controls to a much higher standard.

There is an urgent need world wide to improve these safety controls and to implement programs to actually test all safety controls on boilers on a regular basis. The authors have found that more than one third of the safety controls on industrial and commercial boilers do not operate properly.

References

[1] Dyer, D.F. et al, Boiler Plant Safety Device Testing Manual, 2nd Edition, 2005, Boiler Efficiency Institute; Auburn, Alabama.
[2] CSD-1 - 2006 Controls and Safety Devices for Automatically Fired Boilers, 2006, American Society of Mechanical Engineers.

Modeling of north triumph gas reservoir for carbon-dioxide Sequestration – a case study

M. Newman-Bennett, M. S. Zaman, M. G. Satish & M. R. Islam
Department of Civil and Resource Engineering,
Dalhousie University, Halifax, Canada

Abstract

Carbon-dioxide is considered one of the major factors for climate change despite its importance for the existence of life on our planet. Apart from several other options, CO_2 can be sequestrated into the depleted petroleum reservoirs to maintain the CO_2-ratio. It can also be used for enhanced recovery due to its solvent-like properties at certain temperatures and pressures. Reservoir modeling plays an important role in evaluating the pros and cons of CO_2 sequestration in a particular reservoir. In this study, we present the preliminary modeling results from North Triumph Gas reservoir for CO_2 sequestration and enhanced recovery.
Keywords: reservoir modeling, history matching, CO_2 sequestration.

1 Introduction

Carbon dioxide is present in the atmosphere and plays a critical role in the photosynthesis reaction that allows plants to grow and its presence is crucial. It also acts as an insulator in our atmosphere so that the global surface temperature remains within a reasonable range. However, it has come to the attention of many scientists that anthropogenic CO_2 may be altering the world's climate. Carbon dioxide is being emitted constantly at increasingly greater rates around the globe. The modern industrial age is contributing great amounts of CO_2 to our atmosphere on a daily basis.

There are several ways to reduce the concentration of CO_2 in the earth's atmosphere. The world, as a whole, could burn less fossil fuel or, the CO_2 that is produced could be captured and stored for long term, or at least until the fossil fuel based economy becomes less significant.

WIT Transactions on Engineering Sciences, Vol 59, © 2008 WIT Press
www.witpress.com, ISSN 1743-3533 (on-line)
doi:10.2495/AFM080441

It is possible to capture CO_2 and store it in locations such as the ocean, coal seams, saline aquifers or oil and gas fields. Each of these sequestration methods has associated advantages and disadvantages.

This paper models a depleted gas field offshore of Nova Scotia for CO_2 sequestration and for enhanced natural gas recovery. For modeling, the geological and petrophysical information available from the Canada Nova Scotia Offshore Petroleum Board (CNSOPB) is reviewed. This information includes the Development Application Plan (DPA) for the field, well logs, geological descriptions, well test reports and historical production data. From this information, a full field scale simulation grid was constructed and initialized honoring the geometry and petrophysical properties of the subject gas field. The simulation model was also initialized with an updated value of initial gas in place, calculated with a material balance equation based on actual production data. Once the model was constructed and initialized, the simulation was run and history matched to finalize the model.

2 Related works

As mentioned earlier, several CO_2 sequestration methods exist, including biomass storage, deep ocean storage, and geological storage.

Biomass sequestration utilizes the photosynthetic process used by plants. It is estimated that a total of 700 million hectares of land might be available globally that could sequester between 220-320 Gt CO_2 (Houghton *et al* [1]). This represents only about 11 -16% of the CO_2 emissions expected till the year 2050 (Davison *et al* [2]).

Another potential option for storage of CO_2 at deep ocean depths may lower the pH level of water. Increased biological production of organisms that take up carbon dioxide may offset the CO_2 storage too, according to Ormerod et al [3]. It is also unclear how CO_2 would affect marine life and under current international law, it is illegal to dispose of CO_2 in the ocean (Gale [4]).

There are three main options available for subsurface CO_2 sequestration, namely saline aquifers, unminable coal seams and existing oil and gas fields. Of these three options, injection into existing oil and gas fields or unminable coal seams have the potential to be economically feasible due to the possibility of enhanced oil and gas recovery [4].

There are several advantages to injecting CO_2 into an oil or gas reservoir, namely, increase in sweep efficiency and incremental recovery, more storage of CO_2 compared to saline aquifers (Chadwick *et al* [5]) and proven ability to store oil and gas for geological period of time.

However, existing literature for CO_2 sequestration in depleted natural gas reservoir is very limited, especially when we consider enhanced recovery as well. Van der Burgt *et al* [6] were primarily interested in disposing of CO_2 in a depleted gas field. Although the authors did note that additional natural gas might be recovered due to their scheme, the primary focus of the study was to study the viability of an abandoned gas field as a disposal option for the produced CO_2.

Oldenburg *et al* [7] were concerned with the physical process of injecting CO_2 into a depleted gas field. The authors concluded that incremental natural gas could be recovered both during and after the injection of CO_2. Oldenburg and Benson [8] used finite difference method to model the same Rio Vista gas field. The authors constructed a two dimensional model with one injector and one recovery well, where pressure and breakthrough time were reported for the wells and various grid blocks. The authors also constructed a three dimensional, 5-spot, model and again pressure and breakthrough time were reported for the wells and various grid blocks. This study was concerned only with the injection of pure CO_2.

Sinisha *et al* [9] investigated enhanced gas recovery through carbon dioxide sequestration. The authors modeled two different injection strategies of carbon dioxide into a natural gas field. Based on the study, the researchers concluded that the highest recovery of natural gas can be achieved by injecting CO_2 once the field has reached its economic limit. However, no effort was made to optimize the storage of the CO_2.

It can be seen that the injection of CO_2 into depleted gas fields can both lead to incremental recovery of natural gas as well as the sequestration of carbon. In this paper, the modeling part of our study is discussed and the results for various options for gas recovery and carbon dioxide sequestration processes will be presented in the conference.

3 Reservoir data

The North Triumph reservoir is a rollover anticline that is bounded by major listric faults and divided by minor en echelon faults. The gas is trapped in a single pool of a gas column of 171 meters from the top of the anticline down to the gas water contact. Log correlation between wells completed in the North Triumph field is good, as is pressure communication, indicating stratigraphic continuity over most, or all, of the structure ExxonMobil DPA [10].

The North Triumph field is at a depth of 3,640 m subsea, and extends over an area of 19 square kilometers. A total of two exploratory wells, B-52 and G-43, were completed in the North Triumph field. Average porosity, water saturation and permeability values for the B-52 and G-43 wells are 0.18 and 0.20, 0.36 and 0.15, and 60 mD and 70-100 mD, respectively.

A total of two production wells, NT-1 and NT-2, were also drilled and logged as part of the field development. These logs include information on porosity, water and gas saturation, density, permeability, and perforations. Two layers out of eight layers exhibit a very low permeability (0.1mD), porosity (0.01) and zero gas saturation and are likely shale layers. In the sandstone layers however, the permeability ranged from 1 to 300 mD, the porosity ranged from 0.10 to 0.20, and the gas saturation ranged from 0.5 to 0.80. It is to be noted that the values within a layer are consistent but not homogeneous.

The field is bounded by normal faults to the northeast and south. These faults are a barrier to flow as no gas has been interpreted to be present on the opposite side or the faults, even where juxtaposed with sandstone [10]. Also, two en

echelon faults are present in the southern portion of the gas field. The en echelon faults bisect the gas field vertically, but terminate within the reservoir laterally.

The reported temperature gradient for the North Triumph field is 32 degrees Celsius per 1000 meters [10]. This is approximately consistent with the temperature gradient for other fields in the Sable Sub-basin.

The field is hydrostatically pressured and the initial free water level was 3771 meters subsea. No water drive is present in this gas field.

The PVT properties for the reservoir rock, water and gas are presented in two well test reports and included below in Table 1. This information is used for our simulation model.

Table 1: Select PVT properties for the North Triumph Reservoir from well test reports

Well ID	Formation Compressibility (kPa^{-1})	Init. Gas Viscosity (μPa.S)	Init. Gas FVF (m^3/m^3)	Init Water Viscosity (mPa.S)	Water Compressibility (kPa^{-1})
NT1	5.8176E-07	25.2416	3.8033E-03	0.22876	4.2535E-07
NT2	5.9273E-07	24.7124	3.8306E-03	0.23186	4.1917E-07

Results of special core analysis were not available for review during this study. As a result, the actual laboratory determined relative permeability and capillary pressure curves were not available for input. However, the endpoint relative permeabilites were provided by a representative from the field operator, ExxonMobil Canada Ltd., and these endpoints are listed below:

$$S_{wc} = 0.35,\ K_{rw} = 0;\ S_{wmax} = 0.75\ K_{rw} = 0.05;\ S_{gmin} = 0.35,\ K_{rg} = 0;$$
$$S_{gmax} = 0.65,\ K_{rg} = 0.95$$

The production history for the field is publicly available from the CNSPOB and is used to validate the simulation model through history matching.

For North Triumph gas field the mean initial OGIP (Original Gas in Place) was estimated to be 15.2 E9 m^3 with 72% recovery factor. However, based on the actual production data collected from the CNSOPB, only 5.46 E9 m^3 of natural gas was produced from the field. It seems clear then, that the initial evaluation and calculations did not capture the true nature of the gas reservoir.

The production data was used to calculate a new value for OGIP using material balance equation from Garb and Smith [11]. The calculated value for OGIP is 10.3 E9 m^3. The simulation grid was constructed such that the OGIP was equivalent to the new calculated value.

4 Simulation model

The model was constructed using Petrel® and Eclipse® software provided by Schlumberger Canada. Eclipse E100, also known as the Eclipse black oil simulator, is a finite difference simulator that allows the user to specify the

phases present in the model, and also has various add-ons available, such as the *hysteresis* and *solvent* options. This model assumes isothermal conditions and does not incorporate various components of each phase. The simulator is based on two governing equations, Darcy's Law and the Material Balance Equation.

The Eclipse simulator solves a combination of Darcy's Law and the Material Balance Equation for each grid block and for each time step. Eclipse allows the user to select implicit or explicit solution method and to determine the maximum time step size. For the current simulation problem, the fully implicit solution method was chosen and time steps ranged in size from many days to a few minutes depending on the complexity of the problem.

The grid was built using the Petrel software package. The geometry of the grid was based on figures presented in the DPA. The same surface was then used to define the top and bottom of each of the eight layers. Faults were also input into the model. The boundaries of the model are defined by faults to the north, northeast and south. Also, two smaller en echelon faults are present in the southern portion of the field. The faults are believed to be sealing, so the faults are modeled as no flow barriers.

Sensitivity analysis was completed using Petrel to determine an appropriate grid size for the simulation. The final grid size was established as being 58 by 30, and 8 layers thick. This represents a total of 13,920 grid cells.

Corner point geometry was used as in Eclipse, this allows for non-neighbor connections (NNC) to exist without being specified by the user. This is important when there is displacement and communication across a fault. Also, the corner point geometry allows for more realistic grids to be created, with smooth surfaces, as opposed to block-centered grids.

In our model, two shale layers were modeled as inactive layers, with a limited number of active cells to allow pressure communication between the layers. It helps the model to run faster while maintaining pressure communication between layers opposite to the shale layers. The layers were initialized with petrophysical properties obtained from well logs but were varied to a small degree within specific layers. This was done to represent the heterogeneity in the actual reservoir rocks.

This particular model has three phases, gas, oil and water. Even though the field is a dry gas field, a three-phase model was chosen so that the solvent model option could be used for CO_2 sequestration. Various PVT and SCAL data was entered into the model. However, the exact relative permeability and capillary pressure curves were not known and is dealt differently.

The production history of the field was also entered into the model. The production history covered the time period from December 1999 to May 2006.

The production wells were defined within Eclipse. Both production wells are vertical wells. These wells were placed in the grid according to coordinates that were provided in end of well reports.

Both production wells were placed in local grid refinements. These grid refinements were defined in Eclipse and are radial in nature. The radial grid refinement option was chosen, as opposed to the Cartesian grid refinement, as the radial option allowed for the model to run more efficiently.

5 Results

Once the model was developed and populated with relevant data, the model was run. Figure 1 shows the initial gas saturation for the model in December 1999. The free water level was set at –3771 meters, subsea, as presented in the DPA.

The history match was achieved by adjusting the relative permeability curve, capillary pressure curves and the net to gross ratio (NTG). Various laboratory-determined data including porosity, compressibility and saturations were honored for the modeling purpose.

The NTG was adjusted such that the correct OGIP would be predicted by the model. The representative from Exxon stated that the model saturations, porosities and gas-water contact looked reasonable, therefore, to achieve the correct OGIP, the NTG needed to be adjusted downward.

As the actual relative permeability curves and capillary pressure curves were not known, the default curves available from the Petrel software package were used first and then based on the end-point permeability values these curves were adjusted gradually to achieve an acceptable history match.

In Figure 2, the historical water production rate and predicted water production rate for well NT1 is shown. It can be seen that the trends for the peaks and troughs do generally match. However, there is some discrepancy that is likely caused by the model not successfully capturing the finer details of the actual reservoir geology. Things such as high permeability channel deposits or localized low permeability shale breaks were not accommodated by the simulation model and it is possible for these zones of high or low permeability to affect water production rates due to variations in associated capillary pressures.

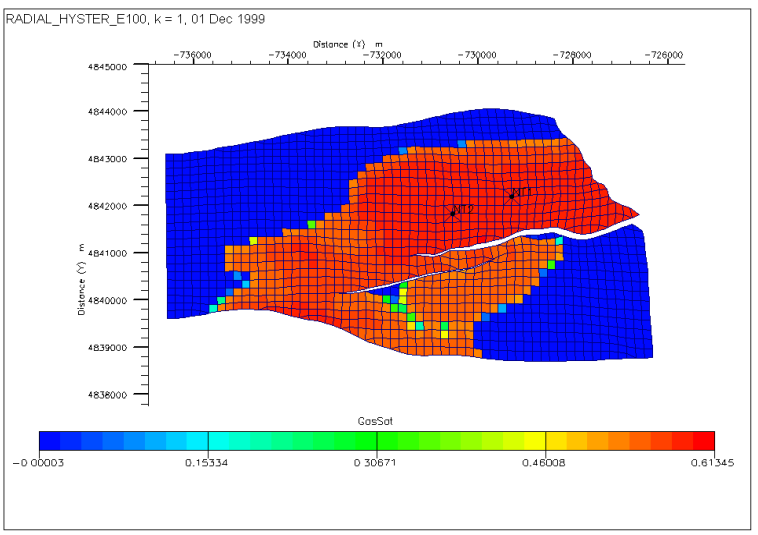

Figure 1: Initial gas saturation for the North Triumph Simulation Model, layer 1 (December 1999).

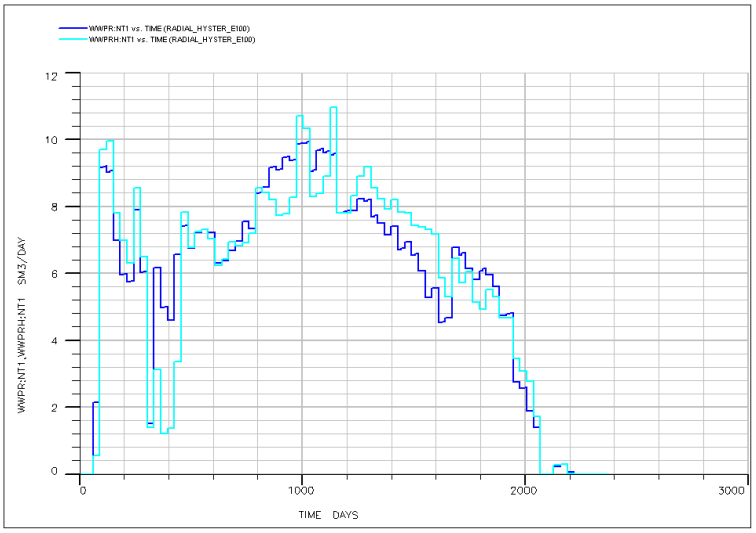

Figure 2: Water production history for well NT1. The historical water production rate (dark blue) and the predicted water production rate (light blue).

Water production at the other well, cumulative water production and bottom-hole pressure were also used for history matching and were found to be reasonably close to the actual production data.

6 Conclusions

In this study, modeling of North Triumph Gas reservoir is carried out successfully using limited data available. Laboratory tested data, like porosity, were honored and the heterogeneity of natural reservoir was also taken into account. The model was then validated through history matching with the actual production data. For the unavailable dataset, the standard curves were modified honoring the end points from the partially available data to fit the history match trend.

The results from the modeling study for various options related to gas recovery and carbon dioxide sequestration processes will be presented in the conference.

References

[1] Houghton, J.T., Ding, Y., Griggs, D.J., Noguer, M., van der Linden, P. J., & Xiaosu, D., (Eds.) *Climate Change 2001: The scientific basis*, Summary for Policymakers and Technical Summary, IPCC, Geneva, Switzerland. pp 98

[2] Davison, J., Freund, P. & Smith, A., *Putting carbon back into the ground, IEA Greenhouse gas R&D Programme*, February, 2001
[3] Ormerod, W.G., Freund, P. & Smith, A., *Ocean storage of CO_2, IEA Greenhouse Gas R&D Programme*, February, 1999
[4] Gale, J., *Why do we need to consider geological storage of CO_2?* Geological Society, London, Special Publications, v. 233, pp. 7–15, 2004.
[5] Chadwick, R.A., Holloway, S., Brook, M.S., & Kirby, G.A., *The case for underground CO2 sequestration in northern Europe*. *In*: Baines, S.J. & Worden, R.H. (eds). *Geological Storage of Carbon Dioxide.* (pp 16-28) Geological Society, London, Special Publications, pp. 16–28, 2004
[6] Van der Burgt, M.J., Cantle, J., & Boukman, V.K., *Carbon dioxide disposal from coal-based IGCC's in depleted gas fields*, Energy Conversion Management, 33(5-8), pp 603–610, 1992
[7] Oldenburg, C.M., Pruess, K., & Benson, S.M., *Process modeling of CO_2 injection into Natural Gas Reservoir for Carbon Sequestration and Enhanced Gas Recovery*, Energy and Fuels, 15, pp. 293, 2001.
[8] Oldenburg, C.M., & Benson, S.M., *CO_2 Injection for Enhanced Gas Production and Carbon Sequestration*, SPE International Petroleum Conference and Exhibition: Villahermosa, Mexico, 10–12 February 2002.
[9] Sinisha, A.J., Smith, D.H., Sams, W.N., & Bromhal, G.S., *Enhanced Gas Recovery (EGR) with Carbon Dioxide Sequestration: A Simulation Study of Effects of Injection and Operational Parameters*, SPE 84813, presented in the SPE Eastern Regional Meeting, Pittsburgh, Pennsylvania, September 6–10, 2003.
[10] ExxonMobil, *Development Plan Application (DPA), Sable Offshore Energy Project* website, Volume 2, http://www.soep.com/cgi-bin/getpage?pageid=1/15/0&dpa=2/0/0/0
[11] Garb, F.A., & Smith, G.L., *Petroleum Engineering Handbook,* Editor*:* Bradley, H.B., SPE, Richardson, Texas, pp. 40–7, 1987.

Section 8
Wave studies

This page intentionally left blank

A mathematical and numerical study of roll waves

S. J. D. D'Alessio[1] & J. P. Pascal[2]
[1]*Department of Applied Mathematics, University of Waterloo, Canada*
[2]*Department of Mathematics, Ryerson University, Canada*

Abstract

In this paper we analyze the gravity-driven laminar flow of a shallow fluid layer down an uneven incline with the principal objective of investigating the effect of bottom topography on the instability of the flow. The equations of motion are approximations to the Navier-Stokes equations which exploit the assumed relative shallowness of the fluid layer and fast laminar flow. The explicit dependence on the cross-stream coordinate is eliminated by depth-integrating the equations of motion. A linear stability analysis of the steady flow is carried out by taking advantage of Floquet-Bloch theory. A numerical scheme is devised for solving the nonlinear governing equations and is used to calculate the evolution of the perturbed steady flow. The results are used to confirm the analytical predictions and to investigate the structure of roll waves. The effect of bottom topography for cases where the bottom profile corresponds to periodic undulations is discussed.
Keywords: roll waves, bottom topography, linear stability analysis, non-hydrostatic pressure, integral-boundary-layer equations.

1 Introduction

The instability of a free-surface gravity-driven flow down an incline leads to the formation of a wave pattern consisting of a series of rapid surface variations followed by slowly varying sections. This phenomenon is referred to as *roll waves* and occurs in many artificial and natural settings [1]. The formation of roll waves can have devastating consequences. For example, in mud flows they can have sufficient force to cause serious property damage while in open conduits they can damage flow-rate measuring devices. The potential impact of roll waves can be reduced, or even eliminated, by appealing to theoretical predictions. Mathematical

WIT Transactions on Engineering Sciences, Vol 59, © 2008 WIT Press
www.witpress.com, ISSN 1743-3533 (on-line)
doi:10.2495/AFM080451

and numerical modelling can be used to anticipate the conditions under which a simple steady discharge will lead to the formation of roll waves.

To accurately represent an unsteady and nonuniform flow exhibiting roll waves along its surface, a mathematical model must incorporate all the relevant physical factors and possess the mathematical complexity required to capture the spatio-temporal coupling and nonlinear dynamics of the flow. At the same time, simplifications to the governing equations, warranted by physically justified assumptions, can lead to a more complete and productive mathematical treatment. A successful strategy to model the flow down an incline, first developed by Shkadov [2] and applied in this study, is furnished by the integral-boundary-layer (IBL) approach. In this approach the simplified two-dimensional Navier-Stokes equations are integrated over the depth of the fluid layer in order to eliminate the cross-flow variation. In the present work, we extend the IBL equations to include inclined flows over an uneven surface.

2 Mathematical formulation

We consider the two-dimensional laminar flow of a shallow layer of a Newtonian fluid along an uneven inclined surface as shown in Figure 1. We define an (x, z) coordinate system with the x-axis inclined at an angle θ with respect to the horizontal and pointing in the downhill direction, and with the z-axis pointing in the upward normal direction. The surface over which the fluid is flowing is given by $z = \zeta(x)$, and the fluid velocity is denoted by $\mathbf{u} = (u, w)^T$.

To describe the flow we start with the following equations:

$$\frac{\partial u}{\partial x} + \frac{\partial w}{\partial z} = 0, \tag{1}$$

$$\rho\left(\frac{\partial u}{\partial t} + u\frac{\partial u}{\partial x} + w\frac{\partial u}{\partial z}\right) = -\frac{\partial p}{\partial x} + g\rho\sin\theta + \mu\left(\frac{\partial^2 u}{\partial x^2} + \frac{\partial^2 u}{\partial z^2}\right), \tag{2}$$

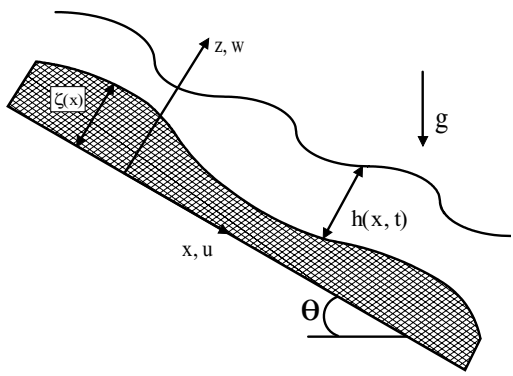

Figure 1: The coordinate system and flow setup.

$$\frac{1}{\rho}\frac{\partial p}{\partial z} + g\cos\theta - \frac{\mu}{\rho}\frac{\partial^2 w}{\partial z^2} = 0, \tag{3}$$

where p is the total pressure, g is the acceleration due to gravity, and ρ, μ are the mass density and the viscosity of the fluid, respectively. For Reynolds numbers which are $O(1)$ these equations represent a second-order non-hydrostatic approximation to the Navier-Stokes equations relative to the shallowness parameter δ given by the ratio of characteristic depth to length.

The dynamic conditions applied at the surface of the fluid layer include

$$\left.\begin{array}{l} p - 2\mu\frac{\partial w}{\partial z} = 0 \\ \frac{\partial u}{\partial z} = 0 \\ w = \frac{\partial h}{\partial t} + u\frac{\partial h}{\partial x} + u\zeta'(x) \end{array}\right\} \text{ at } z = \zeta(x) + h(x,t). \tag{4}$$

Here, we have neglected the effects of surface tension. At the interface between the fluid layer and the impermeable bottom the tangential and normal fluid velocity components are zero. This leads to the usual no-slip conditions

$$u = w = 0 \quad \text{at } z = \zeta(x). \tag{5}$$

Following the approach used by Uecker [3], we next depth average the equations of motion with the aim of eliminating the cross-flow variation. This results in the following one-dimensional problem

$$\frac{\partial h}{\partial t} + \frac{\partial q}{\partial x} = 0, \tag{6}$$

$$\frac{\partial q}{\partial t} + \frac{\partial}{\partial x}\int_{\zeta(x)}^{\zeta(x)+h} u^2 dz = \sin\theta gh - g\cos\theta h\frac{\partial z_1}{\partial x} + \frac{\mu}{\rho}\left[2\frac{\partial^2 q}{\partial x^2} + F + G\right] \tag{7}$$

$$\text{where } F = \left.\frac{\partial u}{\partial z}\right|_{z=z_1} - \left.\frac{\partial u}{\partial z}\right|_{z=\zeta} \quad \text{and}$$

$$G = -2\frac{\partial}{\partial x}\left(u|_{z=z_1}\frac{\partial z_1}{\partial x}\right) - 2\frac{\partial z_1}{\partial x}\left.\frac{\partial u}{\partial x}\right|_{z=z_1} + 2\zeta'(x)\left.\frac{\partial u}{\partial x}\right|_{z=\zeta} + h\frac{\partial}{\partial x}\left(\left.\frac{\partial u}{\partial x}\right|_{z=z_1}\right).$$

In the above $z_1 = h + \zeta(x)$ and q denotes the flow rate which is given by

$$q = \int_{\zeta(x)}^{\zeta(x)+h} u\, dz.$$

In order to convert the explicit dependence on u in equation (7) to a formulation in terms of q and h we must prescribe a specific vertical distribution for the velocity. A commonly used approach involves resorting to the parabolic velocity profile given by

$$u = \frac{3q}{2h^3}[2(h + \zeta(x))z - z^2 - \zeta(x)^2 - 2\zeta(x)h]$$

which satisfies conditions (4) and (5). Incorporating this velocity profile into equation (7) and nondimensionalizing leads to

$$\frac{\partial h}{\partial t} + \frac{\partial q}{\partial x} = 0, \tag{8}$$

$$\begin{aligned}\frac{\partial q}{\partial t} + \frac{6}{5}\frac{\partial}{\partial x}\left(\frac{q^2}{h}\right) &= \alpha\left(h - h\frac{\partial h}{\partial x} - \zeta'(x)h - \frac{q}{h^2}\right) \\ &\quad + \beta\left[\frac{7}{6}\frac{\partial^2 q}{\partial x^2} - \frac{3}{h}\frac{\partial q}{\partial x}\frac{\partial h}{\partial x} + \frac{3q}{h^2}\left(\frac{\partial h}{\partial x}\right)^2 - \frac{3q}{2h}\frac{\partial^2 h}{\partial x^2}\right. \\ &\quad \left. - \frac{2\zeta'(x)}{h}\frac{\partial q}{\partial x} + \frac{2\zeta'(x)q}{h^2}\frac{\partial h}{\partial x} - \frac{\zeta''(x)q}{h} - \frac{2(\zeta'(x))^2 q}{h^2}\right] \end{aligned} \tag{9}$$

where

$$\alpha = \frac{1}{Fr^2}, \quad \beta = 9\left(\frac{Fr}{Re}\right)^2, \quad Fr^2 = \frac{Re}{3\cot\theta}, \quad Re = \frac{\rho Q}{\mu}$$

with Fr denoting the Froude number, Re the Reynolds number and Q the volume flux of the steady flow. Equations (8) and (9) constitute a form of the IBL equations modified to include bottom topography and containing second-order diffusive effects represented by the terms inside the square brackets. If these terms are ignored and an even bottom is assumed by setting $\zeta'(x) \equiv 0$, the equations reduce to the classic first-order IBL equations.

3 Linear stability analysis

The steady-state solution to the governing equations is given by $q = q_s = 1$ and $h = h_s(x)$, where $h_s(x)$ satisfies the ordinary differential equation

$$\begin{aligned}&3\beta[h_s h_s'' - 2(h_s')^2] + \left(2\alpha h_s^3 - 4\beta\zeta' - \frac{12}{5}\right)h_s' + 2\beta\zeta'' h_s - 2\alpha(1-\zeta')h_s^3 \\ &\quad = -2\alpha - 4\beta(\zeta')^2 \end{aligned} \tag{10}$$

where we choose $\zeta(x) = a_b\cos(k_b x)$. Here, primes denote differentiation with respect to x. For small ε, where $\varepsilon = a_b k_b$ is the *waviness* parameter, an approximate solution for $h_s(x)$ can be constructed in the form of a series given by

$$h_s(x) = 1 + \varepsilon h_s^{(1)}(x) + \varepsilon^2 h_s^{(2)}(x) + \cdots,$$

otherwise $h_s(x)$ must be determined by numerically solving (10).

To study how small disturbances will evolve when superimposed on the steady equilibrium solution, we begin by introducing perturbations $\hat{h}$, $\hat{q}$ and set

$$h = h_s(x) + \hat{h}, \quad q = 1 + \hat{q}$$

and then linearize the governing equations.

We first entertain the even bottom case having $\zeta(x) \equiv 0$ and $h_s(x) \equiv 1$. In this case the linearized perturbation equations have constant coefficients and accordingly we introduce normal modes of the form

$$\hat{h} = \tilde{h}e^{\sigma t}e^{ikx} \quad \text{and} \quad \hat{q} = \tilde{q}e^{\sigma t}e^{ikx}.$$

It can be shown that the flow is stable if $Fr < \frac{1}{\sqrt{3}}$ while for $Fr > \frac{1}{\sqrt{3}}$ instability occurs for wavenumbers $k < k_{max}$ where

$$k_{\max} = \frac{10Re}{\sqrt{30}Fr^2}\sqrt{\frac{3Fr^2 - 1}{3Fr^2 + 35 + 12Fr\sqrt{6Fr^2 + 25}}}. \tag{11}$$

Thus, for all values of Re the onset of instability occurs at $Fr = Fr_{crit} = \frac{1}{\sqrt{3}}$ with the neutral stability curve, shown in Figure 2, in the Fr-k plane given by equation (11). It turns out that this neutral stability curve has a maximum at $Fr \approx 0.76286$ which is independent of Re.

For the uneven bottom case the coefficients in linearized equations are periodic functions. We thus apply Floquet-Bloch theory to conduct the stability analysis. Consequently, we represent the perturbations as Bloch-type functions having the form

$$\hat{h} = e^{\sigma t}e^{iKx}\sum_{n=-\infty}^{\infty}\hat{h}_n e^{ink_b x}, \hat{q} = e^{\sigma t}e^{iKx}\sum_{n=-\infty}^{\infty}\hat{q}_n e^{ink_b x}.$$

The exponential factor containing the Bloch wavenumber, K, represents disturbances which interact with the periodic bottom topography via the equilibrium flow, which is represented by the Fourier series composed of the harmonics of

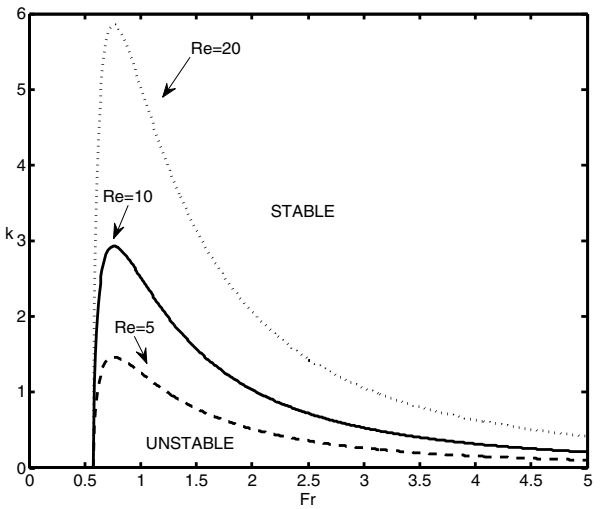

Figure 2: Neutral stability curve for the even bottom case.

k_b. Introducing the Bloch-type functions with truncated series into the perturbation equations yields an algebraic eigenvalue problem. In the case of weak bottom undulations an approximate method of solution, making use of the approximate analytical steady-state solution, can be employed. In the general case the algebraic eigenvalue problem can be solved numerically for the temporal growth rate $\Re(\sigma)$. In this way we can determine the critical Froude number for the onset of instability, and for supercritical flows we can compute the wavelength and speed of unstable disturbances.

Displayed in Figure 3 is the graph of the critical Froude number for the onset of instability as a function of bottom undulation amplitude for several values of the corresponding wavenumber of the bottom undulation. For intermediate values of bottom amplitude the critical Froude number appears to increase with bottom waviness as characterized by an increase in amplitude and wavenumber, thus suggesting that bottom topography tends to stabilize the flow. Our results also reveal that the critical conditions for instability are strongly dependent on the Reynolds number for larger values of bottom amplitude.

In order to understand the nature of the instability as the Froude number is increased to supercritical values, we refer to Figure 4 which illustrates the neutral stability curve in the *Fr*-*K* plane. This plot reveals two major differences between the even and uneven bottom cases. The first is the nose region shown in the insert in Figure 4. That is, for the uneven bottom $Fr_{crit} > \frac{1}{\sqrt{3}}$ occurs at a nonzero Bloch wavenumber and as *Fr* increases slightly beyond Fr_{crit} there is a band of unstable wavenumbers such that $K \in (K_1, K_2)$ where K_1 and K_2 are nonzero and depend

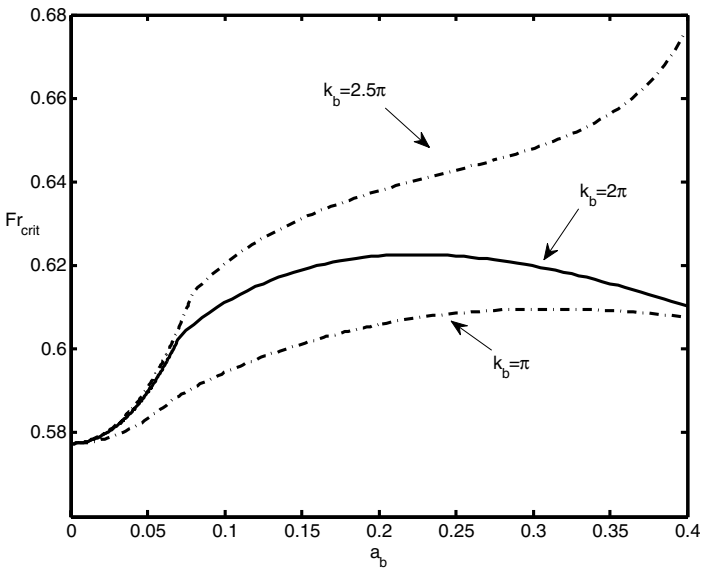

Figure 3: Critical Froude number as a function of bottom amplitude with $Re = 10$.

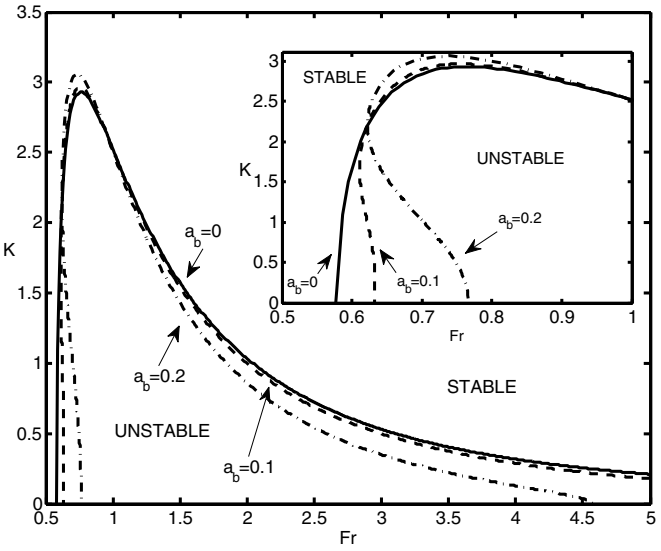

Figure 4: The neutral stability curve for the case with $Re = 10$ and $k_b = 2\pi$.

on Fr. For the even bottom $Fr_{crit} = \frac{1}{\sqrt{3}}$ occurs at $K = 0$ and the band of unstable wavenumbers is such that $K \in (0, K_{\max})$ where $K_{\max}$ is given by (11). The second interesting difference concerns the behaviour for larger Fr. In the even bottom case the flow is always unstable for some band of wavenumbers as long as $Fr > \frac{1}{\sqrt{3}}$ and for large Fr this band gets narrower. On the other hand, the uneven bottom case displays a second critical Froude number beyond which the flow becomes stable again.

4 Numerical solution procedure and results

The instability of a particular steady flow can be determined by tracking the evolution initiated by small disturbances. The development of the flow can be calculated by numerically solving the governing equations. The advantage of this approach is that it incorporates nonlinear interactions of the perturbations and thus captures the entire instability mechanism of the flow.

We begin by expressing the governing equations (8)–(9) in the form

$$\frac{\partial h}{\partial t} + \frac{\partial q}{\partial x} = 0,$$

$$\frac{\partial q}{\partial t} + \frac{\partial}{\partial x}\left(\frac{6}{5}\frac{q^2}{h} + \frac{\alpha}{2}h^2\right) = \Psi(h,q) + \Phi\left(x, h, q, \frac{\partial h}{\partial x}, \frac{\partial q}{\partial x}, \frac{\partial^2 h}{\partial x^2}, \frac{\partial^2 q}{\partial x^2}\right)$$

where the source term $\Psi = \alpha(h - q/h^2)$ and Φ is easily determined from (9). To solve these equations the fractional-step method [4] was adopted. This scheme

decouples the advective and diffusive components, that is, we first solve

$$\frac{\partial h}{\partial t} + \frac{\partial q}{\partial x} = 0,$$
$$\frac{\partial q}{\partial t} + \frac{\partial}{\partial x}\left(\frac{6}{5}\frac{q^2}{h} + \frac{\alpha}{2}h^2\right) = \Psi(h, q)$$

over a time step Δt, and then solve

$$\frac{\partial q}{\partial t} = \Phi\left(x, h, q, \frac{\partial h}{\partial x}, \frac{\partial q}{\partial x}, \frac{\partial^2 h}{\partial x^2}, \frac{\partial^2 q}{\partial x^2}\right)$$

using the solution obtained from the first step as an initial condition for the second step. The second step then returns the solution for q at the new time $t + \Delta t$.

The first step involves solving a nonlinear system of hyperbolic conservation laws which, when expressed in vector form, assumes the form

$$\frac{\partial \mathbf{U}}{\partial t} + \frac{\partial \mathbf{F}(\mathbf{U})}{\partial x} = \mathbf{b}(\mathbf{U}),$$

where

$$\mathbf{U} = \begin{bmatrix} h \\ q \end{bmatrix}, \quad \mathbf{F}(\mathbf{U}) = \begin{bmatrix} q \\ \frac{6}{5}\frac{q^2}{h} + \frac{\alpha}{2}h^2 \end{bmatrix}, \quad \mathbf{b}(\mathbf{U}) = \begin{bmatrix} 0 \\ \Psi \end{bmatrix}.$$

MacCormack's method was implemented to solve this system. This is a conservative second-order accurate finite difference scheme which correctly captures discontinuities and converges to the physical weak solution of the problem.

LeVeque and Yee [5] extended MacCormack's method to include source terms via the explicit predictor-corrector scheme

$$\mathbf{U}_j^* = \mathbf{U}_j^n - \frac{\Delta t}{\Delta x}[\mathbf{F}(\mathbf{U}_{j+1}^n) - \mathbf{F}(\mathbf{U}_j^n)] + \Delta t\ \mathbf{b}(\mathbf{U}_j^n),$$
$$\mathbf{U}_j^{n+1} = \frac{1}{2}(\mathbf{U}_j^n + \mathbf{U}_j^*) - \frac{\Delta t}{2\Delta x}[\mathbf{F}(\mathbf{U}_j^*) - \mathbf{F}(\mathbf{U}_{j-1}^*)] + \frac{\Delta t}{2}\mathbf{b}(\mathbf{U}_j^*)$$

where the notation $\mathbf{U}_j^n \equiv \mathbf{U}(x_j, t_n)$ was adopted, Δx is the grid spacing and Δt is the time step.

The second step reduces to solving the generalized one-dimensional diffusion equation having the form

$$\frac{\partial q}{\partial t} = \frac{7\beta}{6}\frac{\partial^2 q}{\partial x^2} + S_1(x, t)\frac{\partial q}{\partial x} + S_0(x, t)q + S(x, t)$$

where the functions $S(x, t)$, $S_0(x, t)$ and $S_1(x, t)$ are easily obtainable. Since h is known from the first step and remains constant during the second step, the functions $S(x, t)$, $S_0(x, t)$, $S_1(x, t)$ are known and hence the equation is linear. Approximating all spatial derivatives of q by central differences, imposing periodicity conditions, and using the output from the first step as an initial condition, leads to a sparse linear system of equations which can be solved efficiently.

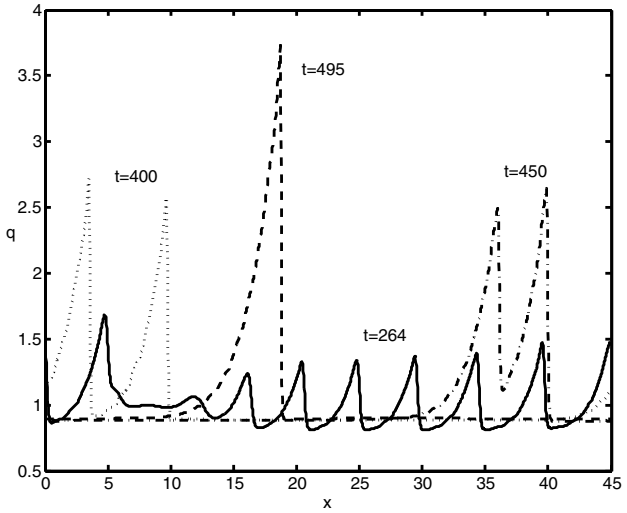

Figure 5: The time evolution of q for the case with $a_b = 0.1$, $k_b = 2\pi$, $Re = 10$ and $Fr = 0.7$ with a computational domain of length 45.

The above numerical method was employed on a periodic spatial domain to compute the evolution of a perturbed equilibrium flow. The initial state was taken to be $q = 1$ and $h = h_s(x)$ where $h_s(x)$ was numerically found by solving (10). The error associated with this numerical solution has the effect of imposing a wide-band perturbation of small amplitude on the steady flow. For Froude numbers less than the critical value, according to the linear theory, we found the perturbations to decay in time thus confirming that the steady flow is stable. For supercritical Froude numbers where the linear analysis predicts flow instability, the perturbations are amplified in time and roll waves eventually emerge provided the computational domain exceeds the minimum wavelength for unstable perturbations, again as predicted by the linear analysis.

Shown in Figure 5 is the progression of an unstable flow. Observed in this plot is the phenomenon of *wave coarsening*, a subharmonic instability whereby bores travelling with different speeds combine to form a wave pattern having fewer and taller bores. As time advances the series of waves begins to coalesce as these waves propagate and interact nonlinearly with each other. This process continues, leaving eventually a single solitary wave profile having the largest possible length scale. The coarsening phenomenon is ubiquitous and can be implicated in other physical systems.

5 Concluding remarks

Investigated in this paper is the formation of roll waves and the effect of bottom topography. A linear stability analysis was carried out which predicted that bottom

topography has a stabilizing effect on the flow and thus can be used to prevent, or at least delay, the formation of roll waves. This prediction was confirmed by nonlinear numerical simulations and is consistent with the findings in [1,6] along with the observations reported in [7]. Further nonlinear analyses to extend the linear stability analysis and to support the coarsening results are currently in progress. Possible extensions of this work could involve exploring how surface tension and a porous wavy bottom would affect our results.

Acknowledgement

Financial support for this research was provided by the Natural Sciences and Engineering Research Council of Canada.

References

[1] Balmforth, N. J. & Mandre, S., Dynamics of roll waves, *J. Fluid Mech.* **514**, pp. 1–33, 2004.
[2] Shkadov, V. Y., Wave conditions in flow of thin layer of a viscous liquid under the action of gravity, *Izv. Akad. Nauk SSSR, Mekh. Zhidh. Gaza* **1**, pp. 43–50, 1967.
[3] Uecker, H., Approximation of the integral boundary layer equation by the Kuramoto-Sivashinsky equation, *SIAM J. Appl. Math.* **63**, pp. 1359–1377, 2003.
[4] LeVeque, R. J., *Finite volume methods for hyperbolic problems*, Cambridge University Press, Cambridge, UK, 2002.
[5] LeVeque, R. J. & Yee, H.C., A study of numerical methods for hyperbolic conservation laws with stiff source terms, *J. Comput. Phys.* **86**, pp. 187–210, 1990.
[6] Wierschem, A., Lepski, C. & Aksel, N., Effect of long undulated bottoms on thin gravity-driven films, *Acta Mechanica* **179**, pp. 41–66, 2005.
[7] Montes, S., *Hydraulics of Open Channel Flow*, ASCE Press, Reston, USA, 1998.

Long axisymmetrical waves in a viscous ocean around a circular island

A. Bandyopadhyay
Department of Mathematics, Khalisani College, Chandannagar, India

Abstract

The problem of long waves due to any applied normal surface stress in a viscous liquid ocean surrounding a circular island is solved. The expression of the surface displacement ζ correct to $O(\nu)$ terms, ν being the coefficient of viscosity, is obtained. Assuming the stress to be time-periodic the surface displacement ζ, is shown to attain a steady-state and the resulting wave forms at any distance from the island are determined. Numerical studies of the results along with illustrations are provided to bring out the effect of viscosity and the presence of an island on the ocean waves otherwise devoid of them.

Keywords: coefficient of viscosity, long wave motion, asymptotic analysis, turbulence.

1 Introduction

The three-dimensional problem of short waves due to arbitrary initial time-dependent surface pressure together with an elevation of the surface in a viscous fluid of finite depth h without any other boundaries has been investigated by Nikitin and Potetyunko [2] and Bandyopadhyay [3, 4]. Assuming the same fluid regime, Oborotov studies the problem of free long waves in the axisymmetric case in which however the condition of zero tangential stress on the surface was not fully utilized. In the oceanographic context it is, however, natural to investigate problems in the presence of a boundary, enclosed or otherwise, in the ocean. Recently, Das and Ghosh analyzed the initial value problem of generation of storm surges by a symmetrically distributed and time-periodic surface wind near a circular island with variable topography [11,12]. For this purpose, Das used a depth-averaged Reynolds' equation together with the usual assumption of shallow water wave theory and the f-plane approximation. It seems that hitherto

WIT Transactions on Engineering Sciences, Vol 59, © 2008 WIT Press
www.witpress.com, ISSN 1743-3533 (on-line)
doi:10.2495/AFM080461

there has been no attempt to analyze the basic non-turbulent non-rotating problem of long axisymmetrical waves formed around a circular island due to suddenly applied arbitrary surface pressure in an ocean of viscous fluid of finite depth. Our objective is to study here this problem, taking into account the complete surface boundary condition of zero tangential stress (contrast Oborotov, who however does not consider any boundary). It is shown that the formal solution [equation (12) or (14)] is achieved by the application of Laplace and Weber-Orr transform. An apparently formidable expression of ζ [equation (16)] is next approximated for small coefficient of viscosity ν correct up to $O(\nu)$ terms under certain conditions on the applied pressure [see condition (A) in Section 3].

We next suppose that the applied pressure is periodic in time and deduce that the motion attains a steady-state as $t \to \infty$. The steady-state surface displacement ζ_1^* [equation (27)] is next analyzed to demonstrate that the surface displacement everywhere consists of a pair of oppositely moving progressive waves accompanied by standing local disturbances. The asymptotic character of these waves' at large distances from the island is easily derived to give a simplified picture of the wave motion.

A numerical study is also undertaken to estimate the range of distances over which the exact solution can be approximated by its asymptotic counterpart and an illustration is also provided to study the nature of the waves to a particular pressure distribution with and without the presence of an island. Last but not the least we note that the Stokes-Navier equations become identical with Reynolds equation for turbulent motion when the horizontal and vertical exchange coefficients become equal, their common value playing the part of ν [13]. Consequently the solutions of v_r, v_z and ζ [equations (10)–(12)] for the long wave axisymmetrical problem obtained here also give the solution of the mean fields in corresponding problem for turbulent motion under preceding condition and the various other conditions (e.g. no surface shear) assumed here.

2 The problem and solution

We consider an initially undisturbed ocean of a viscous homogeneous liquid of uniform depth h and density ρ surrounding a circular island of radius unity. Let (r, θ, z) denote the cylindrical coordinates of any point in the ocean with the undisturbed free surface taken as the xy-plane, the centre of the island as the origin O, and the vertically upward direction as the z-axis. Motion is generated at t = 0+ by the action of an axisymmetrical surface pressure distribution $p_0(r, t)$. Let v_r, v_z, and ζ denote respectively the velocities in the direction of increasing r and z and the surface displacement at any point and time.

The linearised Stokes-Navier equations of motion are

$$\frac{\partial v_r}{\partial t} = -\frac{1}{\rho}\frac{\partial p_1}{\partial r} + \nu(\nabla^2 v_r - \frac{v_r}{r^2}), \tag{1}$$

$$\frac{\partial v_z}{\partial t} = -\frac{1}{\rho}\frac{\partial p_1}{\partial z} + \nu \nabla^2 v_z \tag{2}$$

where

$$p_1 = p + \rho g z, \quad \nabla^2 \equiv \frac{\partial^2}{\partial r^2} + \frac{1}{r}\frac{\partial}{\partial r} + \frac{\partial^2}{\partial z^2} \ .$$

The equation of continuity is

$$\frac{\partial v_r}{\partial r} + \frac{v_r}{r} + \frac{\partial v_z}{\partial z} = 0 \tag{3}$$

The boundary and initial conditions from the continuity of tangential and normal stresses, the kinematic surface condition, the zero-velocity condition on a rigid surface, and the all-quiet condition of the fluid just before the start:

(i) on $z = \zeta \approx 0, r > 1$,

$$\frac{\partial v_r}{\partial z} + \frac{\partial v_z}{\partial r} = 0, \qquad -p_1 + \rho g v_z + 2\mu \frac{\partial v_z}{\partial z} = -p_0, \qquad \frac{\partial \zeta}{\partial t} = v_z(r,0,t)$$

(ii) on $z = -h$, $r > 1$, $v_r = v_z = 0$; on $r = 1$, $v_r = v_z = 0$ (4)–(9)

(iii) at $t = 0$, $v_r = 0 = v_z$, $\zeta = 0$, $\dot{v}_r = -\rho^{-1}(\partial p_0 / \partial r)$

To the above equations and conditions, we apply the usual assumptions adopted for the long wave motion. These are that

(a) p is given by hydrostatic formula, and

(b) the vertical acceleration is negligible and the viscous force in the z-direction is negligible.

The formal solution of the problem may be affected by introducing the Laplace transform and the Weber-Orr transform (Erdélyi et al. [5])

$$v_r = \frac{1}{2\pi i \rho}\int_{c-i\infty}^{c+i\infty} e^{ts} ds \int_1^\infty \frac{ms\tilde{\tilde{P}}_0}{D_1}\big[(k^2 + m^2)(\cosh mz - \cosh mh) - k^2\{\cosh m(z+h) -$$
$$- mh \sinh m(z+h) - 1\}\big] \times \ [J_1(kr)Y_1(k) - Y_1(kr)J_1(k)]\ k\,dk \tag{10}$$

$$v_z = -\frac{1}{2\pi i \rho}\int_{c-i\infty}^{c+i\infty} e^{ts} ds \int_1^\infty \frac{s\tilde{\tilde{P}}_0}{D_1}[(k^2 + m^2)(\sinh mz + \sinh mh) + k^2\{mh\cosh m(z+h) - \sinh m(z+h) - mh\} -$$
$$- m(z+h)\{(k^2 + m^2)\cosh mh - k^2\}] \times \left[J_0(kr)Y_1(k) - Y_0(kr)J_1(k) + \frac{1}{kr}\right] k^2\,dk \tag{11}$$

$$\zeta = -\frac{1}{2\pi i \rho}\int_{c-i\infty}^{c+i\infty} e^{ts} ds \int_1^\infty \frac{\tilde{\tilde{P}}_0}{D_1} m^2[\sinh mh - mh\cosh mh] \times [J_0(kr)Y_1(k) - Y_0(kr)J_1(k) + \frac{1}{kr}] k^2\,dk \tag{12}$$

where

$D_1 = m^2[\nu s m k^2(\cosh mh - 1) - g k^2(\sinh mh - mh\cosh mh) + m^3 \nu s \cosh mh]$,

$m^2 = k^2 + s/\nu$.

In deriving the result for ζ use has been made of the condition $\zeta|_{t=0} = 0$ and a Tauberian theorem (Sneddon, p.185, [7]).

From (12) one gets

$$\zeta = \frac{1}{2\pi i\rho}\int_1^{\infty}\int_{c-i\infty}^{c+i\infty} \frac{(mh - \tanh mh)}{\nu s m k^2(1-\sec h\, mh) + m^3\nu s - gk^2(\tanh mh - mh)} e^{st}\widetilde{\widetilde{P}}_0\, ds \times \times\left[J_0(kr)Y_1(k) - Y_0(kr)J_1(k) + \frac{1}{kr}\right]k^2 dk. \tag{13}$$

By the inversion theorem of Laplace and the convolution theorem we get

$$\zeta = \frac{1}{2\pi i\rho}\int_1^{\infty}\left[\int_0^t \widetilde{P}_0(k, t-\tau)d\tau \int_{c-i\infty}^{c+i\infty} e^{st}\frac{F(\nu^{1/2})}{f(\nu^{1/2})}ds\right]\left(J_0(kr)Y_1(k) - Y_0(kr)J_1(k) + \frac{1}{kr}\right)k^2 dk \tag{14}$$

where

$$\left.\begin{aligned} -F(\nu^{1/2}) &= \nu^{1/2}\tanh\{(s+\nu k^2)/\nu\}^{1/2}h - (s+\nu k^2)^{1/2}h \\ f(\nu^{1/2}) &= \nu^{1/2}s(s+\nu k^2)k^2\left\{1-\sec h\left(\sqrt{\frac{s+\nu k^2}{\nu}}\,h\right)\right\} + s(s+\nu k^2)^{3/2} - \\ &\quad - gk^2\left\{\nu^{1/2}\tanh\left(\sqrt{\frac{s+\nu k^2}{\nu}}\,h\right) - \sqrt{s+\nu k^2}\,h\right\} \end{aligned}\right\} \text{I} \tag{15}$$

it may be of interest to note that the modification of the surface condition (4) as done Oborotov [1] for the case of free waves in the absence of any initial applied surface pressure lead us to a solution of v_r, v_z and ζ which are quite different from that of us obtained in (10) – (12) because of the presence of the island.

3 Wave motion in a slightly viscous fluid

We first state the following result for small ν

$$\zeta = \frac{1}{2\nu i\rho}\int_1^{\infty}\left\{\int_0^t \tilde{P}_0(k, t-\tau)d\tau \int_{c-i\infty}^{c+i\infty} e^{st}\left(\frac{T_1}{\Delta_1}\right)ds\right\}\times\left[J_0(kr)Y_1(k) - Y_0(kr)J_1(k) + \frac{1}{kr}\right]k^2 dk + + o(\nu^{3/2}) \quad \text{as } \nu\to 0 \tag{16}$$

provided $\tilde{P}_o = O\left(k^{-3-n}\right)$, $n' > 0$, uniformly in τ, as $k \to \infty$ (Condition A). Here

$$\left.\begin{aligned} T_1 &= hs - (\nu s)^{1/2} + \frac{1}{2}\nu k^2 h \\ \Delta_1 &= s^3 + \frac{1}{2}\nu k^2(5s^2 + gk^2 h) - gk^2(\nu s)^{1/2} + gk^2 hs \end{aligned}\right\}$$

Evidently the s-integration of (16) in question has a branch point at $s = 0$ as well as possible poles arising from those zeros of Δ_1 for which $T_1 \neq 0$. If $\nu = 0$,

Δ_1 has simple zeros at $s = 0$ and at $s = \pm i\sqrt{gh}\,k$. Corresponding to these three values of s, namely $s_{00} = 0 \quad s_{10} = i\sigma \quad s_{20} = -i\sigma$, where $\sigma = \sqrt{gh}\,k$, we may assume the following expansion for the possible zeros s_j, j = 0, 1, 2 of Δ_1 in powers of $\nu^{1/2}$:

$$s_j = s_{j0} + s_{j1}\nu^{1/2} + s_{j2}\nu + s_{j3}\nu^{3/2} + \ldots \qquad j = 0, 1, 2 \tag{17}$$

It is found that $s_{01} = 0$ and to our degree of accuracy, $T_1(s_0) \equiv T_1(\nu s_{02}) = 0$. Leaving aside then the zero s_0 of Δ_1, and determining the other coefficients $s_{j\ell}$ for ℓ = 1, 2, 3, we find that the s-integration has two simple poles at $s = s_j \approx \alpha_j$ (to our degree of accuracy) given as follows:

$$\alpha_j = (-1)^{j-1} i\sigma - \left\{1 + (-1)^{j-1} i\right\}\frac{1}{2h}\left(\frac{\sigma\nu}{2}\right)^{1/2} - \left(k^2 + \frac{1}{4h^2}\right)\nu \tag{18}$$

The s-integration is now completed by using a modified Bromwich contour (Tranter, 1951, [8]), the result is

$$\zeta = \frac{1}{\rho}\int_1^\infty\int_0^t \widetilde{P}_0(k, t-\tau)\left[J_0(kr)Y_1(k) - Y_0(kr)J_1(k) + \frac{1}{kr}\right]k^2 dk.\, f(k,\tau)d\tau \tag{19}$$

where $$f(k,t) = \sum_{j=1}^{2}\frac{T_1(\alpha_j, k)}{\Delta_1'(\alpha_j, k)}e^{\alpha_j t} - \frac{1}{2\pi i}\int_0^\infty e^{-t\chi}\left\{\left[\frac{T_1}{\Delta_1}\right]_{s=\chi e^{i\pi}} - \left[\frac{T_1}{\Delta_1}\right]_{s=\chi e^{-i\pi}}\right\}d\chi \tag{20}$$

Introducing identity like the above one, we may show that the use of the values $s = s_j$ instead of $s = \alpha_j$ for the roots would add only a term of order $\nu^{3/2}$ to ζ as calculated on the basis of (19)-(20), correct to the first power of ν in the amplitude. We also have

$$-\sum_{j=1}^{2}\frac{T_1(\alpha_j, k)}{\Delta_1'(\alpha_j, k)} = (gk^2)^{-1}e^{-\sigma_2 t}\left[\left(\sigma - \frac{\sigma_1}{2}\right)\sin(\sigma - \sigma_1)t + \left(\frac{\sigma_1}{2} + \nu k^2\right)\cos(\sigma - \sigma_1)t\right] \tag{21}$$

where

$$\sigma_1 = \frac{1}{2h}\left(\frac{\sigma\nu}{2}\right)^{1/2}, \qquad \sigma_2 = \sigma_1 + \left(k^2 + \frac{1}{4h^2}\right)\nu \tag{22}$$

The final expression for ζ results when f(k, t), in (35) is modified in accordance with (21) and (22).

4 Surface displacement for an oscillatory pressure distribution and its asymptotic value for large distances in steady-state

When the applied pressure distribution is of the form $p_0(x,t) = p_0(x)e^{i\omega t}H(t)$, (19) gives by (21) and (22)

$$\zeta = \zeta_1 + \zeta_2 \tag{23}$$

where

$$-\zeta_1 = \frac{1}{\rho g}\int_1^{\infty} \frac{-\sum_{j=1}^{2}(\alpha_j + i\beta_j)e^{\left[(-1)^{j-1}i(\sigma-\sigma_1)-\omega-\sigma_2\right]t} + A + iB}{(\sigma_2 + i\omega)^2 + (\sigma-\sigma_1)^2} \times F(k,r)\tilde{P}_0(k)e^{i\omega t}\,dk \tag{24}$$

and

$$\zeta_2 = -\frac{1}{2\pi i\rho}\int_1^{\infty} F(k,r)\tilde{P}_0(k)k^2 dk \times e^{i\omega t}\int_0^{t} e^{-(i\omega+\chi)\tau}d\tau \times \int_0^{\infty}\left\{\left[\frac{T_1}{\Delta_1}\right]_{s=\chi e^{i\pi}} - \left[\frac{T_1}{\Delta_1}\right]_{s=\chi e^{-i\pi}}\right\}d\chi \tag{25}$$

where

$$\left.\begin{aligned} &F(k,r) = \left[J_0(kr)Y_1(k) - J_0(kr)Y_1(k) + \frac{1}{kr}\right] \\ &A = \sigma^2 - \frac{3\sigma\sigma_1}{2} + \sigma_1^2,\ B = \frac{(\sigma_1 + \nu k^2)\omega}{2},\ C = \sigma\left(\frac{\sigma_1}{2} + \nu k^2 - \sigma_2\right),\ D = \omega\left(\frac{\sigma_1}{2} - \sigma\right) \\ &\text{and}\quad \alpha_j = \frac{A + (-1)^j D}{2},\ \beta_j = \frac{B + (-1)^j C}{2} \end{aligned}\right\} \tag{26}$$

4.1 Exact form of the steady-state wave integral

We may write

$$\zeta_2 = -\frac{1}{2\pi i\rho}\int_1^{\infty} F(k,r)\tilde{P}_0(k)k^2 dk \times e^{i\omega t}\int_0^{1} te^{-(i\omega+\chi)t\tau'}d\tau' \times \int_0^{\infty}\left\{\left[\frac{T_1}{\Delta_1}\right]_{s=\chi e^{i\pi}} - \left[\frac{T_1}{\Delta_1}\right]_{s=\chi e^{-i\pi}}\right\}d\chi$$

It is easy that $t\times\chi$ – integral tends to zero as $t\to\infty$ for $0<\varepsilon<\tau'\le 1$, while the continuity of the $\chi-\tau'$ integral in $0\le\varepsilon<1$ ensures that $\zeta_2\to 0$ as $t\to\infty$. Therefore in this case as $t\to\infty$, r remaining fixed, the steady-state surface displacement ζ^* thus comes out to be ζ_1^* and it is given by

$$\zeta_1^* = -\frac{1}{\rho g}\int_1^{\infty} \frac{(A + iB)}{(\sigma_2 + i\omega)^2 + (\sigma-\sigma_1)^2} F(k,r)\tilde{P}_0(k)e^{i\omega t}dk \tag{27}$$

The dominant contribution of the wave integral corresponding to ζ_1^* comes from the poles of the integrand i.e. the points where

$$R(k) \equiv (\sigma_2 + i\omega)^2 + (\sigma-\sigma_1)^2 = 0\,. \tag{28}$$

For $\nu = 0$, R(k) has always two distinct real roots at $k = \pm\frac{\omega}{\sqrt{gh}} = (\beta_1, \beta_2)$ (say), of these β_2 is inadmissible since $k > 1$ and the zero k_1 of R(k) corresponding to β_1 can be obtained from β_1 by iteration with respect to ν as

$$k_1 = \beta_1 + \nu^{1/2} k_{11} + \nu k_{12} \tag{29}$$

k_{1j} are determined by substituting (29) in (28) and equating the coefficients of $\nu^{1/2}$ and ν of $R(k_1) = 0$ we get

$$k_1 = \frac{\omega}{\sqrt{gh}} + \left(\frac{\omega}{4gh^3}\right)^{1/2} e^{-i\pi/4}\nu^{1/2} - i.\frac{1}{\sqrt{gh}}\left[\frac{3}{8h^2} + \frac{\omega^2}{gh}\right]\nu .$$

To evaluate the k-integral of ζ_1 we consider a contour which essentially is the lower quadrant of a circle of radius R bounded by the lines x = 1 to x = R and y = 0 to y = - R and write the equation (27) as

$$\zeta_1^* = -\frac{e^{i\omega t}}{\rho g}\left[N_1(k_1)\int_1^\infty \frac{F(k,r)}{k-k_1}dk + \int_1^\infty \frac{N_1(k) - N_1(k_1)}{k-k_1} F(k,r)dk \right] \tag{30}$$

where

$$N_1(k) = \frac{(A + iB)'}{R'(k,\nu)}\tilde{P}(k) ,$$

and '$'$' represents $\frac{d}{dk}$. Since $J_0(kr)Y_1(k) - Y_0(kr)J_1(k) = \mathrm{Im}\, H_0^{(2)}(kr)H_1^{(1)}(k)$ (cf. Erdélyi et al. [5]) the first term at the right-hand side of (30) may be written as

$$\zeta_1^* = -\frac{e^{i\omega t}}{\rho g}\left[N_1(k_1)\int_1^\infty \frac{\mathrm{Im}[H_0^{(2)}(kr)H_1^{(1)}(k)] + 1/kr}{k-k_1}dk \right] ,$$

then from (30), the exact value of the steady-state surface displacement is

$$\zeta_1{}^* = -\frac{e^{i\omega t}}{\rho g}\left[\begin{array}{l} \pi\left\{H_0^{(2)}(k_1 r)H_1^{(1)}(k_1) - \overline{H}_0^{(2)}(\overline{k}_1 r)\overline{H}_1^{(1)}(\overline{k}_1)\right\}N_1(k_1) + \\ \qquad + \displaystyle\int_1^\infty \frac{N_1(k) - N_1(k_1)}{k-k_1} F(k,r)dk - \frac{1}{k_1 r}\log(1 - k_1) \end{array} \right] , \tag{31}$$

where $H_1^{(1)}(z)$ and $H_0^{(2)}(z)$ are Hankel functions of the first and second kind of order one and zero respectively. It can be easily verified that the integral-free term in the R.H.S. of (31) represents two progressive wave components in the steady-state motion for all r and t with complex velocities ω/k_1 and $\omega/\overline{k}_1$. The second term of (31) on the other hand represents in general a standing wave having the same frequency as that of the applied disturbances.

Since $H_0^{(2)}(kr) \sim \sqrt{2/\pi kr}\, e^{-i(kr - \pi/4)}$, and also since at large distances the standing waves fade away in comparison to the leading term, denoted by $\zeta_1{}^{**}$ of the asymptotic expression of $\zeta_1{}^*$, we may write, for $r >> 1$

$$\left.\begin{aligned}\zeta_1^{**} &= -\frac{2}{\rho g}\sqrt{\frac{2\pi}{r}}\left\{k_1^{(1/2)}e^{i(\omega t-k_1 r+\pi/4)}H_1^{(1)}(k_1)-\bar{k}_1^{(1/2)}e^{i(\omega t+\bar{k}_1 r-\pi/4)}\overline{H}_1^{(1)}(\bar{k}_1)\right\}N_1(k_1)+O(r^{-1}), \\ &\qquad\qquad \mathrm{Re}\,k_1 \geq 1 \\ &= 0, \qquad\qquad \mathrm{Re}\,k_1 < 1\end{aligned}\right\} \tag{32}$$

The steady-state wave motion at large distances from the island thus consists of two damped simple harmonic progressive waves, having the same velocity of propagation. One of this recedes away from the island and the other moving towards it, both having the same exponential attenuation factor.

5 Illustrative cases

We assume a wind stress model to the one proposed by Jelesnianski [9] as cited by Johns et al [10]. Following this model we write

$$P_0(r) = \tau_0(r/R)^3 \quad \text{when } 0 < r < R \text{ and } P_0(r) = \tau_0(R/r) \text{ when } r \geq R,$$

where R is the ratio of the radii of the maximum wind and the island. Then

$$\begin{aligned}\tilde{P}_0(K) = [\frac{\tau_0}{k^4R^2}\{4S_{3,0}(kR)[J_1(kR)Y_1(k)-Y_1(kR)J_1(k)]-S_{4,1}(kR)[J_0(kR)Y_1(k)-Y_0(kR)J_1(k)]\} \\ +\tau_0R^2S_{0,1}(kR)\{J_0(kR)Y_1(k)-Y_0(kR)J_1(k)\}]/\{J_1^2(k)+Y_1^2(k)\}\end{aligned}$$

where $S_{\mu,\nu}(z)$ denotes Lommel's function.

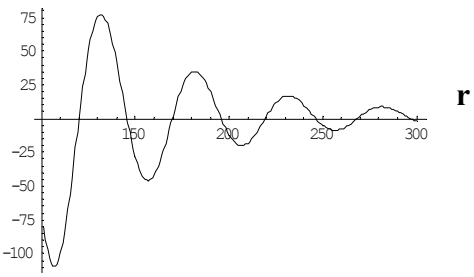

Figure 1: Exact form of the progressive wave part.

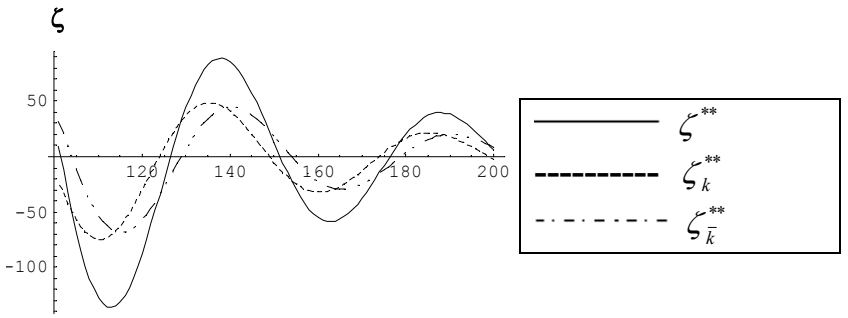

Figure 2: Steady-state large distance wave form.

By means of this result and the values of the non-dimensional parameters $\omega' = \omega\sqrt{h/g}$, $\nu' = \nu/\sqrt{gh^3}$ and $k' = kh$, we obtain the corresponding illustrations of the waves from their exact as well as from asymptotic expression

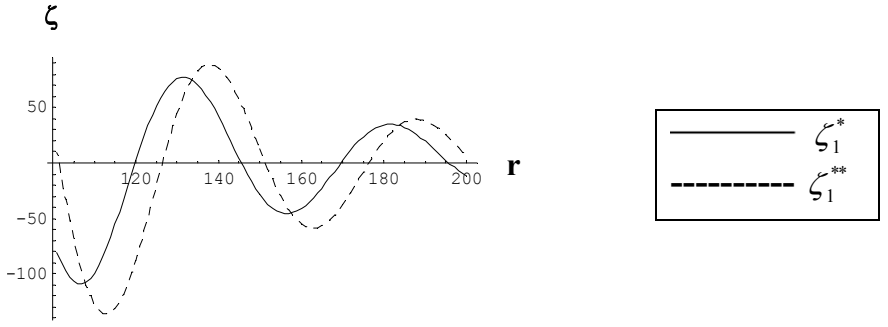

Figure 3: One illustrative comparison of the exact form of the progressive wave part with its asymptotic form.

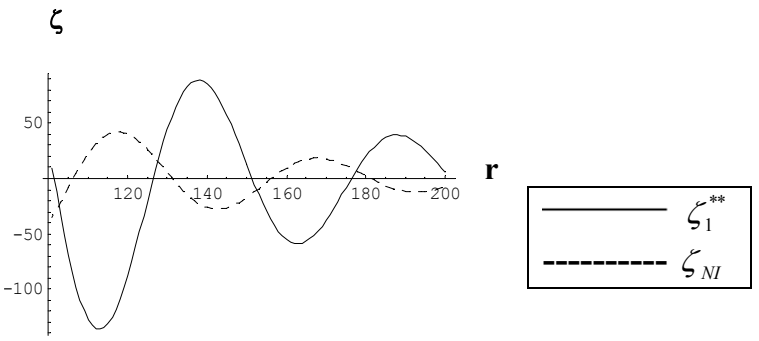

Figure 4: Steady-state waves with and without the presence of an island.

(31) and (32) respectively over different range of distances. A comparison of the nature of these steady-state waves is shown and also a comparison is shown with the large distance steady-state waves for the case of with and without the presence of an island. The Numerical work and the graphical illustrations are done with the help of 'Mathematica' software version 5.2.

6 Conclusion

Wave motion at high Reynolds number will certainly lead to the formation of boundary layers behind the leading wave around the island and also both at the surface and bottom of the open ocean. We will study the order of thickness of

this layer in a subsequent study of this problem. Secondly, a through investigation of the corresponding asymmetrical problem along with its analytical solution will perhaps be a formidable task ahead of us. Lastly, a practical value of this problem may be related to the generation of long waves due to atmospheric point blast in the line with the centre of the island although in that case, I suppose, the non-linear effect of the motion should have to be incorporated.

Acknowledgement

The author is deeply indebted to Professor A. R. Sen of the Department of Mathematics, Jadavpur University, Calcutta, for his help and suggestions during the preparation of this paper.

References

[1] Oborotov, I. P., Long cylindrical waves in a viscous fluid, PMM, Vol – 29, No. – 1, (1965), 196–199.
[2] Nikitin, A. K.; Potetyunko, E. N., The three dimensional Cauchy – Poisson problem for waves on the surface of a viscous liquid of finite depth. Soviet Physics, Doklady, Vol. -12, (1967), 5, 422-424.
[3] Bandyopadhyay, A., Effects of viscosity on linear gravity waves due to surface disturbances in water of finite depth. ZAMM Vol.-83, (2003), No.-3, 205–213.
[4] Bandyopadhyay, A., A study of the waves and boundary layers due to a surface pressure on a uniform stream of slightly viscous liquid of finite depth. Journal of Applied Mathematics [Hindawi Publishing Corporation, Pp. 1–24], Accepted on 22nd November 2006.
[5] Erdélyi, A. et al., Higher Transcendal Function. Vol. II (McGraw –Hill, 1954)
[6] Gradshteyn, I. S. and I. M. Ryzhik, Tables of Series, Products and Integrals, Academic Press, New York (1963).
[7] Sneddon, I. N. The use of Integral Transforms. McGraw-Hill, (1972), p. 185
[8] Tranter, C. J. Integral Transforms in Mathematical Physics, Methuen. 1951.
[9] Jelesnianski, C. P. A numerical calculation of storm tides induced by a tropical storm impinging on a continental shelf, Mon. Wea. Rev, Vol.- 93, 343–358 (1965).
[10] Johns, B., Rao, A.D., Dube, S.K. and Sinha, P.C. Numerical modelling of the tide-surge interaction in the Bay of Bengal, Phil. Trans. R. Soc. Lond., Vol- A313, 507–535 (1985).
[11] Das. S. Storm surges due to a symmetrical wind stress near a circular island, Geophys. Astrophys. Fluid Dynamics, Vol. 57, pp. 49–60 (1991)
[12] Ghosh. S. Surges from winds near a circular island, Geophys. Astrophys. Fluid Dynamics, Vol. 81, Issue 1 & 2, pp. 21–32 (1995)
[13] Pedlosky, J. Geophysical Fluid Dynamics. Springer-Verlag, Berlin (1979)

Travelling waves for two coupled Korteweg-de Vries equations

F. P. Barrera[1] & T. Brugarino[2]
[1]*Dip. di Ingegneria dei Trasporti*
[2]*Dip. di Metodi e Modelli Matematici Università di Palermo, Facoltà d'Ingegneria, 90128 Palermo, Italy*

Abstract

The aim of this paper is to apply the auxiliary equation method to obtain solutions of the system of two coupled Korteweg-de Vries equations which have many applications in the study of two-wave modes in stratified liquid. As an auxiliary equation we consider a reducible hyperelliptic equation.
Keywords: non linear equations, exact solutions, KdV equations.

1 Introduction

We consider the two coupled Korteweg-de Vries equations:

$$\begin{cases} u_t + \alpha_1 u_x + \alpha_2 v_x + \alpha_3 u u_x + \alpha_4 u_{xxx} = 0 \\ v_t + \beta_1 v_x + \beta_2 u_x + \beta_3 v v_x + \beta_4 v_{xxx} = 0 \end{cases} \tag{1}$$

which have many applications in the study of two-wave modes in stratified liquid [1–3].

Recently a large number of methods, such as the tanh method [4,5], generalized tanh method [6,7] and the Jacobi elliptic function expansion method [8], have been proposed to construct explicit analytical solutions for nonlinear wave equations.

Using the reducible hyperelliptic equation [9]:

$$p_\xi^2(\xi) = a_0 + a_2 p^2(\xi) + a_4 p^4(\xi) + a_6 p^6(\xi) \tag{2}$$

we obtain travelling wave solutions of Eqns (1). These solutions are expressed in terms of the Weirestrass elliptic function $\wp$.

WIT Transactions on Engineering Sciences, Vol 59, © 2008 WIT Press
www.witpress.com, ISSN 1743-3533 (on-line)
doi:10.2495/AFM080471

In sect. 2 we show how the solution of Eqn. (2) was obtained. In sect. 3 we describe the method for finding the travelling wave of Eqns (1). In sect. 4 we provide a brief conclusion.

2 Solutions of the hyperelliptic differential equation

The hyperelliptic differential equation (2) via the substitution:

$$\phi(\xi) = b + \frac{a}{c - p^2(\xi)}, \tag{3}$$

with $a \neq 0$, b and c arbitrary constants, is reduced to the elliptic differential equation of Weirestrass type [10]:

$$\phi_\xi^2(\xi) = \hat{a}_0 + 4\hat{a}_1\phi(\xi) + 6\hat{a}_2\phi^2(\xi) + 4\hat{a}_3\phi^3(\xi) + \hat{a}_4\phi^4(\varsigma), \tag{4}$$

where the coefficients are defined as follows:

- $\hat{a}_0 = 4(a^4a_6 + a^3a_4b + a^2a_2b^2 + aa_0b^3 + 4a^3a_6bc + 3a^2a_4b^2c + 2aa_2b^3c + a_0b^4c + 6a^2a_6b^2c^2 + 3aa_4b^3c^2 + a_2b^4c^2 + 4aa_6b^3c^3 + a_4b^4c^3 + a_6b^4c^4)/a^2$
- $\hat{a}_1 = -(a^3a_4 + 2a^2a_2b + 3aa_0b^2 + 4a^3a_6c + 6a^2a_4bc + 6aa_2b^2c + 4a_0b^3c + 12a^2a_6bc^2 + 9aa_4b^2c^2 + 4a2b^3c^2 + 12aa_6b^2c^3 + 4a_4b^3c^3 + 4a_6b^3c^4)/a^2$
- $\hat{a}_2 = 2(a^2a_2 + 3aa_0b + 3a^2a_4c + 6aa_2bc + 6a_0b^2c + 6a^2a_6c^2 + 9aa_4bc^2 + 6a_2b^2c^2 + 12aa_6bc^3 + 6a_4b^2c^3 + 6a_6b^2c^4)/3a^2$
- $\hat{a}_3 = -(aa_0 + 2aa_2c + 4a_0bc + 3aa_4c^2 + 4a_2bc^2 + 4aa_6c^3 + 4a_4bc^3 + 4a_6bc^4)/a^2$
- $\hat{a}_4 = 4(a_0c + a_2c^2 + a_4c^3 + a_6c^4)/a^2$.

3 The method and the two coupled Korteweg-de Vries equations

In order to determine the travelling waves of the Eqns (1), the following transformation $\xi = x - \omega t$ is needed, were ω is the waves speed. By this substitution, Eqns (1) become:

$$\begin{cases} -\omega u_\xi + \alpha_1 u_\xi + \alpha_2 v_\xi + \alpha_3 u u_\xi + \alpha_4 u_{\xi\xi\xi} = 0 \\ -\omega v_\xi + \beta_1 v_\xi + \beta_2 u_\xi + \beta_3 v v_\xi + \beta_4 v_{\xi\xi\xi} = 0. \end{cases} \tag{5}$$

We seek the following solution of the given system by the expansions [9]:

$$\begin{cases} u(\xi) = \sum_{j=0}^{4} u_j p^j(\xi) \\ v(\xi) = \sum_{j=0}^{4} v_j p^j(\xi) \end{cases} \tag{6}$$

where u_j, v_j are all constant and $p(\xi)$ satisfies the Eqn. (2). Substituting Eqns (6) into Eqns (5) and considering Eqn. (2) and its consequences, from Eqns (5) we obtain two polynomials in $p(\xi)$. Setting each coefficient of the polynomials equal to zero, we have equations for $a_0, \ldots, a_6, a, b, c, u_j$ and v_j. Solving these algebraic equations, we obtain

$$\begin{cases} u_1 = v_1 = u_3 = v_3 = 0, \quad a_0 = \dfrac{4a_2a_4a_6 - a_4^3}{8a_6^2} \\ u_4 = -\dfrac{48a_6\alpha_4}{\alpha_3}, \quad v_4 = -\dfrac{48a_6\beta_4}{\beta_3} \\ u_2 = -\dfrac{24a_4\alpha_4}{\alpha_3}, \quad v_2 = -\dfrac{24a_4\beta_4}{\beta_3} \\ u_0 = \dfrac{3a_4^2\alpha_4^2\beta_3 - a_6(\alpha_2\alpha_3\beta_4 + \alpha_4\beta_3(\alpha_1 + 16a_2\alpha_4 - \omega))}{a_6\alpha_3\alpha_4\beta_3} \\ v_0 = \dfrac{3a_4^2\alpha_3\beta_4^2 - a_6(\alpha_4\beta_2\beta_3 + \alpha_3\beta_4(\beta_1 + 16a_2\beta_4 - \omega))}{a_6\alpha_3\beta_3\beta_4}. \end{cases} \tag{7}$$

Using the values given by the Eqns (7), the substitution (3) and the corresponding solution of the Weirestrass Eqn. (2) we obtain

$$\begin{aligned} u(x,t) = {} & \frac{2}{a_6\alpha_3\alpha_4\beta_3}(3a_4^2 + 4a_4a_6c + 8a_6(a_6c^2 - a_2) \\ & - \sqrt{5a_4^2 - 16a_2a_6}(a_4 + 4a_6c))(54a_4^6\alpha_4^2\beta_3 - 4a_2^2a_6^3(25\alpha_2\alpha_3\beta_4 \\ & + \alpha_4\beta_3(25\alpha_1 + 352a_2\alpha_4 - 25\omega)) + 60a_2a_4^2a_6^2(\alpha_2\alpha_3\beta_4 \\ & + \alpha_4\beta_3(\alpha_1 + 25a_2\alpha_4 - \omega)) - 9a_4^4a_6(\alpha_2\alpha_3\beta_4 \\ & + \alpha_4\beta_3(\alpha_1 + 56a_2\alpha_4 - \omega)) + 12a_6\wp(x - \omega t; g_2, g_3) \\ & \times (-18a_4^4\alpha_4^2\beta_3 - 2a_2a_6^2(5\alpha_2\alpha_3\beta_4 + \alpha_4\beta_3(5\alpha_1 + 128a_2\alpha_4 - 5\omega)) \\ & + 3a_4^2a_6(\alpha_2\alpha_3\beta_4 + \alpha_4\beta_3(\alpha_1 + 46a_2\alpha_4 - \omega)) \\ & - 3a_6(9a_4^2\alpha_4^2\beta_3 + a_6(\alpha_2\alpha_3\beta_4 + \alpha_4\beta_3(\alpha_1 - 32a_2\alpha_4 - \omega))) \\ & \times \wp(x - \omega t; g_2, g_3)))(\sqrt{5a_4^2 - 16a_2a_6} - (a_4 + 4a_6c))^{-2} \\ & \times (10a_2a_6 - 3a_4^2 + 6a_6\wp(x - \omega t; g_2, g_3))^{-2} \end{aligned}$$

and so

$$\begin{aligned} v(x,t) = {} & \frac{2}{a_6\beta_3\beta_4\alpha_3}(3a_4^2 + 4a_4a_6c + 8a_6(a_6c^2 - a_2) \\ & - \sqrt{5a_4^2 - 16a_2a_6}(a_4 + 4a_6c))(54a_4^6\beta_4^2\alpha_3 - 4a_2^2a_6^3(25\beta_2\beta_3\alpha_4 \end{aligned}$$

$$
\begin{aligned}
&+ \beta_4\alpha_3(25\beta_1 + 352a_2\beta_4 - 25\omega)) + 60a_2a_4^2a_6^2(\beta_2\beta_3\alpha_4\\
&+ \beta_4\alpha_3(\beta_1 + 25a_2\beta_4 - \omega)) - 9a_4^4a_6(\beta_2\beta_3\alpha_4\\
&+ \beta_4\alpha_3(\beta_1 + 56a_2\beta_4 - \omega)) + 12a_6\wp(x - \omega t; g_2, g_3)\\
&\times (-18a_4^4\beta_4^2\alpha_3 - 2a_2a_6^2(5\beta_2\beta_3\alpha_4\\
&+ \beta_4\alpha_3(5\beta_1 + 128a_2\beta_4 - 5\omega)) + 3a_4^2a_6(\beta_2\beta_3\alpha_4\\
&+ \beta_4\alpha_3(\beta_1 + 46a_2\beta_4 - \omega)) - 3a_6(9a_4^2\beta_4^2\alpha_3\\
&+ a_6(\beta_2\beta_3\alpha_4 + \beta_4\alpha_3(\beta_1 - 32a_2\beta_4 - \omega)))\\
&\times \wp(x - \omega t; g_2, g_3))(\sqrt{5a_4^2 - 16a_2a_6} - (a_4 + 4a_6c))^{-2}\\
&\times (10a_2a_6 - 3a_4^2 + 6a_6\wp(x - \omega t; g_2, g_3))^{-2}
\end{aligned}
$$

where

$$
g_2 = \frac{4a_2^2}{3} + \frac{a_4^4}{2a_6^2} - \frac{2a_2a_4^2}{a_6}
$$

$$
g_2 = -\frac{(8a_2a_6 - 3a_4^2)(24a_2a_4^2a_6 + 16a_2^2a_6^2 - 9a_4^4)}{432a_6^3}.
$$

4 Conclusion

In this paper, we obtained, using a reducible hyperelliptic equation, travelling waves for two coupled Korteweg-de Vries equations. Of course, the above method can be applied to other nonlinear equations too.

References

[1] J. A. Gear, R. Grimshaw, Stud. Appl, Math. 70, (1984) 235.
[2] J. A. Gear, Stud. Appl, Math. **72**, (1985) 95.
[3] R. Grimshaw, G. Gottwald, *Models for Instability in Geophysical Flows* Proceedings of the IUTAM Symposium, Kluwer, (2000) 153.
[4] L. Huibin, W. Kelin, J. Phys. A 23 (1990) 4097.
[5] W. Malfliet, Am. J. Phys. 60 (1992) 650.
[6] W. X. Ma, Int. J. Non–Linear Mech. 31 (1996) 329.
[7] Y. T. Gao, B. Tian, Comput. Math. Appl. 33 (1997) 115.
[8] Z. Y. Yan, J. Phys. Lett. A 552 (1999) 291.
[9] T. Brugarino, M. Sciacca *Exact Travelling Wave Solutions of Nonlinear Equations by Using the Auxiliary Equation Method* preprint Dip. Metodi e Modelli Matematici Palermo (2007)
[10] E. T. Whittaker, G. N. Watson, *A Course of Modern Analysis* Cambridge U.P. (1973).

Author Index

This page intentionally left blank

This page intentionally left blank